

RD-A162 484

LONG-TERM CORROSION FATIGUE OF WELDED MARINE STEELS(U)

1/3

SOUTHWEST RESEARCH INST SAN ANTONIO TX

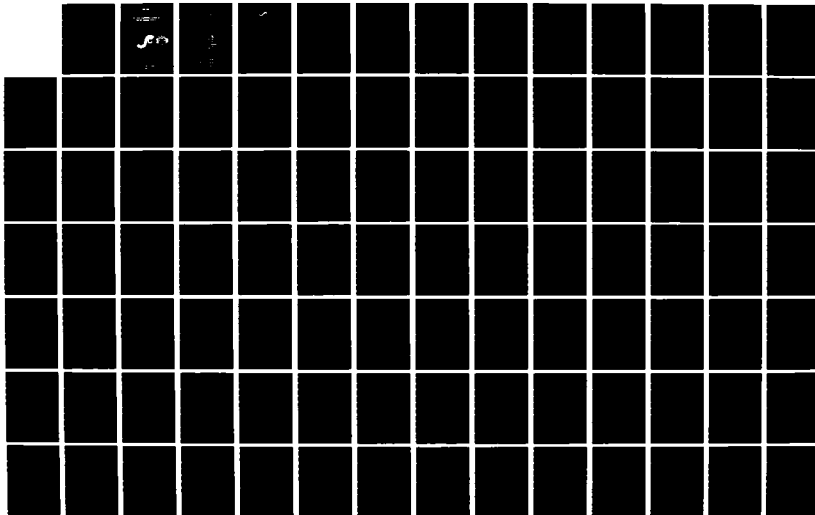
O H BURNSIDE ET AL. 1984 SR-1276 SSC-326

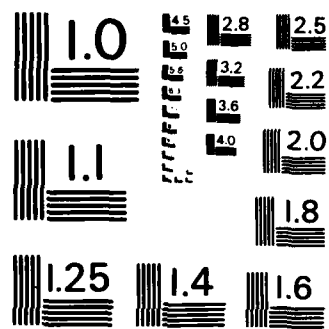
UNCLASSIFIED

DTCG23-80-C-20028

F/G 11/6

NL





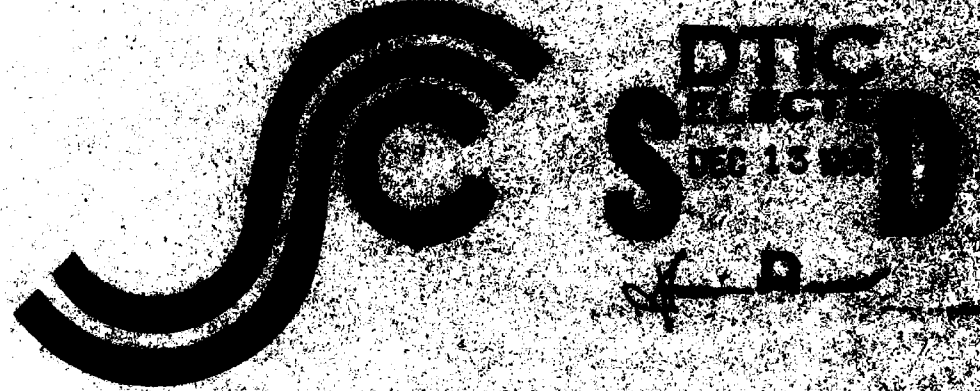
MICROCOPY RESOLUTION TEST CHART
NATIONAL BUREAU OF STANDARDS - 1963 - A

1

SSC-326

**LONG-TERM CORROSION FATIGUE OF
WELDED MARINE STEELS**

AD-A162 484



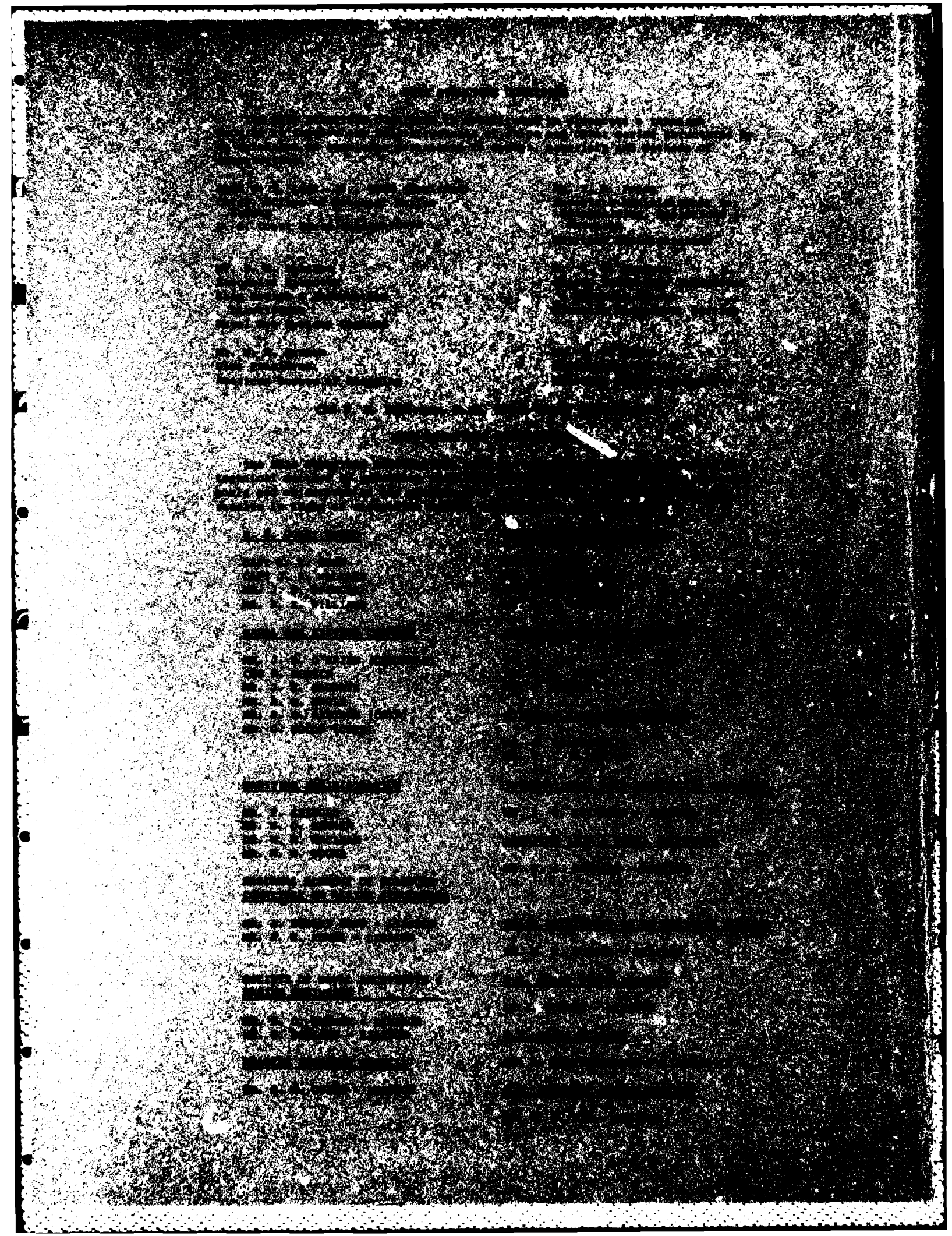
This document has been approved
for public release and sale; its
distribution is unlimited

JMC FILE COPY

SHIP STRUCTURE COMMITTEE

1984

85 12 13 028



Member Agencies:

*United States Coast Guard
Naval Sea Systems Command
Maritime Administration
American Bureau of Shipping
Military Sealift Command
Minerals Management Service*



Address Correspondence to:

*Secretary, Ship Structure Committee
U.S. Coast Guard Headquarters, (G-M/TP 13)
Washington, D.C. 20593
(202) 426-2197*

An Interagency Advisory Committee
Dedicated to the Improvement of Marine Structures SR-1276

This report represents a first look at corrosion fatigue by the Ship Structure Committee in order to assess those future directions which would be most fruitful for further study. In arriving at this objective, the investigators approached corrosion fatigue from both the deterministic and the probabilistic viewpoints.

Deterministically, a crack initiation and propagation model was pursued for both high and low-cycle fatigue. Probabilistically the model was used to assess the importance of numerous variables in the long-term analysis of corrosion fatigue.

Clyde A. Lusk Jr.
CLYDE A. LUSK, Jr.
Rear Admiral, U.S. Coast Guard
Chairman, Ship Structure Committee

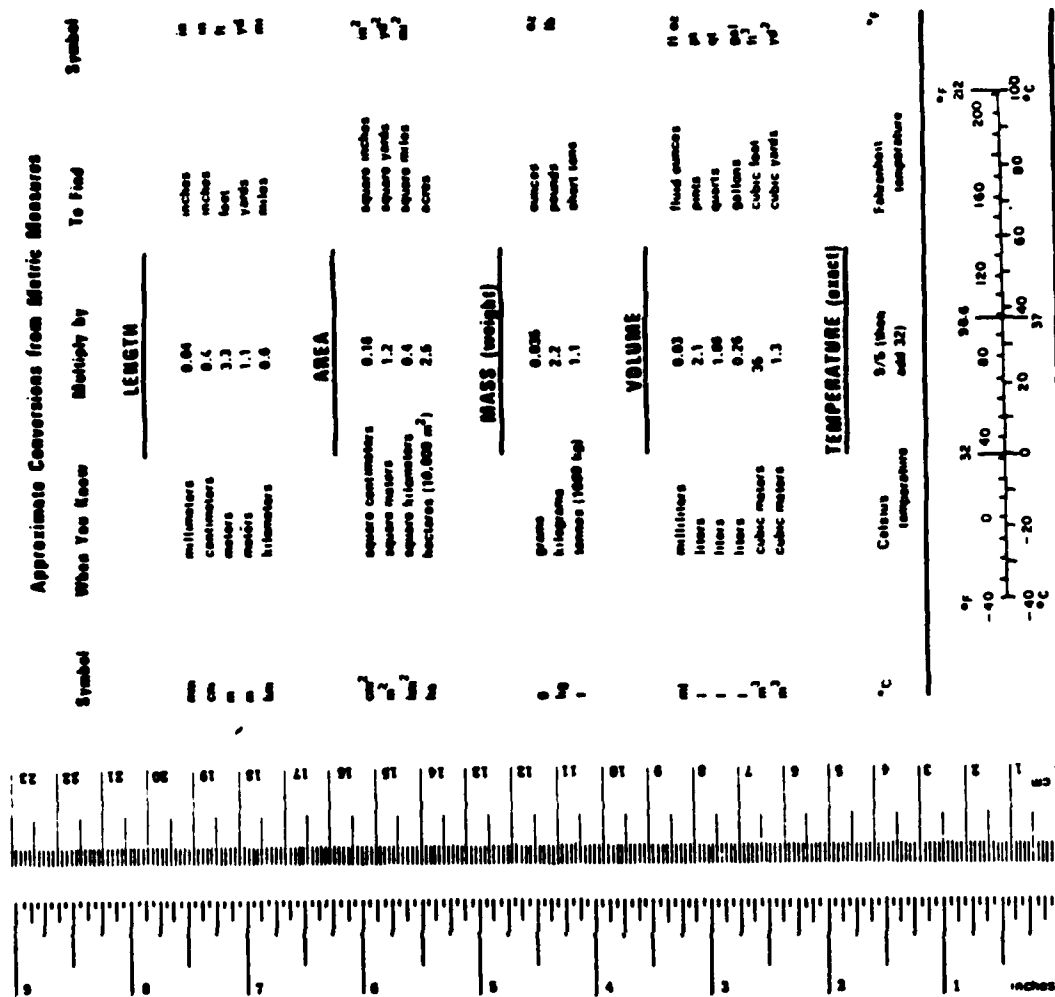
Technical Report Documentation Page

1. Report No. SSC-326	2. Government Accession No. <i>A-162484</i>	3. Recipient's Catalog No.	
4. Title and Subtitle LONG-TERM CORROSION FATIGUE OF WELDED MARINE STEELS		5. Report Date 1984	
7. Author(s) O. H. Burnside, S. J. Hudak, Jr., E. Oelkers, K. Chan, and R. I. Dexter		6. Performing Organization Code Ship Structure Committee	
9. Performing Organization Name and Address Southwest Research Institute P.O. Drawer 28510 San Antonio, Texas 78284		8. Performing Organization Report No. SR-1276	
12. Sponsoring Agency Name and Address U.S. Coast Guard Office of Merchant Marine Safety Washington, D.C. 20593		10. Work Unit No. (TRAVIS) 11. Contract or Grant No. DTCG23-80-C-20028	
		13. Type of Report and Period Covered Final	
15. Supplementary Notes The USCG acts as the contracting office for the Ship Structure Committee		14. Sponsoring Agency Code G-M	
16. Abstract <p>> Corrosion fatigue in welded marine steels and the effects of loading, environmental, material, and fabrication variables on fatigue resistance were reviewed. Mathematical models were formulated which quantified the important environmental and loading variables on fatigue crack initiation and propagation in the high and low cycle life regimes. The initiation model utilized the local stress-strain approach with a modified Neuber rule. The propagation model was based upon fracture mechanics with the stress intensity factor computed using an influence function approach and the uncracked stress state at the toe of the weld.</p> <p>It was concluded that crack initiation constitutes only a small portion of the fatigue life in a welded joint in the low-cycle regime. The analytical predictions for crack growth life generally gave good correlation with experiments on welded planar and tubular joints at low load (R) ratios in air and seawater environments.</p> <p>A probabilistic analysis was also undertaken to quantify the important variables in the high-cycle corrosion fatigue process. Using the fracture mechanics model, the analysis indicated that the single most important variable for reliability predictions is associated with the applied loadings. <i>Keywords:</i></p> <p><i>fatigue, corrosion, prediction,</i></p>			
17. Key Words Fatigue Corrosion Welding, Marine Steels, Marine Environment,	Fatigue Crack Init. >Fatigue Crack Prop. Fracture Mechanics Tubular Joints Long-Term Fatigue Prediction.	18. Distribution Statement This document is available to the public through the National Technical Information Service, Springfield, Virginia 22161	
19. Security Classif. (of this report) UNCLASSIFIED	20. Security Classif. (of this page) UNCLASSIFIED	21. No. of Pages 420	22. Price

METRIC CONVENTION FACTORS

Approximate Conversions to Metric Measures			
What You Know	Simply by	To Find	
Symbol			
		<u>LENGTH</u>	
inches	2.5	centimeters	
feet	30	meters	
yards	0.9	kilometers	
miles	1.6		
		<u>AREA</u>	
square inches	0.06	square centimeters	
square feet	0.09	square meters	
square yards	0.84	square kilometers	
square miles	0.4		
		<u>MASS (weight)</u>	
ounces	28	grams	
ounces	0.035	kilograms	
ounces	0.9		
ounces (avoirdupois)			
		<u>VOLUME</u>	
teaspoons	5	milliliters	
tablespoons	15	milliliters	
Fluid ounces	30	liters	
cup	0.24	liters	
pints	0.47	liters	
quarts	0.95	liters	
gallons	2.0	cubic meters	
cubic feet	0.03	cubic meters	
cubic yards	0.76		
		<u>TEMPERATURE (exact)</u>	
Fahrenheit	5/9 (lower multiplier)	Celsius	
temperature	32	temperature	

1993-1994. The 1993-1994 convention and major historical leaders are held here. Page 205.



ACKNOWLEDGEMENTS

The authors wish to express their appreciation to those individuals who contributed to the preparation of this report: C. W. Dean, editorial and typing; V. J. Hernandez, drafting; R. H. Rivas, word processing; and D. D. Skerhut, J. W. Cardinal, and J. P. Buckingham, computer programming.

The authors also wish to acknowledge The Committee on Marine Structures Program Advisory Committee: Mr. P. W. Marshall, Chairman; Professor P. Wirsching, member; and Dr. R. D. Glasfeld, member; for their motivation and suggestions.

Accesion For	
NTIS	CRA&I
DTIC	TAB
Unannounced	
Justification	
By _____	
Distribution /	
Availability Codes	
Dist	Avail and/or Special
A-1	



TABLE OF CONTENTS

	<u>Page</u>
LIST OF TABLES	xi
LIST OF FIGURES	xiii
LIST OF PRINCIPAL SYMBOLS	xxv
1.0 INTRODUCTION	1.1
1.1 Problem Statement	1.1
1.2 Historical Perspective and Concerns	1.1
1.3 Philosophy of Program's Approach	1.6
CHAPTER 1.0 REFERENCES	1.8
2.0 CHARACTERIZATION OF APPLIED LOADS	2.1
2.1 General	2.1
2.2 Load Classification	2.2
2.3 Wind and Current Loads	2.3
2.4 Wave Loads	2.4
2.4.1 Prediction of Structural Response to Waves	2.7
2.4.2 Forecasting the Stress Range History	2.9
2.5 Consideration of Corrosion Fatigue Testing	2.17
2.6 Summary	2.21
CHAPTER 2.0 REFERENCES	2.23
3.0 EFFECT OF LOADING VARIABLES ON CORROSION FATIGUE RESISTANCE	3.1
3.1 Introduction	3.1
3.2 Effect of Stress and Stress Intensity Factor	3.2
3.3 Effect of Mean Stress or Load Ratio	3.5
3.4 Effect of Cyclic Frequency and Waveform	3.8
3.5 Effect of Transient Crack Growth Rates	3.12
3.6 Effect of Crack Size—"The Small Crack Problem"	3.13
3.7 Mathematical Representation of Crack Growth Rate Data	3.15
3.8 Selection of Steady-State $da/dN (\Delta K)$ Relations For Various Loading and Environmental Conditions	3.18
CHAPTER 3.0 REFERENCES	3.25
4.0 EFFECT OF ENVIRONMENTAL VARIABLES ON CORROSION FATIGUE RESISTANCE	4.1
4.1 Effect of Temperature on Corrosion Fatigue Resistance	4.1
4.2 Effect of Solution Chemistry on Corrosion Fatigue Resistance	4.5
4.3 Effect of Electrode Potential on Corrosion Fatigue Resistance	4.9
CHAPTER 4.0 REFERENCES	4.13

TABLE OF CONTENTS (Continued)

	<u>Page</u>
5.0 EFFECT OF MATERIALS AND FABRICATION VARIABLES ON FATIGUE RESISTANCE	5.1
5.1 Materials	5.1
5.1.1 General	5.1
5.1.2 Composition	5.1
5.1.3 Strength	5.2
5.1.4 Microstructure	5.3
5.2 Fabrication	5.3
5.2.1 Historical Perspective	5.3
5.2.2 Geometry	5.4
5.2.3 Thickness Effects	5.9
5.2.4 Fatigue Improvement Techniques	5.12
CHAPTER 5.0 REFERENCES	5.19
6.0 PREDICTION METHODOLOGIES FOR FATIGUE	6.1
6.1 Introduction	6.1
6.2 Classical S-N Approach	6.1
6.3 Fracture Mechanics Approach to Crack Initiation	6.3
6.4 Local Strain Approach to Crack Initiation	6.3
6.5 Application of Local Strain Approach to Welded Joints	6.6
6.5.1 Introduction	6.6
6.5.2 Stress Concentrations at Crack Initiation Sites	6.6
6.5.3 Strain-Life to Crack Initiation	6.9
6.5.4 Cyclic Stress-Strain Conversion	6.12
6.5.5 Notch Strain Analysis	6.13
6.5.6 Cycles to Crack Initiation Calculation	6.14
6.6 Fracture Mechanics Approach to Crack Growth	6.14
6.6.1 Introduction	6.14
6.6.2 Formulation of the Stress Intensity Factor	6.17
6.6.3 Extension of the Stress Intensity Factor to Two Dimensions	6.21
6.6.4 Stress Distribution at the Toe of a Welded Joint	6.24
6.6.5 Crack Propagation Calculation Strategies	6.25
CHAPTER 6.0 REFERENCES	6.30
7.0 ANALYTICAL AND EXPERIMENTAL STUDIES RELATED TO FATIGUE LIFE IN WELDED JOINTS	7.1
7.1 Introduction	7.1
7.2 Crack Initiation and Propagation of Welded Joints in Air	7.1
7.2.1 Crack Initiation	7.1
7.2.2 Crack Propagation	7.5
7.3 Crack Initiation and Propagation of Welded Joints in Seawater	7.8
7.3.1 Crack Initiation	7.8
7.3.2 Crack Propagation	7.10

TABLE OF CONTENTS (Continued)

	<u>Page</u>
7.4 Effect of Seawater on Fatigue Life	7.12
7.5 Sensitivity Studies	7.12
7.5.1 Stress Distribution and Stress Concentration Factor	7.12
7.5.2 Effect of Weld Toe Geometry on Stress Intensity Factor	7.13
7.5.3 Initial Crack Depth	7.14
7.5.4 Final Crack Depth	7.17
7.5.5 Sensitivity of Life to One- and Two-Dimensional Fracture Models	7.18
7.6 Comparison of Experimental and Analytical Stress Intensity Factor Expressions for Tubular Joints	7.20
7.7 Closing Remarks on Fatigue Life Predictions	7.23
CHAPTER 7.0 REFERENCES	7.25
 8.0 PROBABILISTIC METHODOLOGY APPLIED TO THE CORROSION FATIGUE PROBLEMS	8.1
8.1 Introduction	8.1
8.2 Distribution of the Input Variables	8.2
8.2.1 Distribution of the Initial Flaw Size	8.5
8.2.2 Distribution of Weld Toe Radius and Parameters Y and K _t	8.6
8.2.3 Distribution of Crack Growth Parameters C, A ₁ , and A ₂	8.8
8.2.4 Distribution of Number of Load Cycles in Service Life	8.9
8.2.5 Distribution of Stress Range and Once-in-Lifetime Stress	8.10
8.3 Linear S-N Model, Sensitivity, and Probabilistic Analysis	8.11
8.3.1 Sensitivity with Linear Model	8.13
8.3.2 Probabilistic Analysis with the Linear Model	8.14
8.4 Three-Component Model Approximate Analytical Expression	8.17
8.4.1 Three-Component Model Sensitivity Analysis	8.23
8.4.2 Three-Component Model Probabilistic Analysis	8.23
8.5 Summary and Conclusions	8.26
CHAPTER 8.0 REFERENCES	8.27
 9.0 SUMMARY, CONCLUSIONS, AND RECOMMENDATIONS	9.1
9.1 Summary	9.1
9.2 Conclusions and Recommendations	9.2
9.3 Recommendations for Research Plans	9.7
 APPENDIX A: GLOSSARY OF TERMS IN THE FIELDS OF CORROSION, FATIGUE, AND WELDING	A.1
APPENDIX B: ECSC OFFSHORE TUBULAR JOINT TEST DATA SHEET	B.1
APPENDIX C: FIRST-ORDER, SECOND-MOMENT EXAMPLE CALCULATION	C.1
APPENDIX D: THREE-COMPONENT HIGH-CYCLE MODEL PARTIAL DERIVATIVES	D.1

LIST OF TABLES

<u>Table</u>		<u>Page</u>
1.1	Classification of Typical Marine Environments, From [1.2]	1.9
1.2	Corrosion Factors for Carbon Steel Immersed in Seawater, From [1.2]	1.10
1.3	Summary of Major Variables Influencing the Corrosion Fatigue Crack Initiation Behavior of Carbon Steels in Seawater-Type Environments, From [1.8]	1.11
2.1	Influence of Various Loadings on Fatigue and Fast Fracture in Marine Structures	2.26
3.1	Material and Data Sources for ΔK_{th} Results Given in Figure 3.4	3.31
3.2	Summary of Conditions for Crack Growth Data	3.32
3.3	Constants in Three-Component Crack Growth Law	3.34
4.1	Potential Influence of Temperature on Corrosion Fatigue Crack Growth Rates	4.16
4.2	Guidance on Minimum Design Current Densities (mA/m^2) for Cathodic Protection	4.17
5.1	Structural Steel Plates and Shapes (From [5.1])	5.22
5.2	Structural Steel Pipe (From [5.1])	5.22
5.3	European Steels Used in Corrosion Studies	5.23
5.4	Results of Regression Analysis on Tubular Joint Fatigue Tests (From [5.23])	5.23
6.1	Advantages and Disadvantages of Fatigue Analysis Approaches	6.33
6.2	Elastic Concentration Coefficients for Various Weldments, From [6.14]	6.35
6.3	Mechanical Properties of Base, Weld, and Heat-Affected Materials for ASTM Specification A36 Steel Welds, From [6.13]	6.36

LIST OF TABLES (Continued)

<u>Table</u>		<u>Page</u>
6.4	Cyclic and Fatigue Properties of Base, Weld, and Heat-Affected Materials for ASTM Specification A36 Steel Welds, From [6.13]	6.36
6.5	σ_f , s_f , b, and c for Several Materials, From [6.13]	6.37
6.6	Mechanical Properties of Base, Weld, and Heat-Affected Materials for ASTM Specification A514 Welds, From [6.13]	6.38
6.7	Cyclic and Fatigue Properties of Base, Weld, and Heat-Affected Materials for ASTM Specification A514 Welds, From [6.13]	6.38
7.1	Chemical Compositions and Mechanical Properties of Selected Steels	7.28
7.2	Cyclic Strain-Strain and Strain Life Properties of Selected Mild Steels	7.29
7.3	Cyclic-Strain and Strain Life Properties of Selected High-Strength Steels	7.30
7.4	Comparison of One- and Two-Dimensional Crack Propagation Analyses--T-Joint, A36 HAZ Material, Asymptotic Growth Law	7.31
8.1	Random Variable Summary	8.28
8.2	A ₁ and A ₂ Distributions	8.28
8.3	Stress Range Uncertainty Factors	8.29
8.4	Linear Model Sensitivities	8.29
8.5	Three-Component Model One-At-A-Time Sensitivities (Without Corrosion Effects, High-Cycle Model)	8.30
8.6	Three-Component Model Variance of Logarithm of N	8.30
9.1	Primary Loading, Environmental, and Materials Variables Affecting Corrosion Fatigue Crack Growth Resistance in Offshore Structures	9.12

LIST OF FIGURES

<u>Figure</u>		<u>Page</u>
1.1	Typical Ocean Stress Spectra, From [1.1]	1.12
1.2	Corrosion Zones on Fixed Offshore Steel Structures, From [1.3]	1.12
1.3	Comparative Effects of Environmental Variations on Fatigue Crack Growth Rates ($R \leq 0.1$), From [1.4, 1.5]	1.13
1.4	Oceanographic Data Taken in the Pacific Ocean at a Site West of Port Hueneme, California, From [1.2]	1.13
1.5	Representation of Variables Which Influence Fatigue, From [1.10]	1.14
2.1	Periodic Wave Theories Providing Best Fit to Dynamic Condition	2.27
2.2	C_I and C_D as Functions of R_e and N_{KC} , Appraised from the Literature for Smooth, Vertical, Surface-Piercing Cylinders	2.27
2.3	Transfer Function for Stress at a Critical Location in the Structure	2.28
2.4	Conceptual Representation of Sea Energy Spectrum	2.29
2.5	Response Spectrum for Stress at a Critical Location in the Structure	2.30
2.6	Wide-Band Stress History Showing Interruption of Large Stress Cycle	2.30
2.7	Narrow-Band Stress History	2.31
2.8	Wave-Scatter Diagram	2.31
3.1	Relation Between Fatigue Cycles Corresponding to Crack Initiation (N_i), Crack Propagation (N_p), and Total Life to Failure (N_f) of Smooth, Uncracked Specimens Tested at Various Stress Levels (S)	3.35
3.2	S-N Data on C-Mn Steel Illustrating Typical Influence of Saltwater Environment on Corrosion Fatigue Resistance (From [3.2])	3.36
3.3	Schematic of Basic Types of Fatigue Crack Growth Behavior (From [3.3])	3.37

LIST OF FIGURES (Continued)

<u>Figure</u>		<u>Page</u>
3.4	Effect of Load Ratio on ΔK_{th} for a Variety of Structural and Low-Alloy Steels Exposed to Laboratory Air Environments	3.38
3.5	Influence of Load Ratio on the Corrosion Fatigue Crack Growth Rates in API X-70 Linepipe Steel in 3.5% NaCl (From [3.30])	3.39
3.6	Fatigue Crack Growth Rate Data on BS 4360 Grade 50D in Laboratory Air at Various Load Ratios	3.40
3.7	Influence of Load Ratio on the Region II Fatigue Crack Growth Rate Data on BS 4360 Grade 50D Steel in Seawater (From [3.9])	3.41
3.8	Effect of Cyclic Frequency on Corrosion Fatigue Strength of a Medium Carbon Steel in a 1% NaCl Solution (From [3.36])	3.42
3.9	Effect of Cyclic Frequency on the Fatigue Crack Growth Rate in an X-65 Linepipe Steel Under Either Cathodic Polarization or Freely Corroding Conditions (From [3.37])	3.43
3.10	Effect of Cyclic Frequency on Fatigue Crack Growth Rate in Several HY-Series Steels in Salt Water	3.44
3.11	Effect of Cyclic Frequency on Fatigue Crack Growth Rates in Various Structural and Alloy Steels in Salt Water	3.45
3.12	Effect of Cyclic Frequency on Fatigue Crack Growth Rate in a Low Carbon Steel (From [3.46])	3.46
3.13	Corrosion Fatigue Crack Growth Rate Data for a 12NI Steel in 3% NaCl Under Various Cyclic Loading Waveforms (From [3.47])	3.47
3.14	Effect of Cyclic Waveform and Frequency on Fatigue Crack Growth Rates in a Ni-Cr-Mo Alloy Steel Exposed to 3.5% NaCl (From [3.47])	3.48
3.15	Dependence of Static-Load Crack Growth Rates on Initially Applied Stress Intensity Factor, K_I (From [3.54])	3.49
3.16	Dependence of Fatigue Crack Growth Rates on Initially Applied Stress Intensity Factor Range, ΔK_I (From [3.55])	3.49
3.17	Effect of Test Interruption Crack Growth Rate Data (From [3.56])	3.50
3.18	Fatigue Crack Growth Rate Response Resulting From a Change in Cyclic Loading Frequency (From [3.56])	3.50

LIST OF FIGURES (Continued)

<u>Figure</u>		<u>Page</u>
3.19	Static Load Crack Growth Rates Under Constant Stress Intensity Factor Conditions Showing Transient and Steady-State Behavior (From [3.5])	3.51
3.20	Use of the Parameter δ_0 to Relate the Smooth Bar Fatigue Strength ($\Delta\sigma_e$) and the Threshold Stress Intensity for Crack Growth (ΔK_{th}) (From [3.65])	3.51
3.21	Comparison of Crack Growth Kinetics for Small and Large Cracks in Both Air and 3% NaCl (From [3.66])	3.52
3.22	Schematic Representation of Asymptotic Crack Growth Rate Equation	3.53
3.23	Schematic Representation of Three Component Crack Growth Rate Equation	3.54
3.24	Crack Growth Data, Air Environment, Low R	3.55
3.25	Crack Growth Data, Air Environment, High R	3.56
3.26	Crack Growth Data, Seawater, Free Corrosion Potential, Low R	3.57
3.27	Crack Growth Data, Seawater, Free Corrosion Potential, High R	3.58
3.28	Crack Growth Data, Seawater, Cathodic Polarization, Low R	3.59
3.29	Crack Growth Data, Seawater, Cathodic Polarization, High R	3.60
3.30	Summary of Three-Component Crack Growth Equations	3.61
4.1	Values of Selected Seawater Parameters Measured Over a One-Year Period at the Marine Materials and Corrosion Laboratory, Florida Atlantic University at Boca Raton on the Atlantic Ocean [4.1]	4.18
4.2	Effect of Temperature on Corrosion Fatigue Behavior of Notched Specimens of Mild Steel [4.3]	4.19
4.3	Comparison of Fatigue Crack Growth Rate in 3-1/2% Aqueous NaCl and Air at 75°F and 30°F [4.6]	4.20
4.4	Influence of Temperature (293 K Silicone Oil and 77 K Liquid Nitrogen) on Fatigue Crack Growth Rates in Mild Steel, 31 kHz R = -1	4.21

LIST OF FIGURES (Continued)

<u>Figure</u>		<u>Page</u>
4.5	Rate of Fatigue-Crack Growth as a Function of Temperature in Mild Steel Exposed to 3.5% NaCl [4.9]	4.22
4.6	Crack-Growth-Rate Data for HY 13C Steel in Flowing Natural Seawater and in Flowing Aqueous 3.5% NaCl Solution Under Freely Corroding Conditions (~-0.665 V VS Ag/AgCl) and Under a Cathodic Potential of -1.05 V VS Ag/AgCl) [4.12]	4.23
4.7	Fatigue Crack Propagation Data for Specimens at an Electrochemical Potential of -1.0 V (Ag/AgCl) in Several Electrolytes [4.8]	4.24
4.8	The Effect of Dissolved Oxygen on the Fatigue Behavior of 1035 Steel in 5% NaCl Solution [4.14]	4.25
4.9	Fatigue Crack Propagation Data for Specimens Freely Corroding in Seawater as a Function of Oxygen Concentration	4.26
4.10	Fatigue Crack Propagation Data for Specimens at an Electrode Potential of -0.8 V in Seawater as a Function of Oxygen Concentration	4.27
4.11	Fatigue Data for Smooth Carbon Steel Specimens in a 3% NaCl-Distilled Water Solution as a Function of Potential [4.15]	4.28
4.12	Fatigue Data for Carbon Steel in Seawater as a Function of Specimen Potential [4.22]	4.28
4.13	Effect of Potential on the Fatigue Crack Propagation Rates for Steel Specimens Stressed at 0.1 Hz in Seawater at 20°C, $\Delta K = 20$ to $40 \text{ MN m}^{-3/2}$, Stress Ratio: $R \leq 0.1$ [4.8]	4.29
5.1	Effect of Thickness, Orientation, and Quality on Fatigue Crack Growth in BS 4360, Grade 50D, Steel, From [5.3]	5.24
5.2	Corrosion-Fatigue Crack-Growth Data, $\sigma_y = 130$ ksi, From [5.4]	5.25
5.3	Corrosion-Fatigue Crack-Growth Data, $\sigma_y = 180$ ksi, From [5.4]	5.26
5.4	Fractographic Features in 835M30 Steel, From [5.3]	5.27
5.5	Fracture Through the HY130 Weldment of the Specimen Tested at $R = 0.9$, Cathodic Potential and 0.1 Hz, in 3.5% NaCl Solution, From [5.5]	5.28

LIST OF FIGURES (Continued)

<u>Figure</u>		<u>Page</u>
5.6	Fatigue Crack-Growth Rates at $R = 0.05$ in 3.5% NaCl Solution at Cathodic Potential and 0.1 Hz, Weld Metal (Points), Base Metal (Dash and Dot Line), and in Air, Weld Metal (Dashed Line), Base Metal (Solid Line), From [5.5]	5.29
5.7	Fatigue Crack-Growth Rates at $R = 0.7$ in 3.5% NaCl Solution at Cathodic Potential and 0.1 Hz, Weld Metal (Points), Base Metal (Dash and Dot Line), and in Air, Weld Metal (Dashed Line), Base Metal (Solid Line), From [5.5]	5.29
5.8	Idealized Corrosion Fatigue Behavior and Associated Fracture Modes, From [5.3]	5.30
5.9	Examples of Simple Tubular Node Joint Geometrics, From [5.15]	5.31
5.10	Models of Brace/Chord Intersection and Corresponding Peak Stresses: (a) Steel Model, (b) Acrylic Model, (c) Thin Shell FEM, and (d) Photoelastic Model, From [5.21]	5.32
5.11	Fatigue Curves, From [5.1]	5.33
5.12	Locations of Strain Gauges for Linear Extrapolation to Weld Toe to Determine Strain Concentration Factor, From [5.24]	5.34
5.13	Results for Transverse Joints Showing Influence of Plate Thickness, Under Bending Loading, Air Environment, From [5.25]	5.35
5.14	Dutch Test Results for T-Joints with Axial Loading or In-Plane Bending Loads Applied to the Brace, From [5.15]	5.36
5.15	Comparison of Mean Experimental S-N Curves, From [5.26]	5.37
5.16	ECSC-Program Test Results Vis A Vis API and AWS Design S-N Curves, From [5.27]	5.38
5.17	Grinding of Weld Toe, From [5.15]	5.39
5.18	Cross-Section of Weld: (a) Location of TIG Dressing, (b) Modified TIG Dressing; d = Distance Between First and Second TIG Runs, From [5.33]	5.39
5.19	Results for Transverse Joints Showing Influence of Improvement Techniques Under: (a) Axial Loading, (b) Bending Loading, From [5.25]	5.40
5.20	Comparison Between Fatigue Test Results, From [5.33]	5.41

LIST OF FIGURES (Continued)

<u>Figure</u>	<u>Page</u>
5.21 Fatigue Behavior of 70-mm T-Shaped Specimens (As Welded and Stress Relieved) in Air at the Stress Ratios R = 0.1 and R = -1, From [5.36]	5.42
5.22 Fatigue Behavior of 70-mm T-Shaped Specimens (As Welded and Stress Relieved) in Seawater at the Stress Ratios R = 0.1 and R = -1, From [5.36]	5.42
5.23 Fatigue Behavior of 40-mm T-Shaped Specimens (Grinding and Plasma Dressing) in Air and Seawater at the Stress Ratio R = 0.1, From [5.36]	5.43
5.24 Results for Transverse Joints, AW and Disc Ground, Stress Ratio = 0, From [5.37]	5.43
5.25 Results of Japanese Tests in Air and Seawater, From [5.38]	5.44
6.1 S-N Data for a 1018 Steel in Various Environments	6.39
6.2 Mean Stress Data for SAE 4340 Steel, From [6.3]	6.40
6.3 Mean Stress Data for SAE 4340 Steel, From [6.3]	6.41
6.4 Dependence of Fatigue-Crack Initiation of HY-130 Steel on Nominal-Stress Fluctuations for Various Notch Geometries, From [6.4]	6.42
6.5 Correlation of Fatigue-Crack Initiation Life with the Parameter $\Delta K_1 / \sqrt{\rho}$ for HY-130 Steel, From [6.4]	6.42
6.6 Flow Chart of Fatigue Damage Analysis for Crack Initiation	6.43
6.7 Monotonic and Cyclic Stress-Strain Curves for Several Engineering Alloys	6.44
6.8 Strain-Life Curves Showing Total Elastic and Plastic Strain Components, From [6.7]	6.45
6.9 Actual Stress Range Versus Elastic Stress Range for a Hole in a Plate	6.46
6.10 Actual Strain Range Versus Elastic Stress Range for a Hole in a Plate	6.47
6.11 History Dependence of Local Notch Mean Stress and Its Effect on Fatigue Life	6.48

LIST OF FIGURES (Continued)

<u>Figure</u>		<u>Page</u>
6.12	Geometry of the Five Welds Analyzed, From [6.14]	6.49
6.13	Variation of $K_t - 1$ with t/r for the Five Welds of Figure 1, From [6.14]	6.50
6.14	Average Fatigue Notch Sensitivity, From [6.16]	6.51
6.15	Variation of $K_{f\max}$ with Strength Level (S_u) and Consequent Changes in the Material Parameter a , From [6.14]	6.52
6.16	Low-Cycle Fatigue Behavior of Annealed 4340 Steel	6.53
6.17	Strain Controlled Fatigue Behavior on A36 HAZ Metal	6.54
6.18	Actuator Displacement Versus Cycles on 168-mm T-Joint Subjected to Out-of-Plane Bending	6.55
6.19	Schematic Illustration of the Use of Fracture-Mechanics Technology in the Design Against Fatigue Failure, From [6.22]	6.56
6.20	Parametric Representation of Results from Fracture-Mechanics Fatigue Crack Growth Analysis Showing Influence of Applied Stress Range	6.57
6.21	Crack Coordinate System and Modes of Deformation, From [6.29]	6.58
6.22	Elliptical Hole Subjected to a Tension Load	6.59
6.23	Comparison of Stress Intensity Values for $(h/d) = 0.05, 0.25,$ and 0.5	6.60
6.24	Comparison of Stress Intensity Values for $(h/d) = 1.0, 4.0,$ and 100.0	6.61
6.25	Representations of One- and Two-Dimensional Cracks at the Toe of a Welded Planar T-Joint	6.62
6.26	Surface Crack in a Finite Plate	6.63
6.27	Surface-Cracked Plate Subjected to Tension or Bending Loads	6.63
6.28	Variation of Stress with Distance Away From the Weld Toe (σ_{yy}/S) and Distance Inward Along the Path the Fatigue Crack Will Follow (σ_{xx}/S)	6.64

LIST OF FIGURES (Continued)

<u>Figure</u>		<u>Page</u>
7.1	Comparison of Initiation and Propagation Lives for Cruciform Planar Joint (Environment - Air)	7.32
7.2	Cyclic Stress-Strain and Strain-Life of HT60 and SM42 Steels, From [7.2]	7.33
7.3	Test Specimen and Crack Initiation Lives of SM41 and HT60 Cruciform Joints, From [7.2]	7.34
7.4	Comparison of Analytical and Experimental Crack Initiation Results for Mild Steels	7.35
7.5	Comparison of Strain-Controlled Fatigue Behavior for A36 HAZ and SM41 Metal (Environment - Air)	7.36
7.6	Comparison of Analytical and Experimental Crack Initiation Results for High-Strength Steels	7.37
7.7	Comparison of Initiation and Propagation Lives for Cruciform Planar Joints (Environment - Air)	7.38
7.8	Comparison of Analytical (Low R) and Experimental Fatigue Results for Cruciform Planar Joints (Environment - Air)	7.39
7.9	Comparison of Analytical (High R) and Experimental Fatigue Results for Cruciform Planar Joints (Environment - Air)	7.40
7.10	Comparison of Analytical and Experimental Fatigue Results for Cruciform Planar Joints (Environment-Air)	7.41
7.11	Comparison of Analytical and Experimental Fatigue Results for Cruciform Planar Joints, (Environment-Air)	7.42
7.12	Comparison of Analytical and Experimental Fatigue Results for Cruciform Planar Joints (Environment-Air)	7.43
7.13	Comparison of Analytical and Experimental Fatigue Results for Tubular Joints, Chord Diameter 168 mm x 6 mm Wall Thickness (Environment-Air)	7.44
7.14	Comparison of Analytical and Experimental Fatigue Results for Tubular Joints, Chord Diameter 457 mm x 16 mm Wall Thickness (Environment-Air)	7.45
7.15	Comparison of Analytical and Experimental Fatigue Results for Tubular Joints, Chord Diameter 914 mm x 32 mm Wall Thickness (Environment-Air)	7.46

LIST OF FIGURES (Continued)

<u>Figure</u>		<u>Page</u>
7.16	Relationship Between Stress-Strain Function, D, and Fatigue Crack Initiation Lives in Air and Seawater, From [7.3]	7.47
7.17	Comparison of Strain-Controlled Fatigue Behavior for SM41 Metal in Air and Seawater	7.48
7.18	Comparison of Analytical Crack Initiation Results for Cruciform Planar Joints in Air and Seawater	7.49
7.19	Comparison of Analytical and Experimental Fatigue Results for Cruciform Planar Joints (Environment-Seawater, Free Corrosion Potential)	7.50
7.20	Comparison of Analytical and Experimental Fatigue Results for Cruciform Planar Joints (Environment-Seawater, Cathodic Polarization)	7.51
7.21	Comparison of Analytical (Low R) and Experimental Fatigue Results for Cruciform Planar Joints (Environment - Seawater, Free Corrosion Potential)	7.52
7.22	Comparison of Analytical (High R) and Experimental Fatigue Results for Cruciform Planar Joints (Environment - Seawater, Free Corrosion Potential)	7.53
7.23	Comparison of Analytical and Experimental Fatigue Results for Tubular Joints, Chord Diameter 457 mm x 16 mm Wall Thickness (Environment-Seawater-Free Corrosion Potential)	7.54
7.24	Comparison of Analytical and Experimental Fatigue Results for Tubular Joints, Chord Diameter 914 mm x 32 mm Wall Thickness (Environment-Seawater-Free Corrosion Potential)	7.55
7.25	Comparison of Analytical and Experimental Fatigue Results for Tubular Joints, Chord Diameter 914 mm x 32 mm Wall Thickness (Environment-Seawater-Cathodic Polarization)	7.56
7.26	Comparison of Analytical and Experimental Fatigue Results for Tubular Joints, Chord Diameter 508 mm x 16 mm Wall Thickness (Environment-Seawater-Cathodic Polarization)	7.57
7.27	Sensitivity of Environment on Analytical Crack Propagation Results for a Cruciform Planar Joint	7.58
7.28	Sensitivity of Environment and R on Analytical Crack Propagation Results for a Tubular Joint	7.59

LIST OF FIGURES (Continued)

<u>Figure</u>		<u>Page</u>
7.29	Stress Gradient at Weld Toe (Uncracked State) Planar T-Joint	7.60
7.30	$\Delta K_I / \Delta S$ Versus Depth of Crack at Weld Toe for a Planar T-Joint	7.61
7.31	Initial Crack Depth Assumption for Crack Growth Analysis	7.62
7.32	Sensitivity of Crack Propagation Life to Weld Toe Radius and Initial Crack Depth, Low R-Ratio	7.63
7.33	Sensitivity of Cycles for Crack Propagation to Initial Crack Depth (Low Load (R) Ratio)	7.64
7.34	Sensitivity of Cycles for Crack Propagation to Initial Crack Depth (High Load (R) Ratio)	7.65
7.35	Influence of Chord Size on Fatigue Life Assuming a Constant Initial Flaw Size of 0.12 mm x 0.24 mm	7.66
7.36	Sensitivity of One-Dimensional Crack Propagation Model to Final Crack Length	7.67
7.37	Sensitivity of Two-Dimensional Crack Propagation Model to Final Crack Length	7.68
7.38	Experimental and Predicted Fatigue-Crack Growth Patterns for a Surface Crack in a Plate Under Tension, From [6.34]	7.69
7.39	Experimental and Predicted Fatigue-Crack Growth Patterns for a Surface Crack in an Aluminum Alloy Cantilever Plate Under Bending, From [6.34]	7.69
7.40	Fatigue Crack Propagation Curve for T-Joint, A36 HAZ Material, Asymptotic Growth Law, Comparison of One-Dimensional and Two-Dimensional Analyses	7.70
7.41	Shape of Crack Front for Planar T-Joint, A36 HAZ Material, 500 MPa Far-Field Bending Stress	7.71
7.42	Shape of Crack Front for Planar T-Joint, A36 HAZ Material, 100 MPa Far-Field Bending Stress	7.72
7.43	Scheme for Determination of Experimental Stress Intensity Factor From Crack Growth Rate Information	7.73
7.44	Variation of Experimentally Determined Stress Intensity Factor With Relative Surface Crack Length for Tension Cycling, From [7.14]	7.74

LIST OF FIGURES (Continued)

<u>Figure</u>		<u>Page</u>
7.45	Comparison of Analytical and Experimental Stress Intensity Factors for a T-Joint	7.75
7.46	Bending Component of the Stress Intensity Ratio in Symmetrically Loaded Shells, From [7.18]	7.76
7.47	Changes in Crack Shape During Fatigue Crack Growth in a T-Joint	7.77
8.1	Probabilistic S-N Model, Linear Model, With Corrosion Effects	8.31
8.2	Probabilistic S-N Model, Linear Model, Without Corrosion Effects	8.32
8.3	Approximation of $h(a)$	8.33
8.4	Comparison of Approximate Analytical Solution with Numerical Integration Results	8.34
8.5	Probabilistic S-N Model, Three-Component Model, Without Corrosion Effects	8.35

LIST OF PRINCIPAL SYMBOLS

A_1, A_2, A_3	constants in three-component crack growth law
a	crack depth
a_f	final crack length
a_i, a_o	initial crack length
a_m	material parameter
B	local stress uncertainty factor
b	fatigue strength exponent
C_d	drag coefficient
C_m	added-mass coefficient
COV	coefficient of variation
c	fatigue ductility exponent
$2c$	surface crack length
D	fatigue damage calculated by Miner's rule
da/dN	rate of fatigue crack growth per cycle
E	modulus of elasticity
e	base of natural logarithm
$e (\Delta e)$	remote or far-field strain (range)
E_{POT}	electrochemical potential of the material environment system
F_I	inertial force
F_0	drag force
$F(\)$	function in two-dimensional crack analysis
f	cyclic frequency
$G(\)$	Green's function
$H(\)$	function in two-dimensional crack analysis
H_s	significant wave height
$K (\Delta K)$	stress intensity factor (range)

K_{exp}	experimentally measured stress intensity factor
$K_{\text{th}} (\Delta K_{\text{th}})$	threshold stress intensity factor (range)
K_c	plane stress fracture toughness (Note: May be crack size or geometry dependent)
K_f	fatigue strength reduction factor
$K_{f\max}$	maximum value of K_f
K_t	theoretical elastic stress concentration factor, a constant for a given geometry and loading mode
K_σ	stress concentration factor defined as σ divided by S ; not a constant when yielding occurs
K_e	strain concentration factor defined as e divided by e ; not a constant when yielding occurs
K'	cyclic strength coefficient
M_b	back "free surface" magnification factor
M_f	front "free surface" magnification factor
M_k	magnification factor for a local stress gradient arising from geometrical stress concentration
n	power of ΔK in crack growth rate
N_f	total fatigue life in cycles ($N_f = N_i + N_p$)
N_i	crack initiation fatigue life
N_{kc}	Keulegan-Carpenter number
N_p	crack propagation fatigue life
N_T	applied load cycles during service life
n_1, n_2	exponents in three-parameter crack growth law
n'	cyclic strain hardening coefficient
Q	flaw shape parameter
q	notch sensitivity factor
R	load ratio (minimum stress/maximum stress)
r	radius at toe of weld or notch root radius
r_{crit}	radius at toe of weld where $K_f = K_{f\max}$

S_a	remote or far-field stress amplitude
$S(\Delta S)$	remote or far-field stress (range)
S_o	once-in-a-lifetime stress range level
S_u	ultimate material strength
T	temperature, wave period
T_o	mean wave period
t	material thickness
$u, du/dt$	velocity, acceleration
a	factor in stress concentration (K_t) relationship which is dependent on weld geometry and mode of loading
$\delta(\cdot)$	Dirac-delta function
ξ	Weibull shape parameter
s_f	fatigue ductility coefficient
$s(\Delta s)$	local strain (range) at notch root
ϕ	crack shape correction factor
ρ	water density
σ_a	stress amplitude
$\sigma(\Delta\sigma)$	local stress (range) at notch root
σ'_f	fatigue strength coefficient
σ_o	mean stress
σ_r	equivalent reversed stress amplitude
$\sigma_{\ln x}^2$	variance of the logarithm (base e) of x
$u_{\ln x}$	mean of the logarithm (base e) of x

1.0 INTRODUCTION

1.1 Problem Statement

With the ever-increasing need for more energy and more resources from the sea, marine structures are being built in deeper waters and in increasingly hostile environments. These taller structures are becoming more compliant and will have greater response to the more severe wave loadings than conventional platforms.

If these structures are going to operate for the time required to make them economically feasible, then they must be designed with 30-50 year operating lives. Within this period of time, they will be subjected to up to about 4×10^8 cycles of variable-amplitude loading. The increased compliance, magnitude of wave forces, and extended design lives all contribute to the fatigue damage of the structure.

Conventionally, designers use large factors of safety in the design of structural elements, with the result that conservative structures are being built. The need for large factors of safety stems from a belief that there is considerable uncertainty in structural loadings and a lack of adequate understanding of the response of structural materials to environment. Years of work by researchers and years of experience with existing marine structures suggest that the time has come to take stock of the available information and update design practices. Long-term effects, particularly corrosion fatigue, play an important part in structural life predictions. The lack of sufficient information on material behavior in a corrosive environment beyond 10^7 cycles makes design against high-cycle corrosion fatigue uncertain.

The objective of the research program described in this report is to define and evaluate currently available technology for assessing the long-life corrosion fatigue behavior of welded joints in seawater.

1.2 Historical Perspective and Concerns

Offshore structures have been operational in various parts of the world for over 30 years. Early experience was in the Gulf of Mexico where water

A glossary of terms in the areas of corrosion, fatigue, and welding is given in Appendix A.

depths typically range up to 100 meters. However, technology has advanced to the point where the largest template drilling and production platform *Cognac* stands in 310 meters of water 24 km southeast of the Mississippi River Delta. Currently there are about 3800 offshore platforms of various types in the United States with the vast majority built for Gulf of Mexico service. These platforms typically operate in sea states which are relatively calm for much of the time and only experience severe loadings from occasional hurricanes. This is illustrated in Figure 1.1, which shows a stress spectrum typical of Gulf of Mexico platforms. The plot shows that within a 50-year period, the platform would experience 4×10^8 waves, but only 2×10^6 cycles would be above 5 percent of the design stress. Marshall [1.1]* indicates that in the Gulf of Mexico fatigue failures in fixed platforms have not been a serious problem.

This type of loading is not typical, however, of rough weather areas like the North Sea and the Gulf of Alaska. At the present time, there are about 100 to 150 structures working in the North Sea in water depths from 150 to 200 meters. These North Sea platforms are exposed to an environment that is severe most of the year. This is reflected in the typical stress spectrum shown in Figure 1.1. Notice that the North Sea spectrum does not sag at the higher number of cycles as the Gulf of Mexico spectrum does. This indicates that a larger number of cycles are being applied at a greater proportion of the design load for the North Sea and Gulf of Alaska sea states. Under these more severe loadings, more stringent requirements are placed upon the design, materials, and fabrication aspects of the structure. Fatigue plays an increasingly important role because the structure is subjected to a higher stress level for a greater part of its life.

Marine structures operate in a complex environment. Seawater properties such as salinity, temperature, oxygen content, pH level, and chemistry can vary according to site location and water depth. Table 1.1 describes the environment in different marine zones (Figure 1.2) and indicates the nature of general corrosion attack on steels. Offshore structures are cathodically protected with systems of sacrificial anodes or impressed current. These systems deliver a current density to the protected metal surface which inhibits the corrosion process. The amount of required current density is a function of

*Numbers in brackets denote references listed at the end of each chapter.

environmental factors such as temperature, oxygen content, and flow rate of the seawater. Consequently, even if a structure is globally cathodically protected there may be local areas which are either under or overprotected. Table 1.2 describes qualitatively the effect of various environmental variables on general corrosion attack.

The degree of cathodic protection is measured by the electrode potential at the surface of the cathode and referenced to either a silver-silver chloride (Ag/AgCl) or a copper-copper sulfate (Cu/CuSO_4) electrode. The free corrosion potential (Ag/AgCl) (no protection) is approximately -0.65 volt (V) and normal cathodic protection is about -0.85 V. For more negative potentials the structure is said to be overprotected.

The fatigue phenomenon is enhanced by the corrosive seawater environment. One can gain an appreciation of the various environmental effects by considering Figure 1.3 [1.4, 1.5], which shows the effects of the important variables in seawater. These are: cyclic frequency, temperature, oxygen content, level of cathodic protection, and pH. The base line case takes as unity the propagation rate in air at a temperature of 20°C and a loading frequency of greater than 1 Hz. The remaining data show the increase in crack growth for seawater with respect to air under a variety of conditions. The quantities highlighted in the boxes were varied from a standard seawater test under a free corrosion potential. Conditions are representative of the splash zone in which corrosion is most aggressive. A typical variation with depth is illustrated in Figure 1.4 from data taken in the Pacific Ocean near Port Hueneme, California. The oxygen content of 7 ppm in the standard test represents fully oxygenated seawater. The salinity of open-ocean seawater typically ranges from 32 to 38 parts per thousand (ppt) [1.2].

One should recognize, however, that the crack propagation data on which Figure 1.3 is based was generally taken at crack growth rates no lower than about 10^{-8} meters/cycle. This corresponds to a change in stress intensity factor of approximately $10 \text{ MPa} \sqrt{\text{m}}$. A 10^{-8} meters/cycle of growth rate is too high for structures which have to endure on the order of 4×10^8 ocean waves. For such structures, the average growth rates in a 50-mm weld would be about 1×10^{-10} meters/cycle. This means that, in the region of interest, much slower crack growth data are required at a stress intensity range of 1 to $3 \text{ MPa} \sqrt{\text{m}}$. Work is progressing in this area, as will be reviewed in Chapter 4.0.

Figure 1.3 indicates that, under standard loading rates in the ocean, one could expect crack propagation rates from 1 to 3 times the in-air values. It is generally believed that adequate cathodic protection restores the in-air crack propagation rates, although there is concern with overprotection being detrimental due to hydrogen embrittlement. It is also important to note that if the loading frequency in seawater is increased above 1 Hertz, then the crack propagation rates decrease to the in-air values. This is quite an important observation since it means that the corrosive effects are dependent upon the loading frequency. This is bad from an experimental point of view because it requires that fatigue tests must be made at the correct frequency if one expects to appropriately account for the effects of the corrosive environment. For long-term corrosion fatigue testing, the situation is even worse because one is trying to test into the range of 10^8 to 10^9 cycles. Of course, it is clearly impossible to do laboratory tests with this number of cycles at frequency because the tests would last on the order of 50 years. This has motivated the development of analytical tools to enable the long-term corrosion effects to be accounted for without conducting such high-cycle tests.

The effect different variables have on fatigue crack initiation is not well understood. Reference 1.6 indicates that there are at least four types of mechanisms associated with corrosion fatigue crack initiation. They are:

- (1) Pitting, where crack nucleation is related to stress concentrations at pits formed by corrosive attack.
- (2) Preferential dissolution of highly deformed material acting as a local anode with undeformed material acting as a local cathode.
- (3) Film rupture, where protective surface films such as oxides are cracked by cyclic deformation, allowing corrosion to occur.
- (4) Surface energy reduction caused by adsorption of environmental species and enhancement of microcrack propagation.

Early investigators of corrosion fatigue favored the stress-concentration-pit theory, because physical examination of failed specimens indicated a number of large cracks originating at large hemispherical pits at the metal surface [1.7]. Certainly pits caused by an aggressive environment do reduce fatigue life. However, Reference 1.7 reports that low-carbon steels were fatigued in a 3 percent NaCl solution and examined metallographically after a small

portion of total fatigue life. Even though hemispherical pits were observed on the specimen surface, no crack could be attributed to their presence.

In 1977 an American Petroleum Institute study [1.8] discussed crack initiation in smooth, notched, and welded specimens and summarized a number of earlier investigations. Although it is not possible to quantify the effects of various environmental variables as in Figure 1.3, Table 1.3 ranks them qualitatively according to importance. Reference 1.8 indicates that frequency, cathodic potential, and oxygen level have a primary effect, and temperature and pH level are secondary for the ranges of values normally anticipated in actual service.

The fatigue life of a structure in seawater is influenced by parameters other than those listed in Figure 1.3. For example, the applied load, the materials, and fabrication techniques all play a significant role in determining the fatigue life of a structure. Wirsching [1.9] lists major sources of uncertainty in the fatigue analysis process. This list, supplemented by the present project, includes:

1. Mechanisms of corrosion fatigue and their effects on structural life are not well known.
2. Fatigue data are subject to wide statistical scatter. (Difficulties also arise in normalizing data from different test programs, i.e., coupon tests vs S-N tests vs structural tests.)
3. Fatigue data are dependent on the welded joint geometry, weld profile, and size of the welded components.
4. Defects and discontinuities in welded joints complicate the prediction of fatigue crack initiation and propagation.
5. Fabrication parameters such as weld shapes (profile), weld surface preparations (as welded, ground, peened), and residual stresses (fabrication, welding, and post-weld heat treatment) all play a role in establishing the fatigue life.
6. The ocean wave process is complicated, with the magnitude and period of the waves being random in nature and multi-directional.
7. Hydrodynamic loadings such as due to waves and currents are not accurately known.
8. The detailed stresses that cause fatigue at a particular welded joint are subject to uncertainty in the structural analysis procedure used

for a platform. These stresses are a function of the global structural geometry, type of connection, weld profile, and local weld irregularities.

This section has discussed the corrosion fatigue problem and the major factors affecting fatigue life in an ocean environment. Hartt [1.10] has represented both primary and secondary variables in Figure 1.5, and these will be discussed in greater detail throughout this report. With all of the uncertainties listed above and the concerns that accompany them, rational decisions must still be made to assess the long-term corrosion fatigue behavior of welded joints. This program is dedicated to establishing a framework in which the state-of-the-art can be assessed, developing prediction methods for crack initiation and propagation life which consider the major environment variables, and identifying those areas requiring additional research.

1.3 Philosophy of Program's Approach

In the past five years, there have been major research programs undertaken to investigate the integrity of welded steel structures in an offshore environment. Most of the studies that are published in the open literature are being conducted in the United States and in Europe. Research into corrosion fatigue forms only one part of the overall effort to attempt to understand the long-term behavior of these structures. Such areas include:

1. Static and dynamic response of marine structures to ocean loads
2. Stress analysis of tubular joints
3. Strain measurements in tubular joints
4. Fatigue tests on tubular joints in air and ocean environments
5. Fatigue tests of replica welded joints in air and ocean environments
6. Fatigue crack growth behavior of steels in air and corrosive environments
7. Techniques for predicting fatigue life by both conventional fatigue damage laws and fracture mechanics techniques
8. Techniques for improving fatigue life of welded joints in air and corrosive environments
9. Techniques for establishing design criteria based upon probability methods
10. Calibration of analytical technique by using field data

Previous efforts in the United States have been undertaken for the American Petroleum Institute, the Welding Research Council, and for the Department of Defense through the Metals and Ceramics Information Center. Other programs are sponsored in the private sector primarily by oil companies, but the results are usually proprietary and not published in the open literature. A large research program, the United Kingdom Offshore Steels Research Project (UKOSRP), was approved in 1973 to review the problems of fatigue and fracture of complex welded steel structures required for North Sea oil and gas fields. The European Coal and Steel Community (ECSC) initiated a parallel program of research in 1976. The objective of the program was to obtain the necessary technical background for design and fabrication of large sea structures necessary for exploration and production of offshore oil and gas fields within western Europe. The ECSC program is now participating with the UKOSRP in a coordinated effort since the overall objectives of each of these efforts are basically the same.

The first-year effort of the present program was directed primarily at the state-of-the-art literature review. This was done by identifying applicable references in the open literature. If available, these references were obtained, and they were further scanned to determine their applicability to the present program. From this review, it was quickly determined that most of the current research in fatigue behavior of offshore structures is being conducted in Europe under the UKOSRP and ECSC programs. That work was summarized in papers from individual research programs at the European Offshore Steel Research Seminar held in Cambridge, November 1978 [1.11]. Later results from the UKOSRP effort were presented in a conference, Fatigue in Offshore Structural Steel [1.12], held in London, February 1981, and the ECSC results were presented at the International Conference on Steel and Marine Structures [1.13] held in Paris, France, October 1981.

The objectives of the current research are to (1) take the voluminous amount of information gathered and to distill it into a statement of the critical issues concerned with long-term corrosion fatigue of welded steel structures, (2) prepare and validate methods for predicting the long-term fatigue behavior of welded steels in the marine environment, and (3) identify those areas requiring additional research. This report documents the findings of this program.

CHAPTER 1.0 REFERENCES

- 1.1 Marshall, P. W., "Problems in Long-Life Fatigue Assessment for Fixed Offshore Structures," Preprint 2638, ASCE National Water Resources and Ocean Engineering Convention, San Diego, California, April 5-8, 1976.
- 1.2 Schumaker, M., editor, Seawater Corrosion Handbook, Noyes Data Corporation, Park Ridge, New Jersey, 1979.
- 1.3 Graff, W. J., Introduction to Offshore Structures, Gulf Publishing Company, Houston, Texas, 1981.
- 1.4 Johnson, R., et al., "The Effect of Sea Water Corrosion on Fatigue Crack Propagation in Structural Steel," Paper VI/P, European Offshore Steels Research Seminar, Cambridge, November 1978, published by The Welding Institute, Cambridge, 1980.
- 1.5 Thorpe, T. W., et al., "The Effect of North Sea Service Conditions on Fatigue Crack Growth in Structural Steel," Paper 5, Fatigue in Offshore Structural Steel Conference, Institution of Civil Engineers, London, February 1981.
- 1.6 Jaske, C. E., et al., Corrosion Fatigue of Metals in Marine Environments, Metals and Ceramics Information Center, Report MCIC-81-42, July 1981.
- 1.7 Duquette, D. J., "Environmental Effect I: General Fatigue Resistance and Crack Nucleation in Metals and Alloys," Fatigue and Microstructure, American Society for Metals, Metals Park, Ohio, 1979.
- 1.8 Jaske, C. E., et al., "Interpreting Report on Corrosion Fatigue of Welded Carbon Steels for Application to Offshore Structures," for American Petroleum Institute Committee on Offshore Safety and Anti-pollution Research, Battelle Columbus Laboratories, February 1977.
- 1.9 Wirsching, P. H., "Probability-Based Fatigue Design Criteria for Offshore Structures," Final Reports, First- and Second-Year Effort, API-PRAC Project No. 80-15, American Petroleum Institute, Dallas, Texas, November 1979 (First-Year Report), February 1981 (Second-Year Report).
- 1.10 Hartt, W. H., "Influence of Sea Water and Cathodic Protection Upon Fatigue of Welded Steel," Report to American Petroleum Institute, 1981.
- 1.11 European Offshore Steels Research Seminar, Cambridge, England, November 1978, published by the Welding Institute, 1980.
- 1.12 Fatigue in Offshore Structural Steel Conference, Institution of Civil Engineers, London, February 1981.
- 1.13 International Conference on Steel in Marine Structures, Commission of the European Committees, Paris, France, October 1981.

TABLE 1.1. CLASSIFICATION OF TYPICAL MARINE ENVIRONMENTS, FROM [1.2]

Marine Zone	Description of Environment	Characteristic Corrosion Behavior of Steel
Atmosphere (above splash)	Minute particles of sea salt are carried by wind. Corrosivity varies with height above water, wind velocity and direction, dew cycle, rainfall, temperature, solar radiation, dust, season, and pollution. Even bird droppings are a factor	Sheltered surfaces may deteriorate more rapidly than those boldly exposed. Top surfaces may be washed free of salt by rain. Coral dust combined with salt seems to be particularly corrosive to steel equipment. Corrosion usually decreases rapidly as one goes inland.
Splash.	Wet, well-aerated surface, no fouling	Most aggressive zone for many metals, e.g., steel. Protective coatings are more difficult to maintain than in other zones.
Tidal	Marine fouling is apt to be present to high-water mark. Oil coating from polluted harbor water may be present. Usually, ample oxygen is available.	Steel at tidal zone may act cathodically (well aerated) and receive some protection from the corrosion just below tidal zone. In case of a continuous steel pile isolated steel panels show relatively high attack in tidal zone. Oil coating on surface may reduce attack
Shallow water (near surface and near shore)	Seawater usually is saturated with oxygen. Pollution, sediment, fouling, velocity, etc., all may play an active role.	Corrosion may be more rapid than in marine atmosphere. A calcareous scale forms at cathodic areas. Protective coatings and/or cathodic protection may be used for corrosion control. In most waters a layer of hard shell and other biofouling restricts the available oxygen at the surface and thus reduces corrosion. (Increased stress on structure from weight of fouling must be provided for).
Continental-shelf depths	No plant fouling, very much less animal (shell) fouling with distance from shore. Some decrease in oxygen, especially in the Pacific, and lower temperature.	
Deep ocean	Oxygen varies, tending to be much lower than at surface in Pacific but not too different in Atlantic. Temperature near 0 C. Velocity low, pH lower than at surface	Steel corrosion often less. Anode consumption is greater to polarize same area of steel as at surface. Less tendency for protective mineral scale.
Mud	Bacteria are often present, e.g., sulfate reducing type. Bottom sediments vary in origin, characteristics, and behavior.	Mud is usually corrosive, occasionally inert. Mud-to-bottom water corrosion cells seem possible. Partly embedded panels tend to be rapidly attacked in mud. Sulfides are a factor. Less current than in seawater is consumed to obtain cathodic polarization for buried part of structure.

TABLE 1.2. CORROSION FACTORS FOR CARBON STEEL
IMMERSED IN SEAWATER, FROM [1.2]

Factor in Seawater	Effect on Iron and Steel
Chloride ion	Highly corrosive to ferrous metals. Carbon steel and common ferrous metals cannot be passivated. (Sea salt is about 55 percent chloride.)
Electrical conductivity	High conductivity makes it possible for anodes and cathodes to operate over long distances, thus corrosion possibilities are increased and the total attack may be much greater than that for the same structure in fresh water.
Oxygen	Steel corrosion is cathodically controlled for the most part. Oxygen, by depolarizing the cathode, facilitates the attack, thus a high oxygen content increases corrosivity.
Velocity	Corrosion rate is increased, especially in turbulent flow. Moving seawater may (1) destroy rust barrier and (2) provide more oxygen. Impingement attack tends to promote rapid penetration. Cavitation damage exposes fresh steel surface to further corrosion.
Temperature	Increasing ambient temperature tends to accelerate attack. Heated seawater may deposit protective scale, or lose its oxygen; either or both actions tend to reduce attack.
Biofouling	Hard-shell animal fouling tends to reduce attack by restricting access of oxygen. Bacteria can take part in corrosion reaction in some cases.
Stress	Cyclic stress sometimes accelerates failure of a corroding steel member. Tensile stresses near yield also promote failure in special situations.
Pollution	Sulfides, which normally are present in polluted seawater greatly accelerate attack on steel. However, the low oxygen content of polluted waters could favor reduced corrosion.
Silt and suspended sediment	Erosion of the steel surface by suspended matter in the flowing seawater greatly increases the tendency to corrode.
Film formation	A coating of rust, or rust and mineral scale (calcium and magnesium salts) will interfere with the diffusion of oxygen to the cathode surface, thus slowing the attack.

TABLE 1.3 SUMMARY OF MAJOR VARIABLES INFLUENCING THE CORROSION
FATIGUE CRACK INITIATION BEHAVIOR OF CARBON STEELS
IN SEAWATER-TYPE ENVIRONMENTS, FROM [1.8]

Variable	Effect of Variable
Cyclic frequency	Slower frequencies cause reduced fatigue resistance for unprotected steel
Cathodic potential	Appropriate cathodic protection restores fatigue resistance to levels observed in air
Oxygen level	Fatigue resistance in deaerated seawater is similar to that in air
Temperature	Although decreasing temperature results in increased oxygen levels, the overall effect of decreasing temperature is that fatigue resistance is improved to some extent in range of 13 to 45°C
pH level	Over broad range of values (4 to 10), there is little effect of pH on fatigue resistance. Low values (<4) decrease fatigue resistance and high values (>10) improve fatigue resistance to levels similar to those observed in air

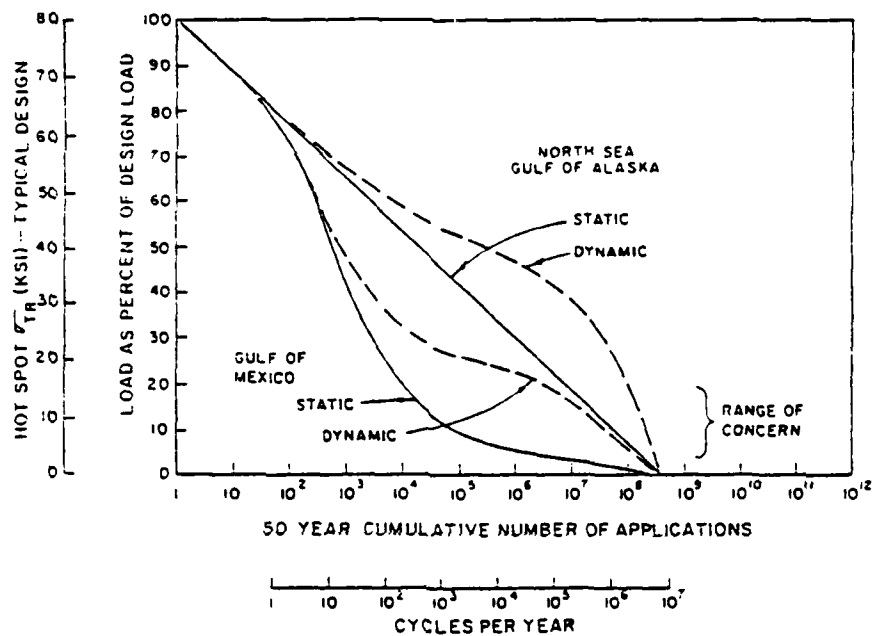


FIGURE 1.1. TYPICAL OCEAN STRESS SPECTRA, FROM [1.1]

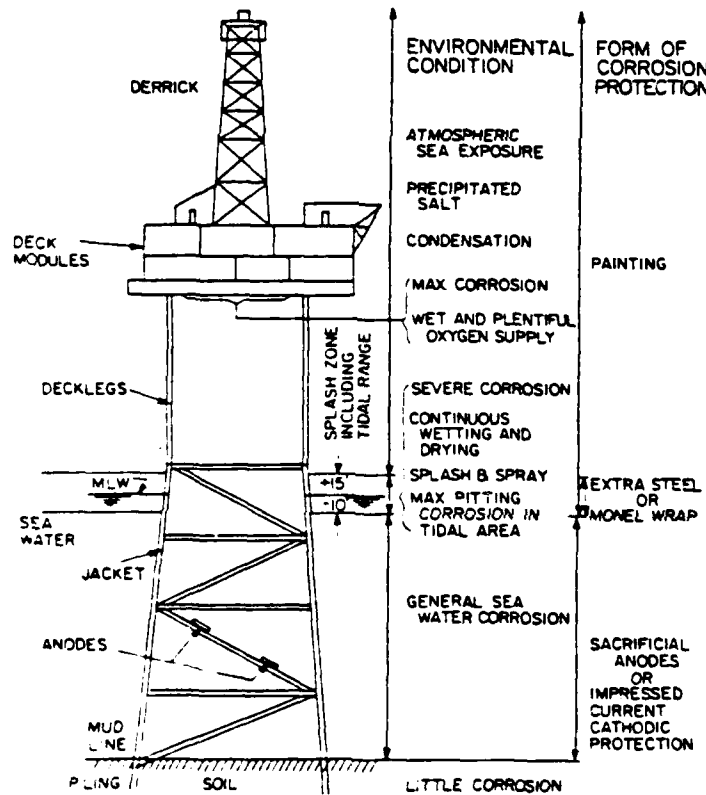


FIGURE 1.2. CORROSION ZONES ON FIXED OFFSHORE STEEL STRUCTURES, FROM [1.3]

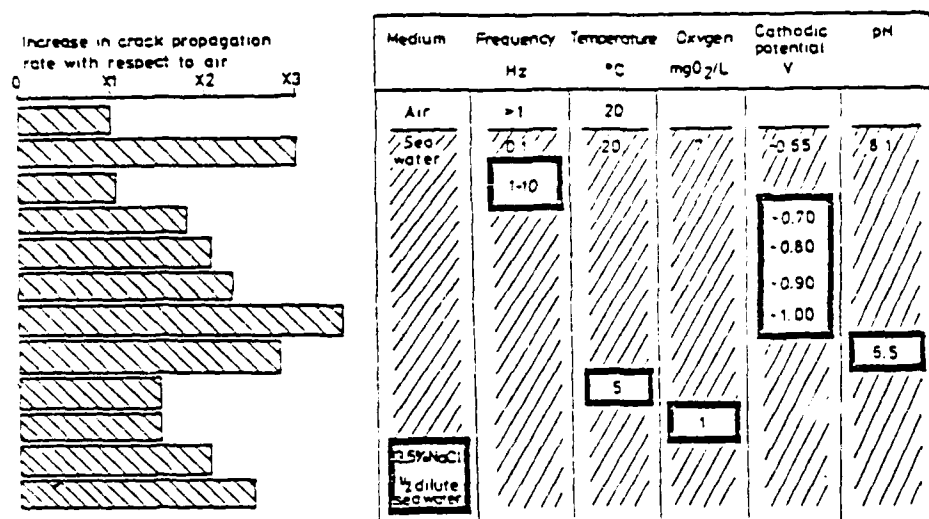


FIGURE 1.3. COMPARATIVE EFFECTS OF ENVIRONMENTAL VARIATIONS ON FATIGUE CRACK GROWTH RATES ($R \leq 0.1$), FROM [1.4, 1.5]

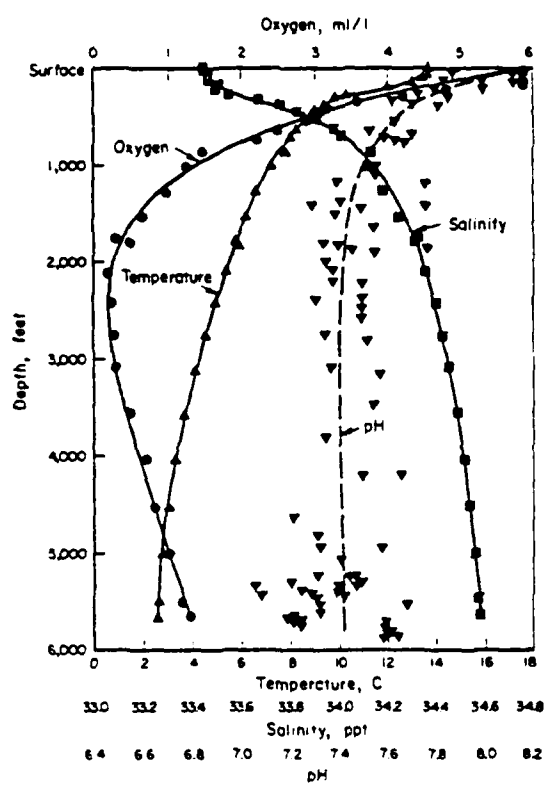


FIGURE 1.4. OCEANOGRAPHIC DATA TAKEN IN THE PACIFIC OCEAN AT A SITE WEST OF PORT HUENEME, CALIFORNIA, FROM [1.2]

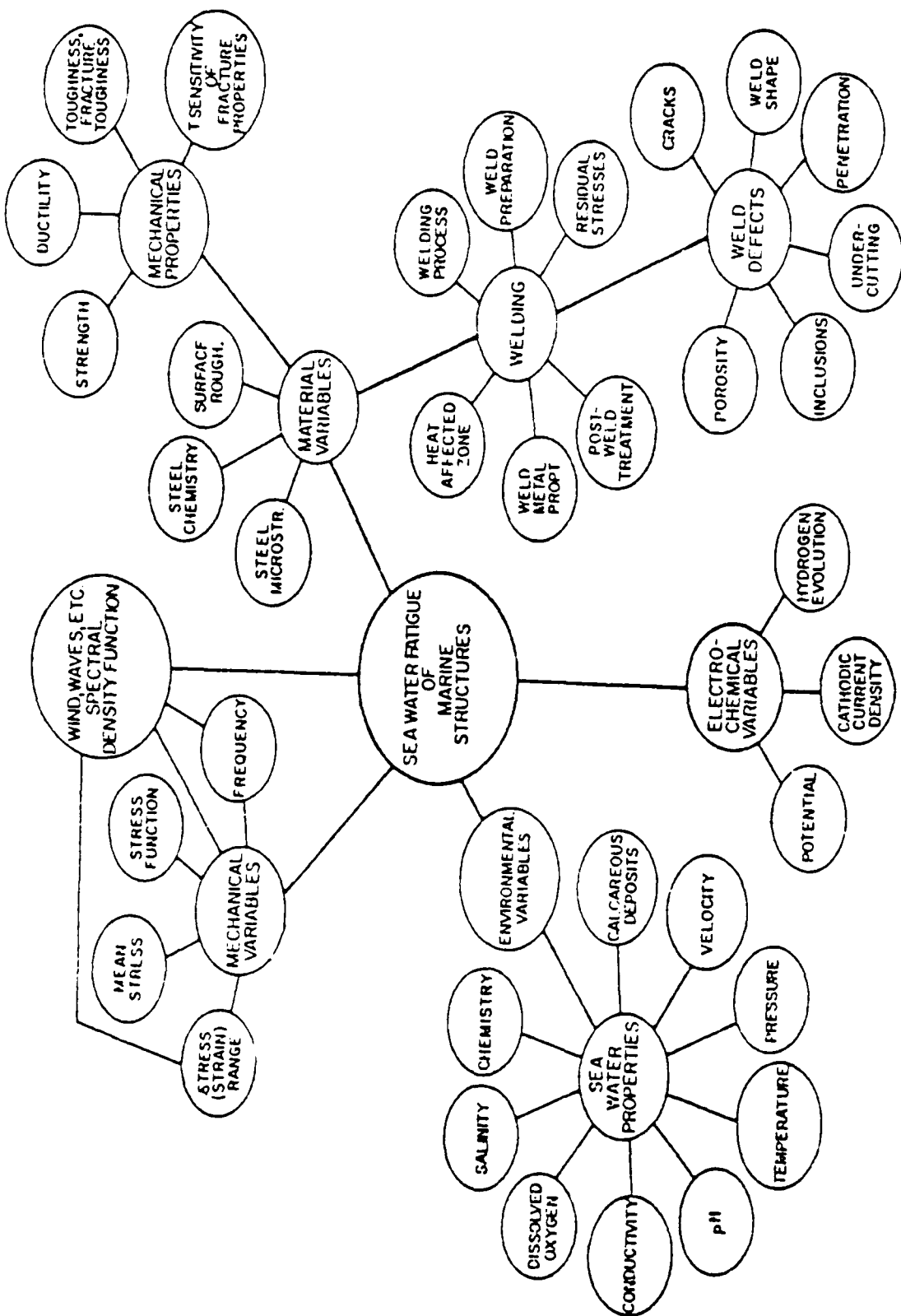


FIGURE 1.5. REPRESENTATION OF VARIABLES WHICH INFLUENCE FATIGUE, FROM [1.10]

2.0 CHARACTERIZATION OF APPLIED LOADS

2.1 General

The discussion of applied loads will be limited to structures exposed to seawater in a loading regime where high-cycle fatigue can lead to failure. Fatigue in offshore welded tubular joints has been identified as a problem for over 20 years [2.1], and as discussed in this report, significant progress has been made in its understanding.

Offshore structures include a variety of components from seabed pipelines to fixed platforms to floating ships. Since this study is directed at corrosion-enhanced fatigue, the offshore structures that experience such problems will be emphasized. These include fixed and mobile offshore drilling and production platforms and their associated riser systems. There is also concern with the emerging compliant structures such as the guyed and articulated towers and tension leg platforms.

The problem with corrosion fatigue on ships is not as great for two reasons. First, ships have few structural discontinuities which are directly exposed to seawater such as in a tubular joint connection on a platform. Second, ships are usually drydocked every several years for inspection and maintenance of the hull, and any fatigue cracks can be repaired.

Repair of damage presents a major problem for offshore platforms, especially fixed structures. These structures, which are generally designed as a lattice of tubular members, have a large number of connections with built-in stress concentrations at which cracks can initiate either during fabrication or service. Detection of fatigue cracks underwater in these connections at significant depths is difficult at best and often impossible. Repair by welding in a habitat or by wet-welding techniques is expensive and often not possible at certain times of the year because of seasonal weather conditions. Therefore, it is incumbent upon the designer to produce a structure whose fatigue life exceeds the design service life.

Prediction of the fatigue life requires a quantitative description of the expected stress history for each critical joint in the structure. As discussed in Chapter 3.0, important loading variables to be obtained from the stress history included stress (or strain) range (maximum stress minus minimum stress within a cycle), mean stress or load ratio (ratio of minimum to maximum stress), cyclic frequency, and sequence of stress cycles. Obtaining this

information is the objective of load modeling, the subject of this chapter. The emphasis will be on obtaining cyclic stresses from wave loading.

2.2 Load Classification

It is appropriate to place the loads into three categories: time-invariant or static, dynamic but infrequent, and dynamic and frequent. The static loads include the dead loads, or weight of the structure and permanent equipment, and live loads such as supplies or temporary structures. Slowly varying or time-invariant environmental loads, such as constant current, sustained wind, and ice and snow accumulation, also are considered as live loads. The tidal movements caused by storm, astronomical, wind, or barometric pressure fluctuations vary at so low a frequency that these are also treated as static live loads. The major effects of buoyancy and the loads induced by external pressure on buoyant members are constant once the platform is set in place. Variation in buoyancy due to tidal changes is also quasistatic, but the change in buoyancy with the passage of waves is both dynamic and frequent.

In addition to the static load-induced stresses above, residual stresses resulting from fit-up, weld shrinkage, or heat treatment during fabrication also occur. The total combined stress due to static loads and residuals has an effect upon fatigue life by increasing the mean stress. Effects of mean stress on fatigue are often taken into account by use of the Goodman diagram in conventional S-N analyses or variations in load ratio (R) for crack propagation calculations. However, in welded joints, the stress range is considered to be the important loading parameter, and mean stress is often ignored. This will be discussed later in Chapters 6.0 and 7.0.

The second category is the dynamic but infrequent load. Generally, these are taken as a special case requiring additional treatment. Included are earthquake and the attendant tsunami wave loadings, impact ice loadings, collision from work boats or barges, dropped objects such as drill collars and casings, and explosion and fire. Transportation and erection loads can also be classed as dynamic, but, in the case of fixed platforms, occur only during the initial installation and, therefore, are infrequent. Jackups and semisubmersible offshore platforms experience numerous transportation and erection cycles, which have resulted in fatigue failures. For these structures, such loadings should be included in the fatigue life determination. As in the case of the static loadings, the basic failure modes for these dynamic infrequent

loads are overload, plastic deformation, buckling, and low-cycle, high-strain rate failures caused by earthquake conditions. High-cycle fatigue does not occur, and, therefore, these loads will not be discussed further.

The third category of loads includes those that are both dynamic and frequent. These are the loads which cause long-term fatigue cracking and, therefore, are of primary interest to this discussion. Wave loading is considered to be the primary oscillating load on the structure. The load is caused by viscous drag and wave inertia. The passage of the wave through the structure changes the buoyancy of members, and the slamming of a breaking wave can introduce significant member loads. Wind gusts cause cyclic loads, and the constant sustained wind can induce oscillations from vortex shedding. Vortex shedding can also be brought on by wave action and uniform current. The failure mode for this third category of loading is generally fatigue crack growth to brittle failure or ligament separation.

Table 2.1 summarizes these types of loading and their effects on fatigue life and fast fracture of marine structures. Cyclic stresses induced by wave motion and mean stresses resulting from fabrication most significantly affect the long-life regime of the structure.

2.3 Wind and Current Loads

Wind is estimated to count for only 5 to 10 percent of the load on a fixed platform; however, it can have a significant effect on compliant structures such as tension leg platforms and guyed towers, moored ships and semi-submersible platforms, and on mobile platforms. Jackup rigs have a large exposed surface area for wind loading compared to the wave-induced loads on the legs.

Wind is significant in that it can induce vortex shedding as well as a cyclic loading associated with gusts. Current, on the other hand, is important only in fatigue life determination if it induces vortex shedding. Vortex shedding can increase drag forces by a factor of 4 to 5 [2.2]. Vortex-induced oscillations have caused fatigue cracking of jackup legs that were elevated during transit, and metal spoilers are now commonly used on these large diameter members. The river outflow current has caused vortex-induced fatigue failures on pipeline and drilling risers, and tapered buoyancy modules or streamers are now used to inhibit the formation of the vortex sheets.

Currents generated by tidal action vary only slightly with water depth. On deep-water structures, a uniform current can substantially increase the static load. A current velocity is vectorially added to the orbital wave velocity, and this vector sum is squared in the force equation. The large apparent increase caused by this approach is suspect, and it is generally held that actual forces are less than predicted [2.3]. Alternate approaches that have been proposed include squaring of the wave and current velocities and then vector summation or modification of the drag coefficient as a function of velocity.

2.4 Wave Loads

Ocean waves are a manifestation of energy applied to the water by the shearing action of wind on the water surface. The surface appears chaotic, and the elevation of the water surface at a fixed location is a stochastic process.

Ideally, a wave can be approximated as a sinusoidal-varying elevation of the water surface. This linear, or Airy model, is the simplest formulation and, for many cases, adequately models the real wave behavior. The higher-order nonlinear theories, such as Stokes third or fifth order and the Canoidal, are also used. The range of applicability of the wave theories is shown in Figure 2.1 [2.4]. In this figure, the wave height (H) and water depth (d) are normalized by wave period (T) squared. The breaking wave limit, H_B , which is the extent of applicability for the wave models is shown, as is the lower practical limit, $H_B/4$. The typical offshore platform is in the Stokes 5th regime.

The nonlinear theories give a steeper wave which can be significant in the calculation of the drag and inertia forces on the structure, but, in Reference 2.5, this effect was shown to be minor for gravity type, inertia-force-dominated structures. Except for slender drag-dominated members near the surface, the linear theory produces acceptable and conservative results. It has also been shown that the error in ignoring the variation in immersion length for cylinders penetrating the water surface, when calculating wave force, caused a greater error than the difference between the linear and nonlinear wave theories. The nonlinear theories are used for steel lattice offshore platforms in which drag effects on the tubular members are significant.

The Morison formulation postulates that the total force on a vertical cylinder due to surface waves is made up of inertial and drag components.

$$F = F_I + F_D \quad (2.1)$$

$$= \frac{C_M \rho \pi D^2}{4} \frac{du}{dt} + \frac{1}{2} C_d \rho D u |u|$$

where

F = wave force (per unit length) acting perpendicular to the member axis

F_I = inertia force

F_D = drag force

C_M = 1.0 plus added mass coefficient

C_d = drag coefficient

ρ = mass density of seawater

D = diameter of the cylinder

u = horizontal water particle velocity

$|u|$ = absolute value of u

du/dt = horizontal water particle acceleration

The inertia force is proportional to the acceleration of the water particles. The proportionality constant is the product of one plus the added-mass coefficient and the mass of water displaced by the cylinder. The drag component of the Morison wave force is generated by viscosity of the water. The Morison equation assumes the drag to be proportional to the water particles' relative velocity squared. The constant depends upon the drag coefficient, C_d , the density of the fluid, and the diameter of the member. It should be noted that the drag depends linearly on diameter, whereas the inertia is related to the square of diameter. Accordingly, inertial effects dominate the wave force for small wave height/diameter ratios.

The Morison equation was developed for vertical cylinders and horizontal velocities. Real structures have inclined members, and therefore, vectorial generalization is needed. Unfortunately, there is no agreement to support the correctness of such an extension. Comparison among four approaches [2.6]

showed a variation in calculated base shear of 22 percent on a typical platform design.

Keulegan and Carpenter [2.7] showed that the average water particle orbit width to the cylinder diameter determines the relative importance of wave-induced drag and inertial effects. The Keulegan-Carpenter number N_{kc} is defined as

$$N_{kc} = \frac{VT}{D} \quad (2.2)$$

where

V = maximum horizontal velocity

T = wave period

D = diameter of member

Figure 2.2 [2.8] shows that when $N_{kc} < 5$, inertial effects dominate. This occurs for a decreasing waveheight/diameter ratio. As the diameter/wavelength ratio increases beyond 0.2, diffraction theory should be used [2.9]. Not only do inertial effects dominate in this regime, but diffraction of the incident wave by the structure must be accounted for in fluid loads computations. The types of structure for which diffraction theory should be used are large diameter, reinforced concrete platforms such as those in the North Sea.

The diffraction solution method assumes a linear wave and solves the two-dimensional potential field equation for boundary conditions on the water surface, seabed, and surface of the cylinder. This solution, when coupled with the Bernoulli equation, yields a pressure which, when integrated over the cylinder surface, determines the force. Extensions of diffraction analysis to a nonlinear wave [2.10] and solutions using finite elements [2.11] have been made.

A final phenomenon that can introduce cyclic loadings is vortex shedding. Vortices form when the Keulegan-Carpenter number exceeds 15 [2.6]. This relation shows that vortex formation increases with velocity and wave period and decreases with diameter. Thus, vortex shedding is important in slender members near the water surface (velocity is greater) in long period waves. Since the flow oscillates during wave passage, the development of a vortex

sheet is generally inhibited, as flow separation, which forms during one-half cycle, collapses during the reversal.

The effect of inaccuracies in drag and inertia coefficients and in the treatment of inclined members can substantially affect fatigue life predictions. Unfortunately, erring on the conservative side and designing for higher loads than exist is not only uneconomical, but also, in some cases, not feasible, as the structure becomes too large to build and launch.

2.4.1 Prediction of Structural Response to Waves

Structural response as discussed in this section pertains to the global response of the structure (i.e., the nominal stress in members, as opposed to local or hot-spot stresses). There are generally three methods of analyzing the global structural response to wave loads: the quasi-static method, integration of the structure's equation of motion in the time domain, and linearized solutions of the structure's equation of motion in the frequency domain.

Quasi-Static Method

The deterministic or quasi-static analysis method is widely used both domestically [2.12-2.14] and internationally [2.15-2.17]. For this type of analysis, a selected wave of a given velocity, height, wavelength and wave-form is stepped past the structure, i.e. a static solution of the structure's response to drag and inertial forces is obtained at selected instants as the wave passes by the structure. The difference between the maximum and minimum stress calculated at a particular location in the structure from these solutions is the stress range associated with this wave. These stress ranges are often multiplied by a dynamic amplification factor to account for resonance and inertial forces of the structure.

Time Domain Integration Method

The most sophisticated but, unfortunately, most expensive analysis method is numerical integration of the structure's equation of motion in the time domain. For this type of analysis, a Monte-Carlo simulation of the random wave elevation time history is required for input and a dynamic analysis performed which may account for such illusive phenomena as the nonlinear drag forces, nonlinear structural response, fluid damping and structural damping. The stress history at selected locations in the structure is obtained as output, and stress ranges may be obtained directly by a variety of cycle counting

schemes or indirectly by spectral analysis as discussed later in this chapter. It should be noted that this type of analysis may be the only method available for obtaining a reasonable estimate of the response of compliant structures where relatively large deflection and velocity of the structure complicate the analysis.

The above analysis methods are called deterministic methods because a discrete value of the stress at a location on the structure is obtained for each time step or instant of time in the simulation. Statistical information about the response can be obtained after exhaustive simulation or a fit to an analytical statistical distribution or transformation of the stress-time history to its spectral components.

Frequency Domain Method

The frequency domain analysis method facilitates a probabilistic description of the response with a reduced computational effort. Unfortunately, this reduced effort is obtained only at the expense of the simplifying assumption that the structural response is a linear function of wave height. One of the primary objections to such a linearization is that Morison's equation for wave drag force must be expressed as a linear function of the water particle velocity rather than properly as the square of that velocity. However, linearization is widely defended and is justified by selecting an artificial or linearized drag coefficient chosen to minimize the total error in drag force over a wave cycle [2.18].

Frequency domain models employ spectral analysis techniques. Solutions of the resulting harmonic stress amplitude are obtained for waves of unit amplitude (half the wave height) at many discrete frequencies in the domain of frequencies of interest. These solutions are called response amplitude operators or RAO's. A plot of the RAO's vs frequency (as shown in Figure 2.3) is an approximation of the transfer function, $H(\omega)$, although the analytical form of the transfer function is not usually obtained. The assumption is made that the response of the structure is linearly related to the wave amplitude. Thus, it is only necessary to analyze the structure and obtain one transfer function to examine its response to many varied seastates. However, it is necessary to obtain different transfer functions for varied azimuths of the unidirectional wave train.

The usefulness of the frequency domain analysis in the probabilistic approach to forecasting the fatigue stress history of the structure will be demonstrated below.

2.4.2 Forecasting the Stress Range History

The analysis methods described above enable designers to make predictions of the stress in members of the structure as a function of wave position and wave height for a quasi-static analysis or as a function of time or frequency for dynamic analysis. For fatigue life predictions, the long-term distribution of stress ranges is required.

Depending on the type of fatigue analysis to be performed, additional information may also be required. Mean stresses or load ratios may be important (as discussed in Section 3.3), although for S-N analysis of welded joints these effects are often ignored [2.19]. Cyclic frequency has an important effect in corrosion fatigue as discussed in Section 3.4. Often it is assumed that cyclic loading takes place at a constant characteristic frequency such as the zero-crossing period (the average period between points where the cyclic stress history crosses from below to above the mean stress). It may be possible that if a lower frequency were chosen as characteristic or if fatigue computations take the period of each cycle into account, predicted fatigue life may be considerably shorter. Sequence or load interaction effects can be significant, particularly in high-cycle fatigue. These effects are briefly discussed in Section 7.7. Linear damage models such as Miner's Rule exclude the possibility of taking sequence effects into account.

The following sections review some of the more common methods of forecasting the fatigue stress history and obtaining the required information for fatigue life prediction. Emphasis is placed on how these methods may impact the fatigue analysis and which methods are suitable for different structural and fatigue analysis techniques. The deterministic approach using quasi-static analysis and a wave exceedence diagram is first discussed, followed by the Weibull method for long-term distribution of stress ranges, the Nolte-Hansford model based on long-term distribution of wave heights, and the spectral approach along with cycle counting methods. Finally, consideration is given to properly conducting simulation tests under corrosion fatigue conditions.

Deterministic Method with Wave Exceedence Diagram

A deterministic method is commonly employed for fatigue safety checks in design of offshore structures. Wave exceedence diagrams, which describe the number of exceedences of a given wave height in the design service life of the structure, are obtained from oceanographic data for each wave direction considered. A quasi-static structural analysis is performed to determine a stress range associated with each discrete wave height, and the number of occurrences of that stress range is obtained from the exceedence diagram. Mean stress information may also be obtained from the quasi-static analysis, and cyclic frequency can be assumed to correspond to the wave period provided these data are available. The quasi-static analysis may miss significant dynamic response at resonant frequencies. Sequence effects can only be included by artificially sequencing the stress ranges for fatigue analysis. The value of the deterministic method is its simplicity when used with linear damage accumulation models.

Long-Term Weibull Distribution Method

A simpler method for describing the long-term stress ranges assumes that this distribution can be approximated by a Weibull model. The exceedence curve for such a distribution is given as:

$$P(S \geq s) = e^{-\left(\frac{s}{\delta}\right)^{\xi}} \quad s, \delta, \xi > 0 \quad (2.3)$$

where

$P(S \geq s)$ = the probability of $S \geq s$

S = fatigue stress range, a random variable

s = specific value of stress range (ordinate of the exceedance curve)

δ = scale parameter = $s_m / [\ln N_T]^{1/\xi}$

ξ = Weibull shape parameter

s_m = largest expected stress range during the life of the structure

N_T = total number of stress ranges during the life of the structure

Use of this method involves establishing δ based on the design wave (highest wave height expected during lifetime of the structure) and corresponding design stress range. The shape parameter ξ is established for the location and type of platform; typical values include [2.20]

- o $\xi \leq 0.5$ for shallow water template platforms in the Gulf of Mexico
- o $\xi = 0.5$ to 0.8 for template platforms outside the Gulf of Mexico with some dynamic amplification
- o $\xi = 1.0$ for semisubmersible and gravity platforms
- o $\xi = 1.4$ for an upper bound for platforms in severe wave climate with significant dynamic amplification [2.21,2.22].

This method inherently precludes rational estimation of mean stress, cyclic frequency, and sequence effects because of the limited information involved. However, it is precisely this simplicity which makes the method so attractive for design purposes.

Nolte-Hansford Method

A third method for describing long-term wave and stress range distributions and fatigue linear damage in closed form was developed by Nolte and Hansford [2.23]. Using this method, the long term distribution of wave heights is assumed to be either Weibull or log-normal [2.24]. Unlike linearized analysis, the stress range is described by the empirical form:

$$s = \psi H^\phi$$

where

s = stress range

H = wave height

ψ ; ϕ = parameters determined from quasi-static or dynamic structural analysis

The parameter ϕ ranges from 1.0 (for linear analysis) to 2.0, with 1.5 being a typical value for platforms in the Gulf of Mexico [2.20]. The value of the Nolte-Hansford method is that it provides a simple description of fatigue damage without resorting to computer analyses for the structural response.

Spectral Approach and Cycle Counting

The spectral approach to forecasting the short-term distribution of stress ranges is based on either 1) transfer functions developed with frequency domain analysis and the wave energy spectrum or 2) transformation of stress-time histories obtained with time domain analysis into the power spectral density function of the response called the response spectrum. The

wave energy spectrum (also termed power spectrum or spectral density function) is used to characterize the distribution of the total energy per unit area of the sea surface over all wave directions and frequencies. The sea surface energy is constantly varying in intensity, but if the assumption is made that the sea-state is stationary (i.e., the statistical properties of the wave elevation time history are constant) during a small time interval (e.g., two or three hours), the sea-state can be treated as a stationary random process, and the instantaneous wave elevation at a fixed location may be treated as a stationary random variable.

The wave energy spectrum can be obtained directly from oceanographic data with Fourier transforms of wavestaff records. To obtain directional spectra, multiple wavestaffs are required and the analysis is very complex.

A special case of the wave energy spectrum is the point spectrum, a spectrum which only describes the distribution of energy over frequencies; i.e., the spread of wave energy in different directions is not taken into account. Such a spectrum would be computed from wave amplitude-time histories measured by a single wavestaff at a fixed location. Point spectra are often modified with a "spreading function" to account for directionality of the sea-state [2.25].

The physical interpretation of wave energy spectra is facilitated by considering the point spectrum. The point spectrum, $S_\xi(\omega)$, is a function such that any increment of area under its graph is proportional to the total energy of component waves in that band of frequencies. Since the energy can be stated in terms of the square of the wave amplitude, it follows that the wave amplitude is proportional to the square root of the area under the spectrum.

Consider the sea spectrum in Figure 2.4(a). The wave elevation time history represented by this spectrum, $\xi(t)$, may be represented as the sum of an infinite number of harmonic waves [2.25]:

$$\xi(t) = \lim_{\delta\omega \rightarrow 0} \sum_{n=1}^{\infty} \cos[\omega_n t + \varepsilon(\omega_n)] [2S_\xi(\omega_n)\delta\omega]^{1/2} \quad (2.4)$$

where $\varepsilon(\omega_n)$ is the random phase angle (uniformly distributed from 0 to 2π) of each component. A good mathematical model of the sea is obtained by considering at least 15 component waves [2.25], as shown in Figure 24(b). The algebraic sum of these component waves will resemble a typical wave elevation time history such as that shown in Figure 24(c). Because of the random phase angle, ε , the wave energy spectrum actually represents an ensemble of an infinite number of possible wave elevation-time histories for the particular sea-state.

As an alternative to measuring wave spectra, there are several analytical forms postulated which adequately describe the shape of wave energy spectra particular to certain areas of the world and certain conditions. Probably the most common is the Pierson-Moskowiz [2.26] formulation for fully developed seas (i.e., the wind has sufficient fetch and duration to bring the sea up to steady state) and derivatives of Pierson-Moskowitz formulations (e.g., P-M-B and ISSC) which are not limited to fully developed seas. The JONSWAP model [2.27], developed from North Sea data, is also not limited to fully developed seas. Another spectral formulation commonly used for the South Pacific Ocean is the Bretschneider model [2.28].

These formulations are based on at least two parameters, generally the significant wave height and either the average zero-crossing period or peak spectral frequency. The significant wave height is a traditional parameter for characterizing sea-state intensity and approximates what an observer would estimate the average wave height to be. By definition, the significant wave height is the average of the one-third highest wave heights. The zero-crossing period is the average time interval between consecutive crossings of the wave elevation time history from below to above the mean. The peak spectral frequency is the mode of the wave energy spectrum.

The transfer function obtained from frequency-domain analysis gives the ratio of the amplitude of the resultant stress in a particular location of the structure to the amplitude of a unidirectional wave as a function of frequency. The time varying portion of the stress response can be characterized by a spectrum, $S_R(\omega)$, called the response spectrum. Since the spectral density is proportional to the square of the wave amplitude, it can be shown that

$$S_R(\omega) = H(\omega)^2 S_\xi(\omega) \quad (2.5)$$

where $H(\omega)$ is the transfer function relating stress amplitude to wave amplitude. An example of a response spectrum is shown in Figure 2.5. This response spectrum was calculated from the sea energy spectrum in Figure 2.4 and the transfer function in Figure 2.3. The response spectrum can also be obtained from the simulated stress history output from a time domain analysis by performing a Fourier transform on the stress history.

The distribution of stress ranges during the period of the stationary sea condition is called the short-term statistics. An assumption (supported by empirical data) that the random stress time history is Gaussian or normally distributed enables the description of these statistics by the moments of the stress response spectrum about the origin:

$$M_{n\sigma} = \int_0^{\infty} \omega^n S_R(\omega) d\omega . \quad (2.6)$$

The area under the spectrum, or zero order moment, $M_{0\sigma}$, is equivalent to the variance of the stress time history; thus, the rms (root-mean square or standard deviation) is equivalent to the square root of $M_{0\sigma}$.

The average zero-crossing period, T , or average period of time between which the time history passes from below to above the mean of the time history, is related to the zero and second order moments:

$$T_\sigma = 2\pi \sqrt{\frac{M_{0\sigma}}{M_{2\sigma}}} . \quad (2.7)$$

The average period between consecutive peaks, generally smaller than the zero-crossing period, is related to the second and fourth order moments:

$$T_{p\sigma} = 2\pi \sqrt{\frac{M_{2\sigma}}{M_{4\sigma}}} = T_\sigma \sqrt{1 - b_\sigma^2} \quad (2.8)$$

The spectral width parameter, b_σ , a measure of the irregularity of the sea, is defined by $M_{0\sigma}$, $M_{2\sigma}$, and the fourth order moment, $M_{4\sigma}$, as:

$$b_{\sigma} = \sqrt{1 - \frac{M_2^2}{M_{0\sigma} M_{4\sigma}}} \quad 0 \leq b_{\sigma} \leq 1 \quad (2.9)$$

where $b_{\sigma} = 0$ corresponds to an infinitely narrow spectrum; i.e., the response is narrow-banded or concentrated at one frequency.

For nonzero spectral widths (wide-band processes) there exist complicated expressions for the distribution of stress peaks [2.29], but it is not clear how the distribution of stress ranges should be obtained. Offshore structures in general exhibit a wide-banded response, with b_{σ} on the order of 0.5 and larger. It is both conservative and computationally appealing to consider a narrow-banded approximation of the response, as will be discussed below. Such approximations bear little resemblance to the actual wide band response, and in order to get information on the probable sequence and magnitude of individual stress ranges, it is necessary to generate a Monte-Carlo simulation of the stress history and perform cycle counting.

There are several schemes for counting stress ranges from a stress-time history. Wirsching [2.30] has provided a review of cycle counting methods and their impact on fatigue design. The rainflow cycle counting method [2.31, 2.32] counts complete stress ranges in terms of closed stress-strain hysteresis loops [2.33]. Thus, this method counts small stress reversals (like those pointed out in the irregular or wide band stress history in Figure 2.5) as well as the larger stress reversals within which they are contained. It is normally agreed that this method produces the best results when used to count cycles for estimation of both crack initiation and propagation fatigue lives [2.33].

Rainflow cycle counting is capable of accounting for all the important loading variables in fatigue: stress range, mean stress, frequency, and sequence. It would be interesting to perform fatigue life calculations on a cycle-by-cycle basis, using a crack growth rate or S-N curve for the particular period (frequency) of each closed stress-strain hysteresis loop. It may be that because of the frequency dependence of corrosion fatigue resistance, cycles at some frequency lower than the assumed characteristic frequency (zero crossing rate or the peak spectral frequency) would be responsible for a larger share of the calculated fatigue damage, even though there might be

fewer cycles with a smaller magnitude at that frequency than at the assumed characteristic frequency.

The approach often taken to counting stress ranges from wide-band spectral data is to make the assumption that the spectral width, b_σ , is equal to zero, thus defining a narrow-band process with a variance equivalent to the corresponding wide-band process. The stress-time history of the equivalent narrow-band process has a very regular appearance (Figure 2.7); i.e., the stress reversals contain no small interruptions like those in Figure 2.6.

There is no need to simulate the stress-time history because for $b_\sigma = 0$ the exceedence curve for stress ranges is given by the Rayleigh function, which is defined by the zero moment or variance of the stress response spectrum:

$$P(S > s) = e^{\frac{-s^2}{8M_0}} \quad (2.10)$$

where:

S = a random variable describing the occurrence of stress ranges

s = a specific value of the stress range

M_0 = the variance of the stress process or zero order moment of the response spectrum

Because offshore structures have spectral widths typically greater than 0.5, one is inclined to assume that the narrow-band assumption is not valid. Recall that the average period between peaks (T_p) and the zero crossing period (T) are related, i.e., $T_p = T \sqrt{1 - b^2}$. Thus for a spectral width of 0.5, $T_p = 0.87T$, indicating that there are 13 percent more peaks than zero crossings. Therefore, the equivalent narrow-band history has 13 percent less cycles than the wide-band history. Since the variance of the narrow-band history is equivalent to that of the wide-band history, the number of occurrences of larger stress cycles is overestimated by the equivalent narrow-band history; consequently, fatigue life predictions based on equivalent narrow-band histories are conservative.

Wirsching [2.30, 2.34] has compared damage calculated with S-N curves and Miner's Rule for both the rainflow and narrow-band methods. His results suggest the narrow-band assumption is conservative in life predictions

by 17 to 38 percent. This is for the exponent in the basic fatigue curve ($NS^m = K$) of 3 to 6, respectively, in comparison with the rainflow method for wide-band ($b_g \geq 0.5$) spectra. Wirsching has also calculated rainflow correction factors to be applied to damage calculated in closed form with the basic fatigue curve and equivalent narrow-band method. These factors vary with the exponent in the fatigue curve and the spectral width and are valid for a wide variety of spectral shapes.

Dexter [2.35] compared crack propagation lives for an ocean structure in a variety of sea-states calculated on a cycle-by-cycle basis with both the rainflow counting method on the wide-band history and with the equivalent narrow-band history method. His results (limited to the particular structure, an ocean mining pipestring, and conditions) indicated that without load interaction effects (i.e., crack growth retardation), life predictions based on the narrow-band method were conservative by less than 25 percent with respect to rainflow counting. However, when interaction effects were included in the crack propagation analyses with the Wheeler model [2.39], this conservatism was reduced to less than 5 percent. The reason for this reduction in conservatism when load interaction effects were included is that the overestimated numbers of large stress cycles in the equivalent narrow-band process caused additional crack growth rate retardation; i.e., the error in the number of occurrences was compensated by the retardation.

With the spectral approach, the long-term distribution of stress ranges can be obtained by a summation or sequencing of a series of short-term stress range distributions according to the long-term distribution of the sea-states. The latter can be obtained from a wave scatter diagram such as that shown in Figure 2.8 [2.29]. This diagram gives occurrences of significant wave height and crossing period combinations over the design life of the structure.

2.5 Consideration of Corrosion Fatigue Testing

The foregoing discussion of forecasting stress histories of offshore structures is relevant to the proper planning and execution of laboratory corrosion fatigue testing. These laboratory tests fall into two categories: 1) constant amplitude tests on conveniently configured coupons aimed at establishing a material's basic resistance to corrosion fatigue crack growth over the range of relevant loading and environmental variables and 2) variable

amplitude tests on a variety of geometries ranging from small coupons to full scale components aimed at simulating actual components and service conditions. Both categories of experiments are related in that basic properties tests are often used to predict the outcome of simulation tests. These exercises are essential to assessing such issues as the applicability of linear versus non-linear damage accumulation models, as well as to the overall evaluation of the utility of methods for corrosion fatigue life predictions. In order for any of the above types of laboratory tests to produce relevant data, information on spectral parameters needs to be considered in the experimental design.

Primary loading variables for constant amplitude tests include stress intensity factor range (or stress range in S-N tests), load ratio, and cyclic frequency. Stress intensity factor ranges of interest include those between the threshold stress intensity factor range (ΔK_{th}) and the critical stress intensity factor range (ΔK_c). ΔK_c can be related to the critical stress intensity and load ratio by the following relation:

$$\Delta K_c = K_c (1-R) \quad (2.11)$$

Typical upper bound values of K_c are on the order of $200 \text{ MPa} \sqrt{\text{m}}$ for materials used in offshore structures.

ΔK_{th} is influenced by a variety of variables, but typical lower bound values are on the order of $2 \text{ MPa} \sqrt{\text{m}}$. For da/dN versus ΔK relations typical for offshore structural steel in corrosion fatigue, these limits of ΔK correspond to a range of crack growth rate (da/dN) of 10^{-11} m/cycle to 10^{-3} m/cycle .

Although load ratios for offshore structures are often negative, the compressive portion of the stress range is generally considered inconsequential, apart from the potential benefits of relaxation of residual stresses. For testing purposes, load ratios from near-zero to 0.9 are of practical interest. The higher values of load ratio (0.7 to 0.9) will be more typical of tendons of tension leg platforms. Load ratio for testing should be chosen carefully since this variable has a profound effect on the crack growth rate and particularly on the threshold stress intensity factor range.

Cyclic frequency is a testing variable for which there is incentive to use values higher than those which occur in actual service. Higher test frequencies are directly related to test time and therefore test cost;

however, evidence indicates (Chapter 3.0) that this temptation should be avoided. Valid frequencies for corrosion fatigue tests range from 0.03 to 0.3 Hz. Most investigators have chosen a frequency between 0.1 and 0.2 Hz, although there is a need for data covering the broader range. The lower end of the frequency range (0.03 to 0.2 Hz) is associated with low-cycle, high- ΔK fatigue, as these frequencies are typical of the larger storm waves and swell which cause large stress ranges. However, tension leg platforms and other buoyant compliant structures may experience slow drift oscillations as low as 0.01 Hz. The upper end of the frequency range (0.1 to 0.3) is associated with high-cycle, low- ΔK fatigue, as these frequencies are typical of mild weather loading. Furthermore, the relevant test frequency depends on the specific structure and location. For example, storm waves at 0.1 to 0.15 Hz are associated with stiff structures in the North Sea, while resonance vibrations at 0.2 to 0.3 Hz are associated with flexible deep water structures such as tension leg platforms.

If it is only possible to test a particular material at one or a few frequencies, choice of the test frequency should be made on the basis of the most damaging frequency in the loading spectrum. A suggested procedure would be to select S-N or da/dN versus ΔK data for a similar material for which the effect of cyclic frequency is known quantitatively. The wide-band stress history should then be obtained from either Monte-Carlo simulation from spectral density functions or directly from time-domain analysis. Cycle-by-cycle fatigue damage calculations should be performed taking the crack growth rate (or damage $1/N$) for each cycle according to the actual frequency of that cycle, thereby taking the frequency effect into account. Tabulation of the resulting damage particular to each frequency should reveal the most damaging frequency for that particular material and the loading spectrum. This frequency may not be the peak spectral frequency. If the crack growth rate is a strong function of frequency, the most damaging frequency may be less than the peak spectral frequency.

The above discussion provides guidelines for selection of loading variables for constant amplitude tests. If the budget permits, it is recommended that test loading conditions be chosen as close as possible to service loading conditions and that the expected range of all variables be considered.

In order to confirm the validity of fatigue life prediction methods, it is useful to perform variable amplitude fatigue tests. The choice of loading for such tests is a formidable task. In general, the loading used in the test should be similar to that expected in service. There is, however, a need for standardized variable amplitude load histories applicable to specific classes of structures and geographic locations.

Ideally, to simulate the short-term wide-band random process of service loading, the short-term test load history should have roughly the same spectral content as the service load history. This means that there are a number of component frequencies in the test load history. The power (function of amplitude) of each frequency component in the test load history should be equivalent to the corresponding frequency component in the service load history. Also the non-stationary nature of the expected service load history should be simulated. Obviously, one can only guess at the sequence and duration of the successive short-term histories, but an educated guess based on the long-term sea-state distribution (e.g., wave scatter diagram) would enable the comparison of predicted lives to experimental lives under the closest to real conditions.

Unfortunately, there has been little corrosion fatigue testing under relevant variable amplitude load histories. Most often, the approach taken is the superposition of several Rayleigh distributed narrow band processes to replicate a long-term distribution, with stress ranges selected at random from this distribution. This was the approach used in the U.K.O.S.R.P. [2.36]. Advantages of the narrow-band histories lie in the ease of testing, including simplified hydraulic actuator demands, function generator programming, and cycle counting. The primary disadvantage is that a large number of small stress ranges are truncated from the history, the importance of which is debatable. Furthermore, there is effectively only one cyclic frequency in the load history, and the succession of various short-term histories is "mixed up," thereby confounding the evaluation of load interaction effects. For example, if successive short-term histories are used, large stress ranges would be succeeded by more large stress ranges if a particularly violent short-term history were in effect. If random selections from a long-term history were used, a large stress range would probably be succeeded by a small stress range, and the interaction would be significantly different. Teledyne Engineering Services, under contract to the Ship Structures Committee [2.37],

recently attempted to evaluate the effects of filtering an as-recorded stress history (to achieve a narrow-banded history) on the resultant lives of fatigue test specimens in air. Their conclusion is that the filtered components of the history were inconsequential; however, their experiment was nonenvironmental (which is not corrosion fatigue, and frequency would not be expected to be important) and consisted of only 25 minutes of one particular stress history.

Hartt of Florida Atlantic University [2.38] is undertaking wide-band corrosion fatigue tests which should be useful in evaluating certain of the above issues.

2.6 Summary

- o Cyclic stresses from repeated wave loading combined with static and residual mean stresses are usually the most significant loads with respect to corrosion fatigue.
- o Wind loading is significant in corrosion fatigue life if vortex shedding occurs or if the wind gusts create a cyclic loading condition. Current can also be important if vortex shedding occurs.
- o Linear wave theories generally produce acceptable estimates of wave forces except for slender, drag-dominated members in the splash zone.
- o Inaccuracies in drag and inertia (added mass) coefficients can substantially affect corrosion fatigue life.
- o There are three widely used methods for prediction of structural response to waves (i.e., quasi-static method, time-domain-integration method, frequency domain method). The time-domain-integration method is the more comprehensive and can accommodate a variety of nonlinear and transient phenomena. The frequency domain method is computationally more efficient and also provides for resonance and structural motion in the dynamic analysis. The transfer function obtained with frequency domain analysis is useful for a spectral approach to stress history forecasting. The quasi-static method is very simple and easy to interpret, ergo the popularity and wide use of this method.
- o A deterministic approach may be taken to forecasting of the stress range history, with a design wave and period and associated stress range defining the response to the particular sea conditions.
Multiple values of design wave and period are used to construct a

stress range history composed of blocks of constant stress ranges. This approach is simple and appealing, but only a few points of the wave energy spectrum are used, providing a limited and possibly unconservative description of the response. The method provides no rational basis for estimating time varying mean stress, frequency, or sequence of stress ranges.

- o The long-term Weibull distribution method for representing stress range distribution is derived from data or analysis and the shape of the Weibull distribution is determined empirically depending on the type and location of the structure. This method is also very simple and attractive, but consequently even more limited in estimating important loading variables in corrosion fatigue than the deterministic approach.
- o The Nolte-Hansford method is based on the long-term distribution of waves and provides an empirical nonlinear relation of stress range to wave height. This method is also limited in extracting important loading variables for corrosion fatigue other than the stress range.
- o The spectral approach can be used directly with frequency domain analysis and provides a probabilistic basis for stress range history forecasting. Used together with Monte-Carlo simulations and rainflow cycle counting, this method produces the best results of the forecasting methods reviewed, and all important loading variables can be ascertained (i.e., stress range, time-varying mean stress, frequency of individual stress cycles, and sequence).
- o The spectral approach is often used conservatively by replacing the wide-band stress response with an equivalent narrow-band process. Unfortunately, the narrow-band assumption precludes extracting relevant information from the stress history on time-varying mean stress, frequency, and sequence effects.

CHAPTER 2.0 REFERENCES

- 2.1 Johnston, L. P., "The Welded Tubular Joint Problem in Offshore Structures," First University of Texas/SPE Drilling and Rock Mechanics Conference, Paper SPE484, January 1963.
- 2.2 Laird, A. D. K., "Water Forces on Flexible Oscillating Cylinders," Proc. ASCE, Waterways and Harbors Div., 88, WW3 (August 1962).
- 2.3 Dolrymple, R. A., "Waves and Wave Forces in the Presence of Currents," Proc. Conf. Civil Engr. in Oceans, University of Delaware, 1975.
- 2.4 Dean, R. G., "Relative Validities of Water Wave Theories," Proc. ASCE Waterways and Harbors Division, 96, WW1, February 1970.
- 2.5 Hogben, N., and Standing, R. G., "Experience in Computing Wave Loads on Large Bodies," OTC Paper 2189, Proc. Offshore Technology Conference, Houston, Texas, 1975.
- 2.6 Wade, B. G., and Dwyer, M., "On the Application of Morison's Equation to Fixed Offshore Platforms," OTC Paper 27, Proc. Offshore Technology Conf., Houston, Texas, 1976.
- 2.7 Keulegan, G. H., and Carpenter, L. H., "Forces on Cylinders and Plates in an Oscillating Fluid," Journal Research National Bureau of Standards, 60, 44-40 (1958).
- 2.8 British Ship Research Association, "A Critical Evaluation of the Data on Wave Force Coefficients," OBFLAG Project 10, No. W278, 1976.
- 2.9 Hogben, N. G., "Fluid Loading of Offshore Structures, a State of Art Appraisal: Wave Loads," R. Inst. Naval Arch., (1974).
- 2.10 Chalerabarti, S. K., "Nonlinear Wave Forces on a Vertical Cylinder," Proc. ASCE, Hydraulics Div., 98, HY11, 1B95-1909, November 1972.
- 2.11 Chen, H. S., and Mei, C. C., "Oscillations and Wave Forces in a Man Made Harbor in the Open Sea," 10th Symposium on Naval Hydrodynamics.
- 2.12 "API Recommended Practice for Designing and Constructing Fixed Offshore Platforms," American Petroleum Institute, Washington, D.C., API RP2A, 11th Edition, January 1980.
- 2.13 "Requirements for Verifying the Structural Integrity of OCS Platforms," United States Geological Survey, Conservation Division, OCS Platform Verification Program, October 1979.
- 2.14 "Rules for Building and Classing Offshore Drilling Units," American Bureau of Shipping, New York, 1973.
- 2.15 "Rules and Regulations for the Construction and Classification of Offshore Platforms," Bureau Veritas, Paris, 1975.

- 2.16 "Offshore Installations Guidance on Design and Construction," Department of Energy, Her Majesty's Stationery Office, London, 1977.
- 2.17 "Rules for the Design, Construction, and Inspection of Offshore Structures," Det norske Veritas, Oslo, Norway, 1977.
- 2.18 Pauling, J. R., "An Equivalent Linear Representation of the Forces Exerted on the OTEC CW Pipe by Combined Effects of Waves and Current," Ocean Engineering for OTEC, OED, Vol. 9, ASME, 1980.
- 2.19 Gurney, T. R., and S. J. Maddox, "A Re-Analysis of Fatigue Data for Welded Joints in Steel," Welding Institute Report E/44/72, Abington, Cambridge, England, 1972.
- 2.20 Wirsching, P. H., "Fatigue Damage Assessment Models for Offshore Structures," Earthquake Behavior and Safety of Oil and Gas Storage Facilities, PVP, Vol. 77, ASME, 1983.
- 2.21 Marshall, P. W., "Problems in Long Life Fatigue Assessment for Fixed Offshore Structures," ASCE Water Resources Convention, San Diego, Preprint 2638, 1976.
- 2.22 Marshall, P. W., and Luyties, W. H., "Allowable Stress for Fatigue Design," presented at BOSS '82, Boston, MA, August 1982.
- 2.23 Nolte, K. G., and Hansford, J. E., "Closed Form Expressions for Determining the Fatigue Damage of Structures Due to Ocean Waves," OTC Paper 2606, May 1976.
- 2.24 Wirsching, P. H., Stahl, B., and Nolte, K. G., "Probabilistic Fatigue Design for Ocean Structures," ASCE Journal of the Structural Division, Vol. 103, No. ST10, October 1977.
- 2.25 J. E. Comstock, ed., Principles of Naval Architecture, SNAME, New York, 1967, p. 616.
- 2.26 Pierson, W. J., and Moskowitz, L., "A Proposed Spectral Form for Fully Developed Wind Seas Based on the Similarity Theory of S.A. Kitaigorodskii," J. Geophys. Res., 69, 5181 (1964).
- 2.27 Chakrabarti, S. K., and Snider, R. H., "Modeling of Wind Waves with JONSWAP Spectra," Proc. Modelling, 120-39 (1975).
- 2.28 Bretschneider, C. L., "Hurricane Design Winds and Waves and Current Criteria for Potential OTEC Sites," University of Hawaii, James K. Look Lab., Report No. 79-45, April 1979.
- 2.29 Vugts, J. H., and Kinra, R. K., "Probabilistic Fatigue Analysis of Fixed Offshore Structures," Journal of Petroleum Technology, April 1978, pp. 657-67.
- 2.30 Wirsching, P. H., "Digital Simulation of Fatigue Damage in Offshore Structures," Computational Methods for Offshore Structures, AMD, Vol. 37, ASME, 1980.

- 2.31 Endo, T., et al., "Damage Evaluation of Metals for Random or Varying Loading - Three Aspects of the Rainflow Method," Proceedings of the 1974 Symposium on Mechanical Behavior of Materials, Vol. 1, The Society of Materials Science, Japan, 1974.
- 2.32 Matsuishi, M., and Endo, T., "Fatigue of Metals Subjected to Varying Stress," presented at the 1968 Japan Society of Mechanical Engineers Conference, held at Fukuoka, Japan.
- 2.33 Dowling, N. E., "Fatigue Failure Predictions for Complicated Stress-Strain Histories," Journal of Materials, Vol. 7, No. 1, March 1972.
- 2.34 Wirsching, P. H., and Light, M. C., "Fatigue Under Wide Band Random Stresses," ASCE Journal of the Structural Division, July 1980.
- 2.35 Dexter, R. J., "Choice of Inspection/Repair Period for Offshore Structures With Replaceable Members," to be published in Proc. Third International and Offshore Mechanics and Arctic Engineering Symposium, ASME, 1984.
- 2.36 Pook, L. P. and A. F. Greenan, "The Effect of Narrow-Band Random Loading on the High Cycle Fatigue Strength of Edge-Cracked Mild Steel Plates," Int. J. Fatigue, January 1989.
- 2.37 Teledyne Engineering Services, "Fatigue Considerations in View of Measured Load Spectra," Ship Structure Committee SR-1254, Tech. Rep. TR-3049-4.
- 2.38 Hartt, et al., Technical Program Review, API Committee Meeting, Houston, 1982 OTC.
- 2.39 Wheeler, O. F., "Spectrum Loading and Crack Growth," J. Basic Eng. Trans. ASME, Series D, Vol. 94, p. 181, 1972.

TABLE 2.1. INFLUENCE OF VARIOUS LOADINGS ON FATIGUE
AND FAST FRACTURE IN MARINE STRUCTURES

Type of Loading	Contribution
Wave	Fatigue Crack Initiation and Propagation
Current and Wind (Static and Quasi-Static)	Mean Stress (R ratio) in Crack Initiation and Propagation Fast Fracture
Current and Wind (Dynamic)	Fatigue Crack Initiation and Propagation
Deadweight	Mean Stress (R ratio) in Crack Initiation and Propagation Fast Fracture
Fabrication	Mean Stress (R ratio) in Crack Initiation and Propagation Fatigue Crack Initiation Initial Flaw Size in Crack Propagation
Launching/Installation	Crack Initiation Fast Fracture
Live Loads	Fatigue Crack Initiation and Propagation Fast Fracture
Transportation	Fatigue Crack Initiation and Propagation Fast Fracture
Buoyant and Hydrostatic	Mean Stress (R ratio) in Crack Initiation and Propagation Crack Initiation Fast Fracture
Foundation Movement/ Earthquake	Crack Initiation Fast Fracture
Floating Ice Impacts	Crack Initiation Fast Fracture

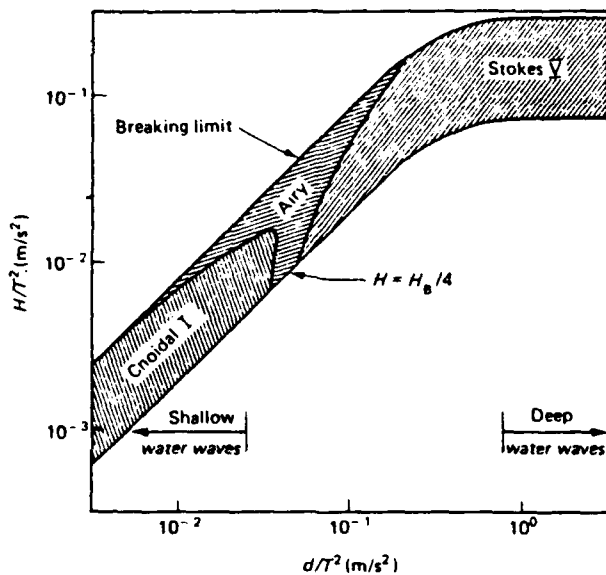


FIGURE 2.1. PERIODIC WAVE THEORIES PROVIDING BEST FIT TO DYNAMIC CONDITION

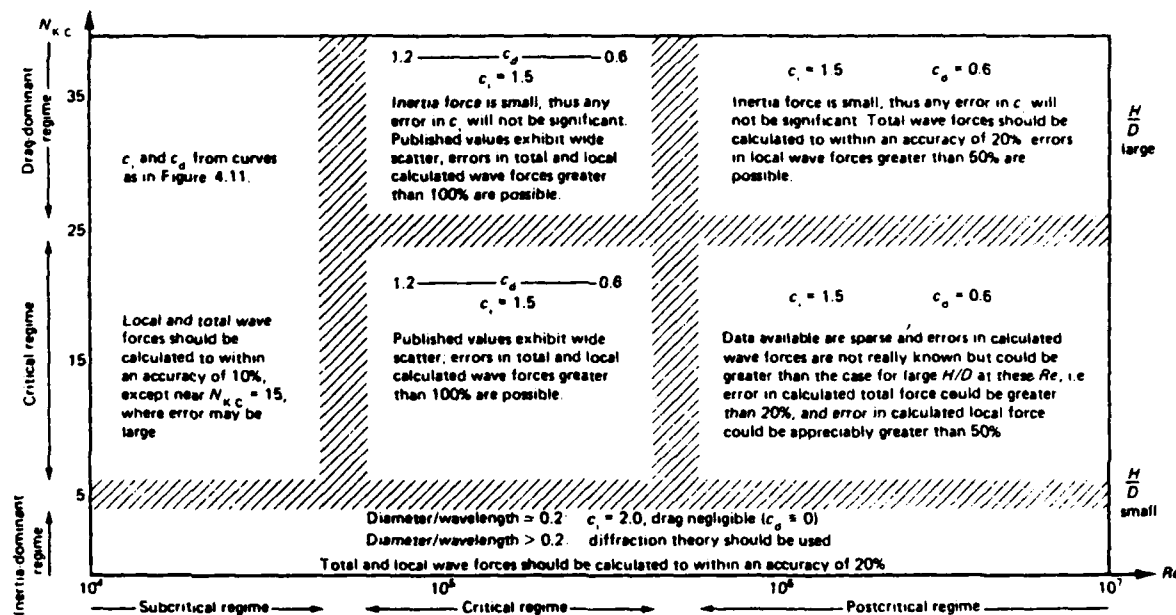


FIGURE 2.2. C_I AND C_D AS FUNCTIONS OF Re AND N_{KC} , APPRAISED FROM THE LITERATURE FOR SMOOTH, VERTICAL, SURFACE-PIERCING CYLINDERS

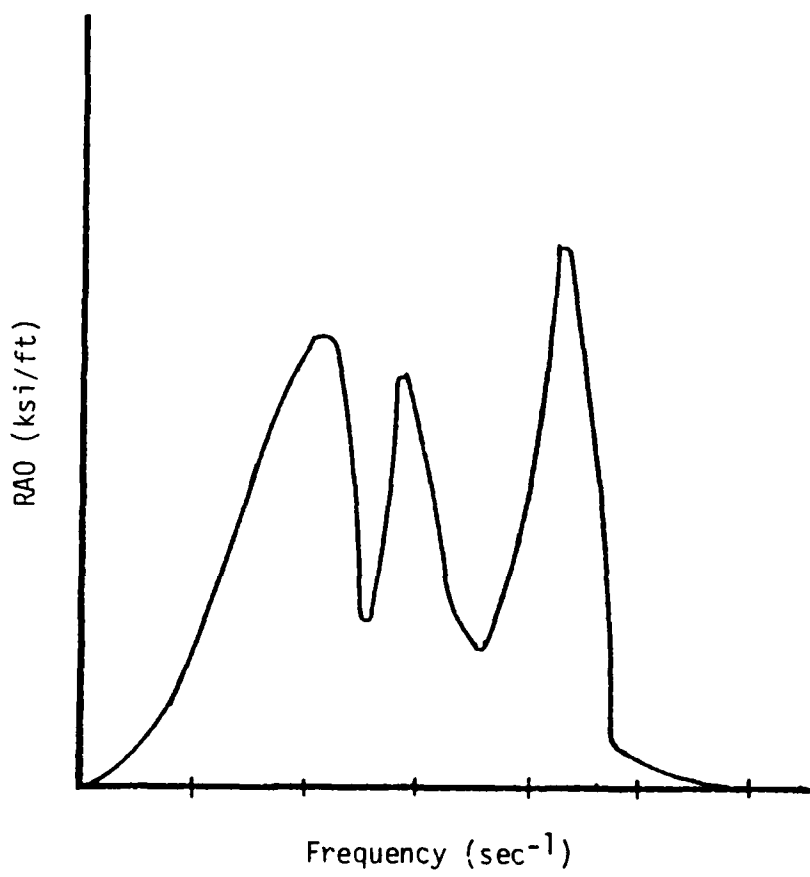
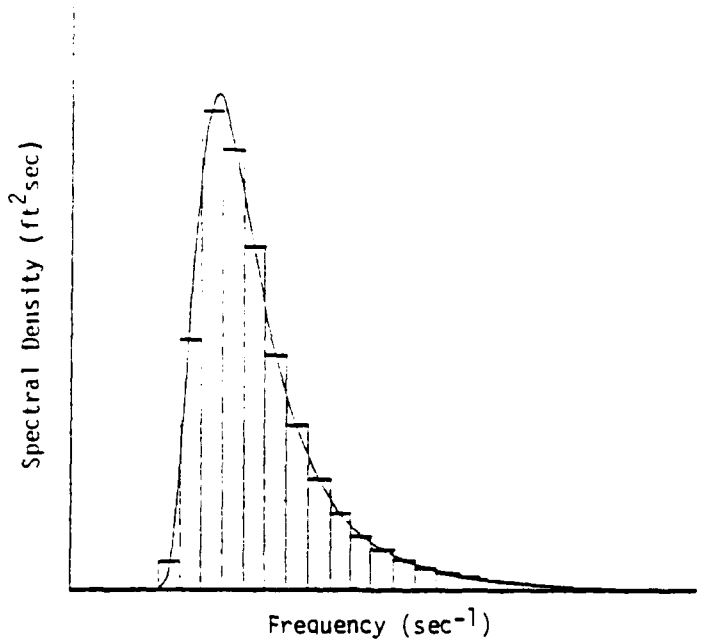
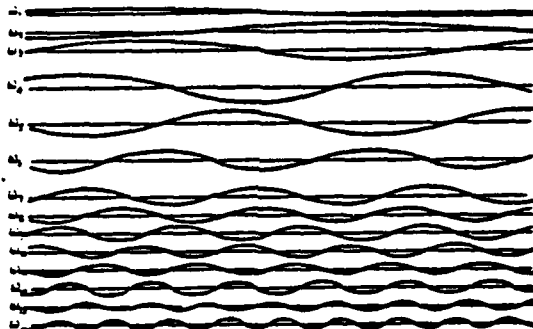


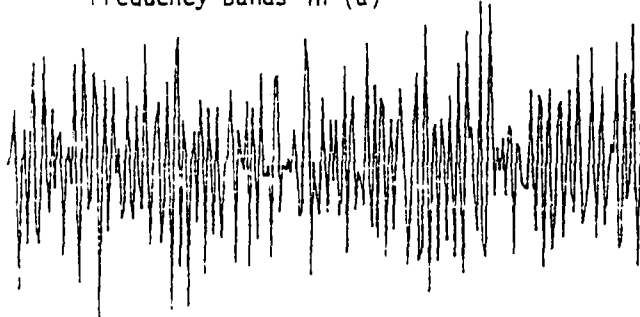
FIGURE 2.3. TRANSFER FUNCTION FOR STRESS AT
A CRITICAL LOCATION IN THE STRUCTURE



(a) Sea Energy Spectrum



(b) Component Waves Represented by Incremental Frequency Bands in (a)



(c) Sum of the Component Waves of Simulated Time History of Wave Elevation

FIGURE 2.4. CONCEPTUAL REPRESENTATION OF SEA ENERGY SPECTRUM

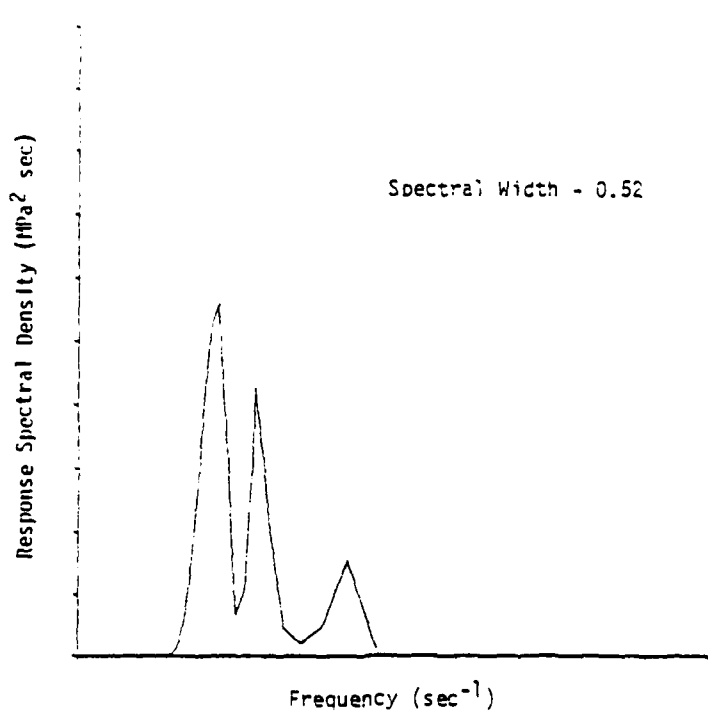


FIGURE 2.5. RESPONSE SPECTRUM FOR STRESS AT A CRITICAL LOCATION IN THE STRUCTURE

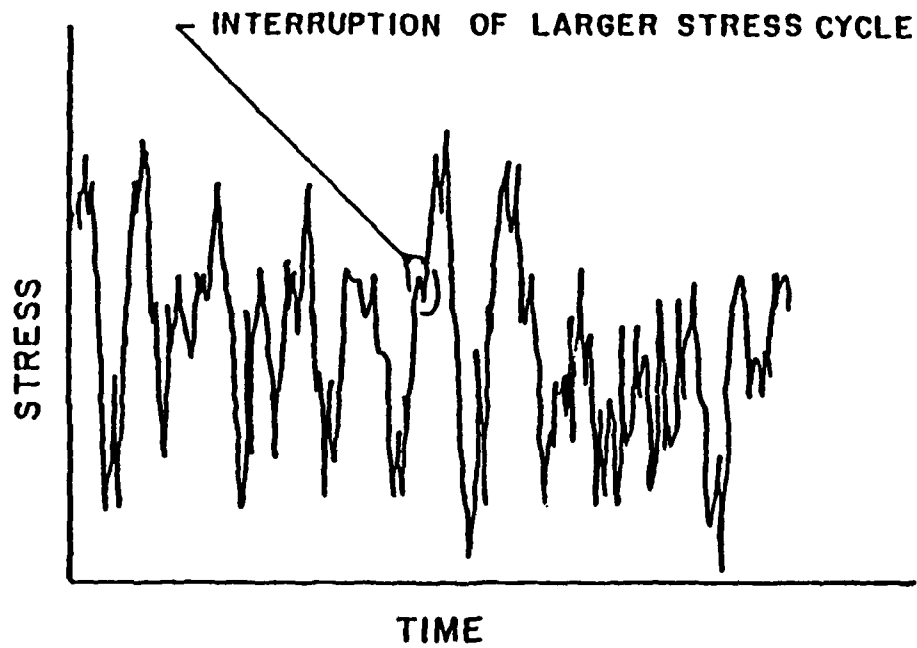


FIGURE 2.6. WIDE-BAND STRESS HISTORY SHOWING INTERRUPTION OF LARGE STRESS CYCLE

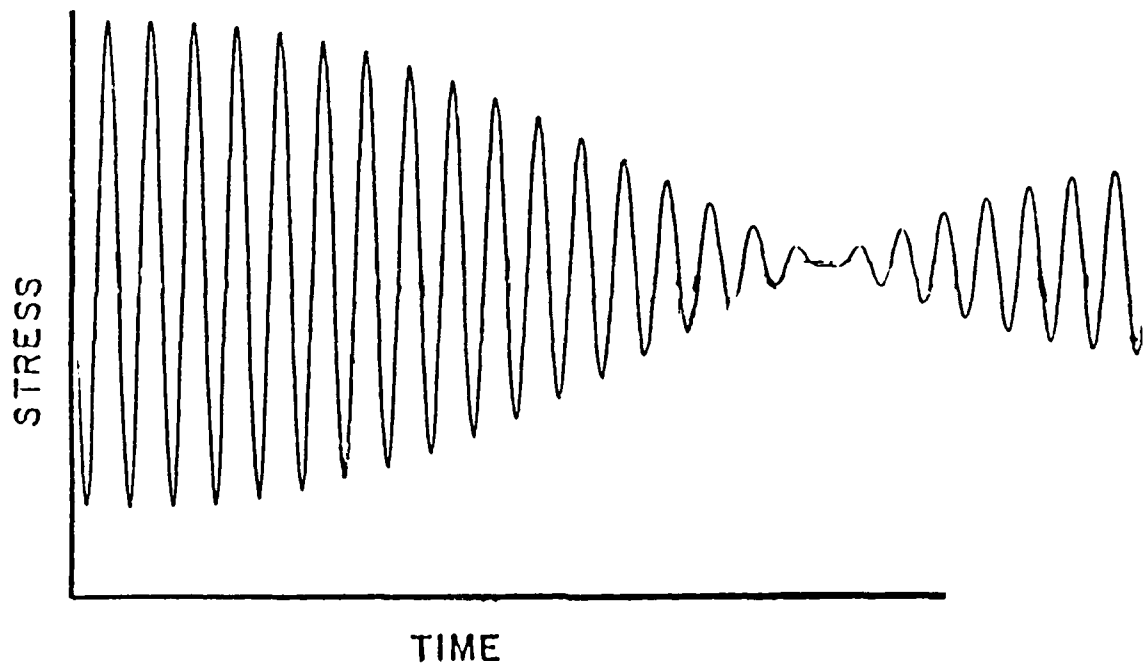


FIGURE 2.7. NARROW-BAND STRESS HISTORY

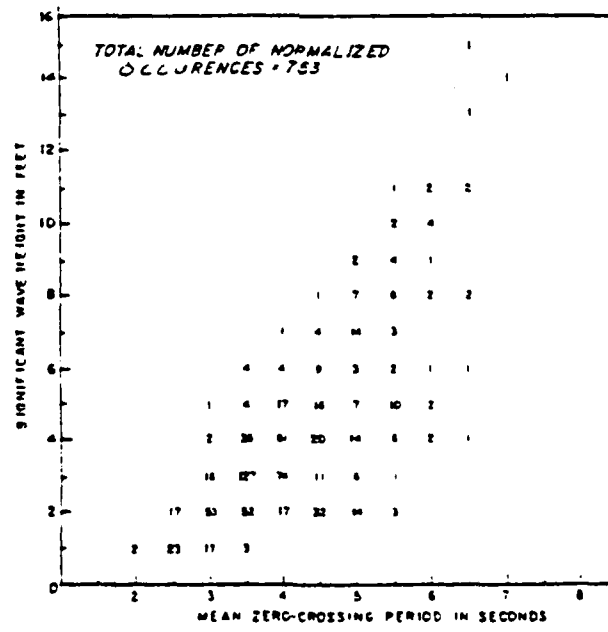


FIGURE 2.8. WAVE-SCATTER DIAGRAM

3.0 EFFECT OF LOADING VARIABLES ON CORROSION FATIGUE RESISTANCE

3.1 Introduction

The resistance of materials to corrosion fatigue is generally characterized using either of two approaches: (1) the classical S-N approach where cycles to failure of initially uncracked, notched or unnotched, specimens are determined as a function of nominal stress, or strain—either maximum or alternating values; or (2) the fracture mechanics approach where the fatigue crack growth rate, da/dN , expressed as the amount of crack extension per fatigue cycle, is determined as a function of the range of stress intensity factor, ΔK .

The S-N approach measures the total fatigue life of a planar or cylindrical specimen. As illustrated schematically in Figure 3.1, the measured total life is composed of cycles required for crack initiation, as well as for crack propagation. Note that in general the initiation and propagation curves of Figure 3.1 cross over each other and demonstrate that high-stress cycling in the so-called "low-cycle fatigue" regime produces specimen lives which are dominated by crack propagation since cracks are initiated very early in the testing; the opposite is true in the low-stress, "high-cycle fatigue regime"—that is, crack initiation is a long process and thereby controls the specimen life. Consequently, lives in the intermediate stress and cycle regime result from varying combinations of initiation and propagation cycles. It should be emphasized that in the high-cycle regime the above generality holds only for smooth specimens of the type most often used in S-N tests which contain no cracks or crack-like defects. This is generally not the case for welded coupons and even less likely the case for large structures containing a multitude of welded joints.

The fracture mechanics approach is based on the premise that the pre-existing cracks or crack-like defects—for example, large unfavorably oriented inclusions or any one of a variety of weld defects—are generally present in large, complex structures from the day they are placed in service. Given these conditions and nominally elastic loading (usually guaranteed by reasonable design), ΔK uniquely characterizes the cyclic stress/strain field at the crack tip and thereby provides a fundamental representation of the "driving force" for the rate of crack growth. The primary advantage of expressing

fatigue crack growth data in these terms is that results are for the most part independent of specimen geometry; thus, not only can data from a variety of test specimens be compared on an equal basis, but more importantly, small specimen results can, through proper analysis, be related to the behavior of large structures as described in Chapter 6.0.

In this chapter, both S-N and fracture mechanics data are considered; however, the latter are emphasized since most of the systematic studies of the primary loading variables have been conducted within the framework of linear elastic fracture mechanics. These primary variables include (1) stress or stress intensity range, (2) mean stress or stress ratio, (3) cyclic frequency, and (4) cyclic waveform. In addition, consideration is given to mathematical representation of data for design as well as to the confounding influences of crack size and nonsteady state crack growth.

The goal of this chapter on loading variables, as well as in the following chapter on environmental variables, is to briefly summarize the influence of the primary variables on corrosion fatigue resistance and identify problem areas. Thus, the objective is a critical state-of-the-art review rather than an exhaustive compilation of data. The latter have been accomplished in several previous reviews, particularly in the recent thorough report of Jaske, et al. [3.1].

The approach taken herein is to first present a general discussion of each of the significant loading variables identified above using data which most clearly illustrate the characteristic influence of the particular variable. Additional factors which can confound the assessment of corrosion fatigue resistance and thereby complicate the prediction of corrosion fatigue life are also discussed. With this information as background, mathematical relations between da/dN and ΔK are established for use in fatigue life predictions under various categories of loading and environmental conditions.

3.2 Effect of Stress and Stress Intensity Factor

Characterizing the corrosion fatigue resistance of structural and low-alloy steels using the S-N approach is typified by the data given in Figure 3.2 for a C-Mn steel tested in laboratory air and in a 1% NaCl environment [3.2]. In both environments the cyclic lives increase exponentially with decreasing stress amplitude.* However, in the air environment the lower

*Stress amplitude is defined as one-half of the stress range.

stress amplitudes produce cyclic lives which become increasingly sensitive to stress amplitude and eventually exceed the test duration. This lower limiting stress amplitude is commonly termed the fatigue limit or endurance limit. The fatigue limit is somewhat arbitrarily defined since it depends on test duration; therefore, it is good practice to reference this measurement to a test duration--typically durations of 10^6 to 10^7 cycles are used. By contrast, the data in Figure 3.2 for the saltwater environment exhibit significantly shorter lives than those in air, at a given stress amplitude. Furthermore, no distinctive endurance limit is detectable even though testing was conducted out to 10^9 cycles. It should be noted that the latter tests were conducted under freely corroding conditions; as discussed in Section 4.3, applying cathodic polarization to the test specimen tends to shift the saltwater data towards the air data. Nevertheless, regardless of the environmental conditions, the cyclic lives are always markedly sensitive to stress amplitude (or range).

While S-N results such as those in Figure 3.2 do provide a measure of corrosion fatigue resistance, it is worth noting that these results are not strictly properties of the material-environment system under investigation. For example, they will also depend on such factors as overall specimen size and geometry, surface finish, and details of machined notches, should they be present.

If one now measures the corrosion fatigue resistance of a material in terms of its crack growth properties and expresses the results in terms of the crack tip stress intensity factor, ΔK , an analogous but somewhat more complex picture emerges than that given by S-N testing. Based on phenomenological observations gathered over the last 20 years, the steady-state corrosion fatigue crack growth rate as a function of ΔK can be grouped into three basic types of response as illustrated in Figure 3.3 [3.3].

In each case, fatigue crack growth data for an inert environment are given in Figure 3.3 as a reference. These results correspond to the purely mechanical process of fatigue crack extension by deformation-controlled mechanisms and are characterized by three distinctly different regions whose growth rate behavior exhibits different dependencies on ΔK . For most steels the Region I slopes of the $\log \Delta K$ - $\log da/dN$ curve range between values of 10 and 30, whereas the Region II slopes range between 2 and 4. Region III corresponds to the onset of unstable crack growth and is controlled by either the materials inherent fracture toughness, or alternatively, in highly ductile

materials, by plastic instability. Differences in growth rate between the "inert" environment curve and the "aggressive" environment curve define the materials sensitivity to corrosion fatigue.

The three types of response to corrosion fatigue are conveniently defined in terms of their relation to K_{ISCC} [3.4], the threshold stress intensity for stress corrosion cracking.* Type A represents those steel-environment systems which are relatively immune to stress corrosion cracking—that is, K_{ISCC} approaches K_{IC} —consequently, the enhancement in fatigue crack growth rates corresponds to a synergism between corrosion and mechanical fatigue. This interaction is manifested by increased growth rates and a decreased ΔK_{th} value. At high ΔK values, the high growth rates corresponding to the onset of mechanical instability become rate controlling. Under these conditions, the environmental component of cracking is negligible; thus crack rates coincide with those for the inert environment. Type B behavior is representative of material-environment systems which exhibit a significant sensitivity to stress corrosion cracking, that is with K_{ISCC} values substantially less than K_{IC} or K_c . Here the environmental effects are quite strong for $K_{max} > K_{ISCC}$ and negligible for $K_{max} < K_{ISCC}$. This type of behavior is predictable from a simple superposition of stress corrosion crack growth and purely mechanical fatigue crack growth [3.7, 3.8]. Type C behavior combines the two extremes of Type A and Type B behavior, with the former predominating when $K_{max} < K_{ISCC}$ and the latter predominating when $K_{max} > K_{ISCC}$.

The exact dependence of the corrosion fatigue crack growth rate on ΔK for any of the above three types of behavior is also dependent on the additional loading variables discussed in the remainder of this chapter, as well as the environmental variables considered in Chapter 4.0. At times it is difficult to discern which of the above categories best represents a given material-environment system, either because of inadequate data—generally in the near threshold regime—or because of confounding effects such as non-steady state crack growth. The latter is discussed in Section 3.5.

Examples from each of the above types of behavior are given in Figures 3.24 through 3.29 which represent data compiled from the literature on

* K_{ISCC} is ideally defined as the value of stress intensity below which stress corrosion crack growth will not occur. In practice this value may be difficult to determine since measurements can be dependent on test technique as well as test duration [3.5, 3.6]

structural and low alloy steels—these results are further discussed in Section 3.8.

3.3 Effect of Mean Stress or Load Ratio

Tensile mean stresses are known to decrease fatigue life, while compressive mean stresses increase fatigue life in smooth specimen tests conducted in laboratory air [3.10-3.12]. Most of these results have been obtained under strain-controlled conditions. This method of loading enables relaxation of the mean stress for large amounts of cyclic plasticity. Thus, mean stress effects tend to be small in the large strain amplitude, low-cycle regime, while becoming increasingly significant in the small strain, high-cycle regime where little or no plasticity precludes relaxation of the mean stress. This changing significance of mean stress is also observed in large structures containing notches since the contained plastic deformation in the notch region is nearly equivalent to strain control.*

Mean stress effects in smooth specimens exposed to aggressive environments are expected to parallel the behavior described above for air environments; however, surprisingly, these effects have not been examined.

Load-controlled tests on either smooth specimens or welded coupons have been extensively employed to study the corrosion fatigue resistance of structural and low alloy steels. These experiments traditionally employ either completely reversed loading or zero-to-tension loading.** Thus, there are little systematic data on the influence of load ratio on the fatigue life of initially uncracked specimens. Data comparisons are further hampered by the fact that load ratios of -1 and 0 often correspond to different specimen geometries as well as loading modes; thus, results are not directly comparable. While S-N tests on welded coupons contain variations in mean stress arising from the welding process, the magnitudes of these stresses are generally unknown.

*Actually, the plastic deformation at notches undergoes a combined stress-strain control, sometimes called Neuber control [3.13] since it is closely approximated by application of Neuber's rule [3.14].

**In load-controlled tests, it is convenient to characterize the mean stress in terms of the load ratio, $R = P_{min}/P_{max} = S_{min}/S_{max}$; thus, completely reversed loading corresponds to $R = -1$, while zero to tension loading corresponds to $R = 0$.

Mean stress effects have been more thoroughly examined in crack growth tests using fracture mechanics techniques. As in load-controlled tests of uncracked specimens, the mean stress is also characterized in terms of the load ratio ($R = P_{\min}/P_{\max} = S_{\min}/S_{\max} = K_{\min}/K_{\max}$). Although increasing mean stress, or load ratio, tends to increase the fatigue crack growth rate over a broad range of growth rates, the exact magnitude of this effect is specific to growth rate regime, material, and environment. Referring to the previously discussed regions of growth given in Figure 3.3 for inert environments, the most significant load ratio effects are observed in Regions I and III.

The increase in growth rates in Region III is linked to the onset of unstable crack growth as K_{\max} increases. Since $K_{\max} = \Delta K/(1-R)$, this behavior is described by letting $K_{\max} = K_{IC}$ or K_c under linear elastic loading. For highly ductile materials, exhibiting high K_{IC} values, Region III behavior generally corresponds to a plastic instability in the uncracked ligament and is given by $P_{\max} = \Delta P/(1-R) = P_{LL}$, where P_{LL} is the fully plastic limit load for the cracked member [3.15]. The relatively high toughness exhibited by materials employed in offshore structures (for example, K_{IC} values generally exceeding $200 \text{ MPa} \sqrt{\text{m}}$), combined with the fact that these structures operate in the high-cycle regime, causes the Region III behavior and its associated load ratio dependence to exert little influence on the fatigue life of these structures. This insensitivity to Region III growth is reflected in an insensitivity of the fatigue life to final crack size and is demonstrated in the sensitivity analysis of Section 7.5.4. The underlying reason for this behavior is the fact that fatigue lives in the high-cycle regime are controlled by the growth of small cracks whose rate of extension is several orders of magnitude less than that of Region III.

The above discussion demonstrates the importance of the Region I growth rates to the fatigue life of offshore structures. As mentioned previously, these near-threshold growth rates are also relatively sensitive to variations in mean stress or load ratio. This sensitivity is also reflected in the load ratio dependence of ΔK_{th} , as shown in Figure 3.4, for a variety of structural and low-alloy steels tested in laboratory air environments. These data were compiled from the literature, including results from two review papers [3.16, 3.17]. The materials and data sources represented in Figure 3.4 are given in Table 3.1. The rather large variability in results in Figure 3.4 is partially

due to the fact that ΔK_{th} , as well as Region I growth rates, is sensitive to steel microstructure (see Reference 3.24, for example). Undoubtedly, however, the complexities associated with low growth rate testing, as well as the lack of a standard test method [3.29], add to the observed variability in results. In addition, the measured ΔK_{th} value depends on test duration—thus, values need to be referenced to a minimum da/dN value in analogous fashion to the specification of a number of cycles for the fatigue endurance limit. Most of the ΔK_{th} values given in Figure 3.4 correspond to da/dN values of 10^{-10} to 10^{-11} m/cycle. This variation in the operational definition of ΔK_{th} further adds to the observed variability.

Several empirical relations have been proposed to describe the influence of R on ΔK_{th} :

Barsom, Reference 3.31

$$\Delta K_{th} = \Delta K_o (1 - aR); R > R' \quad (3.1a)$$

$$\Delta K_{th} = \beta \quad ; R < R' \quad (3.1b)$$

Klesnil and Lucas, Reference 3.32

$$\Delta K_{th} = \Delta K_o (1 - R)^\gamma \quad (3.2)$$

where ΔK_o = the value of ΔK_{th} at $R = 0$
 a, β, γ = empirical constants.

Barsom originally proposed equations (3.1) with $\Delta K_o = 7 \text{ MPa}\sqrt{\text{m}}$, $a = 0.85$ and $\Delta K_{th} = 6 \text{ MPa}\sqrt{\text{m}}$ as a lower bound for ΔK_{th} as a function of R for most steels (line 1, Figure 3.4). Based on Figure 3.5, a more conservative lower bound is provided by equations (3.1) with $\Delta K_o = 5 \text{ MPa}\sqrt{\text{m}}$, $a = 0.8$ and $\beta = 4 \text{ MPa}\sqrt{\text{m}}$ as shown by line 2. Using equation (3.2), with $\Delta K_o = 5 \text{ MPa}\sqrt{\text{m}}$ and $\gamma = 0.5$, provides somewhat different lower bounds to these data (line 3, Figure 3.4). Considering the variability in ΔK_{th} measurements, it is not possible to conclude which of these equations is most representative of the R-dependence of ΔK_{th} . Nevertheless, these results clearly illustrate the strong load ratio dependence of ΔK_{th} , as well as the near threshold growth rates. As

illustrated by the sensitivity analysis in Section 7.5.3, data in this regime will control the fatigue life of offshore structures.

Now let us consider the influence of load ratio on corrosion fatigue crack growth rates for steels exposed to seawater. Figure 3.5 provides results on the influence of load ratio on an X-70 linepipe steel in laboratory air and in 3.5% NaCl under both freely corroding and cathodic polarization conditions [3.30]. In all cases the trends are similar—specifically, growth rates at a given ΔK value increase with increasing R and the sensitivity to R increases at the lower growth rates. In addition, the influence of R on da/dN tends to be accentuated by the presence of the environment—this effect is most pronounced for the cathodically polarized specimen. The tendency for aggressive environments to accentuate load ratio effects is commonly observed. Data in Figures 3.6 and 3.7 on BS 4360 Grade 50D steel in laboratory air and in seawater, respectively, more clearly demonstrate this phenomenon [3.9]. The Region II air data of Figure 3.6 show very little dependence on load ratio, while seawater data of Figure 3.7 exhibit a significant increase in rates as R increases. Note also from Figure 3.7 that for the cyclic frequency of 0.1 Hz the data for $-1 \leq R \leq 0.1$ actually coincide with the air data, indicating no environmental enhancement, while the high- R growth rates are as much as six times faster.

What is clearly lacking with regard to fatigue life predictions in offshore structures is information on the load ratio dependence of ΔK_{th} and Region I growth rates in seawater at representative cyclic frequencies. Quite understandably, these data are sparse because of the extremely long test times and high cost associated with low growth rate, low frequency testing. The limited amounts of available low growth rate data in seawater are included in the summary plots of Section 3.8.

3.4 Effect of Cyclic Frequency and Waveform

In general the influence of time-dependent loading variables on fatigue resistance can have two distinctly different sources: (1) an inherent strain rate sensitivity of the material—this effect is independent of the specific environment and also occurs in inert environments, and (2) a rate dependence of the environmental component of corrosion fatigue. This effect arises from time-dependencies in the underlying kinetic process, or processes, which are

rate controlling*—for example, diffusion of reacting species through the liquid environment, or through solid oxides, a variety of surface reactions, and possibly, hydrogen diffusion, should a hydrogen embrittlement mechanism be operative.

Let us first consider the effect of frequency on fatigue and corrosion fatigue resistance, focusing on structural and low alloy steels. In S-N testing, it is common practice to conduct tests at cyclic frequencies in the range of 10 to 50 Hz using a fixed frequency for a given study, even when environmental influences are being examined. Thus, little information on the effect of cyclic frequency has been obtained in S-N testing. One study by Nishioka, et al., has reported a decrease in the corrosion fatigue strength (at 10^6 cycles) by about a factor of two, in a variety of carbon and low alloy steels in saltwater, as the frequency was lowered from several hundred Hz to about 1 Hz [3.35]. Similarly, Endo and Miyao have observed a frequency dependence of the fatigue life in a medium carbon steel tested in both tap water and saltwater; these results are shown in Figure 3.8 [3.36]. Neither of the above studies considered the possible influence of inherent strain rate effects on the fatigue life.

The influence of cyclic frequency on the fatigue crack growth rate in aqueous solutions has been more thoroughly investigated than have frequency effects in S-N testing. In most cases, fatigue crack growth rates in structural and low alloy steels have been found to increase as cyclic frequency decreases; thus, growth rate data are in qualitative agreement with the limited S-N results. This effect is illustrated in Figure 3.9 by Vosikovsky's data on an X-65 line pipe steel exposed to 3.5% NaCl under both freely corroding conditions, as well as cathodic polarization [3.37]. Interestingly, in both cases the influence of frequency appears to diminish in the low growth rate regime.

Figures 3.10 and 3.11 provide a summary of the influence of cyclic frequency on the intermediate (Region II) growth rates in a variety of structural and alloy steels. Data in Figure 3.10 on several HY-series steels exhibit a similar frequency dependence at ΔK values of $30 \text{ MPa}\sqrt{\text{m}}$ and $50 \text{ MPa}\sqrt{\text{m}}$. At

*These rate-controlling processes are potential sources of time dependencies, regardless of whether the material degradation occurs by a hydrogen embrittlement mechanism [3.33] or by a film rupture/anodic dissolution mechanism [3.34].

frequencies above about 0.01 Hz the rates are approximately proportional to $f^{-0.25}$, while at frequencies below 0.01 Hz the growth rates appear to be approaching a constant value. Figure 3.11 compares the HY steel data at $\Delta K = 30 \text{ MPa}\sqrt{\text{m}}$ with results from a wide range of steels. With the exception of the maraging steels, results tend to converge at 10 Hz. This convergence occurs since the frequency is too fast to allow an environmental contribution to the growth rates. At intermediate frequencies, the dependence of crack growth rate on frequency tends to be somewhat stronger in these steels than in the HY steels. Specifically, between 0.01 and 1 Hz the growth rate is approximately proportional to $f^{-0.5}$ (versus $f^{-0.25}$ in the HY steels). By comparison Hartt's data [3.46, 3.47] on smooth structural steel specimens show that the fatigue life is proportional to $f^{0.3}$ for frequencies of 0.5 Hz and above. Assuming that the fatigue lives of these smooth specimens are controlled by crack growth, and recognizing that $da/dN \propto N_f^{-1}$, gives crack growth rates which are proportional to $f^{-0.3}$. This result is in reasonable agreement with the frequency dependence shown in Figure 3.11, provided $f \geq 0.5$ Hz. Once again, several of the curves exhibit a tendency to level off at about 0.01 Hz, indicating a saturation of the environmental effect. This being the case, the maximum environmental effect for low load ratios in Region II is about a factor of ten. However, information on the frequency sensitivity of the important Region I rates is absent.

The only information on the role of material strain rate sensitivity on cyclic frequency effects is provided by results from a recent study by Davidson and Lankford on crack growth in a low carbon steel [3.48]. As shown in Figure 3.12, growth rates in both dry nitrogen—presumably a relatively inert environment for this material—and moist air respond to changes in frequency in opposite fashion to previously discussed results. These results suggest a significant influence of strain rate sensitivity on frequency effects in carbon steels. The strain rate sensitivity persists even when the growth rates are enhanced by the moist air environment (relative to the dry nitrogen environment). The convergence of results from both environments at about 6 Hz is consistent with the general observation that environmental effects in steels exposed to aqueous environments are absent at these frequencies. These results suggest that high strain rates, at least in carbon steels, promote fatigue damage. Presumably this process parallels the well-known loss of ductility which can accompany high strain rates in monotonic

loading. If this hypothesis is correct, it follows that the inherent frequency-environmental interaction in carbon steels is actually larger than that given in Figure 3.11 since these results also contain a frequency-strain rate interaction which acts in the opposite direction. From the practical viewpoint, there is no problem if these two effects are coupled, provided that their overall influence is empirically established. However, this complexity makes data extrapolation uncertain. These two sources of frequency effects need to be isolated when formulating physical models which may be utilized to extrapolate empirical results.

Variations in cyclic waveform have also been observed to influence fatigue crack growth rates in steels exposed to 3.5% NaCl. Barsom's data on a 12Ni-5Cr-3Mo steel subjected to five different waveforms are shown in Figure 3.13 [3.49]. Data generated in laboratory air were found to be independent of waveform and all fell within the indicated scatterband. In 3.5% NaCl at a frequency of 0.1 Hz, waveforms with rapid rise times gave rates nearly equal to the air data, while those with slow rise times showed a significant environmental effect. These results demonstrate the importance of rise time and suggest that most of the interaction between the material and environment occurs during the increasing portion of the loading cycle.

A more recent study of waveform effects in corrosion fatigue crack growth in a Ni-Cr-Mo steel provides additional support for the significance of rise time in the cycle [3.50]. Twenty-five different triangular and trapezoidal waveforms, having the characteristic components shown in Figure 3.14, gave growth rates which could be normalized by a waveshape parameter containing the rise time and total period of the cycle.

From a fundamental viewpoint the influences of cyclic frequency and waveform on corrosion fatigue behavior are likely to be controlled by the same underlying kinetic process, or processes. The identification and modeling of these rate-controlling processes is currently an active research area. Such studies have led to the correct prediction of the functional form of the frequency dependence of crack growth in the aluminum-water vapor system [3.51], although predictions of the absolute rates have not yet been achieved.

Regarding the practical significance of cyclic frequency and waveform effects, the former would appear to be of primary importance. The frequency cited as being most typical of offshore structures is about 0.1 Hz. However, these structures are also likely to experience loading cycles having both

higher and lower frequencies than this average or typical frequency. It would appear necessary to utilize established correlations between cyclic loading frequency and amplitude (that is, response spectra) in order to assess which cycles are most damaging and thus which frequencies are most significant. To our knowledge, this exercise has not been conducted for corrosion fatigue where damage accumulation is inversely related to cyclic frequency.

Although cyclic waveform effects represent interesting phenomena which should be useful in elucidating the fundamental nature of the material-environment interaction, their practical significance would appear to be minimal in offshore structures. Since these structures respond primarily to wave loading, the relevant waveforms will be approximately sinusoidal, triangular, or trochoidal [3.52-3.54]. Based on data in Figures 3.13 and 3.14, this class of waveforms should give nearly identical results--that is, a maximum corrosion fatigue crack growth rate. Since most empirical crack growth studies employ sinusoidal waveforms, these results can be appropriately used in cyclic life predictions without the need to include additional factors for waveform into the analysis.

3.5 Effect of Transient Crack Growth Rates

The basis of the fracture mechanics approach to structural lifetime prediction is a one-to-one relationship between the rate of crack growth and the crack tip stress intensity factor. However, data on a variety of low-alloy steels exposed to aqueous environments show that under certain conditions the growth rate is not uniquely defined by the crack-tip stress intensity factor [3.55]. For example, data in Figures 3.15 and 3.16 show that growth rates under static [3.56] and cyclic loading [3.57], respectively, are dependent on the initially applied value of stress intensity. In addition, perturbations in da/dN versus ΔK can occur immediately following test interruption. As shown in Figure 3.17, fatigue crack growth rates in a pressure vessel steel exposed to a pressurized water reactor environment are substantially reduced immediately following a test interruption of ten days [3.58]. Similar effects can be observed immediately following a change in loading variable such as cyclic frequency [3.59]. As illustrated in Figure 3.18, growth rates are slow to respond to a reduction in cyclic frequency from 10 Hz to 0.1 Hz, although eventually a substantially higher growth rate is established.

All of the above effects are believed to be related to transient growth rates--that is, a period of time is required during which the crack growth rate accelerates to its steady-state value, as illustrated in Figure 3.19, for static loading [3.55]. The period of nonsteady-state growth is believed to be controlled by time dependencies in the underlying kinetic processes required to supply reacting species to the crack tip. This position is supported by the fact that the apparent transients are dependent on the nature of the material-environment system--those systems with relatively rapid kinetics do not exhibit the phenomenon.

The above transient growth phenomena are of practical significance in (1) obtaining representative corrosion fatigue and stress corrosion cracking data for use in design, and (2) in formulating mechanistic models. In both cases, errors can be incurred by not recognizing the presence of nonsteady-state effects and thereby making improper inferences--for example, falsely identifying a value for the threshold stress intensity factor under either static or cyclic loading. Currently, no methodology exists for incorporating these factors into design and reliability considerations. Since fracture mechanics life predictions are only valid when steady-state growth rate data are used, it is important to recognize and eliminate these transient growth rate phenomena when selecting data for use in design or reliability assessments.

3.6 Effect of Crack Size—"The Small Crack Problem"

A number of recent studies of the growth of small fatigue cracks have demonstrated that small cracks behave differently than do large cracks when results are analyzed in terms of conventional fracture mechanics concepts [3.60]. Small cracks have been observed to grow faster than large cracks in a variety of materials [3.61-3.65]. The peculiar behavior of small cracks arises from two sources: (1) violation of the small scale yielding requirement of linear elastic fracture mechanics when crack size is on the order of either the crack-tip plastic zone or the notch plastic zone for cracks emanating from a notch or similar stress concentration factor, and (2) violation of continuum mechanics concepts when crack size is on the order of size of microstructural features such as grain boundaries [3.66]. Considering both of these factors, it therefore appears that the true deviation between large and small cracks is in the computed mechanical "driving force" and not in the measured growth

rate response; thus a new "driving force" (other than ΔK) needs to be formulated which accounts for both plasticity effects and microstructural effects.

El Haddad, et al., [3.65] have taken a phenomenological approach and proposed that the transition crack size between "small" and "large" cracks is defined by

$$l_0 = \frac{1}{\pi} \left(\frac{\Delta K_{th}}{\Delta \sigma_e} \right)^2 \quad (3.3)$$

where ΔK_{th} is the threshold stress intensity for fatigue crack growth and $\Delta \sigma_e$ is the conventional, smooth bar, fatigue endurance limit. It has been suggested that l_0 merely be added to the physical crack size to redefine the driving force in terms of an effective ΔK . To date, it has not been possible to link l_0 to a characteristic size in the microstructure. As shown in Figure 3.20, this approach does describe the transition between smooth specimen endurance limit and the fracture mechanics threshold stress intensity [3.67].

Nearly all of the studies of the growth of small cracks under fatigue loading have been conducted in relatively inert environments. The one exception is the recent work of Gangloff [3.68], who studied the growth of small cracks in 4130 steel cyclically loaded ($f = 6$ cpm, $R = 0.10$) in an aqueous solution of 3% NaCl. These data, given in Figure 3.21, showed growth rates for small surface cracks (0.1 to 0.8 mm) to exceed those from large cracks (20-50 mm) by about an order of magnitude. In addition, companion small crack data conducted in air were found to be in reasonably good agreement with large crack data, Figure 3.21. The latter observation is consistent with the fact that the smallest crack size employed was larger than the l_0 value computed from equation (3.3). Thus, the significant small crack effect in the presence of an aggressive environment appears to be unrelated to small crack effects in inert environment fatigue. This suggests that the small crack effect in corrosion fatigue crack growth is related to the environmental component of cracking. Gangloff suggests that the crack tip environment for small cracks is rendered more embrittling due to the effect of hydrolytic acidification, which promotes hydrogen evolution. This view is supported by the fact that corrosion fatigue crack growth in high-strength steels exposed

to aqueous environments is believed to occur by a hydrogen embrittlement mechanism. Furthermore, based on Hartt, et al.'s, [3.69] analysis of fluid mixing during fatigue loading, a small crack is predicted to be a relatively inefficient pump relative to a large crack--thereby promoting local acidification in the small crack. It also should be noted that, as in the case of transient crack growth rates, small crack effects in aggressive environments appear to be related to the overall process of transport of species, or lack thereof, between the bulk and local crack-tip environments.

Although small crack effects in inert and aggressive environments appear to be fundamentally different, the practical significance is the same in both cases--namely, crack size effects can potentially cause nonconservative life predictions when conventional fracture mechanics procedures are employed. However, the practical significance of small crack effects is specific to the structural application--in particular, to the size of the preexisting flaw which must be assumed in the fracture mechanics analysis. Generally, if the initial flaw size is greater than several mm, small crack effects are likely to be insignificant and can be ignored. This limit is particularly true for fatigue in inert environments; however, it is less certain for corrosive environments where crack geometry may also influence the limiting crack size since the effect is thought to be due to alterations in the transport of reacting species between the bulk environment and local crack tip environment.

3.7 Mathematical Representation of Crack Growth Rate Data

The early work of Paris and Erdogan established the crack tip stress intensity factor, ΔK , as a proper measure of the "driving force" for the rate of fatigue crack growth, da/dN [3.70]. Furthermore, an analysis of available fatigue crack growth rate at that time suggested that the functional relationship between da/dN and ΔK could be expressed as the following simple power law:

$$da/dN = C(\Delta K)^n \quad (3.4)$$

where C and n are empirical constants. Although this simple relationship provided little understanding of the nature of the fatigue crack growth process, it established $da/dN(\Delta K)$ as a fatigue crack growth property which

is largely independent of specimen geometry, and thereby provides a powerful tool for design and analysis of structures.

In the 20 years since equation (3.4) was first established, extensive studies of the fatigue crack growth resistance of a wide range of materials have established that da/dN is also sensitive to load ratio and environment--the latter giving rise to additional loading and environmental variables which are discussed in this chapter as well as Chapter 4.0. During this time it also became clear that, in general, equation (3.4) was only valid over two to three orders of magnitude in growth rate. For example, $da/dN(\Delta K)$ in inert environments, examined over a broad range of rates, generally exhibited the sigmoidal shape shown in Figure 3.3. Following this realization, $da/dN(\Delta K)$ relationships have been in a state of continual evolution.

Forman proposed the following modification to equation (3.4) to account for the upturn in the $da/dN(\Delta K)$ curve in Region III as K_{max} approaches the fracture toughness (K_c) of the material [3.71].

$$da/dN = \frac{C\Delta K}{(1-R)K_c - \Delta K}^n \quad (3.5)$$

Similarly the fatigue crack growth threshold, ΔK_{th} , was introduced to create a lower asymptote to the $da/dN(\Delta K)$ curve, thereby representing rates in Region I [3.72] by:

$$da/dN = C(\Delta K - \Delta K_{th})^n \quad (3.6)$$

Figure 3.22 provides a graphical representation of equation (3.6) and serves to define the parameters of this equation and illustrate its asymptotic nature.

Numerous equations of added complexity followed the above simple representations [3.73]. Several of these utilized common mathematical functions which possessed the characteristic sigmoidal shape of the $da/dN(\Delta K)$ curve--for example, the hyperbolic sine and inverse hyperbolic tangent functions [3.73]. Although several of these more complex equations were capable of equally representing a given set of data, many of them have the disadvantage of being extremely sensitive to the selection of ΔK_{th} --a parameter which is difficult to measure, has no consensus operational definition, nor standard test technique. Furthermore, nonconservative values are frequently selected

because of misinterpretation of data, often caused by the transient growth phenomena discussed in Section 3.5. For example, it has been pointed out that equations which are asymptotic in Region I tend to select asymptotes which are about 10% below the lowest ΔK value contained in a data set, regardless of the fact that cracks could propagate significantly below this value [3.74]. In computations of fatigue life in the high-cycle regime, this procedure could result in fatigue life predictions which are nonconservatively in error by orders of magnitude.

In order to avoid the above problem, a so-called "three-component model" was developed which does not contain an asymptote in Region I [3.74, 3.75]. This mathematical model is based on adding the materials' resistance to fatigue crack growth--that is, $(da/dN)^{-1}$ in the three commonly observed regions of crack growth, Figure 3.3. The characteristic equation describing da/dN as a function of ΔK (for other loading and environmental variables held constant) is given by

$$\frac{1}{da/dN} = \frac{A_1}{\Delta K^{n_1}} + \frac{A_2}{\Delta K^{n_2}} - \frac{A_2}{[(1-R) K_c]^{n_2}} \quad (3.7)$$

where A_1 , n_1 , A_2 , n_2 and K_c are empirical constants which are defined as illustrated in Figure 3.23. Each term in equation (3.7) represents a given region shown in Figure 3.23; growth rates in transition regions are represented by combinations of adjacent terms. The exponents n_1 and n_2 are the slopes in Regions I and II, respectively; the constants A_1 and A_2 are reciprocals of the intercepts (at $\Delta K = 1$) in Regions I and II, respectively. The constant K_c characterizes the onset of final instability--this value may not equal the plane strain fracture toughness, K_{Ic} , and is best obtained from fatigue crack growth tests on material having the same thickness as the structure of interest. Note also that setting A_1 equal to zero and K_c to infinity reduces equation (3.7) to the simple Paris law, equation (3.4). The form of the three-component model also facilitates the representation of load ratio effects by expressing A_1 and A_2 as functions of R since these effects are known to be specific to Regions I and II. Furthermore, the added complexities arising in the $da/dN(\Delta K)$ curve as the result of environmental effects can be easily represented by adding additional terms to equation (3.7). For example, the plateau in rates which sometimes occurs under cathodic

polarization in seawater can be represented by adding a constant term to equation (3.7) as illustrated in Section 3.8.

The important feature of equation (3.7), with regard to offshore structures, is the fact that low growth rates below those which are practical to measure in laboratory tests are given by a power law extrapolation. Thus, inadequately low growth rate data will result in conservative predictions of cyclic life rather than in nonconservative predictions which can result from asymptotic-type models.

3.8 Selection of Steady-State da/dN(ΔK) Relations For Various Loading and Environmental Conditions

One of the necessary inputs to the fracture mechanics analysis of offshore structures is the characterization of the fatigue crack growth rate resistance for the material-environment systems of interest. As previously discussed, it is most appropriate to express this resistance to crack growth in terms of the rate of crack growth (da/dN) as a function of the stress intensity factor range (ΔK) since the latter provides a geometry-independent measure of the "driving force" for crack propagation. Thus, $da/dN(\Delta K)$ is a material-environment property which can be determined empirically with small-coupon laboratory testing, but which also describes the rate at which fatigue cracks grow in full-scale structures. Based on information presented in this chapter, as well as Chapter 4.0, the general form of the growth rate equation is as follows:

$$da/dN = da/dN(\Delta K, R, f, w/f, \phi, C_i, T, M) \quad (3.8)$$

where:

- R = load ratio = $P_{min}/P_{max} = K_{min}/K_{max}$, and serves to characterize the mean stress;
- f = cyclic frequency, an important variable when time-dependent processes such as environmental effects occur;
- w/f = cyclic waveform, reasonably constant for offshore structures, thus not a critical variable;
- ϕ = electrode potential for the material-environment system, in this application the electrode potential will be either under "freely corroding" conditions or at some level of cathodic polarization to impart protection from generalized corrosion;

C_i = chemical composition of the aggressive environment;
 T = temperature of the environment; and
 M = material composition and/or microstructure.

The influence of the above factors on the corrosion fatigue crack growth rate was discussed in detail in previous sections of this chapter and in Chapter 4.0. Unfortunately, due to the number of variables involved and, in some cases, interactions among these variables, equation (3.8) cannot be completely described due to a lack of empirical data, combined with the absence of a generalized theory to quantitatively relate these factors to crack growth. Thus, the approach taken here was to define simplified crack growth rate equations for the primary variables for which data were available (ΔK , R , f , ϕ), while holding other variables as nearly constant as possible. In order to conduct this task, it was necessary not only to find the appropriate data in the literature but also to translate them into the same units and display them on equal graphical scales. These tasks were accomplished by digitizing all data and entering them into computer files for subsequent replotting using computer graphics.

The data collection focused on structural steels since they are typically used in current offshore structures. Data were separated into the following major categories:

1. Air environment, low-R
2. Air environment, high-R
3. Seawater environment, free corrosion potential, low-R
4. Seawater environment, free corrosion potential, high-R
5. Seawater environment, cathodic polarization, low-R
6. Seawater environment, cathodic polarization, high-R

where low-R is defined as $R < 0.2$, and high R is defined as $R \geq 0.5$.

Data from the above categories are shown in Figures 3.24-3.29, respectively. Table 3.2 provides a detailed list of the sources of data, as well as specific material, loading, and environmental variables represented in these figures.

Mathematical representations of these data were developed using the three-component model given in equation (3.7). The solid curves in Figures 3.24 through 3.29 were judged to provide the best representation of the data using equation (3.7); values of the constants in this equation, corresponding

to these solid curves, are provided in Table 3.3. Category 6, seawater with cathodic polarization at high R, contains insufficient data to establish a meaningful growth rate equation since data are limited and highly variable. Wherever possible, an attempt was made to critically assess data—for example, by not considering anomalous results such as those arising from such factors as nonsteady-state phenomena (Section 3.5). A discussion of each of the data categories, including additional factors considered in the selection process, is given below.

Not surprisingly, the laboratory air data at low load ratios ($R < 0.2$), shown in Figure 3.24, represent the most complete data category. Growth rate data on a mild steel from the study of Stanzel and Tscheegg [3.78] are available to extremely low growth rates—less than 10^{-13} m/cycle. These data were generated at ultrasonic frequencies (21 kHz) using a pulsed technique to avoid adiabatic heating of the crack tip. In spite of the high cyclic frequency, these results merge with data generated at conventional frequencies (5–20 Hz) in the regime of 10^{-9} to 10^{-8} m/cycle. This frequency independence of the data is in agreement with results from Figure 3.12 for a moist air environment. Although the high frequency results were obtained at $R = -1$, only the tensile portion of the loading cycle was used to compute ΔK ; thus, results should be in agreement with other low-R data. Taking the operational definition of ΔK_{th} to be the ΔK value corresponding to $da/dN = 10^{-10}$ m/cycle, gives $\Delta K_{th} = 4 \text{ MPa}\sqrt{\text{m}}$ using equation (3.8)—the solid curve in Figure 3.24. This value is in good agreement with the lower bound ΔK_{th} data previously given in Figure 3.4. The results of Endo, et al., also on a mild steel, give a higher value of $5.5 \text{ MPa}\sqrt{\text{m}}$ for ΔK_{th} . Although the two values differ by only about 30%, the two data sets give significantly different Stage I rates because of the strong ΔK -dependence in this regime. This fact illustrates the problem encountered when selecting a design curve in the low growth rate regime. By contrast, the rates in Region II are in reasonable agreement considering the fact that data are from a variety of sources and for somewhat different materials.

Results for the air environment at high R, given in Figure 3.25, are less extensive than those at low R. The actual load ratios represented in these data ranged from 0.5 to 0.85—the higher R data being concentrated in the da/dN range between 10^{-9} and 10^{-8} m/cycle. These data were heavily weighted in selecting the solid curve in order to give results most representative of

$R \sim 0.8$. Since data were not available in Region I, ΔK_{th} results from Figure 3.4 were utilized to establish the curve in the low growth rate regime by assuming the same operational definition of ΔK_{th} as given above. A comparison of data from Figures 3.24 and 3.25 indicates a modest influence of load ratio in Region II where increasing R causes da/dN to increase by a factor of 2.5 to 3. However, as discussed in Section 3.2, the Region I rates are much more sensitive to load ratio. Consistent with the lower bound ΔK_{th} data of Figure 3.4, increasing R decreases the ΔK_{th} value from about 4 MPav^m to 2 MPav^m . The other major influence of R is seen in the occurrence of Region III behavior at high ΔK values in Figure 3.25. As shown in Table 3.3, the Region II slopes are equal to 3.15 for both high- and low- R values, while the Region I slope is greater at low- R than at high R --this difference is in qualitative agreement with low growth rate data on a variety of materials.

The seawater data at low- R , given in Figure 3.26, exhibit more apparent variability than do the air data. However, most of this variation is due to a layering of the data with respect to cyclic frequency. Specifically, data sets of Endo, et al., [3.77] on a mild steel at 5 Hz and Vosikovsky on X-65 steel at 1 Hz [3.78] exhibit significantly slower growth rates than most of the other data which are for 0.01 to 0.1 Hz. The above trend is particularly true at lower ΔK values where differences are as great as a factor of forty. These lower ΔK data of Endo, et al., are interesting in that the rates in 1% NaCl were found to be less than those in air; this phenomenon was attributed to a decrease in the effective ΔK for the saltwater tests due to the wedging action of corrosion products within the crack. However, it is uncertain as to why this same phenomenon did not similarly influence the low growth rate results from the other studies. Possibly, the wedging is sensitive to alloy composition or to differences in environment--for example, chloride and/or oxygen content.

As in the low- R air tests, the seawater results down to 10^{-13} m/cycle are from the study of Stanzel and Tscheegg on a mild steel at 21 kHz [3.80]. Where data are available in the same ΔK range, the 21 kHz data are about six times slower than the 0.1 Hz data, but faster than the 5 Hz data which were reported to be affected by oxide wedging. The solid curve in Stage II in Figure 3.26 is given by equation (3.10) in Table 3.3 and was weighted towards the data at 0.1 Hz since this frequency is most applicable to offshore structures, as

discussed in Section 2.0. The Stage I portion of this curve was dictated by the only data available namely, those at 21 kHz.

The seawater, high-R data shown in Figure 3.27 are from studies of Silvester and Scott [3.76] and Bardal, et al., [3.81,3.82] on BS 4360-50D steel and from Bristol, et al., [3.83,3.84] on steel 52 (DIN 17100), a C-Mn structural steel similar to BS 4360-50D. Data at the lower growth rates appear to be layered with respect to cyclic frequency; specifically, below 10^{-9} m/cycle the data of Bristol, et al., which were obtained at 0.2 Hz, are consistently faster than those of Bardal, et al., obtained at 1 Hz. These two data sets diverge as growth rates decrease until a difference of about a factor of ten occurs near 10^{-10} m/cycle. The solid curve fit through the data in Figure 3.27 follows the 0.2 Hz data in Region I since this lower frequency is applicable to offshore structures and also corresponds to the frequency employed in tests of welded coupons and tubular joints which are compared with fracture mechanics predictions in Section 7.0. In Figure 3.27, data points with downward arrows at 5×10^{-11} m/cycle indicate no detectable crack extension in 4×10^5 cycles, assuming a crack length measurement precision of ± 0.02 mm. Often points of detectable and nondetectable crack growth occurred at equal values of ΔK , indicating either test-to-test variations or temporarily arresting cracks in a single test. Such behavior is not uncommon in low growth rate crack growth testing and is sensitive to the details of how the load, and thereby stress intensity factor, is decreased during the course of the test [3.29, 3.85]. Thus, in establishing the solid curve in Figure 3.27, the points corresponding to detectable crack growth were more highly weighted than those corresponding to nondetectable crack growth. Using this interpretation, the low growth rate data of Figure 3.27 appear to merge with those in Figure 3.25 representing the case of air at high R values. Thus, the fitting constants A_1 and n_1 for both air and freely corroding seawater at high-R are identical in Table 3.3. However, it should be noted that in both cases data are lacking in this low growth rate regime.

The seawater data at low-R with cathodic polarization, given in Figure 3.28, contain data on X-65 steel from Vosikovsky [3.78] and on BS 4360 steel from Silvester and Scott [3.76] and from Bardal, et al. [3.81]. As indicated in Figure 3.28, results are layered with respect to cyclic frequency, particularly in the regime where growth rates exhibit a plateau. At low growth rates the data of Vosikovsky and of Bardal, et al., on X-65 and BS 4360,

respectively, agree quite well. However, at higher growth rates and a frequency of 0.1 Hz, Vosikovsky's data on X-65 and Silvester and Scott's data on BS 4360-50D disagree significantly. The high growth rate data of Vosikovsky on X-65 at 0.1 Hz were used to establish the solid curve in Figure 3.28 and constants in equation (3.12), Table 3.3. Again, this particular frequency was chosen because of its relevance to offshore structures.

As mentioned in Section 3.8, the rates in the plateau regime were modeled by adding an additional constant to equation (3.7). This constant is simply the reciprocal of the plateau velocity—a value of 1×10^6 m/cycles for the 0.1 Hz data of Figure 3.28. To model the upturn in the data from the plateau value at higher ΔK values, an additional term similar to the first two terms in equation (3.7), but containing different constants, would be necessary. However, instead of adding this complexity to the model, the life predictions of Section 7.0 were simply made to merge with laboratory air predictions at high stress levels.

Figure 3.29 contains data in the category seawater, cathodic polarization, high-R. As discussed in Section 4.3, these conditions can produce crack growth rates which are faster than those for seawater under freely corroding conditions. This enhancement in rates is believed to be associated with the increased production of atomic hydrogen caused by the cathodic polarization. Assuming this mechanism to be correct, the data of Bristol and Roeleveld [3.84] obtained in an environment of seawater saturated with H_2S ($pH \approx 4.5$) are also included in Figure 3.29 for comparison with data obtained under cathodic polarization since the presence of H_2S in aqueous solutions is known to increase the amount of atomic hydrogen in aqueous solutions by hindering the hydrogen recombination reaction. Thus, the influence of H_2S should be qualitatively similar to that of cathodic polarization. As indicated, the H_2S -saturated results of Bristol and Roeleveld (Δ) appear to provide an upperbound to the cathodic polarization data. However, because of the high variability exhibited by all data, as well as the uncertainty as to how to quantitatively relate the H_2S -saturated seawater data to offshore structures, no mathematical representation of these data was developed.

Figure 3.30 provides a summary of the curves selected for categories 1 through 6. Several interesting comparisons emerge from this summary. Recalling the discussion of Section 3.1 (Figure 3.3), two distinct types of behavior can be noted. At low R values, the seawater data under freely

corroding conditions exhibit Type A corrosion fatigue behavior. In contrast, the seawater data under cathodic polarization exhibit Type C behavior, except for the fact that low growth rates fall below the air curve, apparently due to the decrease in the effective ΔK caused by the wedging action of calcareous deposits.

This exercise of reviewing the literature and selecting parameter values for the mathematical representation of corrosion fatigue crack growth rates of materials employed in offshore structures has served to emphasize the fact that data are inadequate under certain loading and environmental conditions—for example, high-R data in air and seawater, both with and without cathodic polarization. This lack of data makes many of the above conclusions on the influence of certain variables tentative, as well as hampers the assessment of the long-term durability of offshore structures. A few laboratories have begun to acquire the near-threshold, low-frequency data which are currently lacking; however, the long test duration and high cost of these tests will require a concerted, industry-wide effort.

CHAPTER 3.0 REFERENCES

- 3.1 Jaske, C. E., Payer, J. H. and Balint, U. S., "Corrosion Fatigue of Metals in Marine Environments," Report No. MCIC-81-42, Metals and Ceramics Information Center, Battelle Columbus Laboratories, Columbus, Ohio, July 1981.
- 3.2 Endo, K., Komai, K. and Kinoshita, S., "Long-Life Corrosion-Fatigue Strength of a Carbon Steel," Proceedings of the 22nd Japan Congress on Materials Research, Kyoto, Japan, 1978, pp. 193-198.
- 3.3 McEvily, A. J., and Wei, R. P., "Fracture Mechanics and Corrosion Fatigue," in Corrosion Fatigue: Chemistry, Mechanics and Microstructure, NACE-2, 381-395, 1972.
- 3.4 Brown, B. F. and Beachem, C. D., "A Study of the Stress Factor in Corrosion Cracking by Use of the Precracked Cantilever-Beam Specimen," Corrosion Science, 5, 1965.
- 3.5 Wei, R. P., Novak, S. R. and Williams, D. P., "Some Important Considerations in the Development of Stress Corrosion Cracking Test Methods," Mat'l. Res. & Std., ASTM, 12, 25, 1972.
- 3.6 Wei, R. P., et al., "Characterization of Environmentally Assisted Cracking for Design: State of the Art," National Materials Advisory Board, NMAB-386, National Academy Press, Washington, D.C., 1982.
- 3.7 Wei, R. P. and Landes, J. D., "Correlation Between Sustained-Load and Fatigue Crack Growth in High Strength Steels," Mat'l. Res. & Std., ASTM, 9, 7, pp 25-28, 1969.
- 3.8 Miller, G. A., Hudak, S. J., Jr. and Wei, R. P., "The Influence of Loading Variables on Environment-Enhanced Fatigue Crack Growth in High Strength Steels," J. of Testing and Eval., JTEVA, 1, (7), pp. 524-531, 1973.
- 3.9 Scott, P. M. and Silvester, D.R.V., "The Influence of Mean Tensile Stress on Corrosion Fatigue Crack Growth in Structural Steel Immersed in Seawater," Department of Energy, UK Offshore Steels Research Project, Interim Technical Report UKOSRP 3/02 May 25, 1977.
- 3.10 Morrow, J., "Fatigue Properties of Metals," Section 3.2 of Fatigue Design Handbook, Society of Automotive Engineers, 1968. Section 3.2 is a summary of a paper presented at a meeting of Division 4 of the SAE Iron and Steel Technical Committee, Nov. 4, 1964.
- 3.11 Smith, K. N., Watson, P., and Topper, T. H., "A Stress-Strain Function for the Fatigue of Metals," Journal of Materials, Vol. 5, No. 4, Dec. 1970.
- 3.12 Topper, T. H. and Sandor, B. I., "Effects of Mean Stress and Prestrain on Fatigue Damage Summation," Effects of Environment and Complex Load History on Fatigue Life, ASTM STP 462, 1970.

- 3.13 Morrow, JoDean, Wetzel, R. M. and Topper, T. H., "Laboratory Simulation of Structural Fatigue Behavior," Effect of Environment and Complex Load History on Fatigue Life, ASTM STP 462, American Society for Testing and Materials, pp. 74-91, 1970.
- 3.14 Neuber, H., "Theory of Stress Concentration for Shear-Strained Prismatic Bodies with Arbitrary Nonlinear Stress-Strain Law," Transactions, American Society of Mechanical Engineers, Journal of Applied Mechanics, Vol. 8, December 1961.
- 3.15 Dowling, N. E., "Fatigue Crack Growth Rate Testing at High Stress Intensities," in Flaw Growth and Fracture, ASTM STP 631, 1977.
- 3.16 Lindley, T. C. and Richards, C. E., "Near-Threshold Fatigue Crack Growth in Materials Used in the Electricity Supply Industry," in Fatigue Thresholds--Fundamentals and Applications, Vol. II, Engineering Materials Advisory Services Ltd., U.K., 1981.
- 3.17 Ritchie, R. O., Suresh, S. and Liaw, P. K., "A Comparison of Environmentally-Influenced Near-Threshold Fatigue Crack Growth Behavior in High and Lower Strength Steels at Conventional Frequencies," in Ultrasonic Fatigue, AIME, 1982.
- 3.18 Priddle, E. K., Int. J. Press. Vessel and Piping, 4, 1976.
- 3.19 Frost, N. E., Pook, L. P. and Denton, K., Eng. Fract. Mech., Vol. 3 p. 109, 1971.
- 3.20 Cooke, R. J. and Beevers, C. J., Eng. Fract. Mech., 5, 1973.
- 3.21 Paris, P. C., Bucci, R. J., Wessel, E. T., Clark, W. G. and Mager, T. J., ASTM STP, 513, 1972.
- 3.22 Masounave, J. and Bailon, J. P., Scripta Met., 10, 1976.
- 3.23 Masounave, J. and Bailon, J. P., Scripta Met., 9, 1975.
- 3.24 Ritchie, R. O., International Metals Review, 20, 516, 1979.
- 3.25 Ritchie, R. O., Suresh, S. and Moss, C. M., J. Engr. Matls. & Tech., Trans. ASME, SerH, 102, 1980.
- 3.26 Suresh, S., Zamiski, G. S. and Ritchie, R. O., Met. Trans., 12A, 1981.
- 3.27 Stewart, A. T., Eng. Fract. Mech., 13, 1980.
- 3.28 Liaw, P. K., Hudak, S. J., Jr. and Donald, J. K., "Near-Threshold Fatigue Crack Growth Investigation of NiMoV Steel in Hydrogen Environment," ASTM STP 791, 1983.
- 3.29 Hudak, S. J., Jr., Saxena, A., Bucci, R. J., and Malcolm, R. C., "Development of Standard Methods of Testing and Analyzing Fatigue Crack Growth Rate Data," Air Force Materials Laboratory, Technical Report AFML-TR-78-40, May 1978.

RD-R162 484

LONG-TERM CORROSION FATIGUE OF WELDED MARINE STEELS(U)

2/5

SOUTHWEST RESEARCH INST SAN ANTONIO TX

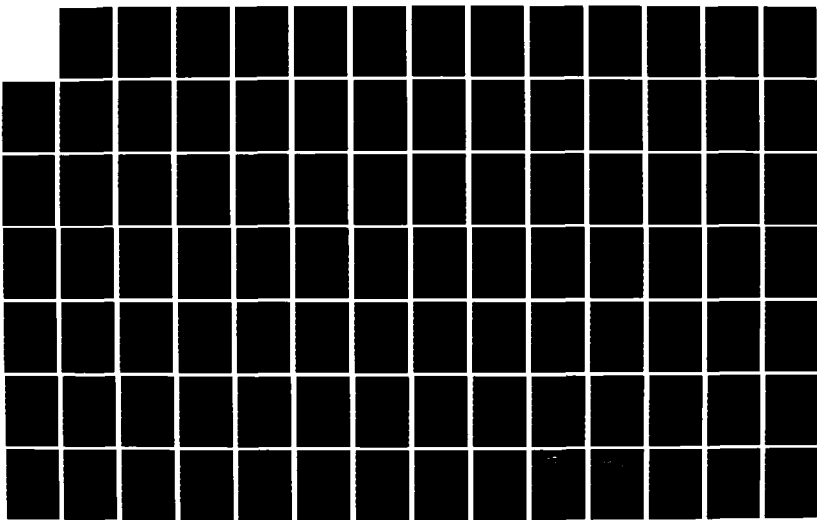
O H BURNSIDE ET AL. 1984 SR-1276 SSC-326

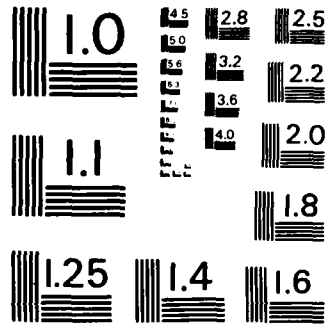
UNCLASSIFIED

DTCG23-89-C-28828

F/G 11/6

NL





MICROCOPY RESOLUTION TEST CHART
NATIONAL BUREAU OF STANDARDS - 1963 - A

- 3.30 Vosikovsky, O., "Fatigue-Crack Growth in an X-65 Line-Pipe Steel at Low Cyclic Frequencies in Aqueous Environments," Trans. ASME, J. Eng. Mater. and Technol., Series H, 97(4), 298-304, October 1975.
- 3.31 Barsom, J. M., "Fatigue Behavior of Pressure-Vessel Steels," WRC Bulletin 194, Welding Research Council, New York, May 1974.
- 3.32 Klesnil, M. and Lukas, P., Matls. Sci. Eng., 9, 1972.
- 3.33 Wei, R. P., "On Understanding Environment Enhanced Fatigue Crack Growth--A Fundamental Approach," ASTM STP 675, 1979.
- 3.34 Ford, F. P., "Mechanisms of Environmental Cracking in Systems Peculiar to the Power Generation Industry," EPRI Report NP-2599, Electric Power Research Institute, Sept. 1982.
- 3.35 Nishioka, K., Hirakawa, K., and Kitaura, I., "Low Frequency Corrosion Fatigue Strength of Steel Plate," The Sumitomo Search, No. 16, 40-54, November 1976.
- 3.36 Endo, K. and Miyao, Y., "Effects of Cyclic Frequency on the Corrosion Fatigue Strength," Bull. JSME, 1, 374-380, 1958.
- 3.37 Vosikovsky, O., J. Eng. Mat. and Tech., Trans. ASME, Series H, 97, 1975.
- 3.38 Vosikovsky, O., "Frequency, Stress Ratio, and Potential Effects on Fatigue Crack Growth of HY130 Steel in Salt Water," J. Test. and Eval. JTEVA, 6 (3), 1978.
- 3.39 Gallagher, J. P., Ryder, J. T., and Hadley, J. C., "The Salt Water Corrosion Fatigue Crack Propagation Behavior of Two Steels," Proceedings of the 1971 International Conference on Mechanical Behavior of Materials, Japan, August 15 to 20, Vol. III, 1971.
- 3.40 Bogar, F. D., and Crooker, T. W., "The Influence of Bulk-Solution-Chemistry Conditions on Marine Corrosion Fatigue Crack Growth Rate," J. Test. and Eval. JTEVA, 7 (3), 155-159, May 1979.
- 3.41 Gallagher, J. P., "Corrosion Fatigue Crack Growth Behavior Above and Below KISCC," Final Report NRL-7064, AD708377, May 28, 1970.
- 3.42 Pettit, D. E., Ryder, J. T., Krupp, W. E., and Hoeppner, D. W., "Environment Aspects of Subcritical Crack Growth," Proceedings of Second International Conference on Mechanical Behavior of Materials, August 16 to 20, pp. 680-684, 1976.
- 3.43 Barsom, J. M., "Corrosion-Fatigue Crack Propagation Below KISCC," Engineering Fracture Mechanics, 3, 15-25, July 1971.
- 3.44 Atkinson, J. D., and Lindley, T. C., "The Effect of Frequency and Temperature on Environmentally Assisted Fatigue Crack Growth Below KISCC in Steels," Proc. of Conf. on the Influence of Environment in Fatigue, Inst. Mech. Engrs., London, May 1977.

- 3.45 Scott, P. M. and Silvester, D.R.V., "The Influence of Mean Tensile Stress on Corrosion Fatigue Crack Growth in Structural Steels Immersed in Seawater," Dept. of Energy, UKOSRP, Interim Technical Report UKOSRP 3/02, May 25, 1971.
- 3.46 Hartt, W. H., "Fatigue of Welded Structural Steel in Sea Water," Proc. 13th Annual OTC, Paper No. OTC 3962, 1981.
- 3.47 Hartt, W. H., "Spectrum Fatigue Properties of Welded Steel as Applicable to Offshore Structures," API Report, June 1981.
- 3.48 Davidson, D. L. and Lankford, J., "Crack Tip Plasticity Associated With Corrosion Assisted Fatigue," Office of Naval Research, Interim Contract Report, Contract N00014-75-C-1038, May 31, 1979.
- 3.49 Barsom, J. M., "Effect of Cyclic Stress Form on Corrosion Fatigue Crack Propagation Below KISCC in a High Yield Strength Steel," in Corrosion Fatigue: Chemistry, Mechanics and Microstructure, NACE-2, 1972.
- 3.50 Kawai, S. and Koibuchi, K., "Effect of Waveform on Corrosion Fatigue Crack Growth," Fatigue of Engineering Materials and Structures, 1 (4), 1979.
- 3.51 Wei, R. P. and Simmons, G. W., "Surface Reactions and Fatigue Crack Growth," in Fatigue: Environment and Temperature Effects, Proc. of Army Materials Research Conference, Vol. 27, Syracuse Univ. Press., 1983.
- 3.52 Jahns, H. O. and Wheeler, J. D., "Long-Term Wave Probabilities Based on Hindcasting of Severe Storms," J. of Petroleum Tech., April, 1973.
- 3.53 Robinson, R. J., Brannon and Kattawar, G. W., "Storm Wave Characteristics," Society of Petroleum Engineers Journal, AIME, March, 1967.
- 3.54 Lambrakos, K. F. and Brannon, H. R., "Wave Force Calculations for Stokes and Non-Stokes Waves," Sixth Annual OTC, Paper OTC 2039, 1974.
- 3.55 Hudak, S. J. and Wei, R. P., "Consideration of Nonsteady State Crack Growth in Materials Evaluation and Design," Int. J. Pres. Ves. & Piping, 9, p. 63, 1981.
- 3.56 Landes, J. D. and Wei, R. P., Int. J. of Fracture, 9 (3), p. 277, 1973.
- 3.57 Scott, P. M. and Silvester, D.R.V., "The Influence of Mean Tensile Stress on Corrosion Fatigue Crack Growth in Structural Steel Immersed in Sea Water," Tech. Rep. UKOSRP 3/02, Harwell Corrosion Service, UKAEA, May 1977.
- 3.58 Bamford, W. H. and Ceschini, L. J., "Effects of High Temperature Primary Reactor Water on Fatigue Crack Growth of Reactor Vessel Steels," HSST Quart. Prog. Rep. ORNL-NUREG-TM-194, pp. 25-35, May 1978.
- 3.59 Pao, P. S., Wei, W. and Wei, R. P., "Environment Sensitive Fracture of Engineering Materials (Z. A. Fououlis, ed.)," The Metallurgical Society of AIME, Warrendale, PA, USA, 15086, pp. 565-580, 1979.

- 3.60 Hudak, S. J., Jr., "Small Crack Behavior of the Prediction of Fatigue Life," Transactions of the ASME, 103, January 1981.
- 3.61 Kitagawa, H., Takahashi, S., Suh, C. M., and Miyashita, S., "Quantitative Analysis of Fatigue Process-Microcracks and Slip Lines Under Cyclic Strains," Fatigue Mechanisms, ASTM STP 675, p. 420, 1979.
- 3.62 Taira, S., Tanaka, K., and Hoshina, M., "Grain Size Effect on Crack Nucleation and Growth in Long-Life Fatigue of Low-Carbon Steel," Fatigue Mechanisms, ASTM STP 675, p. 135 (1979).
- 3.63 Nakai, Y. and Tanaka, K., "Grain Size Effect on Growth Threshold for Small Surface-Cracks and Long Through-Cracks Under Cyclic Loading," Proc. Jap. Cong. Mat. Res., 1980.
- 3.64 Pearson, S., Eng. Frac. Mech., 7, p. 235, 1975.
- 3.65 Morris, W. L., "Crack Closure Stress Effects on the Rate of Propagation of Surface Microcracks During the Fatigue of Al 2219-T851," Met. Trans. A, 11A, 1980.
- 3.66 Chan, K. S., and Lankford, J., "A Crack-Tip Strain Model for the Growth of Small Fatigue Cracks," Scripta Met., 17, 1983.
- 3.67 El Haddad, M. H., Smith, K. N. and Topper, T. H., "Fatigue Crack Propagation of Short Cracks," Trans. ASME, Series E, 101, p. 42 (1979).
- 3.68 Gangloff, R. P., "The Criticality of Crack Size in Aqueous Corrosion Fatigue," to be published in Res. Mechanica Letters, 1983.
- 3.69 Hartt, W. H., Tennant, J. S., and Hooper, W. C., "Solution Chemistry Modification Within Corrosion-Fatigue Cracks," ASTM STP 642, 5-18, 1978.
- 3.70 Paris, P. C. and Erdogan, F., "A Critical Analysis of Crack Propagation Laws," Trans. ASME, Journal of Basic Engineering, Vol. 85, pp. 528-534, December, 1963.
- 3.71 Forman, R. G., Kearney, U. E., and Engle, R. M., "Numerical Analysis of Crack Propagation in Cyclic Loaded Structures," J. Basic Eng. ASME Trans., Series D, 89, September 1967.
- 3.72 Liu, H.W., Fatigue - An Interdisciplinary Approach, Proc. of Tenth Sagamore Army Materials Research Conference, Syracuse, Univ. Press., 1964.
- 3.73 Miller, M. S. and Gallagher, J. P., "An Analysis of Several Fatigue Crack Growth Rate (FCGR) Descriptions," ASTM STP 738, 1981.
- 3.74 Saxena, A., Hudak, S. J., Jr. and Jouris, G. M., "A Three Component Model for Representing Wide-Range Fatigue Crack Growth Rate Behavior," Engineering Fracture Mechanics, 12, 1979.

- 3.75 Saxena, A. and Hudak, S. J., Jr., "Evaluation of the Three Component Model for Representing Wide Range Fatigue Crack Growth Rate Data," Journal of Testing and Evaluation, JTEVA, 8, 5, 1980.
- 3.76 Silvester, D.R.V., Scott, P. M., et al, "The Effects of Sea Water Corrosion on Fatigue Crack Propagation in BS4360:50D Steel," UK Atomic Energy Authority Northern Division Report, ND-R-194(S), September 1978.
- 3.77 Endo, K., Komai, K. and Shikida, T., "Crack Growth by Corrosive Dissolution and Threshold Characteristics in Corrosion Fatigue of a Steel," Proceedings of ASTM Symposium on Corrosion Fatigue: Mechanics, Metallurgy, Electrochemistry, and Engineering, St. Louis, Missouri, October 1981.
- 3.78 Vosikovsky, O., "Fatigue-Crack Growth in an X-65 Line-Pipe Steel at Low Cyclic Frequencies in Aqueous Environments," Internal Report PM-M-74-11, Canada Department of Energy, Mines, and Resources, Ottawa, July 1974.
- 3.79 Dowling, N. E. and Walker, H., "Fatigue Crack Growth Rate Testing of Two Structural Steels," SAE Paper 790459, Society of Automotive Engineers, 1979.
- 3.80 Stanzel, S. and Tschegg, E., "Influence of Environment on Fatigue Crack Growth in the Threshold Region," Acta Metallurgica, Vol. 29, pp. 21-32, 1981.
- 3.81 Bardal, E. B., Haagensen, P. J., and Solli, O., "Corrosion Fatigue--Offshore," SINTEF/DnV Final Report, NTNF Project B.0601.5185, October 1978.
- 3.82 Bardal, E., et al, "Measurements of Very Low Fatigue Crack Growth Rates in Structural Steel in Artificial Seawater," Underwater Systems Design, August/ September 1982, pp 16-20; also see Proceedings of the International Symposium on Fatigue Thresholds, Stockholm, June 1981.
- 3.83 Bristoll, P. and Opdam, J.J.G., "Fatigue of Offshore Structures: The Prediction of Fatigue Crack Propagation Under Conditions of Random Loading," Oceanology International '75, Brighton, March 1975.
- 3.84 Bristoll, P. and Roeleveld, J. A., "Fatigue of Offshore Structures: Effect of Sea Water on Crack Propagation in Structural Steel," Paper 18, Marine Tech. Conf., Cambridge, 1978.
- 3.85 Bucci, R. J., "Development of a Proposed ASTM Standard Test Method for Near-Threshold Fatigue Crack Growth Rate Measurement," in Fatigue Crack Growth Measurement and Data Analysis, ASTM STP 738, pp. 5-28, 1981.

TABLE 3.1 MATERIAL AND DATA SOURCES FOR ΔK_{th} RESULTS GIVEN IN FIGURE 3.4

Symbol	Steel	Yield Strength, MPa	Source	Reference
A	Low carbon	309	Priddle (1976)	3.18
B	Low carbon	232	Frost, Pook and Denton (1971)	3.19
C	Medium carbon	337-434	Cooke and Beevers (1973)	3.20
D	Medium carbon	399-590	Cooke and Beevers (1973)	3.20
E	Low alloy	—	Frost, Pook and Denton (1971)	3.19
F	ASTM A533B	479	Paris, et al. (1972)	3.21
G	ASTM A508	479	Paris, et al. (1972)	3.21
H	2-1/2 NiCrMoV	618	Lindley and Richards (1982)	3.16
I	Low carbon	168-192	Masounaue and Bailon (1976)	3.22
J	High carbon	477-493	Masounaue and Bailon (1975)	3.23
K	High carbon	532	Masounaue and Bailon (1975)	3.23
L	2-1/2 NiCrMoV	618	Lindley and Richards (1982)	3.16
M	3-1/2 NiCrMoV	742	Lindley and Richards (1982)	3.16
N	3-1/2 NiCrMoV	607	Lindley and Richards (1982)	3.16
O	ASTM A533B	445-463	Lindley and Richards (1982)	3.16
P	ASTM SA387*	290	Ritchie (1979)	3.24
Q	ASTM SA516-70	327	Ritchie, Suresh and Moss (1980)	3.25
R	ASTM SA592-3*	500	Suresh, Zamiski and Ritchie (1981)	3.26
S	ASTM SA542-2*	575	Suresh, Zamiski and Ritchie (1981)	3.26
T	2 NiCrMoV	575	Stewart (1980)	3.27
U	3-1/2 NiCrMoV	602	Stewart (1980)	3.27
V	NiMoV	661	Liaw, Hudak and Donald (1982)	3.28
W	ASTM SA542-2	769	Suresh, Zamiski and Ritchie (1981)	3.26
X	API X65	460	Vosikovsky (1975)	3.29

*2-1/4 Cr⁻¹ Mo Pressure Vessel Steels

TABLE 3.2. SUMMARY OF CONDITIONS FOR CRACK GROWTH DATA

Condition	Symbol	Reference	Source	Figure in Reference	Material	Frequency (Hz)	N	Remarks
Air, Low-E (Figure 1.24)	□	3.74 3.76 3.75	Sylvester and Scott (1978) Sylvester and Scott (1978) Endo et al (1981)	7 8 3	BS4460:50D BS4460:50D Mild Steel	1-10 1-10 5	0-0.1 0-0.1 0.1	
	○	3.75	Endo et al (1981)	3	Mild Steel	5	0.1	
	△	3.75	Endo et al (1981)	3	X-65 Linepipe	15	0.2	
	+	3.75	Vasilevsky (1974)	1	Man-Ten Steel	2-20	0.1	
	×	3.76	Dwelling and Walker (1979)	2	Man-Ten Steel	2-20	0.1	
	○	3.77	Dwelling and Walker (1979)	3	WV-100	21 kHz	-1	In Silicon Oil
	◊	3.77	Stanzel and Tscherr (1981)	4	Mild Steel	5 Hz	0.02-0.04	
	×	3.78	Berdal et al (1978)	6	BS4460:50D			
	◻	3.78	Sylvester and Scott (1978)	7	BS4460:50D	1-10	0.5-0.85	
	○	3.78	Sylvester and Scott (1978)	8	BS4460:50D	1-10	0.5-0.85	
Air, High-E (Figure 1.25)								
Semiarid, Free Corrosion Potential, Low-E (Figure 1.26)	□	3.76 3.75	Sylvester and Scott (1978) Endo et al (1981)	9 3	BS4460:50D Mild Steel	0.1 5	0.0-0.1 0.1	Natural Seawater, 0-10°C, -0.65 V (Ag/AgCl)
	○	3.76 3.75	Endo et al (1981)	3	Mild Steel	5	0.1	12 NaCl, 25°C, Flow Rate = 0.4 l/min.
	△	3.75	Endo et al (1981)	3	Mild Steel	0.1	0.1	12 NaCl, 25°C, Flow Rate = 0.4 l/min.
	+	3.75	Endo et al (1981)	3	Mild Steel	0.01	0.1	12 NaCl, 25°C, Flow Rate = 0.4 l/min.
	×	3.75	Endo et al (1981)	3	X-65 Linepipe	1.0	0.2	12 NaCl, 25°C, Flow Rate = 0.4 l/min.
	○	3.76	Vasilevsky (1974)	1	X-65 Linepipe	0.1	0.7	Changed Every 24 Hours
	◊	3.76	Vasilevsky (1974)	3	X-65 Linepipe	0.1	0.7	1.52 NaCl, pH = 6.5-7.5, Solution
	×	3.76	Vasilevsky (1974)	3	X-65 Linepipe	0.01	0.2	Changed Every 24 Hours
	◻	3.78	Stanzel and Tscherr (1981)	4	Mild Steel	21 kHz	-1	1.52 NaCl, pH = 6.5-7.5, Solution
	○	3.79	Berdal et al (1978)	7	BS4460:50D	0.167-1.0	0.05	Changed Every 24 Hours
	×	3.79	Berdal et al (1978)	7	BS4460:50D			Synthetic Seawater (ASTM-D1141-52)

TABLE 3.2. SUMMARY OF CONDITIONS FOR CRACK GROWTH DATA (Concl'd)

Condition	Symbol	Reference	Source	Plates in Reference	Material	Frequency (Hz)	R	Remarks
Seawater, Free Corrosion Potential, High-R (Figure 3.27)	□	3.74 1.80	Silvester and Scott (1978) Bardal et al (1981)	9 5b	BS4 360:50D BS4 360:50D	0.1 0.167 & 1	0.5-0.85 0.5	Natural Seawater, -10°C , -0.65 V (Ar/ArCl)
	○							Synthetic Seawater (ASTM D1141-52), 12°C , pH = R.2, Air Saturated, Flow Rate = 0.4 m/s,
	△	3.84	Bristoll et al (1978)	5	Steel 521 DIN 17100	0.2	0.6-0.8	Synthetic Seawater (ASTM D1141-52), 20°C , pH = R.2, Flowing, Refreshed Monthly
Seawater, Cathodic Polarization, Low-R (Figure 3.28)	□	3.74	Silvester and Scott (1978)	10	BS4 360:50D	0.1	0-0.1	Natural Seawater, -10°C , -0.85 V (Ar/ArCl)
	○	3.74	Silvester and Scott (1978)	11	BS4 360:600	0.1	0-0.1	Natural Seawater, -10°C , -1.10 V (Ar/ArCl)
	△	3.76	Vashkovsky (1974)	2	X-65 Linepipe	10	0.7	1.52 NaCl, 25°C , -1.16 V (Ar/ArCl)
	+	3.76	Vashkovsky (1974)	2	X-65 Linepipe	1	0.2	1.52 NaCl, 25°C , -1.16 V (Ar/ArCl)
	×	3.76	Vashkovsky (1974)	2	X-65 Linepipe	0.1	0.2	1.52 NaCl, 25°C , -1.16 V (Ar/ArCl)
	◊	3.76	Vashkovsky (1974)	2	X-65 Linepipe	0.01	0.2	1.52 NaCl, 25°C , -1.16 V (Ar/ArCl)
	◆	3.79	Bardal et al (1978)	6	BS4 360:50D	0.167 & 1	0.2-0.06	Synthetic Seawater (ASTM D1141-52), 12°C , -0.8 and -1.1 V (Saturated Calcium Electrode)
Seawater, Cathodic Polarization, High-R (Figure 3.29)	□	3.74	Silvester and Scott (1978)	10	BS4 360:50D	0.1	0.5-0.85	Natural Seawater, -10°C , -0.85 V (Ar/ArCl)
	○	3.74	Silvester and Scott (1978)	11	BS4 360:50D	0.1	0.5-0.85	Natural Seawater, -10°C , -1.1 V (Ar/ArCl)
	△	3.84	Bristoll et al (1978)	6	Steel 521 DIN 17100	0.2	0.6-0.8	Synthetic Seawater, Saturated with H_2S , pH = 4.5

TABLE 3.3. CONSTANTS IN THREE-COMPONENT CRACK GROWTH LAW

Condition	Equation Number	A_1	A_2	n_1	n_2	K_c (MPa \sqrt{m})	R
Air, Low R	3.8	1.9×10^{29}	2.5×10^{11}	32.0	3.15	250	< 0.2
Air, High R	3.9	1.0×10^{14}	9.1×10^{10}	13.3	3.15	250	> 0.5
Seawater, Free Corrosion Potential, Low R	3.10	1.9×10^{20}	3.3×10^{11}	17.5	3.65	250	< 0.2
Seawater, Free Corrosion Potential, High R	3.11	1.0×10^{14}	1.7×10^{11}	13.3	3.65	250	> 0.5
Seawater, Cathodic Polarization*, Low R	3.12	8.0×10^{34}	2.9×10^{13}	32.0	5.93	250	< 0.2
Seawater, Cathodic Polarization, High R	-					250	> 0.5
Constants Not Estimated Because of Lack of Experimental Data							

$$\frac{1}{da/dN} = \frac{A_1}{n_1} + \frac{A_2}{n_2} - \frac{A_2}{[(1-R)K_c]^2} \left(\frac{da}{dN} \text{ in meters/cycles, } \Delta K \text{ in MPa}\sqrt{m} \right) \quad (\text{Equation 3.7})$$

* The plateau rates occurring under these conditions were modeled by adding an additional constant to the above equation equal to 1×10^6 cycles/m for the 0.1 Hz data.

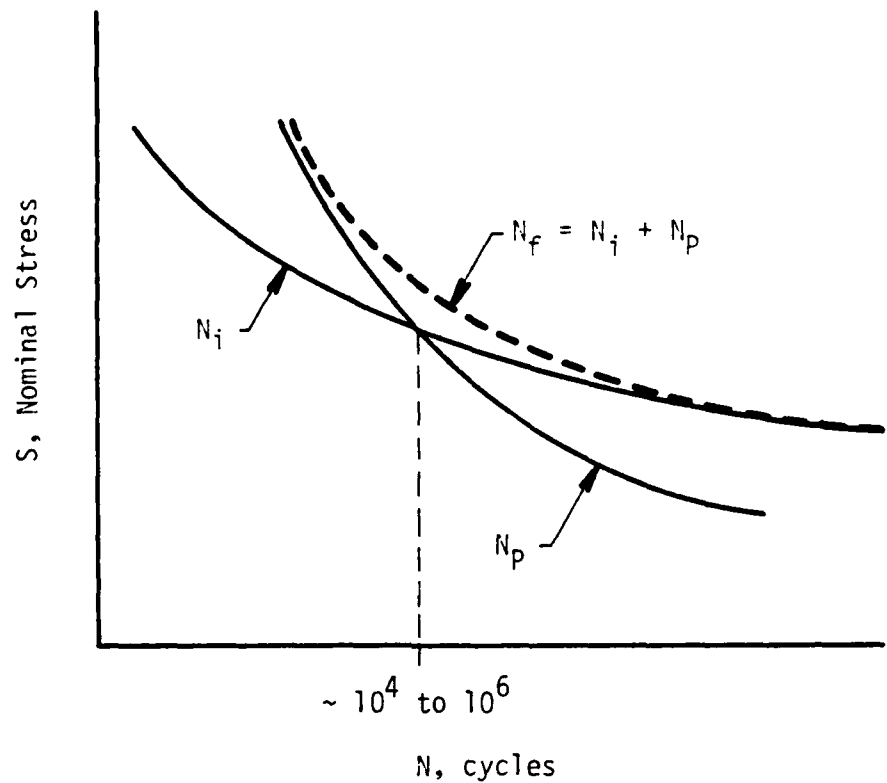


FIGURE 3.1. RELATION BETWEEN FATIGUE CYCLES CORRESPONDING TO CRACK INITIATION (N_i), CRACK PROPAGATION (N_p), AND TOTAL LIFE TO FAILURE (N_f) OF SMOOTH, UNCRACKED SPECIMENS TESTED AT VARIOUS STRESS LEVELS (S)

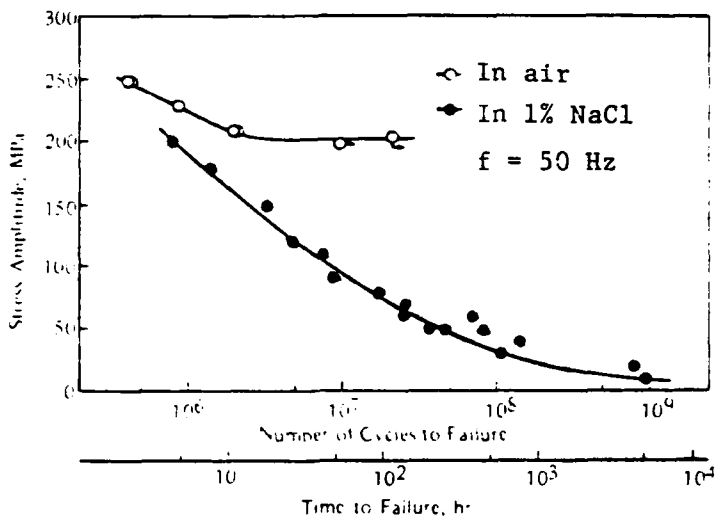


FIGURE 3.2. S-N DATA ON C-Mn STEEL ILLUSTRATING
TYPICAL INFLUENCE OF SALTWATER ENVIRONMENT
ON CORROSION FATIGUE RESISTANCE
(FROM [3.2])

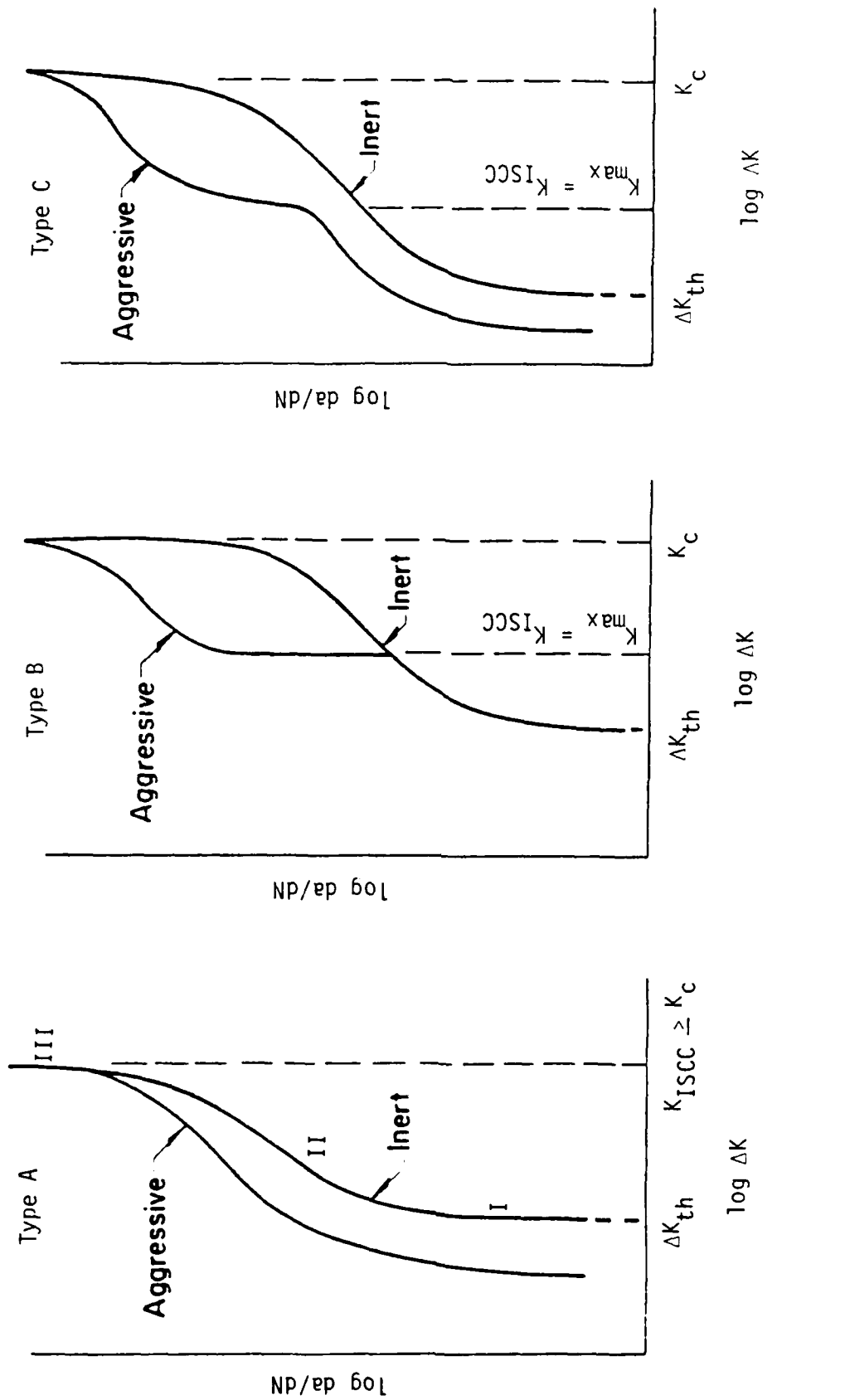


FIGURE 3.3. SCHEMATIC OF BASIC TYPES OF FATIGUE CRACK GROWTH BEHAVIOR ([FROM [3.3]])

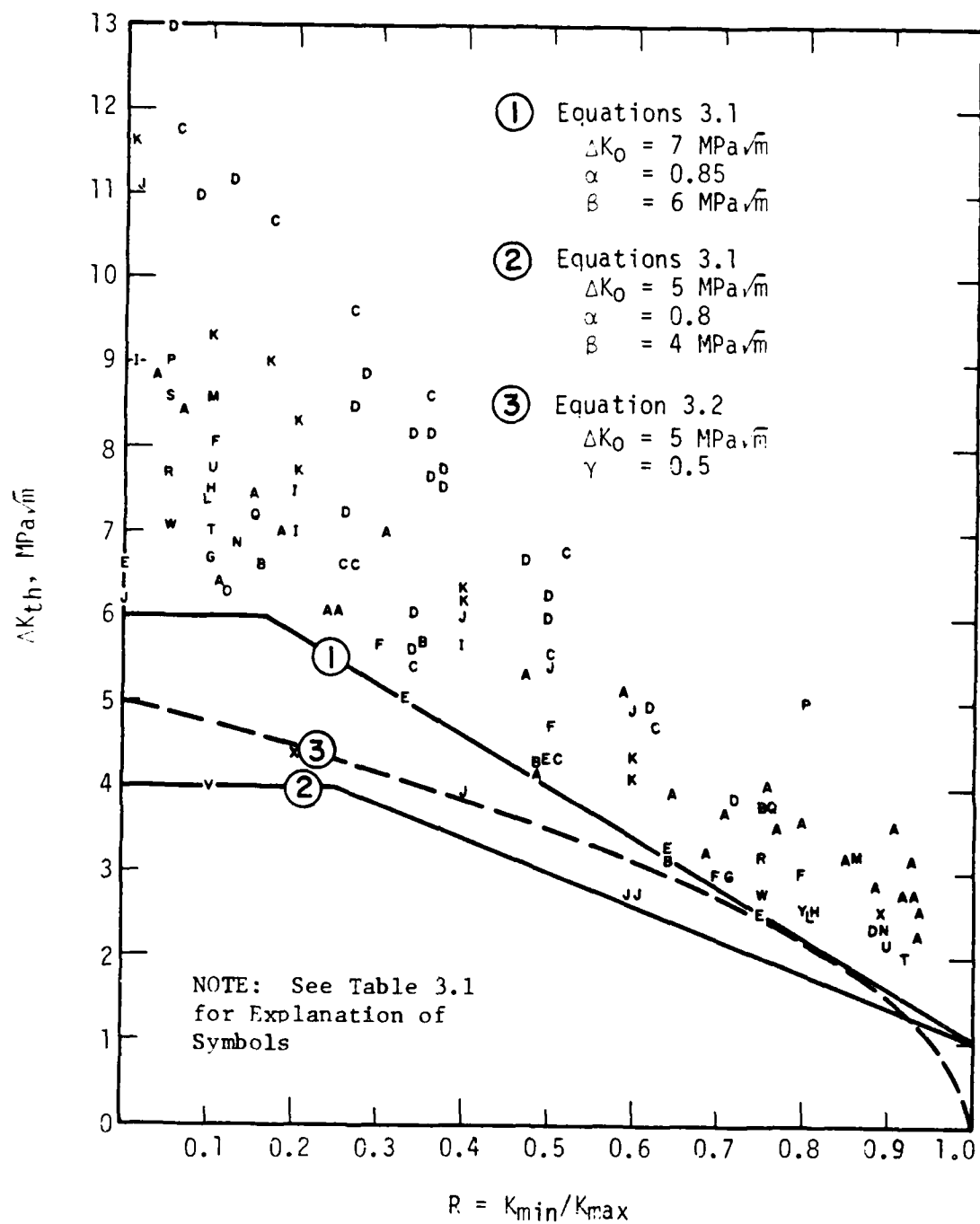


FIGURE 3.4. EFFECT OF LOAD RATIO ON ΔK_{th} FOR A VARIETY OF STRUCTURAL AND LOW-ALLOY STEELS EXPOSED TO LABORATORY AIR ENVIRONMENTS

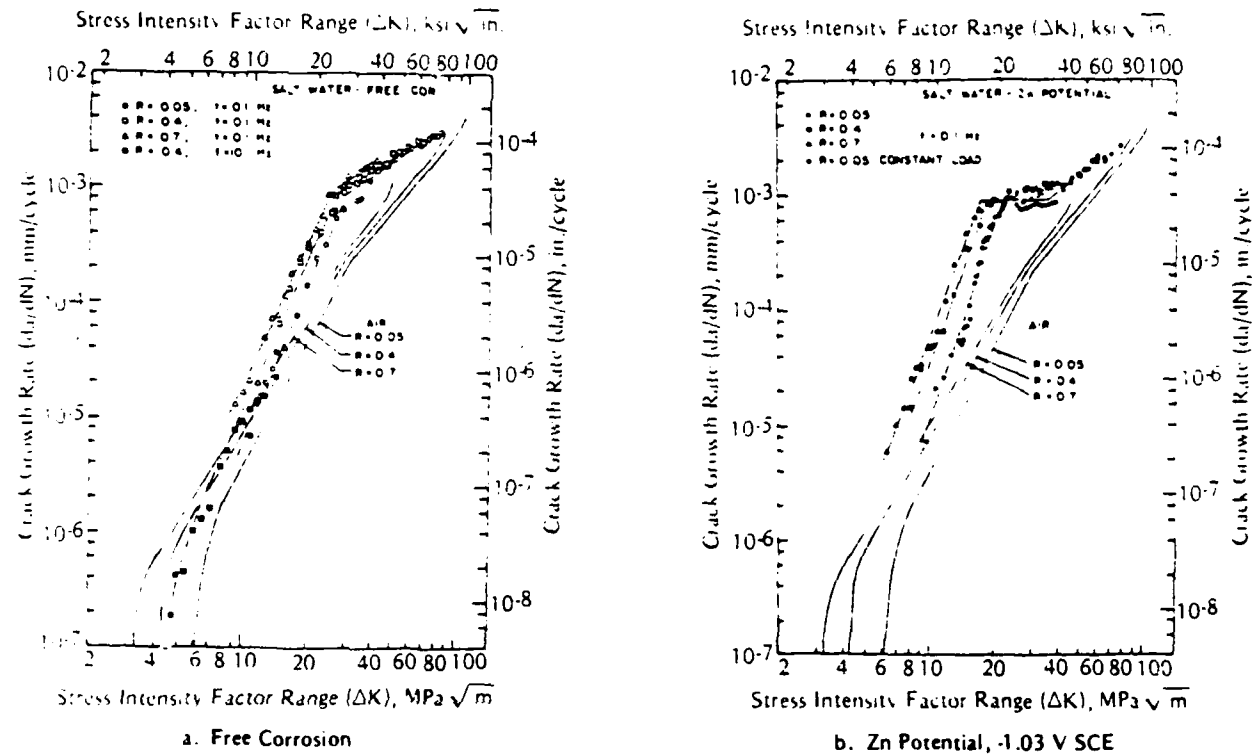


FIGURE 3.5. INFLUENCE OF LOAD RATIO ON THE CORROSION FATIGUE CRACK GROWTH RATES IN API X-70 LINEPIPE STEEL IN 3.5% NaCl (FROM [3.30])

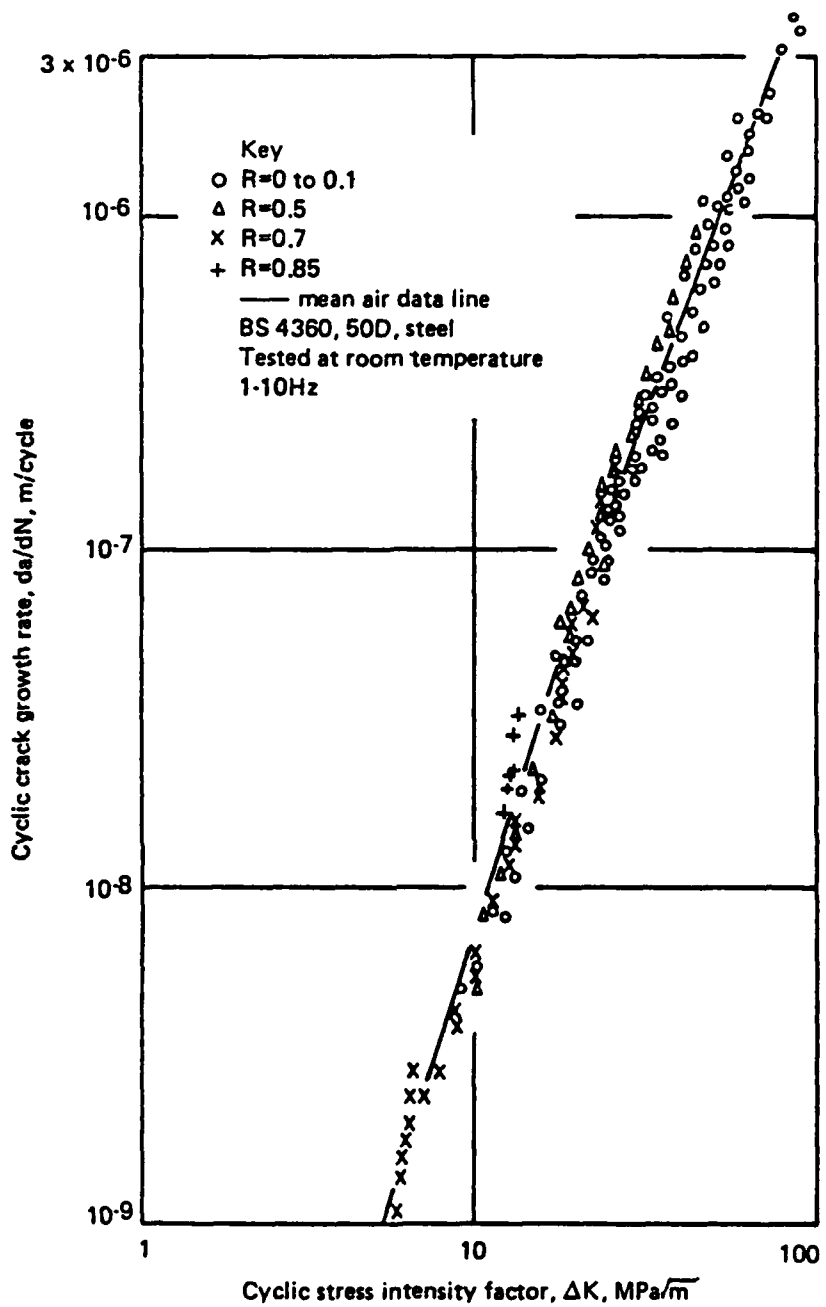


FIGURE 3.6. FATIGUE CRACK GROWTH RATE DATA ON BS 4360 GRADE 50D IN LABORATORY AIR AT VARIOUS LOAD RATIOS. NOTE THE RELATIVE INSENSITIVITY OF THESE REGION II GROWTH RATES TO LOAD RATIO.
 (FROM [3.9])

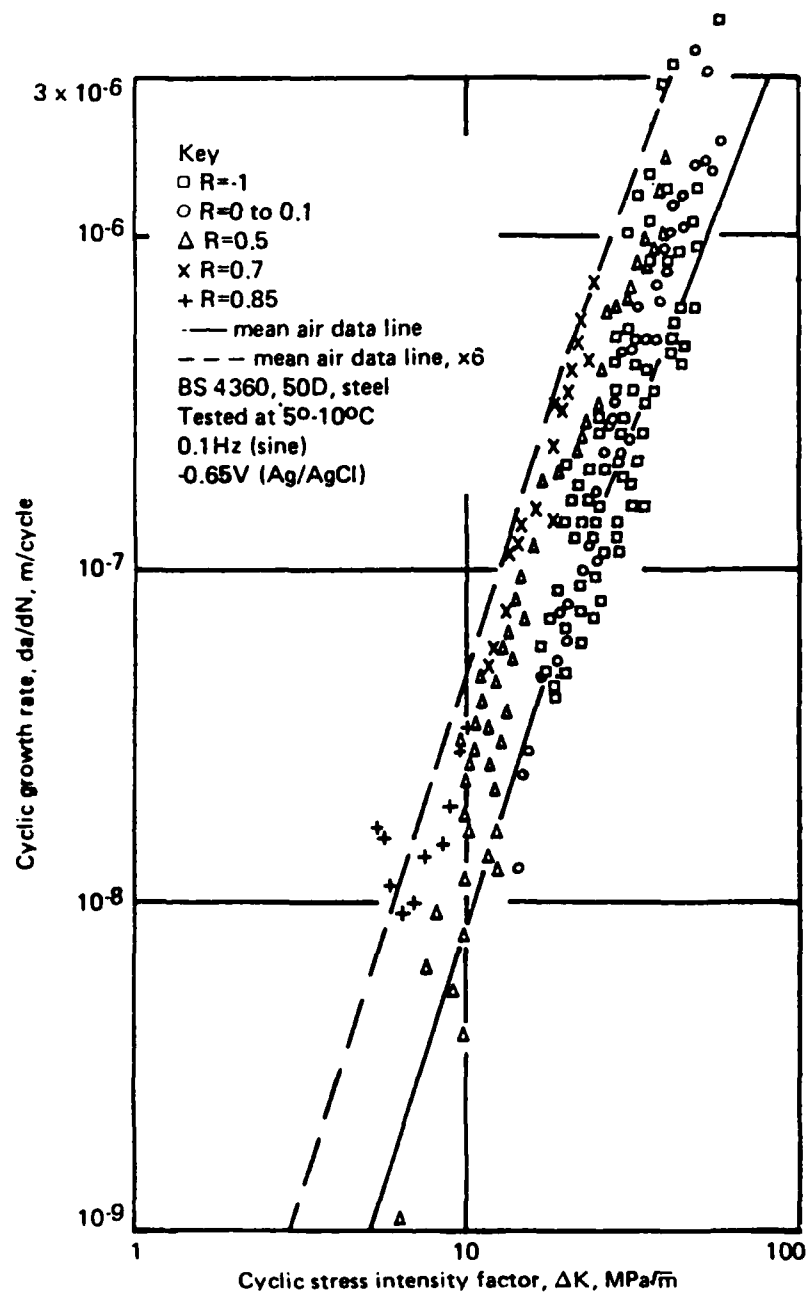


FIGURE 3.7. INFLUENCE OF LOAD RATIO ON THE REGION II FATIGUE CRACK GROWTH RATE DATA ON BS 4360 GRADE 50D STEEL IN SEAWATER (FROM [3.9])

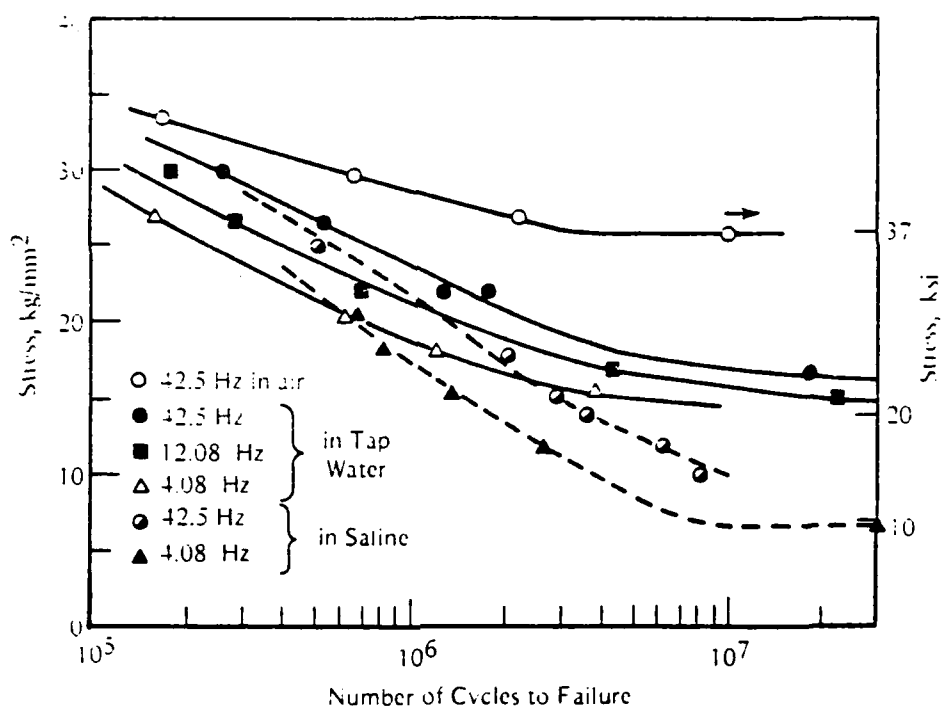


FIGURE 3.8. EFFECT OF CYCLIC FREQUENCY ON CORROSION FATIGUE STRENGTH OF A MEDIUM CARBON STEEL IN A 1% NaCl SOLUTION (FROM [3.36])

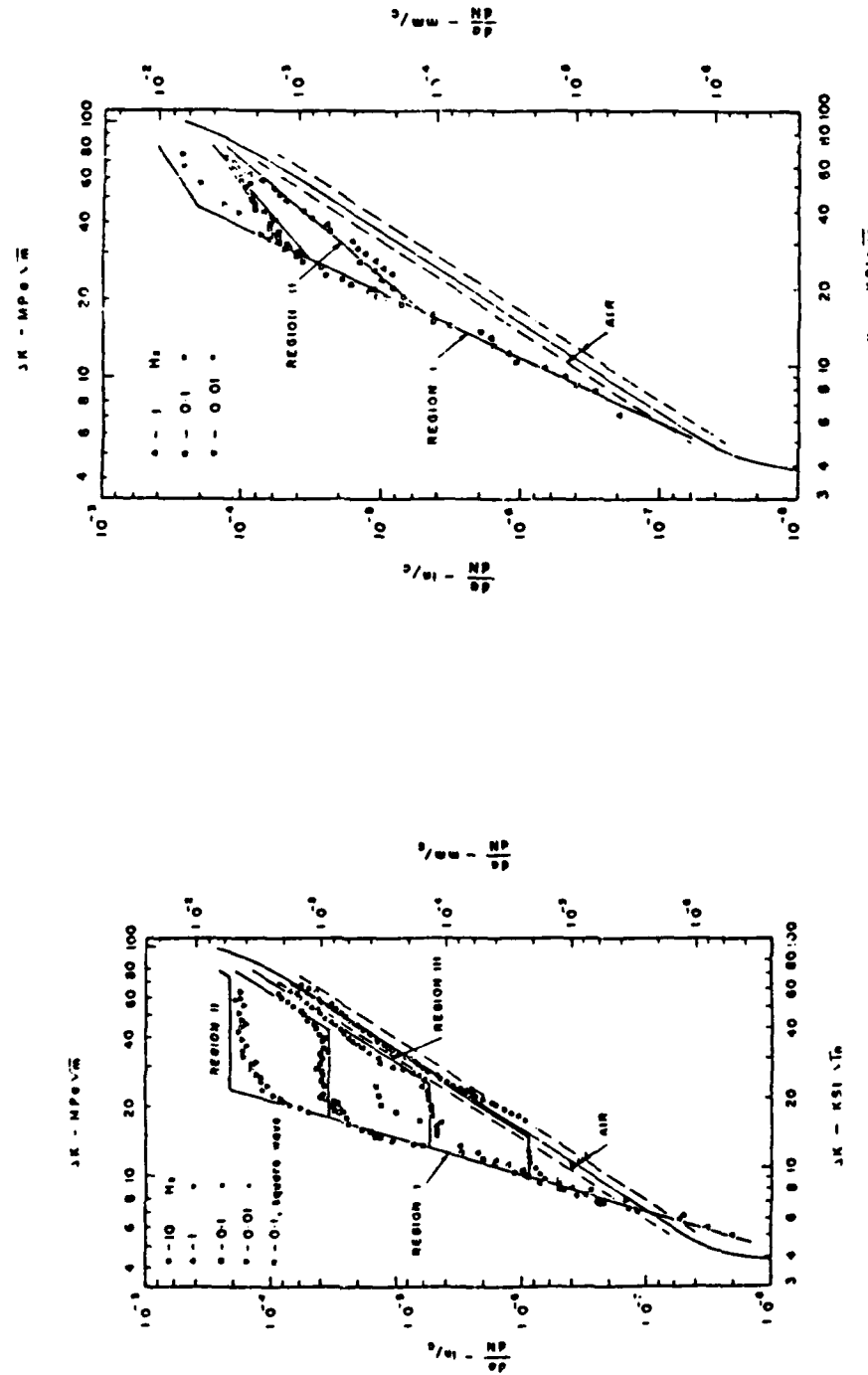


FIGURE 3.9. EFFECT OF CYCLIC FREQUENCY ON THE FATIGUE CRACK GROWTH RATE IN AN X-65 LINEPIPE STEEL UNDER EITHER CATHODIC POLARIZATION OR FREELY CORRODING CONDITIONS (FROM [3.37])

(a) Cathodic Polarization,
-1.04 V (Ag/AgCl)

(b) Freely Corroding, -0.68 V (Ag/AgCl)

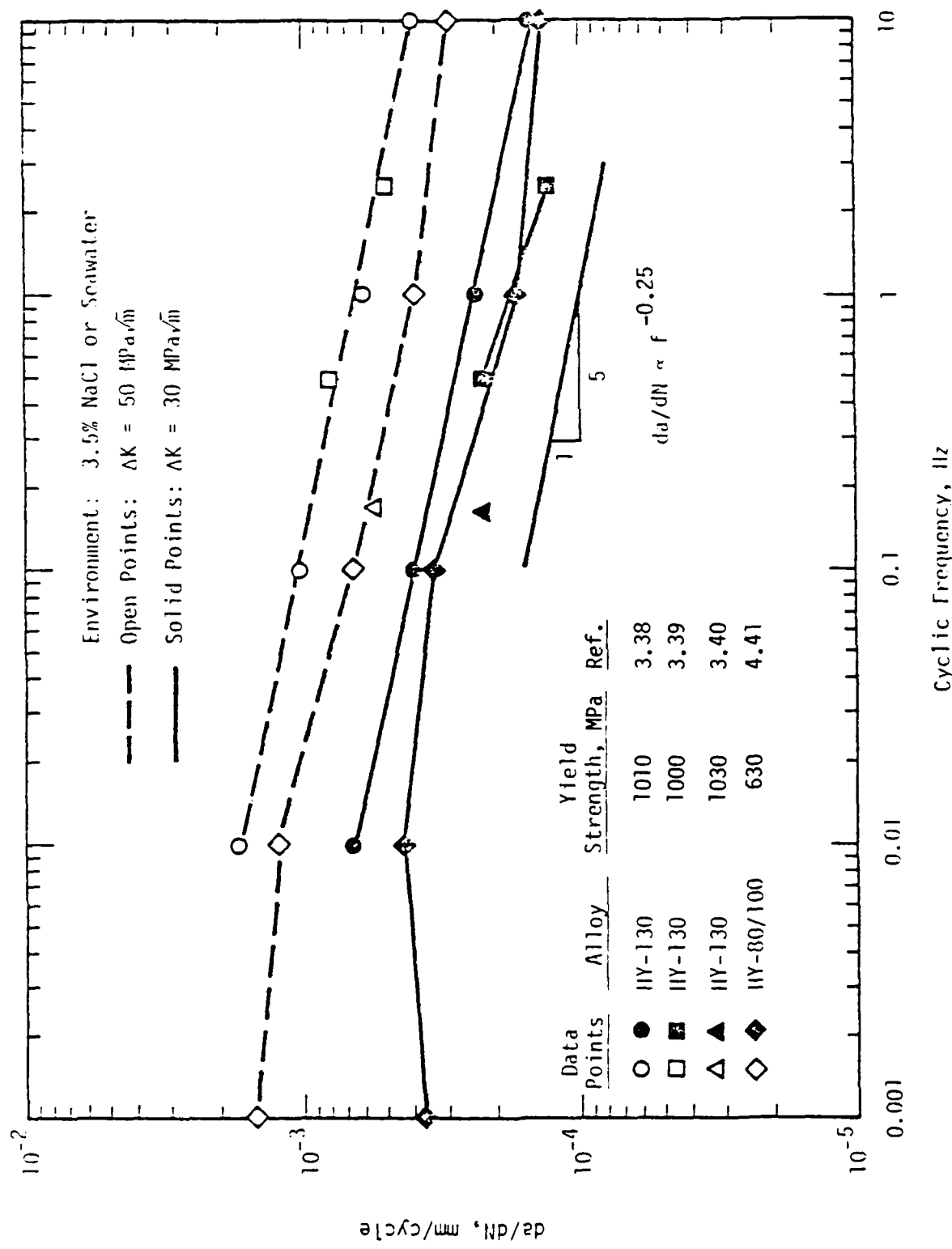


FIGURE 3.10. EFFECT OF CYCLIC FREQUENCY ON FATIGUE CRACK GROWTH RATE IN SEVERAL HY-SERIES STEELS IN SALT WATER

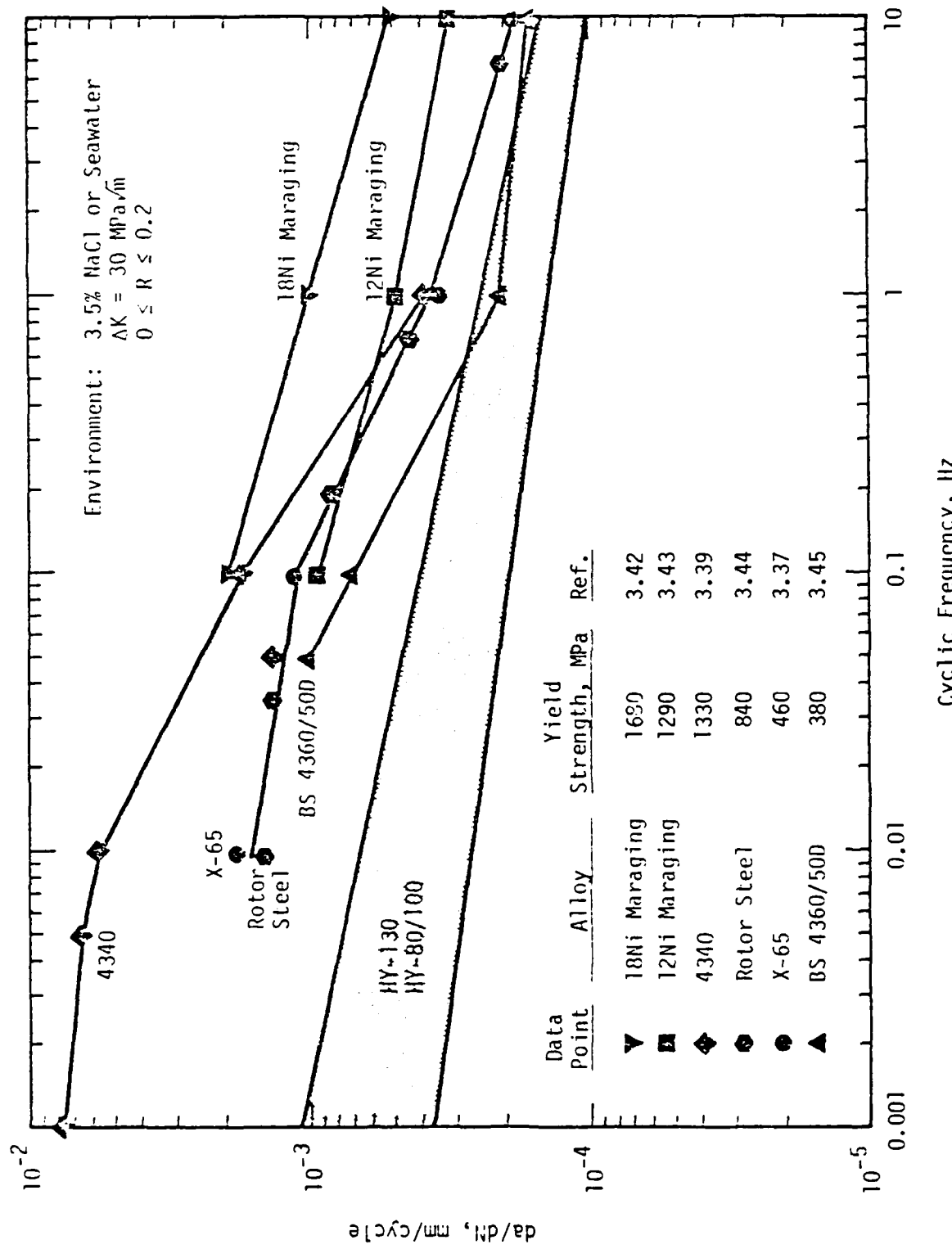


FIGURE 3.11. EFFECT OF CYCLIC FREQUENCY ON FATIGUE CRACK GROWTH RATES IN VARIOUS STRUCTURAL AND ALLOY STEELS IN SALT WATER

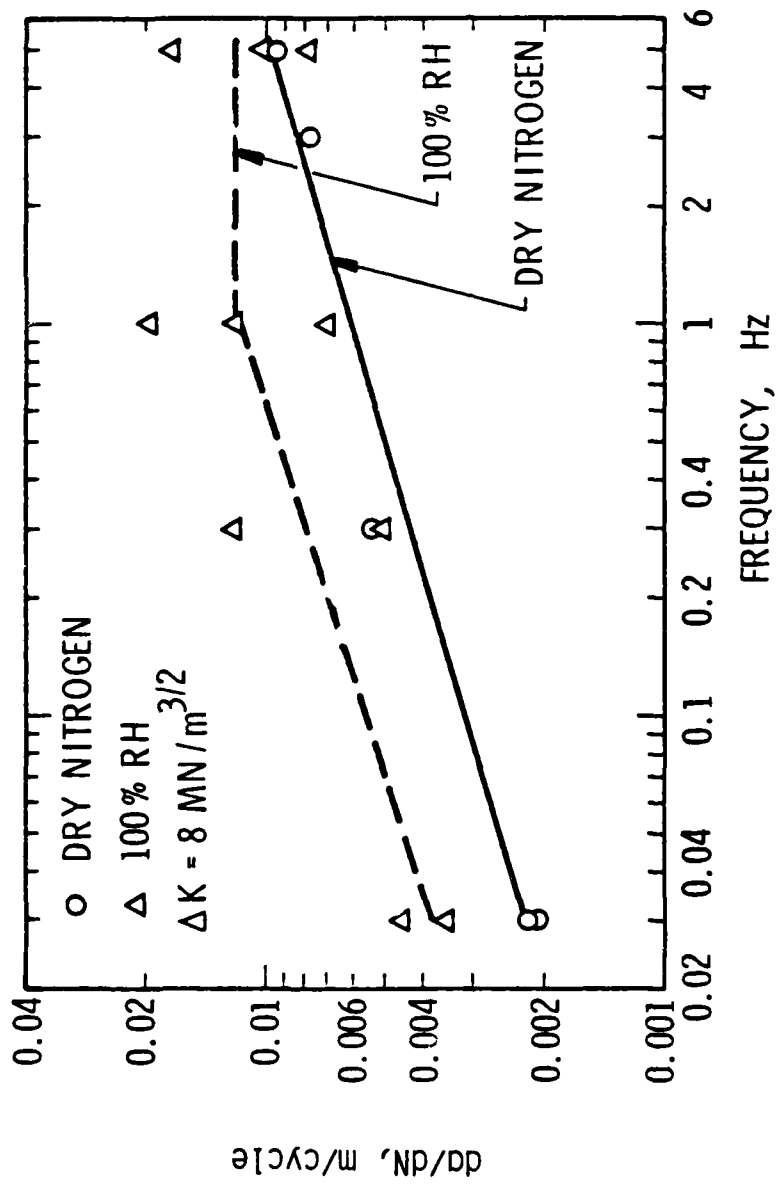
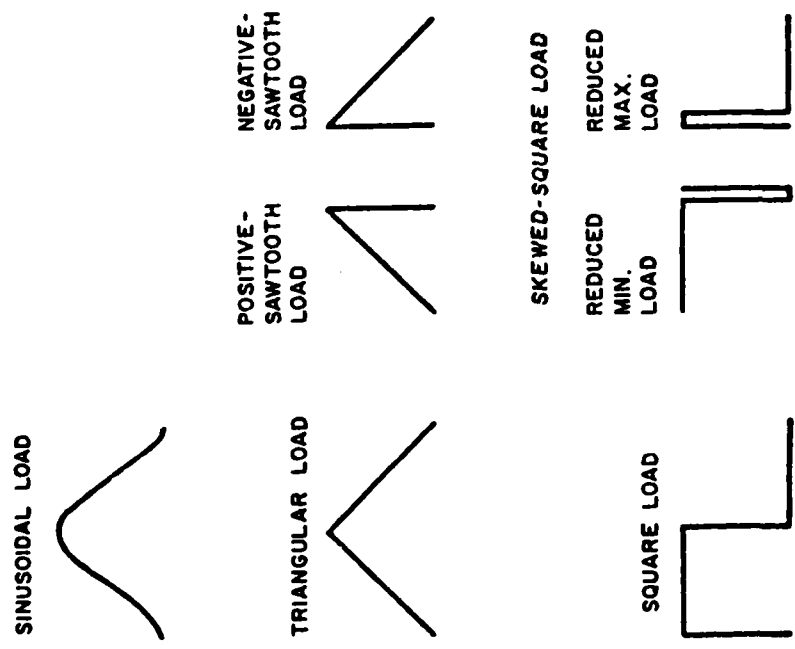
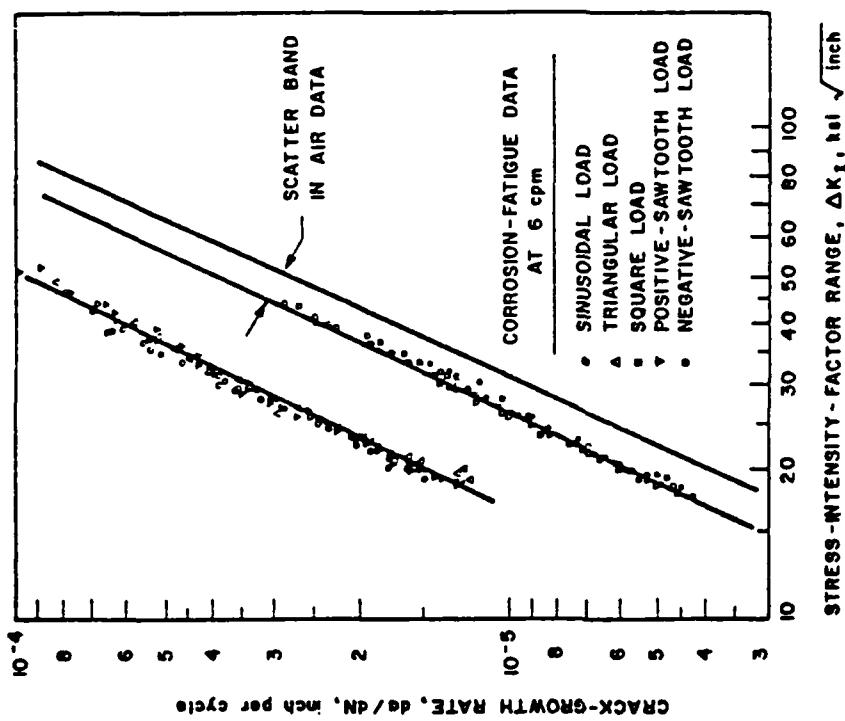


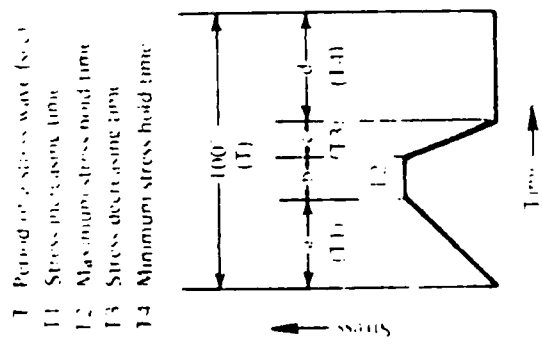
FIGURE 3.12. EFFECT OF CYCLIC FREQUENCY ON FATIGUE CRACK GROWTH RATE
IN A LOW CARBON STEEL
(FROM [3.46])



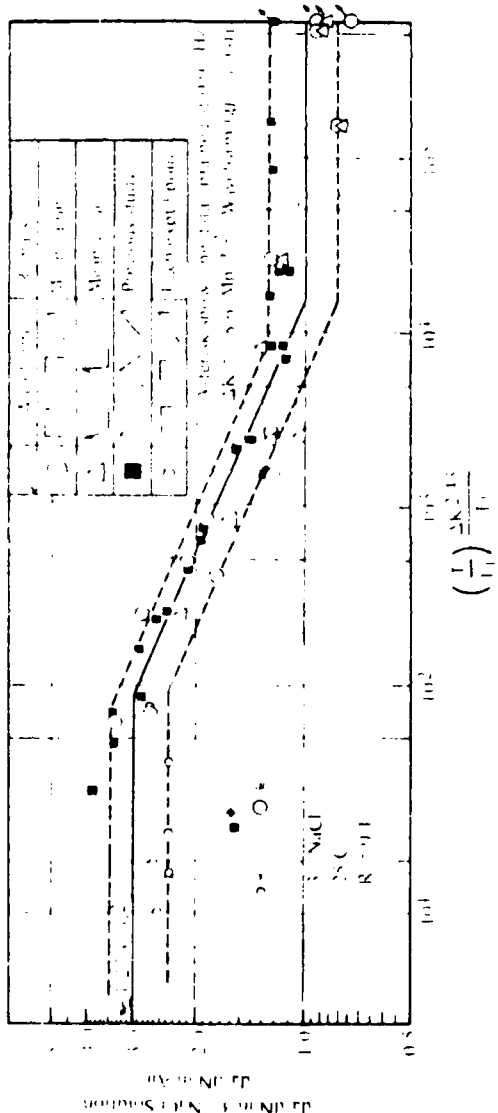
(a) Various Waveforms Studied

(b) Crack Growth Rate Data

FIGURE 3.13. CORROSION FATIGUE CRACK GROWTH RATE DATA FOR A 12NI STEEL IN 3% NaCl UNDER VARIOUS CYCLIC LOADING WAVEFORMS (FROM [3.47])



(a) Definition of Characteristic Times in Waveforms Studied



(b) Growth Rate Versus Waveshape Parameter

FIGURE 3.14. EFFECT OF CYCLIC WAVEFORM AND FREQUENCY ON FATIGUE CRACK GROWTH RATES IN A Ni-Cr-Mo ALLOY STEEL EXPOSED TO 3.5% NaCl (FROM [3.47])

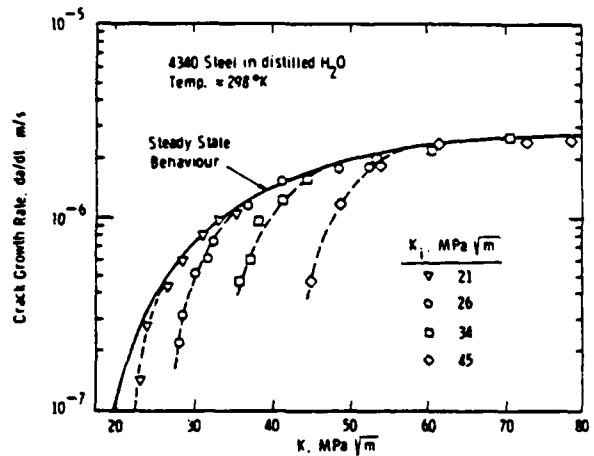


FIGURE 3.15. DEPENDENCE OF STATIC-LOAD CRACK GROWTH RATES ON INITIALLY APPLIED STRESS INTENSITY FACTOR, K_i (FROM [3.54])

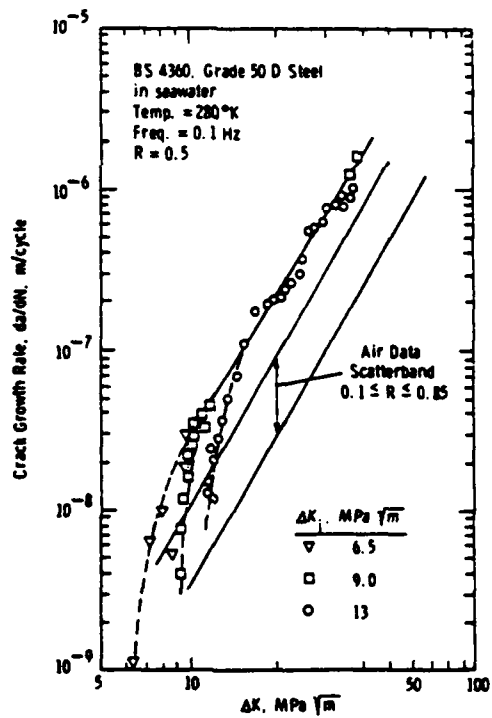


FIGURE 3.16. DEPENDENCE OF FATIGUE CRACK GROWTH RATES ON INITIALLY APPLIED STRESS INTENSITY FACTOR RANGE, ΔK_i (FROM [3.55])

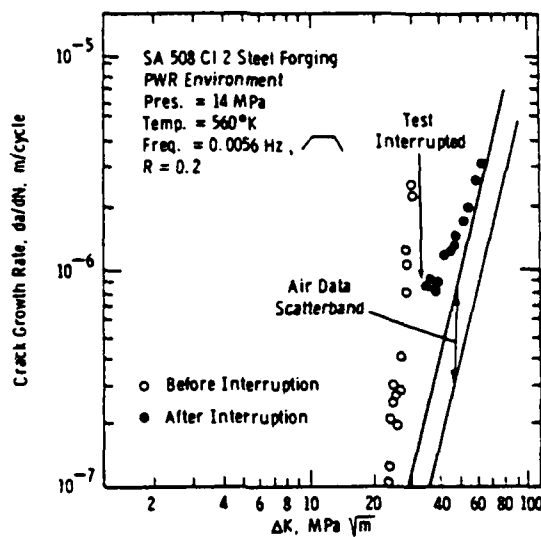


FIGURE 3.17. EFFECT OF TEST INTERRUPTION ON FATIGUE CRACK GROWTH RATE DATA (FROM [3.56])

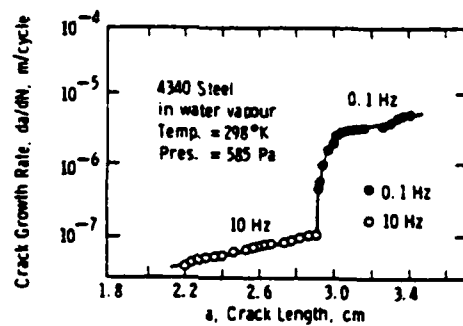


FIGURE 3.18. FATIGUE CRACK GROWTH RATE RESPONSE RESULTING FROM A CHANGE IN CYCLIC LOADING FREQUENCY (FROM [3.56])

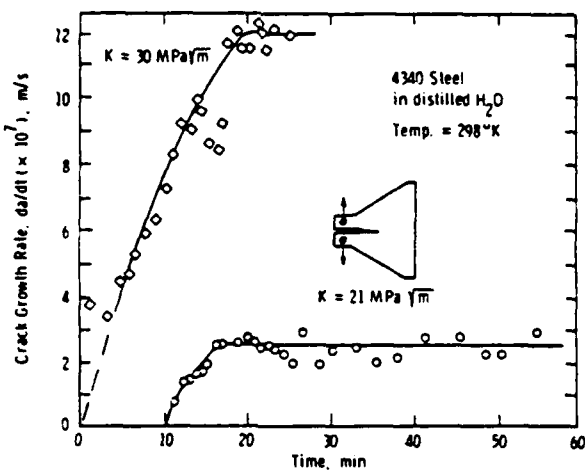


FIGURE 3.19. STATIC LOAD CRACK GROWTH RATES UNDER CONSTANT STRESS INTENSITY FACTOR CONDITIONS SHOWING TRANSIENT AND STEADY-STATE BEHAVIOR (FROM [3.53])

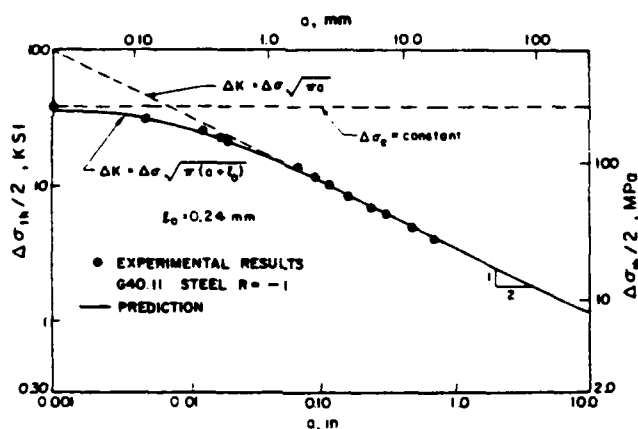


FIGURE 3.20. USE OF THE PARAMETER σ_0 TO RELATE THE SMOOTH BAR FATIGUE STRENGTH ($\Delta\sigma_e$) AND THE THRESHOLD STRESS INTENSITY FOR CRACK GROWTH (ΔK_{th}) (FROM [3.65])

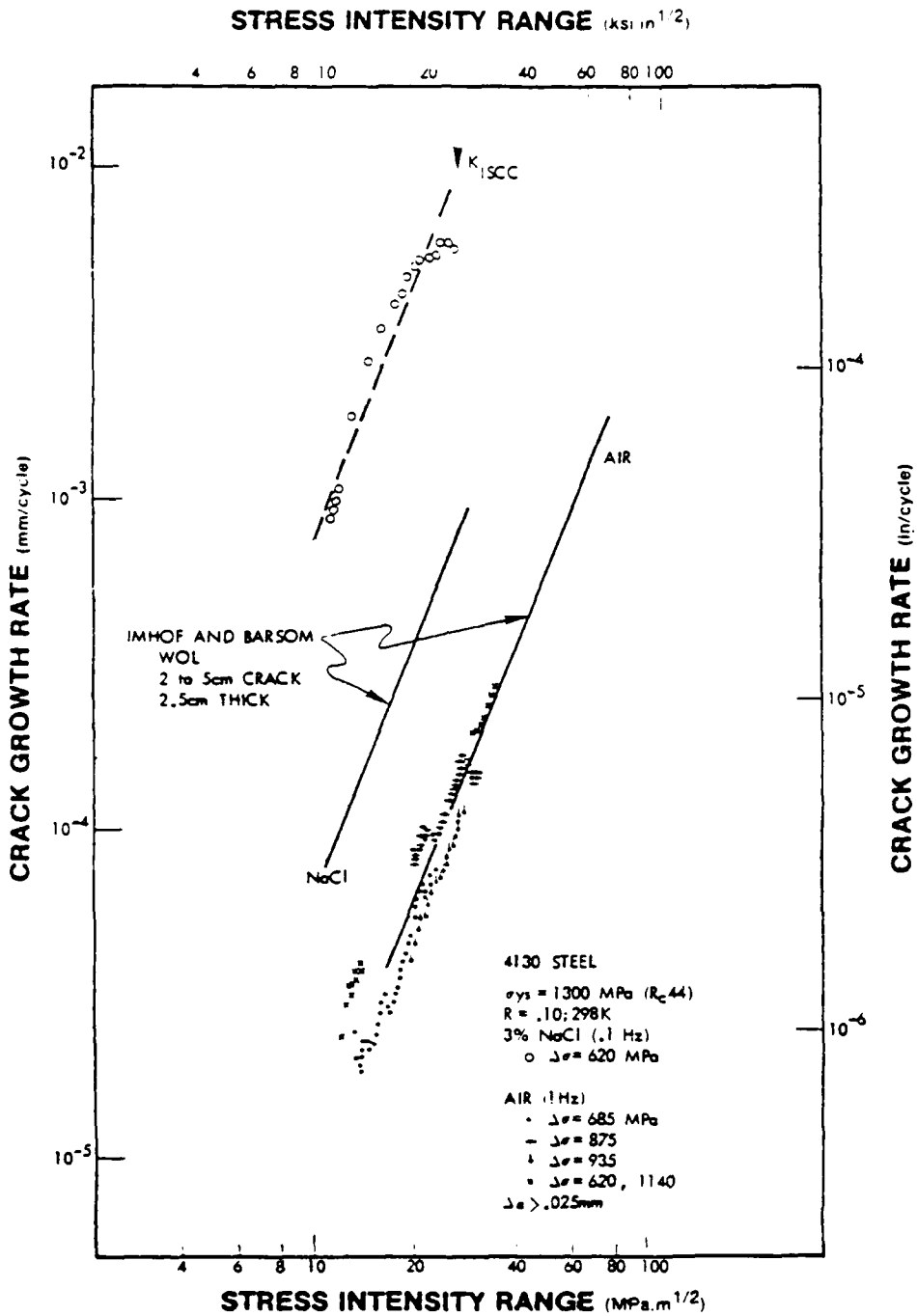


FIGURE 3.21. COMPARISON OF CRACK GROWTH KINETICS FOR SMALL AND LARGE CRACKS IN BOTH AIR AND 3% NaCl
(FROM [3.66])

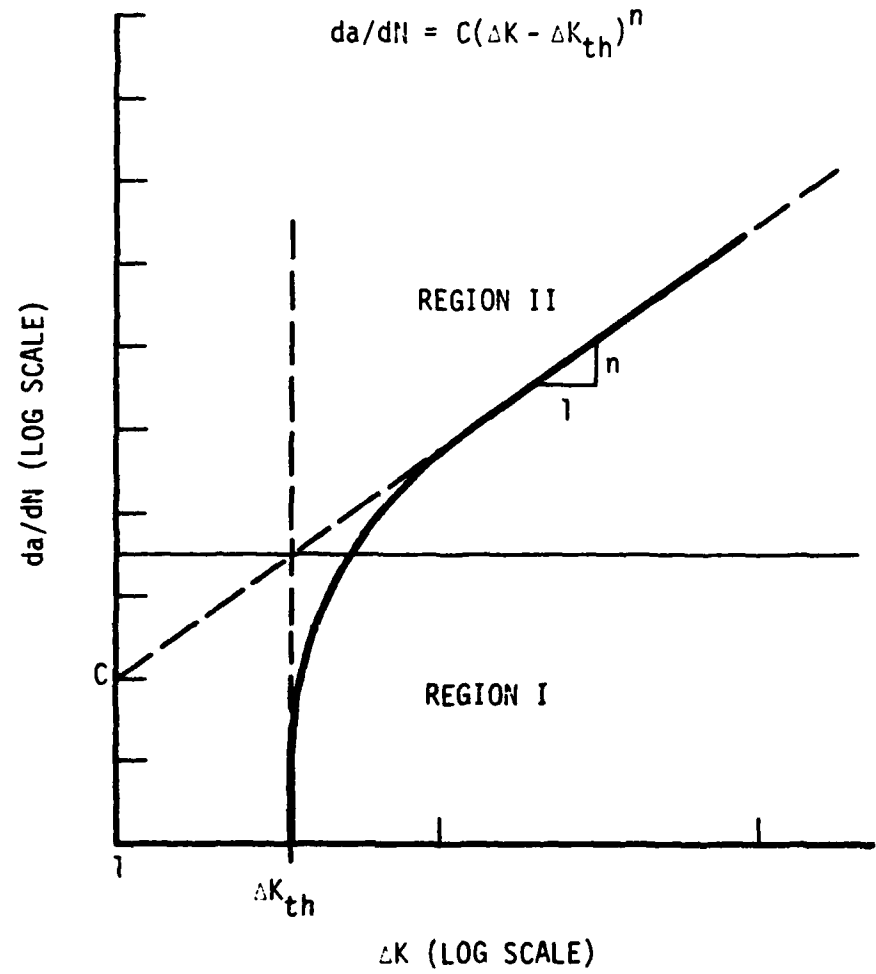


FIGURE 3.22. SCHEMATIC REPRESENTATION OF ASYMPTOTIC CRACK GROWTH RATE EQUATION

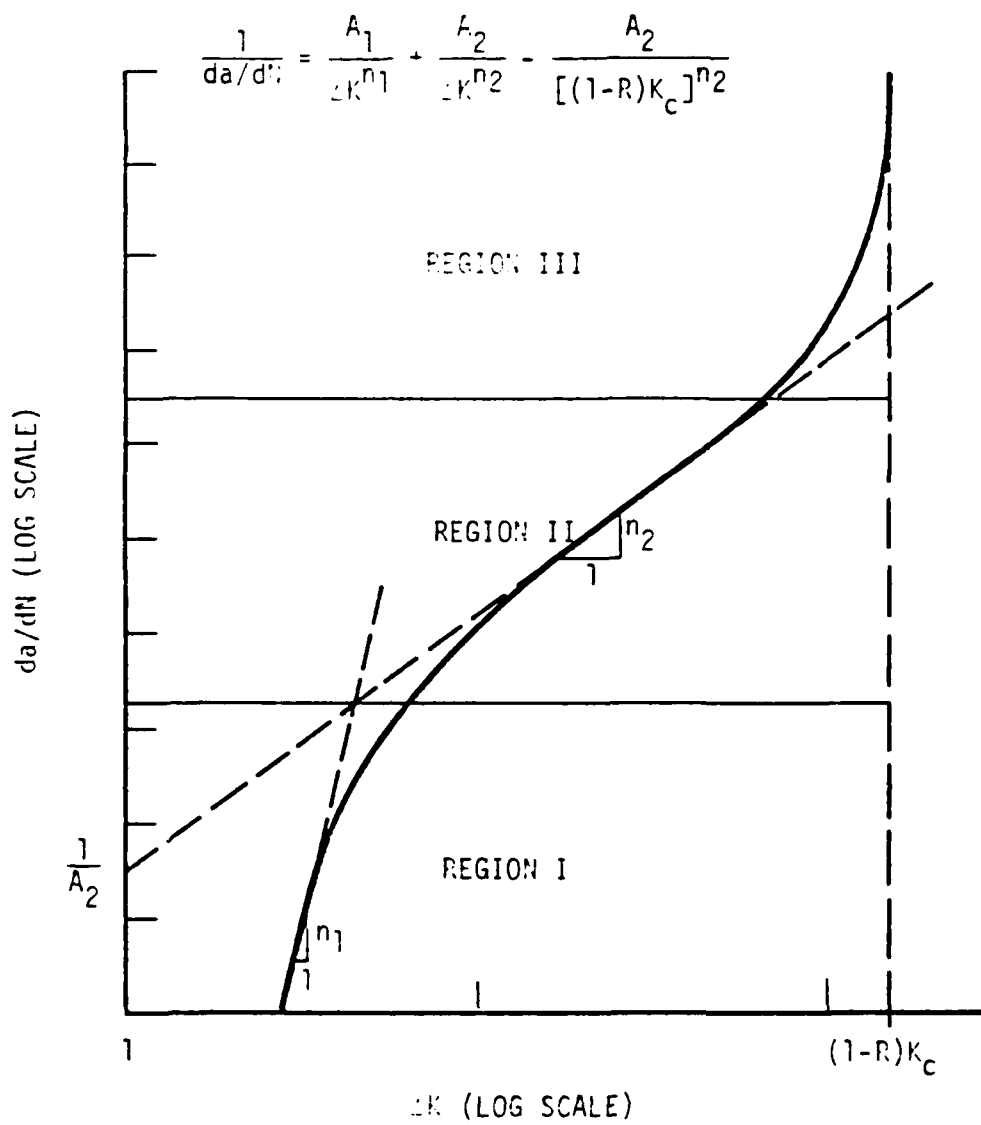


FIGURE 3.23. SCHEMATIC REPRESENTATION OF THREE COMPONENT CRACK GROWTH RATE EQUATION

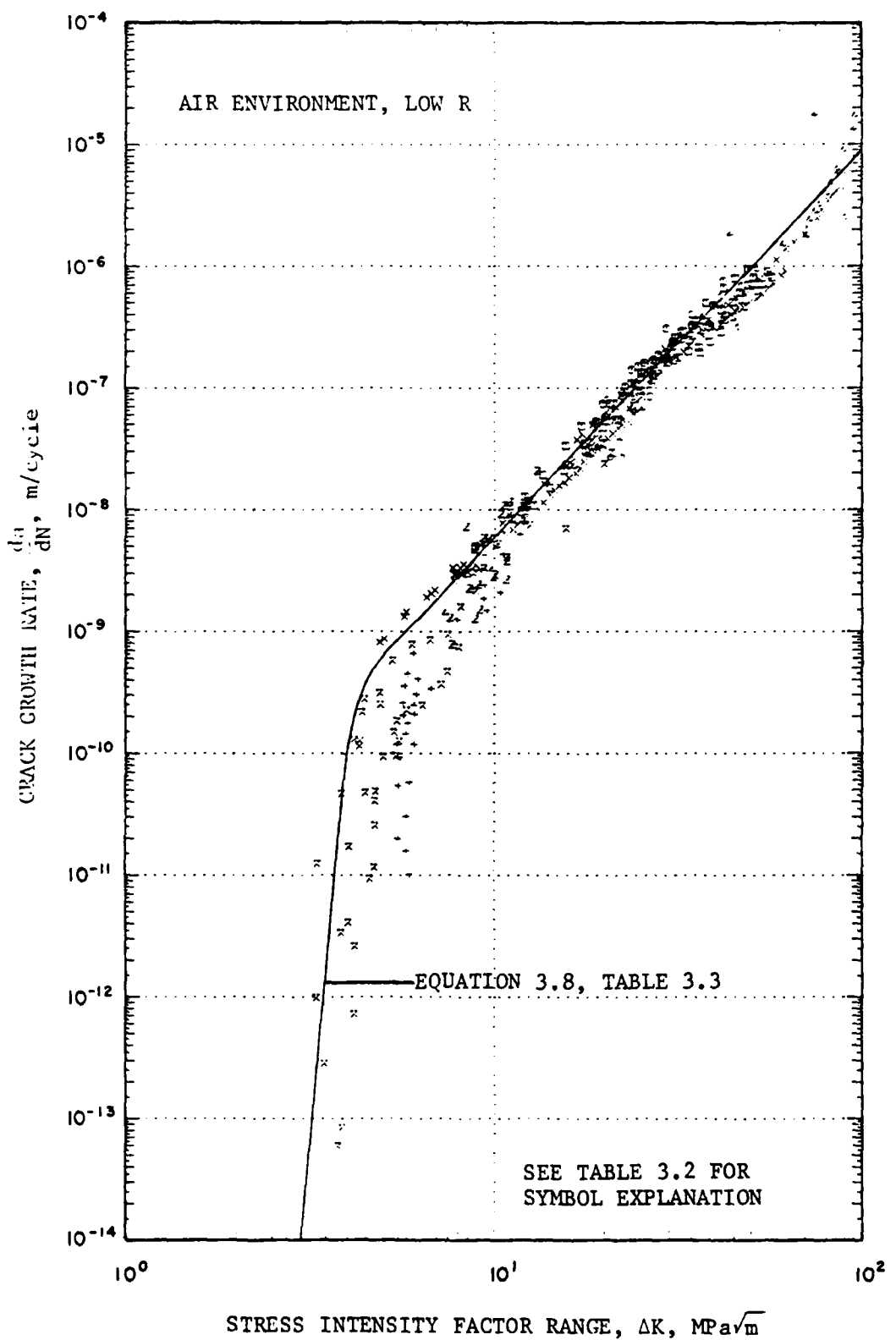


FIGURE 3.24. CRACK GROWTH DATA, AIR ENVIRONMENT, LOW R

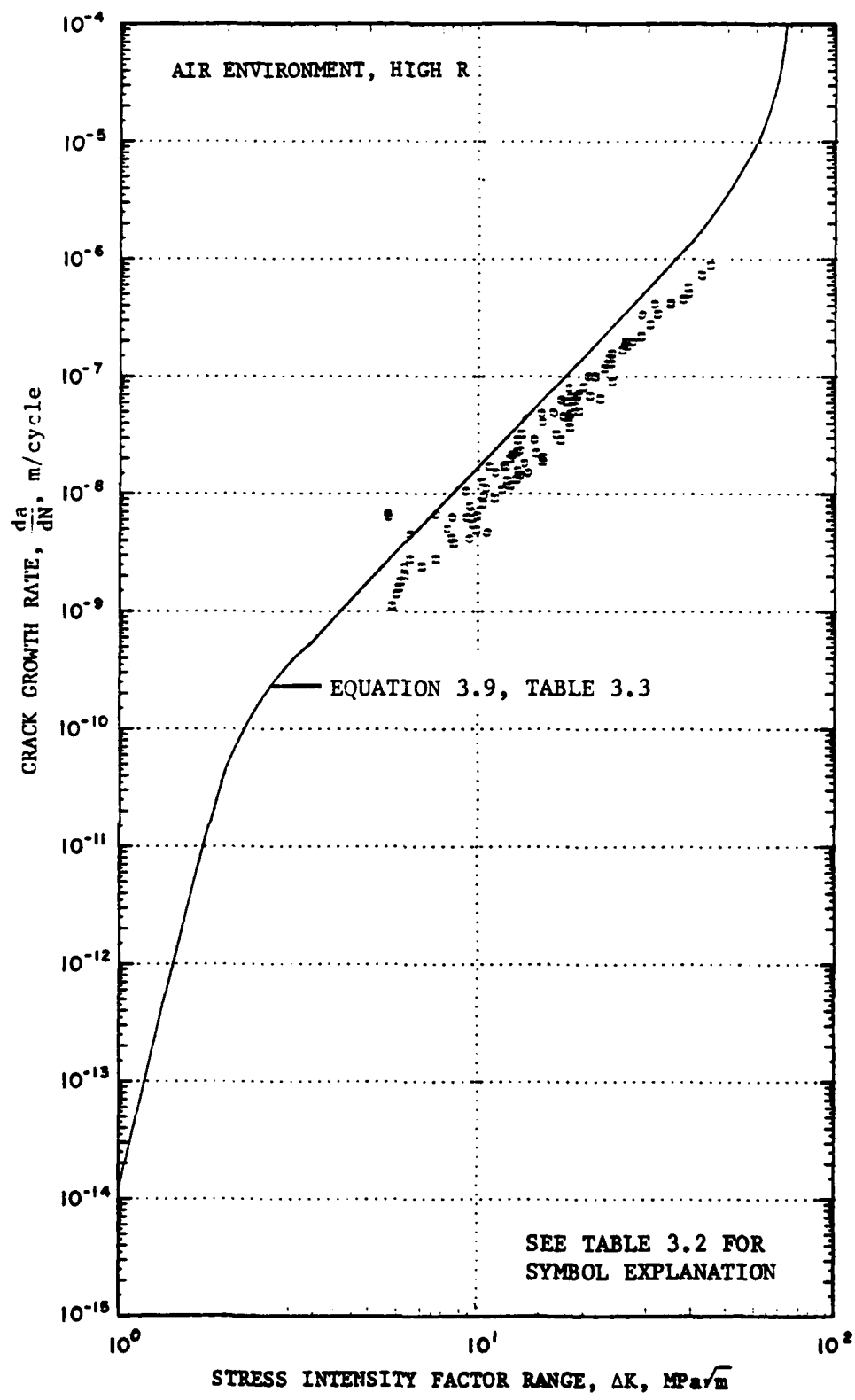


FIGURE 3.25. CRACK GROWTH DATA, AIR ENVIRONMENT, HIGH R

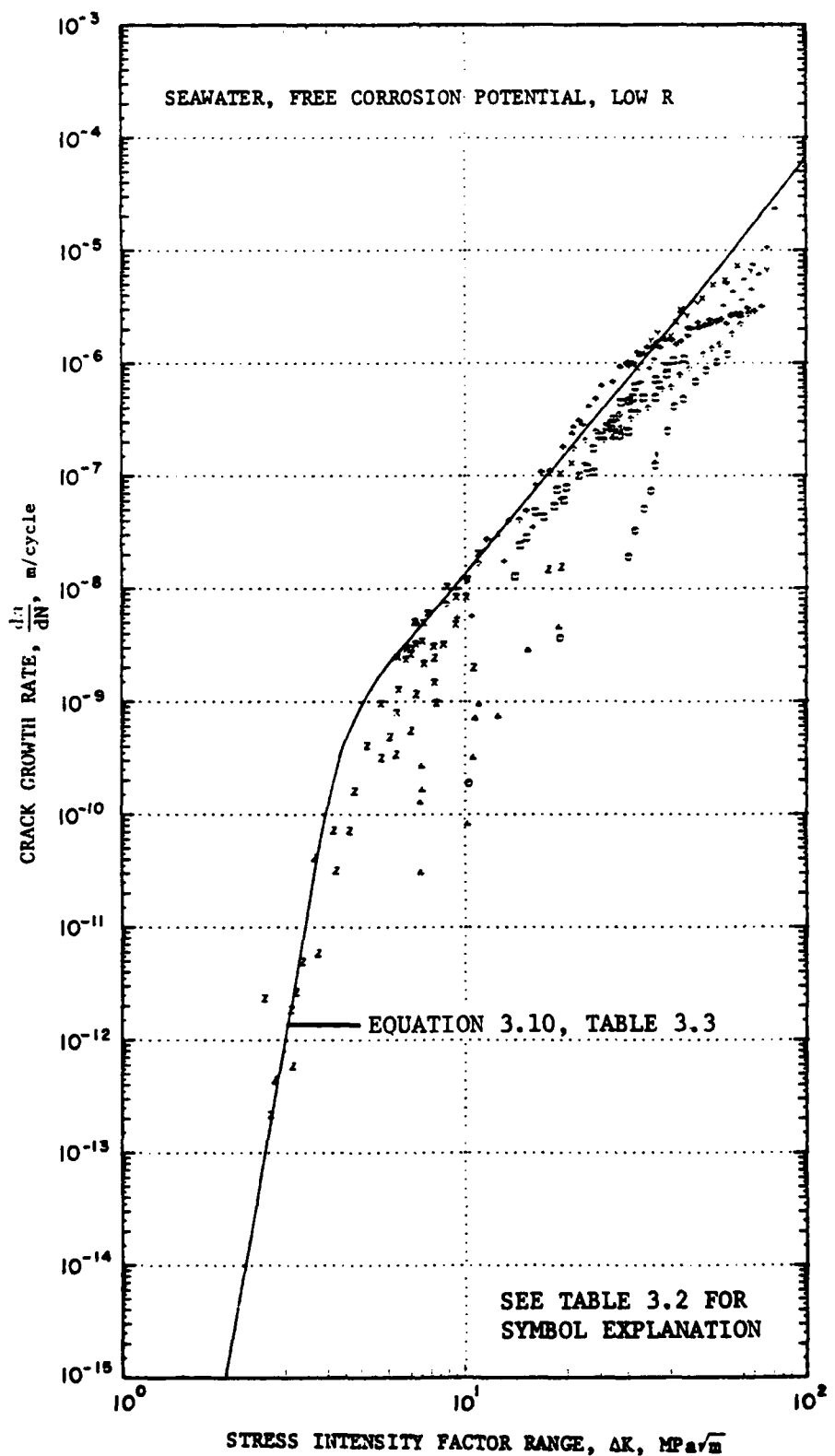


FIGURE 3.26. CRACK GROWTH DATA, SEAWATER,
FREE CORROSION POTENTIAL, LOW R

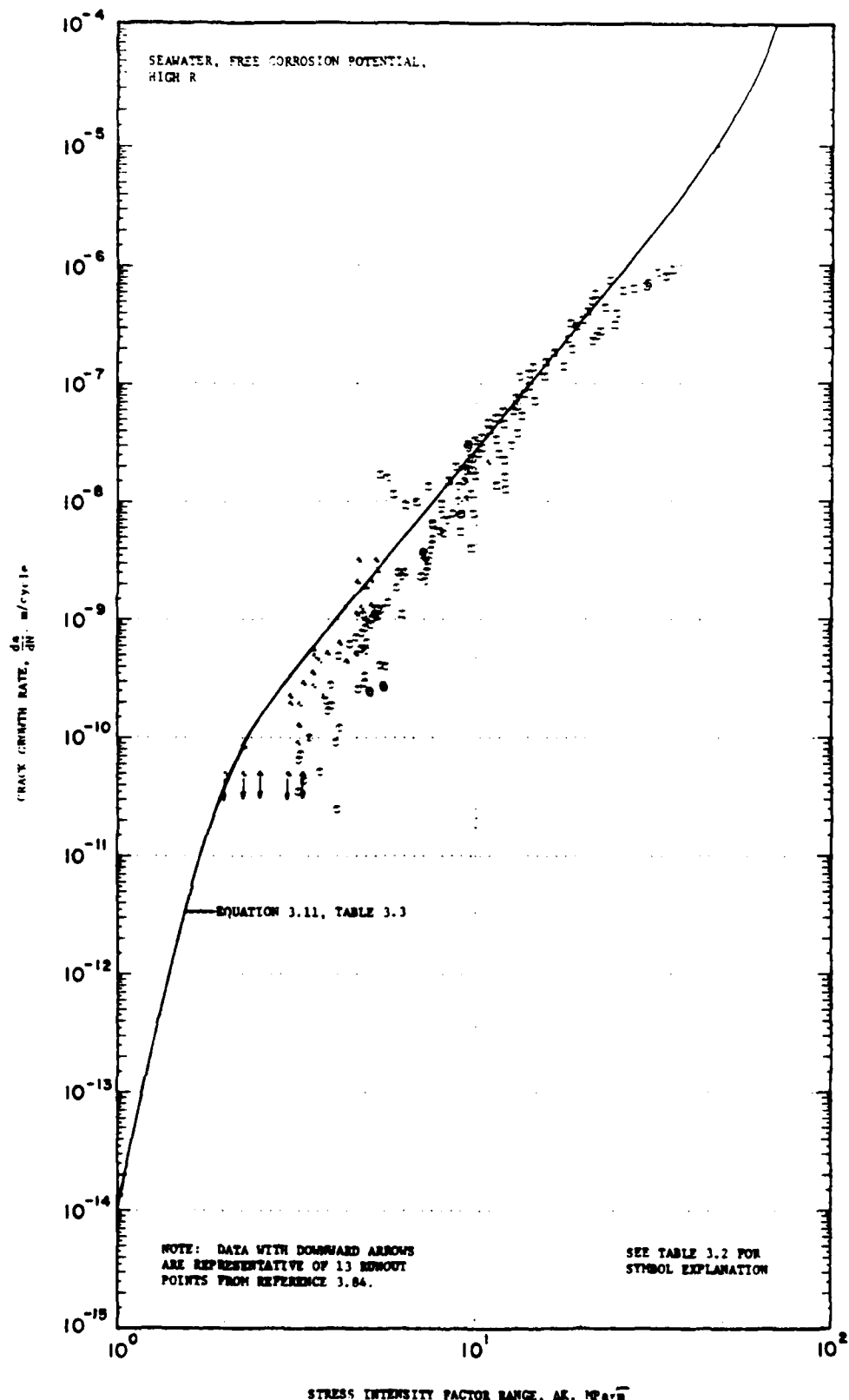


FIGURE 3.27. CRACK GROWTH DATA, SEAWATER,
FREE CORROSION POTENTIAL, HIGH R

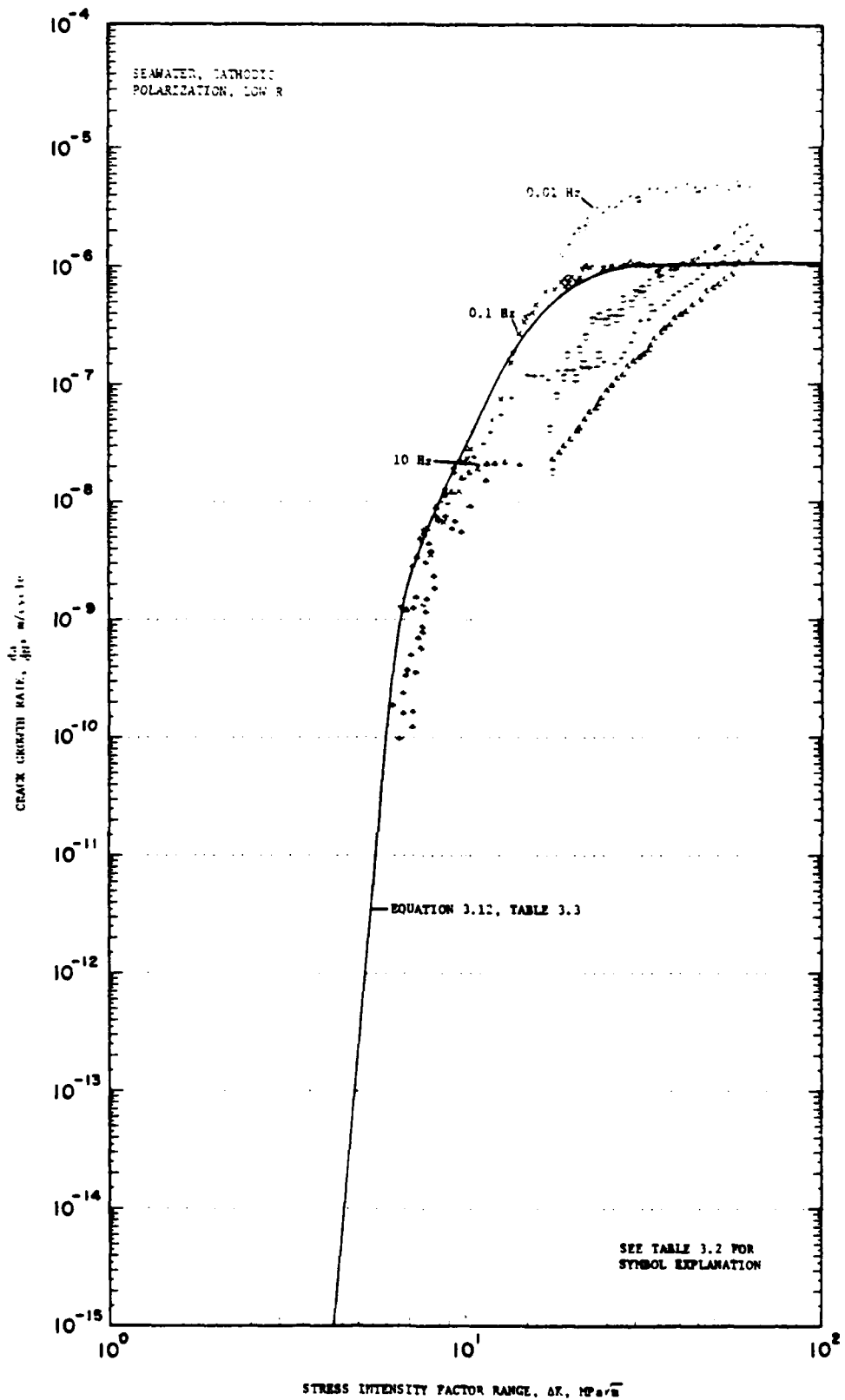


FIGURE 3.28. CRACK GROWTH DATA, SEAWATER,
CATHODIC POLARIZATION, LOW R

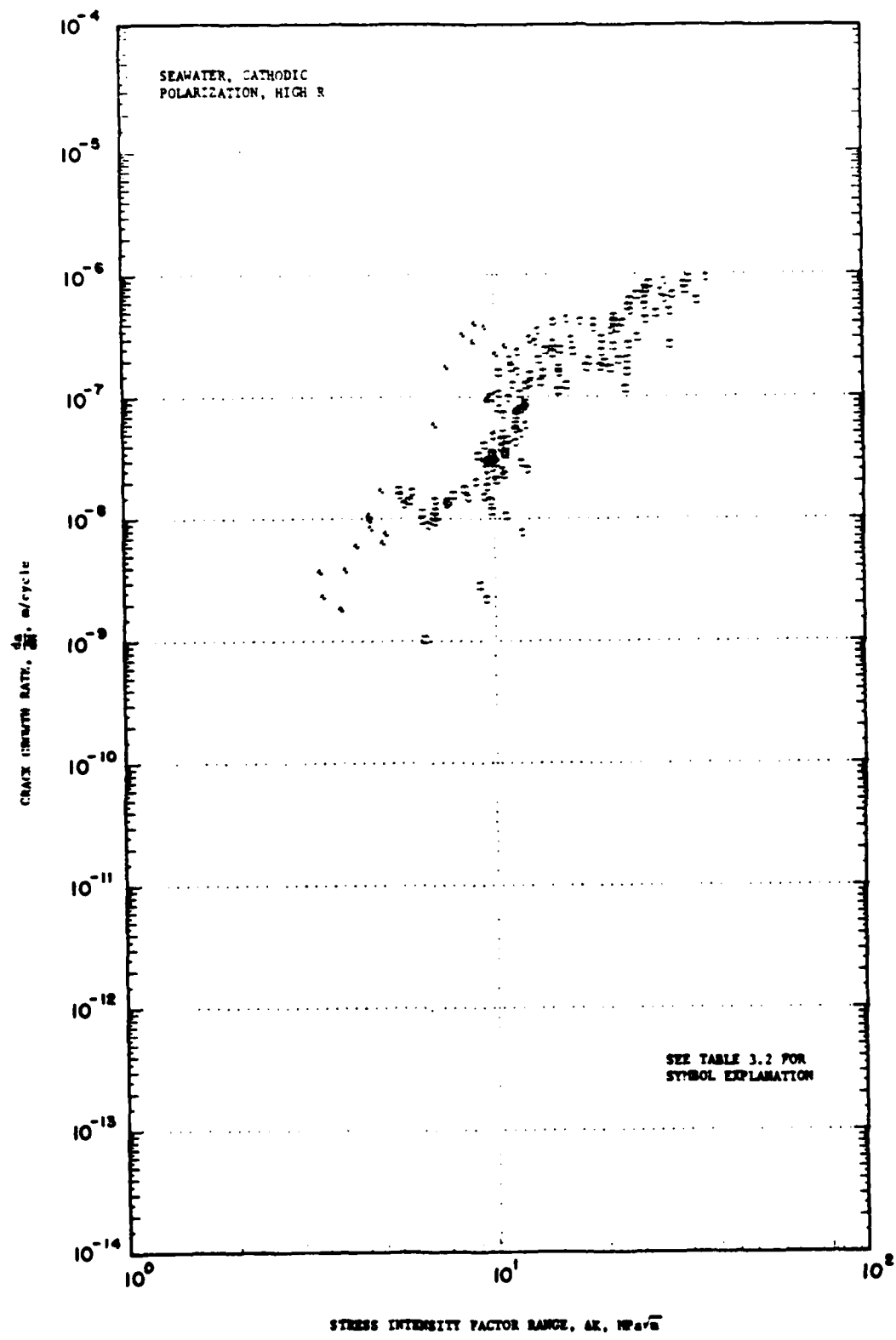


FIGURE 3.29. CRACK GROWTH DATA, SEAWATER,
CATHODIC POLARIZATION, HIGH R

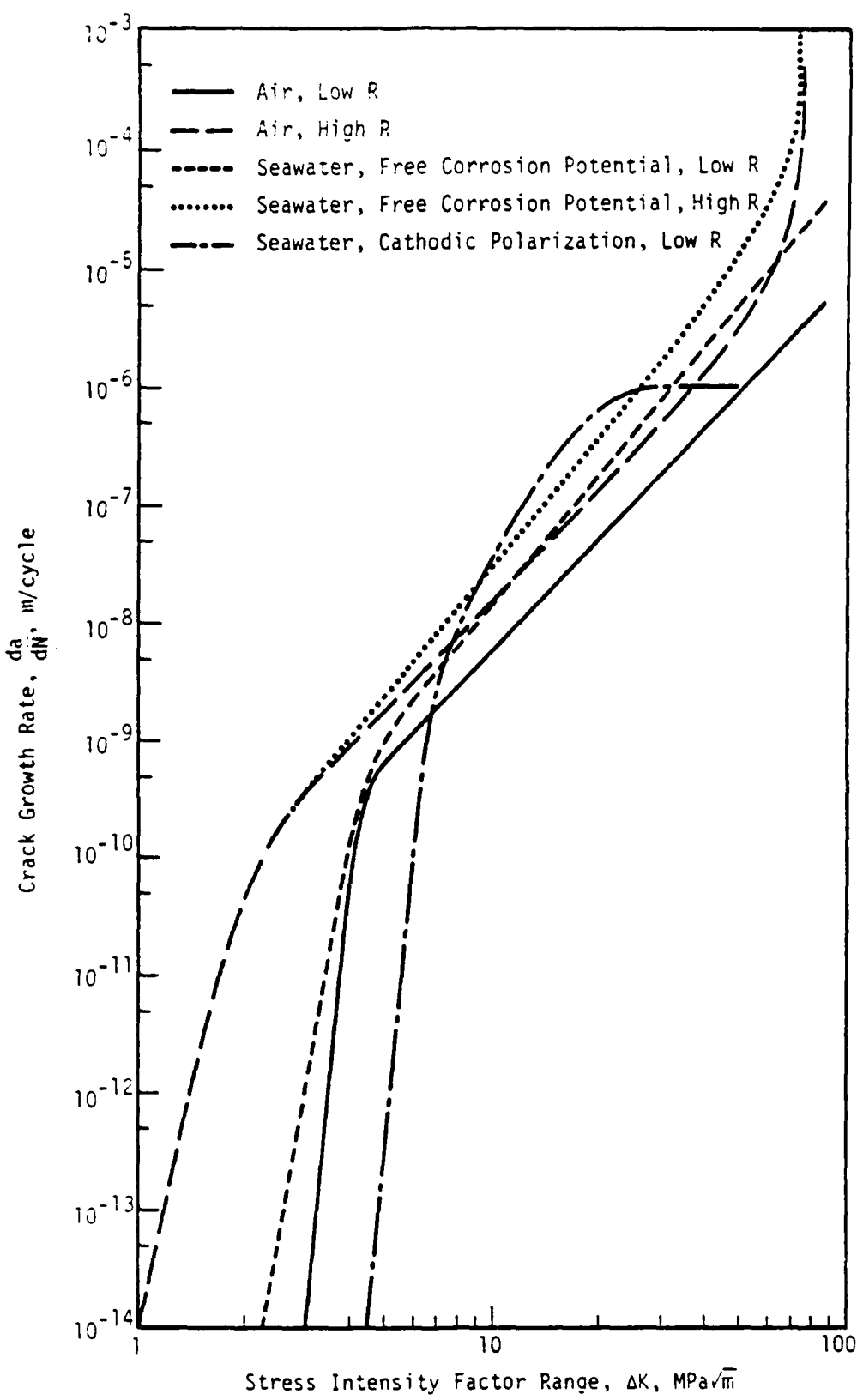
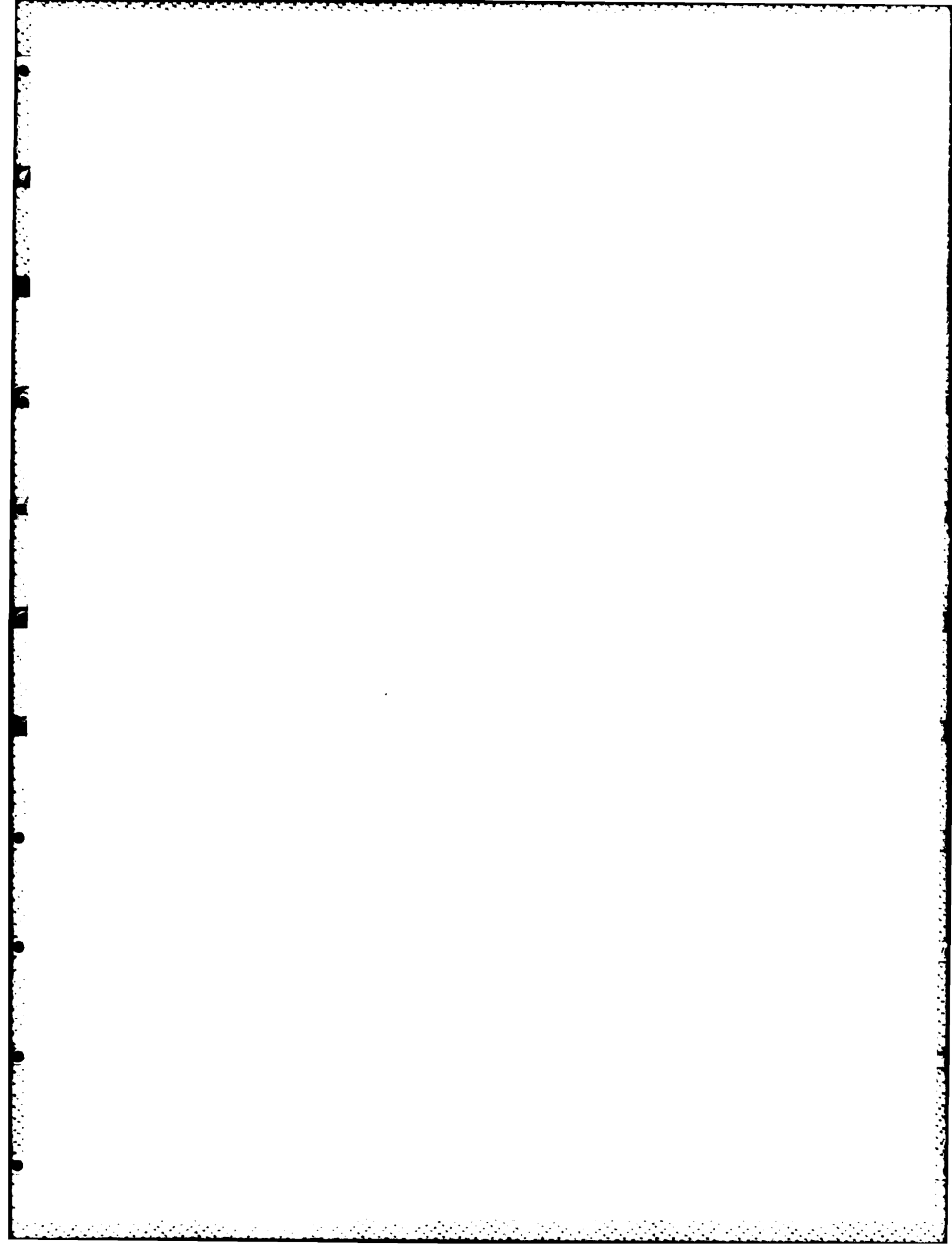


FIGURE 3.30. SUMMARY OF THREE-COMPONENT CRACK GROWTH EQUATIONS



4.0 EFFECT OF ENVIRONMENTAL VARIABLES ON CORROSION FATIGUE RESISTANCE

The major environmental variables associated with corrosion fatigue of offshore structures are (1) temperature of the seawater, (2) chemistry of the seawater, and (3) electrode potential of the seawater-steel interface. The primary difficulty in assessing the influence of each of the above variables is that many of them are inextricably related. For example, the application of a cathodic potential increases the oxygen reduction reaction, thereby increasing the pH of solution near the metal surface; this in turn can reduce the solubility of certain salts in seawater and result in chalk-like deposits on the metal surface. In addition, this chain of events is sensitive to temperature since the oxygen reduction reaction and solubility of salts are thermally-activated processes. The chemistry of seawater also varies with time, as indicated in Figure 4.1, where values of five common water hydrology parameters, typical of semitropical Atlantic Ocean surface waters, are given for an annual cycle [4.1].

The environmental variables will be discussed in the order listed above, thereby building to the key practical issue of the effectiveness of cathodic protection systems.

4.1 Effect of Temperature on Corrosion Fatigue Resistance

Offshore structures can experience temperatures ranging from about 0°C to 30°C depending on geographic location, time of the year, and water depth. Qualitatively, it has been clearly established that a decrease in temperature causes an increase in the materials resistance to both fatigue and corrosion fatigue. This trend has been observed in S-N tests, as well as in fatigue crack growth tests, in steels, aluminum alloys, and titanium alloys exposed to a variety of environments ranging from inert to chemically aggressive. The following discussion attempts to quantify the effect of temperature on the fatigue and corrosion fatigue of structural steels.

In S-N tests, on both smooth [4.2] and notched [4.3] specimens of carbon steels in saltwater environments, the cycles to failure have been observed to decrease significantly as temperature is increased. Data from Dugdale [4.3] obtained on notched specimens of a 0.22% C steel exposed to saturated brine and cycled at 25 Hz are shown in Figure 4.2. At low stress amplitudes, the

cyclic life is about four times greater at 13°C than at 33°C. Due to the severity of the notch employed in these experiments (V-notch with a root radius of 0.005 cm), cracks are likely to have initiated early in the lives of these specimens [4.4]. Thus, these results actually demonstrate the temperature sensitivity of crack growth rather than crack initiation. The low fatigue strengths shown in Figure 4.2 are also indicative of the fact that cracks initiated early in these tests. Assuming this to be the case, one can reinterpret these results using the analytical solution for K in a circumferentially cracked cylinder in bending [4.5]. Using the in-air value of the endurance limit gives a fatigue crack growth threshold of $\Delta K_{th} = 6 \text{ MPa}\sqrt{\text{m}}$. This value is reasonably consistent with in-air values of ΔK_{th} summarized in Section 3.0 of this report. Similar computations using the brine data of Figure 4.2 give ΔK_{th} values of less than $1 \text{ MPa}\sqrt{\text{m}}$. This value is considerably less than those summarized in Section 3.0 for saltwater environments. This discrepancy is likely due to the high concentration of salt and oxygen present in Dugdale's experiments since saturated brine was periodically sprayed into the notch throughout the test.

Several studies have directly examined the influence of temperature on the fatigue and corrosion fatigue crack growth in structural steels [4.6-4.9]. However, before examining these results, it is useful to introduce a general framework for quantifying and comparing these data. As in any thermally activated process, the temperature dependence of fatigue crack growth can be expressed by an Arrhenius equation of the following form:

$$da/dN = A \exp(-Q/RT) \quad (4.1)$$

where

- da/dN = fatigue crack growth rate at temperature, T
- A = a temperature-independent, preexponential factor
- Q = apparent activation energy in units of cal/mole
- R = universal gas constant, $1.98 \text{ cal}/(\text{mole } ^\circ\text{K})$
- T = absolute temperature in $^\circ\text{K}$.

It follows from the form of Equation 4.1 that a plot of $\ln(da/dN)$ versus $1/T$ is linear with a slope equal to $-Q/R$. Values of Q are useful for comparing the magnitude of the temperature sensitivity (temperature sensitivity

increases with increasing Q), as well as indicating which underlying phenomenon is responsible for the observed temperature dependence.

Data from Socie and Antolovich in Figure 4.3 show fatigue crack growth rates for a 0.15% C-Mn-Si steel (ASTM A 537) which were obtained in a 3.5% NaCl solution at temperatures of 24°C and -1°C. Analyzing these data in terms of Equation 4.1 gives an activation energy of about 9000 cal/mole. Although the test frequency used to obtain these data was not specified, the correspondence between data at 24°C in-air and in 3.5% NaCl indicates that the frequency was too fast to enable an environmental component of cracking to be operative. Thus, the observed temperature dependence probably reflects the temperature sensitivity of deformation processes at the crack tip.

Additional data on the temperature dependence of fatigue crack growth in a mild steel in the absence of an environmental component are given by the results of Tschegg and Stanzl in Figure 4.4. In spite of the fact that these data were generated at 21 kHz*, the room temperature results agree quite well with those of Figure 4.3 for the region of overlapping data. As in the previous results, growth rates are shown to decrease with decreasing temperature. However, the data at -196°C in Figure 4.4 differ very little from those at -1°C in Figure 4.3, suggesting that the activation energy decreases as temperature decreases. It is also interesting to note that the growth rates in Figure 4.4 become increasingly sensitive to temperature as ΔK is decreased. These changes in temperature sensitivity with temperature and ΔK are believed to be caused by corresponding alterations in the crack-tip deformation mechanisms [4.7].

Two studies have measured the temperature dependence of structural steels in 3.5% NaCl at cyclic frequencies which were slow enough to allow environment enhancement of the growth rate [4.8, 4.9]. Scott and Silvester found the fatigue crack growth rate in a structural steel (BS 4360 Grade 50D) to decrease by about a factor of two as the temperature was decreased from 20°C to 5°C; this change is consistent with an activation energy of about 8000 cal/mole. These results were obtained at a cyclic frequency of 0.1 Hz and data in 3.5% NaCl were five times faster than those in air. Thus, the measured temperature dependence is expected to be at least partially

*A pulsed ultrasonic technique and an inert fluid (silicone oil) was used to prevent adiabatic heating of the crack-tip region during testing.

controlled by some elemental process in the environmental component of cracking—e.g., bulk or ionic transport down the crack, the near-surface reaction at the crack-tip, or possibly hydrogen diffusion into the steel, should hydrogen embrittlement be contributing to the crack growth process.

The results of Telseren and Doruk [4.9], obtained on a 0.15% C-Mn-Si steel in 3.5% NaCl, are shown in Figure 4.5. As in the above results, the cyclic frequency was slow enough (0.23 Hz) to allow an environmental component of cracking. As indicated in Figure 4.5, the measured activation energy was 4200 cal/mole—significantly lower than that of 8000 cal/mole measured by Scott and Silvester [4.8]. However, it should be pointed out that the results of Telseren and Doruk [4.9] are uncharacteristic in several respects. First, the measured growth rates are about an order of magnitude faster than those reported by other investigators (e.g., see Section 3.0). Secondly, K-independent growth rates were observed in air as well as in 3.5% NaCl. These anomalies may have been due to the fact that tests were conducted at nominal stresses which were above the materials' yield strength. Under these conditions, the linear-elastic analysis which was used to analyze the results is inappropriate, and an interpretation of the measured temperature dependence is uncertain.

In addition to the uncertainty caused by elastic-plastic loading, there are other possible reasons for differences between the measured activation energies (4200 cal/mole versus 8000 cal/mole) for corrosion fatigue of carbon steel. First, the value of 8000 cal/mole corresponding to Scott and Silvester's [4.8] data was for a constant oxygen content (8 mg/l). In the study by Telseran and Doruk, the oxygen content was not specified; thus, it was probably not controlled. This would result in a decreasing oxygen content in the aqueous solution as temperature was increased. Under these conditions, a counteracting effect would occur—that is, the accelerating effect of increasing temperature would be mitigated to some extent by the decelerating effect of lower oxygen content. (The latter effect is discussed in the next section.) Differences in activation energies may also have arisen due to differences in cyclic frequency and/or ΔK level, as has been reported for a high-strength steel in 3.5% NaCl [4.10]. In other words, a more general form of Equation 4.1 would be

$$\frac{da}{dN} = A \exp \left[\frac{-Q(f, \Delta K)}{RT} \right] \quad (4.2)$$

where $Q(f, \Delta K)$ is the activation energy which depends on both cyclic frequency, f , and ΔK .

Table 4.1 gives the change in da/dN which would accompany a change in temperature from 0°C to 30°C for the range of activation energies which have been reported. If these differences are due to variations in oxygen content as described above, the lower activation energy would be more relevant to actual structures where oxygen content will vary with temperature. This lower value is also consistent with the temperature dependence which is normally assumed for general corrosion of structural steels in seawater [4.11].

4.2 Effect of Solution Chemistry on Corrosion Fatigue Resistance

As indicated previously through Figure 4.1, the precise chemical content of seawater varies in seasonal cycles for a given location. Furthermore, as in the case of temperature, additional changes in chemical composition occur as a function of geographic location, as well as seawater depth. The influence of all of these changes on corrosion fatigue behavior of structural steels has not been examined in detail. Nevertheless, information is available to make judgments on the significance of such factors as synthetic versus natural seawater under flowing and quiescent conditions, dilution of seawater by river estuaries, solution pH, and dissolved oxygen content.

Regarding the issue of what constitutes a suitable environment for laboratory tests, Bogar and Crooker [4.12] compared the relative influence of fresh natural seawater, aqueous solution of 3.5% NaCl, and ASTM D 1141-75 substitute seawater on the fatigue crack growth behavior of various high-strength materials, including a low-alloy steel, two precipitation hardening stainless steels, and an aluminum alloy. Results on an HY-130 steel are most relevant for our purposes and are given in Figure 4.6. For both the freely corroding potential and an applied cathodic potential, flowing natural seawater resulted in faster rates of crack growth--the effect varying from a factor of about 1.5X to 2.0X, depending on potential and ΔK level. Based on these and other results, Bogar and Crooker concluded that natural seawater was a more aggressive environment than either 3.5% NaCl or ASTM substitute seawater and that flowing (~200 ml/min) and quiescent (static with changes twice per eight-hour daily testing period) conditions gave equivalent results. However, results of Scott and Silvester [4.8] on a structural steel (BS 4360 Grade 50D) appear to be in conflict with this conclusion. Within the scatter

of their experimental data, no consistent differences occurred in fatigue crack growth rates obtained in natural seawater ($\text{pH} = 8.1$), half diluted seawater ($\text{pH} = 8.1$), seawater with 2 mg/l HCO_3 ($\text{pH} = 6.5$), and $3.5\% \text{ NaCl}$ ($\text{pH} = 6.5$) at either the freely corroding potential or applied cathodic potentials of -0.8 V (Ag/AgCl) and -1.0 V (Ag/AgCl) *—results from the latter potential are given in Figure 4.7. The reason for this apparent difference between the two studies is uncertain. The influence of bulk solution chemistry on fatigue crack growth rates may depend on material composition. Alternatively, it should be noted that the scatter in Scott and Silvester's data may preclude resolving differences of $1.5X$ to $2.0X$ in growth rates; thus, results may not be in conflict with those of Bogar and Crooker.

As will be discussed later, one factor which appears to contribute to the sometimes observed beneficial effect of cathodic polarization on corrosion fatigue resistance is the reduction in the crack tip stress intensity factor due to the wedging action of calcareous deposits formed within cracks in cathodically polarized specimens. This process, which one would expect to become increasingly important in the near-threshold crack growth regime, could give rise to slower growth rates in natural and synthetic seawater than in $3.5\% \text{ NaCl}$. Unfortunately, the influence of such changes in bulk solution chemistry has not been systematically examined in this important low-growth rate regime.

Based on the above information it is concluded that the use of either natural or synthetic (ASTM D1141-75) seawater is preferable to aqueous NaCl solutions for corrosion fatigue testing. Although natural seawater may appear to be more representative of offshore environments than synthetic seawater, the inherently variable nature of this environment can confound the interpretation of results. For example, as indicated previously in Figure 4.1, factors such as dissolved oxygen, pH , temperature, salinity and ionic conductivity in natural seawater can fluctuate within a given year, as well as from year-to-year, even for a single geographic location. For high-cycle, low-frequency tests, times of one year or more are not uncommon; thus, test programs using fresh, natural seawater will inherently include uncontrolled variations in seawater chemistry, both within a given specimen and from

*Refers to electrode potentials measured with respect to a silver/silver chloride reference electrode.

specimen to specimen. These variations confound the interpretation of results, thereby causing the influence of controlled test variables on corrosion fatigue resistance to be uncertain, particularly in crack growth rate testing where measurements are obtained periodically throughout the test. These variations can be minimized to some extent if the seawater is stored and processed prior to use so that variables such as oxygen content, pH, and temperature can be controlled. However, even with such effort seasonal variations in ionic species would cause periodic variations in the test environment depending on when, how much, and how often the seawater was obtained. Of course the nominal composition would only be representative of the location from which it was obtained. Finally, storage of the environment would render it biologically inactive. In fact, even in the case of freshly supplied seawater, pumping over distances as short as 15 m can alter the biological activity of seawater.

In view of the above variables associated with the use of natural seawater, synthetic seawater appears to be preferable for corrosion fatigue testing, both for technical and economic reasons. The use of ASTM D1141-75 provides a consistent standard of comparison from test to test, program to program, and laboratory to laboratory. Control of primary environmental variables such as temperature, pH, oxygen content, and electrode potential could still be employed as deemed necessary to simulate specific geographic locations, water depths, and critical locations in the structure.

The influence of solution pH on the S-N behavior of a low-carbon steel in NaCl + NaOH has been studied by Radd, et al., [4.13] over a broad range of pH: 6.6 to 13 plus. Results show highly alkaline solutions ($\text{pH} \geq 12$) to be beneficial in that fatigue lives were substantially increased and a clearly defined fatigue limit occurred. However, pH values in the near-neutral range, which is typical of seawater ($\text{pH} = 6.5$ to 8.3), appear to have little influence on the corrosion fatigue resistance of structural steels [4.8].

The importance of dissolved oxygen concentration on the corrosion fatigue resistance of a wide range of materials, including structural steels, follows the long-established trends for general corrosion. Although resistance to both crack initiation (to the extent reflected in smooth specimen tests) and crack growth decreases with increasing oxygen concentration, the effect on initiation appears to be more pronounced. For example, results of Mehdizadel, et al., [4.14] in Figure 4.8 shows the fatigue strength in a 1035 steel in 5%

NaCl solution to be dramatically improved by complete deaeration--in fact, under this condition, the fatigue limit which occurs in air tests can be restored. These results, which have also been confirmed by Duquette and Uhlig [4.15] for a 3.5% NaCl solution and for distilled water, indicate that dissolved oxygen is essential for corrosion fatigue crack initiation in near-neutral pH solutions.

The influence of dissolved oxygen on corrosion fatigue crack growth in structural steels exposed to seawater has been examined by Scott and Silvester [4.8]. Data obtained at the freely corroding potential parallel the above S-N results as shown in Figure 4.9; however, data obtained under applied cathodic potentials exhibited little or no beneficial effect of lowered dissolved oxygen concentration as shown in Figure 4.10. The latter test results are understandable since the electrode potential, a measure of oxidizing power, was maintained constant during these tests. Thus, the effective oxygen content at the specimen surface was forced to be equivalent irrespective of bulk oxygen contents. The only difference between these two test conditions is that the high oxygen content solution would require a greater current density to maintain the specified potential. Consequently, these results are not directly applicable to offshore structures and should not be interpreted to mean that oxygen content of the seawater is not an important variable affecting crack growth in cathodically "protected" structures. Under these service conditions, where polarization is achieved by sacrificial anodes, a higher oxygen content in the seawater will cause a more rapid consumption of the anodes. This anode consumption is also likely to result in a change in the growth rates since the imposed potential, as well as the current density, will be changing in proportion to the consumption kinetics of the anode.

It is important to point out, however, that the beneficial effect of decreased oxygen can be mitigated by the growth of sulfate-reducing bacteria in biologically active seater [4.16]. These bacteria thrive under conditions of low oxygen in the pH range of about 5.5 to 8.6. The process of reducing inorganic sulfates to sulfides involves iron reduction, thereby resulting in accelerated general corrosion rates--however, the potential influence of this reaction on the corrosion fatigue behavior has not been assessed.

As indicated above, a change in dissolved oxygen content can cause a change in potential through the oxygen reduction reaction and the process of activation polarization [4.16]. Thus, the influence of dissolved oxygen,

discussed above, is closely tied to the influence of potential, which is discussed in the following section.

4.3 Effect of Electrode Potential on Corrosion Fatigue Resistance

Electrode potential is the "driving force" for aqueous corrosion and thus is a fundamental variable in general corrosion, as well as in corrosion fatigue. Control of this variable through the widespread use of cathodic protection provides a means of minimizing corrosion of steel structures exposed to seawater.

Before discussing the effectiveness of this variable in improving corrosion fatigue resistance, it is useful to first briefly review the processes involved in cathodic protection. Cathodic protection is achieved either by an impressed current from a d.c. power supply or, more frequently, by a galvanic system using sacrificial anodes—usually Zn-Al-Cd, Al-Zn-Hg, or Al-Zn-In alloys—the result being an enhancement in the cathodic process (either oxygen reduction or proton reduction) and a corresponding suppression of the anodic process (metal dissolution). The oxygen reduction reaction gives rise to an increase in the pH near the metal surface, which in turn alters the solubility of calcium and magnesium salts in the seawater, resulting in precipitation of calcareous deposits of calcium carbonate and magnesium hydroxide. The presence of adherent calcareous deposits is beneficial since they reduce the current density required for protection by (1) decreasing the detrimental effects of water velocity [4.17] and (2) forming a barrier to the diffusion of oxygen to the metal surface [4.18]. Since the kinetics of formation of these deposits is temperature dependent, the current required for adequate protection also depends on temperature. Furthermore, the growth of certain bacteria (as discussed in the preceding section) may increase the required current density. The combined experience from laboratory studies of the above factors, as well as operating histories of cathodic protection systems, has resulted in empirical guidelines for minimum current densities; for example, see Table 4.2 [4.19]. As indicated in Table 4.2, the required current densities for the U.S. West Coast and the Gulf of Mexico are generally less demanding than those of the North Sea due to higher temperatures (which give lower oxygen and favor calcareous deposits) and lesser currents and storm turbulence (which give lower oxygen and slower water velocity).

Numerous studies have examined the influence of cathodic polarization on the corrosion fatigue behavior of structural steels in saltwater or seawater in order to define the minimum potential (or current density) which affords immunity to corrosion fatigue. A review paper by Jaske, et al., [4.20] covers most of the results published prior to 1977. Although additional studies have been conducted since then, the general conclusions on the influence of cathodic protection have not changed appreciably, although two distinctly different views on the benefit of overprotection have been strengthened in the ensuing time. These positions are summarized below and are followed by a discussion of fundamental issues in an attempt to reconcile these apparent differences.

Studies employing S-N testing have reported that results on structural steels in saltwater and seawater can be made to return to the in-air results when adequate cathodic protection is applied [4.1, 4.15, 4.21-4.30]. For example, Figure 4.11 provides results from Duquette and Uhlig [4.15] on a carbon steel in a 3% NaCl solution which show that a cathodic potential of -0.74 V (Ag/AgCl)* gives an endurance limit which is equivalent to that observed in air; more negative potentials also give the same results. Minami and Yakada [4.22] found that a larger cathodic potential, -1.06 V (Ag/AgCl), was necessary to restore the fatigue strength of a carbon steel in seawater to that measured in air. Numerous other studies have drawn similar conclusions, with the minimum required potential being between -0.74 V and -1.06 V (Ag/AgCl). Hartt, et al., [4.30] have shown that the minimum required potential for full protection can depend on cyclic frequency, as well as on the specific specimen geometry—that is, results differ somewhat for smooth versus notched specimens and for different notch geometries. In addition, Kochera, et al., [4.29] have shown that results under overprotected conditions can depend on test technique. Specifically, it was demonstrated that ineffective protection in the range of -1.2 V to -1.37 V (Ag/AgCl) occurred when an insufficient amount of uncirculating solution was used and the pH decreased to 5. It was argued that such results are not relevant to actual structures where the ample supply of fresh seawater would prevent reductions in pH.

*Electrode potentials ϕ in this section are given with respect to the silver/silver chloride (Ag/AgCl) reference electrode.

Corrosion fatigue crack growth studies on structural steels exposed to saltwater and seawater have developed a somewhat different picture. Although cathodic protection has been observed to decrease the crack growth rate relative to that of the freely corroding potential [4.8, 4.29, 4.31, 4.32], overprotection has in some cases resulted in faster growth rates than those at the freely corroding potential [4.8, 4.32]. For example, Figure 4.13 gives results of Scott and Silvester on a structural steel (BS 4360 Grade 50D) in seawater which show that optimum cathodic potentials of -0.7 V to -0.8 V (Ag/AgCl) result in growth rates which approach those measured in air. However, as the cathodic potential is increased from this range, the growth rates increase measurably, until at -1.1 V (Ag/AgCl), the rates are nearly twice as fast as those at the freely corroding potential and as much as six times faster than those in air. Similar trends have been reported by Vosikovsky in an X-65 line-pipe steel in 3.5% NaCl [4.32] and for several high-strength steels in saltwater [4.33-4.35]. It is generally accepted that the detrimental effect of overprotection is due to hydrogen embrittlement in high-strength steels. Based largely on the parallelism of behavior that can be drawn with high-strength steels, it has been suggested that the detrimental effect of overprotection in structural steels is also due to hydrogen embrittlement [4.8, 4.32], although this view is not popularly accepted because of the long-standing belief that structural steels in this strength level are immune to hydrogen embrittlement. However, recent results of Nelson [4.36] show a significant enhancement in fatigue crack growth rates in carbon steel due to the presence of dry gaseous hydrogen, thereby demonstrating that these materials can be embrittled by hydrogen under cyclic loading.

The different responses to overprotection exhibited by S-N testing and fatigue crack growth rate testing are likely to be related to (1) differences in the response of crack initiation versus crack growth to applied potential and (2) differences between bulk and local environment conditions for specimens containing small versus large cracks. For example, with respect to the latter, Brown, et al., [4.33] have shown that regardless of the pH of the bulk environment and applied cathodic potential at the surface, the conditions at the tip of a growing stress corrosion crack are favorable for the discharge of hydrogen in high-strength steels exposed to aqueous environments. Although Hartt, et al., [4.37] have shown, through a simple model of mass transfer,

that mixing is promoted by movement of the crack surfaces under cyclic loading, similar differences between bulk and local environment are likely to also occur during corrosion fatigue. This view is consistent with many of the phenomenological observations in corrosion fatigue, notably: (1) the decrease in effectiveness of cathodic protection as cracks deepen [4.34], (2) the dependence of cathodic protection on specimen geometry [4.30], and (3) the observation of non-steady state crack growth which results in growth rates which appear to depend on the initial ΔK level and crack length [4.38, 4.39] (see Sections 3.5 and 3.6, respectively).

The critical question to be resolved is how these effects relate to actual structures. Undoubtedly, the use of cathodic protection, when adequately applied, increases the materials' resistance to corrosion fatigue crack initiation. However, a false sense of security may develop if local current densities fall below those required for full protection, either because of the uncertainty in the current "throwing power" at complex structural joints or within cracks or crack-like defects.

The current inability to define differences between bulk and local environments is a major limitation in formulating predictive models for the growth of cracks in corrosion fatigue and stress corrosion cracking. Recently, models for mass and ionic transport to these occluded regions have provided some insight into the problem [4.40-4.43]. The role of corrosion products, including calcareous deposits under cathodic polarization conditions, may also be a significant factor in understanding these problems for two reasons: (1) they can impede transport of species between the bulk and local environments, and (2) they can induce wedging forces at the crack tip which reduce the effective ΔK —particularly in the low-growth rate regime. Additional basic research in these areas is needed to advance our mechanistic understanding of these problems as well as to answer practical questions such as the effectiveness of cathodic protection, particularly in cracked members.

CHAPTER 4.0 REFERENCES

- 4.1 Hartt, W. H., Henke, T. E., and Martin, P. E., "Influence of Sea Water and Cathodic Protection Upon Fatigue of Welded Steel Plates, as Applicable to Offshore Structures," Engineering and Industrial Experiment Station, Florida Atlantic University, Report No. TR-OE-80-1, prepared for American Petroleum Institute, March 20, 1980.
- 4.2 Gould, A. J., Engineering, Vol. 141, 1936, pp. 495-496.
- 4.3 Dugdale, D. S., "Corrosion-Fatigue of Sharply Notched Steel Specimens," Metallurgia, January 1962, pp. 27-28.
- 4.4 Allery, M.B.P., and Birkbeck, G., "Effect of Notch Root Radius on the Initiation and Propagation of Fatigue Cracks," Engineering Fracture Mechanics, Vol. 4, 1972, pp. 325-331.
- 4.5 Tada, H., Paris, P. C., and Irwin, G. R., The Stress Analysis of Cracks Handbook, Del Research Corporation, Hellertown, PA, 1973.
- 4.6 Socie, D. F., and Antolovich, S. D., "Subcritical Crack Growth Characteristics in Welded ASTM A 537 Steel," Welding Research Supplement, June 1974, pp. 267-S - 271-S.
- 4.7 Tscheegg, E., and Stanzl, S., "Fatigue Crack Propagation and Threshold in b.c.c. and f.c.c. Metals at 77 and 293 K," Acta Metallurgica, Vol. 29, 1981, pp. 33-40.
- 4.8 Scott, P. M., and Silvester, D.R.V., "The Influence of Seawater on Fatigue Crack Propagation Rates in Structural Steel," Department of Energy, UK Offshore Steels Research Project, Interim Technical Report UKOSRP 3/03, December 19, 1975.
- 4.9 Telseren, A., and Doruk, M., "Temperature Dependence of Water-Inhanced Fatigue-Crack Growth in Mild Steel," Engineering Fracture Mechanics, Vol. 6, 1974, pp. 283-286.
- 4.10 Ryder, J. T., and Gallagher, J. P., "Temperature Influence on Corrosion Fatigue Behavior of 5Ni-Cr-Mo-V Steel," Journal of Testing and Evaluation, JTEVA, Vol. 2, No. 3, 1974, pp. 180-189.
- 4.11 Walter, J. C., Steensland, O., and Eliassen, S., "Safety Against Corrosion Damages Offshore," Det Norske Veritas Publication No. 94, April 1976, pp. 3-7.
- 4.12 Bogar, F. D., and Crooker, T. W., "The Influence of Bulk-Solution-Chemistry Conditions on Marine Corrosion Fatigue Crack Growth Rate," Journal of Testing and Evaluation, JTEVA, Vol. 7, No. 3, 1979, pp. 155-159.
- 4.13 Radd, F. J., Crowder, L. H., and Wolfe, L. H., Corrosion, Vol. 16, 1960, p. 415t.

- 4.14 Mehdizadeh, P., McGlasson, R. L., and Landers, J. E., Corrosion, Vol. 22, 1966, p. 325.
- 4.15 Duquette, D. J., and Uhlig, H. H., Transactions ASM, Vol. 61, 1968, p. 449.
- 4.16 Uhlig, H. H., Corrosion and Corrosion Control, Wiley, 1971.
- 4.17 Sawyer, L.J.E., Routley, A. F., Chapman, D. A., and Crennell, J. T., "Current Density Required for Cathodic Protection," Journal of Applied Chemistry, Vol. 15, 1965, p. 182.
- 4.18 Cornet, I., Pross, T. W., Jr., and Bloom, R. C., "Current Requirements for Cathodic Protection of Disks Rotating in Salt Water--A Mass Transfer Analysis," Proceedings Paris, Editions du Centre de Recherches et d'Etudes Oceanographiques (1965), p. 175.
- 4.19 Grundwell, R., Cathodic Protection of Offshore Structures, Petroleum Engineer International, October 1980, pp. 76-84.
- 4.20 Jaske, C. E., Broek, D., Slater, J. E., and Anderson, W. E., "Corrosion Fatigue of Structural Steels in Seawater and for Offshore Applications," Corrosion Fatigue Technology, ASTM STP 642, 1978, pp. 19-47.
- 4.21 Evans, V. R., and Simnad, M. T., "The Mechanism of Corrosion Fatigue in Mild Steel," Proceedings of Royal Society, London, A188, 1947, p. 387.
- 4.22 Minami, Y., and Takada, H., "Corrosion Fatigue and Cathodic Protection of Mild Steel," Boshoku Gijutsu, Vol. 7, No. 6, 1958, p. 336.
- 4.23 Glikman, L. A., Corrosion-Mechanical Strength of Metals, Butterworths, London, 1962, translated by J. S. Shapiro.
- 4.24 Nichols, J. L., "Cathodic Protection Reduces Corrosion Fatigue of Steel in Sea Water," Materials Protection, Vol. 2, No. 2, 1963, p. 46.
- 4.25 Jones, D. A., Corrosion Science, Vol. 11, No. 6, 1971, pp. 439-451.
- 4.26 Hudgins, C. M., Jr., Casad, B. M., Schroeder, R. L., and Patton, C. C., "The Effect of Cathodic Protection on the Corrosion Fatigue Behavior of Carbon Steel in Synthetic Sea Water," Journal of Petroleum Technology, March 1971, pp. 283-293.
- 4.27 Hartt, W. H., Fluet, J. E., and Henke, T. E., "Cathodic Protection for Notched Mild Steel Undergoing Corrosion Fatigue in Sea Water," Offshore Technology Conference Paper No. OTC 2380, AIME, 1975.
- 4.28 Lyaschenko, A. E., Glikman, L. A., and Zobachev, Y. E., Soviet Materials Science, Vol. 9, 1975, p. 496.
- 4.29 Kochera, J. W., Tralmer, J. P., and Marshall, P. W., "Fatigue of Structural Steel for Offshore Platforms," Offshore Technology Conference, Paper No. OTC 2604, AIME, 1976.

- 4.30 Hartt, W. H., and Hooper, W. C., "Endurance Limit Enhancement of Notched 1018 Steel in Sea Water--Specimen Size and Frequency Effects," Corrosion, Vol. 36, No. 3, 1980.
- 4.31 Pook, L. P., and Greenan, A.F., in Fatigue Testing and Design, Vol. 2, The Society of Environmental Engineers, April 1976, pp. 30.1-30.33.
- 4.32 Vosikovsky, O., ASME Transactions, Journal of Engineering Materials and Technology, October 1975, pp. 298-304.
- 4.33 Smith, J. A., Peterson, M. H., and Brown, B. F., Corrosion, Vol. 26, 1970, p. 539.
- 4.34 Barsom, J. M., International Journal of Fracture, Vol. 7, No. 2, 1971, pp. 163-182.
- 4.35 Crooker, T. W., Bogar, F. D., and Cares, W. R., "Effects of Flowing Natural Seawater and Electrochemical Potential on Fatigue Crack Growth in Several High Strength Marine Alloys," in Corrosion Fatigue Technology, ASTM STP 642, 1978, pp. 189-201.
- 4.36 Nelson, H. G., "Hydrogen-Induced Slow Crack Growth of a Plain Carbon Pipeline Steel Under Conditions of Cyclic Loading," in Effect of Hydrogen on Behavior of Materials, AIME, 1976.
- 4.37 Hartt, W. H., Tennant, J. S., and Hooper, W. C., "Solution Chemistry Modification Within Corrosion-Fatigue Cracks," in Corrosion Fatigue Technology, ASTM STP 642, 1978, pp. 5-18.
- 4.38 Scott, P. M., "The Effects of Seawater on Corrosion Fatigue in Structural Steels," Harwell Corrosion Service, A.E.R.E., Harwell, March 17, 1980, to be published in Metals Science, 1981.
- 4.39 Hudak, S. J., Jr., and Wei, R. P., "Consideration of Non-Steady-State Crack Growth in Materials Evaluation and Design," International Journal of Pressure Vessels and Piping, Vol. 9, 1981, pp. 63-74.
- 4.40 Alkire, R., and Siitari, D., "The Location of Cathodic Reaction During Localized Corrosion," Journal of the Electrochemical Society: Electrochemical Science and Technology, Vol. 126, No. 1, 1979, pp. 15-21.
- 4.41 Newman, J., "Mass Transport and Potential Distribution in the Geometries of Localized Corrosion," in Localized Corrosion, NACE, 1974., p. 45.
- 4.42 Beck, T. R., and Grens, E. A., Journal of the Electrochemical Society: Electrochemical Science and Technology, Vol. 116, 1969, p. 177.
- 4.43 Turnbull, A., and Gardner, M. K., "The Distribution of Potential and pH in a Crevice of the Steel BS 4360:50D in 3.5% NaCl and in Artificial Seawater," National Physical Laboratory Report DMA(A)22, 1980.

TABLE 4.1. POTENTIAL INFLUENCE OF TEMPERATURE ON CORROSION
FATIGUE CRACK GROWTH RATES

<u>Activation Energy,* Q, cal/mole</u>	<u>Increase in da/dN for Temperature change from 0°C to 30°C</u>
4200	2.1 X
8000	4.3 X

*Q may depend on cyclic frequency and ΔK ; see equation (4.2).

TABLE 4.2. GUIDANCE ON MINIMUM DESIGN CURRENT DENSITIES (mA/m^2) FOR CATHODIC PROTECTION

	<u>Initial Value</u>	<u>Mean Value</u>	<u>Final Value</u>
North Sea (southern)	130	100	90
North Sea (northern)	150	115	100
Gulf of Mexico	65	-	-
U.S. West Coast	87	-	-
Cook Inlet	440	-	-
Persian Gulf	108	-	-
Indonesia	65	-	-
Australia (southern)	130	90	85
Brazil	130	90	85
Stagnant seawater (initial)	75	50	40
Pipelines (burial specified)	50	50	50
Saline mud (ambient temp)	20	20	20

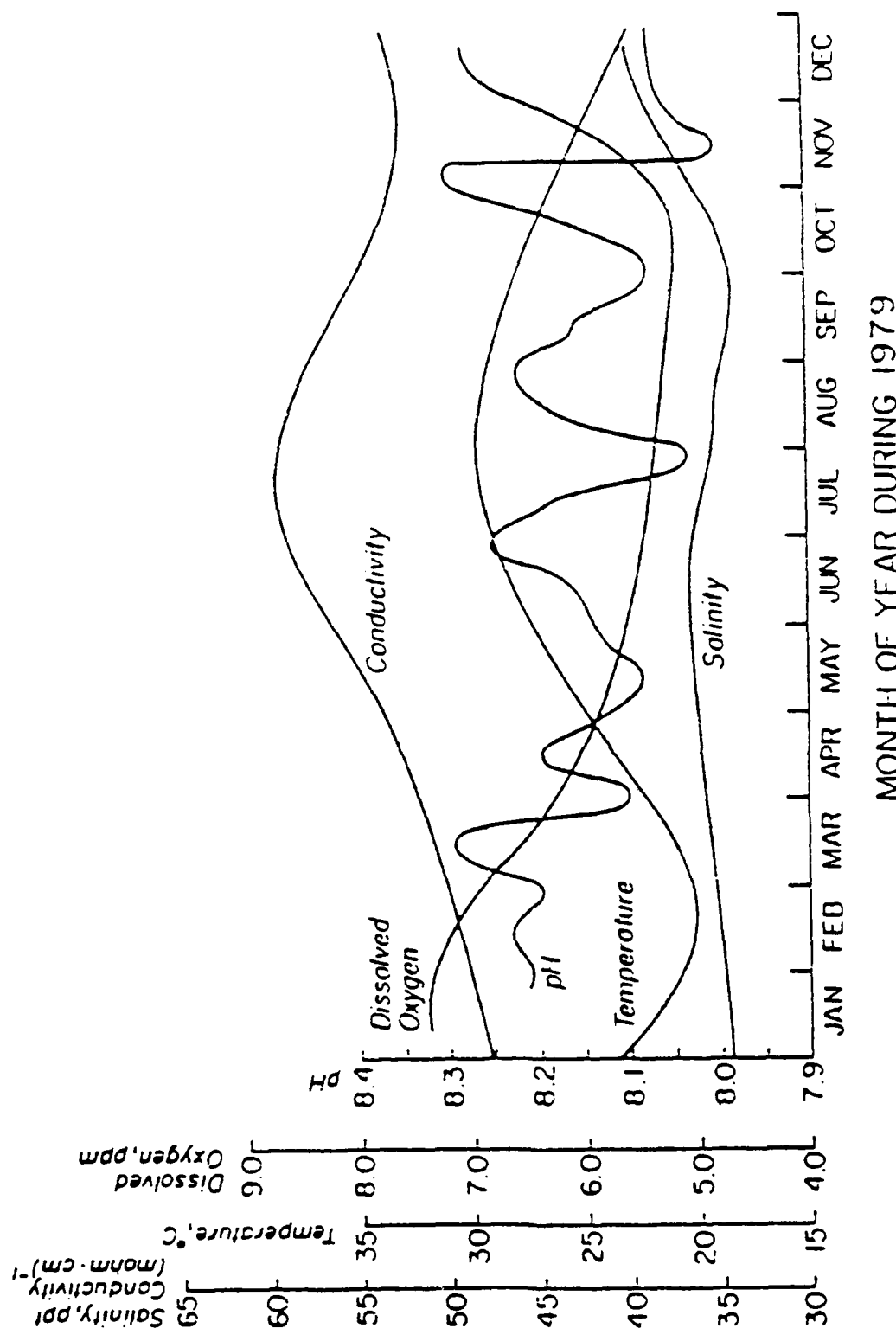


FIGURE 4.1. VALUES OF SELECTED SEAWATER PARAMETERS MEASURED OVER A ONE-YEAR PERIOD AT THE MARINE MATERIALS AND CORROSION LABORATORY, FLORIDA ATLANTIC UNIVERSITY AT BOCA RATON ON THE ATLANTIC OCEAN [4.1]. NOTE THAT OVER THIS PERIOD THE DATA ARE NOT EXACTLY PERIODIC, INDICATING YEAR-TO-YEAR VARIATIONS IN THESE PARAMETERS AS WILL.

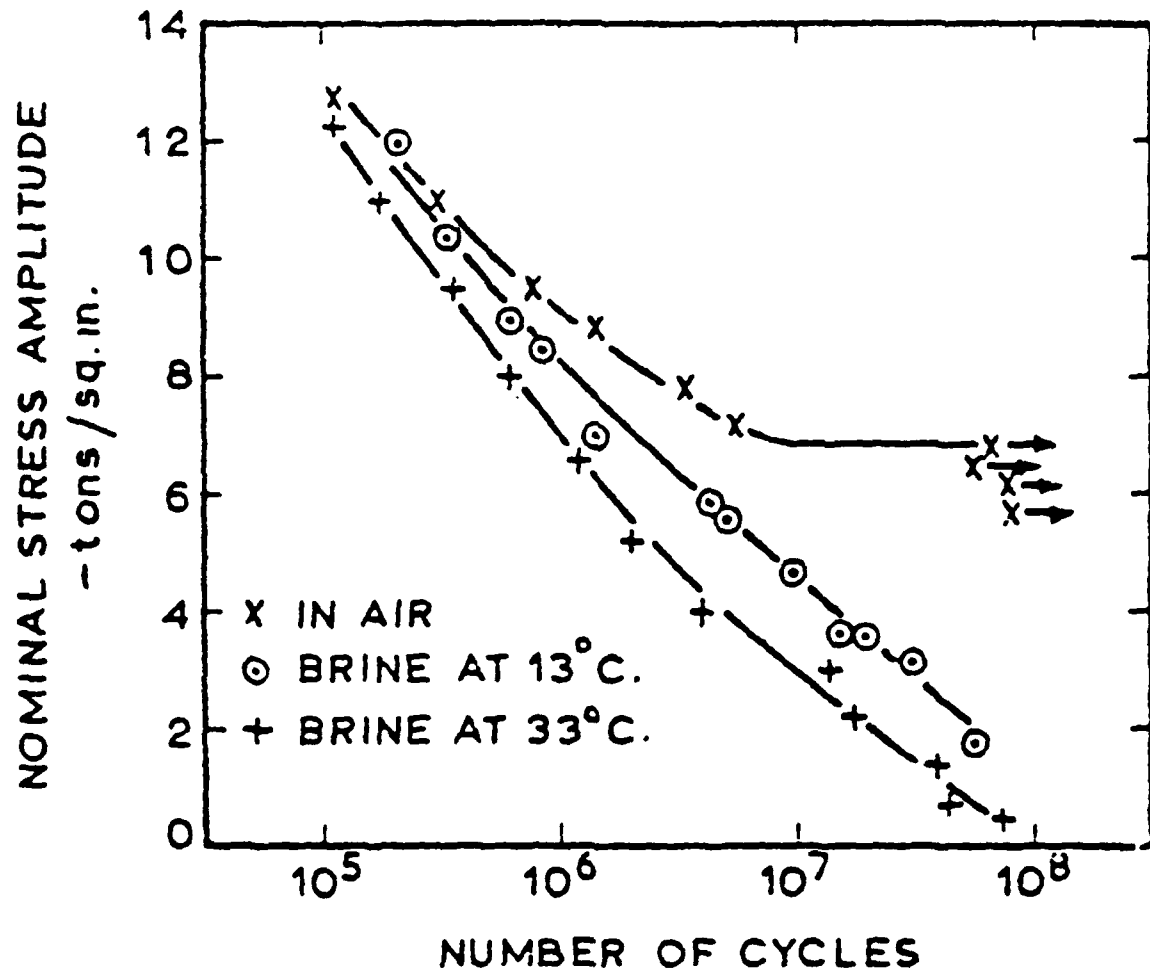


FIGURE 4.2. EFFECT OF TEMPERATURE ON CORROSION FATIGUE BEHAVIOR OF NOTCHED SPECIMENS OF MILD STEEL [4.3]

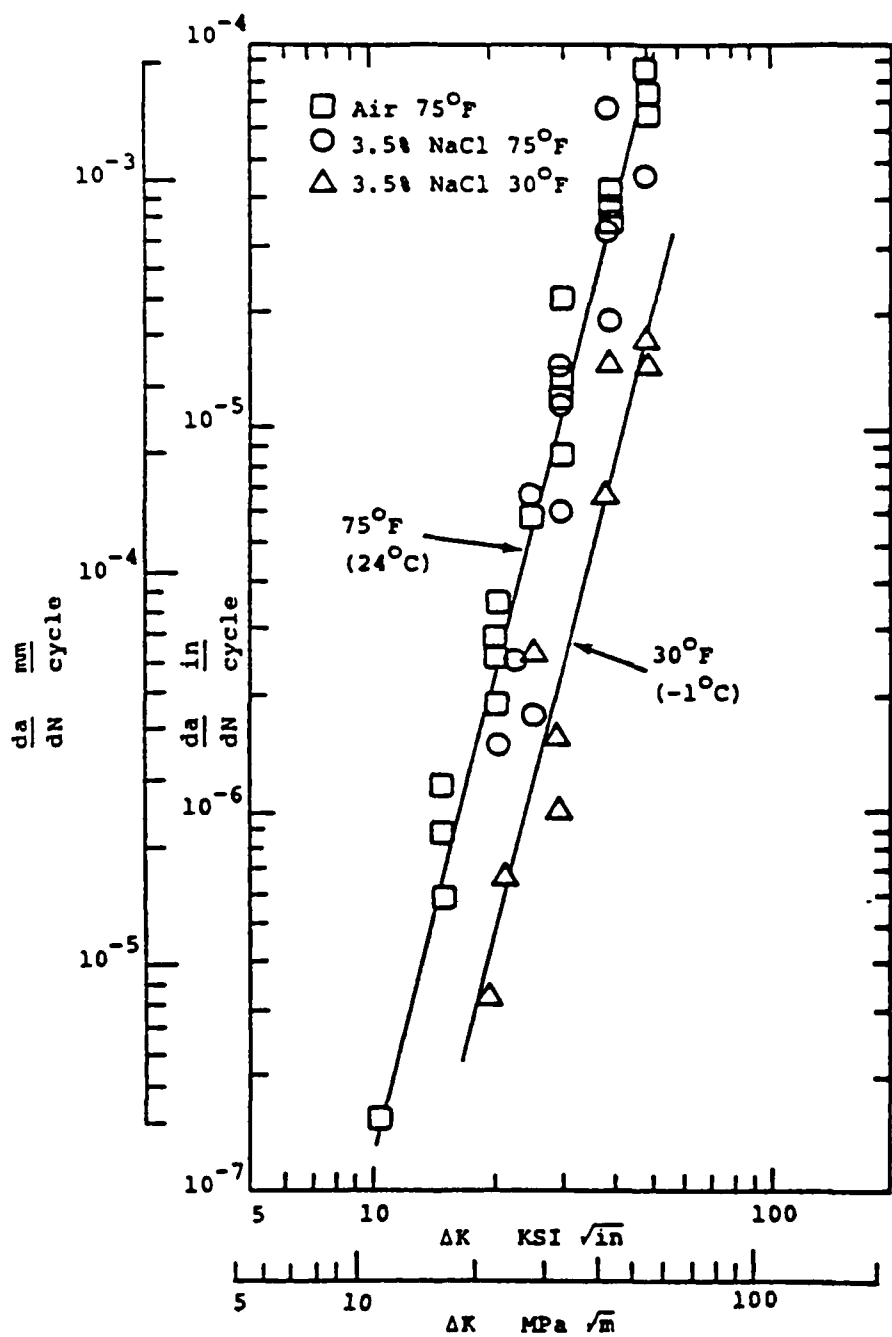


FIGURE 4.3. COMPARISON OF FATIGUE CRACK GROWTH RATE IN
3½% AQUEOUS NaCl AND AIR
AT 75°F AND 30°F [4.6]

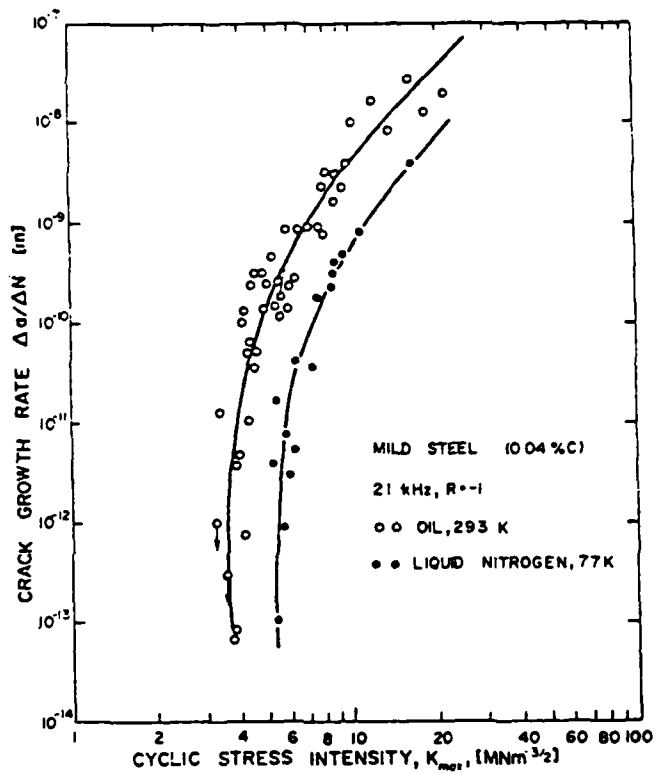


FIGURE 4.4. INFLUENCE OF TEMPERATURE (293 K SILICONE OIL AND 77 K LIQUID NITROGEN) ON FATIGUE CRACK GROWTH RATES IN MILD STEEL, 21 kHz R = -1.
Data analyzed using positive portions of the loading cycle only, that is,
 $\Delta K = K_{max}$ [4.7].

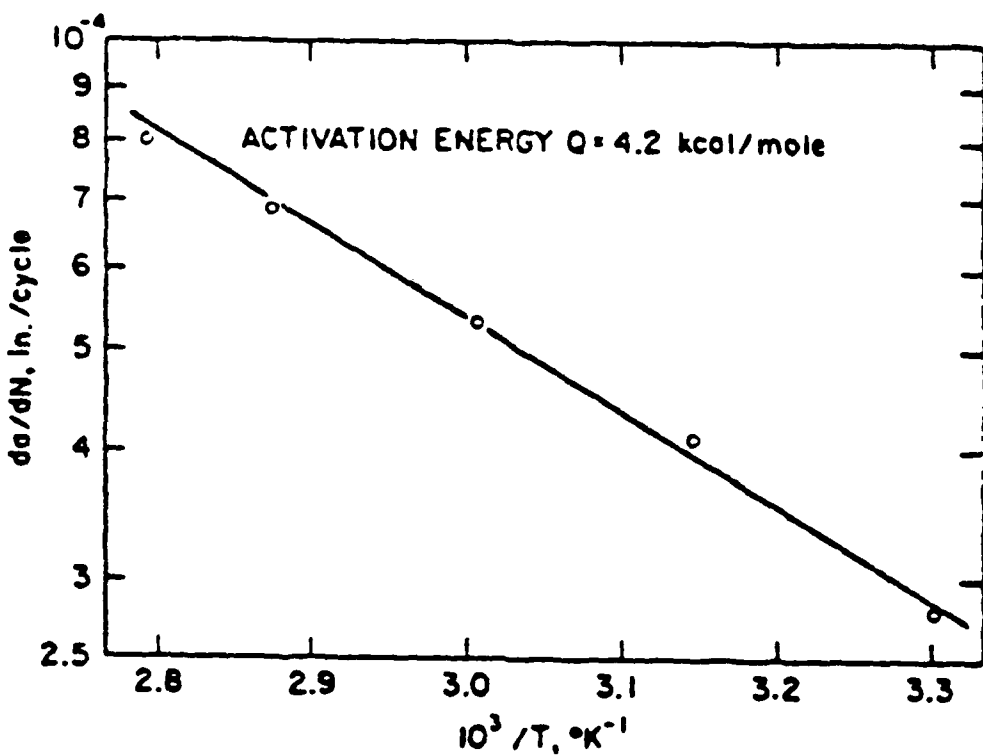


FIGURE 4.5. RATE OF FATIGUE-CRACK GROWTH AS A
FUNCTION OF TEMPERATURE IN MILD STEEL
EXPOSED TO 3.5% NaCl [4.9]

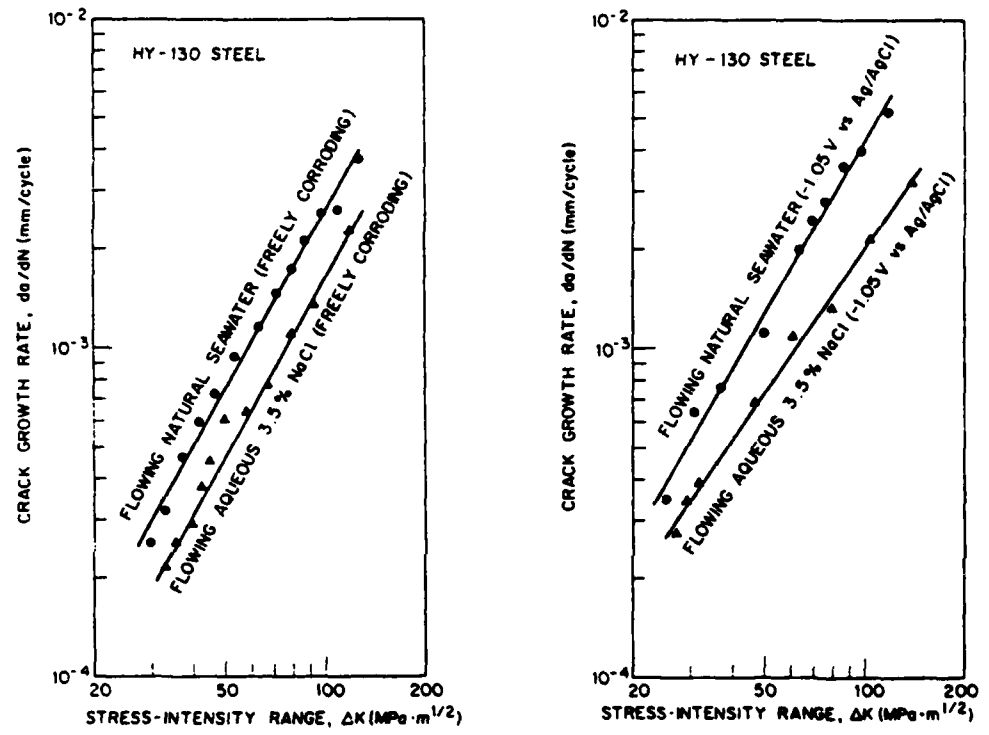


FIGURE 4.6. CRACK-GROWTH-RATE DATA FOR HY 130 STEEL IN FLOWING NATURAL SEAWATER AND IN FLOWING AQUEOUS 3.5% NaCl SOLUTION UNDER FREELY CORRODING CONDITIONS (~ -0.665 V VS Ag/AgCl) AND UNDER A CATHODIC POTENTIAL OF -1.05 V VS Ag/AgCl [4.12]

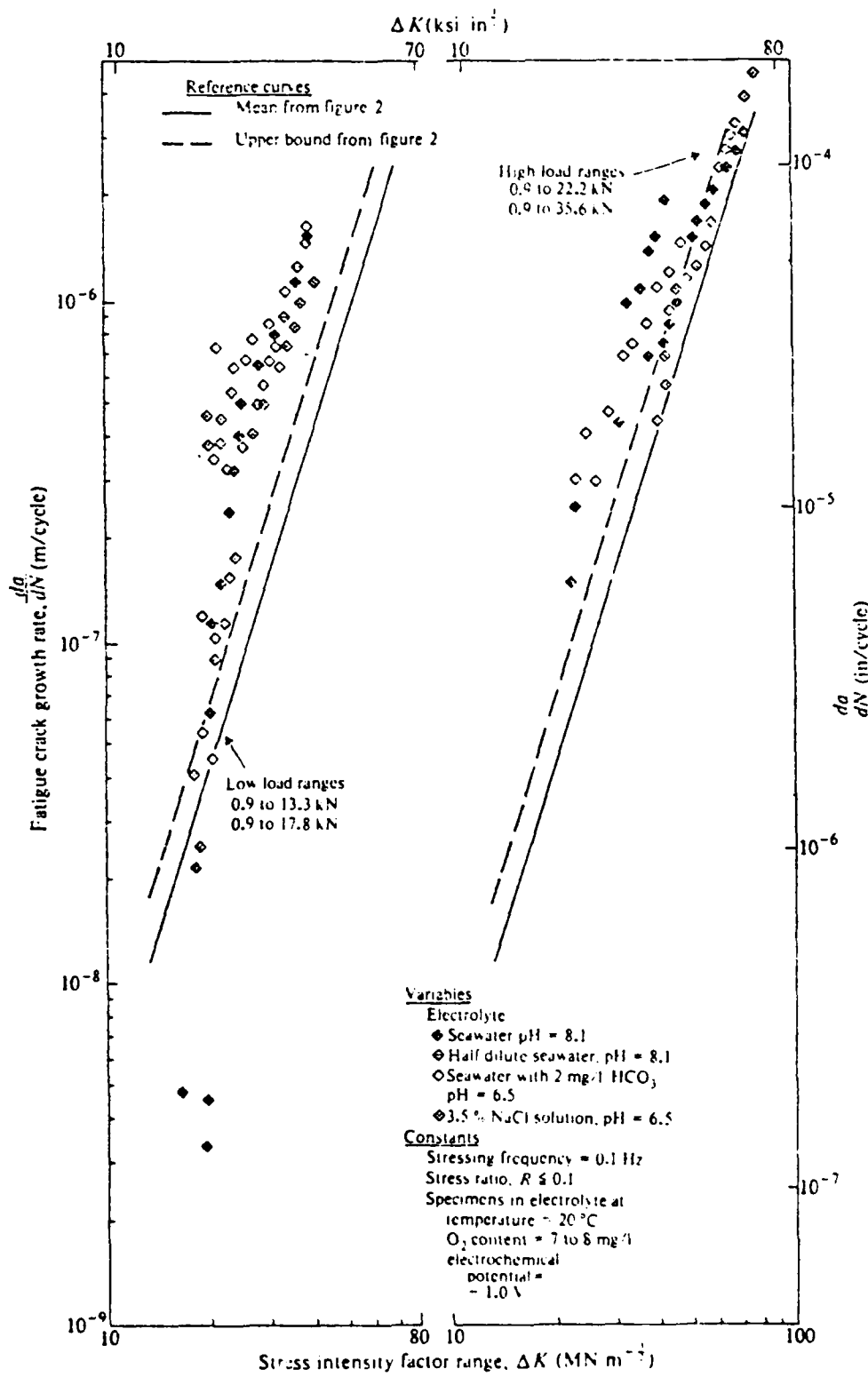


FIGURE 4.7. FATIGUE CRACK PROPAGATION DATA IN BS 4360/50D STEEL AT AN ELECTRODE POTENTIAL OF -1.0 V (Ag/AgCl) IN SEVERAL ELECTROLYTES [4.8]

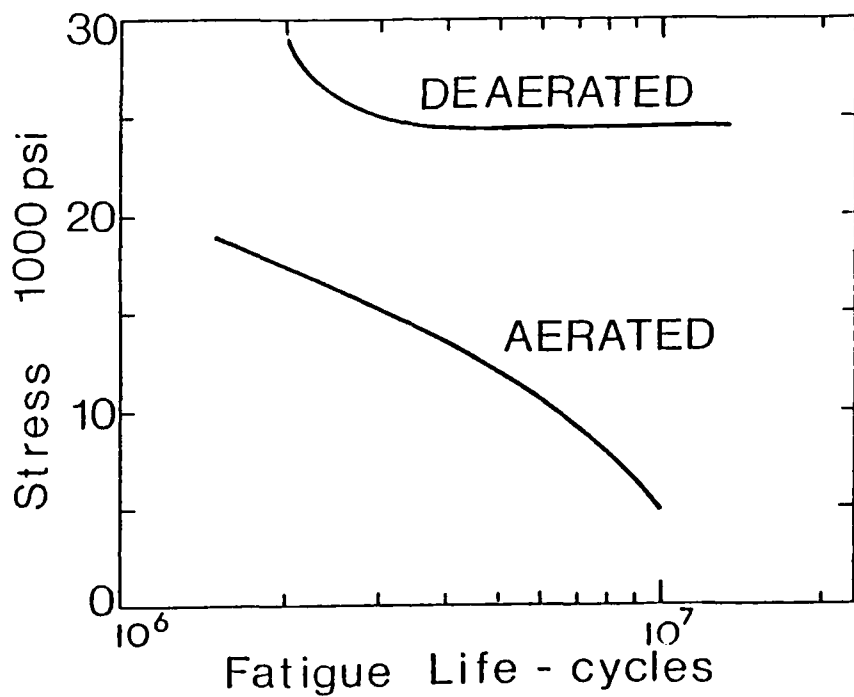


FIGURE 4.8. THE EFFECT OF DISSOLVED OXYGEN ON THE FATIGUE BEHAVIOR OF 1035 STEEL IN 5% NaCl SOLUTION [4.14]

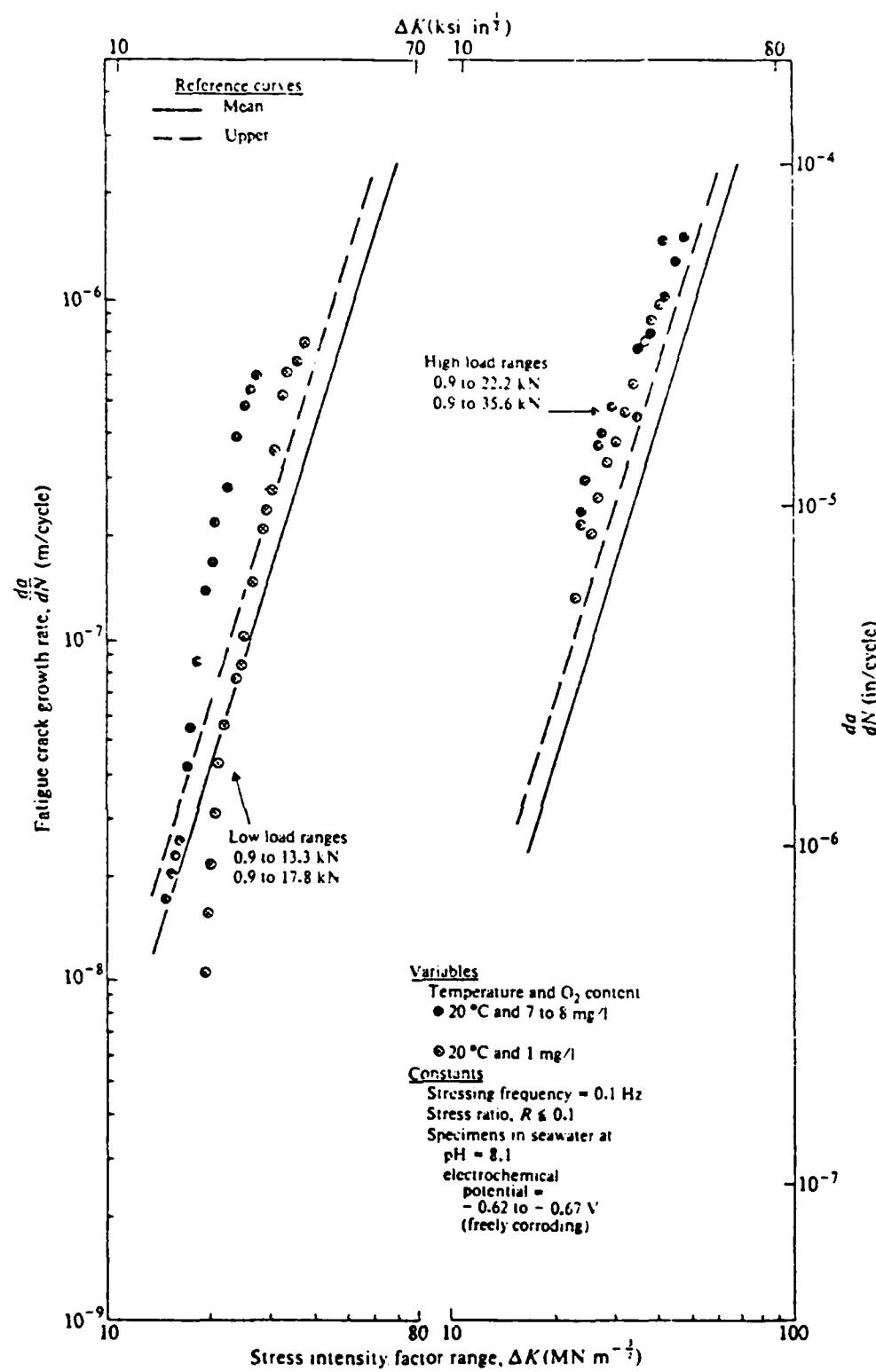


FIGURE 4.9. FATIGUE CRACK PROPAGATION DATA IN BS 4360/50D STEEL UNDER FREELY CORRODING CONDITIONS IN SEAWATER AS A FUNCTION OF OXYGEN CONCENTRATION. Reference curves are from air data [4.8].

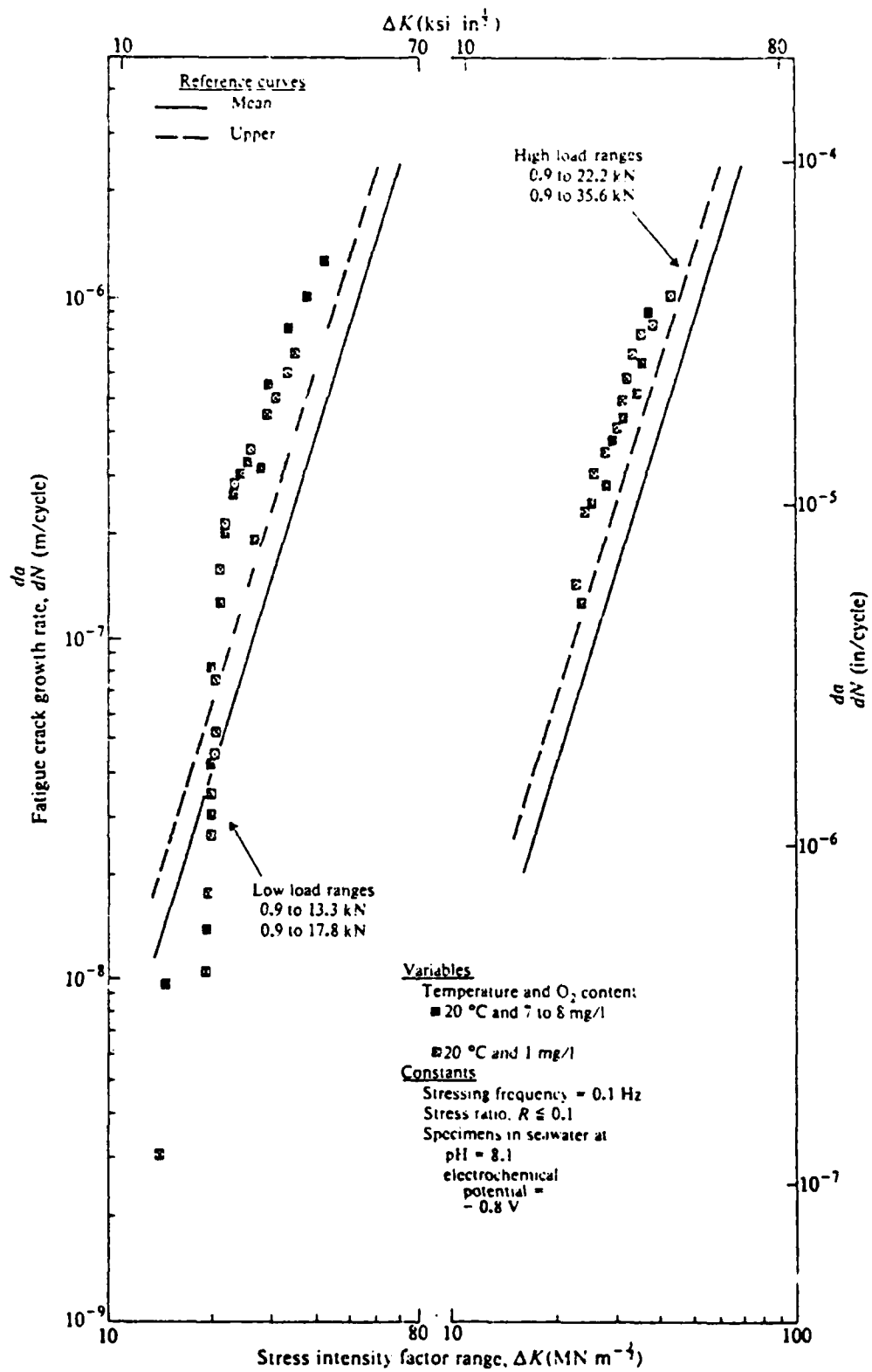


FIGURE 4.10. FATIGUE CRACK PROPAGATION DATA IN BS 4360/50D STEEL AT AN ELECTRODE POTENTIAL OF -0.8 V IN SEAWATER AS A FUNCTION OF OXYGEN CONCENTRATION. Reference curves are from air data [4.8].

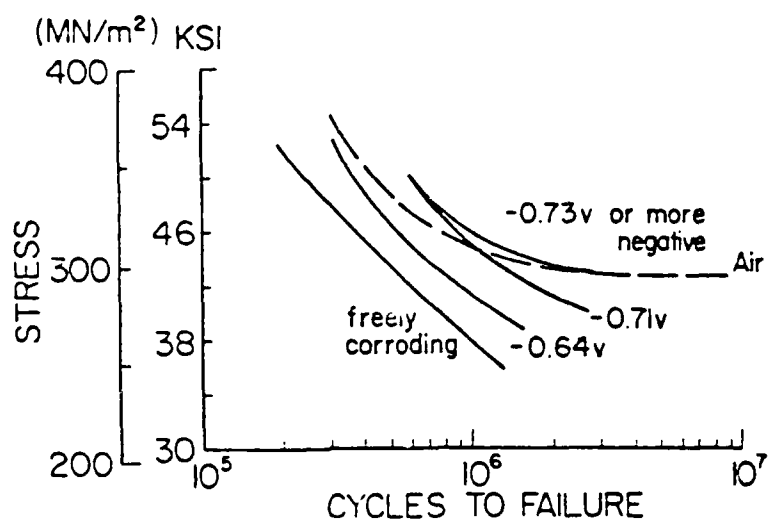


FIGURE 4.11. FATIGUE DATA FOR SMOOTH CARBON STEEL SPECIMENS IN A 3% NaCl-DISTILLED WATER SOLUTION AS A FUNCTION OF POTENTIAL [4.15]

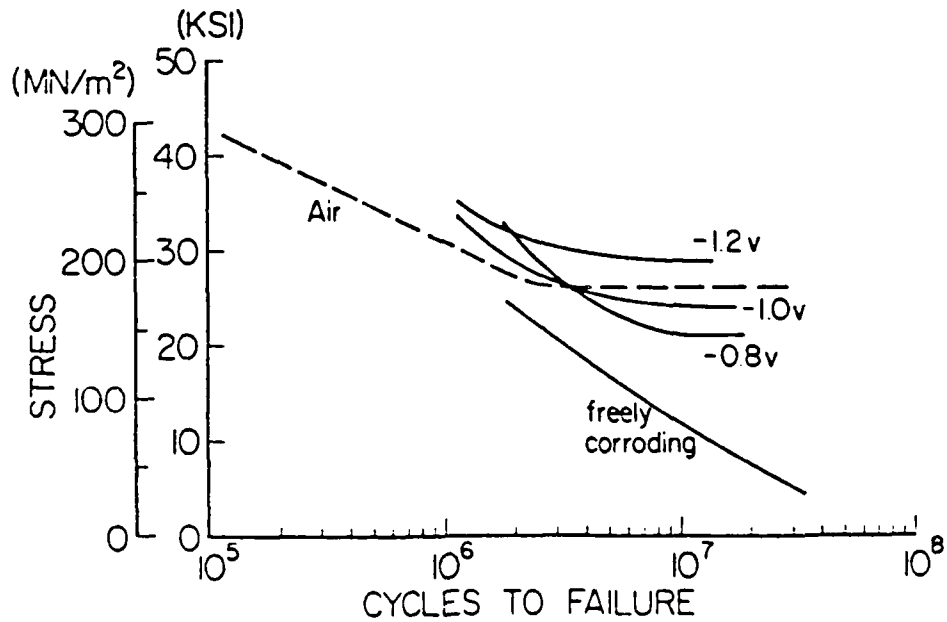


FIGURE 4.12. FATIGUE DATA FOR CARBON STEEL IN SEAWATER AS A FUNCTION OF SPECIMEN POTENTIAL [4.22]

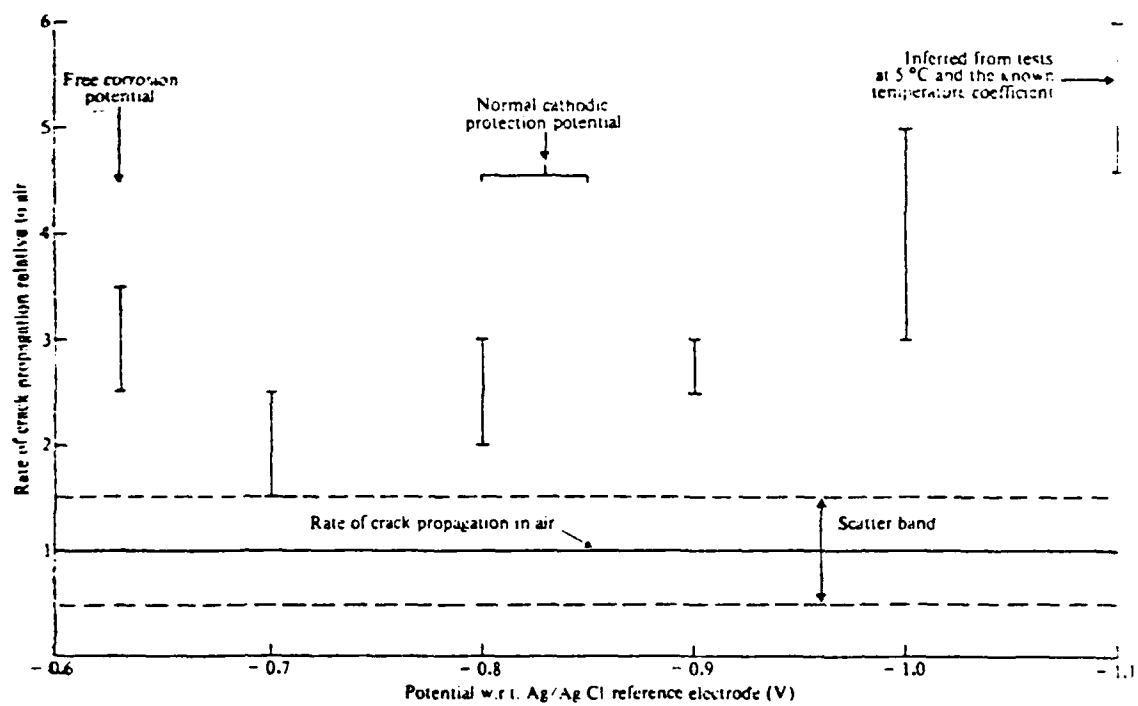


FIGURE 4.13. EFFECT OF ELECTRODE POTENTIAL ON THE FATIGUE CRACK PROPAGATION RATES FOR BS 4360/50D STEEL SPECIMENS STRESSED AT 0.1 Hz IN SEAWATER AT 20°C, $\Delta K = 20$ TO $40 \text{ MN m}^{-3/2}$, STRESS RATIO: $R \leq 0.1$ [4.8]

5.0 EFFECT OF MATERIALS AND FABRICATION VARIABLES ON FATIGUE RESISTANCE

5.1 Materials

5.1.1 General

In the United States, materials for welded steel offshore structures are chosen to meet the recommendations in API RP2A, Planning, Designing, and Constructing Fixed Offshore Platforms. Steels are specified in Reference [5.1] according to a group and class. The group designation indicates the minimum yield strength, and the steel class designates its intended application. Tables 5.1 and 5.2, reproduced from Reference [5.1], show the three groups, 1, 2, and 3, and the steel classifications A, B, and C. The API-recommended practice also gives guidance for steel selection for tubular joints. The groups are defined based on strength levels and welding characteristics. The classes for steels are determined from the material notch-toughness characteristics.

Table 5.3 presents a list of steels commonly used in corrosion fatigue studies in Europe.

5.1.2 Composition

There is a general lack of corrosion fatigue data on different kinds of structural steels. The effect of composition on corrosion fatigue may be of secondary importance to the corrosion aspects of marine steels. Recently, Solli [5.2] reported corrosion fatigue data on two welded CMn steels with the following characteristics.

1. Steel A

$$\sigma_y \text{ Min.} = 355 \text{ MPa (50 ksi)}$$

C	Si	Mn	P	S	Ni
0.06	0.3	0.7	0.01	0.01	2.4

2. Steel B (Quenched and Tempered CMn Steel)

$$\sigma_y \text{ Min.} = 490 \text{ MPa (70 ksi)}$$

Weld Composition in Percent

C	Si	Mn	Mo
0.06	0.4	1.3	0.4

Fatigue tests were conducted in air, synthetic seawater, and with cathodic protection with potentials of -780 and -1100 mV v. SCE. The tests were conducted at 1 Hz frequency and at a temperature of 10°-12°C. It was found that for Steel A the cathodic protection (-780 mV v. SCE) restored the fatigue strength in air, while Steel B did not recover the in-air fatigue strength for the same cathodic protection. Hence, the degree of cathodic protection would be the more important factor in determining corrosion fatigue crack growth.

In-air fatigue crack-growth tests performed on different qualities, thicknesses, and orientations of BS 4360 Grade 50D steel have been reported by Austen [5.3]. The data are shown in Figure 5.1. The in-air data show little effect of the metallurgical parameters on crack growth rate for $\Delta K > 20 \text{ MPa}\sqrt{\text{m}}$. However, in the slow growth region below 10^{-8} m/c , significant differences may exist.

5.1.3 Strength

Many of the high-strength steels exhibit low values of K_{ISCC} . Imhof and Barsom [5.4] studied the corrosion fatigue crack growth behavior in a 3 percent NaCl solution of 4340 steel heat-treated to different yield strengths. Figures 5.2 and 5.3 are corrosion fatigue crack-growth data for 4340 steels of 130 ksi (900 MPa) and 180-ksi (1240 MPa) yield strengths, respectively [5.4]. Fatigue crack-growth rates below K_{ISCC} increased by a factor of two for the 130 ksi (900 MPa) yield strength material tested at 6 cpm. However, the crack-growth rate under similar conditions increased five to six times for the 180 ksi (900 MPa) yield strength material. In other words, corrosion fatigue crack-growth rates increase with increase in yield strength of the material and are accompanied by a decrease in K_{ISCC} . Since most of the crack-growth data generated by Imhof and Barsom [5.4] at $R \approx 0.1$ were at ΔK less than K_{ISCC} , the mechanism of crack growth can be classified as true corrosion fatigue.

5.1.4 Microstructure

Fractographic examinations [5.3] of steels explain the various mechanisms involved in corrosion fatigue crack-growth process. Fractographs of 835M30 steel are shown in Figure 5.4. True corrosion fatigue is

characterized by brittle fatigue striations, Figure 5.4(b). Figure 5.4(c) shows an inter-granular cracking for the stress corrosion fatigue mechanism.

Corrosion rate is structure-sensitive and increased attack can take place in weld areas in marine environments. The effect depends on other parameters like composition and weld heat input.

Vosikovsky [5.5] measured fatigue crack growth in HY 130 steel weldments in air and 3.5 percent NaCl solution. The study found that in air at high stress ratios, crack-growth data for base metal is a conservative estimate for weld metal. However, in saltwater at high mean stress, cracks could grow faster in weld metal. Figure 5.5 is the fracture surface for a weld specimen. At high mean stress, a fatigue crack can grow faster in the weld metal because the boundaries of columnar dendrites appear to be susceptible to environmental cracking. Figures 5.6 and 5.7 show the fatigue growth rate differences between weld metal and base metal for two R-ratio cases, respectively.

Figure 5.8 illustrates a schematic representation of the various micro-structural phenomena associated with corrosion fatigue behavior. Additional testing programs are required to correlate the microstructural aspects with fatigue crack-growth predictions.

5.2 Fabrication

5.2.1 Historical Perspective

The exploration for oil and gas offshore first began off the coast of California in the late 1890's [1.3]. Wells were drilled from wharves which extended about 500 ft (150 m) from the shoreline. For the next three decades, exploration continued in California, in the marshes and swamps of Louisiana, and on Lake Maracaibo, Venezuela. These early platforms were fabricated from timber with wooden piles and generally stood in waters not exceeding 20 ft (6 m). Because of attack on the timber by shipworms and the need to drill in deeper waters, steel pilings were introduced in the mid-1940's. The importance of proper welding was not recognized in the early tubular joints of these platforms and there was little information on the proper design or fabrication. Graff [1.3] indicated that failure of tubular joints was a recurring problem in the early platforms, but redundancy of braces and on-site repairs successfully contended with the situation.

The U.S. oil industry and government recognized a need to further knowledge of tubular connections used in offshore platforms. Early research was conducted under the guidance of the Welding Research Council (WRC) in a number of cooperatively sponsored programs [5.6-5.8]. In the late 1960's, several studies conducted at Southwest Research Institute addressed the effect of notches on fatigue crack initiation and propagation life [5.9, 5.10]. The analysis techniques were extended to tubular joints and predictions compared with experiments in [5.11]. More recent WRC publications [5.12, 5.13] have summarized and evaluated procedures and data used in offshore tubular joint design.

Much of the work in the period through the mid-1970's concentrated on the static and fatigue strength of welded offshore connections. Procedures were developed to evaluate the stress concentration factors in tubular joints, and experimental fatigue tests were conducted to collect data which now form the basis of design S-N curves such as given in Reference 5.1.

The Offshore Technology Conference (OTC) held annually since 1969 in Houston, Texas, has served as a forum between researchers worldwide in the field of offshore structures. For example, one of the early applications of fracture mechanics to fatigue in welded tubular joints was presented at the 1970 OTC [5.14]. Recent interest has turned to the next generation of offshore structures such as tension leg platforms and guyed and articulated towers.

5.2.2 Geometry

The fatigue life of a welded connection is strongly influenced by the geometry of the joint. This is because the local stresses are a function of the stress concentration factor, which is geometry dependent, and these stress levels strongly influence fatigue crack initiation and propagation. The detrimental effect of stress concentration on fatigue strength has been known ever since the early days of fatigue testing. Wöhler, from his classic experiments on railway axles, came to the conclusion that sudden changes in diameter reduce the fatigue strength. He also noted that the number of cycles that an axle could endure depended on the condition of the surface, with a polished specimen surviving much longer than one that had been turned or filed.

In welded structures with simple geometry, such as fillet welds, stress concentrations have been computed both analytically and experimentally.

Most stress concentration factors (K_t) computed analytically use the finite element method, while photoelastic techniques are widely employed in experimental investigations. Gurney [5.15] gives the stress concentration factor for a number of fillet-welded joints. These joints are idealized since the weld face profile is a flat plane. Therefore, these concentration factors only include what may be termed the geometry of the connection and do not include local irregularities such as undercut at the weld toe. The total stress concentration factor for the joint may be considered as composed of two factors, which reflect both the local weld toe radius and the geometry of the connection. In a welded joint, the peak stresses usually occur at the toe or at the root of the weld, and there are separate stress concentration factors for these locations. In Section 6.5.2 the effect of the geometry on K_t is further discussed, and an expression which relates K_t to the toe radius, weld geometry, mode of loading, and plate thickness is given.

The locations where fatigue cracks initiate depend upon the geometry of the weld and the mode of loading. Normally in fillet-weld type joints used in offshore structures, cracks initiate at the weld toe. However, in some situations, depending upon the loading and thickness of the members, cracks may initiate at the weld root. The British Standards Institution document DD55, Draft for Development—Fixed, Offshore Structures [5.16], gives fatigue curves for a number of welded joints of simple geometry. Curves are given for both air and seawater, with the difference being the endurance limits for joints in seawater are lower than those in air. However, for a weld of a given class, both the air and seawater curves have the same slope when the fatigue curve is plotted as log-stress range versus log-cycles to failure.

In an offshore structure, the majority of the load-bearing welded joints subject to fatigue are in welded tubular connections. These are commonly classified as T, Y, X, and K joints, as shown in Figure 5.9. These are the basic types of joints. However, in real offshore structures, many of the joints are geometrically much more complicated, and it is common to have structural nodes with ten or more brace members intersecting a single chord. The stress concentration factors in these complex joints are more difficult to determine than the simple configurations mentioned earlier. This is because of the complex geometry, the multiplanar nature of the loading, and the variability in the local weld profile.

A considerable amount of research has been undertaken in recent years to determine stress concentration factors at tubular joint connections. These may be divided into analytical and experimental investigations. The analytical work generally uses thin-shell, finite element theory, although thick-shell theory and the use of solid finite elements have also been undertaken. Such numerical work under the ECSC and UKOSRP programs is being conducted by Parkhouse [5.17] and Gibstein [5.18]. Work in photoelastic models is being conducted by Fessler [5.19] and acrylic measurements by Wordsworth [5.20].

The difficulty in using the analytical and experimental techniques to determine stress concentrations in an actual welded structure is illustrated in Figure 5.10 [5.21]. The actual weld profile connecting the chord and brace is shown in Figure 5.10(a). What is required from any analytical or experimental technique is to determine the stress in the weld at a location such as the weld toe. Even with a full-scale welded specimen, this could not be accomplished exactly. The technique that is commonly used is to install strain gauges in the vicinity of the weld toe and to extrapolate the results back to the weld toe. Figure 5.10(a) shows that this extrapolation is usually done linearly and the extrapolated value is called the hot-spot strain or stress. However, this is more of a matter of convenience rather than an attempt to represent the actual physical stress gradient in the vicinity of the welded connection. As will be seen in Chapter 6.0, a very high stress gradient exists at the weld toe. The use of the hot-spot strain (stress) concept eliminates weld toe variances and put similar tubular joints on a common basis.

For the acrylic model shown in Figure 5.10(b), the stresses or strains are determined in a manner similar to actual steel specimens, that is, by extrapolating results back to the intersection of the brace and the chord. The weld profile is not included in the acrylic model technique, and the results more closely resemble those obtained by thin-shell analysis.

The basis of a thin-shell, finite element analysis is given in Figure 5.10(c). Here the mid-plane of the brace and chord members is described by finite element nodes with the thickness of the element being included directly in the finite element formulation. The intersection of the outer surface of the brace and chord is fictitious, and the difficulty comes in choosing the stress on the outer brace and chord members to use in

calculating the stress concentration factor. There is a question of accuracy using thin-shell finite element theory to determine peak stresses at the intersection. This is based upon the belief that the stiffness of the welded joint is not accurately represented by the finite element two-dimensional formulation. This inaccuracy may decrease as the thickness-to-diameter ratio of the joint decreases and may not be too significant for the larger tubular joints.

Both the acrylic and thin-shell finite element models are more extensively used for parametric evaluation of stress concentration factors rather than actual determination. They simply cannot take into account the three-dimensional effect and accurately determine the stress at the weld toe. To formulate a more realistic model, thick-shell isoparametric finite elements have been used to represent the geometry of the welded connection. The photoelastic technique is also able to include the weld profile and thereby is able to include three-dimensional effects. Figure 5.10(d) shows the typical stress distribution found from photoelastic analysis and indicates the continuous increase in stress as one passes from the chord wall to the brace wall. This method is widely used to evaluate stress distributions in very complex joints that are difficult to model analytically. Fortunately, work in the determination of stress concentration has progressed to a point where formulas are available for the designer. These stress concentration factors are based on work by investigators such as Kuang [5.22], Gibstein [5.18], and Wordsworth and Smedley [5.23]. Formulas are given for a variety of geometry and loading conditions; for example,

- o K and KT joints, balanced axial load
- o K joints, out of plane bending moment
- o K and KT joints, in plane bending moment

Reference 5.13 gives a good summary of the recent state-of-the-art in calculating hot-spot stresses and stress concentration factors for various tubular joint connections.

In making actual fatigue calculations, the difficulty for the designer is choosing the correct stress value to correspond to a given fatigue curve. It is standard practice in tubular joint connection to present fatigue curves in terms of total cyclic strain or stress range versus number of cycles to failure. A typical example from API RP2A [5.1] is given in Figure 5.11. Here the stress or strain is given in terms of the so-called hot-spot value,

which is the strain or stress at the toe of a welded joint. Of course, exact determination of the strain or the stress at this location cannot be achieved in reality because of the difficulties in making measurements or performing an analysis at this location. In Figure 5.11, for example, curves D', X, and K presume the welds merge smoothly with adjoining base metal. If a smooth transition as defined by the API RP2A criterion is not met, then the dashed curves should be used. The X curve with hot-spot strain range is preferred for a tubular connection. The hot-spot strain range is defined as that which would be measured by a strain gauge element adjacent to and perpendicular to the toe of the weld after stable strain cycles have been achieved. The D', E', and K curves in Figure 5.11 are for other welded joint connections as defined in Reference 5.1. It is also interesting to note that the curves in Figure 5.11 assume effective cathodic protection. API RP2A indicates that for splash zone conditions having free corrosion or excessive cathodic protection, an appropriate reduction to the allowable cycles should be considered. However, no recommendations are given for what the reduction should be. Reference 5.1 also indicates that joints in the splash zone should be avoided.

In the working groups for the ECSC and UKOSRP programs, there has been apparent agreement on the location of strain gauges to determine the hot-spot strain ranges in welded joint fatigue tests. The standard practice is to mount two strain gauges, one close to the toe of the weld and the other a distance away, as illustrated in Figure 5.10. From strain measurements, a linear extrapolation technique is used to compute the hot-spot strain range at the toe of the weld. The innermost gauge should be near to the weld to reduce extrapolation errors, but it should be outside the notch region. The outermost gauge should be in the region where the decay of geometric stress is still linear. Figure 5.12 shows recommended locations for placement of the gauges on both the chord and brace member. The values are given in terms of the radius and thickness of the respective members. However, the distance from the weld toe should not be smaller than 4 mm. Figure 7.29 in Section 7.5.1 shows a typical stress distribution in the vicinity of the weld toe for a planar T-Joint. At distances greater than about 2 mm, the toe notch no longer has an effect on the stress field.

For the ECSC program, along with the standardization of placement of strain gauges, there has been standardization of data which are collected with respect to the various tests. The purpose of doing this is to allow a

more ready comparison of the test results from one laboratory to the next. An example of this standard test data sheet is given in Appendix B. The first page describes the tubular joint geometry, the properties of the base metal, the welding filler materials, electrodes, and describes the weld bead geometry at the hot-spot. It also documents the location of the strain gauges in relationship to their weld toe and records the shakedown of the gauges before fatigue testing. Information is also provided on crack initiation and propagation. Initiation is usually defined as a drop of 15 percent in strain levels as measured by gauges adjacent to the weld toe. At this drop in strain, cracks are difficult, if not impossible, to detect with the naked eye. Data on small (approximately 30 mm) visual cracks and through cracks in the chord wall (usually detected by monitoring with pressure differentials) are also provided. The propagation of the crack is usually monitored and presented by polar plots.

5.2.3 Thickness Effects

The fatigue curves presented in the usual codes such as API are based upon test data attained from plate weldments, tubular joints, or other typical geometries. The thickness of the test specimens is relatively thin compared with that of the actual structure, and usually tests are conducted with components about 1/2 in. thick. However, in most offshore structures, plate thicknesses are usually much larger than that, and there is concern that using fatigue data from thin specimens may be unconservative when applied to the size of the structures being built today. As a consequence of the concern for the thickness effect, a series of investigations has been conducted under the ECSC and UKOSRP programs for both tubular and nontubular welded joints.

This thickness effect has been observed experimentally, both in replica planar specimens and also in tubular joint fatigue results. Typical results from cruciform testing are shown in Figure 5.13 [5.25]. Results indicate a drop in fatigue life for a 38-mm-thick plate compared with 25 mm. These results were made in air at an R-ratio of 0. Session 3 of the 1978 European Offshore Steel Research Seminar contained several papers from experimental investigators in Germany, Norway, and the United Kingdom reporting on the effect of plate thickness on planar type specimens.

There has also been considerable experimental work done to determine the effect of wall thickness on the fatigue life of welded tubular connections. Most of the work on size effects in tubular joints is being conducted in the Netherlands at TNO and the University of Delft, and at the National Engineering Laboratory (NEL) and the Welding Institute in the United Kingdom. Figure 5.14 summarizes some of the earlier Dutch tests. These tests were performed on T joints with axial or in-plane bending loads applied to the brace. The tests were done on three different chord diameters; however, the ratios of the chord thickness to diameter for all three sets of results are the same. The results shown in Figure 5.14 clearly indicate that for increasing chord thickness, there is a decrease in fatigue life of the joint. Results from the UKOSRP program conducted by the NEL and the Welding Institute also confirm the influence of thickness. Tests were done on T and K joints, with four separate chord diameters of 168, 457, 914, and 1830 mm. The chord thicknesses were chosen such that for the four sizes tested, the average chord diameter-to-thickness ratio was about 27. Reference 5.26 gives details on the testing procedure and test results for individual specimens. Generally the longest test conducted was to 2×10^7 cycles. A linear regression analysis was performed on each set of results for a specific chord diameter, and these results are shown in Figure 5.15, where the ordinate is given in terms of hot-spot strain range. The hot-spot strain was extrapolated back to the toe of the weld from two gauges mounted as described in Section 5.2.1. The straight lines are the result of a linear regression analysis on the fatigue data, where the mean fatigue curve is assumed to be a straight line on a log-log plot. The form of equation is

$$N(\Delta e)^m = C \quad (5.1)$$

The parameters m and C for the different chord diameters are shown in Table 5.4. Figure 5.15 shows a decrease in fatigue strength with increasing chord diameter, although it is not understood why the 457-mm chord thickness crosses both the 914-mm curve at a low number of cycles and the 168-mm curve at a high number of cycles. The largest diameter tested, 1830 mm, lies below the other curves for less than 107 cycles, but crosses the 914-mm line at about 107. It should be noted that the large 1830-mm T joints were stress relieved, and only about five of these were tested.

Gibstein [5.27] at Det norske Veritas has also considered the effect of thickness and how it relates to current design fatigue curves. Figure 5.16 shows some selected results on tubular joint tests from the Netherlands, the United Kingdom, and Norway for various chord diameters. The API X and API X' design curves (Figures 5.11), as well as the API X design curve at the 97.5 percent and the corresponding mean curve at the 50 percent survival levels, are also shown. Clearly, two test results on 914 maximum diameter joints from the Dutch program fall on or slightly above the API X design curves in the high-cycle region. These results, taken strictly by themselves, would indicate that the curve given for design is nonconservative. However, there was no grinding or stress relief applied to the Dutch test specimens and there is a question the reduced fatigue life was a result of poor weld profile. It also must be realized that the API curve, for example, was based upon strains measured by gauges some distance from the weld toe. Current fatigue curves are presented in terms of strain or stress at the weld toe versus number of cycles to failure. These strains are obtained by linear extrapolation of strain gage results placed close to the weld toe as discussed in Section 5.2.2. It can be argued that the existing code fatigue curves are not underconservative since the basis for determining the hot-spot strain or stresses is not the same now as when the curves were established.

Nevertheless, with the evidence from the extensive experimental work which has been conducted on the effect of plate thickness, it appears that consideration should be given to include some allowance of this plate thickness effect in the design fatigue curves. A drafting panel has recommended revisions to the fatigue section of the UK Department of Energy's document installations: Guidance on Design and Construction [2.16]. Such changes are discussed in Reference [5.28] and recommended accounting for the thickness effect in the design fatigue curves.

The effect of plate thickness on fatigue life can also be addressed through linear elastic fracture mechanics. Section 6.6.4 presents mathematical expressions for the stress concentration factor K_t at the weld toe and the stress distribution in the vicinity of the weld. The equation for K_t indicates that for two joints with equal toe radii, the joint with the larger thickness will have the large stress concentration factor. The analysis agrees with Gurney's [5.15] qualitative explanation that for a thicker plate, the high-stress region extends further into the plate than for a thin

one. Therefore, for two joints with the same initial defect size and two different thicknesses of plate, the crack tip in the thicker plate will be situated in a region of higher stress than the corresponding crack tip in the thinner plate. In a higher stress region, the crack will propagate faster, particularly in the small crack stage where most of the fatigue life is expended. Other calculations [5.29, 5.30] which have been conducted for fillet-welded joints confirm, at least qualitatively, the thickness effect. Chapter 7.0 in this report compares fracture mechanics crack propagation analytical predictions with experimental tests and again confirms the reduction in fatigue strength with increased joint thickness.

5.2.4 Fatigue Improvement Techniques

The previous two sections of this report discussed how joint geometry and plate thickness influence the fatigue life of a weld. This section reviews the most commonly used post-weld treatments to improve fatigue life and what increases can be expected. In general, improvements in fatigue life of an already-fabricated weld can be achieved in two ways:

- o Reduce geometrical discontinuities
- o Create more favorable surface stresses distribution

Gurney [5.15] discusses these techniques in some detail and presents an extensive bibliography. However, Gurney's work and most of the literature until recently consider fatigue improvements of welds in air and not in seawater. As the main thrust of this present work is on long-term corrosion fatigue, the following discussions will generally be restricted to what effect the marine environment has on these life improvement techniques. However, some comments on the specific techniques are first in order.

Weld Toe Grinding: Section 5.2.2 discussed how fatigue strength is related to the stress concentration at a welded joint. The stress concentration factor was considered to be influenced by the joint and local weld toe geometries. By grinding the weld, either with a rotary burr or disc grinder, the entire weld surface, or just the toe of the weld, can be smoothed to remove irregularities and to help reduce this so-called local stress concentration factor. This technique does not, of course, return the fatigue strength of the joint back to base material because the joint stress concentration still exists. It also can remove slag intrusions that exist at the

weld toe. This technique of improving fatigue strength is discussed by Gurney [5.15], and Figure 5.17 shows that the grinding must extend below the parent plate surface as shown in Part B in order to remove toe defects.

Investigations have shown that if adequate grinding is not performed, then the increase in fatigue strength is negligible. Work at The Welding Institute suggests that the depth of the grinding should be approximately 0.5 mm below the bottom of any visible undercut. Chapter 7.0 indicates that for plate thicknesses ordinarily used in offshore structures, the initial crack length used for a fracture mechanics analysis would be less than 0.5 mm. Grinding, therefore, not only helps reduce the stress concentrations by improving the weld toe profile, but it helps eliminate initial crack-like defects in the joint. It should be remembered that grinding can only improve fatigue life for failures initiating on the weld surface. In some instances, fatigue cracks initiate at the weld root and propagate through the thickness. This is not a normal failure mode in a typical offshore structure, however, and so, improvements in fatigue life can be expected by grinding.

TIG Dressing: Another technique for improving the shape at the weld toe uses the tungsten inert gas (TIG) process. In addition to improvements in profile, the TIG dressing can remove entrapped inclusions at the weld toe. The process usually requires that the weld surface be clean in order to produce a satisfactory bead. It is also preferable to lightly grind the surface and brush the weld toe to remove contaminants before remelting the TIG dressing. The TIG process does have its advantages over grinding because it is easy to use and can be conducted in a relatively good working environment with much less noise and dust.

However, there are some disadvantages using TIG dressing because it is known to increase hardness in the heat-effective zone near the remelted weld in excess of 400 VHN 10.* This, for example, exceeds the maximum allowed hardness for offshore structures given in Reference 5.31. For submerged arc welding, the American Welding Society Structural Welding Code, AWS D1.1-83 [5.32], limits the hardness in the heat-effective zone of the base metal to less than 225 VHN for steel having a minimum tensile strength not exceeding 60 ksi and 480 VHN for steels having a minimum specified tensile strength greater

*VHN10 - Vickers hardness number obtained with a 10-kg load.

than 60 ksi, but not exceeding 70 ksi. These allowed hardness limits are established to prevent stress corrosion cracking and brittle failure in the weldments. Work has been conducted under the ECSC program in Norway by Haagensen [5.33] on techniques to reduce the hardness to an acceptable level by employing a second TIG dressing run to temper the martensite formed in the heat-affecting zone left by the first run. Figure 5.18 schematically shows a cross-section of a TIG-dressed weld. Part (a) indicates the dressing at the weld toe, and Part (b) shows the profile between the first and second TIG runs.

Stress Relieving: When two components are joined together, there is usually a zone of residual stresses in the welded joint. For example in a butt weld, tensile forces exist in the weld and the base metal immediately adjacent to it. These tensile stresses are balanced by compressive stresses at locations further away from the weld. Of course, the tensile and compressive forces must be balanced to provide overall static equilibrium to the joint. The earlier work on residual stresses seems to indicate little effect on fatigue life. This was based on comparative tests of as-welded and stress-relieved butt specimens under pulsating tension loading. The general trend indicates there is little effect of stress relief on fatigue life for welded structures with completely nominal tensile loads. However, if there is a partial compressive nominal load on the joint, then improvements in life can be obtained by stress relieving.

Large residual stresses are found near the weldments in tubular and plate connections as a result of the welding process. These stresses raise the mean load experienced by cracks growing from a weldment to the point where the entire fatigue stress range can be tensile and thus damaging. It is for this reason that the present design codes for welding connections require that only the cyclic stress range and not the mean stress be considered for calculation of fatigue endurance. Improvements in post-weld heat treatment have been demonstrated in the life of plate weldments subject to nominal tensile-compressive ($R = -1$) loading. If this effect applies to tubular joints, then the heat treatment offers an opportunity in certain cases for significant improvement in fatigue life. However, the cost for such heat treatment is large and must be justified by the anticipated gain in structural performance of the joint.

If a connection is stress relieved by post-weld heat treatment, then the residual stresses are greatly reduced, and the mean stress in the crack-growth region falls back to that due to the applied loading, provided this loading is not entirely tensile. Part of the fatiguing stress cycle is then compressive and less damaging. This decreases the fatigue damaging cyclic stress range and increases the fatigue endurance of the connection. The amount of such an increase will depend on the mean stress of the applied loading, and, thus, the fatigue life of a post-weld heat treatment connection depends upon the applied mean stress as well as the cyclic stress range. It is not possible to calculate tensile stresses for post-weld heat treatment connections simply from knowledge of the applied mean stress and the stress range. This is because not all stresses may be removed, and the residual stress distribution may depend upon plate thickness.

The theoretical predictions for both crack initiation and crack propagation developed in Chapter 6.0 account for residual stress effects either by including a mean stress or modifying the R-ratio. Examples are presented and discussed in Chapter 7.0.

Peening: Peening is a cold-working process which consists of battering the surface of the component, usually either with a high-velocity stream of metal particles or with a tool operated by a pneumatic hammer. The objective of peening is to introduce compressive residual stresses in the surface layer. The process produces plastic deformations in the material, with the surface trying to expand laterally, but prevented by doing so by the elastic material underneath. This restraint of the elastic metal introduces compressive stresses on the surface. In addition to providing a favorable stress state on the surface, the peening reduces the sharpness of notches and thus reduces the severity of the stress concentration. This in itself has a beneficial effect on fatigue life.

Attention will now turn to what improvements in fatigue life can be expected from the four techniques just mentioned. Figure 5.19 shows fatigue curves for crucible joints under bending and tensile loading. As-welded results are compared to TIG-dressed, ground, and peened welds. These results show that peening resulted in the greatest increase in fatigue strength, followed by grinding and then TIG dressing. Results in air were similar for both axial ($R = 0$) and bending ($R = 0$) loading. The results

reported in Reference 5.25 are similar to those of other investigations [5.34, 5.35]. The literature seems to indicate that the variability in improving fatigue life is greatest with TIG dressing techniques. The reason for this is not understood; however, it may be due to the TIG process itself and also to the condition of the original weld before it is TIG dressed. As an example, consider Figure 5.20 [5.33], which shows best-fit curves from Haagensen's bending tests on the joint geometry shown in Figure 5.18. Haagensen's and Booth's results cannot be quantitatively compared because of the different joint geometries. However, qualitatively, they show conflicting trends in fatigue life. Booth's results, Figure 5.19, indicate little difference between the fatigue performance of as-welded and TIG-dressed joints at a low number of cycles (approximately 10^5) with an increasing divergence in results over 10^6 cycles. Haagensen, Figure 5.20, on the other hand, shows wide dispersion between the air test and the TIG test at 10^5 cycles, but indicates a converging of the two fatigue curves at cycles above 10^6 . There is no explanation of this trend at the present time.

Stress-relieved tests were not conducted on the specimens given in Figure 5.19, so a direct comparison is not possible. However, Reference 5.36 does compare the effects of post-weld heat treatments on a welded plate T-type connection subjected to bending. The results are shown in Figure 5.21 for R-ratios of 0.1 and -1. These results confirm the observations reported earlier that for the post-weld heat treatment to be most effective, the loading mode should be tension-compression. Although there is some improvement at $R = 0.1$, the greatest improvement in fatigue life is under tension-compression ($R = -1$).

Work has also been conducted to look at the effect of a seawater environment on the increase in fatigue life due to post-weld heat treatment. Figure 5.22 presents results from tests run in the Netherlands with plates 70-mm thick. The tests in seawater were conducted at a loading frequency of 0.2 Hz. These tests indicate that stress relief still has a favorable effect on fatigue of welds in seawater. However, there is less of an increase than in air. For example, at $R = 0.1$, the post-weld heat treatment shows little improvement in fatigue life. Greater improvement, however, is gained when the loading is tension-compression ($R = -1$).

Work has also been conducted in The Netherlands to consider the effect of seawater on toe grinding and TIG dressing. The results of a limited set of tests are presented in Figure 5.23. This figure presents fatigue curves for as-welded joints in air and seawater. Figure 5.23 indicates about the same improvement for both the TIG and ground welds. This is not entirely consistent with Booth's [5.25] results conducted in air, which show the toe ground welds have an improved fatigue life over the TIG dressed. Although there is an improvement in life in both air and seawater, the test results seem to indicate there is less relative improvement for the tests conducted in seawater. This effect is illustrated even more clearly in results obtained by Booth [5.37], and Figure 5.24 shows results from cruciform specimens conducted in air and constant immersion in seawater. The toes of the welds were either ground or left in an as-welded condition. The air results, as shown by the solid line, show the usual large increase in fatigue life when the toes of the welds were ground to reduce the local stress concentration or remove slag inclusions. However, for the tests conducted in seawater, very little improvement in fatigue life can be noted. The explanation of this is that in air, the grinding removes defects at the weld toe that serve as initiation sites for fatigue propagation. By removing these defects, the initiation phase can be delayed and fatigue life improved. In the seawater environment, however, corrosion attacks the weld surface. This causes development of pits that could serve as crack initiation sites, thereby negating some of the beneficial effects of the weld grinding.

The Japanese have also been active in looking at the performance of TIG-dressed welds in a seawater environment. The results of one such investigation are given in Reference 5.38. Butt and fillet-welded joints were subjected to pulsating tensile stresses at a cycling rate of 10 cycles per minute and a seawater environment of 30°C. The toes of the as-welded fillet welds were modified by using TIG dressing and also depositing what the Japanese termed an "additional welding" bead. The cross-sectional geometry of the weld is shown in Figure 5.25(a). Fatigue curves for the welded and base metal specimens in both seawater and in air are presented in Figure 5.25(b). As expected, the Japanese results indicate an improvement in fatigue life by using TIG dressing, and their results indicate an improvement in fatigue life by using TIG dressing and their "additional weld" techniques. The results are

surprising in that the fatigue lives using these two improvement methods approach that of the base material in both seawater and in air. Figure 5.25 also indicates that there may be less relative improvement in fatigue life for welds subjected to a seawater environment than in air.

The Japanese have also been concerned with the question of hardness in a TIG-dressed weld. The general literature indicates that stress corrosion cracking is not a problem in ordinary structural steel in normal seawater. The critical hardness for stress corrosion cracking in seawater contaminated with 1 to 30 parts per million of sulfide is 360 to 400 Vickers hardness [5.35]. The problem occurs, of course, for seawater contaminated with sulfide or for high-strength steels. For the tests conducted in Reference 5.35, the following Vickers hardnesses were reported in the weld zone:

Base Metal:	150-163
Deposited Metal:	203-222
TIG Dressing:	216-225
Additional Welding:	274-183

The Japanese results indicate that with controlled procedures the increase in hardness due to the TIG or additional welding processes is not sufficient to create problems with stress corrosion cracking. The fatigue results indicate that this hardened weld toe region will have negligible effects on corrosion fatigue.

In summary, this section has discussed various weld fatigue improvement techniques, either by changing the geometrical discontinuities at the weld toe or altering the weld surface stresses. Tests have indicated that substantial increases in fatigue life can be gained by employing these techniques when the structure is loaded in an air environment. Increases in fatigue life can also be gained in a seawater environment. However, the relative improvements in fatigue life do not seem to be as great. The question that still needs to be answered is what effect on fatigue life can be expected when these techniques are used in conjunction with cathodic protection, which is standard practice in offshore structures. This includes, of course, continuous protection, intermediate protection, and overprotection. These are areas of research that are still under investigation.

CHAPTER 5.0 REFERENCES

- 5.1 "API Recommended Practice for Planning, Designing, and Constructing Fixed Offshore Platforms," API RP2A, Eleventh Edition, American Petroleum Institute, Dallas, Texas, January 1980.
- 5.2 Solli, O., "Corrosion Fatigue of Welded Joints in Structural Steels and the Effect of Cathodic Protection," Paper 10, IV/P10-1, European Offshore Steels Research Seminar Proceedings, Cambridge, UK, 27-29 November 1978.
- 5.3 Austen, I. M., "Factors Affecting Corrosion Fatigue Crack Growth in Steels," Paper No. 14, European Offshore Steels Research Seminar, Cambridge, UK, 27-29 November 1978.
- 5.4 Imhof, E. J., and Barsom, J. M., "Fatigue and Corrosion-Fatigue Crack Growth of 4340 Steel at Various Yield Strengths," Progress in Flaw Growth and Fracture Toughness Testing, ASTM STP 536 (1973).
- 5.5 Vosikovsky, O., "Fatigue Crack Growth in HY130 Steel Weldments in Air and Water," Welding Research Supplement, September 1980, pp 255-s to 258-s.
- 5.6 Bouwkamp, J. G., "Research on Tubular Connections in Structural Work," Welding Research Council Bulletin 71, August 1961.
- 5.7 Toprac, A. A., "An Investigation of Welded Steel Pipe Connections," Welding Research Council Bulletin 71, August 1961.
- 5.8 Toprac, A. A., Johnston, L. P., and Noel, J., "Welding Tubular Connections: An Investigation of Stresses in T-Joints," Welding Journal, Vol. 45, No. 1, Research Supplement pp 1-S to 12-S, January 1966.
- 5.9 Pickett, A. G., and Grigory, S. C., "Prediction of the Low Cycle Fatigue Life of Pressure Vessels," Transactions of the ASME, Journal of Basic Engineering, Vol. 89, Series D, No. 4, December 1967.
- 5.10 Pickett, A. G., "Prediction of Low-Cycle Fatigue Life of Specimens with Fabrication Flaws," Transactions of the ASME, Journal of Engineering for Industry, Vol. 90, Series B, 1968.
- 5.11 Grigory, S. C., "A Study to Develop a Design Procedure for Analysis of Plastic Fatigue Life of Tubular Joints on Offshore Structures," Southwest Research Institute Final Report, Project No. 03-1882, Shell Development Company, Houston, Texas, May 1969.
- 5.12 Marshall, P. W., "Basic Considerations for Tubular Joint Design in Offshore Construction," Welding Research Council Bulletin 193, April 1974.
- 5.13 Rodabaugh, E. C., "Review of Data Relevant to the Design of Tubular Joints for Use in Fixed Offshore Platforms," Welding Research Council Bulletin 256, January 1980.

- 5.14 Becker, J. M., Gerberich, W. W., and Bouwkamp, J. C., "Fatigue Failure of Welded Tubular Joints," Offshore Technology Conference Paper OTC1 228, April 1970.
- 5.15 Gurney, T. R., Fatigue of Welded Structures, Second Edition, Cambridge University Press, 1979.
- 5.16 British Standards Institution, DD55 Draft for Development, Fixed Offshore Structures, 1978.
- 5.17 Parkhouse, J. G., "Computer-Aided Analysis of Tubular Connections," Paper 1X/P28, European Offshore Steels Research Seminar, Cambridge, November 1978, published by The Welding Institute, 1980.
- 5.18 Gibstein, M. B., "Parametric Stress Analysis of T Joints," Paper 1X/P26, European Offshore Steels Research Seminar, Cambridge, November 1978, published by The Welding Institute, 1980.
- 5.19 Fessler, H., et al., "Stresses in a Tubular K Joint Subjected to Out-of-Plane Bending," Paper 1X/P29, European Offshore Steels Research Seminar, Cambridge, November 1978, published by The Welding Institute, 1980.
- 5.20 Wordsworth, A. C., "Stress Concentration Factors at K and KT Tubular Joints," Paper 7, Fatigue in Offshore Structural Steel Conference, Institution of Civil Engineers, London, February 1981.
- 5.21 Clayton, A. M., and Irvine, N. M., "Stress Analysis Methods for Tubular Connections," Paper 1X/P30, European Offshore Steels Research Seminar, Cambridge, November 1978, published by The Welding Institute, 1980.
- 5.22 Kuang, J. G., et al., "Stress Concentrations in Tubular Joints," Offshore Technology Conference Paper 2205, Houston, Texas, 1975.
- 5.23 Wordsworth, A. C., and Smedley, G. P., "Stress Concentrations at Unstiffened Tubular Joints," Paper 1X/P31, European Offshore Steels Research Seminar, Cambridge, November 1978, published by The Welding Institute, 1980.
- 5.24 Irvine, N. M., "UKOSRP Management, Stress Analysis of Tubular Joints," Paper 6, Fatigue in Offshore Structures Conference, Institution of Civil Engineers, London, February 1981.
- 5.25 Booth, G. S., "Constant Amplitude Fatigue Tests on Welded Steel Joints Performed in Air," Paper III/P4-1, European Offshore Steels Research Seminar, Cambridge, November 1978, published by The Welding Institute, 1980.
- 5.26 McDonald, A., and Wylde, J. G., "Experimental Results of Fatigue Tests on Tubular Welded Joints," Paper 10, Fatigue in Offshore Structural Steel Conference, Institution of Civil Engineers, London, February 1981.
- 5.27 Gibstein, M. B., "Fatigue Failure of T-Joints," Norwegian Maritime Research, Vol. 7, No. 4, 1979.

- 5.28 Tomkins, B., "Fatigue Design Rules for Steel Welded Joints in Offshore Structures," Offshore Conference Technology Paper OTC 4403, May 1982.
- 5.29 Johnston, G. O., "Influence of Plate Thickness on Fatigue Strength," Welding Institute Report 3549/3/1978.
- 5.30 Gurney, T. R., and Johnston, G. O., ' A Revised Analysis of the Influence of Toe Defects on the Fatigue Strength of Transverse Non-Load-Carrying Fillet Welds," Welding Institute Report 62/1978/E.
- 5.31 Det norske Veritas, "Rules for the Design, Construction, and Inspection of Fixed Offshore Structures," 1974.
- 5.32 American Welding Society, "Structural Welding Code - Steel," AWS D1.1-1983.
- 5.33 Haagensen, P. J., et al., "Fatigue Performance in Air and Sea Water and Fracture Toughness of TIG-Dressed Steel Weldments," Paper III/P8, European Offshore Steels Research Seminar, Cambridge, November 1978, published by The Welding Institute, 1980.
- 5.34 Schofield, K. G., "Improving the Fatigue Strength of Fillet-Welded Joints by Disc Grinding the Weld Toe - Progress Report," Welding Institute Members Report, E60/75, 1975.
- 5.35 Knight, J. W., "Improving the Fatigue Strength of Fillet Welded Joints by Grinding and Peening," Welding Institute Members Report 8/1976/E.
- 5.36 van Leeuwen, J. L., de Back, J., and Vaesser, G.H.G., "Constant Amplitude Fatigue Tests on Welded Steel Joints Performed in Air and Seawater," International Conference - Steel in Marine Structures, Paris, October 1981.
- 5.37 Booth, G. S., "Constant Amplitude Fatigue Tests on Welded Steel Joints Performed in Sea Water," Paper IV/P9, European Offshore Steels Research Seminar, Cambridge, November 1978, published by The Welding Institute, 1980.
- 5.38 Todoroki, R., "Effects of Toe Profile Improvement on Corrosion Fatigue Properties of Welded Joint," International Institute of Welding Document XIII-875-78, July 1978.

TABLE 5.1. STRUCTURAL STEEL PLATES AND SHAPES, FROM [5.1]

GROUP	CLASS	SPECIFICATION & GRADE	YIELD STRENGTH		TENSILE STRENGTH	
			ksi	MPa	ksi	MPa
I	C	ASTM A36 (to 2" thick)	36	250	58-80	400-550
		ASTM A131 Grade A (to $\frac{3}{8}$ " thick)	34	235	58-71	400-490
		ASTM A235 Grade C (to $\frac{3}{4}$ " thick)	30	205	55-75	380-515
I	B	ASTM A131 Grades B, D	34	235	58-71	400-490
		ASTM A516 Grade 65	35	240	65-85	450-585
		ASTM A573 Grade 65	35	240	65-77	450-530
		ASTM A709 Grade 36T2	36	250	58-80	400-550
I	A	ASTM A131 Grades CS, E	34	235	58-71	400-490
II	C	ASTM A441 (strength varies w/thickness)	42-50	290-345	63-70 min.	435-485
		ASTM A572 Grade 42 (to 2" thick)	42	290	60 min.	415 min.
		ASTM A572 Grade 50 (to $\frac{3}{8}$ " thick*)	50	345	65 min.	450 min.
		ASTM A588 (to 2" thick)	50	345	70 min.	485 min.
II	B	ASTM A709 Grades 50T2, 50T3	50	345	65 min.	450 min.
		ASTM A131 Grade AH32	45.5	315	68-85	470-585
		ASTM A131 Grade AH36	51	350	71-90	490-620
II	A	API Spec 2H	42	290	62-80	430-550
		ASTM A131 Grades DH32, EH32	45.5	315	68-85	470-585
		Grades DH36, EH36	51	350	71-90	490-620
		ASTM A537 Class I (to $2\frac{1}{2}$ " thick)	50	345	70-90	485-620
		ASTM A633 Grades A, B	42	290	63-83	435-570
		Grades C, D	50	345	70-90	485-620
III	A	ASTM A678 Grade A	50	345	70-90	485-620
		ASTM A537 Class II	60	415	80-100	550-690
		ASTM A633 Grade E	60	415	80-100	550-690
		ASTM A678 Grade B	60	415	80-100	550-690

*To 2" Thick For Type 1. Killed, Fine Grain Practice.

TABLE 5.2. STRUCTURAL STEEL PIPE, FROM [5.1]

GROUP	CLASS	SPECIFICATION & GRADE	YIELD STRENGTH		TENSILE STRENGTH	
			ksi	MPa	ksi	MPa
I	C	API 5L Grade B	35	240	60 min.	415 min.
		ASTM A53 Grade B	35	240	60 min.	415 min.
		ASTM A135 Grade B	35	240	60 min.	415 min.
		ASTM A139 Grade B	35	240	60 min.	415 min.
		ASTM A381 Grade Y35	35	240	60 min.	415 min.
		ASTM A500 Grade A	33-39	230-270	45 min.	310 min.
		ASTM A501	36	250	58 min.	400 min.
I	B	ASTM A106 Grade B	35	240	60 min.	415 min.
I	A	ASTM A524 (strength varies w/thickness)	30-35	205-240	55-85	380-585
II	C	API 5LX Grade X42 2% max. cold expansion	42	290	60 min.	415 min.
		API 5LX Grade X52 2% max. cold expansion	52	360	66 min.	455 min.
		ASTM A500 Grade B	42-46	290-320	58 min.	400 min.
		ASTM A618	50	345	70 min.	485 min.
II	B	API 5LX Grade X52 with SR5, SR6 or SR8	52	360	66 min.	455 min.

TABLE 5.3. EUROPEAN STEELS USED IN CORROSION STUDIES

<u>Steel</u>	<u>Yield or Proof Strength (MPa)</u>	<u>K_IC or K_Q (MPa/m)</u>	<u>K_{ISCC}</u>
835M30	1350 (200 ksi)	75.0	14.3
X65	496 (70 ksi)	49.8	—
BS4360 50D	370 (55 ksi)	—	—

TABLE 5.4. RESULTS OF REGRESSION ANALYSIS ON TUBULAR JOINT
FATIGUE TESTS (FROM 5.26)

<u>Chord Diameter (mm)</u>	<u>Constants in Fatigue Equation</u>	
	<u>m</u>	<u>C</u>
168	2.56	1.27×10^{14}
457	3.50	3.98×10^{16}
914	2.69	1.07×10^{14}
1830	3.14	1.66×10^{15}

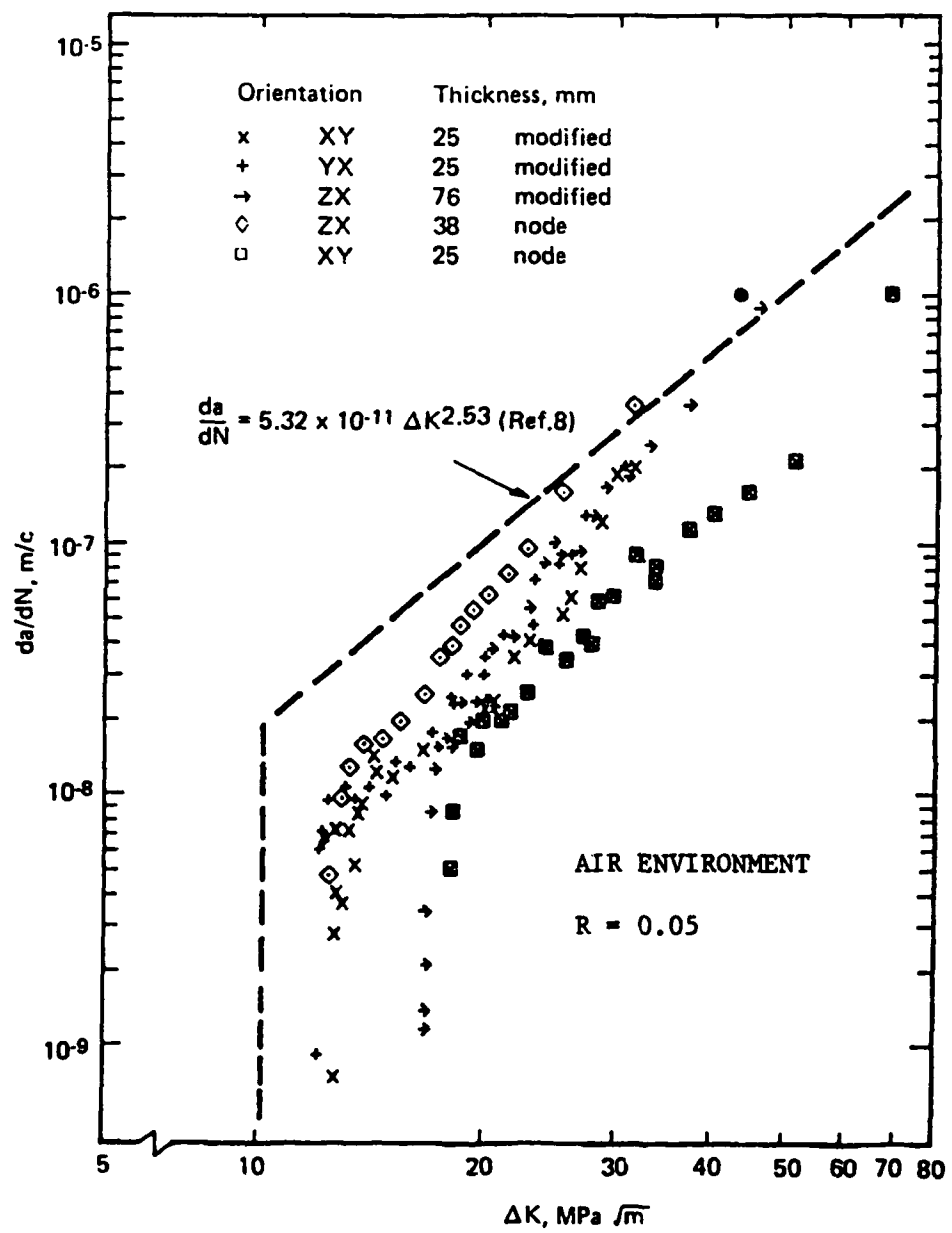


FIGURE 5.1. EFFECT OF THICKNESS, ORIENTATION, AND QUALITY ON FATIGUE CRACK GROWTH IN BC 4360, GRADE 50D, STEEL, FROM [5.3]

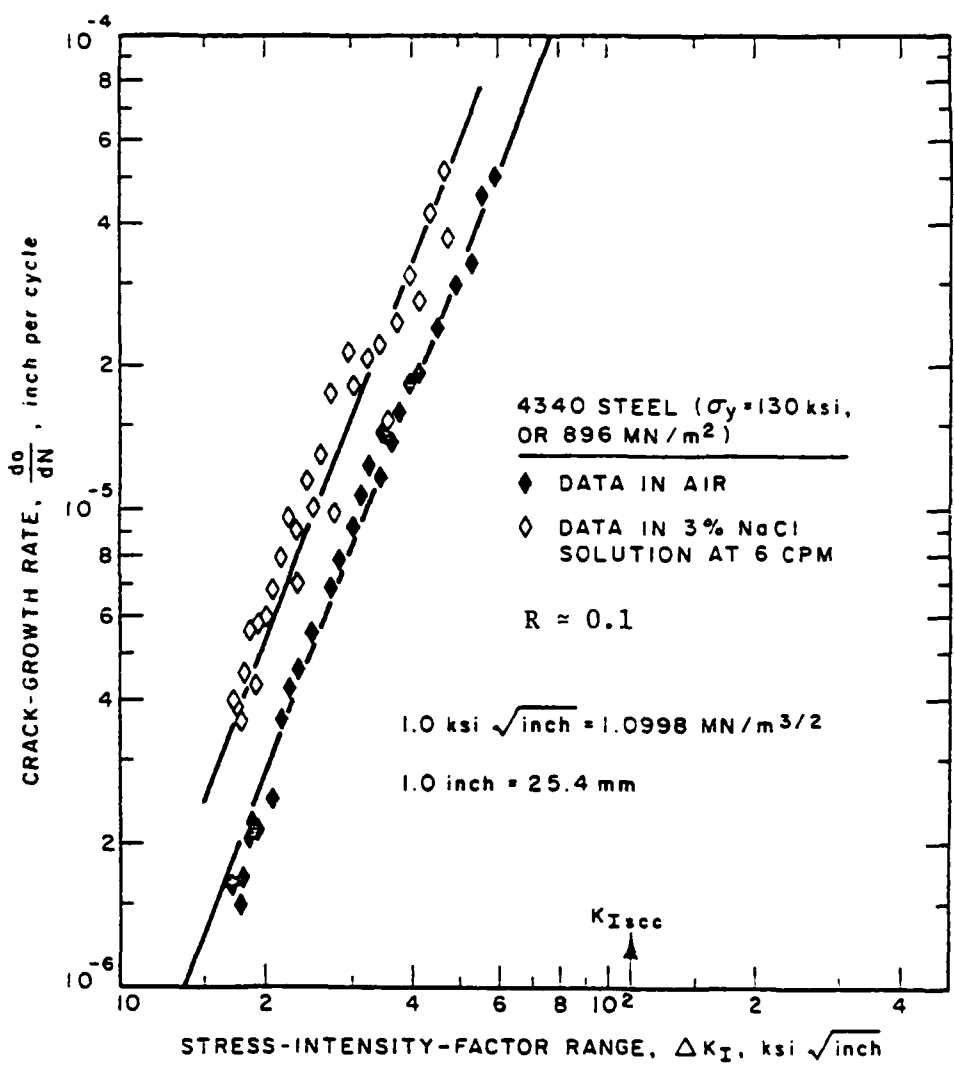


FIGURE 5.2. CORROSION-FATIGUE CRACK-GROWTH DATA,
 $\sigma_y = 130$ KSI, FROM [5.4]

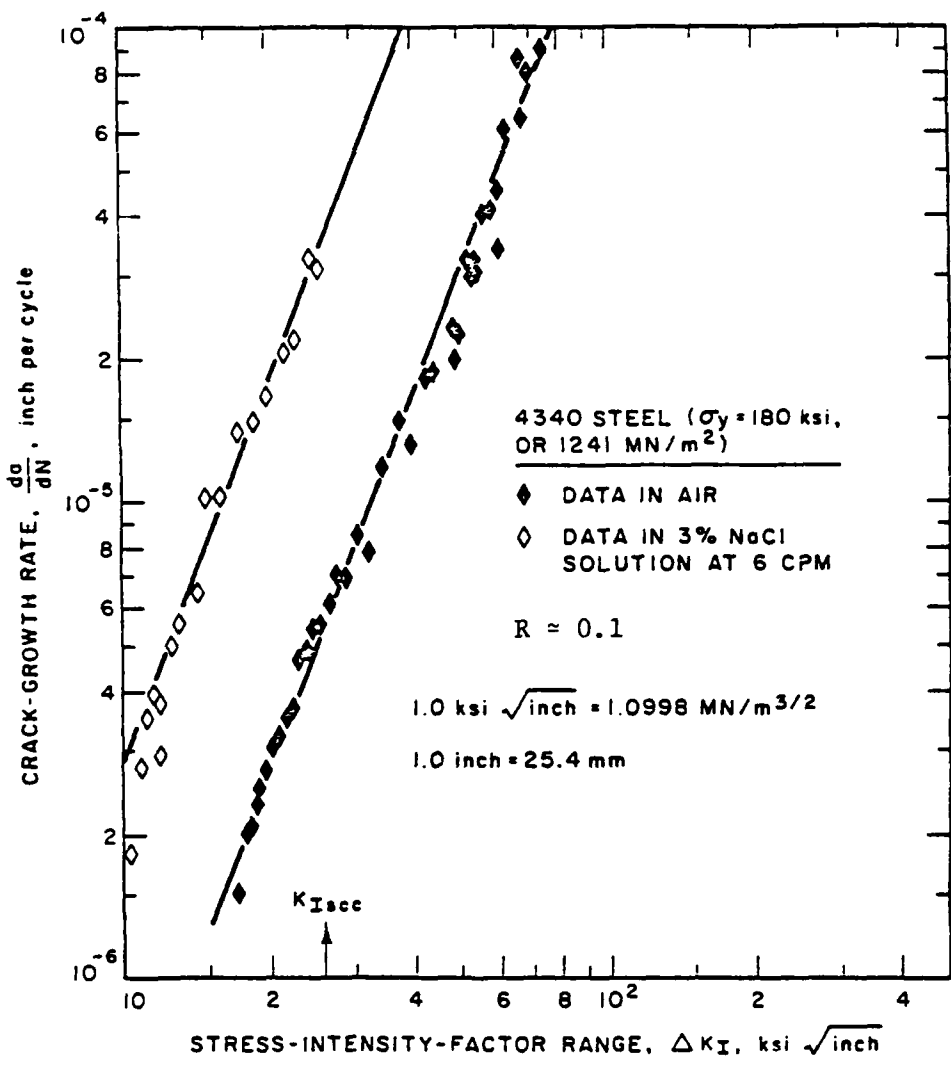
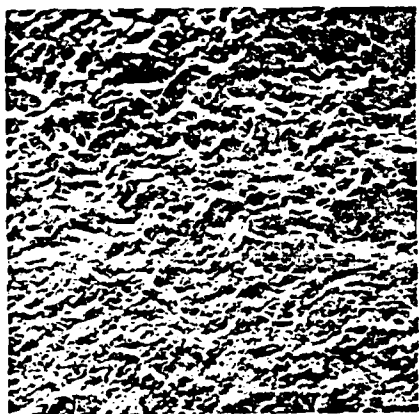
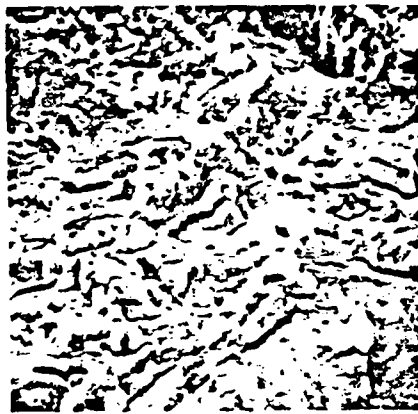


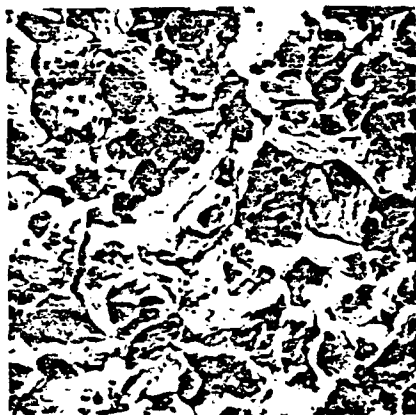
FIGURE 5.3. CORROSION-FATIGUE CRACK-GROWTH DATA,
 $\sigma_y = 180 \text{ KSI}$, FROM [5.4]



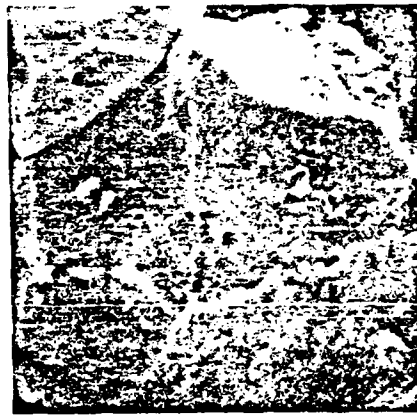
(a) corrosion fatigue initiation
from precrack ($\times 210$), 45° tilt



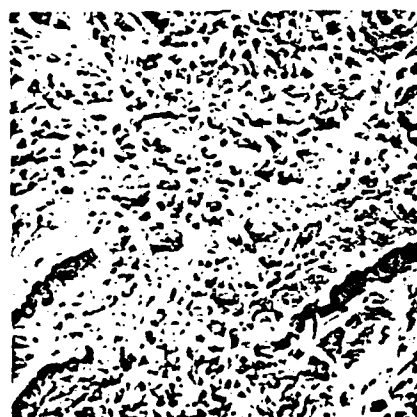
(b) fatigue striations
($\times 1100$), 20° tilt



(c) intergranular fracture
($\times 580$), 0° tilt



(d) intergranular facets
($\times 1700$), 45° tilt



(e) rapid fracture by
microvoid coalescence
(note inclusions) ($\times 485$), 0° tilt



(f) terminal fatigue
($\times 2050$) 0° tilt

FIGURE 5.4. FRACTOGRAPHIC FEATURES IN 835M30 STEEL, FROM [5.3]

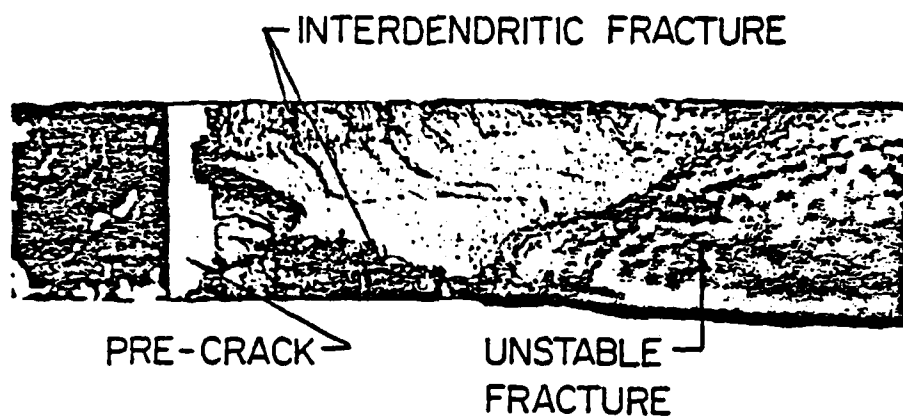


FIGURE 5.5. FRACTURE THROUGH THE HY130 WELDMENT OF THE
SPECIMEN TESTED AT $R = 0.9$, CATHODIC POTENTIAL AND 0.1 Hz,
IN 3.5% NaCl SOLUTION, FROM [5.5]

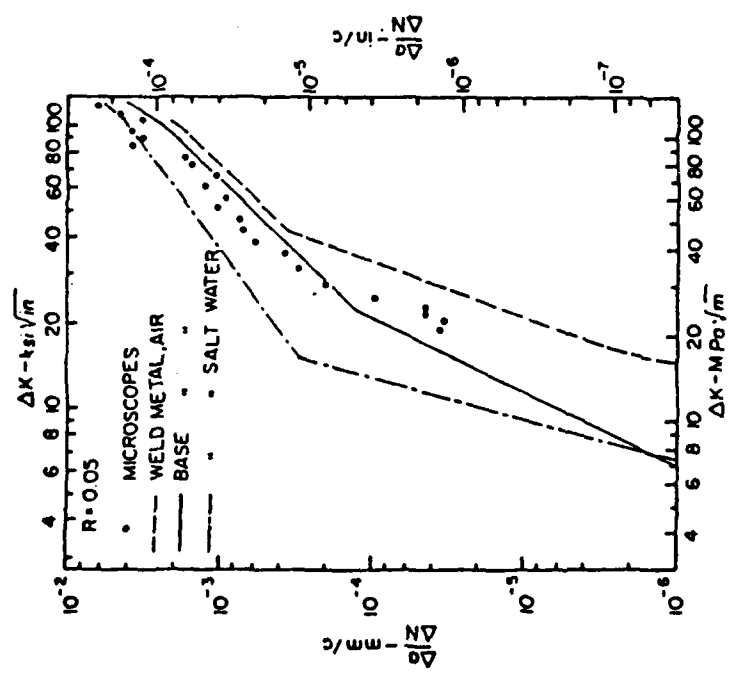


FIGURE 5.6. FATIGUE CRACK-GROWTH RATES AT
 $R = 0.05$ IN 3.5% NaCl SOLUTION AT CATHODIC
 POTENTIAL AND 0.1 Hz, WELD METAL (POINTS),
 BASE METAL (DASH AND DOT LINE), AND IN AIR,
 WELD METAL (DASHED LINE), BASE METAL
 (SOLID LINE), FROM [5.5]

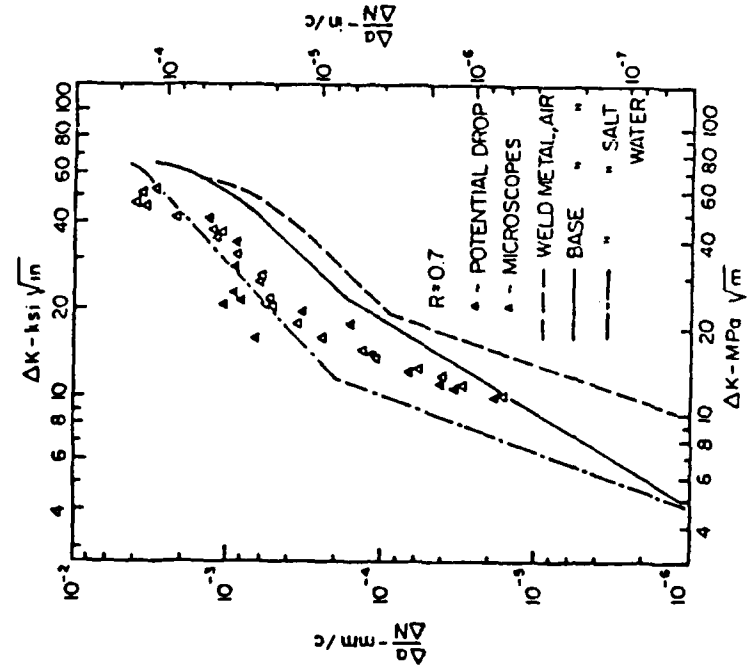


FIGURE 5.7. FATIGUE CRACK-GROWTH RATES AT
 $R = 0.7$ IN 3.5% NaCl SOLUTION AT CATHODIC
 POTENTIAL AND 0.1 Hz, WELD METAL (POINTS),
 BASE METAL (DASH AND DOT LINE), AND IN AIR,
 WELD METAL (DASHED LINE), BASE METAL
 (SOLID LINE), FROM [5.5]

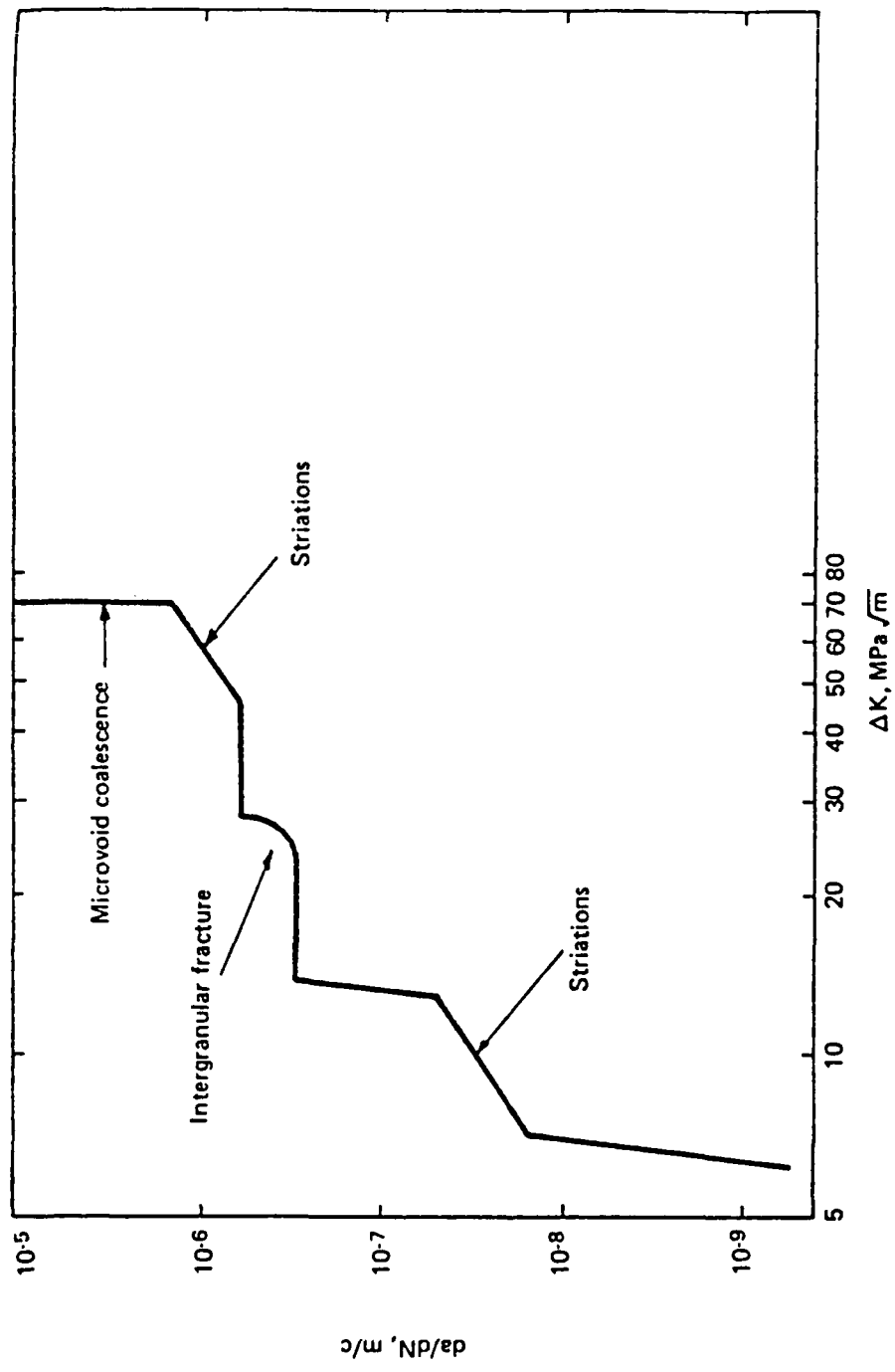


FIGURE 5.8. IDEALIZED CORROSION FATIGUE BEHAVIOR AND ASSOCIATED FRACTURE MODES, FROM [5.3]

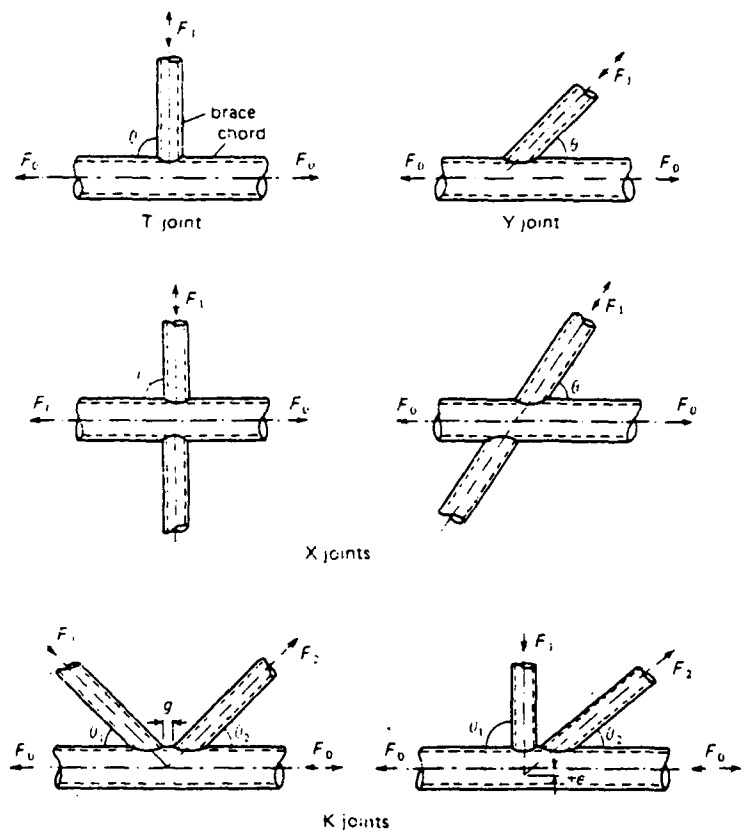


FIGURE 5.9. EXAMPLES OF SIMPLE TUBULAR NODE JOINT GEOMETRICS, FROM [5.15]

AD-A162 484

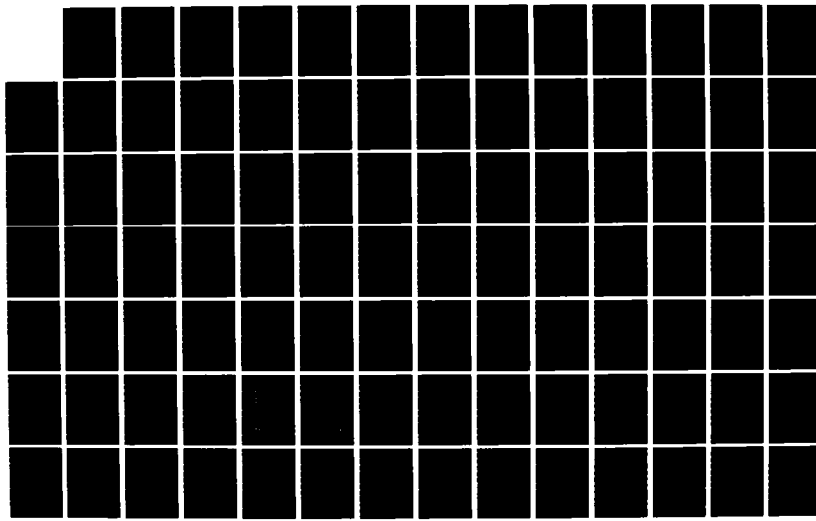
LONG-TERM CORROSION FATIGUE OF WELDED MARINE STEELS(U) 3/3
SOUTHWEST RESEARCH INST SAN ANTONIO TX
O H BURNSIDE ET AL. 1984 SR-1276 SSC-326

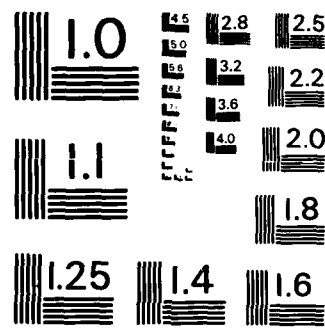
UNCLASSIFIED

DTCG23-80-C-20028

F/G 11/6

NL





MICROCOPY RESOLUTION TEST CHART
NATIONAL BUREAU OF STANDARDS - 1963 - A

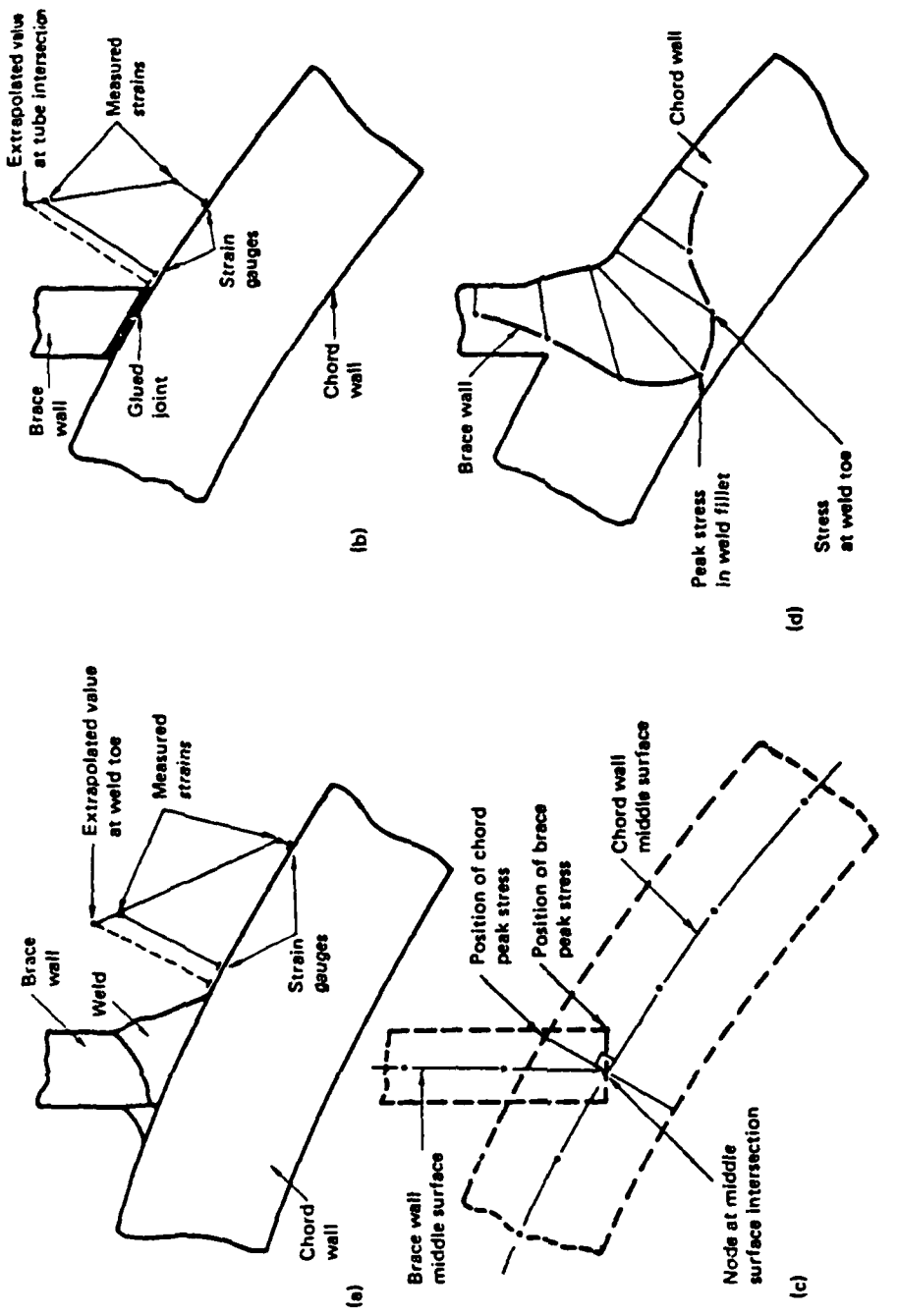
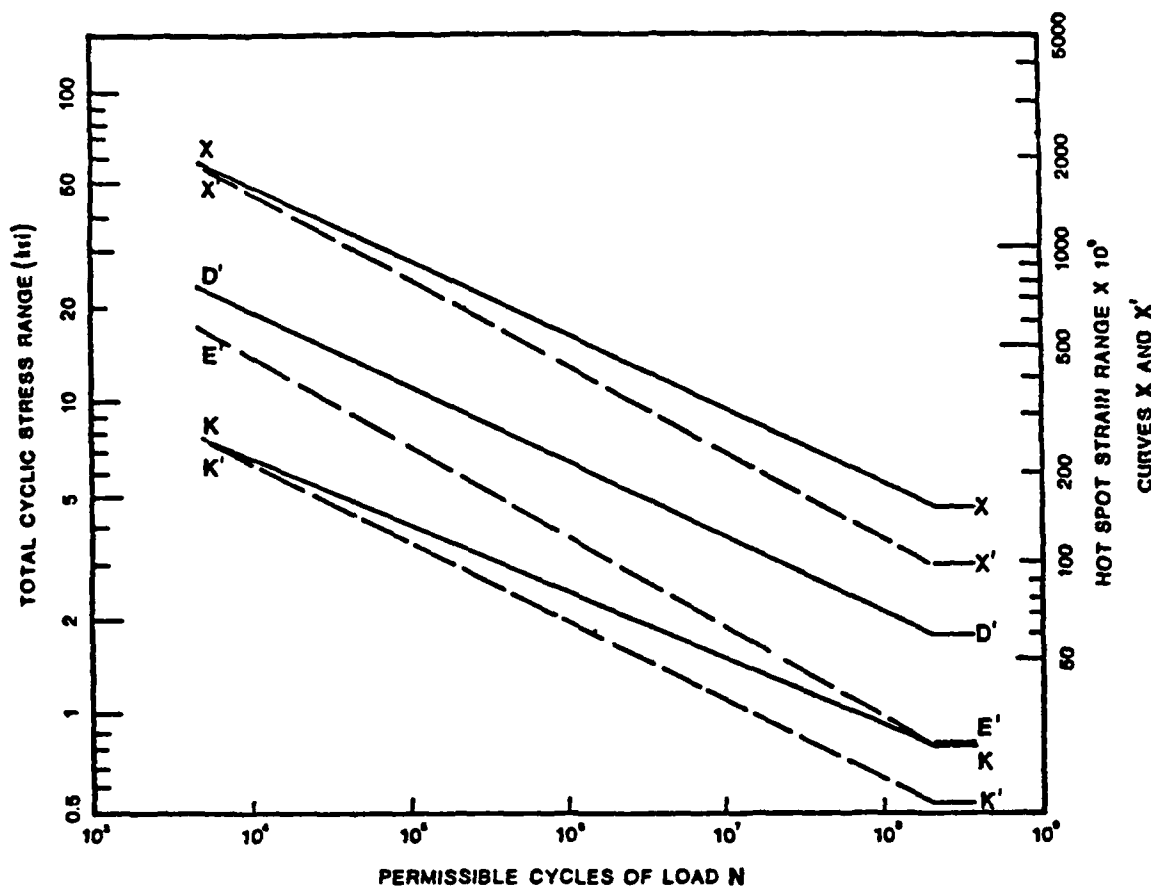


FIGURE 5.10. MODELS OF BRACE/CHORD INTERSECTION AND CORRESPONDING PEAK STRESSES:
 (a) STEEL MODEL, (b) ACRYLIC MODEL, (c) THIN SHELL FEM, AND
 (d) PHOTOELASTIC MODEL, FROM [5.21]



NOTE--These curves may be represented mathematically as

$$N = 2 \times 10^6 \left(\frac{\Delta \sigma}{\Delta \sigma_{ref}} \right)^{-m}$$

where N is the permissible number of cycles for applied cyclic stress range $\Delta \sigma$, with $\Delta \sigma_{ref}$ and m as listed below.

<u>CURVE</u>	<u>$\Delta \sigma_{ref}$</u> <u>STRESS RANGE AT 2 MILLION CYCLES</u>	<u>m</u> <u>INVERSE LOG-LOG SLOPE</u>
X	14.5 ksi (100 MPa)	4.38
X'	11.4 ksi (79 MPa)	3.74
D'	5.8 ksi (40 MPa)	4.38
E'	3.0 ksi (21 MPa)	3.48
K	2.15 ksi (15 MPa)	4.66
K'	1.7 ksi (12 MPa)	4.19

FIGURE 5.11. FATIGUE CURVES, FROM [5.1]

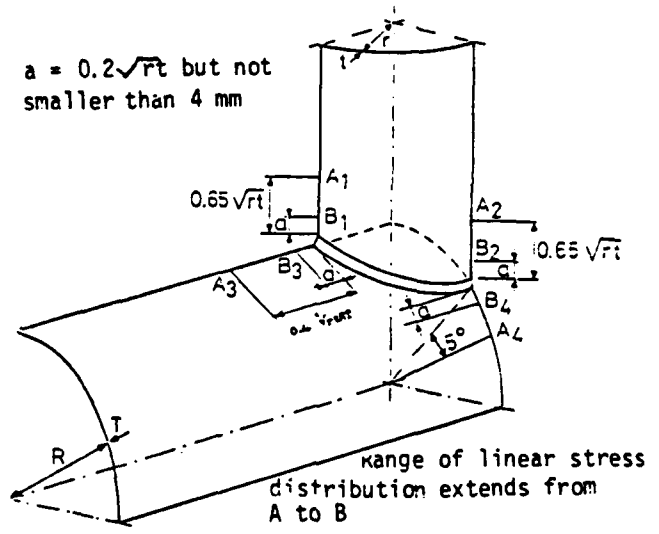


FIGURE 5.12. LOCATIONS OF STRAIN GAUGES
 FOR LINEAR EXTRAPOLATION TO WELD TOE
 TO DETERMINE STRAIN CONCENTRATION
 FACTOR, FROM [5.24]

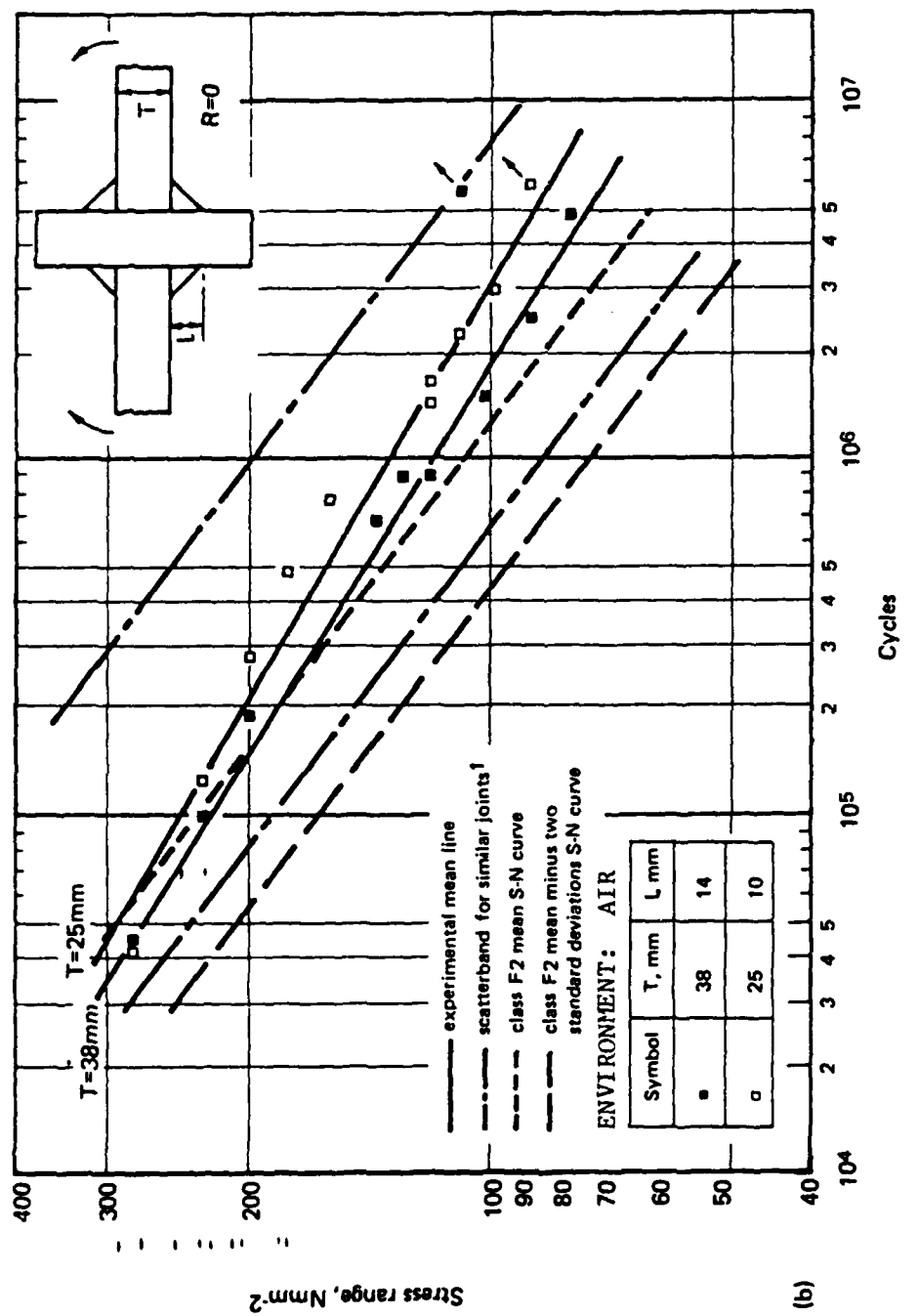


FIGURE 5.13. RESULTS FOR TRANSVERSE JOINTS SHOWING INFLUENCE OF PLATE THICKNESS, UNDER BENDING LOADING, AIR ENVIRONMENT, FROM [5.25]

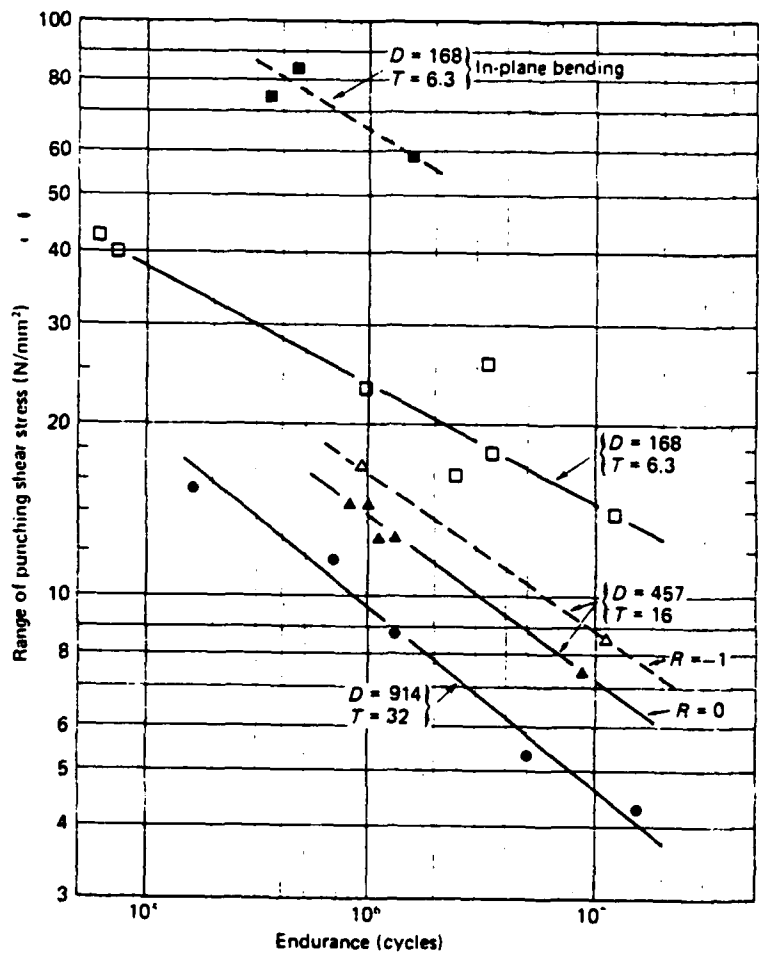


FIGURE 5.14. DUTCH TEST RESULTS FOR T-JOINTS WITH AXIAL LOADING OR IN-PLANE BENDING LOADS APPLIED TO THE BRACE, FROM [5.15]

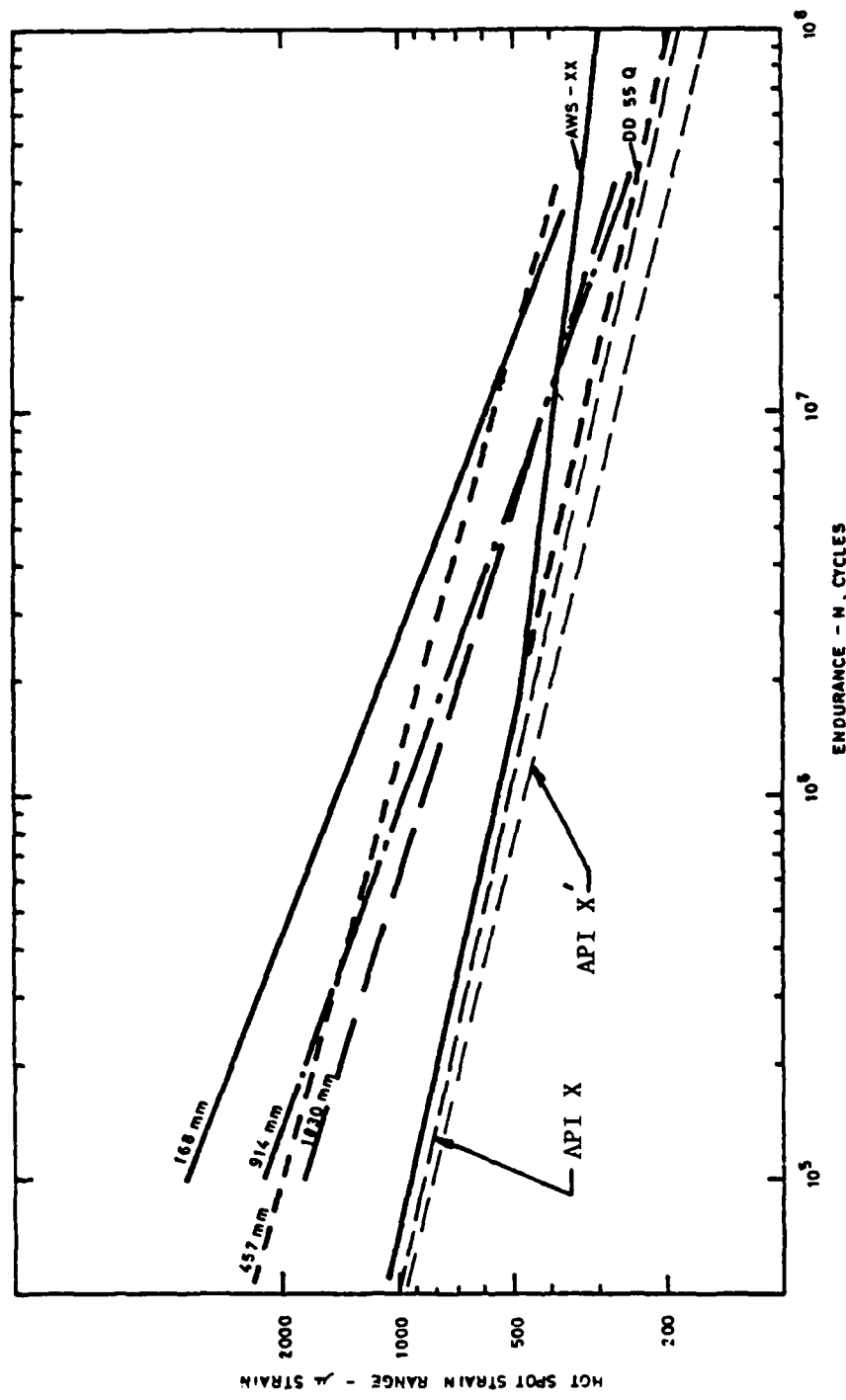


FIGURE 5.15. COMPARISON OF MEAN EXPERIMENTAL S-N CURVES, FROM [5.26]

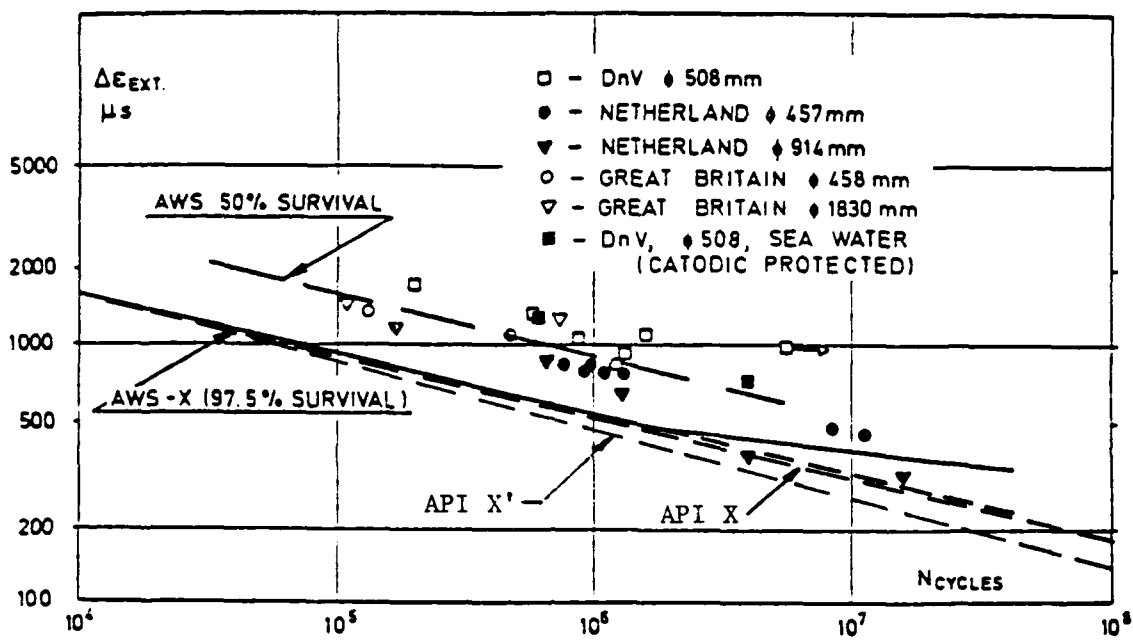


FIGURE 5.16. ECSC-PROGRAM TEST RESULTS VIS A VIS API AND AWS DESIGN S-N CURVES, FROM [5.27]

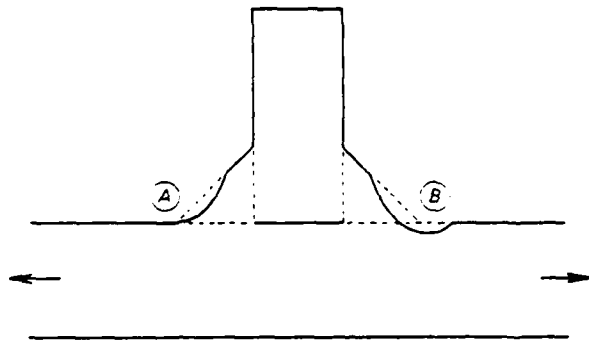
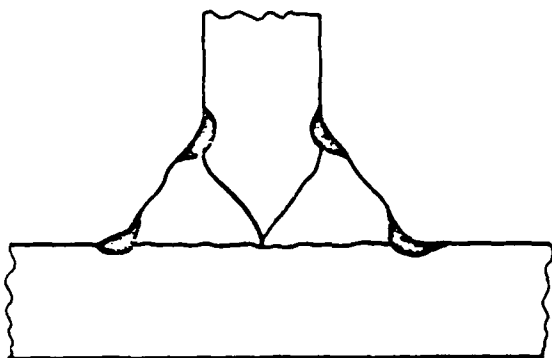
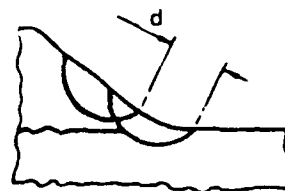


FIGURE 5.17. GRINDING OF WELD TOE, FROM [5.15]

(Grinding a weld toe tangentially to the plate surface, as at A, will produce little improvement in strength. Grinding must extend below the plate surface, as at B, in order to remove toe defects.)

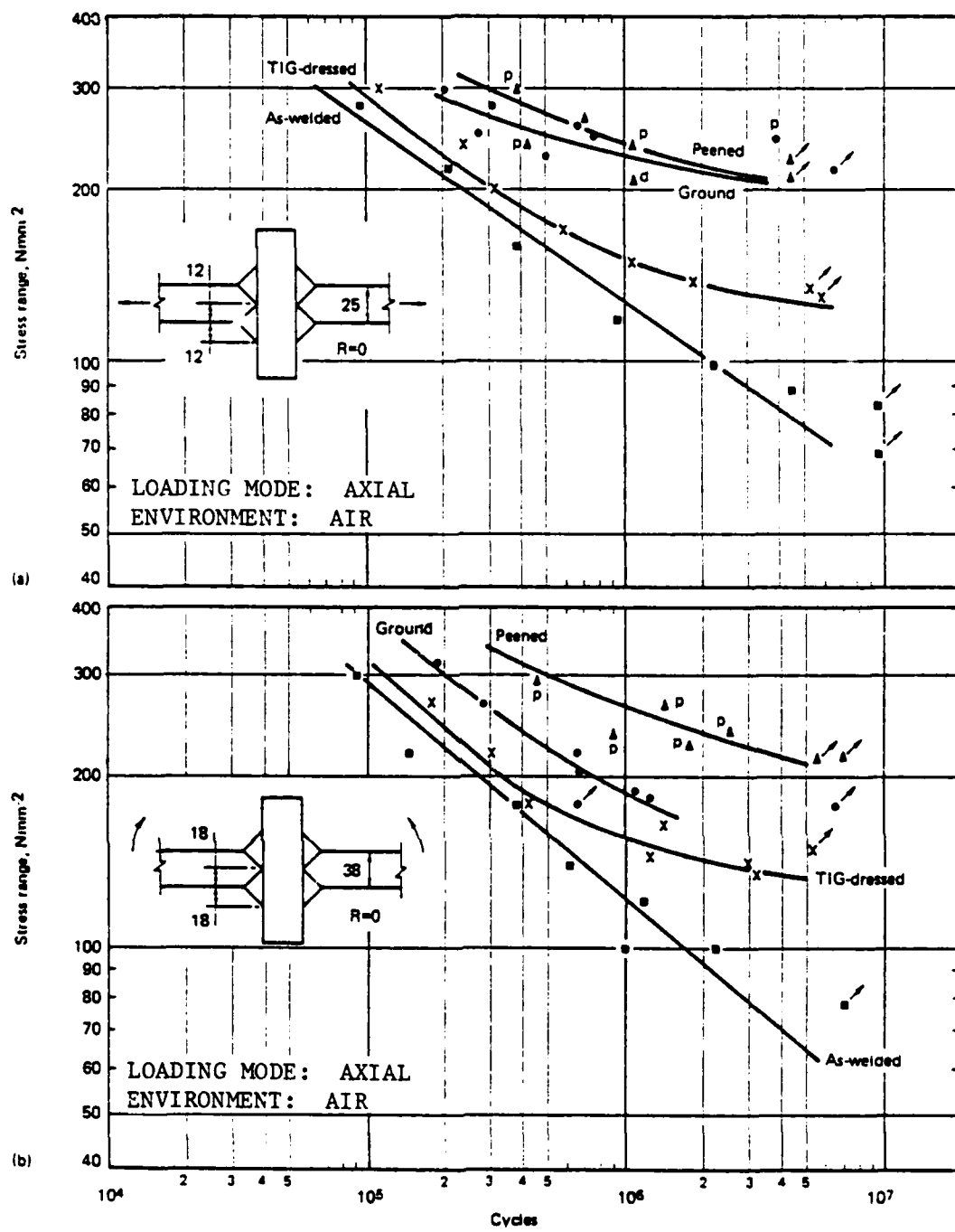


(a)



(b)

FIGURE 5.18. CROSS-SECTION OF WELD: (a) LOCATION OF TIG DRESSING,
 (b) MODIFIED TIG DRESSING; d = DISTANCE BETWEEN FIRST AND
 SECOND TIG RUNS, FROM [5.33]



■ - as-welded; ● - heavy disc ground; ▲ - four-pass hammer-peened;
 X - TIG-dressed; p - plate failure; d - premature failure caused by
 weld defect

FIGURE 5.19. RESULTS FOR TRANSVERSE JOINTS SHOWING INFLUENCE
 OF IMPROVEMENT TECHNIQUES UNDER: (a) AXIAL LOADING,
 (b) BENDING LOADING, FROM [5.25]

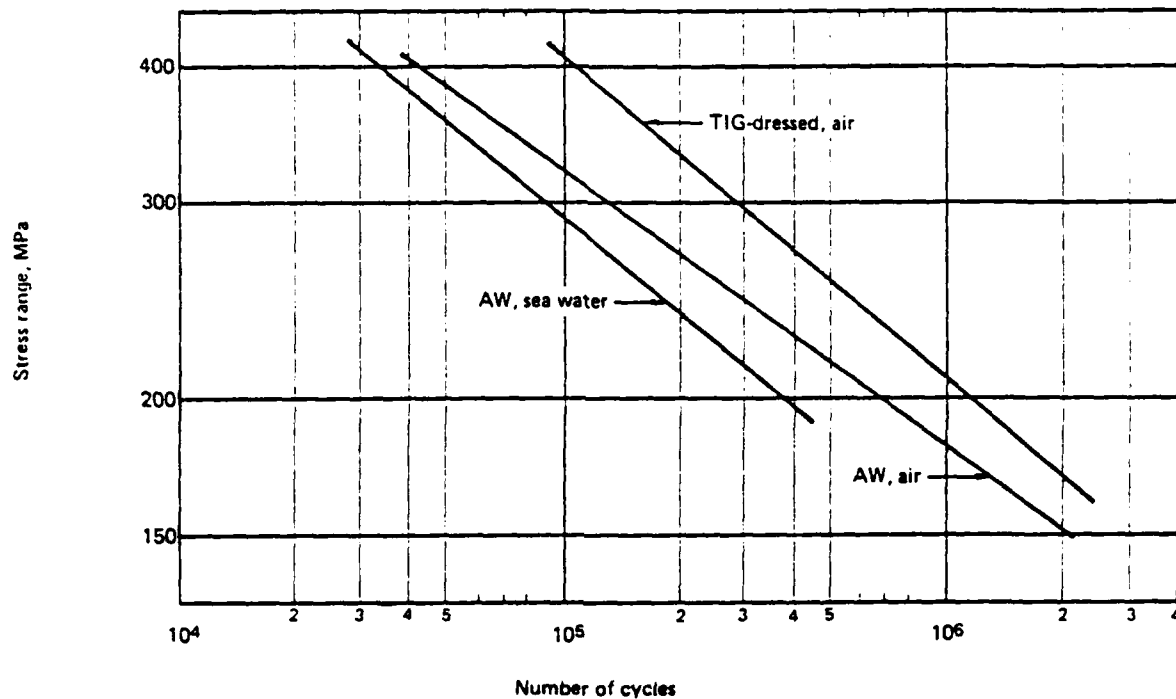


FIGURE 5.20. COMPARISON BETWEEN FATIGUE TEST RESULTS,
FROM [5.33]

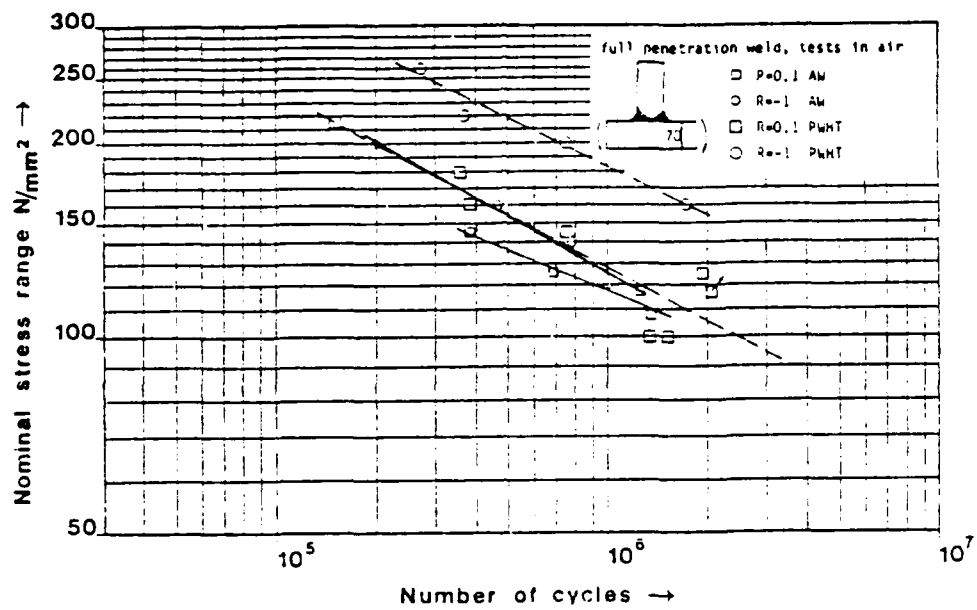


FIGURE 5.21. FATIGUE BEHAVIOR OF 70-mm T-SHAPED SPECIMENS (AS WELDED AND STRESS RELIEVED) IN AIR AT THE STRESS RATIOS $R = 0.1$ AND $R = -1$, FROM [5.36]

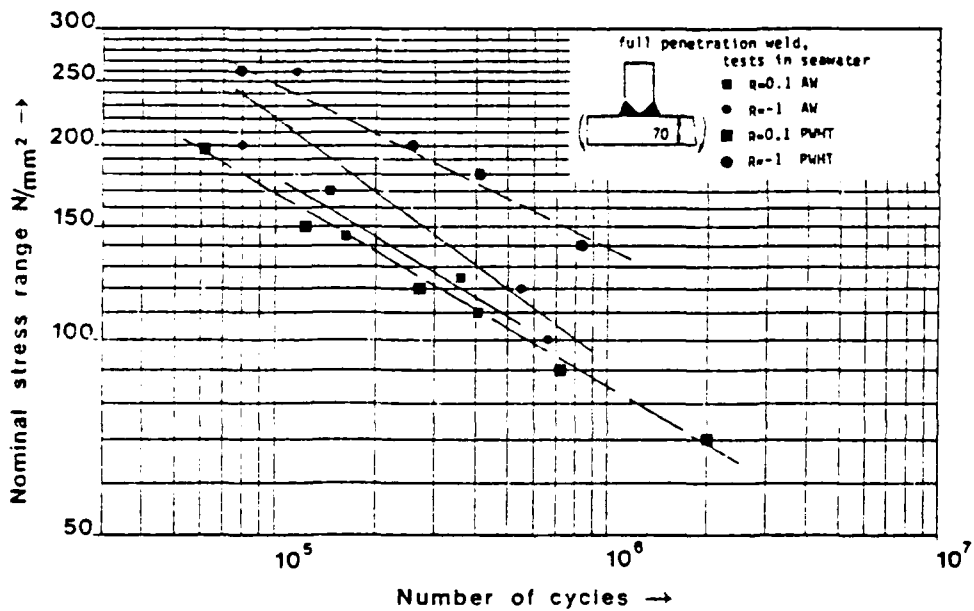


FIGURE 5.22. FATIGUE BEHAVIOR OF 70-mm T-SHAPED SPECIMENS (AS WELDED AND STRESS RELIEVED) IN SEAWATER AT THE STRESS RATIOS $R = 0.1$ AND $R = -1$, FROM [5.36]

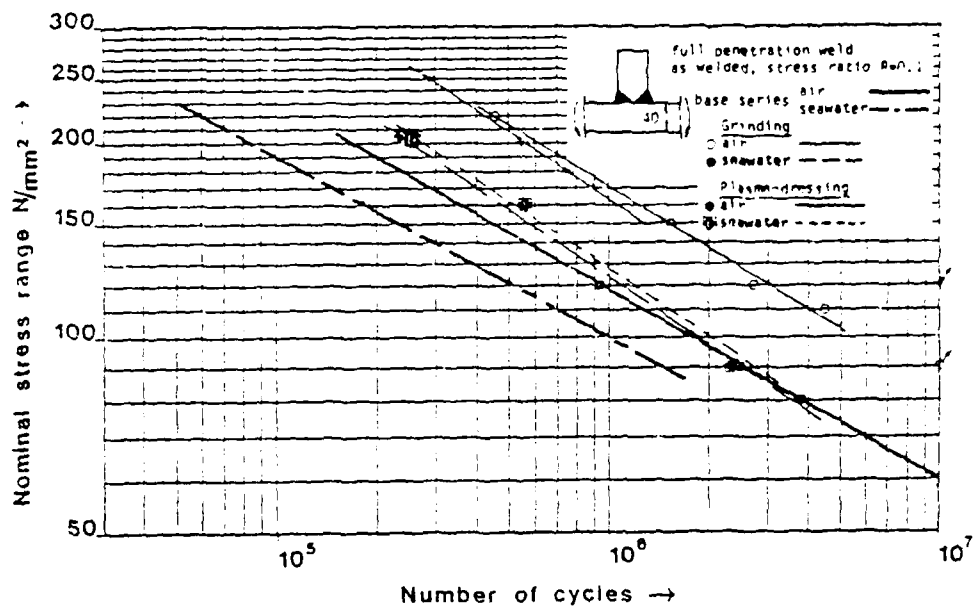


FIGURE 5.23. FATIGUE BEHAVIOR OF 40-mm T-SHAPED SPECIMENS
(GRINDING AND PLASMA DRESSING) IN AIR AND SEAWATER
AT THE STRESS RATIO $R = 0.1$, FROM [5.36]

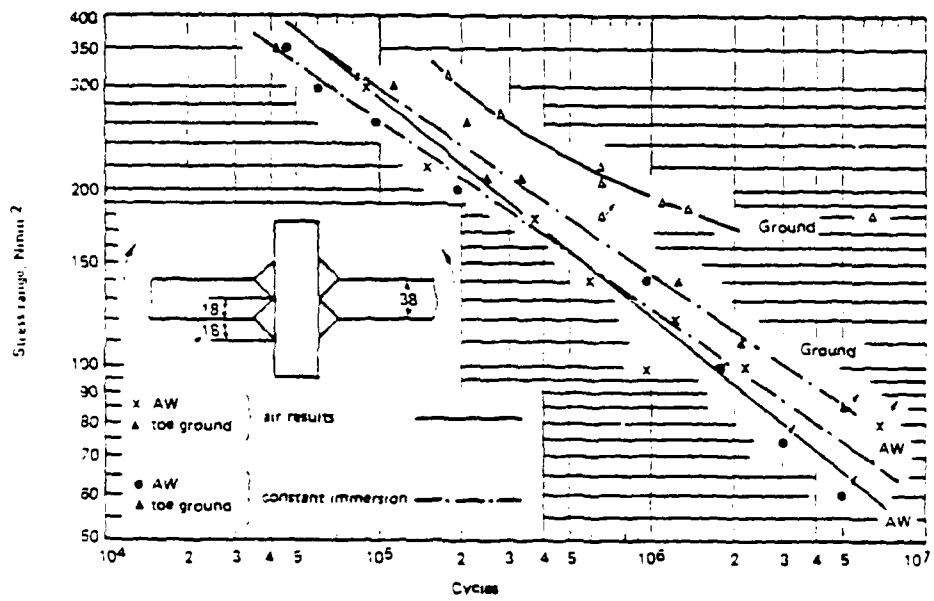
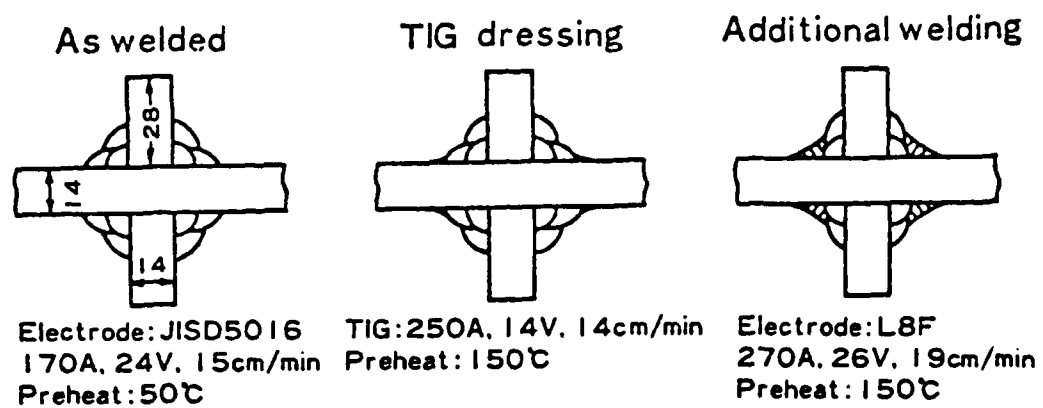
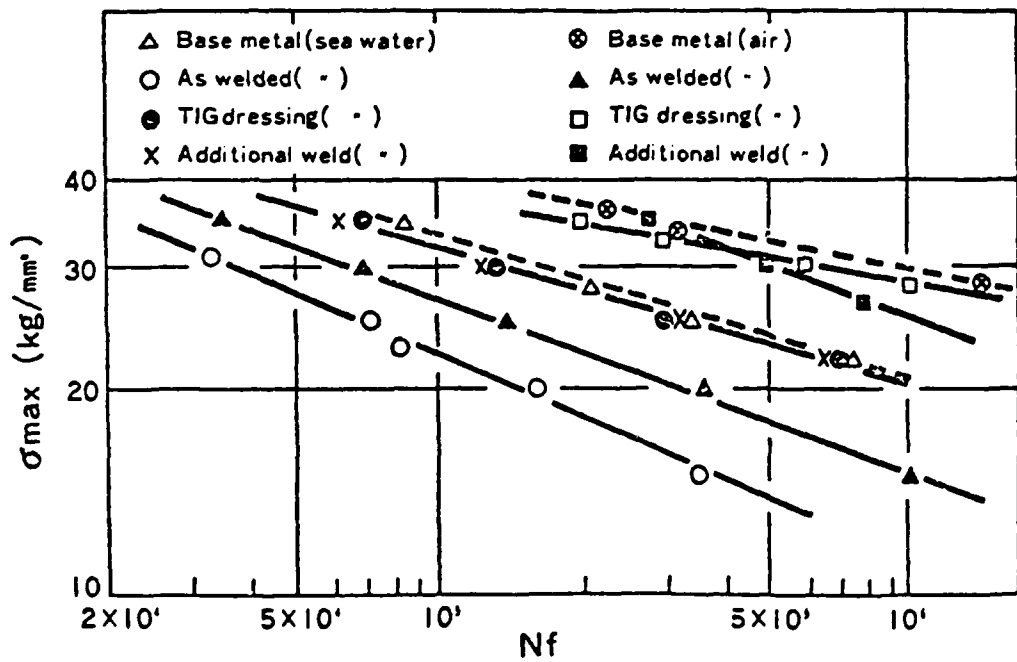


FIGURE 5.24. RESULTS FOR TRANSVERSE JOINTS, AW AND DISC GROUND,
STRESS RATIO = 0, FROM [5.37]



(a) Improvement Conditions of Toe Profile



(b) S-N Curves of Base Metal and Fillet-Welded Specimens in Air and in Sea Water (30°C)

FIGURE 5.25. RESULTS OF JAPANESE TESTS IN AIR AND SEAWATER, FROM [5.38]

6.0 PREDICTION METHODOLOGIES FOR FATIGUE

6.1 Introduction

Several distinctly different approaches have evolved for designing against fatigue failures; these can be categorized as follows: (1) classical S-N approach, (2) local-stress strain approach, (3) fracture mechanics approach to crack initiation, and (4) fracture mechanics approach to crack growth. The first two approaches are directed at crack initiation, although neither approach obtains explicit information on initiation of a crack of specific size; rather, data are acquired in terms of complete specimen failure. The third approach is also directed at crack initiation; however, information is obtained in terms of the number of cycles required to initiate a crack of a given size, typically 0.25 mm (0.01 inch). The fourth approach deals exclusively with the propagation of preexisting cracks. In addition, combinations of crack initiation and crack propagation analyses have recently been employed to predict the total fatigue life of structures. Important features of all of these approaches are briefly summarized below, and advantages and disadvantages of each are noted.

This information, when combined with the phenomenological observations on corrosion fatigue presented in other sections of this report, will provide the background upon which an evaluation of the most relevant corrosion fatigue design philosophy for offshore structures can be made. The primary objective of this effort would be to explore how classical design procedures can be combined with newly evolving technologies, such as fracture mechanics. The former will likely continue as the primary design tool, while the latter might provide a new tool for evaluating existing nondestructive evaluation requirements, assessing structural reliability once cracks are detected in service, and determining the feasibility of extending the lives of existing structures beyond their original design lives.

6.2 Classical S-N Approach

The philosophy of this approach is relatively simple and has changed little since it was first used by Wöhler in his pioneering studies of metal fatigue in 1860 [6.1]. The materials' fatigue properties are characterized in terms of the applied nominal stress, S , and the resulting cycles to failure, N_f . Most often testing is conducted under completely reversed bending or tension

so that S corresponds to the nominal stress amplitude at zero mean stress. As depicted in Figure 6.1, the principal characteristics of the S-N curve are: (1) increased cycles to failure as the applied stress amplitude is decreased; and (2) the presence or absence of a fatigue limit as the applied stress amplitude is decreased. The S-N curve is sensitive to many variables which have been reviewed in numerous books on fatigue. Variables include bending versus tension loading, specimen size and geometry, notch acuity, temperature, chemical environment, and localized residual stress. Factors giving rise to size and geometry dependencies appear to result from not distinguishing between crack initiation and crack growth and not recognizing the existence of nonpropagating cracks in notched specimens [6.2].

All of these variables are incorporated into the fatigue analysis using empirically based correction factors. For example, mean stress is generally treated by developing expressions such as those depicted in Figures 6.2 and 6.3. Here the stress amplitude, σ_a , and mean stress, σ_0 , are combined to give an equivalent, completely reversed stress amplitude, σ_r , such as the conventional Goodman diagram.

The analysis used to relate the S-N fatigue properties to structural behavior is idealized in the sense that local plasticity is not considered. The local stress in regions of stress concentration in the component is assumed to be $K_t S$, where K_t is the elastic stress concentration factor. Thus, design against fatigue merely involves manipulating K_t and S so that their product is less than either the fatigue limit or a desired fatigue life.

The advantages and disadvantages of the classical S-N approach are given in Table 6.1. As noted, the major limitation of this approach is the fact that plasticity effects are not considered. Thus, for complex geometries the local stress and strain conditions are unknown at geometrical stress concentrations where fatigue crack initiation will inevitably occur, such as at the toe of a welded joint. Under this condition, the utility of the S-N approach for effectively treating high stress amplitude, low-cycle fatigue is greatly limited, particularly for variable amplitude loading. Of course, this limitation does not apply to high-cycle fatigue where plasticity is greatly reduced.

6.3 Fracture Mechanics Approach to Crack Initiation

This approach is based on the fact that the maximum elastic stress, σ_{\max} , in a notched member can be derived from the linear elastic stress intensity factor, K_I , using the following relationship:

$$\sigma_{\max} = \frac{2 K_I}{\sqrt{\pi r}} = K_t S \quad (6.1)$$

where

r = the notch root radius

K_t = the elastic stress concentration factor

S = nominal stress

Equation (6.1) is exact in the limit as r approaches zero; thus, it is most accurate for sharp notches where conventional elastic analyses to determine K_t are most uncertain. Thus, fracture mechanics principles merely provide a convenient means to obtain $K_t S$ for notched members.

Experimental data (Figure 6.4) utilizing this approach to characterize fatigue crack initiation are very similar to those obtained in S-N testing, except here notched specimens are employed. As indicated in Equation (6.1), K_I/\sqrt{r} is proportional to $K_t S$, and results are usually expressed as K_I/\sqrt{r} , as shown in Figure 6.5 [6.4]. The application of this information to the prediction of crack initiation in the structure is also analogous to that employed in the S-N approach.

The advantages and disadvantages of the fracture mechanics approach to crack initiation are given in Table 6.1. Both advantages and disadvantages are similar to those of the S-N approach. However, as indicated in Table 6.1, the fracture mechanics approach has the advantage that crack initiation is measured rather than complete specimen failure.

6.4 Local Strain Approach to Crack Initiation

This approach recognizes the fact that fatigue is a localized process and, therefore, focuses on the regions of stress concentration in the structure where crack initiation is most likely to occur. Since these regions will generally experience local plastic deformation, plasticity effects are explicitly treated.

The essential ingredients of the local stress-strain approach are illustrated in the flow chart of Figure 6.6. Input information consists of load and environment histories of the structural component as well as the materials' fatigue properties. As indicated, the information on the component's history provides guidelines for the selection and/or generation of representative fatigue properties. The mechanics analysis subsequently uses all of this information to relate the nominal loadings to the actual stress amplitudes, strain amplitudes, and mean stresses in the critical region of stress concentration. This detailed information is used to assess fatigue damage by using rules for cycle counting and damage accumulation. Each of these components of the analysis is briefly described below.

The relevant materials' fatigue properties consist of the cyclic stress-strain relation and the strain-life relation, both of which are empirically determined. Figures 6.7 and 6.8 provide typical examples of such data. Results are mathematically expressed in the following functional form.

Cyclic Stress-Strain Relation

$$\frac{\Delta \epsilon}{2} = \frac{\Delta \sigma}{2E} + \left(\frac{\Delta \sigma}{2K'} \right)^{1/n'} \quad (6.2)$$

Cyclic Strain-Life Relation

$$\frac{\Delta \epsilon}{2} = \frac{\sigma'_f}{E} (2N_i)^b + \epsilon'_f (2N_i)^c \quad (6.3)$$

where

$\Delta \epsilon$ = notch strain range

$\Delta \sigma$ = notch stress range

E = elastic modulus

σ'_f = fatigue strength coefficient

ϵ'_f = fatigue ductility coefficient

b = fatigue strength exponent

c = fatigue ductility exponent

n' = monotonic strain hardening coefficient

K' = cyclic strength coefficient

N_i = cycles for crack initiation

The specific values of σ'_f , ϵ'_f , b, c, n' and K' are determined from regression analyses of the type of data represented in Figures 6.7 and 6.8.

A mechanics analysis is used to establish a relationship between the far-field stress (ΔS), the far-field strain (Δe), the notch stress ($\Delta \sigma$), and the notch strain ($\Delta \epsilon$) ranges as illustrated in Figures 6.9 and 6.10. These relations can either be determined from elastic-plastic finite element analysis or from simpler engineering approximations such as Neuber's rule [6.8, 6.9]. Neuber postulated that for a material which deforms nonlinearly, the theoretical stress concentration factor, K_t , is equal to the geometric mean of the actual stress K_σ , and strain concentration, K_ϵ , factors. That is,

$$K_t = (K_\sigma K_\epsilon)^{1/2} \quad (6.4)$$

where

K_t = theoretical stress concentration factor, a constant for a given geometry and loading

K_σ = stress concentration factor, σ divided by S , not a constant when yielding occurs

K_ϵ = strain concentration factor, ϵ divided by e , not a constant when yielding occurs

Section 6.5 will discuss a modified Neuber rule to include the notch effect at the toe of a weld and develop a numerical procedure to apply the local stress-strain approach to crack initiation in a welded joint.

For complex load histories, procedures must be established for counting fatigue cycles. Dowling has shown that the so-called "rain flow" method, which counts cycles as closed stress-strain hysteresis loops, is most effective for a wide range of variable amplitude histories [6.3]. The other aspect of damage assessment, namely damage accumulation, is adequately treated using linear damage laws such as the Palmgren-Miner rule [6.10-6.11]. Although such linear damage laws cannot account for load interactions, these effects can be accounted for when generating the cyclic strain-life information [6.5].

The advantages and disadvantages of the local stress-strain approach are given in Table 6.1. As indicated, the major disadvantage of the approach is its relatively complexity--as compared to the S-N approach, for example. However, the need for detailed input information and analytical complexity

accounts for the general utility of the approach as reflected in the advantages listed in Table 6.1. For example, the importance of realistically dealing with plasticity effects is demonstrated by the data in Figure 6.11. Here, two slightly different loading sequences are shown to result in significantly different fatigue lives. This difference is due to the effect of plasticity on determining the local mean stress, which for history A is tensile and for history B is compressive. An S-N approach would predict identical fatigue lives and could not account for such effects. The local stress-strain approach can predict such effects since it realistically deals with plasticity.

The disadvantage of relative complexity of the local stress-strain approach can be overcome by developing computer algorithms to perform the analysis. One such computer code was developed as part of this study, and a set of results is presented and discussed in Chapter 7.0.

6.5 Application of Local Strain Approach to Welded Joints

6.5.1 Introduction

This discussion extends the local strain approach outlined in Section 6.4 to prediction of crack initiation in welded joints. The procedure is based upon earlier pioneering work in fatigue of notched members by Neuber [6.8] and Peterson [6.12] and later investigations by Fuchs [6.7] and Lawrence [6.13, 6.14]. The initiation life of the welded joint, which is assumed to contain a small notch, is related to the life of small unnotched specimens cycled to the same strains as the material at the weld notch root. The initiation period is the time required for a small, but detectable, fatigue crack to develop. At the present time it is difficult to quantitatively define the size of a crack to the end of the initiation and beginning of the propagation periods, but such cracks are on the order of 0.1 - 0.5 mm.

6.5.2 Stress Concentrations at Crack Initiation Sites

The first step in the calculation process is to identify likely crack initiation locations. For welds typically found in offshore structures, cracks usually initiate at the weld toe. Lawrence [6.13, 6.14] has conducted finite element analyses on weld geometries shown in Figure 6.12 and has computed stress concentration factors K_t in the form

$$K_t = 1 + a \left(\frac{t}{r}\right)^{1/2} \quad (6.5)$$

where

a = a factor depending on the weld geometry and mode of loading

r = radius at weld toe

t = plate thickness

Figure 6.13 plots Equation (6.5) for tension loading, and Table 6.2 presents results for both tension and bending for the five weld geometries.

The functional form of Equation (6.5) follows that of an elliptical hole in an infinite plate with the load applied normal to the major axis [6.15], i.e.,

$$K_t = 1 + 2 \left(\frac{a_0}{r}\right)^{1/2} \quad (6.6)$$

where

$2a_0$ = major diameter of ellipse

r = radius at major axis

The calculation method will also require calculation of the so-called fatigue stress concentration factor, K_f , where

$$K_f = \frac{S_n \text{ for unnotched specimens}}{S_n \text{ for notched specimens}} \quad (6.7)$$

S_n is the fatigue endurance limit or the endurance strength at a large number of cycles such as 5×10^8 . K_f is related to K_t by

$$q = \frac{K_f - 1}{K_t - 1} \quad (6.8)$$

or

$$K_f = 1 + q (K_t - 1) \quad (6.9)$$

where q is a measure of the notch sensitivity and ranges between 0 and 1. A material which is completely notch sensitive ($q = 1$) experiences the full effect of the notch and thus $K_f = K_t$. A completely non-notch-sensitive material ($q = 0$) feels no effect of the stress concentration and $K_f = 1$. Figure 6.14 shows how the average notch sensitivity varies as a function of notch radius. Peterson [6.12] has proposed the following simple formula for q which is widely used

$$q = \frac{1}{1 + \frac{a_m}{r}} \quad (6.10)$$

where

a_m = material parameter
 r = notch radius

K_f may now be expressed as

$$K_f = 1 + \frac{\frac{K_t - 1}{a_m}}{1 + \frac{a_m}{r}} \quad (6.11)$$

Numerous tests have found that the material constant a_m , which has dimensions of length, can be related to the ultimate tensile strength, S_u . Peterson [6.16], based upon experimental tests, has suggested the following approximate relationship between a_m and S_u .

$$\begin{aligned} a_m &\approx 2.5 \times 10^{-5} \left(\frac{2068}{S_u} \right)^{1.8} && \text{(SI Units)} \\ &\approx 9.8 \times 10^{-4} \left(\frac{300}{S_u} \right)^{1.8} && \text{(ksi, English units)} \end{aligned} \quad (6.12)$$

Combining Equations (6.5) and (6.11) gives

$$K_f = 1 + \frac{\frac{a}{r} \left(\frac{t}{r} \right)^{1/2}}{1 + \frac{a_m}{r}} \quad (6.13)$$

By differentiating Equation (6.13) with respect to r and solving for the maximum value of K_f , Lawrence [6.13, 6.14] demonstrated that $K_{f\max}$ occurs when $r_{crit} = a_m$ in Equation (6.13). Therefore

$$K_{f\max} = 1 + \frac{a}{2} \left(\frac{t}{a_m} \right)^{1/2} \quad (\text{at } r = a_m) \quad (6.14)$$

Equation (6.14) shows that the maximum fatigue stress concentration factor is a function of weld type and mode of loading (a), size of weldment (t), and ultimate tensile strength of the material through the parameter a_m . The value of K_f , Equation (6.11), depends both on the weld configuration (macro-geometry) and the notch root radius (micro-geometry). However, the value of $K_{f\max}$, Equation (6.14), depends on the macro-geometry only. Lawrence [6.13] argues that since almost any notch radius can exist at the weld toe, it is realistic to take $K_f = K_{f\max}$. This gives the most conservative estimate of the crack initiation life N_i .

Figure 6.15 plots K_t and K_f for a butt weld for 572MPa (83 ksi) and 966MPa (140 ksi) ultimate strength materials. For an ASTM A 36 steel, which is commonly used in offshore structures, Tables 6.3 and 6.4 give mechanical and cyclic fatigue properties of base (BM), weld (WM), and heat-affected materials (HAZ). The critical radii for these materials calculated from Equation (6.12) are

<u>A 36 Material</u>	<u>$r_{crit} = a_m$</u>
Base	0.45 mm (0.018 in.)
HAZ	0.19 mm (0.008 in.)
Weld Metal E605-WM(1 Pass)	0.17 mm (0.007 in.)
Weld Metal E605-WM(2 Pass)	0.26 mm (0.01 in.)

6.5.3 Strain-Life to Crack Initiation

Section 6.4 presented the cyclic stress-strain and strain-life relationships used in the local strain approach to crack initiation. This and the following sections will discuss further those relationships and how they are used in calculation procedures for welded joints.

Figure 6.8 schematically shows the fatigue life of small, polished specimens plotted in terms of total strain amplitude. Tests are usually

conducted between about 10 and 10^6 cycles. These strain-controlled curves are often designated low-cycle data because much of the testing is for less than about 10^5 cycles. Above about 10^6 cycles, the strain is predominately elastic, and load or stress controlled tests can be conducted. As an example, data for annealed 4340 steel are presented in Figure 6.16.

Figure 6.16b indicates that the stress amplitude, σ_a , can be expressed as

$$\sigma_a = \frac{\Delta\sigma}{2} = \sigma'_f (2N_i)^b \quad (6.15)$$

where

$\Delta\sigma$ = stress range

σ'_f = fatigue strength coefficient

b = fatigue strength exponent

N_i = number of cyclic reversals to initiate a small crack

As pointed out in Table 6.1, the strain-life data are generated by smooth specimen tests conducted to total failure (N_f) rather than crack initiation (N_i).

The behavior expressed by Equation (6.15), first proposed by Basquin [6.17] in 1910, is generally not elastic. σ'_f is related to the true fracture stress in a monotonic tensile test. The constant b ranges between about -0.06 to -0.14 with -0.1 as an average value.

For the plastic strain amplitude, Figure 6.16c indicates the straight line may be represented by

$$\frac{\Delta\varepsilon_p}{2} = \varepsilon'_f (2N_i)^c \quad (6.16)$$

where

$\frac{\Delta\varepsilon_p}{2}$ = plastic strain amplitude

ε'_f = fatigue ductility coefficient

c = fatigue ductility exponent

ϵ'_f is related to the true fracture strain in a monotonic tensile test. The constant c ranges between about -0.5 and -0.7 with -0.6 as an average value. Table 6.5 shows values for these coefficients for several different materials. Equation (6.16) is called the Manson-Coffin relationship [6.18, 6.19], first proposed in the early 1960's.

The total strain amplitude, $\frac{\Delta\epsilon}{2}$, may be separated into elastic and plastic components, i.e.

$$\frac{\Delta\epsilon}{2} = \frac{\Delta\epsilon_e}{2} + \frac{\Delta\epsilon_p}{2} \quad (6.17)$$

where

$$\frac{\Delta\epsilon_e}{2} = \text{elastic strain amplitude } \left(\frac{\Delta\sigma}{2E} \right)$$

$$\frac{\Delta\epsilon_p}{2} = \text{plastic strain amplitude}$$

If Equations (6.15) and (6.16) are substituted into Equation (6.17), the following relationship for total strain amplitude is obtained

$$\frac{\Delta\epsilon}{2} = \frac{\sigma'_f}{E} (2N_i)^b + \epsilon'_f (2N_i)^c \quad (6.18)$$

Raske and Morrow [6.20] have suggested that the strain-life relationship, Equation (6.18), can be modified to account for mean stress by reducing the fatigue strength coefficient by an amount equal to the mean stress σ_0 , i.e.,

$$\frac{\Delta\epsilon}{2} = \frac{\sigma'_f - \sigma_0}{E} (2N_i)^b + \epsilon'_f (2N_i)^c \quad (6.19)$$

where σ_0 is positive for a tensile and negative for a compressive mean stress.

At small strains, the elastic strain component in Equations (6.18) and (6.19) is predominant, and the cyclic hardening and softening effects on initiation life can be neglected. At large strains, plasticity effects at the notch control the initiation, and the effect of mean stress becomes

negligible. Figure 6.17 shows strain life data for A 36 Heat-Affected-Zone (HAZ) metal and indicates the plastic strain amplitude is small compared with the elastic strain for $N_f > 10^5$. The transition fatigue life, where $\frac{\Delta e_p}{2} = \frac{\Delta e_e}{2}$, occurs at about 13,000 cycles.

6.5.4 Cyclic Stress-Strain Conversion

The next step in the calculation process is to determine the relationship between notch stresses and strains. For non-cyclic (monotonic) loading, an equation of the following form is widely used:

$$\epsilon = \frac{\sigma}{E} + \left(\frac{\sigma}{K}\right)^{1/n} \quad (6.20)$$

where ϵ = notch strain

σ = notch stress

K = monotonic strength coefficient

n = monotonic strain hardening coefficient.

If repeated loadings are involved, Equation (6.20) is usually expressed as

$$\frac{\Delta \epsilon}{2} = \frac{\Delta \sigma}{2E} + \left(\frac{\Delta \sigma}{2K'}\right)^{1/n'} \quad (6.21)$$

where $\Delta \epsilon$ = notch strain range

$\Delta \sigma$ = notch stress range

K' = cyclic strength coefficient

n' = monotonic strain hardening coefficient

Figure 6.7 compares the monotonic and cyclic stress-strain response for several common engineering alloys. For example, A 36 HAZ and weld metal cyclically soften, while the base metal softens at low strains and hardens at high strains. Figure 6.7c shows A514 cyclically softens in all cases. Tables 6.6 and 6.7 give the mechanical and fatigue properties of the A514 steel. Other data on metals can be found in Reference [6.7].

6.5.5 Notch Strain Analysis

Section 6.4 discussed that the final ingredient required to compute crack initiation life is the relationship between the far-field stress (ΔS), far-field strain (Δe), notch-stress ($\Delta \sigma$), and notch strain ($\Delta \varepsilon$) ranges. This is provided by the Neuber rule, Equation (6.4)

$$K_t = (K_{\sigma} K_{\varepsilon})^{1/2} \quad (6.4)$$

In applying Neuber's rule to the notch fatigue problem, Topper [6.21] replaced K_t by K_f , the fatigue strength reduction factor, discussed in Section 6.5.2. When K_{σ} and K_{ε} are expressed in terms of ranges of stress and strain, Equation (6.4) can be written as

$$K_f = \left(\frac{\Delta \sigma}{\Delta S} \frac{\Delta \varepsilon}{\Delta e} \right)^{1/2} \quad (6.22)$$

or in the more standard form

$$K_f (\Delta S \Delta e E)^{1/2} = (\Delta \sigma \Delta \varepsilon E)^{1/2} \quad (6.23)$$

where

ΔS and Δe = nominal (net action) stress and strain ranges applied to a notched member,

$\Delta \sigma$ and $\Delta \varepsilon$ = local stress and strain ranges at the notch root, and
 E = elastic modulus.

The far-field stress range is usually assumed to remain elastic,
i.e.,

$$\Delta S = \Delta e E \quad (6.24)$$

and Equation (6.23) becomes

$$K_f \Delta S = (\Delta \sigma \Delta \varepsilon E)^{1/2} \quad (6.25)$$

6.5.6 Cycles to Crack Initiation Calculation

All relationships required to compute initiation life are now available and are summarized below:

Fatigue Strength Reduction Factor - Weld Geometry and Loading Relationship

$$K_{f\max} = 1 + \frac{a}{2} \left(\frac{t}{a_m}\right)^{1/2} \quad (6.14)$$

Material Parameter a_m - Ultimate Strength Relationship

$$a_m \approx 2.5 \times 10^{-5} \left(\frac{2068}{S_u}\right)^{1.8} \quad (6.12)$$

Strain-Life Relationship

$$\frac{\Delta\varepsilon}{2} = \frac{\sigma'_f}{E} (2N_i)^b + \varepsilon'_f (2N_i)^c \quad (6.18)$$

Cyclic Stress - Strain Relationship

$$\frac{\Delta\varepsilon}{2} = \frac{\Delta\sigma}{2E} + \left(\frac{\Delta\sigma}{2K'}\right)^{1/n'} \quad (6.21)$$

Modified Neuber Rule

$$K_f \Delta S = (\Delta\sigma \Delta\varepsilon E)^{1/2} \quad (6.25)$$

A computer program was written to solve this system of nonlinear algebraic equations. Example cases applied to welded joints are presented in Chapter 7.0.

6.6 Fracture Mechanics Approach to Crack Growth

6.6.1 Introduction

It is now generally accepted that the total fatigue life of structures is comprised of cycles required for crack initiation as well as those required for crack propagation; that is:

$$N_f = N_i + N_p \quad (6.26)$$

where

- N_f = total cycles to failure;
- N_i = cycles to crack initiation; and
- N_p = cycles for crack propagation.

Reasonable success has been demonstrated by combining the local stress-strain approach to crack initiation and the fracture mechanics approach to crack propagation [6.22-6.24]. Although this combined initiation and propagation approach to fatigue life prediction is both physically correct and generally applicable, the relative magnitudes of N_i and N_p in Equation (6.26) can vary greatly from structure to structure, depending on fabrication history, magnitude of applied loads, and severity of stress concentrations. Generally for large complex structures fabricated by welding, N_i is relatively small compared to N_p . For example, as shown in Figure 6.18, results from a full-scale test of a welded tubular joint typical of that in an offshore structure have demonstrated that engineering-sized cracks of 1 to 3 mm are present at less than 10 percent of the total life. Under these conditions, crack propagation controls the total life of the structure and Equation (6.26) reduces to

$$N_f \approx N_p \quad (6.27)$$

The techniques of Linear Elastic Fracture Mechanics (LEFM) are capable of providing reasonable estimates of N_p [6.27, 6.28]. This approach is well established in the airframe, jet engine, and power generation industries where it is routinely used to make run-retirement-repair decisions on a wide range of structural components.

The fracture mechanics approach has the advantage of being interactive with nondestructive evaluation (NDE). This interaction is embodied within the "fail-safe" design philosophy in which structures are designed to insure safe operation over some reasonable inspection interval. In this way, components can be retired based on combining analysis, periodic inspection, and a consideration of the specific loading history, rather than by establishing an arbitrary limit on service time.

The primary purpose of this section is to outline a procedure for predicting the residual fatigue life of offshore structures using LEFM. Subsequent sections treat the problem in more detail and identify difficulties which are peculiar to offshore structures.

The LEFM approach is based on the fact that the crack-tip stress intensity factor, ΔK , defined by linear elasticity, uniquely characterizes the stress-strain field at the crack-tip and thereby provides a measure of the "driving force" for crack propagation. Consequently, expressing the rate of fatigue crack growth (da/dN) as a function of the range of stress intensity factor (ΔK) provides a geometry-independent material property. This growth rate equation can be empirically established and has the following general form:

$$da/dN = da/dN(\Delta K, R, f, w/f, \phi, C_i, T, M) \quad (6.28)$$

where

$R = \text{load ratio} = P_{\min}/P_{\max} = K_{\min}/K_{\max}$, and serves to characterize the mean stress;

$f = \text{cyclic frequency}$, an important variable when time-dependent processes such as corrosion occur;

$w/f = \text{cyclic waveform}$, also an important variable for time-dependent processes;

$\phi = \text{electrode potential for the material environment system}$, in this application either at the "open circuit" or "freely corroding" potential or at some level of cathodic polarization to impart protection from generalized corrosion;

$C_i = \text{chemical composition of the aggressive environment}$;

$T = \text{temperature of the environment}$; and

$M = \text{material composition and microstructure}$.

Having established Equation (6.28) empirically, one then integrates this expression to determine the crack propagation life (N_p) as follows:

$$N_p = \int_{a_i}^{a_f} \frac{1}{F[\Delta K(a), \dots]} da \quad (6.29)$$

where a_i and a_f are the initial and final crack lengths, respectively. The form of the relation between the range of stress intensity factor and crack length, $\Delta K(a)$, makes the analysis specific to a given structural member and must be determined either from a stress analysis of the crack structure or from approximations using existing solutions for analogous configurations. When preexisting cracks are present in the structure, a_i is determined from NDE results, or alternatively, from destructive measurements, such as metallography, on selected critical components. The value of a_f is determined from fracture toughness properties of the material or from operational requirements—for example, loss of stiffness or load bearing capacity. The above procedure is schematically illustrated in Figure 6.19. Results from such an analysis can be parametrically expressed as shown in Figure 6.20 to facilitate use of this information in design.

The advantages and disadvantages of the fracture mechanics approach to crack growth are given in Table 6.1. The primary advantage is the fact that it provides a rational procedure for incorporating the influence of flaws on the fatigue performance of materials. The major disadvantage is its relative complexity. However, as in the case of the local strain approach, this can largely be overcome by developing computer algorithms. The other disadvantages listed in Table 6.1 are actually limitations, rather than true disadvantages, which represent currently active research areas. Nevertheless, this approach has proven to be extremely useful in the aircraft industry, where it forms the basis of the "safe-life" design philosophy [6.28].

The following sections give consideration to the application of LEFM to evaluate the residual fatigue life of welded joints. Specifically addressed is the evaluation of stress intensity factors for one- and two-dimensional surface cracks at the weld toe.

6.6.2 Formulation of the Stress Intensity Factor

The integration of the crack growth expression, equation (6.28) requires that the relationship between the stress intensity factor, crack size and shape, and mode of loading be known. For a two-dimensional surface crack the functional form of this relationship may be expressed as

$$\Delta K = \Delta K (a, c, \phi, \Delta S)$$

(6.30)

where

a = crack depth

$2c$ = surface crack length

ϕ = crack shape

ΔS = far-field stress range and mode of loading

Expressions for stress intensity factor have been widely published in the technical literature. References [6.29] and [6.30] have collected K_I (Mode I - inplane crack opening), K_{II} (Mode II - inplane shear), and K_{III} (Mode III - out of plane shear) values for a variety of crack geometries and loadings. These modes are shown in Figure 6.21. Mode I is the most commonly found in practical situations and is believed to control crack propagation at the toe of a welded joint. Therefore, for the discussions related to this investigation, the Mode I stress intensity K_I factor will be designated simply as K . Likewise ΔK is the change in the mode I stress intensity factor due to a change in far-field stress ΔS .

This study uses the Green's function method of determining stress intensity factors for cracks in a welded joint. This approach is discussed by Cartwright and Rooke in Reference [6.31]. The Green's function, first postulated by George Green in 1828, is defined as the response of a system to a standard input. The input is usually in the form of an impulse, and in elasticity, the stress is the response of the body to a point force. The advantage of this approach is that the stress intensity factor can be evaluated by knowledge of the body's stress state in the uncracked configuration if the appropriate Green's function is known. This avoids computing K by more complicated and time-consuming techniques such as the finite element method.

For a one-dimensional crack this approach requires evaluation of an integral of the form

$$K(a) = \frac{1}{\sqrt{\pi a}} \int_0^a G(\bar{a}) \sigma(\bar{a}) d\bar{a} \quad (6.31)$$

where

$K(a)$ = Mode I stress intensity factor;

$\sigma(a)$ = stress field normal to path of crack in absence of the crack;

$G(a)$ = Green's function;

a = depth of crack; and

\bar{a} = dummy variable of integration.

For a crack starting at a notch, Reference [6.31] suggests that a valid approximation for $G(\bar{a})$ is

$$G(\bar{a}) = 1.12 \pi a \delta(\bar{a} - a) \quad (6.32)$$

where $\delta(\bar{a}-a)$ is the Dirac-delta function with the properties

$$\begin{aligned} \delta(\bar{a} - a) &= 0 && \text{at } \bar{a} \neq a \\ &= \infty && \bar{a} = a \end{aligned} \quad (6.33)$$

The Dirac-delta function represents a singularity at the crack tip.

Integration of Equation (6.31) gives

$$K(a) = 1.12 \sigma(a) \sqrt{\pi a} \quad (6.34)$$

This relationship requires knowledge of the stress distribution over the crack site in the uncracked body. The factor 1.12 accounts for the front-surface effects. To gain some understanding of the accuracy of using the $G(\bar{a})$ as a suitable Green's function for cracks propagating from small notches, a verification analysis was made. Consider an elliptical hole shown in Figure 6.22 under a tension loading normal to the major diameter.

The stresses along the X-axis, $x \geq d$, (without the presence of the crack) are [6.15]

$$\sigma_{xx} = F_1(s) - F_2(s) \quad (6.35)$$

$$\sigma_{yy} = F_1(s) + F_2(s) \quad (6.36)$$

where

$$s = \frac{x}{2B} + \sqrt{\left(\frac{x}{2B}\right)^2 - m} \quad (6.37)$$

and

$$F_1(s) = \frac{\sigma}{2} \left[1 + \frac{2(1+m)}{s^2 - m} \right] \quad (6.38)$$

$$F_2(s) = \frac{\sigma}{2} \left\{ 1 + \frac{m^2 - 1}{s^2 - m} \left[1 + \left(\frac{m-1}{s^2 - m} \right) \left(\frac{3s^2 - m}{s^2 - m} \right) \right] \right\} \quad (6.39)$$

$$B = \frac{1}{2} (h + d) \quad (6.40)$$

$$m = \frac{d-h}{d+h}$$

Equation (6.34) can now be written as

$$K(a) = 1.12 [F_1(s) + F_2(s)] \sqrt{\pi a} \quad (6.41)$$

or since $a = x-d$

$$K(x) = 1.12 [F_1(s) + F_2(s)] \sqrt{\pi(x-d)}, \quad x \geq d \quad (6.42)$$

Rooke and Cartwright [6.29] have computed the solution for various h/d and x/d values. Solutions are shown in the attached Figures 6.23 and 6.24 for the nondimensional ratio

$$\frac{K(x)}{K_o} = \frac{K(x)}{\sigma \sqrt{\pi x}} \quad (6.43)$$

where K_0 is the Mode I stress intensity for an infinite plate under tension. The expression for the nondimensional K/K_0 by the Green's function approach is then

$$\frac{K(x)}{K_0} = \frac{1.12 [F_1(s) + F_2(s)] \sqrt{\pi(x-d)}}{\sqrt{\pi x}} \quad (6.44)$$

Equation (6.44) was evaluated and the results are compared with those of Rooke and Cartwright on Figures 6.23 and 6.24 for various values of h/d and x/d . This problem has been studied by other investigators [6.32, 6.33], and the results are believed to be accurate within 1 percent. Green's function approximation is a function of both the ellipse geometry (h/d) and crack length to major axis (x/d) ratios. In the worst case, the "exact" and "approximate" solutions generated by the Green's function differ a maximum of about 20 percent. Therefore, the Dirac-delta function has the possibility of providing reasonably accurate values of K for cracks propagating from notches if the uncracked stress state is known. Still in the high-cycle fatigue regime where the slope of the crack growth curves is steep, an acceptable engineering estimate of K could produce considerable error in fatigue life predictions. This accentuates the need for having as accurate stress intensity factor values as possible.

6.6.3 Extension of the Stress Intensity Factor to Two Dimensions

The evaluation of K in Section 6.6.2 considered the crack to be one dimensional with depth a . The length of the crack along the surface was assumed to be infinitely long. Metallurgical examinations of fatigue cracks indicate that in the early stages of propagation cracks have shapes which may be considered semi-elliptical. They propagate through the plate thickness and along the surface as shown in Figure 6.25 for a welded planar T-joint. When the surface length $2c$ is large compared with the crack depth, the highly elliptical crack can be considered as one dimensional.

The fracture analysis will be extended to two dimensions with the aid of the following stress intensity equation for combined tension and bending cyclic loads proposed by Newman and Raju [6.34]:

$$K = (\sigma_t + H \sigma_b) \sqrt{\pi a / Q} F\left(\frac{a}{t}, \frac{a}{c}, \frac{c}{b}, \phi\right) \quad (6.45)$$

where

a, t, c, b , = are geometry parameters defined in Figure 6.26.

σ_t, σ_b = are tensile and bending stresses defined in Figure 6.27.

F, H, Q = are functions depending on the crack size, crack shape, plate thickness, and location on crack (angle ϕ)

Equation (6.45) is limited to the parameter ranges

$$0 \leq \frac{a}{t} < 1.0$$

$$\frac{c}{b} < 0.5 \quad (6.46)$$

$$0 \leq \phi \leq \pi$$

In Equation (6.45), Q is the flaw shape parameter, and a useful approximation developed by Rawe and used in Reference [6.35] is

$$Q = 1.464 \left(\frac{a}{c}\right)^{1.65} \quad \frac{a}{c} \leq 1 \quad (6.47)$$

$$= 1.464 \left(\frac{c}{a}\right)^{1.65} \quad \frac{a}{c} > 1$$

The functions F and H are defined so that the boundary-correction factor for tension is equal to F and the boundary-correction factor for bending is equal to the product of H and F . The function F given by Newman and Raju [6.34] is

$$F = [M_1 + M_2 \left(\frac{a}{t}\right)^2 + M_3 \left(\frac{a}{t}\right)^3] f_\phi f_w g \quad (6.48)$$

where

$$M_1 = 1.13 - 0.09 \left(\frac{a}{c}\right) \quad \frac{a}{c} \leq 1.0$$

$$= \sqrt{c/a} \left(1 + 0.03 \frac{c}{a}\right) \quad \frac{a}{c} > 1.0$$

$$M_2 = -0.54 + \frac{0.89}{0.2 + \left(\frac{a}{c}\right)}$$

$$M_3 = 0.5 - \frac{1.0}{0.65 + \left(\frac{a}{c}\right)} + 14 \left(1.0 - \frac{a}{c}\right)^{24}$$

$$g = 1 + [0.1 + 0.35 \left(\frac{a}{t}\right)]^2 (1 - \sin \phi)^2 \quad (6.49)$$

$$f_\phi = \left[\left(\frac{a}{c}\right)^2 \cos^2 \phi + \sin^2 \phi \right]^{1/4}$$

$$f_w = \left[\sec \left(\frac{\pi c}{2b}\right) \sqrt{a/t} \right]^{1/2}$$

The function f_ϕ comes from the embedded elliptical-crack solution [6.36], and the function f_w is a finite width correction from [6.37]. The function H , developed in [6.34], has the form

$$H = H_1 + (H_2 - H_1) \sin^p \phi \quad (6.50)$$

where

$$p = 0.2 + \frac{a}{c} + 0.6 \frac{a}{t} \quad (6.51)$$

$$H_1 = 1 - 0.34 \frac{a}{t} - 0.11 \left(\frac{a}{c}\right) \left(\frac{a}{t}\right)$$

and

$$\begin{aligned} H_2 &= 1 + G_1 \left(\frac{a}{t}\right) + G_2 \left(\frac{a}{t}\right)^2 \\ G_1 &= -1.22 - 0.12 \frac{a}{c} \\ G_2 &= 0.55 - 1.05 \left(\frac{a}{c}\right)^{0.75} + 0.47 \left(\frac{a}{c}\right)^{1.15} \end{aligned} \quad (6.52)$$

6.6.4 Stress Distribution at the Toe of a Welded Joint

The use of the Green's function approach discussed in Section 6.6.2 requires that the stress at the path of the crack in uncracked geometry be known. For a welded joint, this requires knowledge of the stress distribution across the weld at the toe.

From finite element analyses of joint configurations, such as shown in Figure 6.12, Lawrence [6.38] has developed an approximate relationship for the distribution of stress in the form

$$\sigma(a) = S \left\{ 1 + (K_t - 1) \exp [-35(K_t - 1) \frac{a}{t}] \right\} \quad (6.53)$$

where

a = distance from weld surface (depth of crack);

S = far-field stress;

K_t = stress concentration factor; and

t = plate thickness.

Equation (6.53) represents a rapid decay of stress from

$$\sigma(x) = K_t S \quad \text{at } a = 0 \quad (6.54)$$

to

$$\sigma(x) = S \quad \text{as } a \text{ becomes large}$$

The value of the stress concentration factor can be evaluated from the following relationship which was discussed in Section 6.5.2.

$$K_t = 1 + a \left(\frac{t}{r}\right)^{1/2} \quad (6.5)$$

The value of the radius at the weld toe, r , will be taken as r_{crit} as defined by the crack initiation procedure.

The form of Equation (6.53) is consistent with the stress distribution at the root of a notch, such as shown in Figure 6.28. Equation (6.36) gives the stress distribution along the major axis of an elliptical hole subjected to tension as shown in Figure 6.22. In the neighborhood of the notch tip, $x=d$ for $r \ll d$ on the major axis, the stress σ_{yy} may be approximated by

$$\sigma_{yy} = \frac{\sigma \sqrt{d}}{\sqrt{2a}} \frac{1 + \frac{x}{a}}{(1 + \frac{x}{2a})^{3/2}} \quad (6.55)$$

If Equations (6.53) and (6.55) are expanded in a power series about $x=d$, then terms of like order (up to order $O(a/r)^2$) will be equal provided

$$K_t = 1.28$$

and

$$a = 0.27$$

(6.56)

The value of 1.28 for K_t is somewhat lower than expected in typical welded joints, but $a = 0.27$ agrees well with the values reported in Table 6.4 for welds in tension. Therefore, Equation (6.53) appears to correctly characterize the stress distribution at the notch of a weld toe and will be used in subsequent crack propagation analyses.

6.6.5 Crack Propagation Calculation Strategies

All the ingredients are now available to conduct a series of calculations involving crack propagation and the sensitivity of the various parameters including the effects of environment.

A FORTRAN computer program was written to conduct the following three separate types of analyses for one-dimensional cracks of the type described in Section 6.6.2.

(1) Fatigue Life Sensitivity to Initial Crack Depth

Given the final crack depth and stress range, how does the propagation life vary as a function of initial crack depth?

(2) Fatigue Life Sensitivity to Final Crack Depth

Given the initial crack depth and stress range, how does the propagation life vary as a function of final crack depth?

(3) Fatigue Crack Growth for Typical Block Sea Spectra

Given the initial crack depth and load spectra, what is the final crack depth?

The computational procedure centers around the crack growth equation

$$\frac{da}{dN} = f(\Delta K) \quad (6.57)$$

which for the three-component crack growth law may be written as

$$\frac{1}{da/dN} = [f(\Delta K)]^{-1} = \frac{A_1}{\Delta K^{n_1}} + \frac{A_2}{\Delta K^{n_2}} - \frac{A_2}{[(1 - R) K_c]^{n_2}} \quad (6.58)$$

Integrating Equation (6.57) gives

$$N_p = N(a_f) - N(a_i) = \int_{a_i}^{a_f} \frac{1}{f(\Delta K)} da \quad (6.59)$$

where a_i and a_f are the initial and final crack depths. The functional form of $K(a)$ and hence $f[\Delta K(a)]$ is generally so complex that Equation (6.59) must be integrated numerically.

For the calculation of fatigue crack growth for typical block sea spectra, a function F is defined as follows:

$$F(a_f, a_i, \Delta K, N_p) = \int_{a_i}^{a_f} \frac{1}{f(\Delta K)} da = N_p \quad (6.60)$$

For a given block loading, the number of cycles and stress range are known. If the crack depth at the a_i at the beginning of the block is known, Equation (6.60) can be solved to determine the final crack depth a_f so that

$$F(a_f, a_i, \Delta K, N_p) = 0 \quad (6.61)$$

Equation (6.61) is nonlinear and requires an iterative solution such as Newton's method. If $a_{f,n}$ is an initial guess on the final crack depth, a successive approximation can be found from the relationship

$$\begin{aligned} a_{f,n+1} &= a_{f,n} - \frac{F(a_{f,n}, a_i, \Delta K, N_p)}{\frac{dF}{da_f}(a_{f,n}, a_i, \Delta K, N_p)} \\ &= a_{f,n} - \frac{\int_{a_i}^{a_{f,n}} \frac{1}{f(\Delta K)} da - N_p}{\left. \frac{1}{f(\Delta K)} \right|_{a_{f,n}}} \end{aligned} \quad (6.62)$$

The procedure is repeated until a suitable convergence criterion is met such as

$$\left| \frac{a_{f,n+1} - a_{f,n}}{a_{f,n}} \right| < \varepsilon \quad (6.63)$$

where ε is a small convergence parameter.

Crack growth analyses using Equation (6.57) are one dimensional since only the depth a is considered. The crack length along the surface is assumed to be infinite. In order to account for both the crack depth and the crack length on the surface, Equation (6.57) for the stress intensity factor had to be appropriately modified as discussed in Section 6.6.3.

The computer program already developed for the one-dimensional analysis was modified to consider a two-dimensional surface crack as shown in Figure 6.26. Although Equation (6.45) gives the stress-intensity factor at any location along the crack front, only the values at the maximum-depth point A and at the front surface B are used to predict the crack-growth patterns. The cracks are always assumed to be semi-elliptical with semiaxes a and c .

The crack-growth rates are calculated by assuming that the three-component relationship between crack-growth rate and stress-intensity factor are obeyed independently at points A and B on the crack front.

Thus

$$\frac{da}{dN} = f(\Delta K_A) \quad (6.64)$$

$$\frac{dc}{dN} = f(\Delta K_B^*) \quad (6.65)$$

where ΔK_A and ΔK_B^* are stress intensity factor ranges at points A and B.

Reference [6.34] indicates the experimental results for surface cracks under tension, and bending fatigue loads show that small semicircular cracks tend to grow semicircular for low a/t ratios. The stress intensity factor solution for the small semicircular crack yields a stress intensity at point B about 10 percent higher than at point A. This is due to the expression for g given in Equation (6.49) for small a/t .

Consequently, to ensure that a small semicircular crack would be predicted to initially retain its shape, the value of ΔK_B^* in Equation (6.65) is taken as 0.9 times the value of ΔK_B computed using Equation (6.45) at $\phi = 0$ degrees.

The number of stress cycles required for propagation of a surface crack from depth a_i to a desired a_f is obtained by a numerical integration of Equations (6.64-6.65). This was accomplished by dividing the crack extension ($a_f - a_i$) into a large number (500-1000) of equal increments and assuming that each increment was created at a constant crack-growth rate. The constant growth rate for each increment is determined from Equation (6.64) by using the crack configuration which existed at the start of that growth increment. For

each increment of crack advance Δa in depth, a new increment of crack length Δc computed from

$$\Delta c = \frac{f(\Delta K_B^*)}{f(\Delta K_A)} \Delta a \quad (6.66)$$

This defines the crack configuration for the next growth increment, and the process is repeated until the crack depth reaches the desired value. Since the crack growth rates at A and B are usually different, the shape (or aspect ratio) of the crack thus changes during crack propagation.

The expression for the two-dimensional stress intensity factor, Equation (6.45), was originally developed for a plate subjected to tension and/or bending loads (Figure 6.27). As such, the expression does not consider stress concentrations that would exist at the toe of a welded joint. The present analysis method incorporates such stress concentrations by taking the tensile or bending stresses on the surface ($\phi = 0^\circ$) or at depth "a" ($\phi = 90^\circ$) equal to

$$\sigma(\phi = 90^\circ) = S \left\{ 1 + (K_t - 1) \exp [-35 (K_t - 1) \frac{a}{t}] \right\} \quad (6.67)$$

$$\sigma(\phi = 0^\circ) = K_t S \quad (6.68)$$

where

S = far-field stress in tension or bending

K_t = stress concentration factor in tension or bending

Equation (6.68) shows that on the surface the stress is equal to $K_t S$, which remains constant during crack growth. As the crack gradually grows in depth, the stress at the crack tip, in the absence of the crack, would decrease as indicated in Equation (6.67). For long-cracks (c/a large), the two-dimensional analysis reduced to the one-dimensional case.

This analysis procedure is applied to both two-dimensional planar welds and tubular joints in Chapter 7.0. Results are compared with experimental tests in air and seawater environments.

CHAPTER 6.0 REFERENCES

- 6.1 Wöhler, A., Zeitschrift für Bauwesen, Vol. 10, 1860.
- 6.2 Hudak, S. J., Jr., "Small Crack Behavior and the Prediction of Fatigue Life," Transactions ASME, Journal of Engineering Materials and Technology, Vol. 103, pp. 26-35, January 1981.
- 6.3 Dowling, N. E., "Fatigue Failure Predictions for Complicated Stress-Strain Histories," Journal of Materials, MTLA, Vol. 7, No. 1, pp 71-87, March 1972.
- 6.4 Rolfe, S. T., and Barson, J. M., Fracture and Fatigue Control in Structures, Prentice-Hall, Inc., Englewood Cliffs, NJ, 1977.
- 6.5 Landgraf, R. W., "Cumulative Fatigue Damage Under Complex Strain Histories," Cyclic Stress-Strain Behavior, ASTM STP 519, pp 212-227, 1973.
- 6.6 Higashida, Y., Burk, J. D., and Lawrence, F. V., Jr., "Strain-Controlled Fatigue Behavior of ASTM A 36 and A 514 Grade F Steels and 5083-0 Aluminum Weld Materials," Welding Journal, Vol. 57, 334S-344S, 1978.
- 6.7 Fuchs, H. O., and Stephens, R. I., Metal Fatigue in Engineering, John Wiley and Sons, 1980.
- 6.8 Neuber, H., "Theory of Stress Concentrations for Shear-Strained Prismatical Bodies with Arbitrary Nonlinear Stress-Strain Law," Transactions ASME, Journal of Applied Mechanics, Vol. 8, December 1961.
- 6.9 Dowling, N. E., and Wilson, W. K., "Analysis of Notch Strain for Cyclic Loading," Proceedings of the 5th International Conference on Structural Mechanics in Reactor Technology, L, 13/4.
- 6.10 Palmgren, A., "Ball and Roller Bearing Engineering," translated by G. Palmgren and B. Ruley, SKF Industries, Inc., Philadelphia, pp 82-83, 1945.
- 6.11 Miner, M. A., "Cumulative Damage in Fatigue," Journal of Applied Mechanics, Series E of the Transactions of the ASME, Vol. 12, pp A-159-164, September 1945.
- 6.12 Peterson, R. E., Stress Concentration Factors, John Wiley and Sons, New York, 1974.
- 6.13 Lawrence, F. V., Jr., et al, "Estimating the Fatigue Crack Initiation Life of Welds," Fatigue Testing of Weldments, ASTM STP 648, D. W. Hoeppner, Ed., 1978, pp 134-158.
- 6.14 Lawrence, F. V., Jr., "Predicting the Fatigue Resistance of Welds," Fracture Control Program Report No. 36, College of Engineering, University of Illinois at Urbana-Champaign, October 1980.

- 6.15 Boresi, A. P., et al, Advanced Mechanics of Materials, Third Edition, John Wiley and Sons, New York, 1978.
- 6.16 Peterson, R. E., "Analytical Approach to Stress Concentration Effect in Fatigue of Aircraft Structures," WADS Symposium, Wright Air Development Center, August 1959.
- 6.17 Basquin, O. H., "The Exponential Law of Endurance Tests," Proc. ASTM, Vol. 10, Part II, 1910, p 625.
- 6.18 Tavernelli, J. F., and Coffin, L. F., Jr., "Experimental Support for Generalized Equation Predicting Low Cycle Fatigue," Transactions ASME, Journal of Basic Engineering, Vol. 84, No. 4, p 533, December 1962.
- 6.19 Mason, S. S., "Discussion of Reference 8," Transactions ASME, Journal of Basic Engineering, Vol. 84, No. 4, p 537, December 1962.
- 6.20 Raske, D. and Morrow, J., "Mechanics of Materials in Low Cycle Fatigue Testing," Manual on Low Cycle Fatigue Testing, ASTM STP 465, 1969.
- 6.21 Topper, T. H., et al, "Neuber's Rule Applied to Fatigue of Notched Specimens," ASTM Journal of Materials, Vol. 4, No. 1, March 1969.
- 6.22 N. E. Dowling, "Fatigue at Notches and the Local Strain and Fracture Mechanics Approaches," ASTM STP 677, pp 247-273, 1979.
- 6.23 D. F. Socie, J. Morrow, and W. C. Chen, "A Procedure for Estimating the Total Fatigue Life of Notched and Cracked Members," Journal of Engineering Fracture Mechanics, Vol. 11, No. 4, pp 851-860, 1979.
- 6.24 W. C. Chen, and F. V. Lawrence, "A Model for Joining the Fatigue Crack Initiation and Propagation Analysis," FCP Report No. 32, University of Illinois, Urbana, November 1979.
- 6.25 J. G. Wylde and A. McDonald, "Modes of Fatigue Crack Development and Stiffness Measurements in Welded Tubular Joints," Fatigue in Offshore Structural Steel, Institution of Civil Engineers, Westminster, London, pp 65-74, 1981.
- 6.26 Clark, W. G., Jr., "Fracture Mechanics in Fatigue," Experimental Mechanics, pp 1-8, 1974.
- 6.27 Hoeppner, D. W., and Krupp, W. E., "Prediction of Component Life by Application of Fatigue Crack Growth Knowledge," Engineering Fracture Mechanics, Vol. 6, pp 47-70, 1974.
- 6.28 Gallagher, J. P., and Stalnaker, H. D., Journal of Aircraft, Vol. 12, No. 9, p 669, 1975.
- 6.29 Rooke, D. P., and Cartwright, D. J., Compendium of Stress Intensity Factors, Her Majesty's Stationery Office, London, September 1974.
- 6.30 Tada, H., Paris, P. C., and Irwin, G. R., The Stress Analysis of Cracks Handbook, Del Research Corporation, Hellertown, Pennsylvania, 1973.

- 6.31 Cartwright, D. J., and Cooke, D. P., "Green's Functions in Fracture Mechanics," Fracture Mechanics - Current Status, Future Prospects, Smith, R. A., editor, Proceedings of a Conference held at Cambridge University, March 1979.
- 6.32 Newman, J. C., NASA Technical Note TN D-6376, 1971.
- 6.33 Isida, M., and Nishitani, H., Lecture Meeting of Japan Society of Mechanical Engineering, No. 212, 131, 1969.
- 6.34 Newman, J. C., Jr., and Raju, I. S., "An Empirical Stress-Intensity Factor Equation for the Surface Crack," Engineering Fracture Mechanics, Vol. 15, No. 1-2, pp. 185-192, 1981.
- 6.35 Merkle, J. C., "A Review of Some of the Existing Stress-Intensity Factor Solutions for Part-Through Surface Cracks," U.S. Atomic Energy Commission ORNL-TM-3983 1973.
- 6.36 Green, A. E., and Sneddon, I. N., "The Distribution of Stress in the Neighborhood of a Flat Elliptical Crack in an Elastic Solid," Proc. Cambridge Phil. Soc., Vol. 46, 1950.
- 6.37 Newman, J. C., Jr., "Predicting Failure of Specimens With Either Surface Cracks or Corner Cracks at Holes," NASA TN D-8244, 1976.
- 6.38 Lawrence, F. V., et al, "Predicting the Fatigue Resistance of Welds," Ann. Rev. Materials Science, Vol. 11, 1981, pp. 401-425.

TABLE 6.1. ADVANTAGES AND DISADVANTAGES OF FATIGUE ANALYSIS APPROACHES

CLASSICAL S-N APPROACH TO CRACK INITIATION

Advantages:

- o Data relatively easy to obtain
- o Much data available
- o Method simple to apply

Disadvantages

- o S-N properties based on specimen failure, not crack initiation
- o Does not consider cyclic hardening/softening
- o Plasticity effects not considered; thus:
 - Actual stress amplitude, σ_a , is less than calculated value, $K_t S_a$.
 - Actual mean stress, σ_0 , is not given by $K_t S_0$.
 - Actual strain amplitude is greater than calculated value, $K_t \sigma_a / E$.
 - Cannot rationally count cycles under variable amplitude loading.

FRACTURE MECHANICS APPROACH TO CRACK INITIATION

Advantages

- o Crack initiation measured rather than failure
- o Data relatively easy to obtain
- o Method simple to apply

Disadvantages

- o Ignores physical events at the notch, e.g., plasticity, mean stress, cyclic hardening, and softening
- o Cannot be rationally extended to variable amplitude loading

TABLE 6.1. ADVANTAGES AND DISADVANTAGES OF FATIGUE ANALYSIS APPROACHES

(continued)

LOCAL STRESS-STRAIN APPROACH TO CRACK INITIATION

Advantages:

- o No limitation on irregularity of load history
- o Rationally accounts for plasticity, cyclic alteration of properties, mean stress, over-strain effects
- o Approximation can be used to simplify preliminary analyses
- o Can be used in conjunction with actual component service history data
- o Can be used in conjunction with advanced structural analysis techniques

Disadvantages:

- o Cyclic strain-life properties based on specimen failure, not crack initiation
- o Detailed input information needed
- o Overall approach relatively complex

FRACTURE MECHANICS APPROACH TO CRACK GROWTH

Advantages:

- o Only method which treats crack growth
- o Rationally accounts for influence of flaws on fatigue life
- o Can be used in conjunction with nondestructive testing information
- o Can be used in conjunction with advanced stress analysis techniques

Disadvantages:

- o Method is relatively complex
- o More development is needed to adequately treat:
 - Crack growth under variable amplitude loading
 - Crack growth under elastic-plastic loading
 - Growth of very small cracks

TABLE 6.2. ELASTIC CONCENTRATION COEFFICIENTS
FOR VARIOUS WELDMENTS, FROM [6.14]

Description*	Geometry	Axial α_A	Bending α_B
A. T-Joint, Full Penetration Welds (fixed ends)	$\theta = 45^\circ$	0.35	0.19
B. T-Joint, Fillet Welds (cruciform)	$\theta = 45^\circ$ $2c/t = 0$ $\theta = 45^\circ$ $2c/t = .5$ $\theta = 45^\circ$ $2c/t = .75$ $\theta = 45^\circ$ $2c/t = 1$	0.35 0.38 0.41 0.45	0.19 0.19 0.19 0.19
C. Double Lap Joint Transverse Fillet Welds	$\theta = 45^\circ$ $\ell/t = 1.0$ $\theta = 90^\circ$ $\ell/t = 1.0$ $\theta = 90^\circ$ $\ell/t = 0.5$	0.44 0.60 0.95	0.19 0.24 0.30
D. Butt Joint Full Penetration Double-V Groove Welds	$\theta = 10^\circ$ $\phi = 90^\circ$ $\theta = 15^\circ$ $\phi = 90^\circ$ $\theta = 30^\circ$ $\phi = 90^\circ$ $\theta = 45^\circ$ $\phi = 90^\circ$	0.013 0.18 0.23 0.27	- - - 0.165
E. Single Lap Joint Double Transverse Fillet Welds	$\theta = 45^\circ$ $x/t = 4$ $\theta = 45^\circ$ $x/t = 12$	0.47 0.35	- -

$K_t - 1 = \alpha (t/r)^{\frac{1}{2}}$; α_A = axial coefficient, α_B = bending coefficient

$$K_t \text{ at LOP for axial loads } K_{tA}^{\text{LOP}} = 1 + 1.15 (c/r)^{\frac{1}{2}}$$

$$K_t \text{ at LOP for bending loads } K_{tB}^{\text{LOP}} = .0165 (c/r)^{\frac{1}{2}} K_{tA}^{\text{LOP}}$$

LOP stands for loss of penetration

TABLE 6.3. MECHANICAL PROPERTIES OF BASE, WELD, AND HEAT-AFFECTED MATERIALS FOR ASTM SPECIFICATION A36 STEEL WELDS, FROM [6.13]

Material	ASTM A 36-BM	ASTM A 36-HAZ	E60S-WM(1P)	E60S-WM(2P)
Hardness, DPH/HB	168/160	255/243	245/233	211/201
Modulus of elasticity, E , $\times 10^3$ (MPa)	190	190	190	190
0.2% offset yield strength, (MPa)	224	535	580	408
Ultimate tensile strength, S_u , (MPa)	414	667	711	580
Percent reduction in area, %RA	69.7	52.5	44.6	60.7
True fracture strength, σ_f , (MPa)	800	821	890	870
True fracture ductility, ϵ_f	1.19	0.745	0.590	0.933
Strain hardening exponent, n	0.0146/0.258	0.102	0.098	0.130
Strength coefficient, K , (MPa)	778	980	987	849

TABLE 6.4. CYCLIC AND FATIGUE PROPERTIES OF BASE, WELD, AND HEAT-AFFECTED MATERIALS FOR ASTM SPECIFICATION A36 STEEL WELDS, FROM [6.13]

Material	ASTM A 36-BM	ASTM A 36-HAZ	E60S-WM(1P)	E60-WM(2P)
Cyclic yield strength, 0.2% offset, (MPa)	232	402	385	363
Cyclic strain hardening exponent, n'	0.249	0.215	0.155	0.197
Cyclic strength coefficient, K' (MPa)	1097	1490	1007	1235
Fatigue strength coefficient, σ_f , (MPa)	1014	725	904	1028
Fatigue ductility coefficient, ϵ_f	0.271	0.218	0.607	0.602
Fatigue strength exponent, b	-0.132	-0.066	-0.075	-0.090
Fatigue ductility exponent, c	-0.451	-0.492	-0.548	-0.567
Transition fatigue life, $2N_t$, reversals	200 000	13 234	28 022	19 259

Note: BM = Base Metal

HAZ = Heat Affected Zone

WM = Weld Metal

1P(2P) = One (Two) Passes

6.895 MPa = 1 ksi

TABLE 6.5. σ_f' , ϵ_f' , b, AND C FOR SEVERAL MATERIALS,
FROM [6.13]

<u>Material</u>	<u>σ_f' (MPa)</u>	<u>b</u>	<u>ϵ_f'</u>	<u>c</u>
<u>A 36</u>				
Base Metal	1014	-0.132	0.271	-0.451
HAZ	725	-0.066	0.218	-0.492
Weld E60S-WM(1P)	904	-0.075	0.607	-0.548
Weld E60S-WM(2P)	1028	-0.090	0.602	-0.567
<u>A 514</u>				
Base Metal	1304	-0.079	0.975	-0.699
HAZ	2001	-0.087	0.783	-0.713
Weld E110-WM(1P)	1890	-0.115	0.848	-0.734
Weld E110-WM(2P)	1408	-0.079	0.595	-0.590
<u>5083 Aluminum</u>				
5083 - Base Metal	725	-0.122	0.405	-0.107
5183 - Weld Metal	638	-0.692	0.581	-0.890

TABLE 6.6. MECHANICAL PROPERTIES OF BASE, WELD, AND HEAT-AFFECTED MATERIALS FOR ASTM SPECIFICATION A514 WELDS, FROM [6.13]

Material	ASTM A 514-BM	ASTM A 514-HAZ	E110-WM(IP)	E110-WM(2P)
Hardness, DPH/HB	320/303	496/461	382/362	327/310
Modulus of elasticity, E , $\times 10^3$ (MPa)	209	209	209	209
0.2% offset yield strength, (MPa)	890	1180	835	759
Ultimate tensile strength, S_u , (MPa)	938	1408	1035	911
Percent reduction in area, %RA	63.0	52.7	57.6	59.3
True fracture strength, σ_f , (MPa)	1270	1988	1911	1428
True fracture ductility, ϵ_f	0.994	0.750	0.857	0.899
Strain hardening exponent, n	0.060	0.092	0.092	0.085
Strength coefficient, K , (MPa)	1187	2111	1559	1290

TABLE 6.7. CYCLIC AND FATIGUE PROPERTIES OF BASE, WELD, AND HEAT-AFFECTED MATERIALS FOR ASTM SPECIFICATION A514 WELDS, FROM [6.13]

Material	ASTM A 514-BM	ASTM A 514-HAZ	E110-WM(IP)	E110-WM(2P)
Cyclic yield strength, 0.2% offset, (MPa)	604	938	649	603
Cyclic strain hardening exponent, n'	0.091	0.103	0.177	0.166
Cyclic strength coefficient, K' , (MPa)	1090	1766	2022	1670
Fatigue strength coefficient, σ_f' , (MPa)	1304	2001	1890	1408
Fatigue ductility coefficient, ϵ_f'	0.975	0.783	0.848	0.595
Fatigue strength exponent, b	-0.079	-0.087	-0.115	-0.079
Fatigue ductility exponent, c	-0.699	-0.713	-0.734	-0.590
Transition fatigue life, $2N_t$, reversals	3461	1138	1536	6448

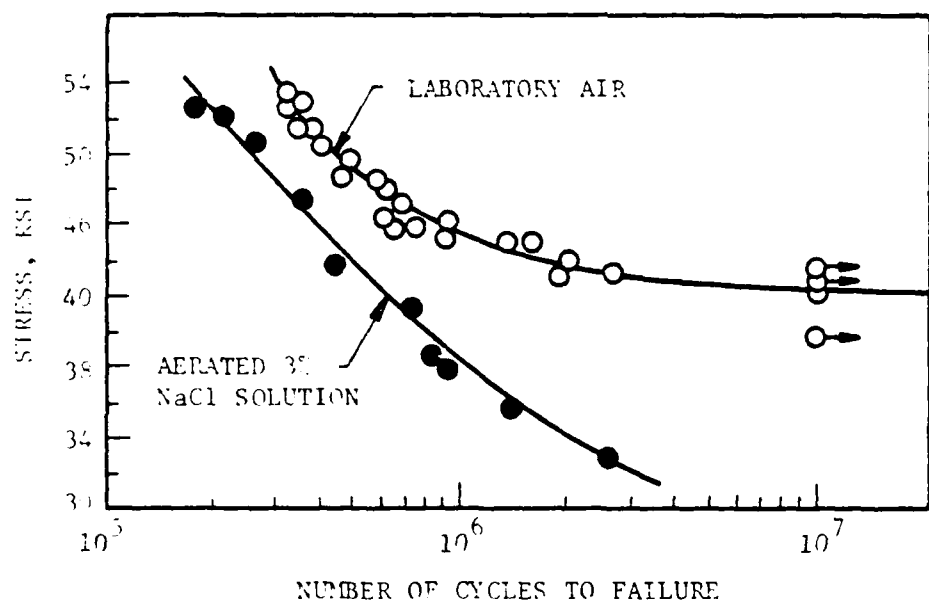


FIGURE 6.1. S-N DATA FOR A 1018 STEEL
IN VARIOUS ENVIRONMENTS

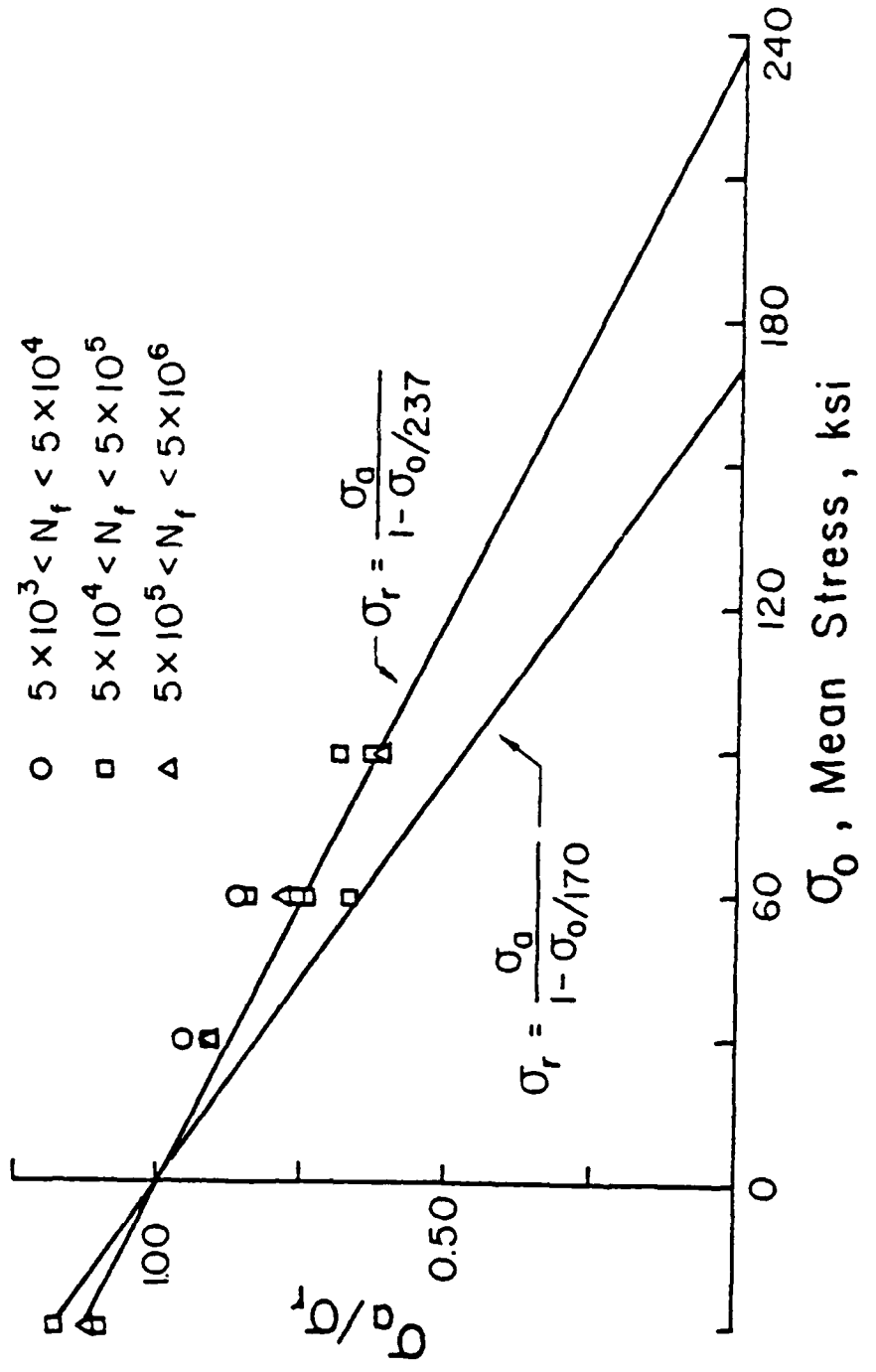


FIGURE 6.2. MEAN STRESS DATA FOR SAE 4340 STEEL,
FROM [6.3]

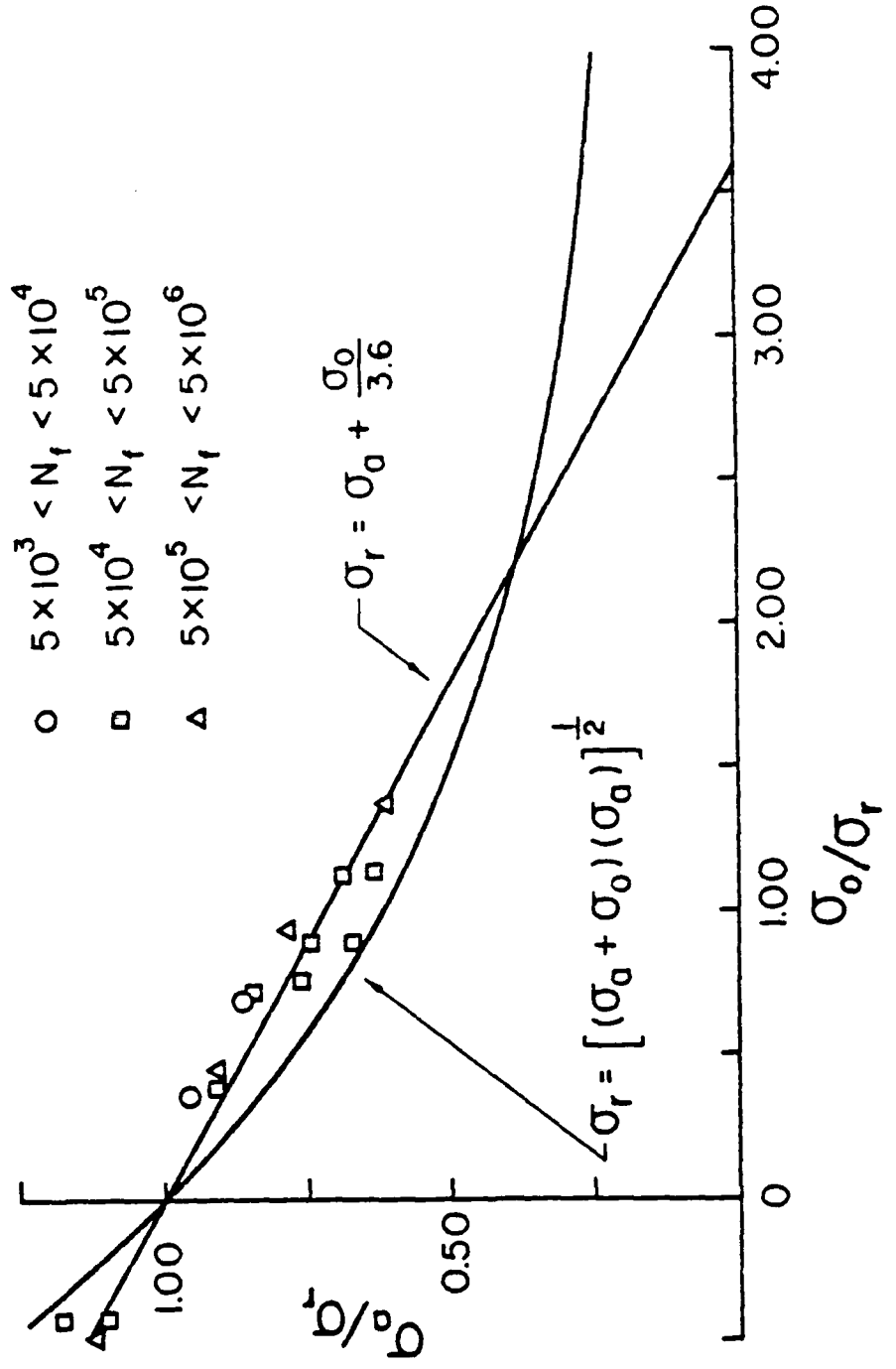


FIGURE 6.3. MEAN STRESS DATA FOR SAE 4340 STEEL,
FROM [6.3]

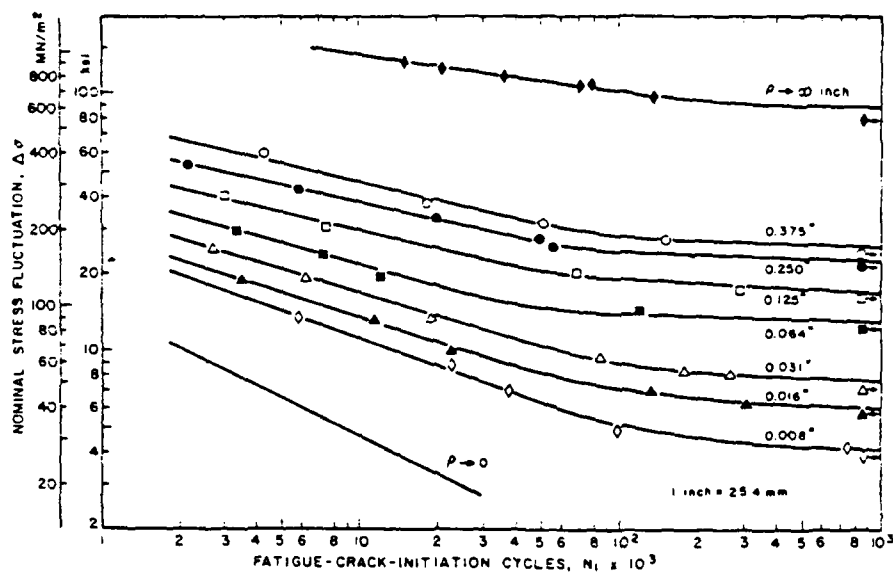


FIGURE 6.4. DEPENDENCE OF FATIGUE-CRACK INITIATION OF HY-130 STEEL ON NOMINAL-STRESS FLUCTUATIONS FOR VARIOUS NOTCH GEOMETRIES, FROM [6.4]

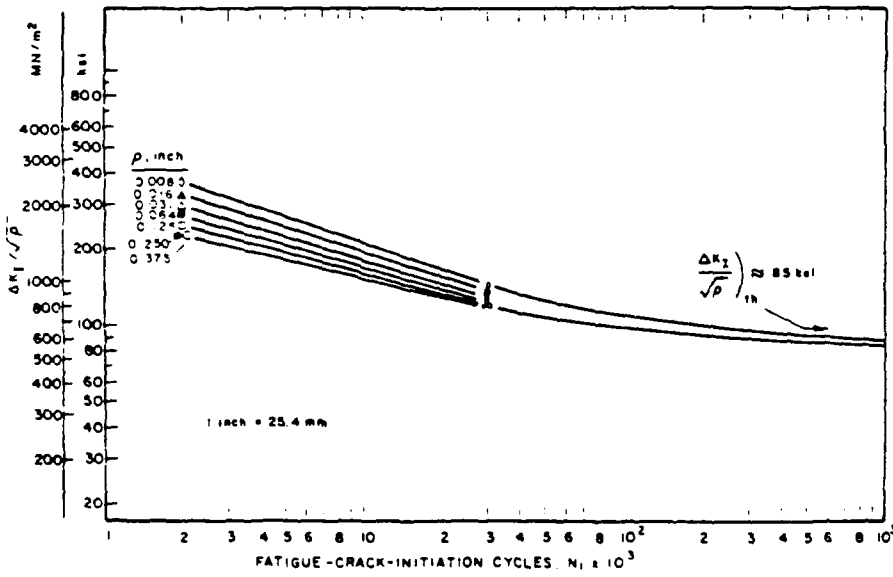


FIGURE 6.5. CORRELATION OF FATIGUE-CRACK INITIATION LIFE WITH THE PARAMETER $\Delta K_1 / \sqrt{\rho}$ FOR HY-130 STEEL, FROM [6.4]

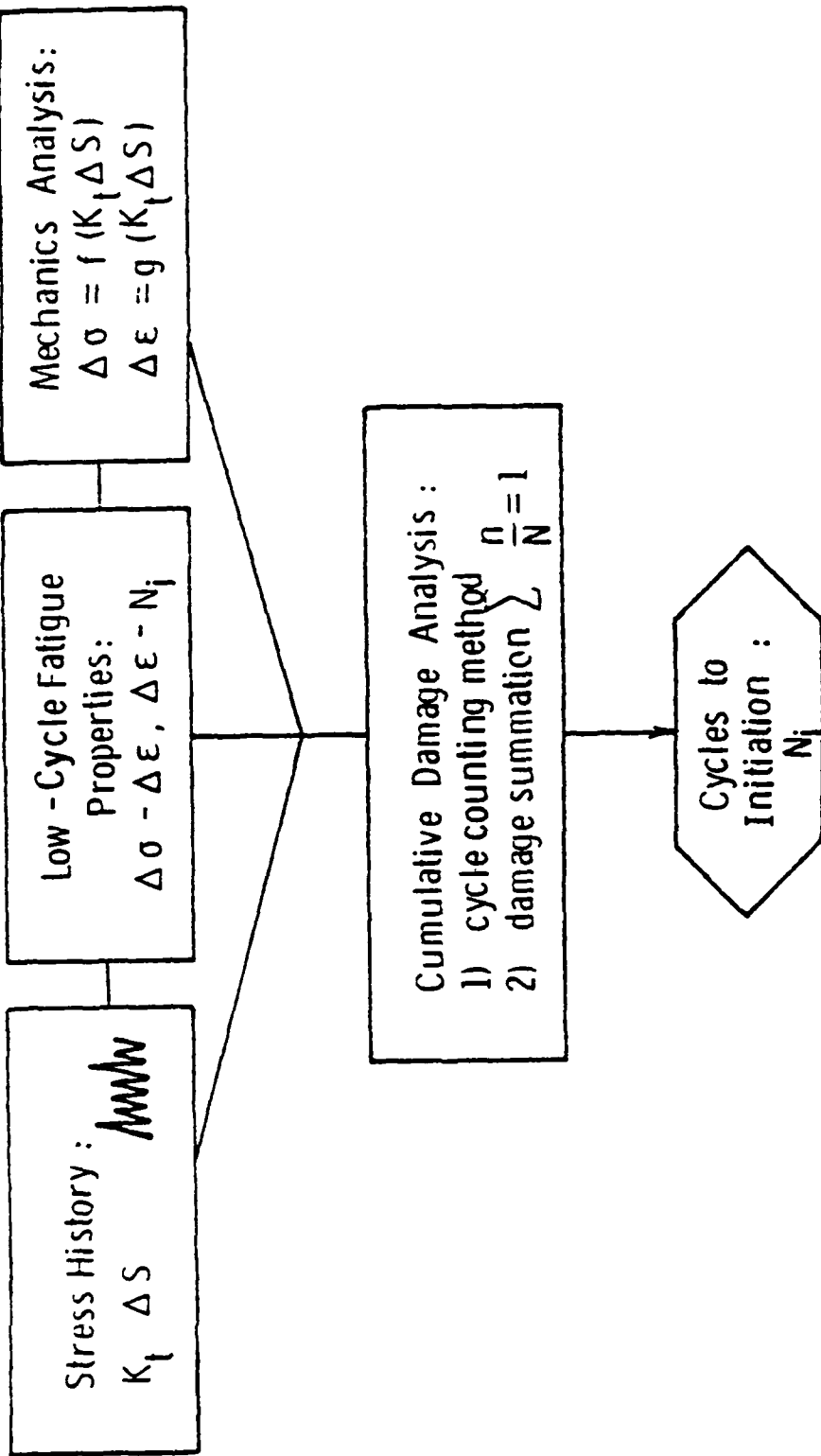


FIGURE 6.6. FLOW CHART OF FATIGUE DAMAGE ANALYSIS FOR CRACK INITIATION

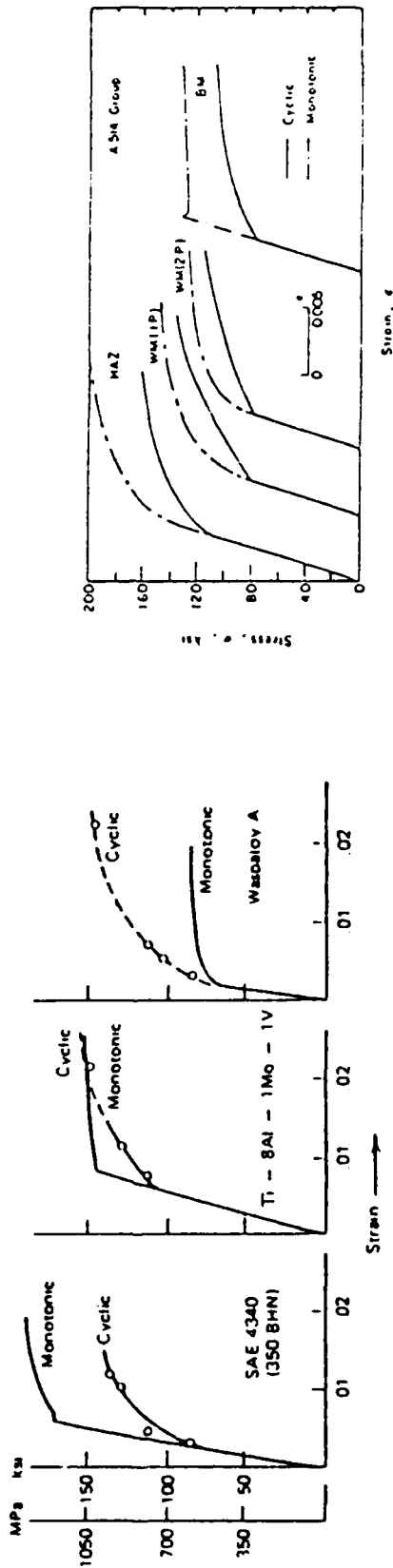
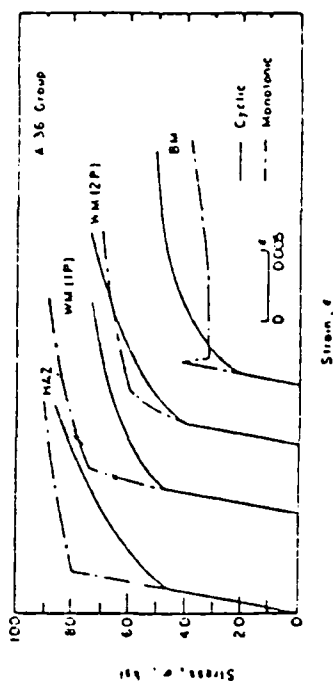
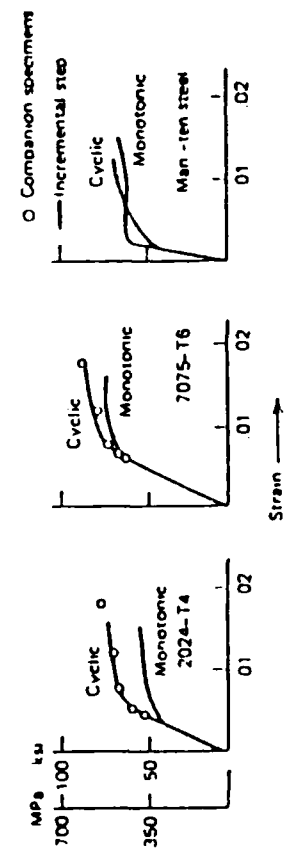


FIGURE 6.7. MONOTONIC AND CYCLIC STRESS-STRAIN CURVES FOR SEVERAL ENGINEERING ALLOYS

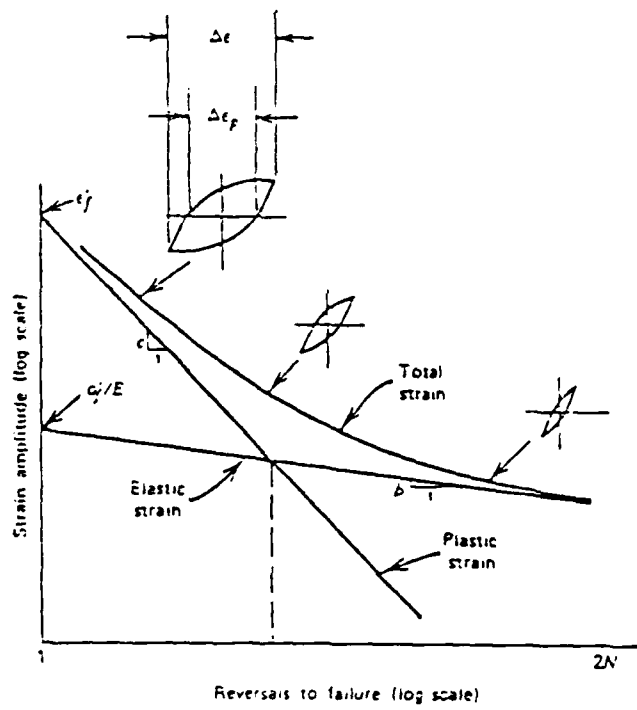


FIGURE 6.8. STRAIN-LIFE CURVES SHOWING TOTAL ELASTIC AND PLASTIC STRAIN COMPONENTS, FROM [6.7]

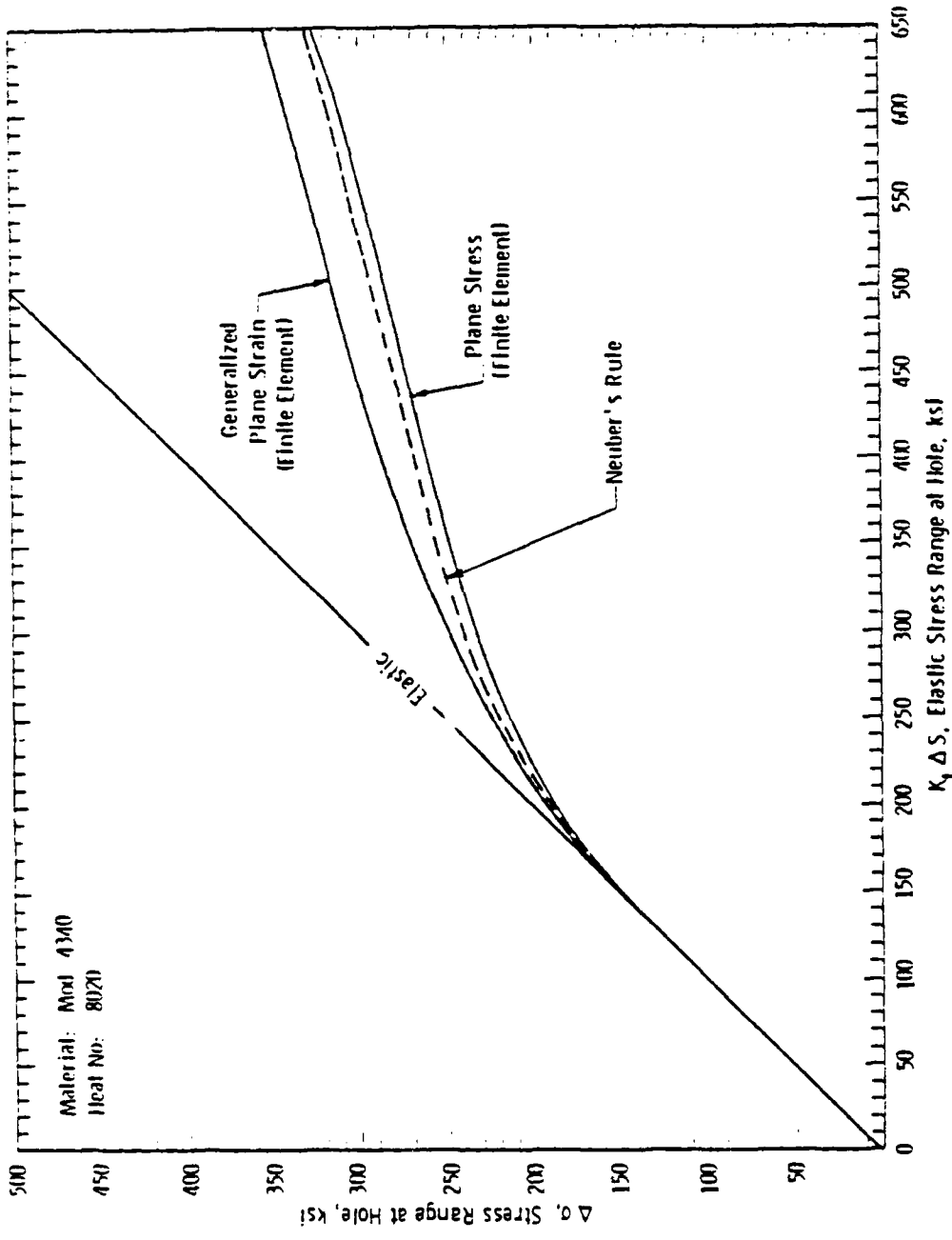


FIGURE 6.9. ACTUAL STRESS RANGE VERSUS ELASTIC STRESS RANGE FOR A HOLE IN A PLATE

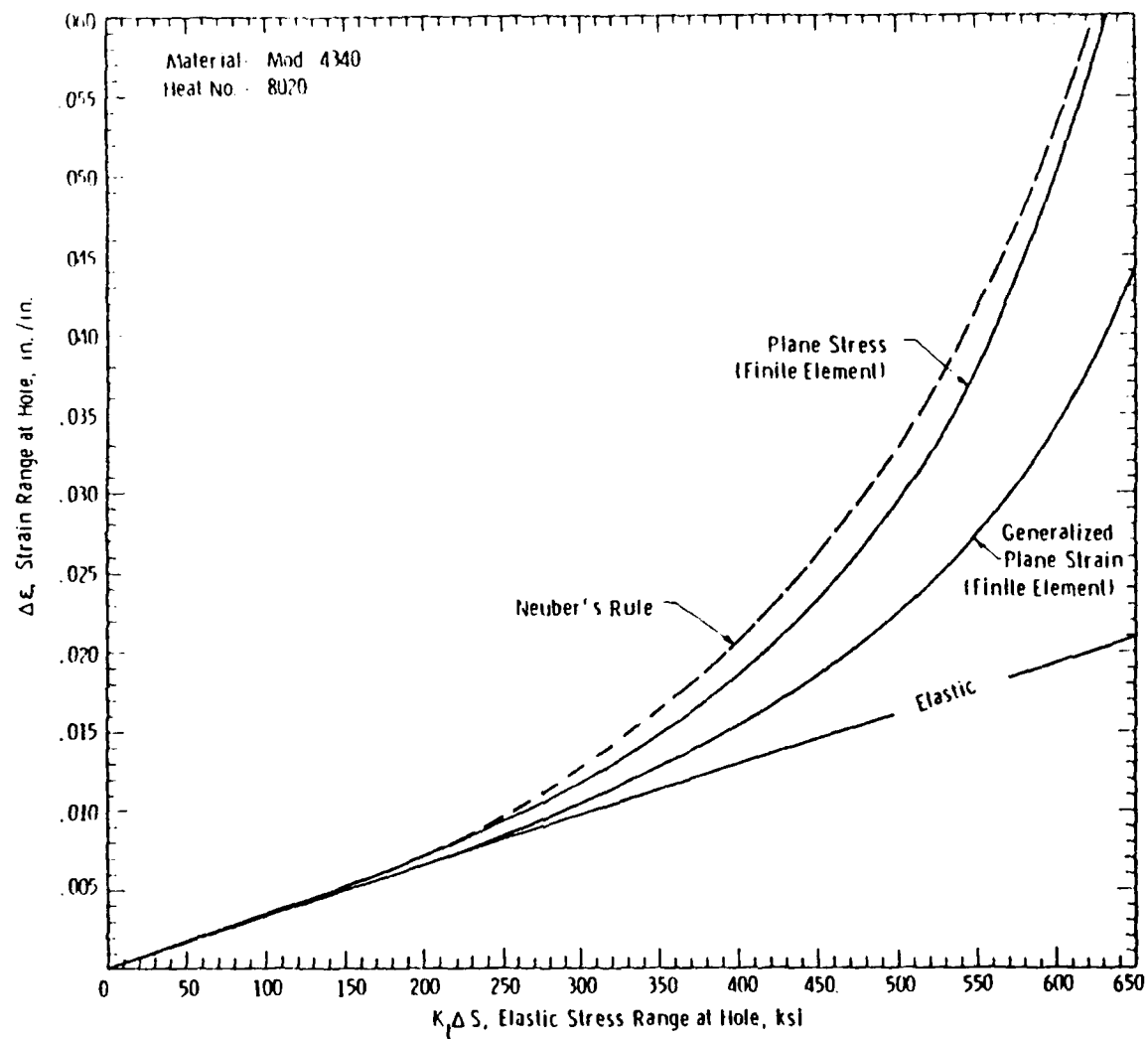


FIGURE 6.10. ACTUAL STRAIN RANGE VERSUS ELASTIC STRESS RANGE FOR A HOLE IN A PLATE

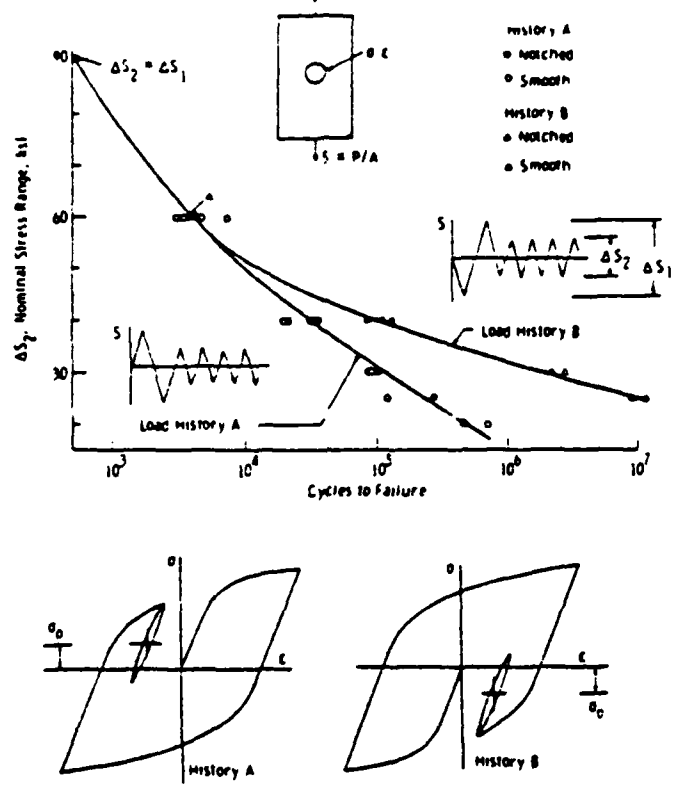


FIGURE 6.11. HISTORY DEPENDENCE OF LOCAL NOTCH MEAN STRESS AND ITS EFFECT ON FATIGUE LIFE

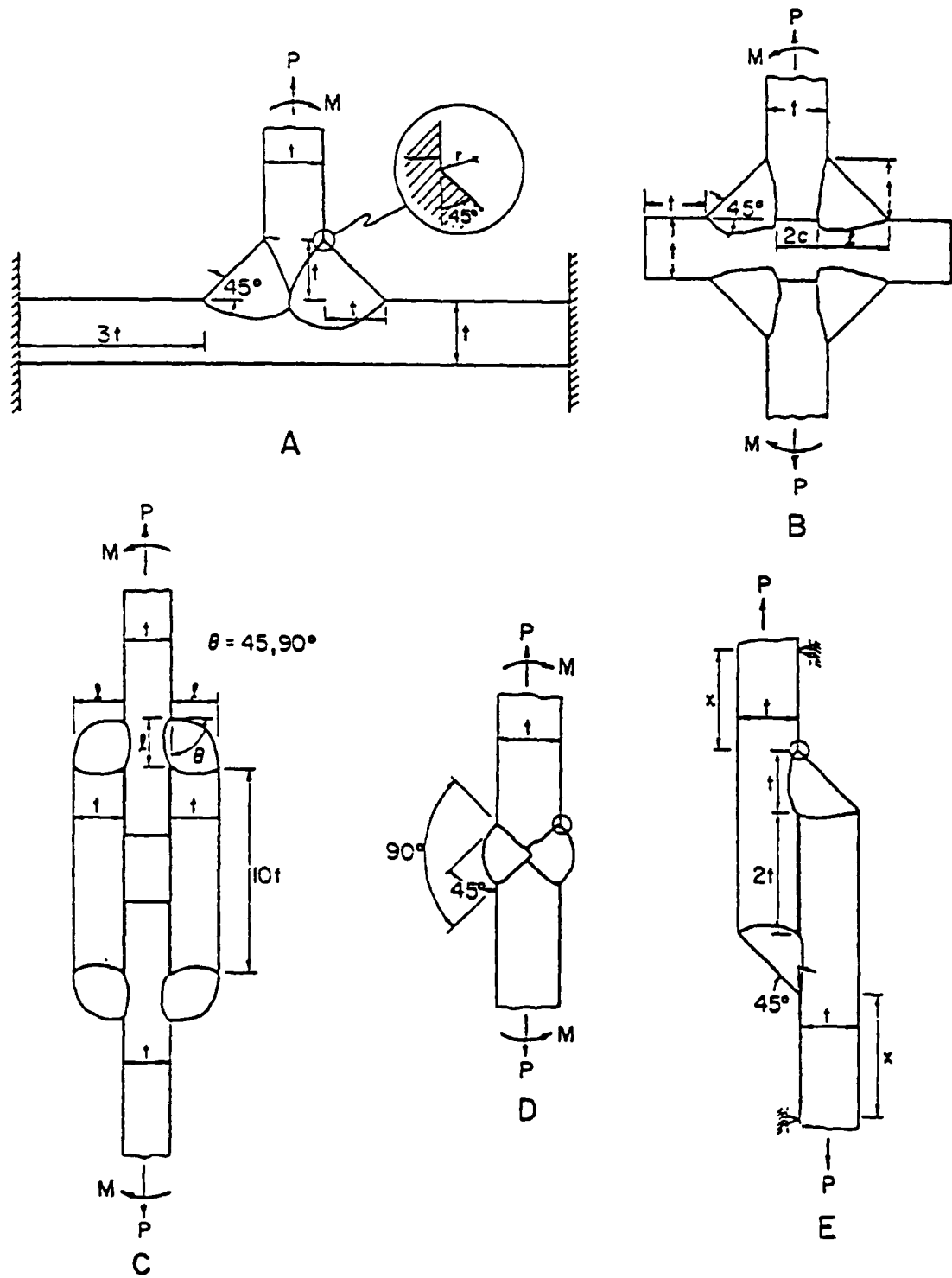


FIGURE 6.12. GEOMETRY OF THE FIVE WELDS ANALYZED, FROM [6.14]

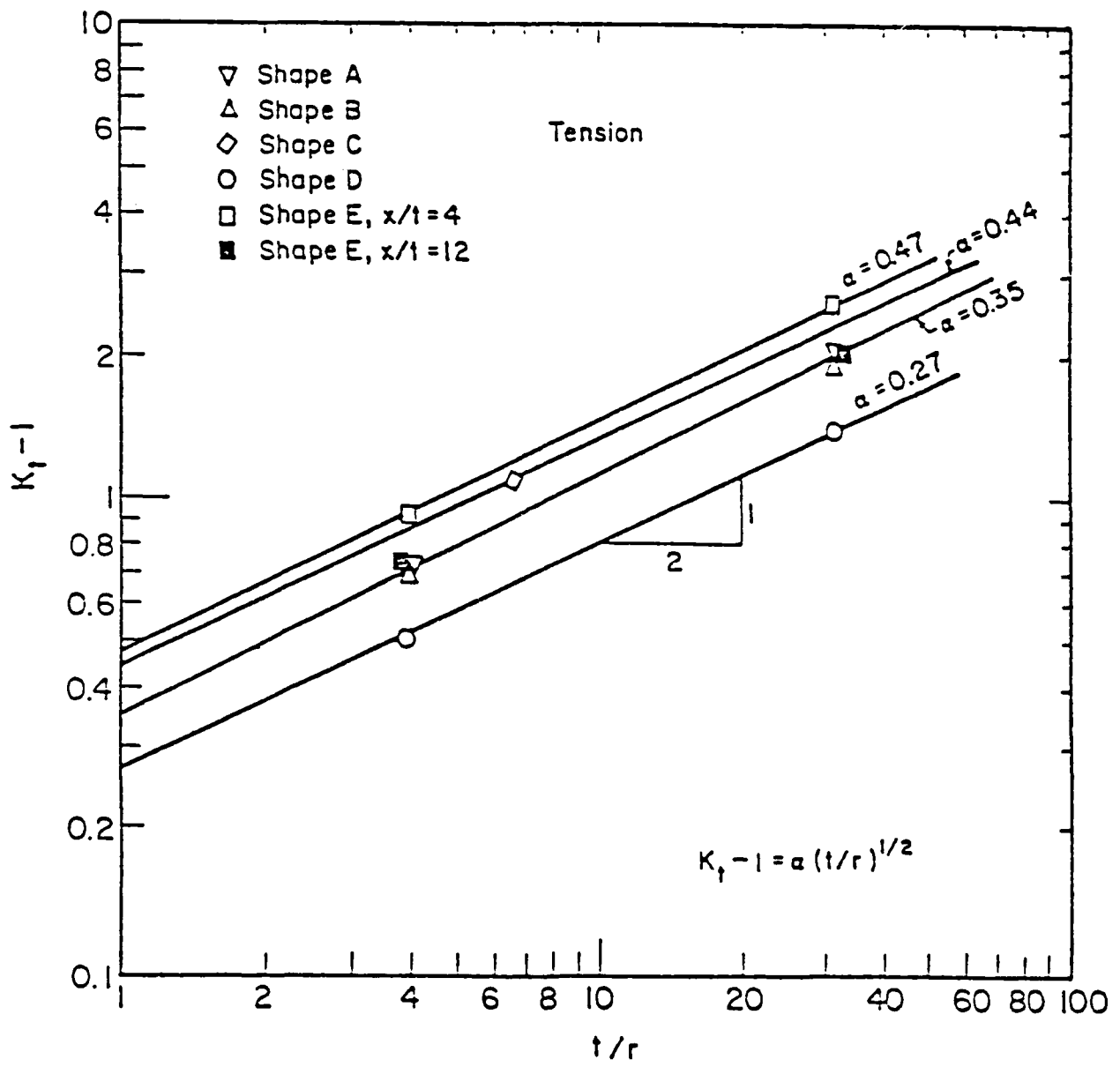


FIGURE 6.13. VARIATION OF $K_t - 1$ WITH t/r FOR THE FIVE WELDS
OF FIGURE 1, FROM [6.14]

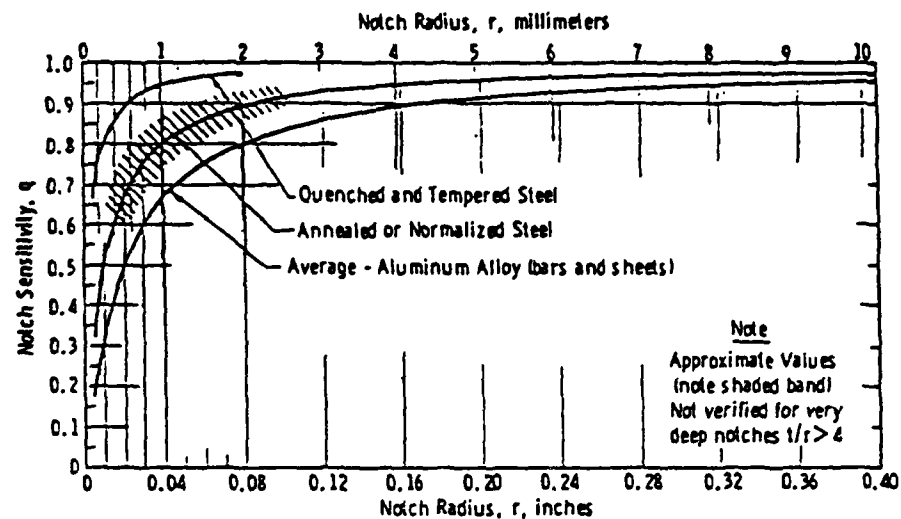


FIGURE 6.14. AVERAGE FATIGUE NOTCH SENSITIVITY,
FROM [6.16]

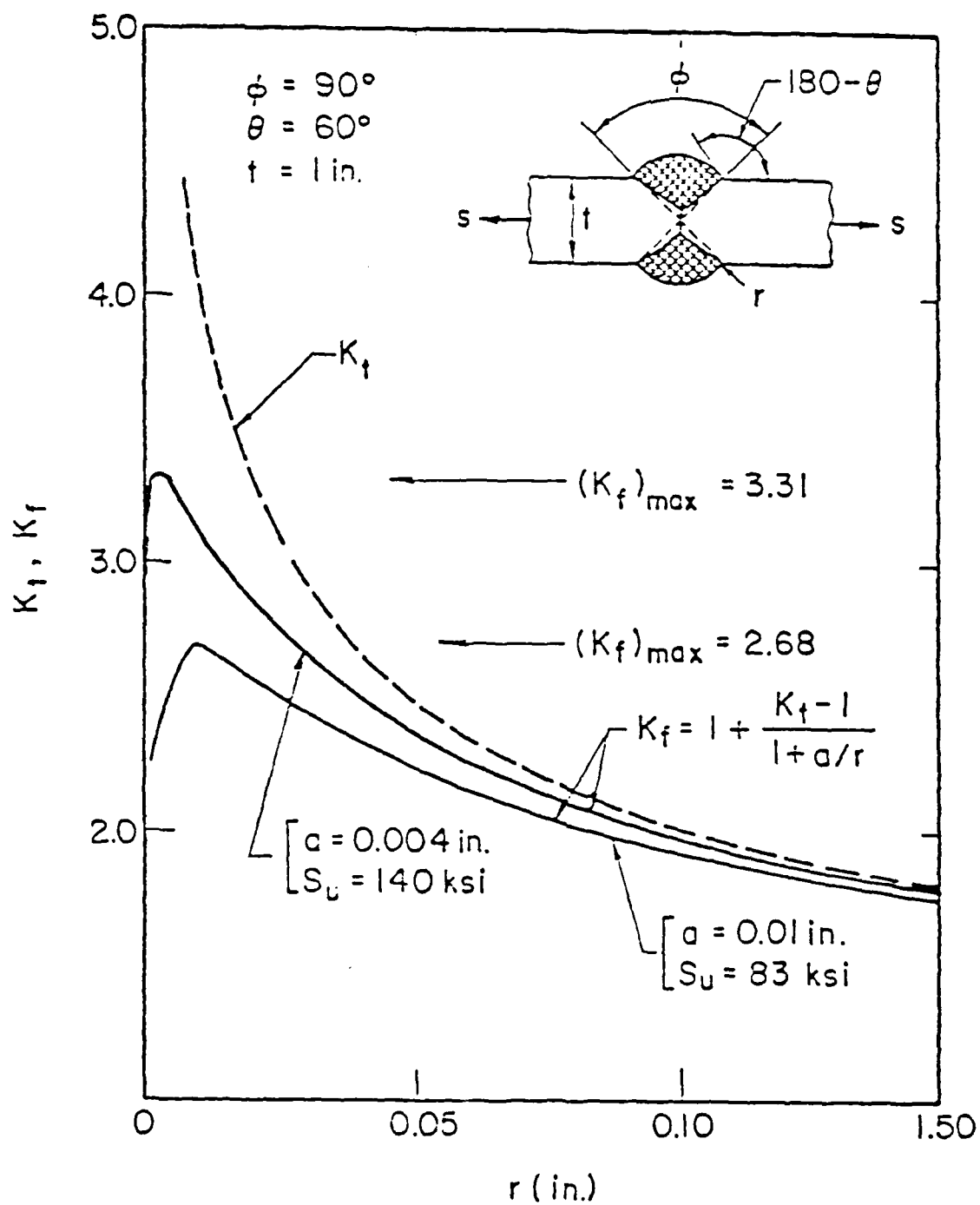


FIGURE 6.15. VARIATION OF $K_{f\max}$ WITH STRENGTH LEVEL (S_u) AND CONSEQUENT CHANGES IN THE MATERIAL PARAMETER a , FROM [6.14]

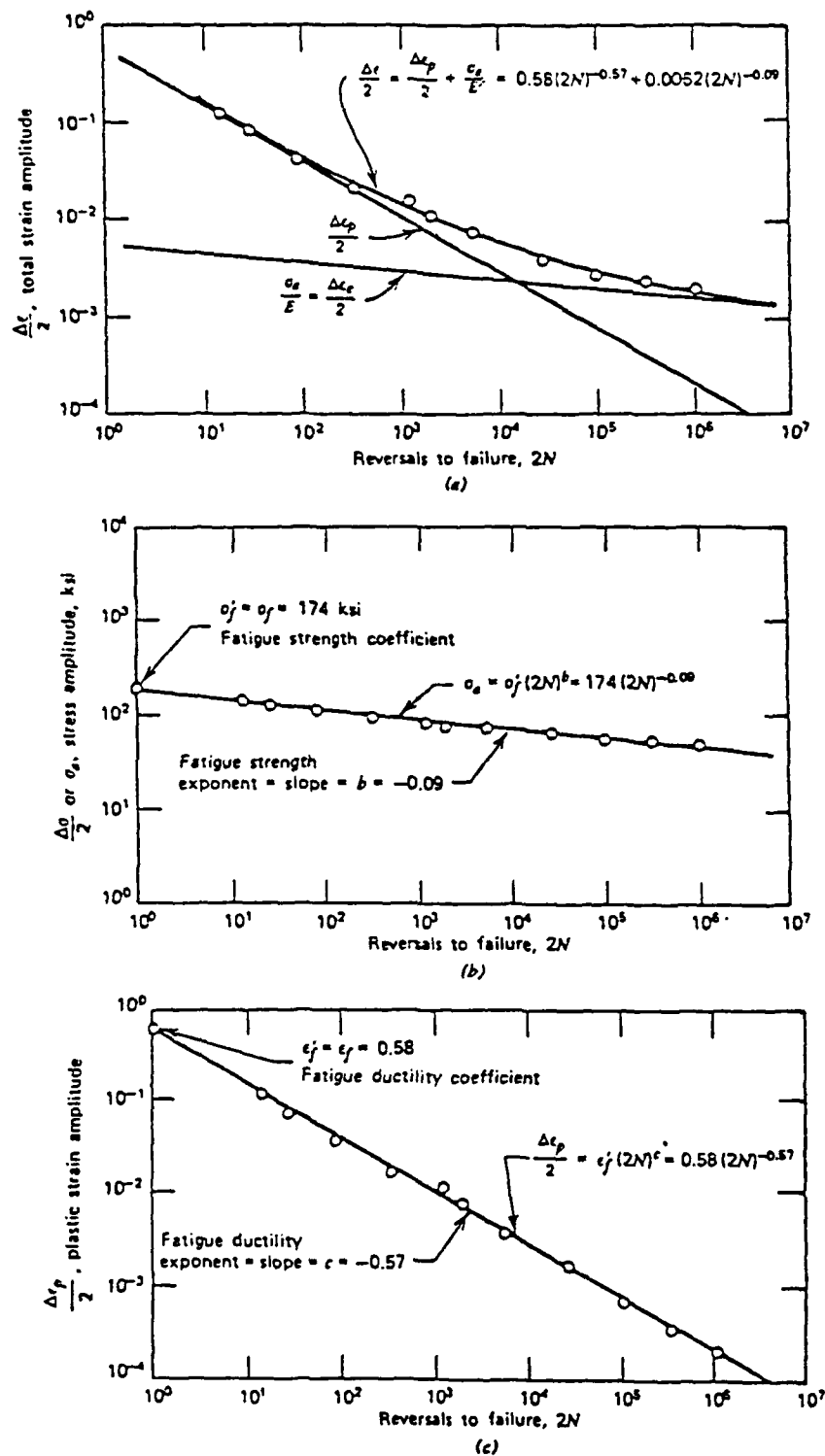


FIGURE 6.16. LOW-CYCLE FATIGUE BEHAVIOR OF ANNEALED 4340 STEEL.
 (a) TOTAL STRAIN AMPLITUDE, (b) ELASTIC STRAIN AMPLITUDE $\frac{\Delta\varepsilon}{2}$,
 (c) PLASTIC STRAIN AMPLITUDE, FROM [6.7]

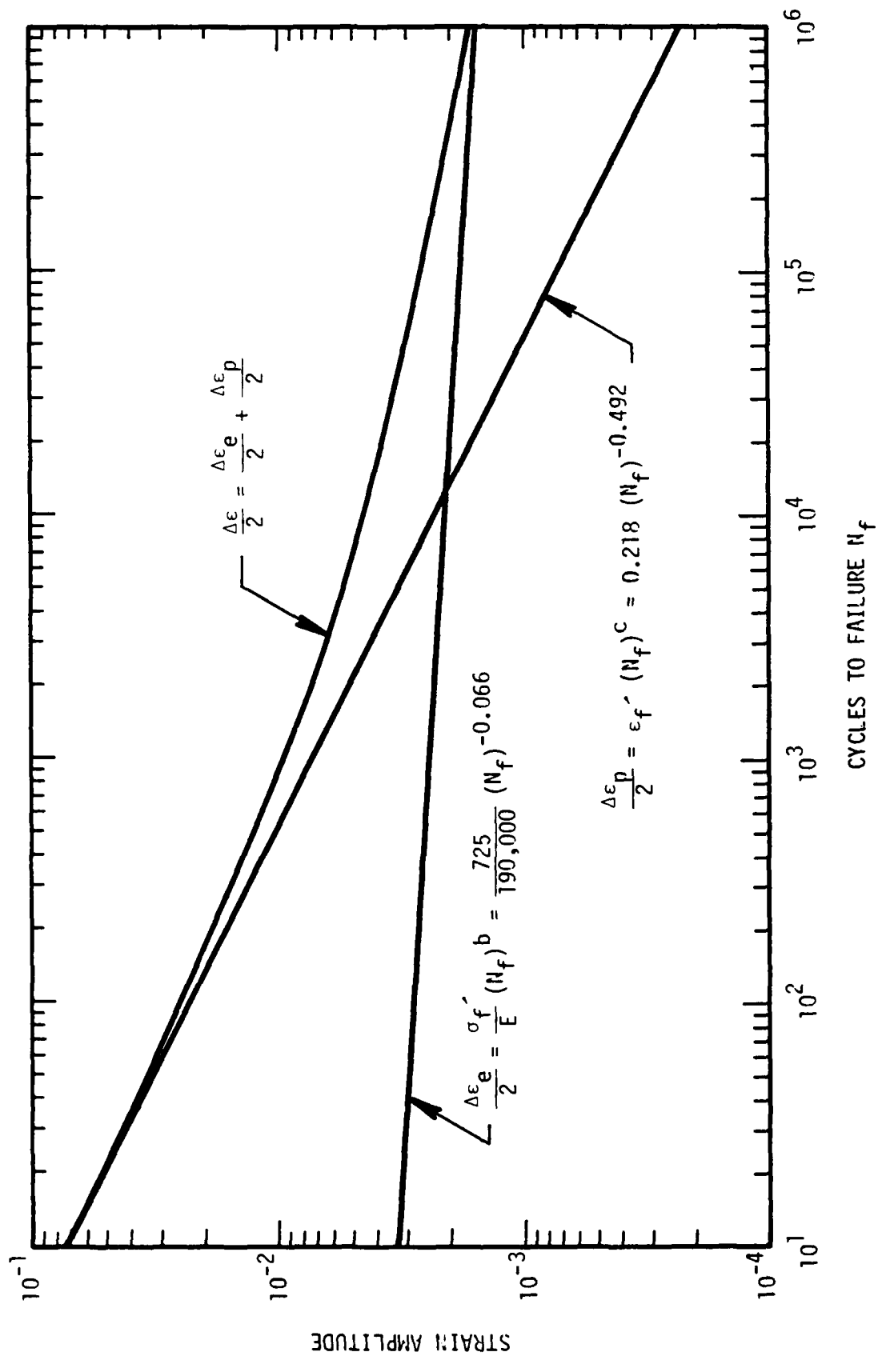


FIGURE 6.17. STRAIN CONTROLLED FATIGUE BEHAVIOR ON A36 HAZ METAL

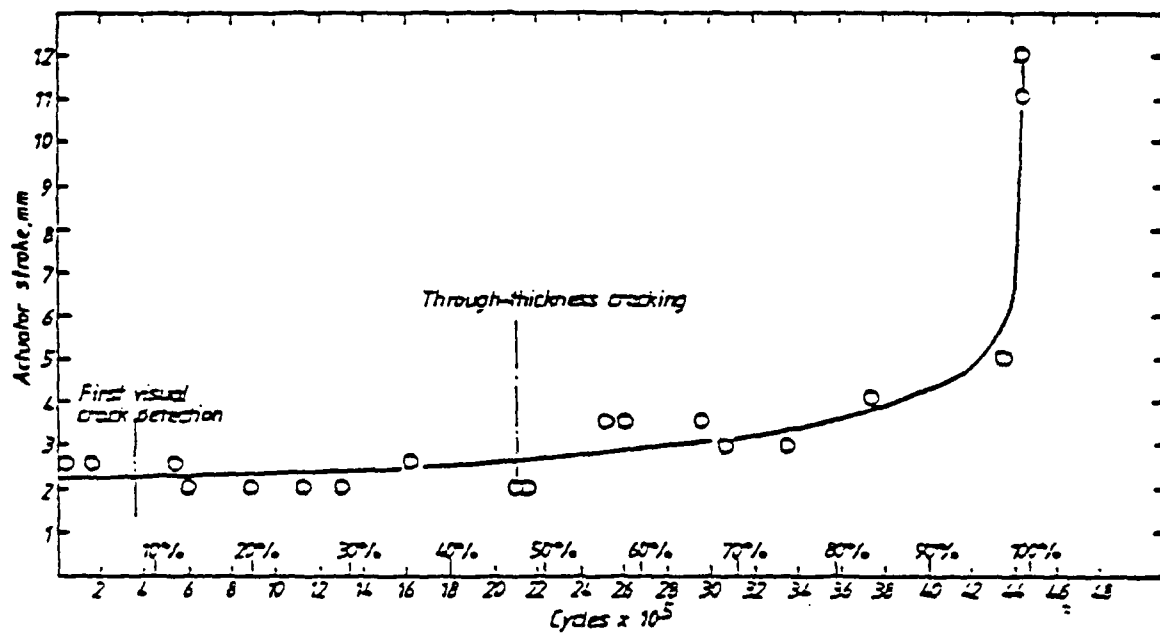


FIGURE 6.18. ACTUATOR DISPLACEMENT VERSUS CYCLES ON 168-mm T-JOINT SUBJECTED TO OUT-OF-PLANE BENDING. NOTE THAT CRACK INITIATION OCCURRED AT LESS THAN 10% OF THE TOTAL NUMBER OF CYCLES REQUIRED FOR FAILURE, FROM [6.25]

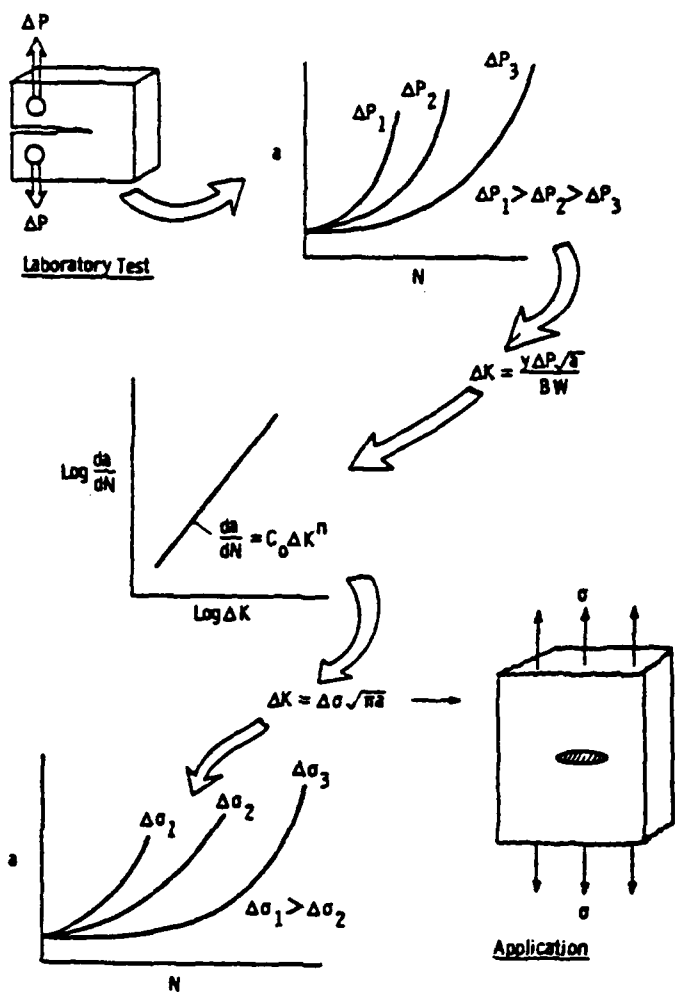


FIGURE 6.19. SCHEMATIC ILLUSTRATION OF THE USE OF FRACTURE-MECHANICS TECHNOLOGY IN THE DESIGN AGAINST FATIGUE FAILURE,
FROM [6.22]

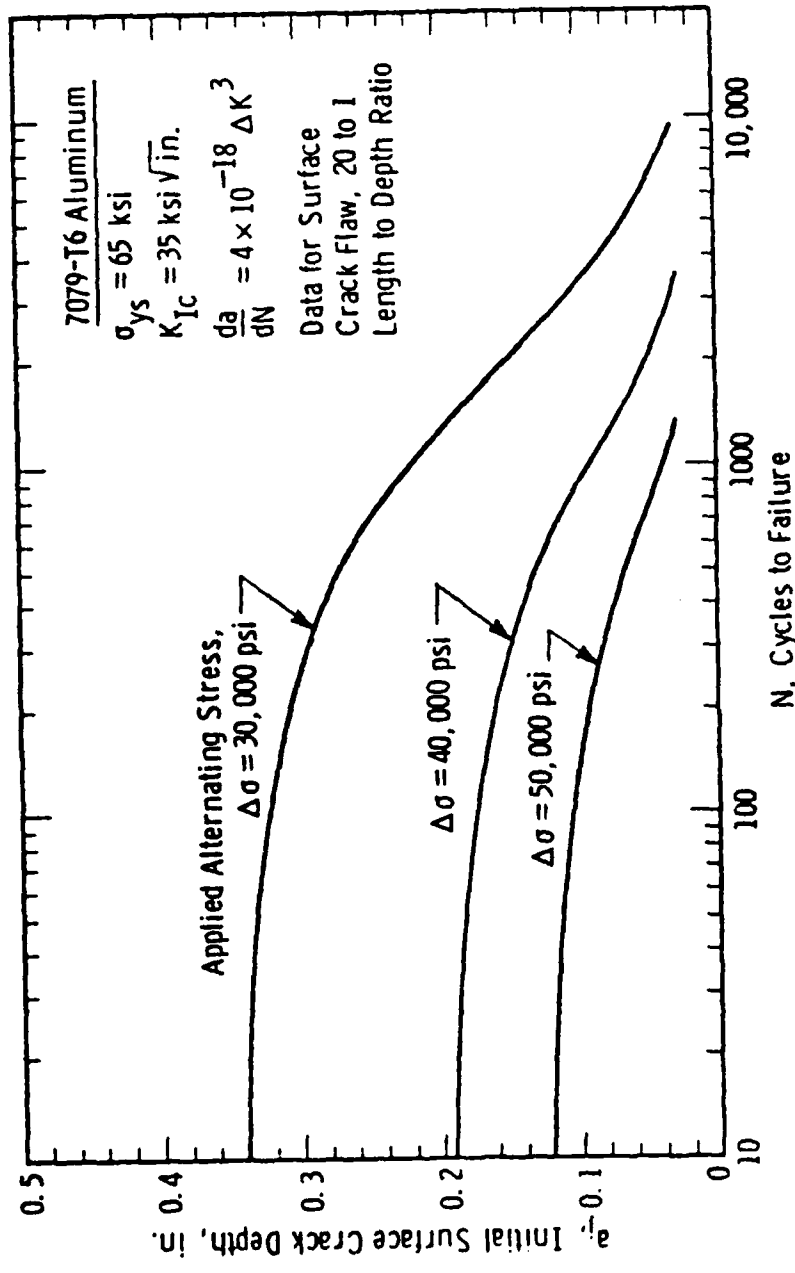


FIGURE 6.20. PARAMETRIC REPRESENTATION OF RESULTS FROM FRACTURE-MECHANICS FATIGUE CRACK GROWTH ANALYSIS SHOWING INFLUENCE OF APPLIED STRESS RANGE

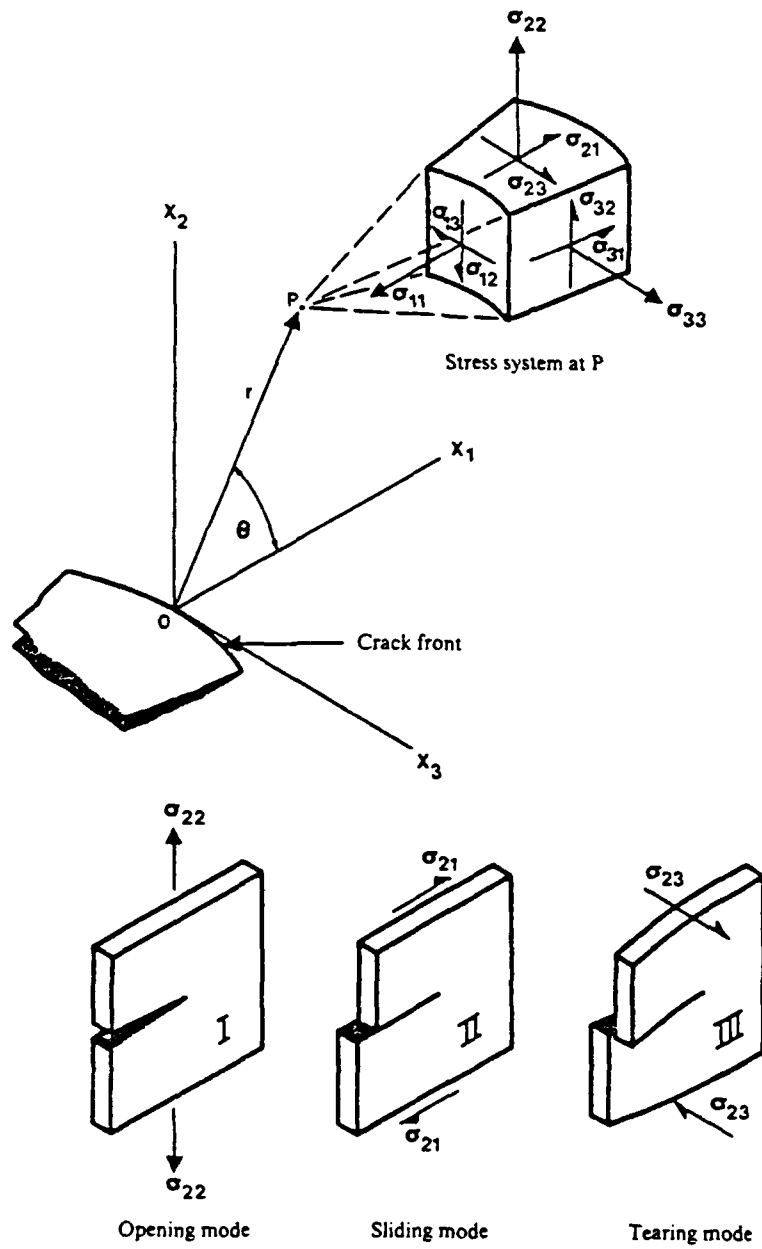


FIGURE 6.21. CRACK COORDINATE SYSTEM AND MODES OF DEFORMATION, FROM [6.29]

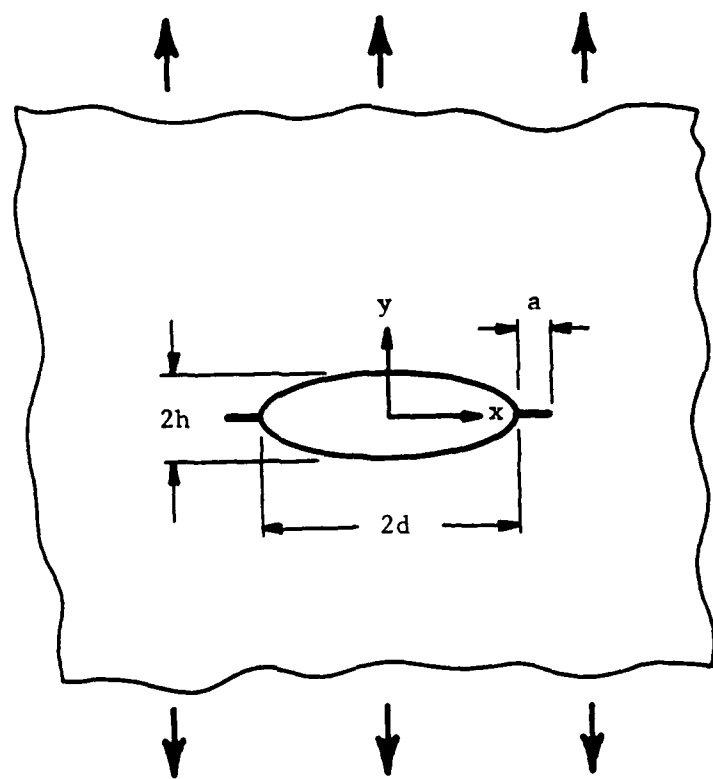


FIGURE 6.22. ELLIPTICAL HOLE SUBJECTED TO A TENSION LOAD

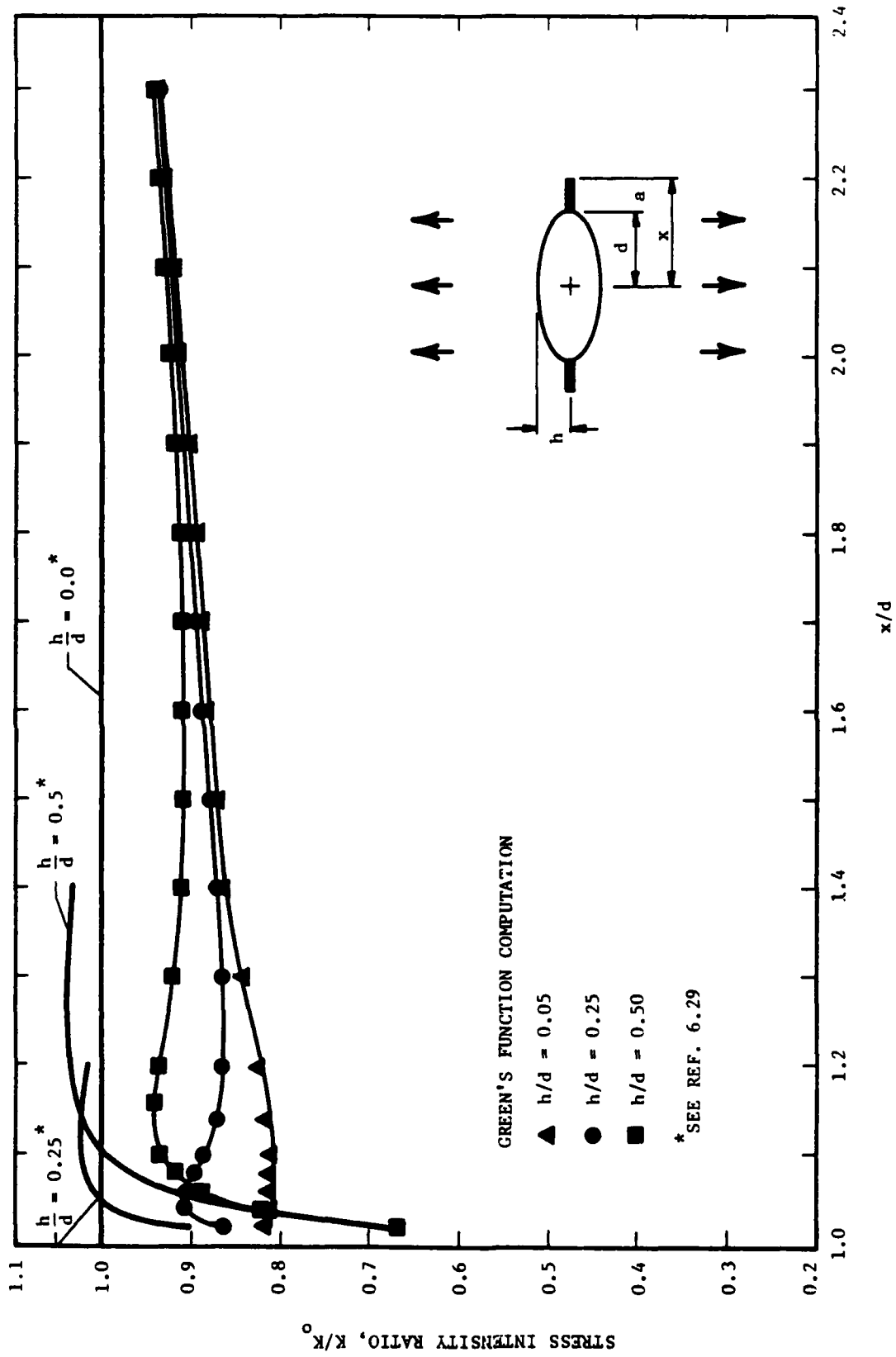


FIGURE 6.23. COMPARISON OF STRESS INTENSITY VALUES FOR $(h/d) = 0.05, 0.25, \text{ AND } 0.5$

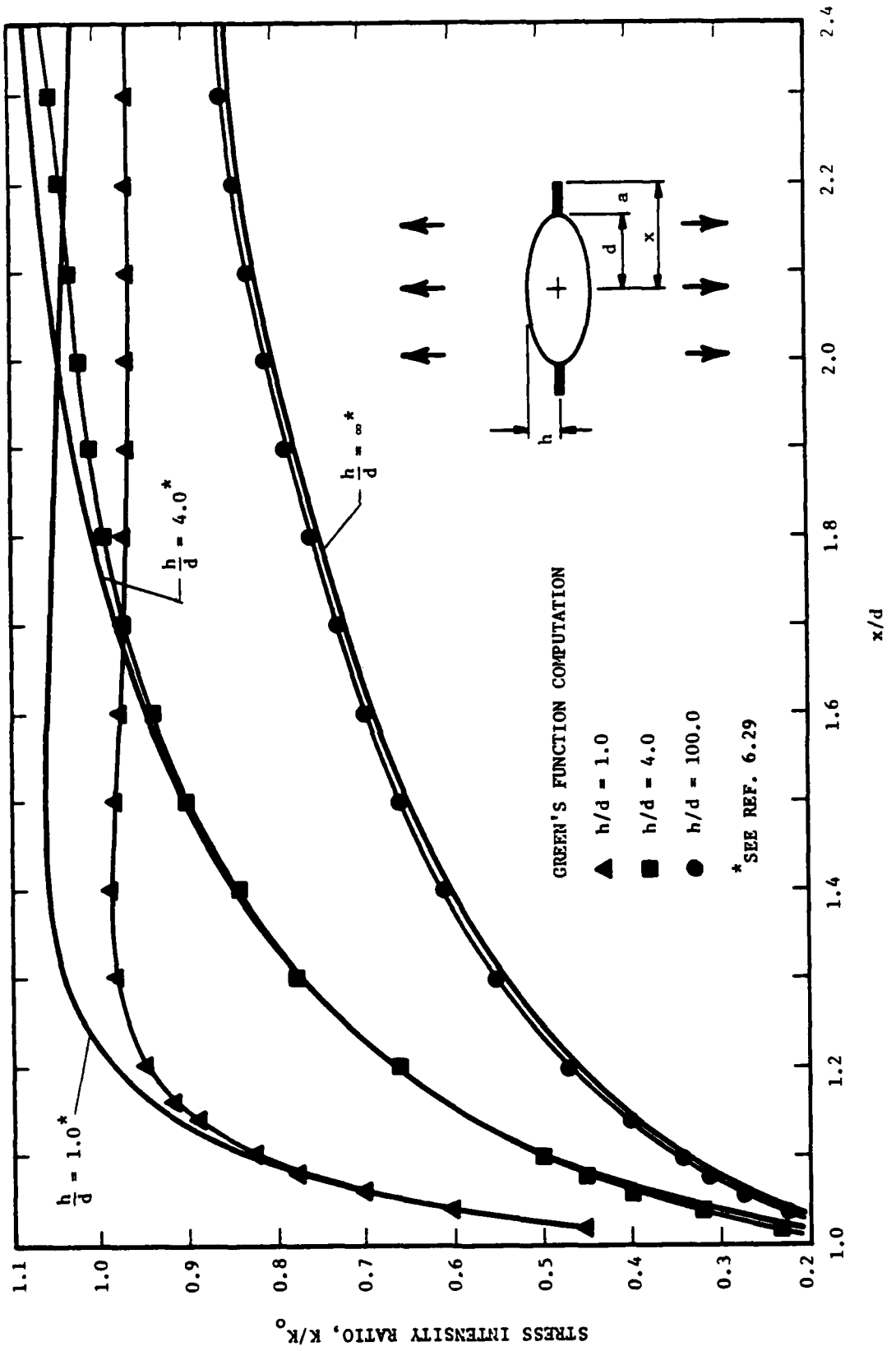


FIGURE 6.24. COMPARISON OF STRESS INTENSITY VALUES FOR $(h/d) = 1.0, 4.0$, AND 100.0

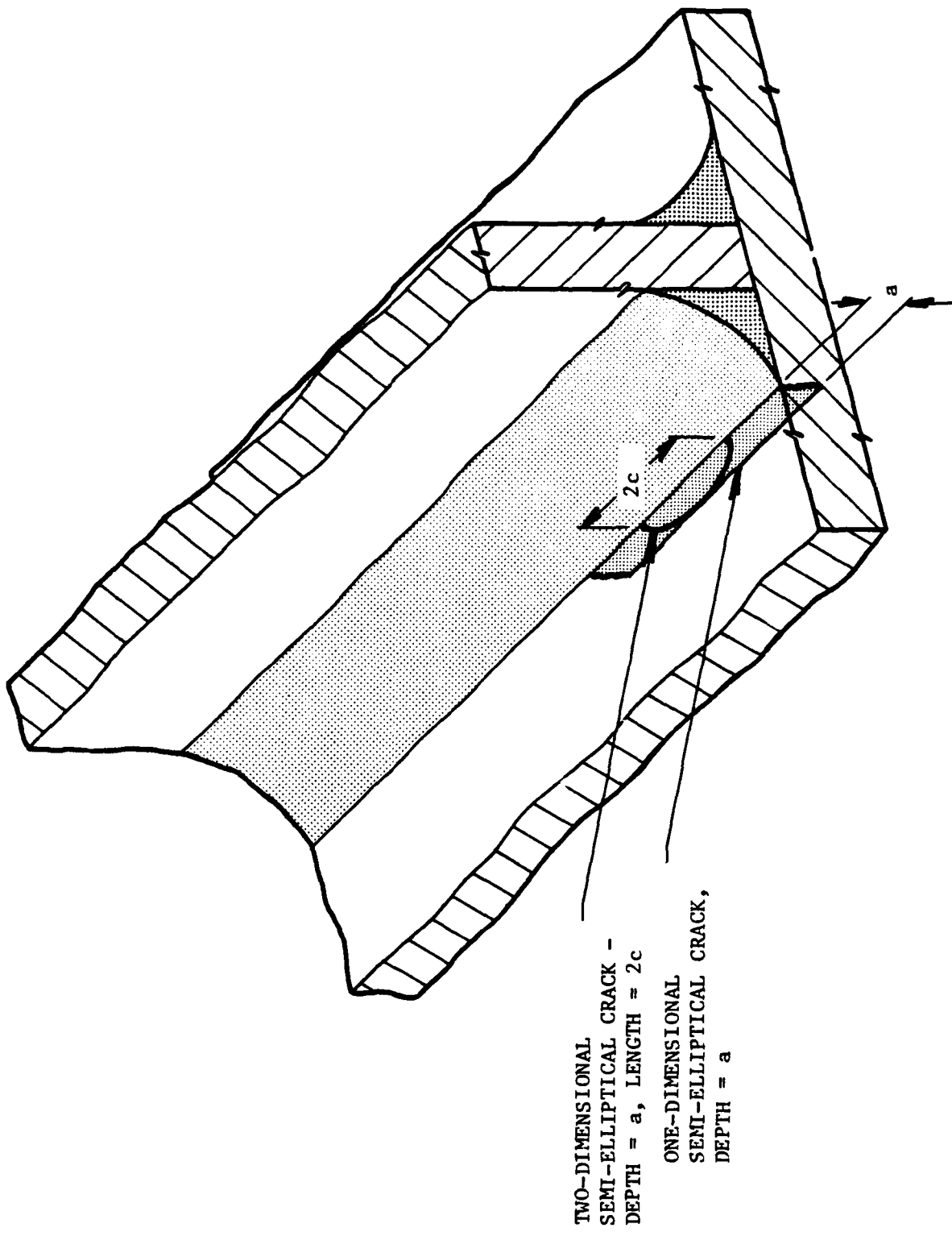


FIGURE 6.25. REPRESENTATIONS OF ONE- AND TWO-DIMENSIONAL CRACKS
AT THE TOE OF A WELDED PLANAR T-JOINT

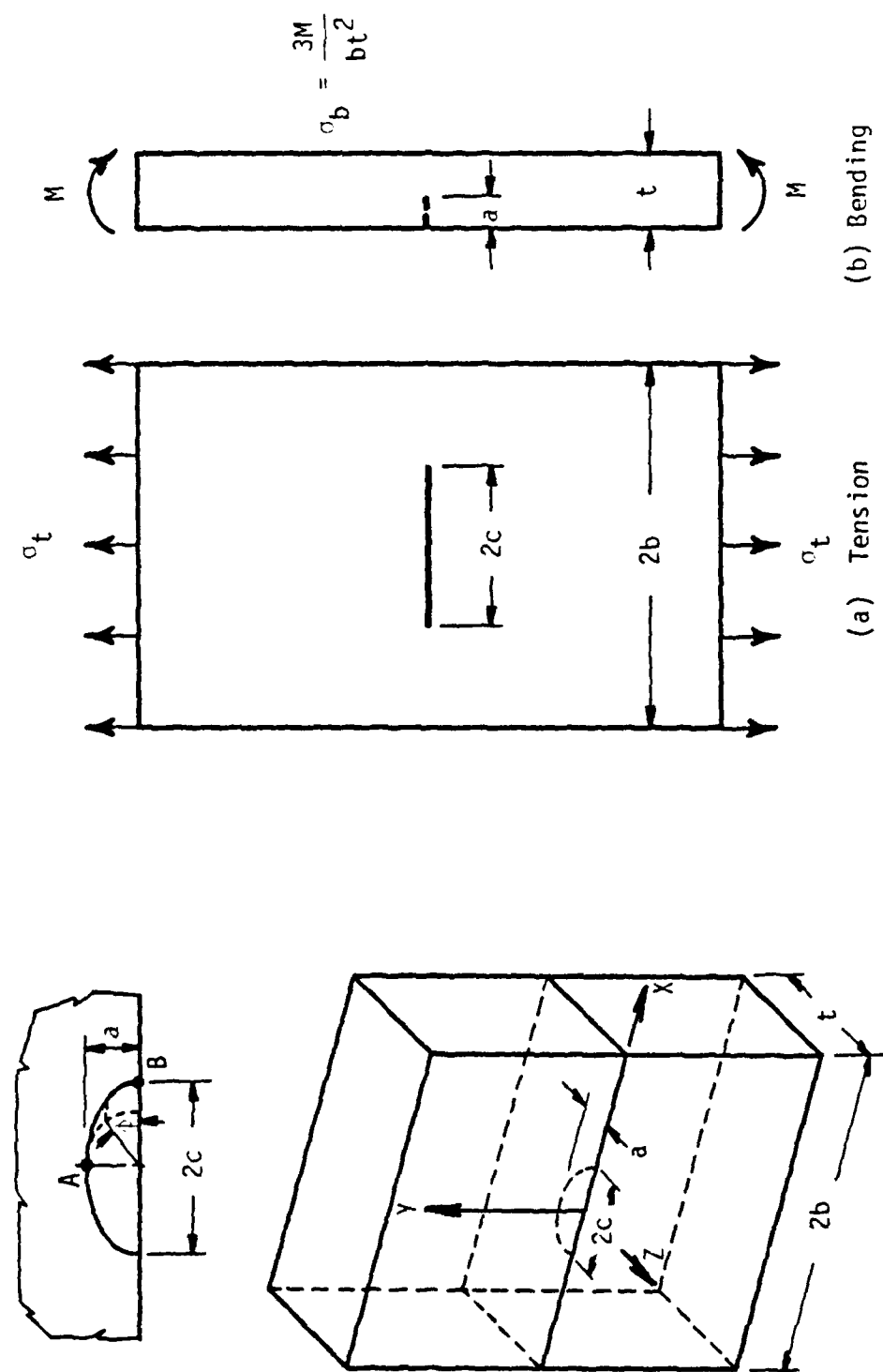


FIGURE 6.27. SURFACE-CRACKED PLATE SUBJECTED TO TENSION OR BENDING LOADS

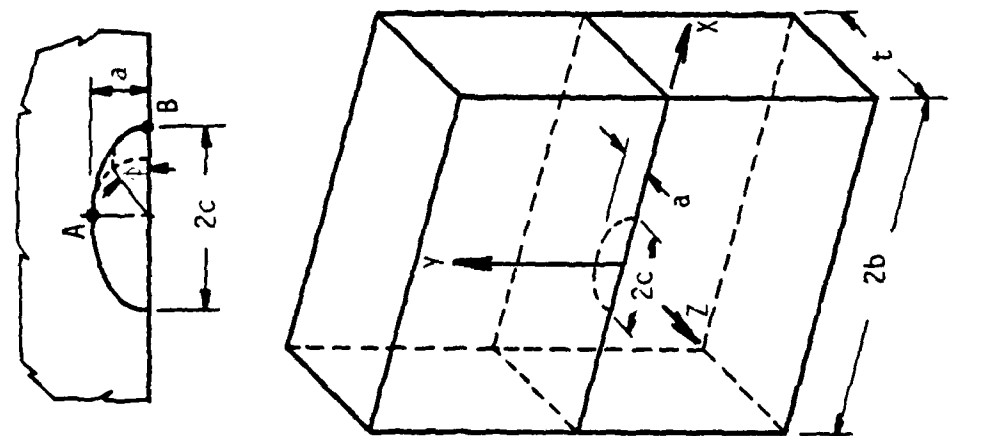


FIGURE 6.26. SURFACE CRACK IN A FINITE PLATE

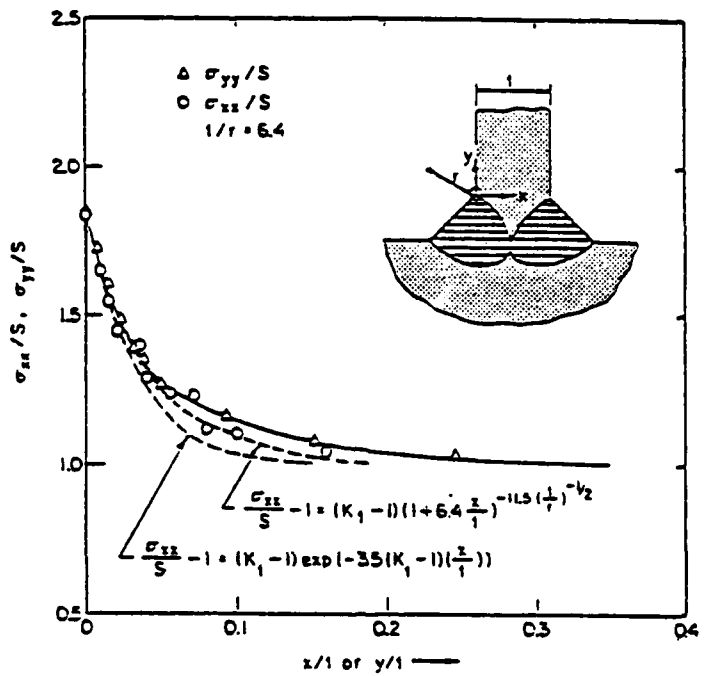


FIGURE 6.28. VARIATION OF STRESS WITH DISTANCE AWAY FROM THE WELD TOE (σ_{yy}/S) AND DISTANCE INWARD ALONG THE PATH THE FATIGUE CRACK WILL FOLLOW (σ_{xx}/S).

(Two mathematical approximations to the finite element stress analysis results are indicated, from [6.14].)

7.0 ANALYTICAL AND EXPERIMENTAL STUDIES RELATED TO FATIGUE LIFE IN WELDED JOINTS

7.1 Introduction

The preceding chapters have formed a framework for predictions of fatigue crack initiation and propagation life in welded joints. One central issue, at least as far as crack propagation calculations are concerned, is the availability of crack growth data for relevant growth rates, and loading and environmental variables discussed in Chapter 3.0.

Chapter 6.0 reviewed computational methodologies for fatigue life assessment and proposed analytical procedures for estimating both crack initiation and growth in welded joints. This chapter applies these procedures, along with available material data, to make fatigue predictions of welded joints in air and seawater and compares the results with experimental tests. As such, this chapter may be considered a validation of the materials' data and the analysis methodologies. Consequently, those instances where analysis and tests indicate poor correlation serve to indicate where additional data or refinements in the analytical procedures may be warranted.

This chapter also evaluates the sensitivity of various parameters in the crack initiation and propagation models. For most of the important variables, e.g., material parameters, load ratio, and environment, their sensitivities to fatigue life are discussed in Sections 7.2-7.4. However, the significance of initial and final crack lengths and crack shape is addressed separately in Section 7.5. Section 7.6 discusses the application of the two-dimensional crack model to tubular joints.

7.2 Crack Initiation and Propagation of Welded Joints in Air

7.2.1 Crack Initiation

The procedures for calculating crack initiation life based on the local strain approach were outlined in Sections 6.4-6.5. The methodology required details of the weld geometry, mode of loading, and materials' cyclic stress- and strain-life properties. To verify the crack initiation analysis, a series of computations was conducted and compared with experimental data. Figure 7.1 shows a set of initiation and propagation calculations and test results for a cruciform joint in tension. The experiments were conducted by Booth [7.1] as part of the UK Offshore Steels Research Program (UKOSRP).

With respect to crack initiation, Figure 7.1 shows that the analysis grossly overpredicts fatigue life in the high-cycle regime, while below about 5×10^3 cycles, crack initiation accounts for about 10 percent of the total life. This percentage is often quoted as the ratio of initiation to total life in a welded structure, and the effect can be seen in Figure 6.18 for a tubular joint.

The material property data for this set of initiation calculations was for the A36 Heat-Affected Zone (HAZ) steel given in Table 6.6. The chemical compositions and mechanical properties for A36 steel (Table 7.1) are similar to those of BS4360 Grade 50D steel used in the UKOSRP tests. No information was available on the strain life properties of BS4360 steel. Obviously, one reason why the initiation lives in Figure 7.1 are overpredicted in the high-cycle regime could be nonrepresentative strain life data. Other sources of data were found from Japanese research work on crack initiation in welded joints. Reference 7.2 summarizes results on joints made of two grades of structural steels designated as SM41 and HT60. Chemical compositions and mechanical properties are given in Table 7.1, and Figure 7.2 shows the cyclic stress-strain properties and strain-life behavior of these base metals. Note that the results in Figure 7.2 account for mean stress in the low-, intermediate-, and high-cycle life regimes. For HT60 steel, estimates of the properties required for crack initiation calculations were made from the slopes and intercepts of the curves in Figure 7.2 and are summarized in Table 7.3. Strain life data were found for SM41 in Reference 7.3 and are presented in Table 7.2.

Crack initiation fatigue tests were also conducted as part of the Japanese study on machined and welded cruciform specimens of the type shown in Figure 7.3(a). Initiation was defined when the crack depth reached 0.2 mm as observed by a 50 magnification microscope. Figure 7.3(b,c) shows the experimental data for various weld profile angles. The set of data for $\beta = 45$ degrees was chosen to compare with analytical predictions. Reference 7.2 defines $K_t(\text{eff})$, an effective stress concentration factor, as the average K_t in the vicinity of the weld toe notch. The value of $K_t(\text{eff})$ given in Reference 7.2 for $\alpha = 45$ degree joint is

$$K_t(\text{eff}) = 3.34 \quad \text{SM41 Steel} \quad (7.1)$$

$$K_t(\text{eff}) = 4.31 \quad \text{HT60 Steel}$$

The fatigue strength reduction factor given by equation (6.14) for a welded joint is

$$K_{f\max} = 1 + \frac{\alpha}{2} \left(\frac{t}{a_m} \right)^{1/2} \quad (7.2)$$

Using

$$\alpha = 0.35 \text{ for a cruciform joint in tension}$$

$$t = 50 \text{ mm}$$

$$a_m = 0.28 \text{ mm, SM41 Weld Metal}$$

$$a_m = 0.20 \text{ mm, HT60 Weld Metal}$$

gives

$$K_{f\max} = 3.34, \quad \text{SM41 Weld Metal}$$

$$K_{f\max} = 3.77, \quad \text{HT60 Weld Metal}$$

The values of $K_{f\max}$ agree exactly with the value of $K_t(\text{eff})$ given in Reference 7.2 for the SM41 Steel and are slightly less than $K_t(\text{eff}) = 4.31$ for the HT60 material. Therefore, the initiation calculations will take $K_{f\max} = K_t(\text{eff})$.

Figure 7.4 compares test results with analytical predictions using properties of A36HAZ material given in Reference 6.13 and SM41 steel from Reference 7.3. When computations were made using the revised properties, excellent analytical and experimental correlation was obtained, as shown in Figure 7.4 with the SM41 data curve with the (o) symbol. These calculations illustrate the sensitivity of initiation predictions in the high-cycle regime to the fatigue strength coefficient σ_f' and fatigue strength exponent b . As an example, let us consider Figure 7.5. The elastic and plastic components of the strain-life curve are plotted for the A36HAZ and SM41 materials. The plastic components given by

$$\frac{\Delta \epsilon_p}{2} = \epsilon_f' (2N_f)^c \quad (7.3)$$

agree very closely, while the elastic components

$$\frac{\Delta \varepsilon_e}{2} = \frac{\sigma_f}{E} (2N_f)^b \quad (7.4)$$

diverge for high-cycle fatigue. Small differences in the values of σ_f and b , which are related to the intercept and slope of the elastic component, can result in large differences in the high-cycle fatigue life.

To judge the initiation sensitivity for a higher strength steel, a comparison of calculations and test results was made for A514 and HT60 steels. Chemical compositions and mechanical properties are shown in Table 7.1. Figure 7.6 again illustrates the sensitivity of initiation life in the high-cycle region to the strain-life parameters, which are given in Table 7.3. The constants used in the analysis for HT60 steel were not explicitly given in Reference 7.2, but were estimated from Figure 7.3. Good correlation in the high-cycle region was found with experimental tests. However, because of fatigue life to the strain-life parameters, graphical estimates of the strain-life parameters for high-cycle fatigue should be made with caution since they can lead to large errors in initiation life predictions.

A set of initiation calculations was made for the axially loaded cruciform joint of Figure 7.1 with the revised SM41 material data from Reference [7.3]. The resulting S-N curve, Figure 7.7, shows that the initiation life is greatly reduced, but the analysis still overpredicts life for $N > 5 \times 10^5$ cycles. Predictions were also made for a 38-mm thick cruciform joint under bending at low and high R and compared with tests in Figures 7.8 and 7.9. For crack initiation at low R the mean stress was taken as zero in equation (6.19). For high R, a mean stress equal to the material's yield value ($\sigma_0 = 345$ MPa) was assumed. In Figure 7.8, the last experimental data point is a runout at 7×10^6 cycles and falls close to the predicted propagation curves. Predictions at high R are shown in Figure 7.9, and the propagation curve lies well below the runout point. The extremely conservative crack propagation predictions at high R are a consequence of the choice of crack growth curve given in Figure 3.25 for the low-growth region.

The comparisons of initiation calculations and experimental tests for the case studied in Figures 7.7-7.9 clearly show that below about 1×10^4 cycles initiation life constitutes only about 10 percent of the total life of the welded joint. The three data points from 5×10^6 to 1×10^7 cycles in Figure 7.7 offer the best correlation with crack propagation predictions and seem to indicate fatigue life in a welded joint is propagation controlled, even in the high-cycle regime. It does not seem realistic to assume that the fatigue life of welds, with all of their inherent crack-life defects, should be controlled by two mechanisms--crack propagation for low-cycle and crack initiation for high-cycle fatigue. Therefore, with the exception of a brief discussion of the seawater environment on initiation life in Section 7.3.1, further computations will only consider crack propagation. This is in agreement with the current philosophy of neglecting crack initiation in welded structures.

7.2.2 Crack Propagation

Booth [7.1, 7.6] at the Welding Institute in Cambridge, England, conducted fatigue tests on cruciform, load-carrying, planar welds under bending and tension loads. The weld geometry and modes of loading for these test specimens correspond to the analytical models for the joints in Chapter 6.0. Booth performed a number of air ($f = 3\text{-}5$ Hz) and seawater, free-corrosion potential and cathodic polarization, tests ($f = 1/6$ Hz) on planar cruciform joints in tension and bending. These results are compared with calculations for low and high R for the air environment.* Comparisons in seawater will be discussed in Section 7.4.

The initial crack depth taken in the calculations depends on the plate thickness t , the material parameter a_m , and the mode of loading through the following relationship, which will be discussed in Section 7.5.3.

$$a_i = \frac{0.0198 \sqrt{ta_m}}{a} \quad (7.5)$$

*For the two-dimensional crack propagation studies the initial crack length $2c_i$ was taken as two times the initial depth a_i , i.e., $2c_i/a_i = 2$.

From Table 6.4 and Section 6.5.2,

$\alpha = 0.35$, Cruciform Joint in Tension

$\alpha = 0.19$, Cruciform Joint in Bending

$$a_m = 2.5 \times 10^{-5} \left(\frac{2068}{S_u} \right)^{1.8} \quad (\text{SI Units})$$

For the BS4360 Grade 50D steel, an average value for the ultimate strength was taken as $S_u = 540$ MPa. This gives $a_m = 2.8 \times 10^{-4}$ m. For the range of plane thickness (25-38 mm) considered in the cruciform joint analyses, the initial crack depth varied from 0.15 to 0.34 mm. The final crack depth was taken as one-half the plate thickness, which is the depth at which Booth indicated the tests were stopped.

Figures 7.10-7.12 show results under tension and bending loads for 25- and 38-mm plate thicknesses. The experimental data generally fall on the low R analytical curves. One can argue that in the high-stress low-cycle regime the experimental results should fall closer to the low R curve because residual stresses would be relieved. On the other hand, in the low-stress, high-cycle region, welding stresses would not be appreciably relieved, and the data should fall closer to the high R curve. This trend is not apparent in these comparisons for the planar joints in air and may indicate overly conservative selections of the Region I crack growth rate curves (Section 3.7).

A comparison of Figures 7.11 and 7.12 shows that the size effect, i.e., the reduction in fatigue life as the plate thickness increases, is correctly predicted.

A great number of tubular joint fatigue tests in air have been performed throughout the world and reported in the literature. Figures 7.13-7.15 show results generated at NEL (UK), WI (UK), TNO (Netherlands), and DnV (Norway). Three different plate thicknesses (6 mm, 16 mm, and 32 mm) were considered, and with the exception of the DnV tests, the diameter/thickness ratio was kept constant.

For the tubular joint tests, there is no standard end-of-test criterion. Progressive fatigue cracking causes increasing loss of member stiffness, and some tests were terminated by the limit of actuator stroke. In other instances, the tests were stopped when cracks branched away from the

weld toe into the chord. Finally, under axial loading, complete separation of the brace from the chord was achieved [7.4]. The lack of a precise definition of failure or end of test is not considered critical because there is rapid crack propagation in the final stages of structural life. Thus, differences in cyclic life for these various definitions of failure will be small.

The ordinate of the life curves is presented in terms of hot-spot stress instead of hot-spot strain, which is usual for presentation of experimental data. Experimental strain was transformed to stress by the simple one-dimensional Hooke's law relationship

$$\sigma = E \epsilon \quad (7.6)$$

From the discussion in Chapter 5.0, the hot-spot stress (strain) is defined as the maximum stress (strain) adjacent to the weld toe, but not influenced by the weld's local notch geometry. Since the stress concentration factor given in equation (6.5) is for the weld toe, the far-field stress in the planar joint analysis will be replaced by the hot-spot stress for the tubular joints. The crack front is still two dimensional, and the analysis does not consider any curvature effects of the chord or brace. Section 7.6 further discusses the extension of the planar joint crack propagation model to tubular structures.

Figures 7.13-7.15 also give predicted lives for three cases: 1) Low-R, Bending; 2) Low-R, Axial; and 3) High-R, Axial. The Low-R predictions, both for bending and tension, provide reasonably good representations of the lower bound of the data. Note that the predicted shape of the curves, as well as the location of the endurance strength, is in good agreement with the experimental results. Since tests were conducted on nonstress relieved joints, one might expect the High-R predictions to be more relevant due to the presence of tensile residual stresses local to the weld. However, this appears not to be the case. At high values of hot-spot stress, it is possible that localized plasticity at the weld-toe caused relaxation of the residual stresses. Although if this were the case, experimental results at low stresses, where plasticity induced relaxation would not be expected to occur, should approach the High-R predictions. Since this is clearly not the case, it appears that welding residual stresses did not significantly influence the overall crack propagation life.

Although the experimental results in Figures 7.13 through 7.15 are for axial, in-plane-bending and out-of-plane bending loading modes, an influence of loading mode could not be resolved within the scatter in results, which is typically an order of magnitude.

The predicted longer fatigue lives for remotely applied bending (versus tension) loading is consistent with general fatigue testing experience and is undoubtably caused by differences in stress gradient between these two loading modes. This effect is not reflected in the experimental results since the hot-spot stresses are dominated by local membrane bending, regardless of whether the joints are loaded axially or in bending. Thus, differences between applied axial versus bending loading are minimized. In addition, this secondary effect is masked by the scatter in the fatigue lives of welded joints. The latter arises due to the randomness introduced by the welding process--including variations in the weld-toe radii and initial defect population. Thus, the lower bound representation of the data by the predictions is understandable, since a "worst-case" notch analysis was employed in the fracture mechanics analysis.

7.3 Crack Initiation and Propagation of Welded Joints in Seawater

7.3.1 Crack Initiation

In Section 7.2.1 it was argued that, for a welded joint in air, crack initiation life constituted a small portion of the total fatigue life and therefore could be neglected. Certainly in seawater, initiation is expected to contribute an even smaller part of the total fatigue life. Consequently, there has been little research on crack initiation of welded joints in seawater. One such study was conducted in Japan, and the effects of environment are summarized in Figure 7.16 [7.3]. The specimen geometry was a 15-mm-thick cruciform butt welded joint loaded in tension and fabricated from SM41 steel. Reference 7.3 indicates that in air, crack initiation was defined when a visible crack at the notch root had grown to 0.5 mm in depth. In seawater, crack initiation is very difficult to detect. Reference 7.3 reported that in the corrosive environment the cycles to crack initiation were estimated from a fracture mechanics analysis and experimental tests on the total number of cycles to failure.

In Figure 7.16, K_t is the elastic stress concentration factor which is used in this study to compute local stress-strain conditions using either Neuber's rule (as given by equation (6.4)):

$$K_t = (K_\sigma K_\epsilon)^{1/2} \quad (7.7)$$

or, alternatively, from Stowell [7.7]

$$K_\sigma = \frac{K_\epsilon}{K_\epsilon - K_t + 1} \quad (7.8)$$

where K_σ and K_ϵ are defined in Section 6.4

Instead of strain-range, the ordinates of Figure 7.16 are expressed in terms of a so-called stress-strain function, D, defined by

$$D = (\Delta\sigma \Delta\epsilon E)^{1/2} = f^k (A_1 N_f^{b_1-2k} + A_2 N_f^{b_2-2k})^{1/2} / c \quad (7.9)$$

where A_1 , A_2 , b_1 , and b_2 are experimentally evaluated constants for air, and c and k are experimentally evaluated constants for seawater (f is the frequency in cpm).

The purpose of utilizing D is an attempt at reducing the experimental results to a common basis. Numerical values of D are given in air (D_A) and in seawater (D_S) in Figure 7.16. Using the definitions of notch stress ($\Delta\sigma$), equation (6.15), and notch strain ($\Delta\epsilon$), equation (6.18), along with the stress-strain function D, numerical values for the strain-life parameters in seawater can be evaluated. These are given in Table 7.2 for a typical wave frequency of 1/6 Hz. Figure 7.17 compares the strain-life parameters for the SM41 steel in air and seawater. In the high-cycle, low-stress regime, the seawater is seen to dramatically reduce fatigue initiation life. It is not understood why, in the low-cycle, high-stress region, the seawater environment seems to enhance initiation life. This may be a consequence of the straight-line extrapolation of the data in Figure 7.16b below 5×10^3 cycles and has no physical significance. Figure 7.18 illustrates the dramatic decrease that seawater has on crack initiation in the high-cycle life regime.

7.3.2 Crack Propagation

Turning now to crack propagation, analysis and experiments show favorable agreement, as can be seen in Figures 7.19 and 7.20. The analysis for a free-corrosion potential is given for both low and high R values (Figure 7.19). The analytical predictions and experimental results remain parallel below 10^6 cycles, but diverge at higher cyclic values. This is a direct consequence of the $da/dN-\Delta K$ curves in Figure 3.30. Under cathodic polarization, only a low-R curve is presented (Figure 7.20), as there was lack of crack-growth data in the lower ΔK region for high R.

Crack initiation was calculated for the previous examples, and predictions are presented in Figures 7.21 and 7.22. In seawater, the initiation predictions clearly correlate better with test data in the low-cycle regime. However, the experimental results are tending to approach the predicted curve in the high-cycle regime.

For tubular joints in a seawater environment, only a handful of tests have been performed. Such tests are extremely expensive because the wave loading frequency needs to be preserved to correctly simulate the corrosion fatigue process. This means that a test performed at a typical frequency of 0.2 Hz for 5×10^6 cycles requires about two years of continuous testing—the longest tubular joint test noted in Figures 7.23–7.26. The Dutch have performed tests on about four tubular T-joints in saltwater at free corrosion and cathodic polarization potentials. The analytical predictions are shown with the three free-corrosion test points in Figures 7.23 and 7.24. The comparisons are amazingly good. One test point for the cathodic polarization is compared with the low R analytical curve in Figure 7.25. The test result is considerably below the prediction curve. Interestingly, the Dutch test results in Figures 7.25 and 7.26 show little change in fatigue life for free corrosion and cathodic polarization potential.

In retrospect, predictions for bending rather than axial loading, would have been more relevant in view of the previous discussion. However, since the bending analysis would have resulted in longer lives, this would only increase the discrepancy between measured and predicted lives.

The extremely nonconservative prediction in Figure 7.25 for the important practical case of cathodic polarization is particularly unsatisfying. Several possibilities may be hypothesized for this lack of agreement. First, since the application of cathodic polarization is geometry-dependent

through the nonuniform distribution of current density in complex geometries, the crack may have grown from a region which was either not polarized or under polarized. The fact that the measured fatigue life was the same for both cathodic polarization and the freely corroding condition supports this view. Secondly, the data base used to establish the crack growth rate curve for seawater under cathodic polarization was limited; thus, the constants used in the growth rate equation may be inaccurate. Thirdly, crack size and/or geometry effects, which are inherently related to the fundamental mechanism of material-environment interaction, may introduce errors in applying data generated in the laboratory in relatively long, through-thickness cracks to structures containing initially small surface cracks.

The final comparisons are with experimental results for two tests on 508-mm OD x 16-mm WT tubular joints conducted at DnV in Norway, Figure 7.26. Tests were performed under cathodic polarization, but at an increased frequency of 1 Hz. The experimental points in Figure 7.26 denote what the Norwegians call crack initiation (\circ), a 20-mm-long surface crack (Δ), and failure (\square). Gibstein [7.5] defines a laboratory-based crack initiation point as one at which a strain gage, located close to the weld toe, has changed ± 15 percent of the full amplitude at the beginning of the test. This definition does not pretend to be precise, but serves to correlate test experience among the various laboratories in the ECSC program. Failure was defined as the point at which the surface crack reached 80-90 percent of the brace circumference.

The analytical curves in Figures 7.25 and 7.26 show an increased slope at about 10^5 cycles. This is a consequence of the crack growth curves presented in Figure 3.28. At a testing frequency of 0.1 Hz, the $da/dN-AK$ curve becomes flat at about 1×10^{-6} m/c. When the frequency is increased to 1 Hz, the point is reduced to 1.5×10^{-7} m/c. As the hot-spot stress is increased further and the cycles for propagation decrease, the effects of corrosion become less important and the curves in air are approached.

Regarding the results in Figures 7.23-7.26, a final point is worth mentioning; namely, the number of available measurements is so few that the comparisons may be inadequate to formulate sound conclusions. This is particularly true in light of the scatter observed in the air tests. Therefore, one indisputable conclusion is the fact that more testing—using both coupon

specimens to generate da/dN (ΔK) data and tubular joint tests to verify crack growth models—is warranted under these environmental conditions.

7.4 Effect of Seawater on Fatigue Life

The previous discussions have made separate comparisons of analytical predictions and test results for initiation and propagation in air and seawater environments. This section summarizes those results so that the effect of the ocean environment on fatigue life can be evaluated.

A comparison of the low R curves, Figures 7.8 and 7.21, and the high R curves, Figures 7.9 and 7.22, demonstrates the detrimental effect that seawater has on both initiation and propagation life. This is a direct result of the curves in Figure 3.30 used to represent the crack-growth data.

As a final set of comparisons illustrating environmental effects, Figures 7.27 and 7.28 summarize crack propagation life predictions on a cruciform and tubular joint. The S-N curves all follow the general shape of the crack growth curves of Figure 3.30, where da/dN is replaced by cycles (N), and ΔK is replaced by stress range (ΔS).

7.5 Sensitivity Studies

7.5.1 Stress Distribution and Stress Concentration Factor

Equation (6.53) in Section 6.6.4 expressed the stress distribution at the toe of a weld as

$$\sigma(a) = S [1 + (K_t - 1) \exp [-35 (K_t - 1) a/t]] \quad (7.10)$$

where

a = distance from weld surface in depth or surface direction,

S = far-field stress,

t = plate thickness.

and the stress concentration factor is given by equation (6.5)

$$K_t = 1 + a(t/r)^{1/2} \quad (7.11)$$

where

a is a factor depending on the weld geometry and mode of loading,

r = radius at weld toe.

As an example of the stress distribution, consider the planar T-joint in Figure 7.29 under a bending loading. For $t = 25.4$ mm and 50.8 mm thicknesses, the following values of K_t can be calculated for A36 and A514 materials using the method and data presented in Chapter 6.0. The results are

	<u>A36 (HAZ)</u>	<u>A514 (HAZ)</u>
S_u (MPa)	667	1408
r_{crit} (a _m) (mm) (Bending Load)	0.19	0.05
K_t , $t = 25.4$ mm	3.2	5.3
K_t , $t = 50.8$ mm	4.1	7.1

Figure 7.29 is a plot of the normalized stress distribution $\sigma(x)/S$ in equation (7.10) for the above four cases. It should be remembered that this distribution is for a toe notch radius, r_{crit} , which would give a maximum value to the fatigue strength reduction factor K_f defined in Section 6.5.2. Because r_{crit} is much smaller for the higher strength A514 steel, the stress concentration factor and gradient is much steeper close to the notch. However, at 1.5 mm away from the notch, the stress is reduced to essentially its far-field value in all cases. In fatigue tests strain gages are usually not installed closer than about 4 mm to the weld toe to avoid the influence of the load toe geometry as discussed in Section 5.2.2; thus, Figure 7.29 indicates such gage readings would not be influenced by the local toe geometry.

7.5.2 Effect of Weld Toe Geometry on Stress Intensity Factor

The one-dimensional stress intensity factor developed using the Green's function approach in Section 6.6.2, given by equation (6.34), is

$$K(a) = 1.12 \sigma(a) \sqrt{\pi a} \quad (6.34)$$

where $\sigma(a)$ is the stress distribution given by equation (7.10). Using the same materials and planar weld configuration discussed in Section 7.5.1, $K(a)$, normalized by the far-field stress, was evaluated and presented in

Figure 7.30. Also shown is the solution for an edge crack in a semi-infinite plate under tension, i.e.,

$$K(a) = 1.12 S \sqrt{\pi a} \quad (7.12)$$

The stress-intensity factors for the weld toe crack have the same characteristics as for notches in a plate given in Figures 6.23 and 6.24. The value of $K(a)$ rapidly rises for small notch depths in the range 0.0 to 0.1 mm. For the A36HAZ material with the smaller stress concentration factors, $K(a)$ remains constant from about 0.3 to 1.0 mm. This is caused by the stress decay in Figure 7.29 being offset by the \sqrt{a} term in equation (6.34). For the larger values of K_t corresponding to the A514HAZ steel, the stress intensity factor actually decreases from about 0.3 to 0.5 mm due to the high stress gradient. As the crack depth reaches 2.0 mm, all solutions approach that of the edge crack since the stress has reached the far-field value.

7.5.3 Initial Crack Depth

The initial crack depth assumption in the propagation calculations is based upon the work of Chen and Lawrence [7.10]. Let us define a_i as the flaw size which is just large enough to propagate from the worst-case weld-toe notch, thereby eliminating nonpropagating cracks from the flaw population. Although this definition may at first appear to be nonconservative, this is not actually the case since we have already made a worst-case assumption in selecting the weld-toe radius. This condition is given by

$$\sigma(a_i) = K_{f\max} S \quad (7.13)$$

According to equation (7.10), the stress at $a = a_i$ is

$$\sigma(a_i) = S \{1 + (K_t - 1) \exp [-35 (K_t - 1) a_i / t]\} \quad (7.10)$$

From the $K_{f\max}$ concept and equations (6.5) and (6.14)

$$K_t^* - 1 = 2(K_{f\max} - 1) \quad (7.14)$$

or

$$K_{f\max} = 1/2(K_t^* + 1)$$

where K_t^* is the stress concentration factor associated with $K_{f\max}$. The criteria for crack propagation given in equation (7.13) become

$$\begin{aligned}\sigma(a_i) &= K_{f\max} S \\ &= [1/2(K_t^* + 1)] S\end{aligned} \quad (7.13)$$

Equating relationships (7.10) and (7.14) gives

$$\exp[-35(K_t^* - 1)a_i/t] = 1/2 \quad (7.15)$$

Using equation (7.11), equation (7.15) reduces to

$$\exp[-35(a/t/a_m)^{1/2}a_i/t] = 1/2 \quad (7.16)$$

or

$$a_i = \frac{0.0198 \sqrt{ta_m}}{a} \quad (7.17)$$

Thus, the initial crack depth is dependent on the plate thickness (t), material strength (a_m), and mode of loading (a).

Figure 7.31 plots equation (7.17) as a function of plate thickness for a planar T-joint under tension and bending loads for A36HAZ and A514HAZ material. For plate thicknesses (20-100 mm) normally used in offshore structures, Figure 7.31 indicates initial crack depths in the ranges should be assumed as (in mm):

A36HAZ

$$\begin{aligned} 0.2 < a_i &< 0.5 \text{ Bending} \\ 0.1 < a_i &< 0.25 \text{ Tension} \end{aligned} \quad (7.18)$$

A514HAZ

$$\begin{aligned} 0.1 < a_i &< 0.25 \text{ Bending} \\ 0.05 < a_i &< 0.10 \text{ Tension} \end{aligned} \quad (7.19)$$

These ranges agree from metallurgical observations of fatigue cracks in welds and the initial crack sizes of 0.2 mm observed in the Japanese studies [7.2, 7.3] and discussed in Section 7.1.1. Section 8.2.1, in the statistical consideration of initial crack size, reported an average depth of 0.125 mm used by Norwegian researchers.

A sensitivity study of crack propagation life to initial crack depth was conducted on a planar T-joint under tension (low R) in a seawater, free-corrosion environment. Analyses were conducted with the one-dimensional crack model at stress ranges $\Delta S = 50, 150$, and 500 MPa at the weld toe radii corresponding to $K_t = 2.3, 2.8$, and 5.1 . For the medium (150 MPa) and high stresses (500 MPa), the propagation life is relative insensitive to K_t and initial crack depth a_i in the range $0.1 < a_i < 0.5$ mm as indicated in Figure 7.32.

For the larger toe radii, there is a marked increase in life as a_i is decreased below 0.1 mm. The $K_t = 5.1$ was evaluated at the toe radius $r_{crit} = 0.28$ mm, which corresponds to K_{fmax} . Since a value of $K_t = 5.1$ is likely to exist somewhere in the joint, Figure 7.32 indicates that at $\Delta S = 150$ and 500 MPa, propagation life is insensitive to initial crack length even below 0.1 mm. At the lower $\Delta S = 50$ MPa stress range, the sensitivity to initial crack size does depend on the toe radius. In the range $0.2 < a_i < 1.0$ mm, the larger toe radii actually have a decreased crack propagation life over that for $K_t = 5.1$. Figures 7.29 and 7.30 indicate this is a consequence of the complex mathematical model of the stress distribution and stress intensity factor whereby the influence of a smaller K_t is felt at a greater depth from the weld toe than for a larger K_t . However, for initial crack depths less than about 0.05 mm, the weld with the smallest K_t has the longest life.

The sensitivity to initial crack size can be presented in terms of standard S-N plots as shown in Figures 7.33 and 7.34 for a planar T-joint under tension at low and high R values. The toe radius was assumed to be $r = 0.28$ mm which gives a stress concentration factor $K_t = 5.1$. These figures confirm the observations that for initial crack depths in the range $0.1 < a_i < 0.5$ mm, crack propagation life is relatively independent of a_i .

The two-dimensional crack model was used to evaluate the sensitivity of initial crack size on fatigue life for the three tubular joints of Figures 7.13-7.15. All parameters were kept constant except the initial crack depth for the 6 mm and 32 mm (wall thicknesses) selected as $a_i = 0.12$ mm, the initial size for the 16 mm joint. A comparison of Figure 7.35 with Figures 7.13 and 7.15 shows little change in life for this case of bending. These results also predict the experimentally observed size dependence of the fatigue life. Thus, it is concluded that the effect of joint size on the fatigue life is due primarily to the dependence of the weld-toe stress concentration on wall thickness through Equation (7.11). Since this influence is local to the weld-toe, it is understandable why hot-spot stress range--operationally defined to avoid weld-toe effects--does not unify the data from various joint sizes.

7.5.4 Final Crack Depth

For crack propagation calculation, the question arises as to what final crack depth should be assumed which defines fatigue life. To assess the effect of final crack depth, a sensitivity study was conducted. The results are presented (Figures 7.36 and 7.37) for the one- and two-dimensional fracture models of a planar T-joint under bending. The final crack depths were taken as $t/10$, $t/2$, and t , where t is the plate thickness. The S-N curve for the one-dimensional model (Figure 7.36) shows little sensitivity to a_f for the three final crack lengths assumed. The two-dimensional model (Figure 7.37) indicates that crack depths equal to $t/2$ and t have little influence on propagation life. For smaller final crack depths, e.g., 3.8 mm, the two-dimensional model is more sensitive than the one-dimensional, as can be seen in Figures 7.36 and 7.37. This is due to the correction factors for the two-dimensional crack presented in Section 6.6.3.

A direct comparison of propagation lives in Figures 7.36 and 7.37 shows conservatism in the one-dimensional analysis in the high-cycle ($>10^6$) region. At stress ranges greater than 150 MPa, there are little differences in life between the one- and two-dimensional models. However, at $\Delta S = 100$ MPa and 75 MPa, the factor on life is about 2 and 10 for the two fracture mechanics models. This indicates that for more accurate long-life predictions, a two-dimensional model may be needed. Further sensitivity of the two models is discussed in the next section.

7.5.5 Sensitivity of Life to One- Versus Two-Dimensional Fracture Models

In Section 6.6.2, the stress intensity factor for a one-dimensional crack of depth a at the toe of a weld was developed. This model was extended to two dimensions (depth a - surface length $2c$) in Section 6.6.3.

As a partial validation in the computer algorithms, calculations on crack size and shape were compared with numerical and analytical results published in Reference [6.34]. Figures 7.38 and 7.39 plot a nondimensional crack shape under tension and bending loads for different plate thicknesses. The "X" values show this investigation's results for the same initial conditions on a/c and a/t given by the solid symbols. The calculations were performed using the asymptotic growth law [7.11].

$$\frac{da}{dN} = C(\Delta K - \Delta K_{th})^m \quad (7.20)$$

where*

$$C = 5.34 \times 10^{-11}$$

$$m = 2.53$$

$$\Delta K_{th} = 2.3 \text{ MPa} \sqrt{\text{m}}$$

The results closely match the predicted values given in Reference [6.34], which used the Paris law and different values of C and m .

*These constants were selected based on limited data early in the program. However, changes in these constants will not alter the conclusions of the sensitivity analysis.

These results demonstrate that crack shape is primarily dependent on loading mode and is relatively insensitive to material, provided the material is isotropic—that is, growth rates do not depend on growth direction, due to microstructural variations, within a given plane of growth. In addition, component geometry—particularly, local notch geometry—will also influence crack shape during fatigue crack growth.

For further verification of the two-dimensional analysis, test cases were conducted for a long crack in a planar T-joint such as illustrated in Figure 6.25. Ideally the results should be equal to the one-dimensional analysis. The ratio of initial crack length to depth was taken as

$$c_i/a_i = 1000 \quad (7.21)$$

Figure 7.40 compares results of the one- and two-dimensional analyses at three different crack lengths for 500 MPa and 100 MPa. On a log S-log N plot, differences in cycles are insignificant. Numerical values are presented in Table 7.4. The investigators attribute differences in computed propagation life to the two different numerical integration techniques and the contribution of a finite thickness plate to the stress intensity factor for the two-dimensional analysis.

Calculations were also performed for an initially semicircular crack with

$$a_i = c_i = 0.48 \text{ mm} \quad (7.22)$$

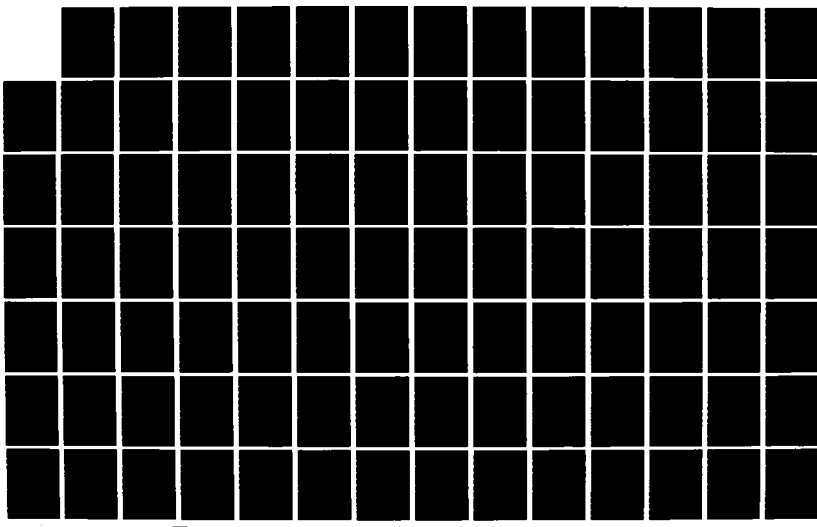
The symbol  on Figure 7.40 shows the cycles required for the crack to reach the plate thickness 25.4 mm. The two-dimensional analysis to reach full thickness increases the calculated life by a factor of 1.9 at 500 MPa and 2.1 at 100 MPa over the one-dimensional approach. The differences in the one-dimensional and two-dimensional results are illustrated even more dramatically in Figures 7.41 and 7.42, which represent the shape of the crack at various numbers of cycles. These results show that the one-dimensional crack model grows faster than its two-dimensional counterpart. Hence, the one-dimensional analysis is more conservative in life predictions. This has been pointed out in Section 7.5.4 and by other investigators in the field.

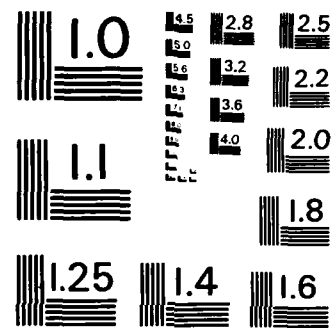
RD-R162 484 LONG-TERM CORROSION FATIGUE OF WELDED MARINE STEELS(U) 4/5
SOUTHWEST RESEARCH INST SAN ANTONIO TX
O H BURNSIDE ET AL. 1984 SR-1276 SSC-326

UNCLASSIFIED DTCG23-88-C-20028

F/G 11/6

NL





MICROCOPY RESOLUTION TEST CHART
NATIONAL BUREAU OF STANDARDS - 1963 - A

7.6 Comparison of Experimental and Analytical Stress Intensity Factor Expressions for Tubular Joints

James and Anderson [7.12] have documented a relatively simple technique for experimentally determining the stress intensity factor from crack growth rate information. This technique, originally suggested by Paris [7.13], is based on the fact that da/dN vs ΔK (or K_{max}) provides a unique geometry-independent material property for a fixed set of environmental and loading variables. Figure 7.43 illustrates how the procedure can be utilized to establish the functional dependence of stress intensity factor on crack size in a tubular joint, although the technique is applicable to any component geometry. Having established the materials' crack growth rate properties, da/dN vs K_{max} , one measures the growth rate versus crack depth in a full-sized or model component under identical loading and environmental conditions. For each crack depth, the measured da/dN is translated into a K_{max} by utilizing the established da/dN vs K_{max} relation. It is convenient to represent results in dimensionless form as $K(exp)/(S \sqrt{\pi a})$, where $K(exp)$ is the experimentally measured stress intensity factor, S is the remote stress, and "a" is the crack size, preferably crack depth in the case of partial penetration cracks.

Pan and Plummer applied this technique to axially loaded, nonoverlapping, tubular K-joints [7.14]. These results are given in Figure 7.44. In this case, results were expressed in terms of the hot spot stress, σ , and the surface crack length, L_c , as defined in Figure 7.44. Although crack growth rate properties for the test material were estimated from S-N data, the overall technique was verified by also measuring $K(exp)$ for a planar, three-point-bend specimen and comparing results with the known analytical solution for this geometry.

Recently, Dover and coworkers measured $K(exp)$ in similar fashion for welded, tubular, T-joints subjects to in-plane bending [7.15, 7.16] and out-of-plane bending [7.16, 7.17], as shown in Figure 7.45. Results were also normalized in terms of the hot-spot stress, although in this case a weighted average value was used since tests were conducted under variable amplitude loading. In addition, results were normalized using crack depth, measured using an alternating current potential drop technique, rather than surface crack length. The normalized stress intensity factor, given in Figure 7.45, can be thought of as a correction factor which accounts for crack shape,

These results demonstrate that crack shape is primarily dependent on loading mode and is relatively insensitive to material, provided the material is isotropic—that is, growth rates do not depend on growth direction, due to microstructural variations, within a given plane of growth. In addition, component geometry—particularly, local notch geometry—will also influence crack shape during fatigue crack growth.

For further verification of the two-dimensional analysis, test cases were conducted for a long crack in a planar T-joint such as illustrated in Figure 6.25. Ideally the results should be equal to the one-dimensional analysis. The ratio of initial crack length to depth was taken as

$$c_i/a_i = 1000 \quad (7.21)$$

Figure 7.40 compares results of the one- and two-dimensional analyses at three different crack lengths for 500 MPa and 100 MPa. On a log S-log N plot, differences in cycles are insignificant. Numerical values are presented in Table 7.4. The investigators attribute differences in computed propagation life to the two different numerical integration techniques and the contribution of a finite thickness plate to the stress intensity factor for the two-dimensional analysis.

Calculations were also performed for an initially semicircular crack with

$$a_i = c_i = 0.48 \text{ mm} \quad (7.22)$$

The symbol  on Figure 7.40 shows the cycles required for the crack to reach the plate thickness 25.4 mm. The two-dimensional analysis to reach full thickness increases the calculated life by a factor of 1.9 at 500 MPa and 2.1 at 100 MPa over the one-dimensional approach. The differences in the one-dimensional and two-dimensional results are illustrated even more dramatically in Figures 7.41 and 7.42, which represent the shape of the crack at various numbers of cycles. These results show that the one-dimensional crack model grows faster than its two-dimensional counterpart. Hence, the one-dimensional analysis is more conservative in life predictions. This has been pointed out in Section 7.5.4 and by other investigators in the field.

loading mode, as well as stress-free surfaces in the tubular joint. Note that this factor decreases with relative crack depth.

Computations for the nondimensional parameters $K/(S\sqrt{na})$ versus a/t were made using the modified plate bending models developed in this study. Predicted values of $K/(S\sqrt{na})$ were generated using the previously developed equation (6.45), employed in the two-dimensional, surface crack model for crack growth in Section 6.6.3. By normalizing this equation for the case of a bending load, one obtains

$$\frac{K}{\sigma_b \sqrt{\pi a}} = \frac{H}{Q} F \left(\frac{a}{t}, \frac{a}{c}, \frac{c}{b}, \zeta \right) \quad (7.23)$$

As indicated in Figure 7.45, the theoretical solutions are in agreement with the downward trend in the experimental results, thereby suggesting that changes in crack shape play a role in decreasing $K/(S\sqrt{na})$ values as a/t increases. The analytical results tend to be higher than the experimental results and diverge with increases in relative crack depth, a/t . At $a/t < 0.05$, the analytical results rise steeply, reflecting the influence of the stress concentrating effect of the weld-toe; experimental results are not available in this region due to the inability to measure crack depth for small flaws along the weld-toe. At $a/t = 0.1$ experimental and analytical results are in closest agreement, but diverge for deeper cracks where they differ by as much as a factor of two. The eventual increase in the analytical results for large a/t values reflects the influence of the interior surface of the tube on the stress intensity factor; experimental results are not available in this region.

The differences in the measurements and predictions for $a/t > 0.2$ could also be caused by curvature effects. In considering a tubular geometry, an additional factor is needed to account for the curvature since equation (7.23) is ideally valid only for a surface-cracked plate. Thus, equation (7.23) becomes

$$\frac{K}{\sigma_b \sqrt{\pi a}} = \frac{H}{Q} F \left(\frac{a}{t}, \frac{a}{c}, \frac{c}{b}, \zeta \right) A_b \quad (7.24)$$

where A_b is the curvature correction factor for an axially-cracked cylinder subjected to out-of-plane bending. The value of A_b was obtained from the analysis of Erdogan and Ratwani [7.18] for a through-wall crack in a cylindrical shell. Figure 7.46 gives A_b as a function of the shell parameter λ defined as:

$$\lambda = [12 (1 - \mu^2)]^{1/4} C_{eq} / \sqrt{Rt} \quad (7.25)$$

where μ is the Poisson's ratio, R is the radius of the cylinder, and C_{eq} is the equivalent half crack length. For a surface crack, A_b is obtained from Figure 7.46 by using the λ based on an equivalent through-wall crack length, which is calculated on the basis of equivalent crack area from the actual crack length and depth assuming a semi-elliptical crack. Thus,

$$C_{eq} = \frac{\pi ac}{4t} \quad (7.26)$$

It is clear that $K/(S\sqrt{ta})$ depends on the crack aspect ratio as well as other geometric parameters. Substituting the analytical crack aspect ratio data from Figure 7.47 into equations (7.25) and (7.26), the shell parameter λ can be calculated for values of a/t . In the region of interest, λ lies in the range $0 < \lambda < 1.8$, which gives, from Figure 7.46, a curvature correction factor $0.95 < A_b < 1.0$. Thus, the analytical results of Figure 7.45 would only be slightly reduced if the correction factor were included. It appears that curvature effects are of secondary importance in the crack growth for this tubular joint.

The deviation between analytical and experimental results in Figure 7.45 cannot be resolved at this time. Possibly the experimental measurements are in error by this amount considering the variabilities associated with determining crack depth in tubular joints as well as those inherent in fatigue crack growth rate measurements. To the investigators' knowledge, the influence of these factors on the experimental results have not been quantified at this time. In addition, differences in crack shape could contribute to the observed discrepancy. For example, Figure 7.47 provides a comparison of measured versus predicted crack shape during fatigue crack growth in tubular joints. The major difference between the predicted and measured results is

believed to be due to the fact that the crack growth model does not consider link-up, or coalescence, of multiple cracks. As discussed previously, multiple cracks having high a/c values are known to occur initially, followed by a decrease in a/c as the cracks lengthen along the surface due to stress concentration at the weld-toe, which then leads to crack link-up and a further decrease in a/c . The hypothesized shape changes during this series of processes are indicated in Figure 7.47.

Additional analytical studies are needed to further explore the influence of crack shape changes on the stress intensity factor. Although crack depth is not commonly measured in tubular joint tests, this additional measurement would enable a more rigorous assessment of fatigue crack growth models. The cost of these additional measurements would be small in relation to the overall cost of full-scale testing.

7.7 Closing Remarks on Fatigue Life Predictions

The analytical results presented herein, along with information gathered from full-scale tubular joint tests and failure analyses of actual offshore structures, all support the use of a fracture mechanics approach to the prediction of fatigue life in offshore structures. The reasonably good agreement between the fracture mechanics model predictions and experimental data on planar joints demonstrated herein provides confidence in this approach. However, lack of adequate crack growth data in the near-threshold regime appears to have led to overly conservative solutions of da/dN (ΔK) properties, which in turn has led to conservative life predictions, particularly at high R values, even for planar welded joints.

It should be recognized that while comparisons of predictions and measurements have not been made for welded joints subjected to variable amplitude loading, it appears that load interaction effects can be significant--particularly in the low-growth rate, high-cycle regime. Data on representative materials indicate that retardation in the growth rate can be significant after overloads [7.21, 7.22]. Furthermore, crack growth predictions using linear damage accumulation have been shown to significantly underestimate the fatigue

life under variable amplitude loading representative of offshore structures [7.19, 7.20]. Although various empirical [7.23-7.27] and analytical [7.28-7.31] models for load interaction in fatigue have demonstrated a certain degree of success, none are available which incorporate environmental effects. The latter will be a fruitful area of research on offshore structures. Other recommended areas of research are given in Chapter 9.0.

CHAPTER 7.0 REFERENCES

- 7.1 Booth, G. S., "Constant Amplitude Fatigue Tests on Welded Steel Joints Performed in Air," Paper III/P4, European Offshore Steels Research Seminar, Cambridge, United Kingdom, November 1978.
- 7.2 Usami, S., et al., "Fatigue Crack Initiation and Propagation at the Toes of Heavy Welded Joints," Paper 3JWS-44, Third International Symposium of the Japan Welding Society, Tokyo, September 1978.
- 7.3 Nagai, K., et al., "Studies of the Evaluation of Corrosion Fatigue Crack Initiation Life for Welded Joints of Mild Steel in Seawater," Paper 3JWS-43, Third International Symposium of the Japan Welding Society, Tokyo, September 1978.
- 7.4 McDonald, A., and Wylde, J.G., "Experimental Results of Fatigue Tests on Tubular Welded Joints," Paper No. 10, Fatigue in Offshore Structural Steels, Institution of Civil Engineers, London, February 1981.
- 7.5 Gibstein, M. B., "Fatigue Failure of T-Joints: the Det Norske Veritas Fatigue Testing Program," Paper X/P33, European Offshore Steels Research Seminar, Cambridge, United Kingdom, November 1978.
- 7.6 Booth, G. S., "Constant Amplitude Corrosion Fatigue Strength of Welded Joints," Paper No. 2, Fatigue in Offshore Structural Steels, Institution of Civil Engineers, London, February 1981.
- 7.7 Stowell, E. Z., "Stress and Strain Concentrations at a Circular Hole in an Infinite Plate," NACA Technical Note, 2073, National Advisory Committee for Aeronautics, April 1950.
- 7.8 de Back, J., "Strength of Tubular Joints," Plenary Session 7, International Conference on Steel in Marine Structures, Paris, October 1981.
- 7.9 Walker, E. F., "Effect of Marine Environment," Plenary Session 4, International Conference on Steel in Marine Structures, Paris, October 1981.
- 7.10 Chen, W. C., and Lawrence, F. V., Jr., "Fracture Control Report No. 32," University of Illinois, Urbana, 1979.
- 7.11 Tomkins, B., and Scott, P. M., "An Analysis of the Fatigue Endurance of Tubular T Joints by Linear Fracture Mechanics," Paper VII, P20, European Offshore Steels Research Seminar, Cambridge, United Kingdom, November 1978.
- 7.12 James, L. A., and Anderson, W. E., "A Simple Experimental Procedure for Stress Intensity Factor Calibration," Engineering Fracture Mechanics, 1, 1969.
- 7.13 Paris, P. C., presentation to the Boeing Company, 1962.

- 7.14 Pan, R. B., and Plummer, F. B., "A Fracture Mechanics Approach to Nonoverlapping, Tubular K-Joint Fatigue-Life Prediction," Journal of Petroleum Technology, April 1977.
- 7.15 Hibberd, R. D., and Dover, W. D., "Random Load Fatigue Crack Growth in T-Joints," Proceedings of the 9th Annual Offshore Technology Conference, OTC 2853, May 1977.
- 7.16 Dover, W. D., and Holdbrook, S. J., "Fatigue Crack Growth in Tubular Welded Connections," International Journal of Fatigue, January 1980.
- 7.17 Dover, W. D., Holdbrook, S. J., Hibberd, R. D., and Charlesworth, F.D.W., "Fatigue Crack Growth in T-Joints; Out-of-Plane Bending," Proceedings of the 10th Annual Offshore Technology Conference, OTC 3252, May 1978.
- 7.18 Erdogan, F., and Ratwani, M., "Fracture of Cylindrical and Spherical Shells Containing a Crack," Nuclear Engineering and Design, 20, 1972.
- 7.19 Pook, L. P., and Greenan, A. F., "The Effect of Narrow-Band Random Loading on the High Cycle Fatigue Strength of Edge-Cracked Mild Steel Plates," International Journal of Fracture, January 1979.
- 7.20 "Fatigue Considerations in View of Measured Load Spectra," Final Report, Ship Structure Committee Project SR-1254, Contract DOT-CG-80359-A, May 1982.
- 7.21 Klesnil, M., and Lukas, P., "Influence of Strength and Stress History on Growth and Stabilization of Fatigue Cracks," Engineering Fracture Mechanics, Vol. 4, pp 77-92, 1972.
- 7.22 Sehitoglu, H., and McDiarmid, D. L., "The Effect of Load Stepdown on Fatigue Crack Arrest and Retardation," International Journal of Fatigue, April 1980.
- 7.23 Wheeler, O. E., "Spectrum Loading and Crack Growth," J. Bas. Eng. ASME, Vol. 94, No. 1, p. 181, 1972.
- 7.24 Willenborg, J. D., Engle, R. M., Jr., and Wood, H. A., "A Crack Growth Retardation Model Using an Effective Stress Concept," AFFDL-TM-71-1-FBR, 1971.
- 7.25 Gallagher, J. P., and Hughes, T. F., "Influence of Yield Strength on Overload Affected Fatigue Crack Growth Behavior in 4340 Steel," AFFDL-TR-74-27, 1974.
- 7.26 Johnson, W. S., "Multi-Parameter Yield Zone Model for Predicting Spectrum Crack Growth," NASA Tech. Mem. 81890, 1980.
- 7.27 Gray, T. D., and Gallagher, J. P., in Mechanics of Crack Growth, ASTM STP 590, American Society for Testing and Materials, 1976, pp. 331-344.
- 7.28 Fuhring, H., and Seeger, T., "Dugdale Crack Closure Analysis of Fatigue Cracks Under Constant Amplitude Loading," Engineering Fracture Mechanics, Vol. 11, pp. 99-122, 1979.

- 7.29 Fuhring, H., and Seeger, T., "Structural Memory of Cracked Components Under Irregular Loading," Fracture Mechanics, ASTM STP-677, C. W. Smith, Ed., American Society for Testing and Materials, pp. 144-167, 1979.
- 7.30 Newman, J. C., Jr., "A Crack-Closure Model for Predicting Fatigue-Crack-Growth Under Aircraft Spectrum Loading," Methods and Models for Predicting Fatigue Crack Growth Under Random Loading, ASTM STP 748, American Society for Testing and Materials, 1981.
- 7.31 Newman, J. C., Jr., "Prediction of Fatigue-Crack Growth Under Variable-Amplitude and Spectrum Loading Using a Closure Model," NASA TM 81942, January 1981.

TABLE 7.1. CHEMICAL COMPOSITIONS AND MECHANICAL PROPERTIES OF SELECTED STEELS

Material	C	Mn	P(max)	S(max)	S ₁	Min. Yield (MPa)	Tensile Strength (MPa)
A36 Base Metal (1) (38-64 mm Plate)	0.26 (max)	0.80-1.20	0.04	0.05	0.15-0.40	250	400-550
SM41 Base Metal (2) Weld Metal	0.19	0.84	0.021	0.013	0.01	287	468
	0.08	0.76	0.010	0.009	0.55	456	542
AS14 Gr. H Base Metal (1) (51 mm max. Thickness Plate)	0.12-0.21	0.95-1.3	0.035	0.04	0.20-0.35	690	760-895
HT60 Base Metal (2) Weld Metal	0.13	1.3	0.020	0.006	0.32	510	600
	0.06	0.87	0.012	0.009	0.38	568	657
BS4360 Gr. 50D Modified(3)	0.22 (max)	1.6 (max)	0.050	0.050	0.10-0.55	345	490-620

(1) Specified in ASTM Standards

(2) From Reference [7.2]

(3) From Reference [7.1]

TABLE 7.2. CYCLIC STRAIN-STRAIN AND STRAIN LIFE PROPERTIES OF SELECTED MILD STEELS

	In Air		In Seawater ($f = 1/6$ Hz)	
	ASTM A36 (From [6.13])	SM41 HAZ BASE	SM41 (Ref. [7.3])	SM41 (Estimated from Ref. [7.3])
Modulus of Elasticity, E (MPa)	190,000	190,000	210,000	210,000
Fatigue Strength Coefficient, σ_f' (MPa)	725	1,014	765**	1,732
Fatigue Ductility Coefficient, s_f'	0.218	0.271	0.342**	0.775
Fatigue Strength Exponent, b	-0.066	-0.132	-0.088**	-0.177
Fatigue Ductility Exponent, c	-0.492	-0.451	-0.509**	-0.598
Cyclic Strain Hardening Exponent, n'	0.215	0.249	0.26*	0.26*
Cyclic Strength Coefficient, K' (MPa)	1,490	1,097	1,000*	1,000*

*Estimated from Reference [7.2]

**Given in Reference [7.3]

TABLE 7.3. CYCLIC-STRAIN AND STRAIN LIFE PROPERTIES
OF SELECTED HIGH-STRENGTH STEELS

	A514 (Ref. [6,13])	HT60 (Ref. [7,21])
Modulus of Elasticity, E (MPa)	290,000	190,000
Fatigue Strength Coefficient, σ_f' (MPa)	2,000	720*
Fatigue Ductility Coefficient, ϵ_f'	0.783	0.35*
Fatigue Strength Exponent, b	-0.087	-0.10*
Fatigue Ductility Exponent, c	-0.713	-0.53*
Cyclic Strain Hardening Exponent, n'	0.103	0.174*
Cyclic Strength Coefficient, K' (MPa)	1,766	1,000*

*Estimated from Reference [7.2]

TABLE 7.4. COMPARISON OF ONE- AND TWO-DIMENSIONAL
CRACK PROPAGATION ANALYSES -- T-JOINT, A36 HAZ
MATERIAL, ASYMPTOTIC GROWTH LAW

Far-Field Stress (MPa)	Final Crack Depth (mm)	Cycles for Crack Propagation	
		1-D Analysis	2-D Analysis
500	2.54	0.444 10^4	0.498 10^4
	6.35	0.648 10^4	0.778 10^4
	25.4	0.877 10^4	0.976 10^4
100	2.54	0.553 10^6	0.658 10^6
	6.35	0.745 10^6	0.923 10^6
	25.4	0.916 10^6	1.07 10^6

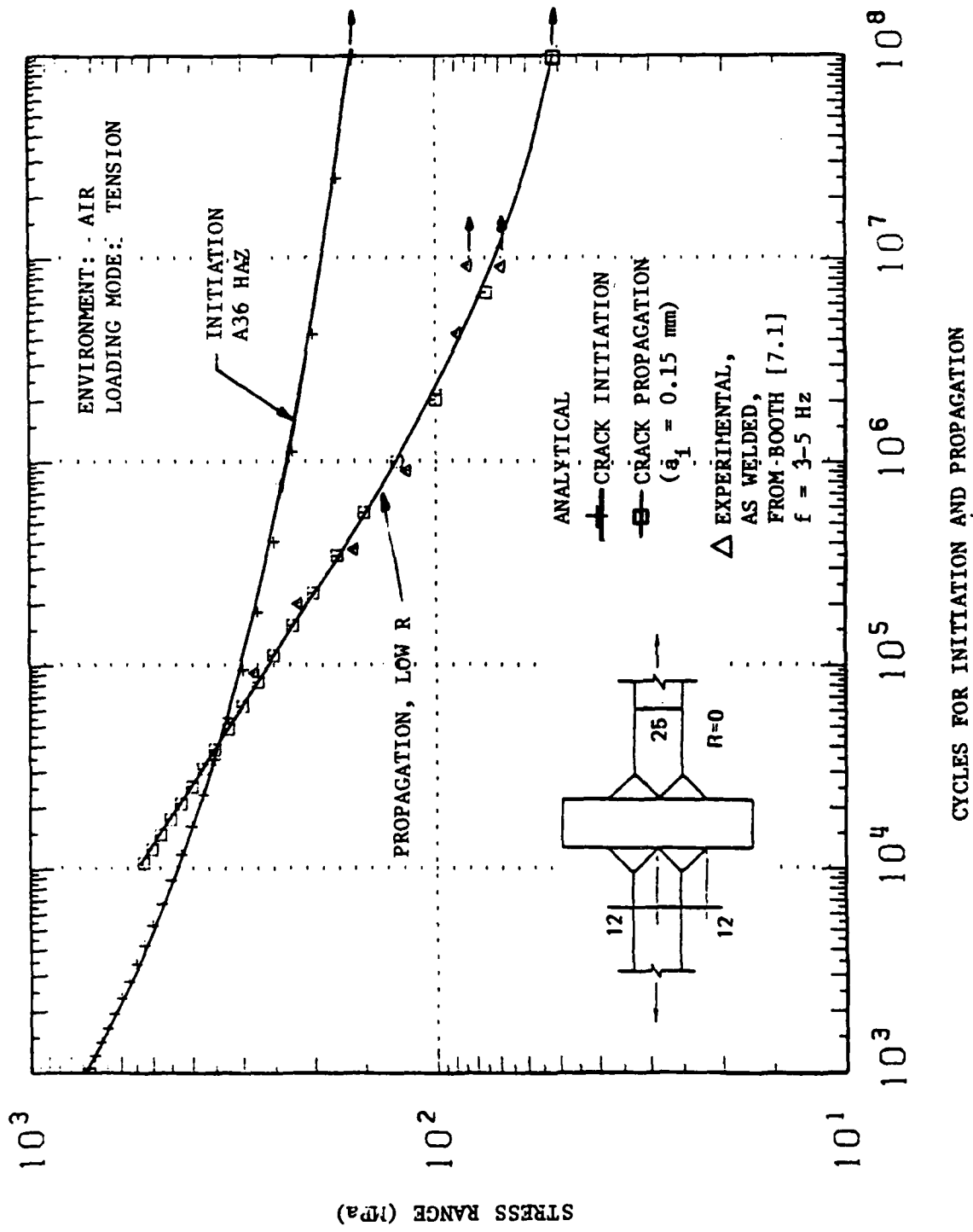
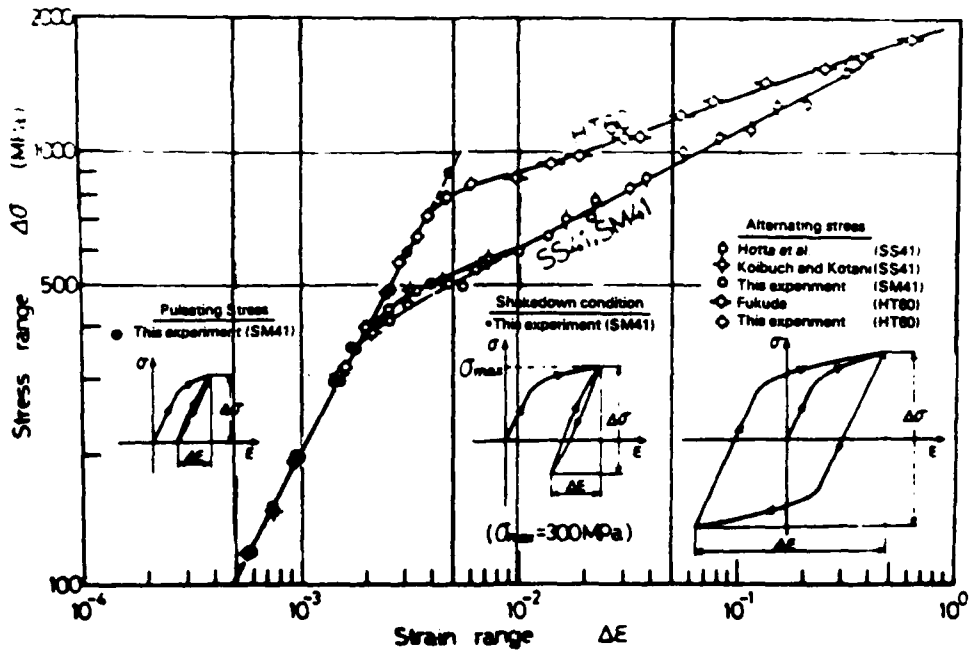
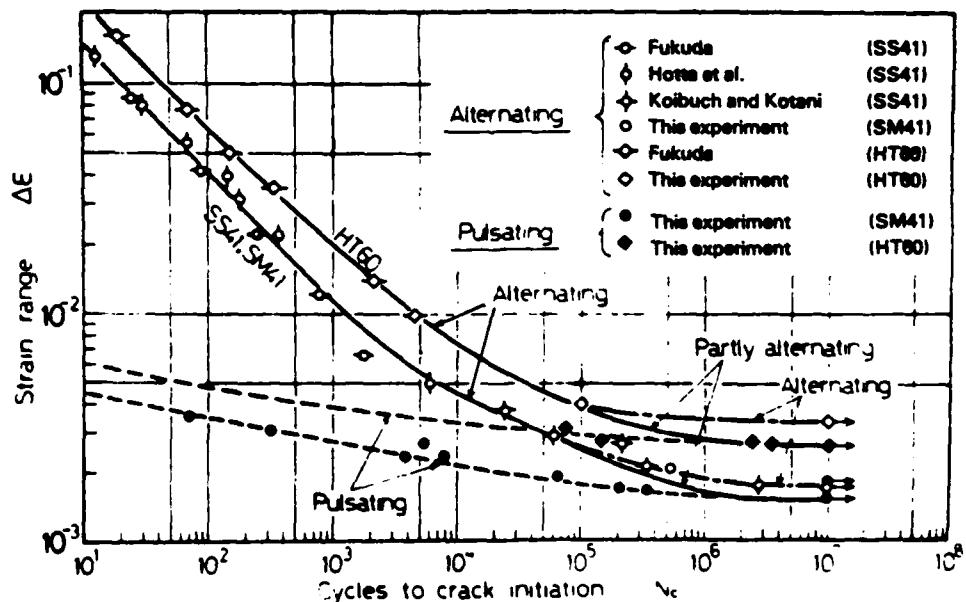


FIGURE 7.1. COMPARISON OF INITIATION AND PROPAGATION LIVES
FOR CRUCIFORM PLANAR JOINT (ENVIRONMENT - AIR)

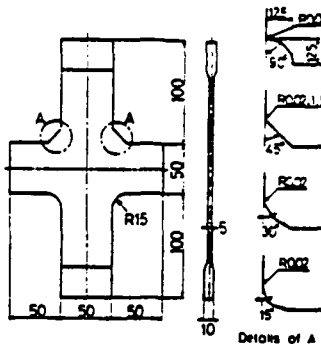


a. Cyclic Stress-Strain Relationships

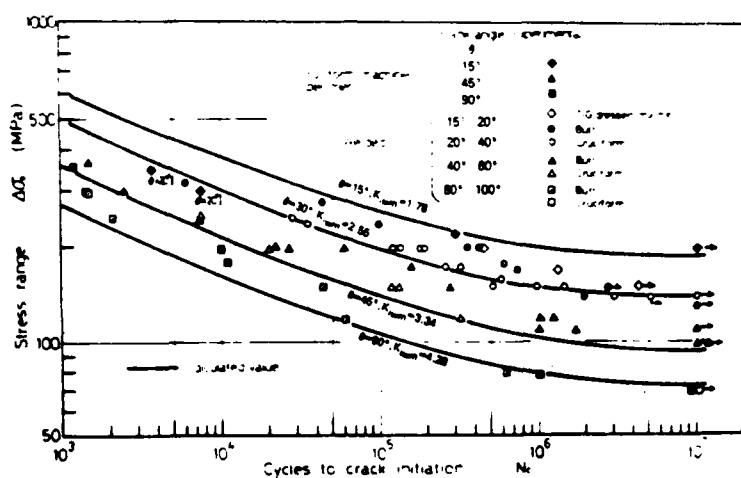


b. Fatigue Crack Initiation Life

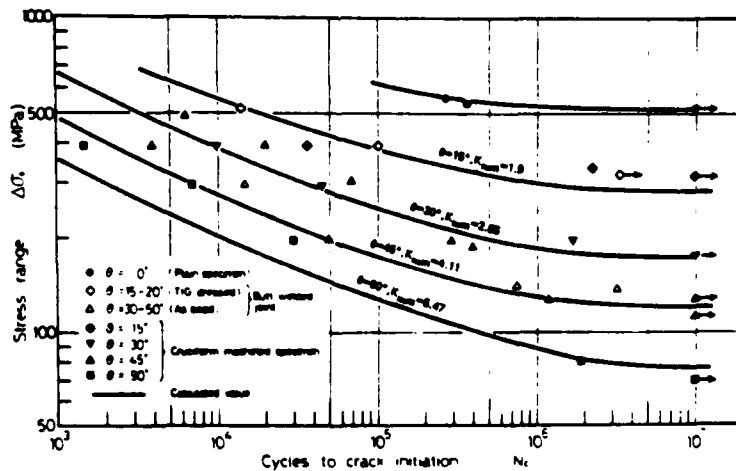
FIGURE 7.2. CYCLIC STRESS-STRAIN AND STRAIN-LIFE OF HT60 AND SM41 STEELS, FROM [7.2]



a. Details of the Machined Specimens



b. Fatigue Crack Initiation Lives at
Toes of SM41 Steel Joints



c. Fatigue Crack Initiation Lives at As-Welded
Toes of HT60 Steel Joints

FIGURE 7.3 . TEST SPECIMEN AND CRACK INITIATION LIVES OF
SM41 AND HT60 CRUCIFORM JOINTS, FROM [7.2]

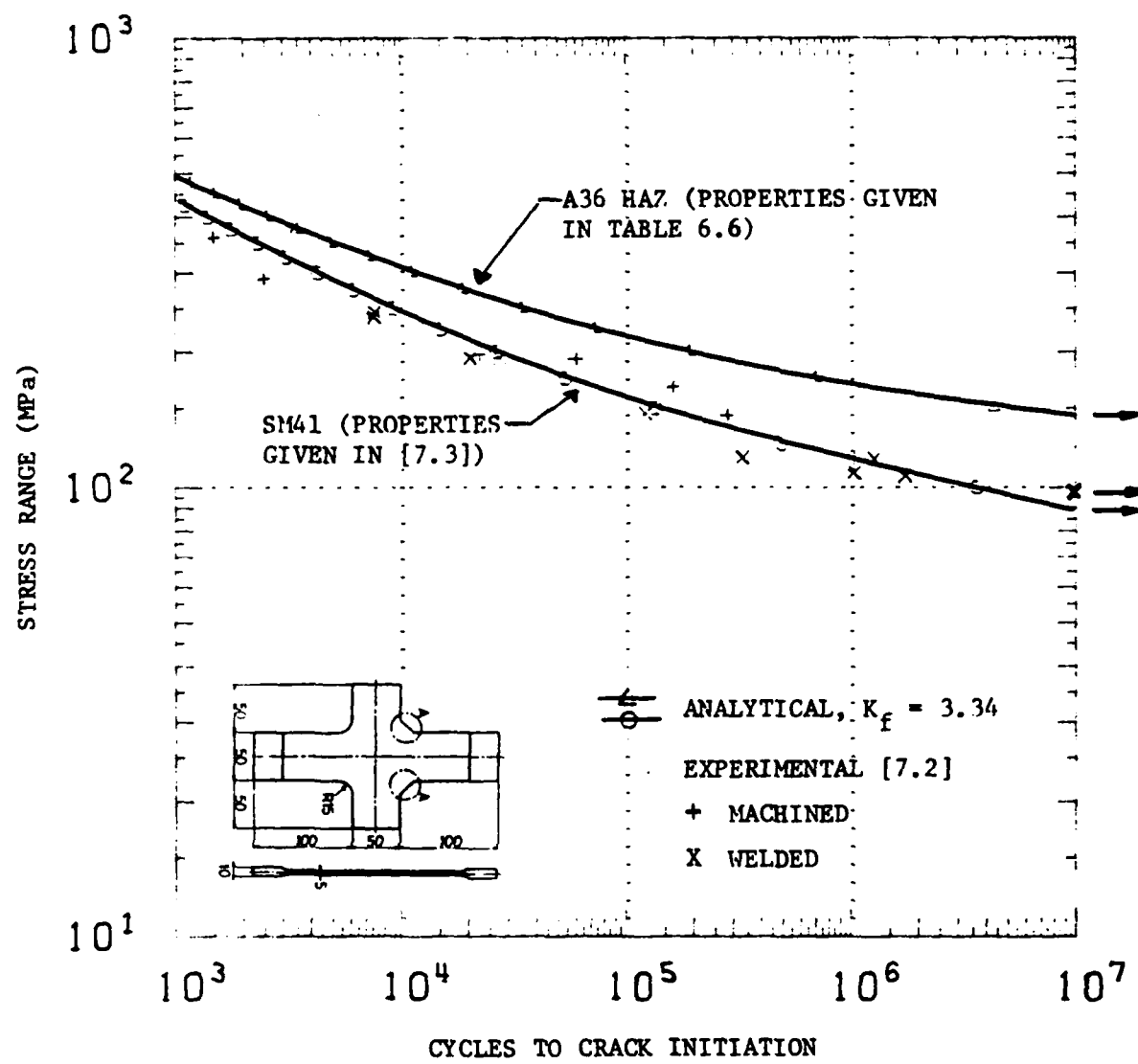


FIGURE 7.4. COMPARISON OF ANALYTICAL AND EXPERIMENTAL CRACK INITIATION RESULTS FOR MILD STEELS

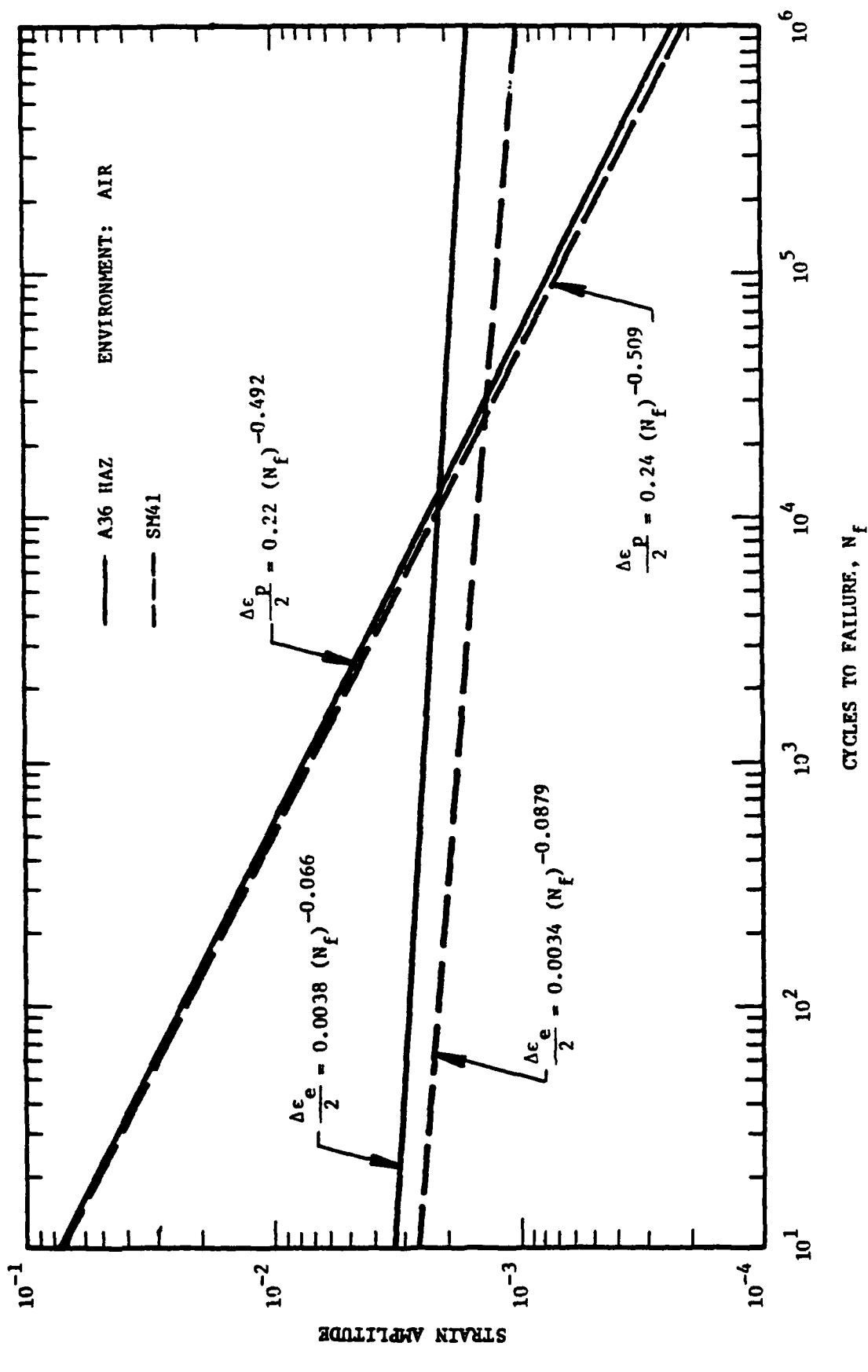


FIGURE 7.5. COMPARISON OF STRAIN-CONTROLLED FATIGUE BEHAVIOR FOR A36 HAZ AND SM41 METAL (ENVIRONMENT - AIR)

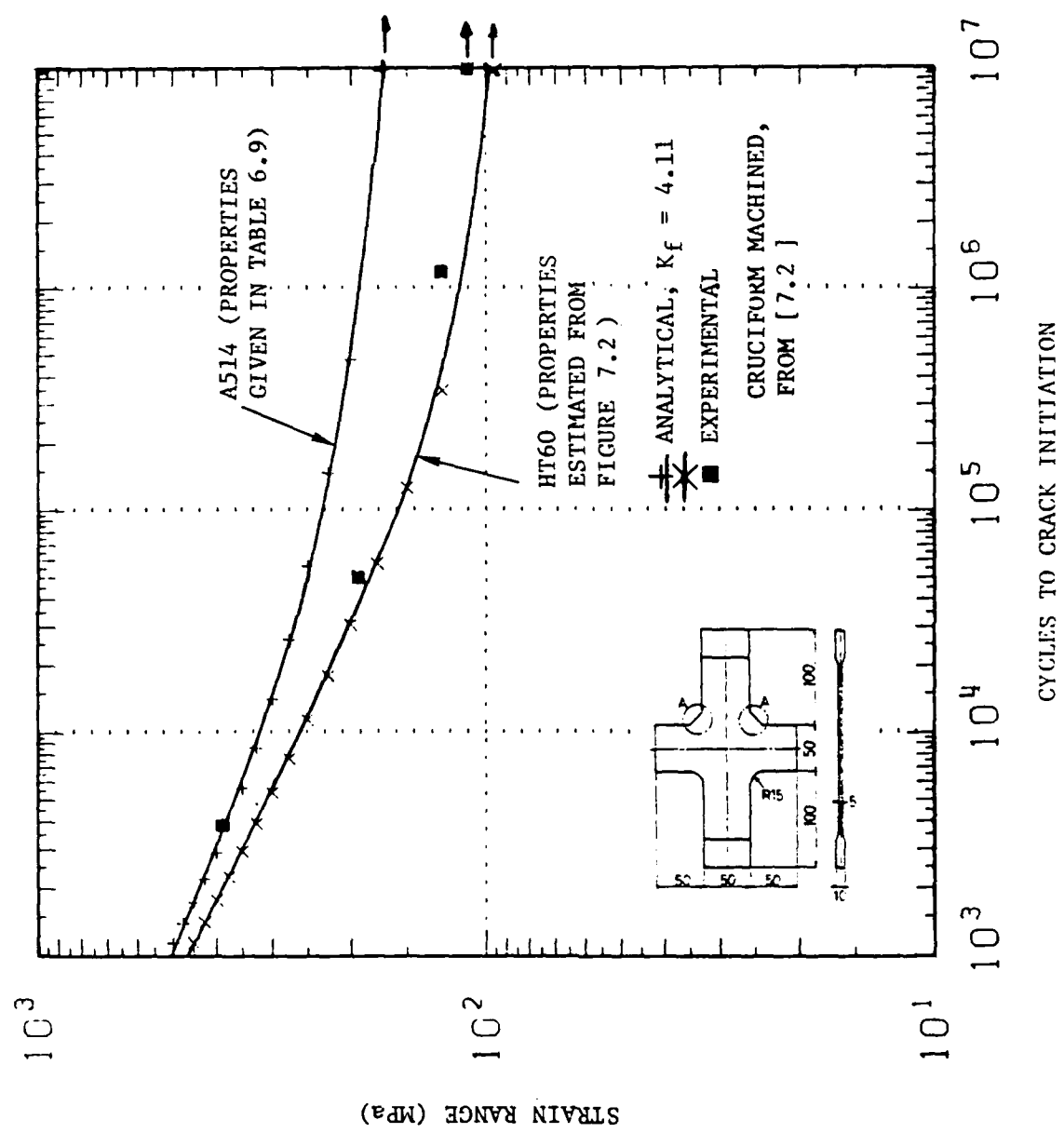


FIGURE 7.6. COMPARISON OF ANALYTICAL AND EXPERIMENTAL CRACK INITIATION RESULTS FOR HIGH-STRENGTH STEELS

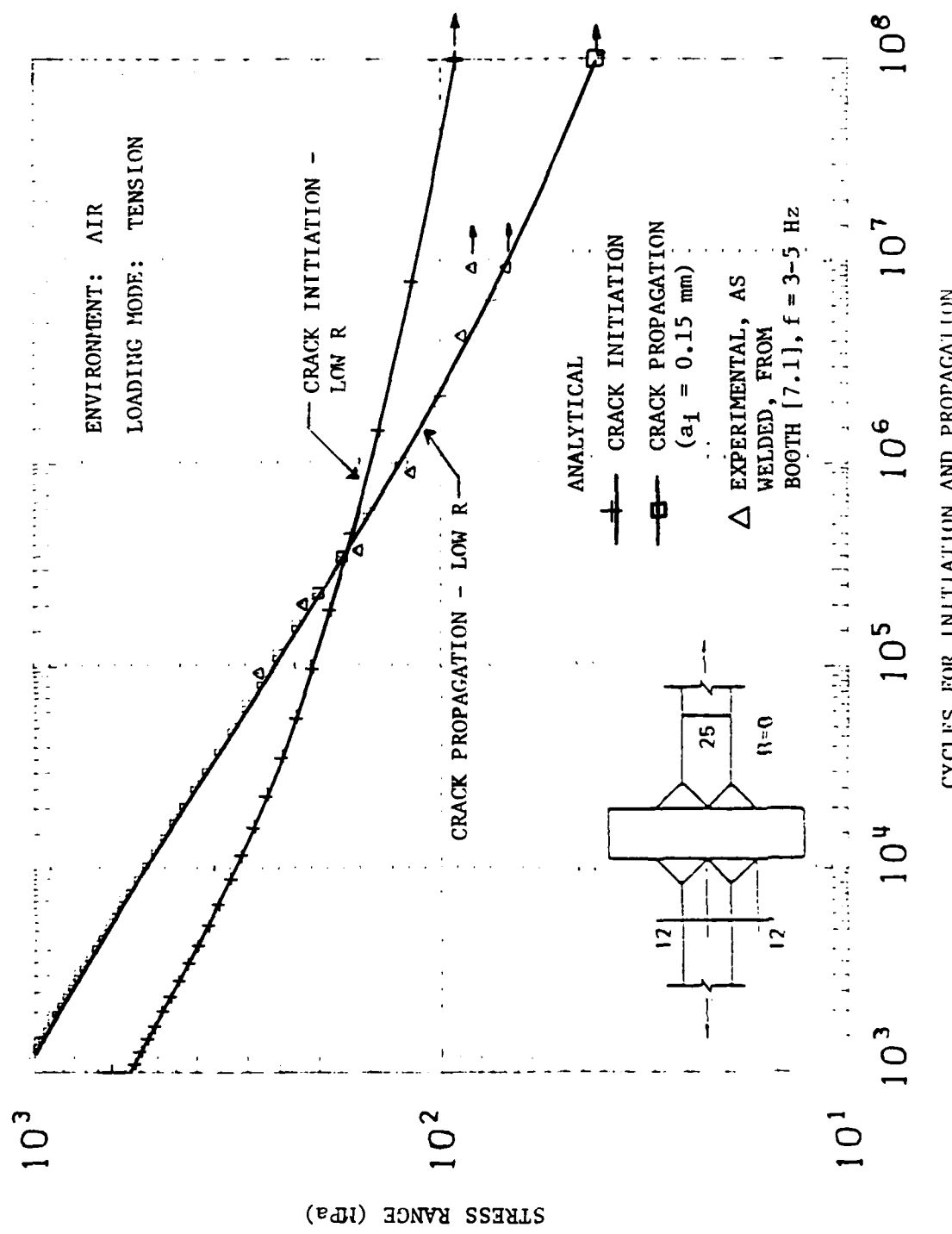


FIGURE 7.7. COMPARISON OF INITIATION AND PROPAGATION LIVES FOR CRUCIFORM PLANAR JOINTS (ENVIRONMENT - AIR)

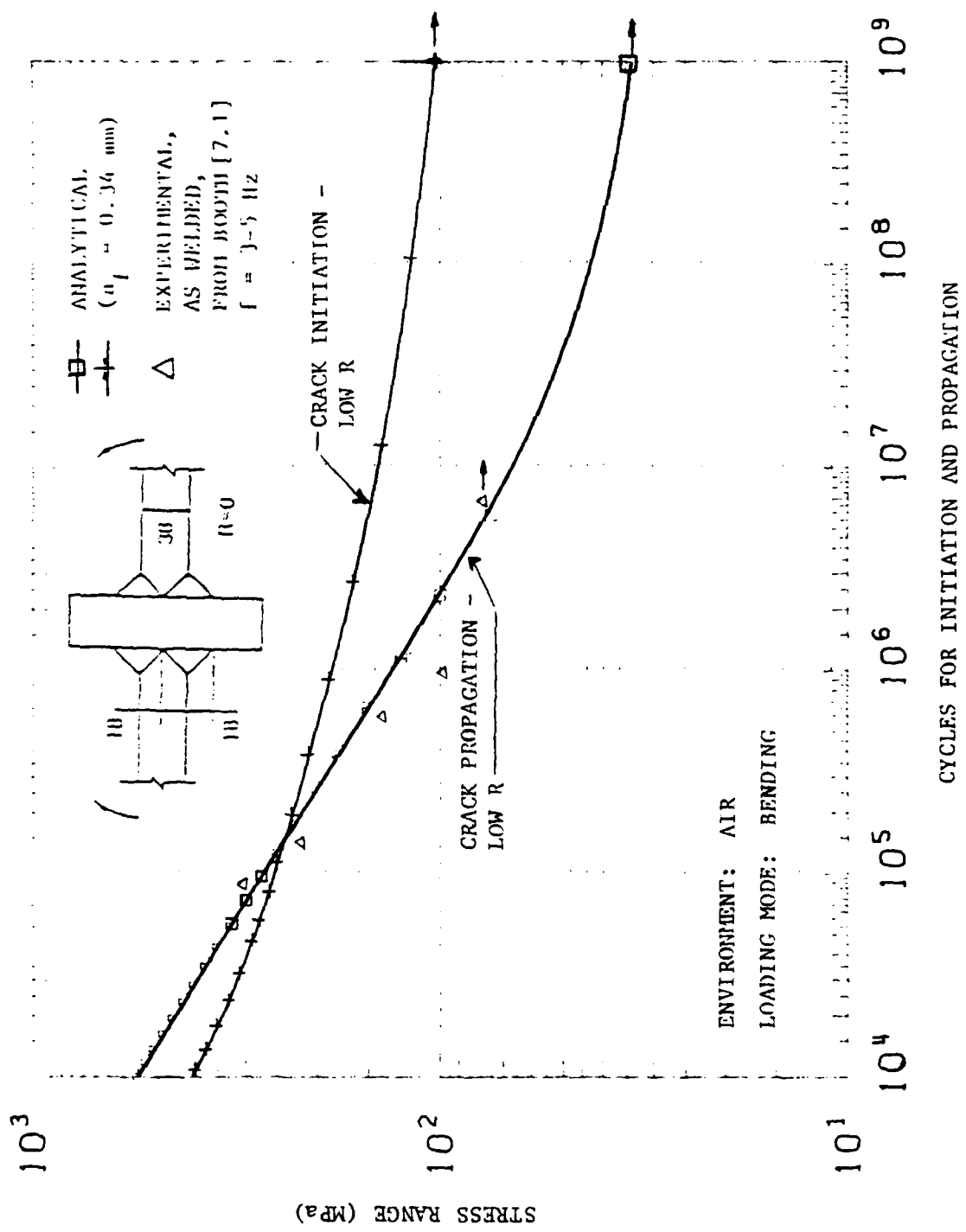


FIGURE 7.8. COMPARISON OF ANALYTICAL (LOW R) AND EXPERIMENTAL FATIGUE RESULTS FOR CRUCIFORM PLANAR JOINTS (ENVIRONMENT - AIR)

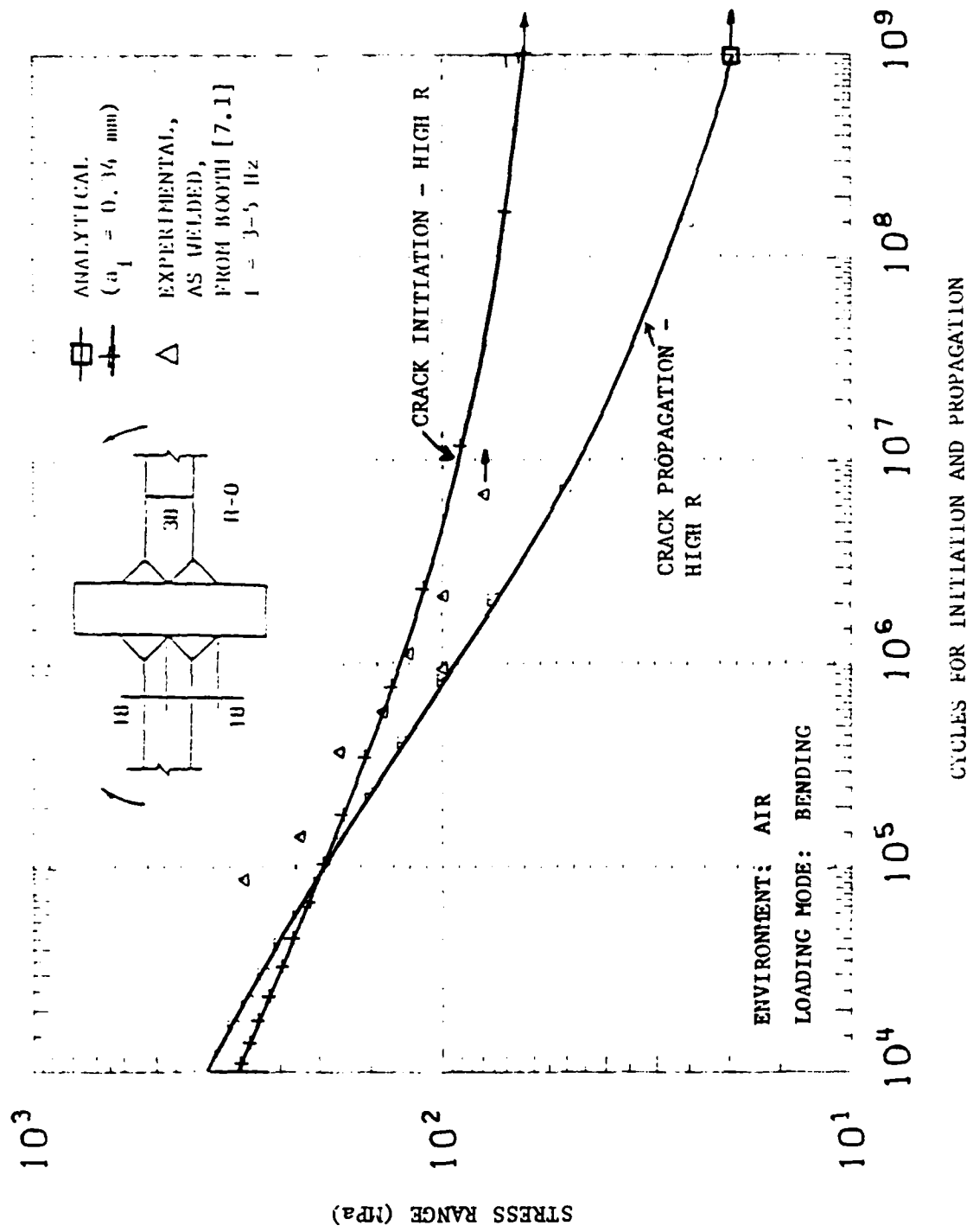


FIGURE 7.9. COMPARISON OF ANALYTICAL (HIGH R) AND EXPERIMENTAL FATIGUE RESULTS FOR CRUCIFORM PLANAR JOINTS (ENVIRONMENT - AIR)

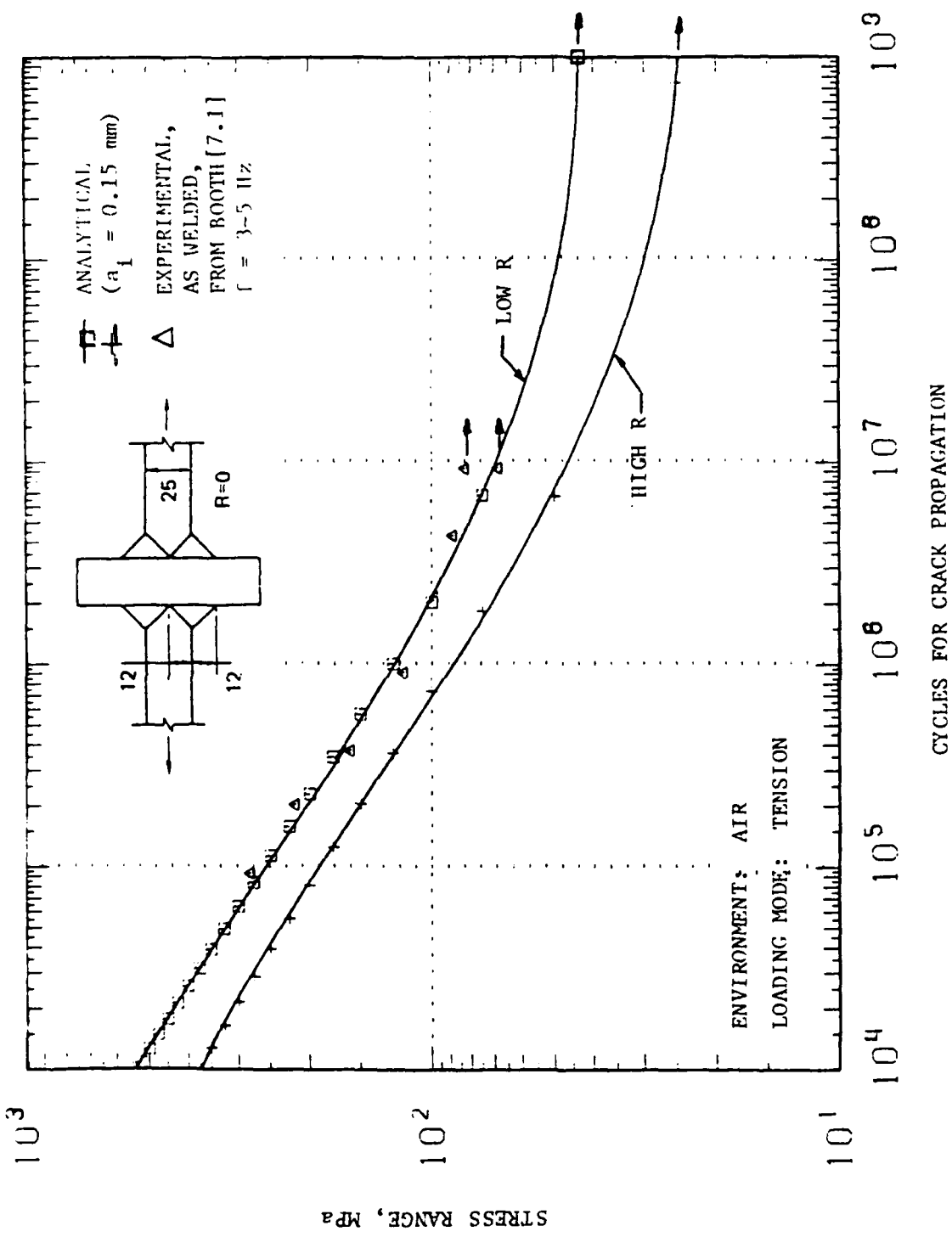


FIGURE 7.10. COMPARISON OF ANALYTICAL AND EXPERIMENTAL FATIGUE RESULTS FOR CRUCIFORM PLANAR JOINTS (ENVIRONMENT-AIR)

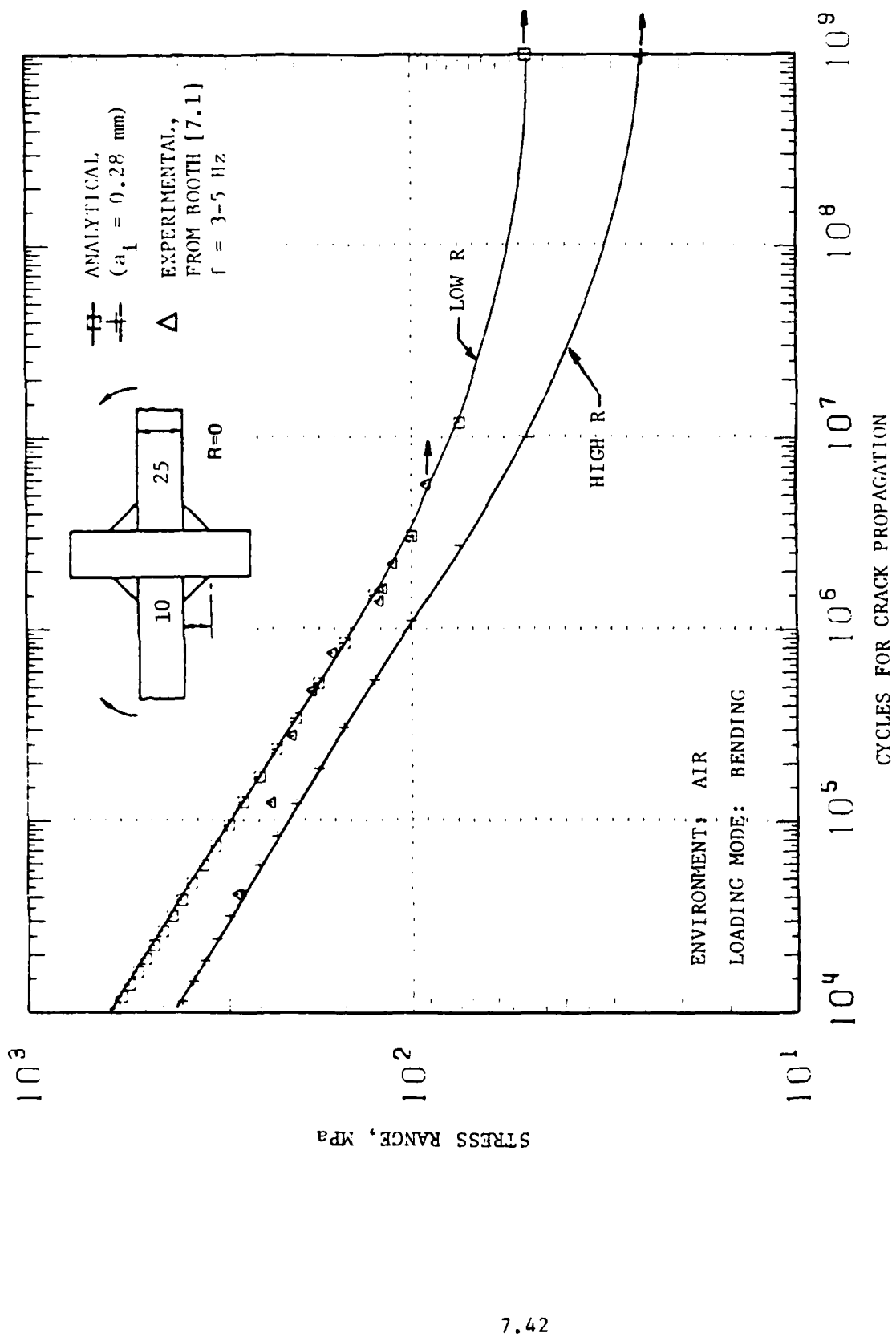


FIGURE 7.11. COMPARISON OF ANALYTICAL AND EXPERIMENTAL FATIGUE RESULTS FOR CRUCIFORM PLANAR JOINTS (ENVIRONMENT-AIR)

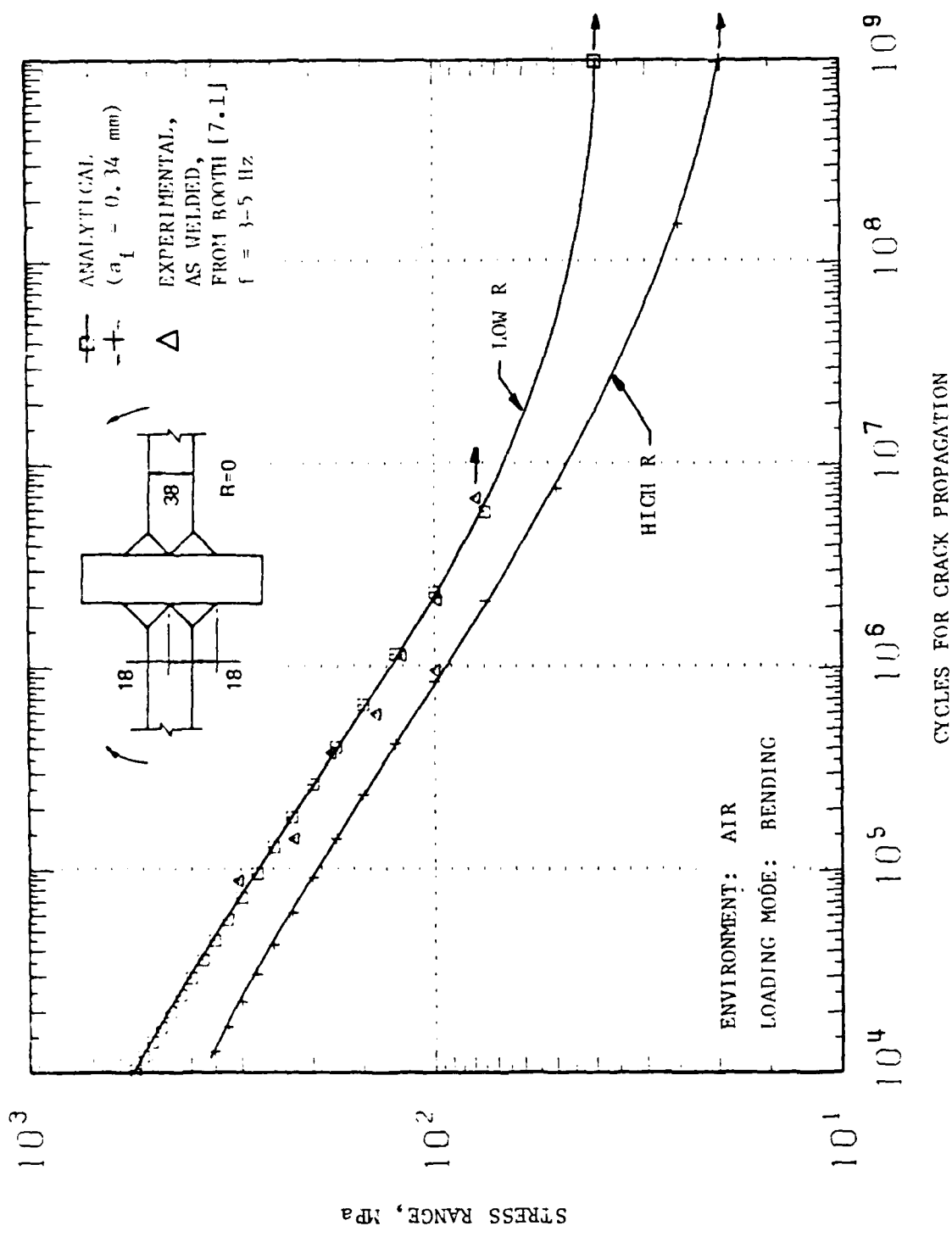


FIGURE 7.12. COMPARISON OF ANALYTICAL AND EXPERIMENTAL FATIGUE RESULTS FOR CRUCIFORM PLANAR JOINTS (ENVIRONMENT-AIR)

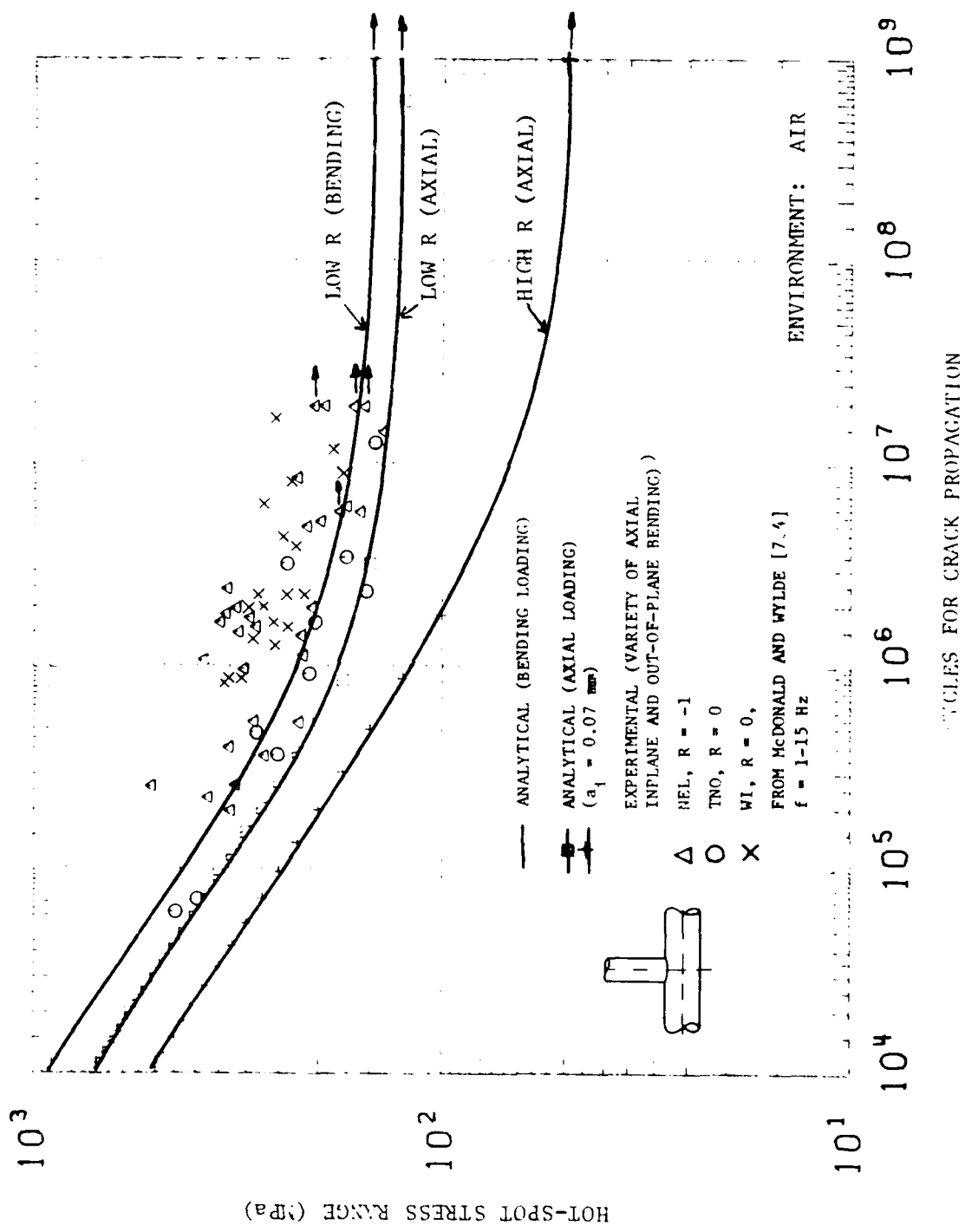


FIGURE 7.13. COMPARISON OF ANALYTICAL AND EXPERIMENTAL FATIGUE RESULTS FOR TUBULAR JOINTS,
CHORD DIAMETER 168 mm x 6 mm WALL THICKNESS (ENVIRONMENT-AIR)

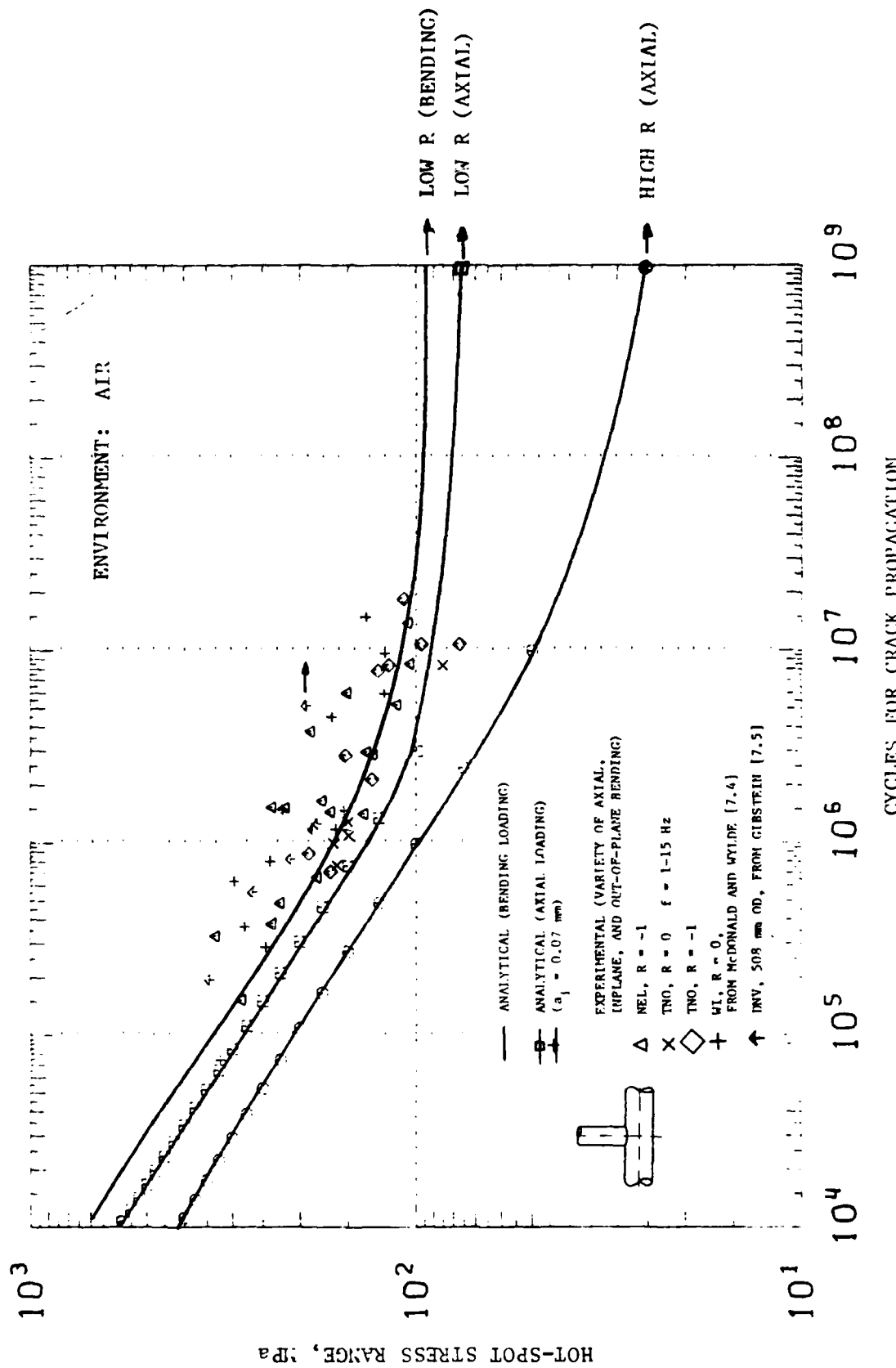


FIGURE 7.14. COMPARISON OF ANALYTICAL AND EXPERIMENTAL FATIGUE RESULTS FOR TUBULAR JOINTS,
CHORD DIAMETER 457 mm x 16 mm WALL THICKNESS (ENVIRONMENT-AIR)

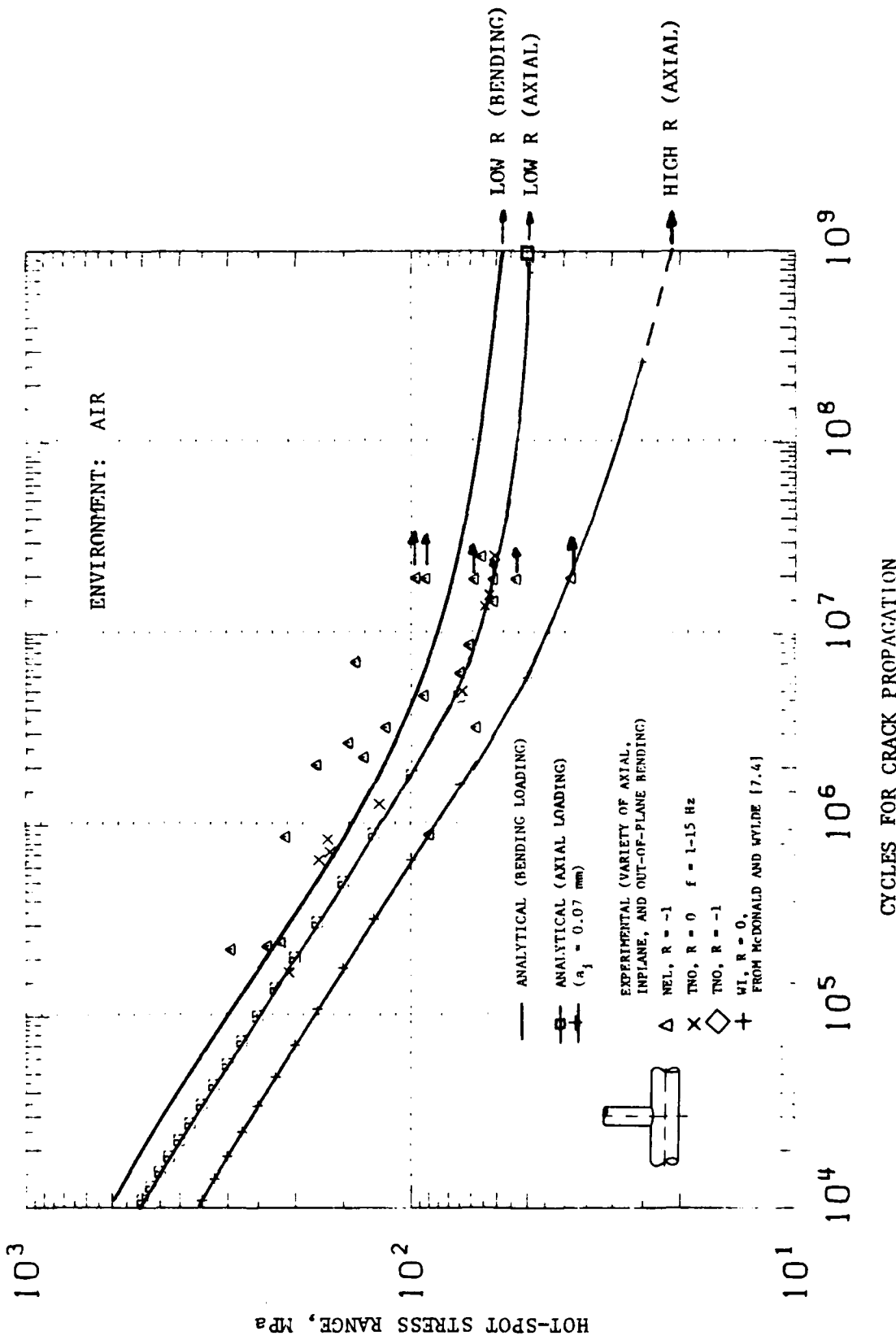
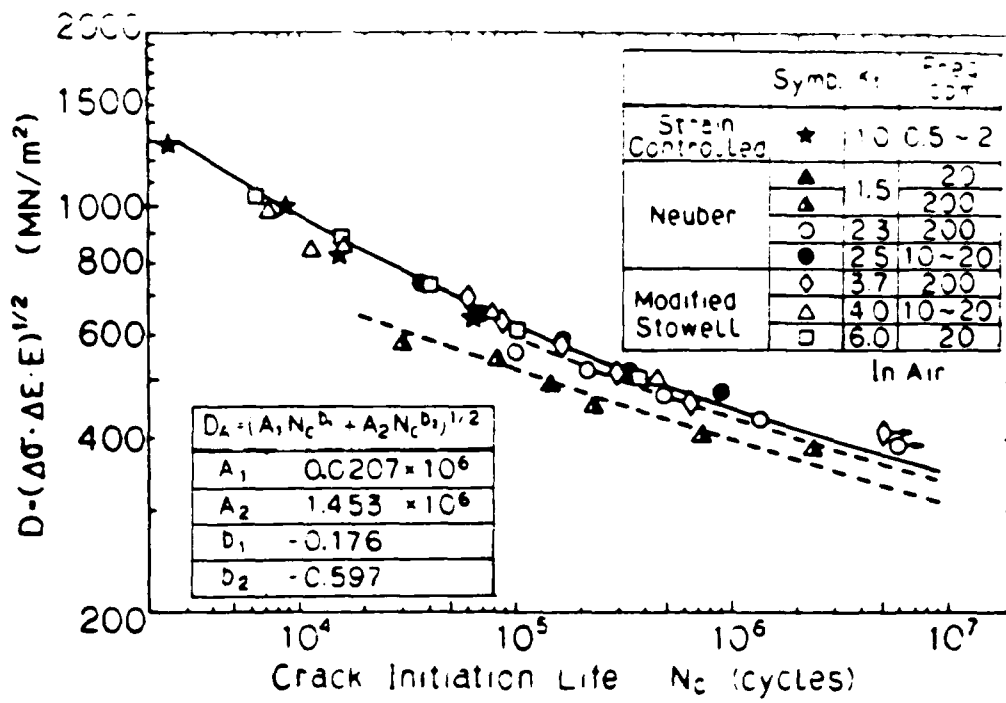
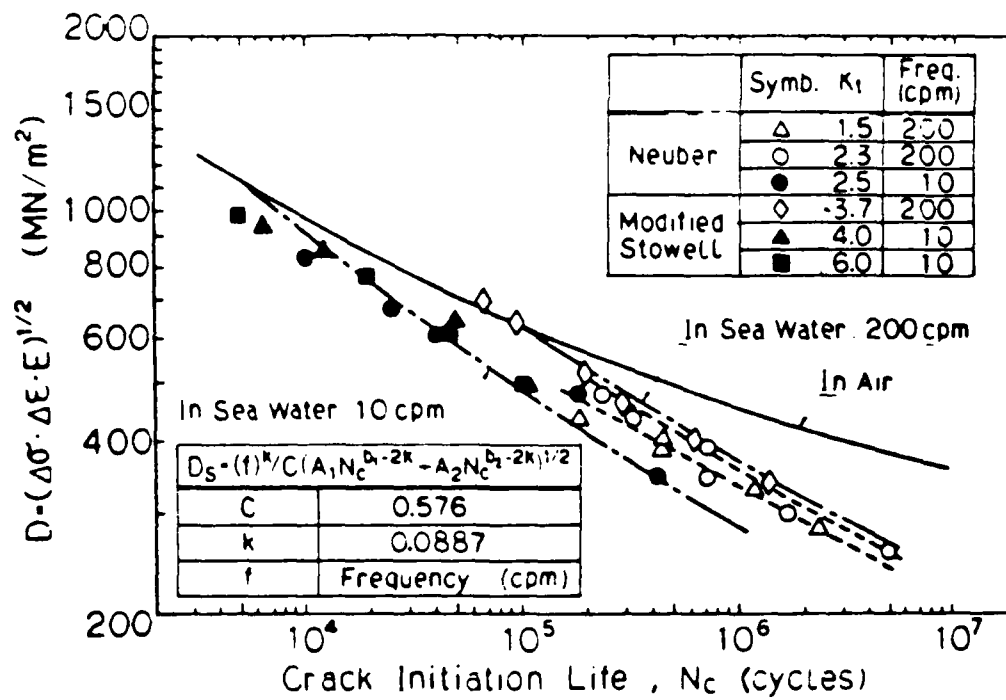


FIGURE 7.15. COMPARISON OF ANALYTICAL AND EXPERIMENTAL FATIGUE RESULTS FOR TUBULAR JOINTS,
CHORD DIAMETER 9.14 mm x 32 mm WALL THICKNESS (ENVIRONMENT-AIR)



a. Air



b. Seawater

FIGURE 7.16. RELATIONSHIP BETWEEN STRESS-STRAIN FUNCTION, D, AND FATIGUE CRACK INITIATION LIVES IN AIR AND SEAWATER, FROM [7.3]

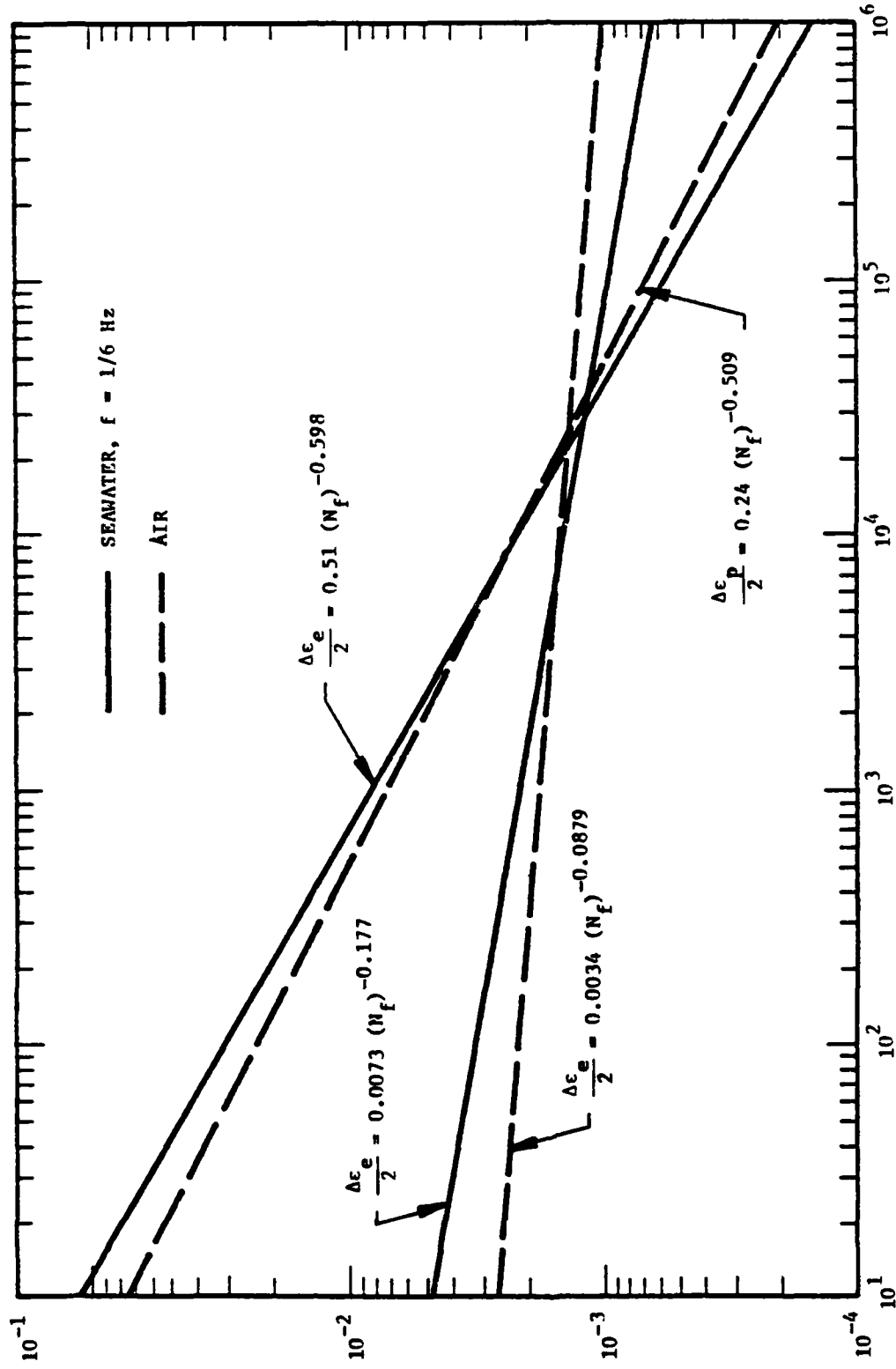


FIGURE 7.17. COMPARISON OF STRAIN-CONTROLLED FATIGUE BEHAVIOR FOR SM41 METAL IN AIR AND SEA WATER

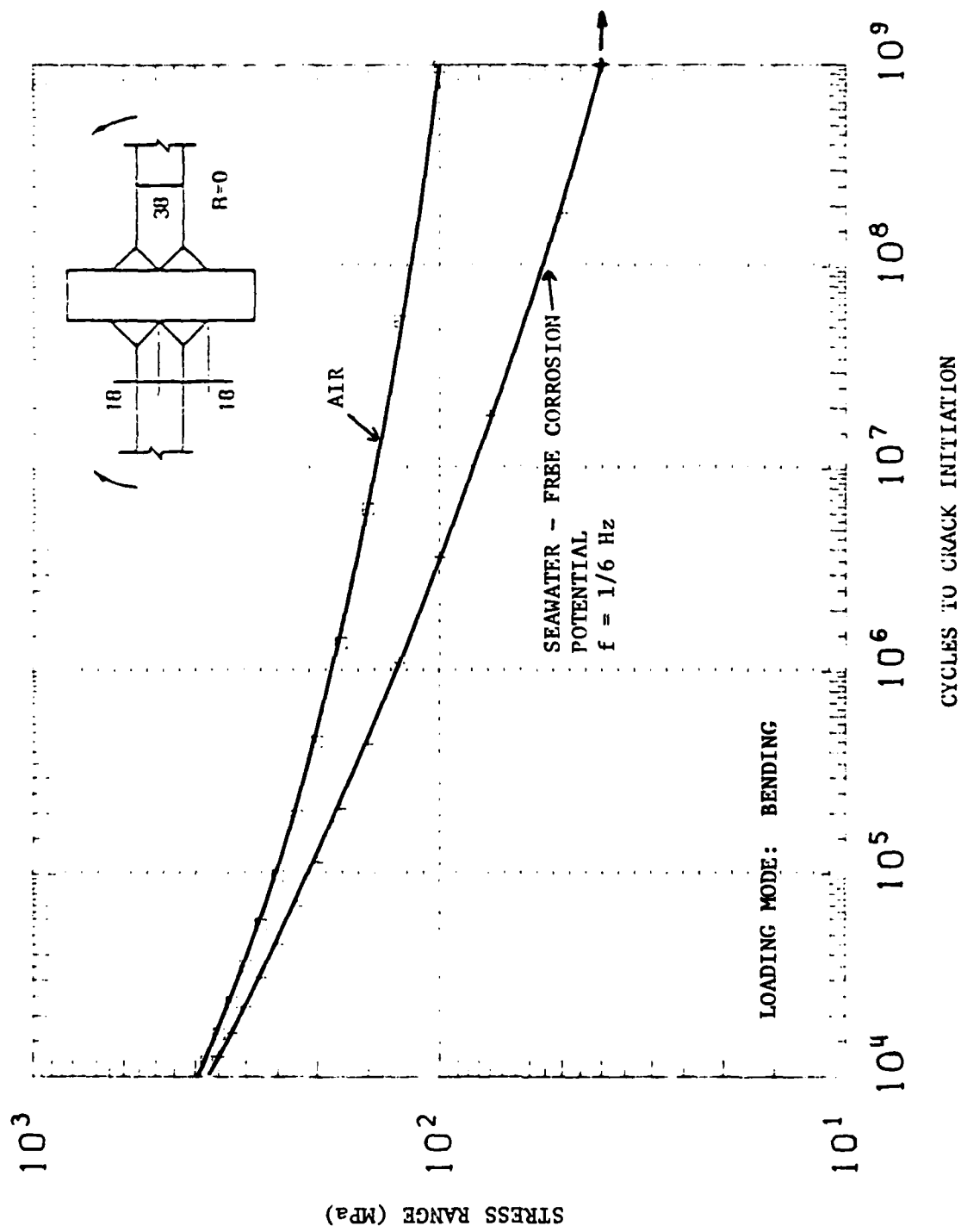


FIGURE 7.18. COMPARISON OF ANALYTICAL CRACK INITIATION RESULTS FOR CRUCIFORM PLANAR JOINTS IN AIR AND SEAWATER

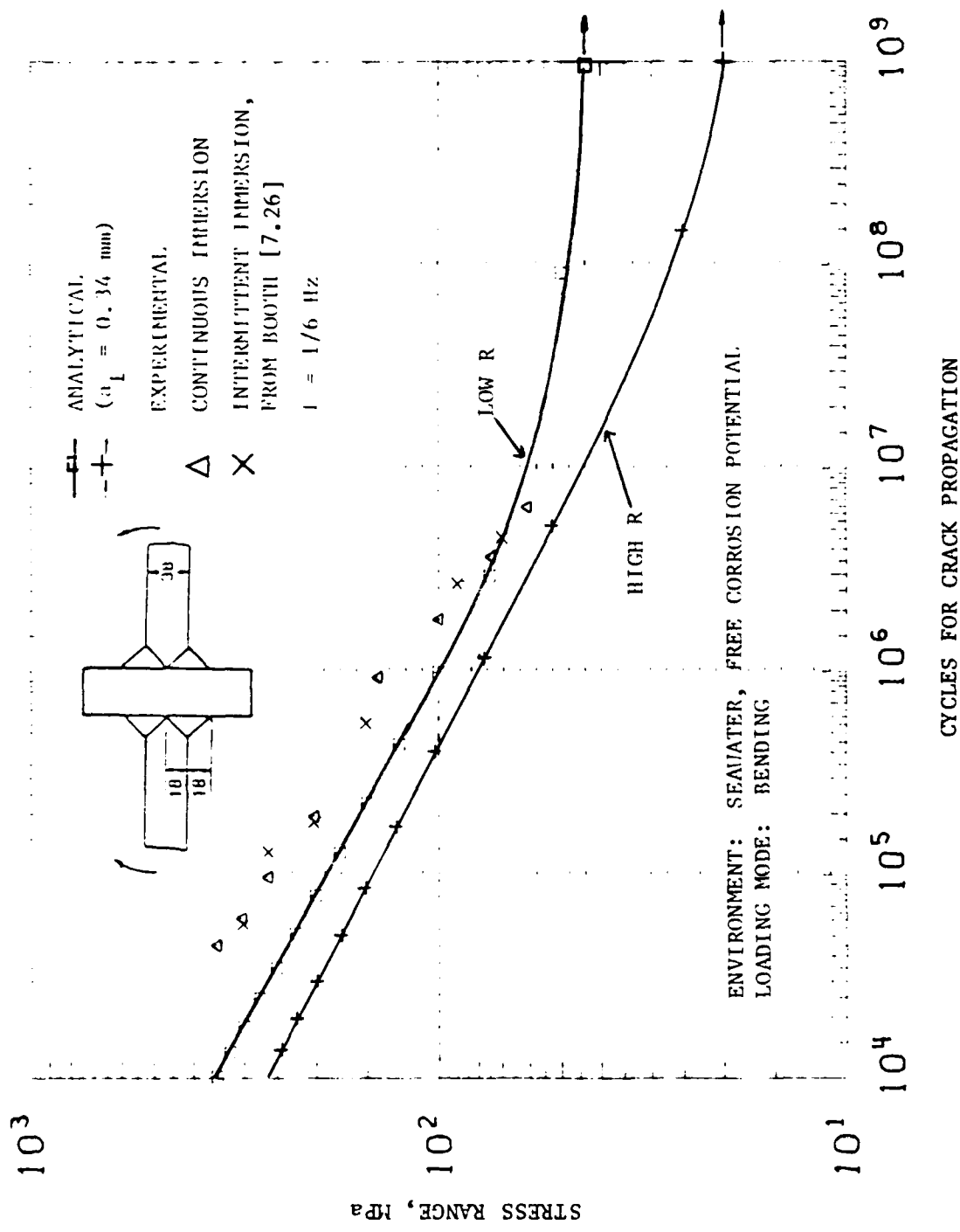


FIGURE 7.19. COMPARISON OF ANALYTICAL AND EXPERIMENTAL FATIGUE RESULTS FOR CRUCIFORM PLANAR JOINTS (ENVIRONMENT-SEAWATER, FREE CORROSION POTENTIAL)

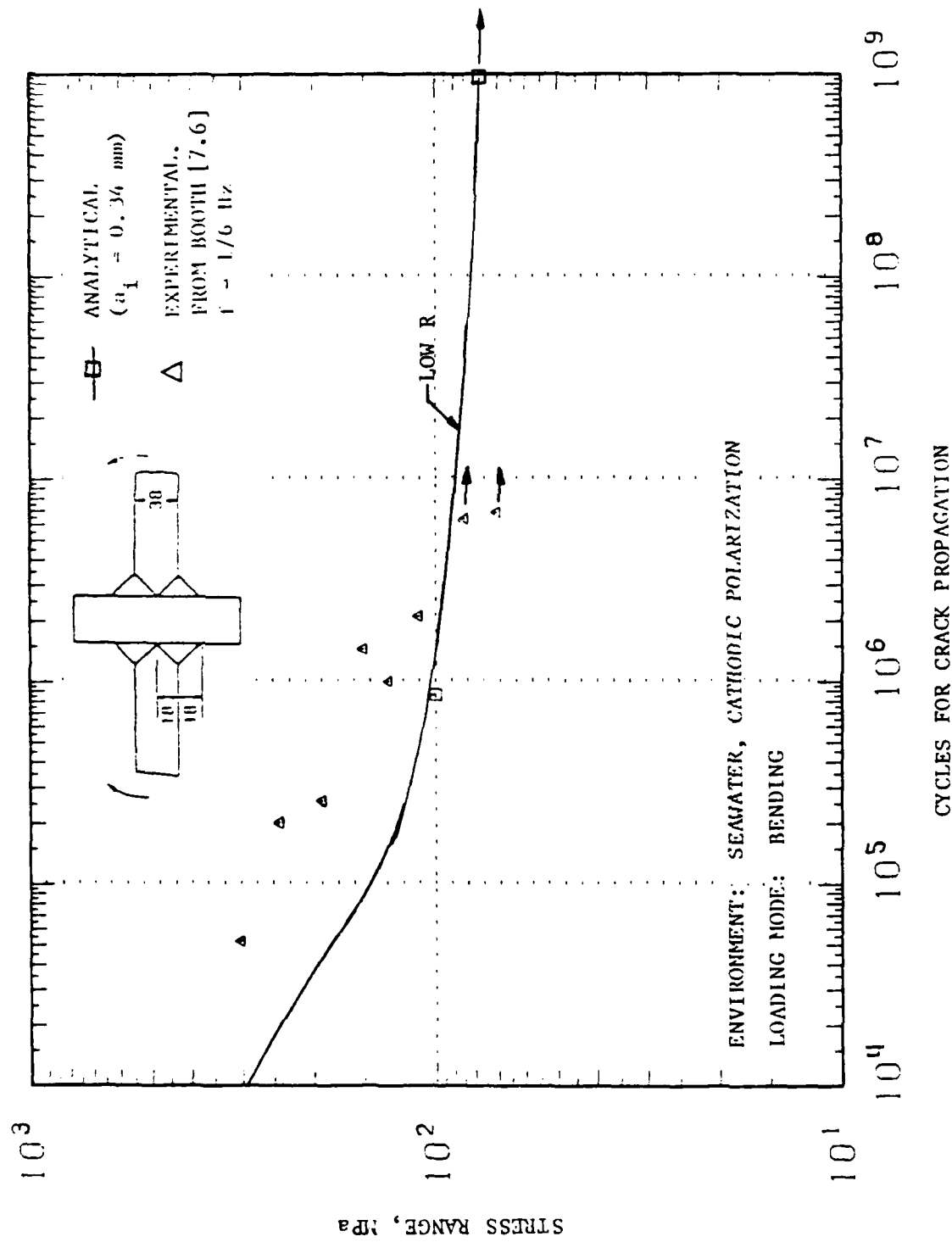


FIGURE 7.20. COMPARISON OF ANALYTICAL AND EXPERIMENTAL FATIGUE RESULTS FOR CRUCIFORM PLANAR JOINTS (ENVIRONMENT-SEAWATER, CATHODIC POLARIZATION)

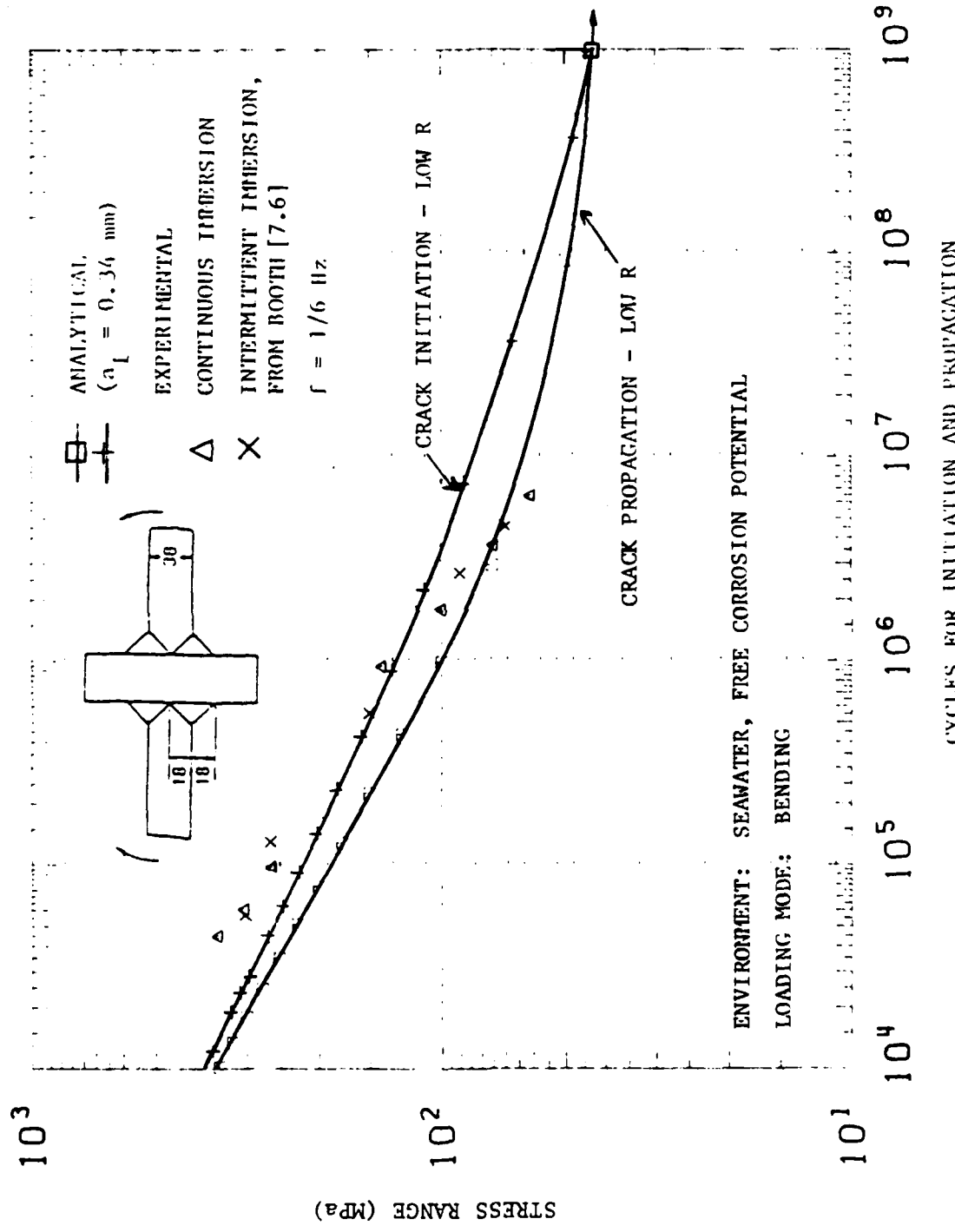


FIGURE 7.21. COMPARISON OF ANALYTICAL (LOW R) AND EXPERIMENTAL FATIGUE RESULTS FOR CRUCIFORM PLANAR JOINTS (ENVIRONMENT - SEAWATER, FREE CORROSION POTENTIAL)

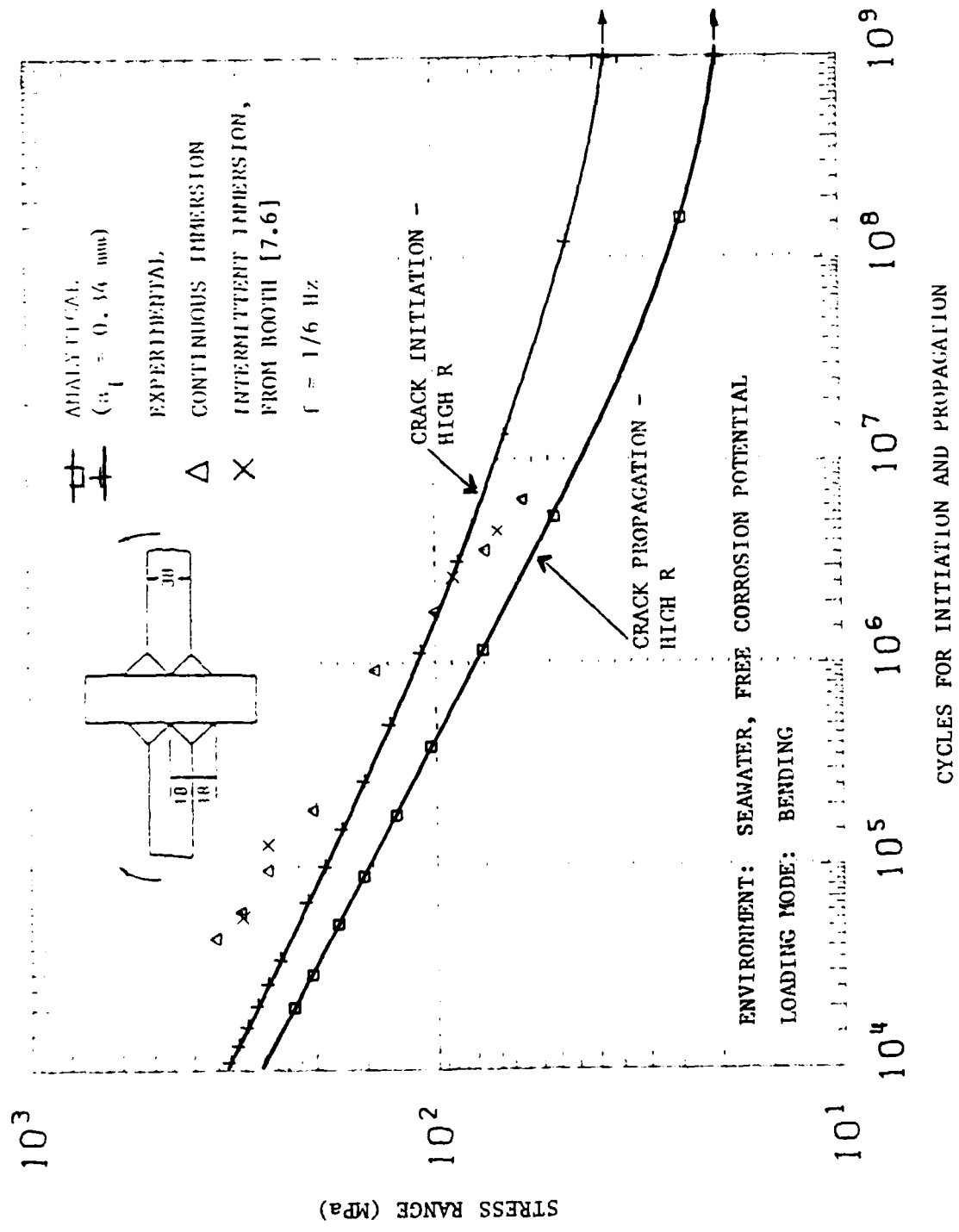


FIGURE 7.22. COMPARISON OF ANALYTICAL (HIGH R) AND EXPERIMENTAL FATIGUE RESULTS FOR CRUCIFORM PLANAR JOINTS (ENVIRONMENT - SEAWATER, FREE CORROSION POTENTIAL)

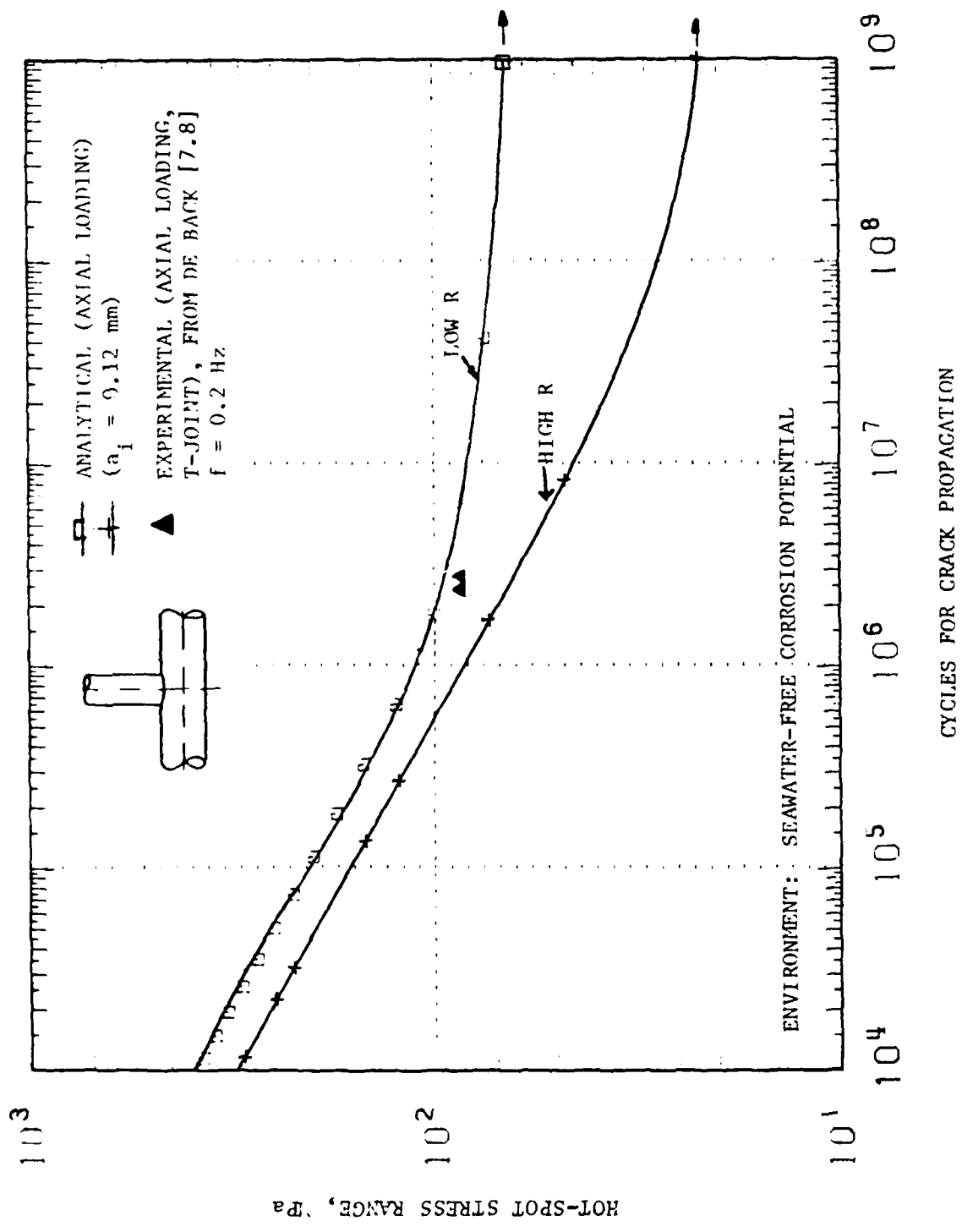


FIGURE 7.23. COMPARISON OF ANALYTICAL AND EXPERIMENTAL FATIGUE RESULTS FOR TUBULAR JOINTS, CHORD DIAMETER 457 mm x 16 mm WALL THICKNESS (ENVIRONMENT-SEAWATER-FREE CORROSION POTENTIAL)

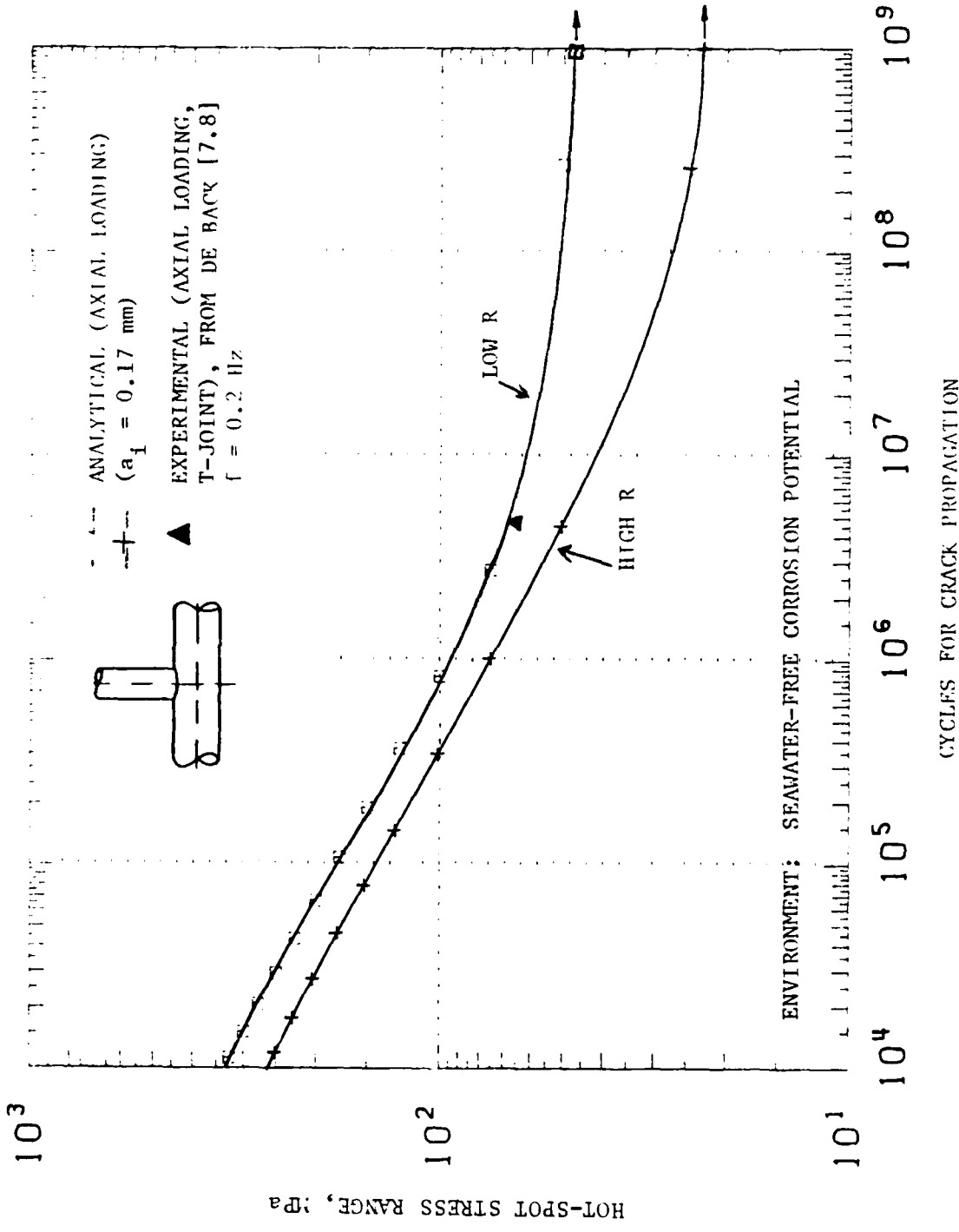


FIGURE 7.24. COMPARISON OF ANALYTICAL AND EXPERIMENTAL FATIGUE RESULTS FOR TUBULAR JOINTS, CHORD DIAMETER 914 mm x 32 mm WALL THICKNESS (ENVIRONMENT-SEAWATER-FREE CORROSION POTENTIAL)

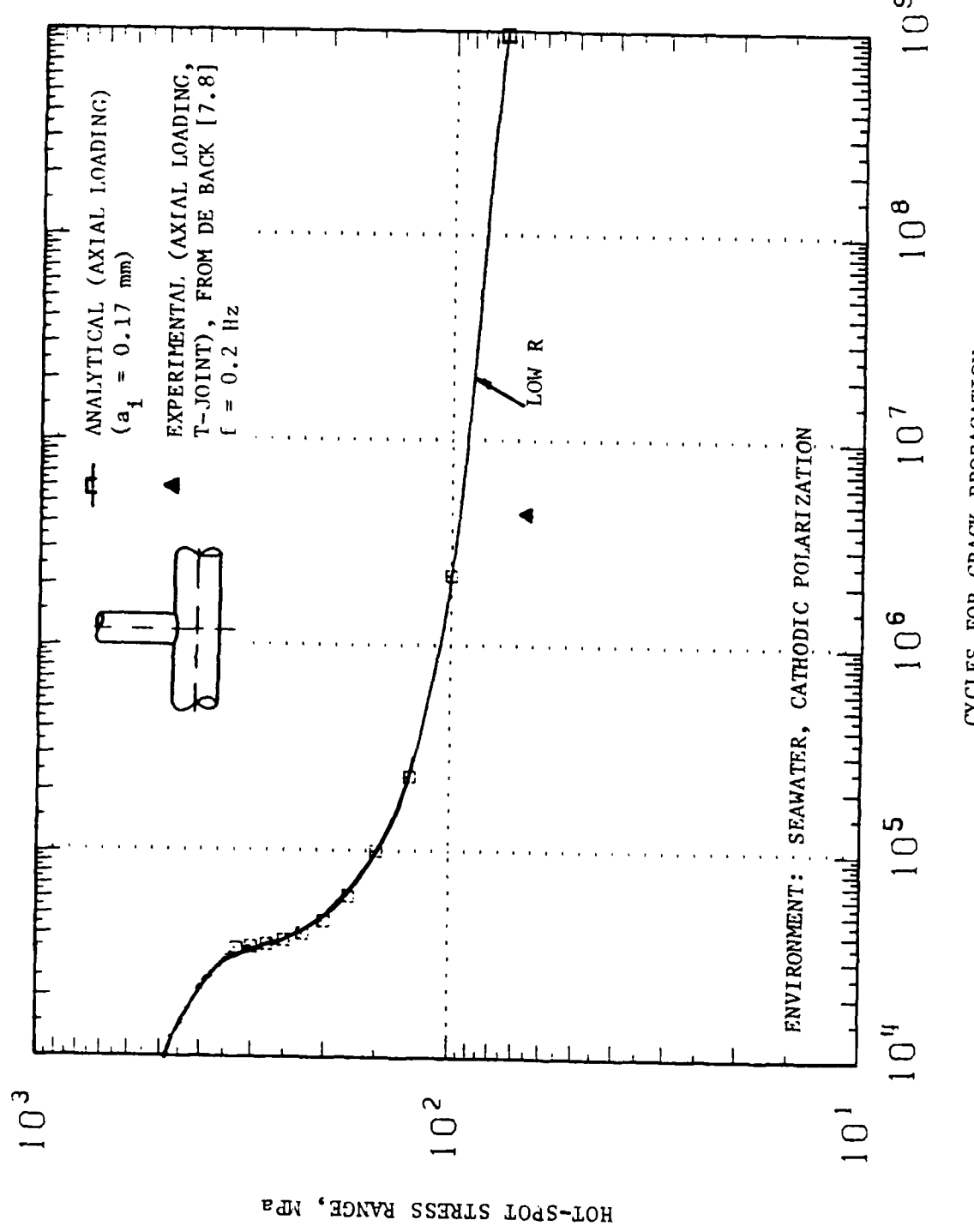


FIGURE 7.25. COMPARISON OF ANALYTICAL AND EXPERIMENTAL FATIGUE RESULTS FOR TUBULAR RESULTS, CHORD DIAMETER 914 mm x 32 mm WALL THICKNESS (ENVIRONMENT-SEAWATER-CATHODIC POLARIZATION)

CYCLES FOR CRACK PROPAGATION

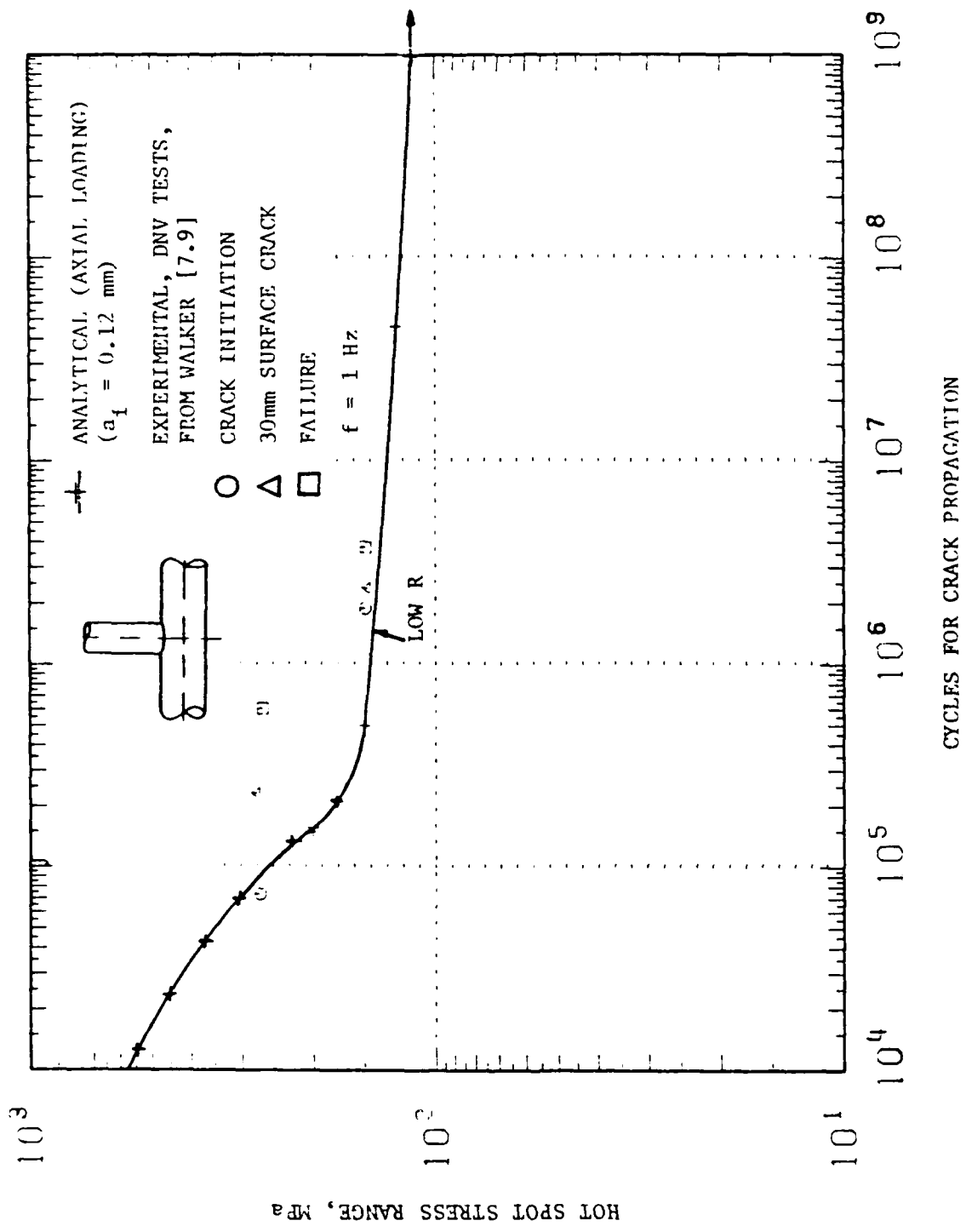


FIGURE 7.26. COMPARISON OF ANALYTICAL AND EXPERIMENTAL FATIGUE RESULTS FOR TUBULAR JOINTS, CHORD
 DIAMETER 508 mm x 16 mm WALL THICKNESS (ENVIRONMENT-SEAWATER-CATHODIC POLARIZATION)

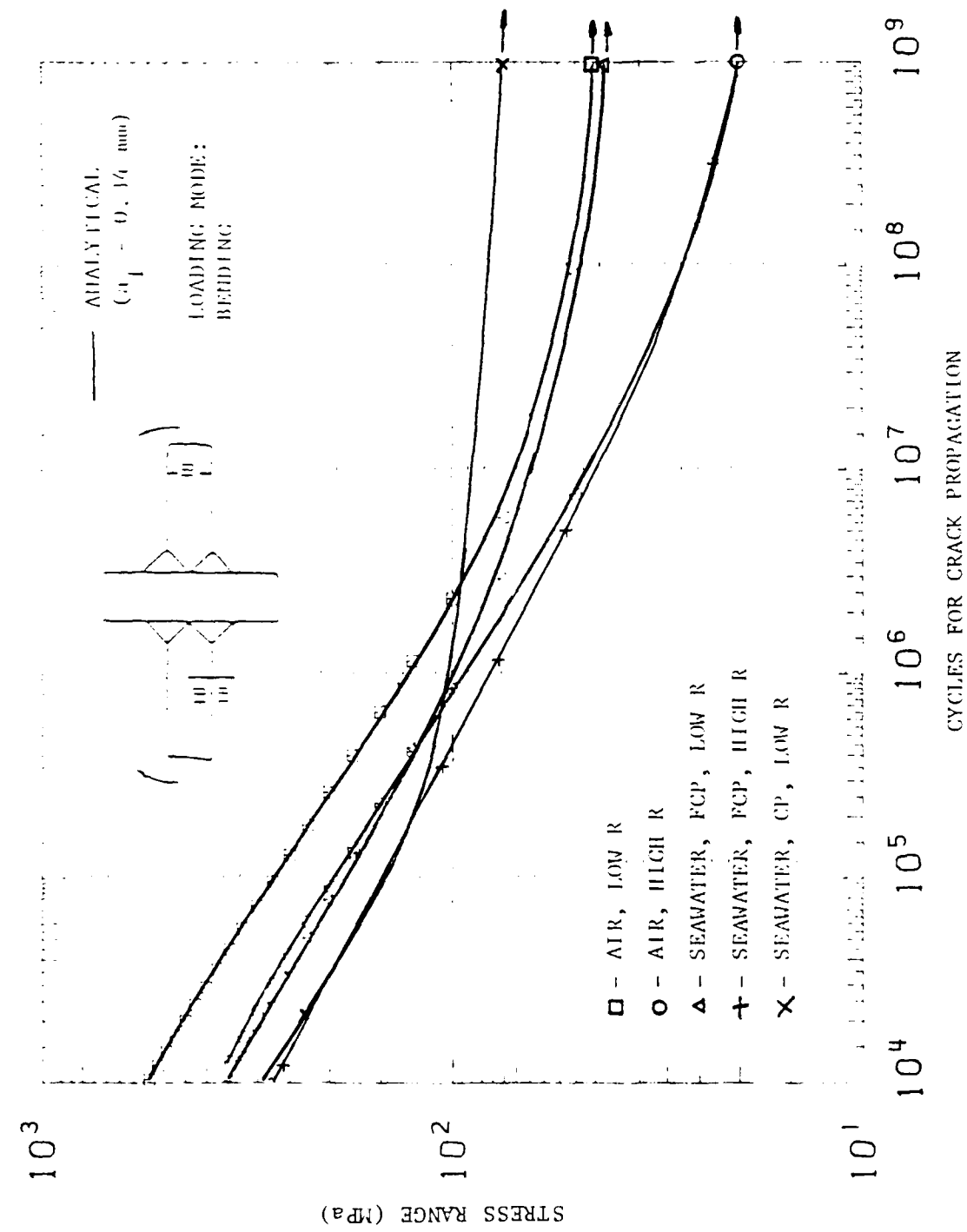


FIGURE 7.27. SENSITIVITY OF ENVIRONMENT ON ANALYTICAL CRACK PROPAGATION RESULTS FOR A CRUCIFORM PLANAR JOINT

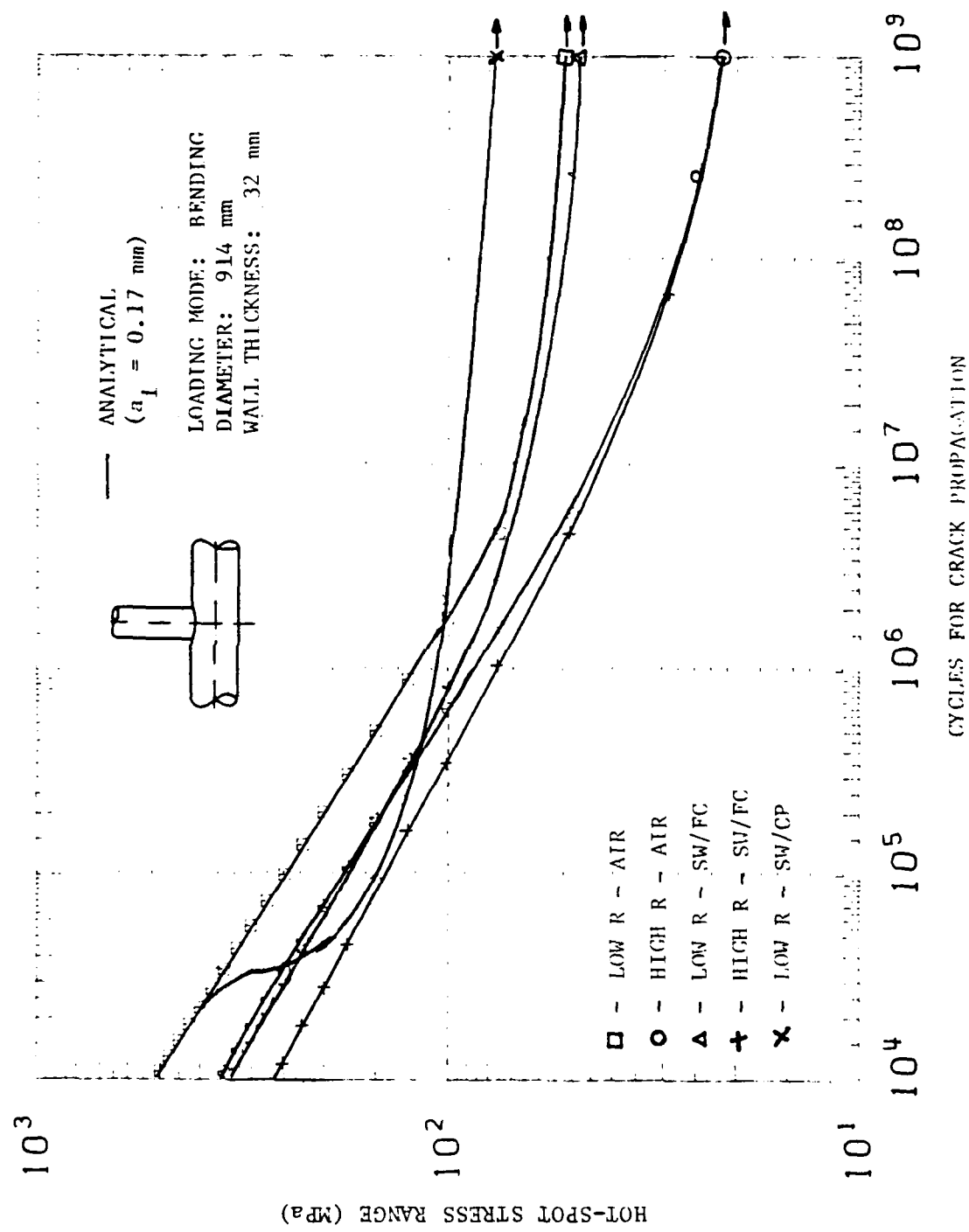


FIGURE 7.28. SENSITIVITY OF ENVIRONMENT AND R ON ANALYTICAL CRACK PROPAGATION RESULTS FOR A TUBULAR JOINT

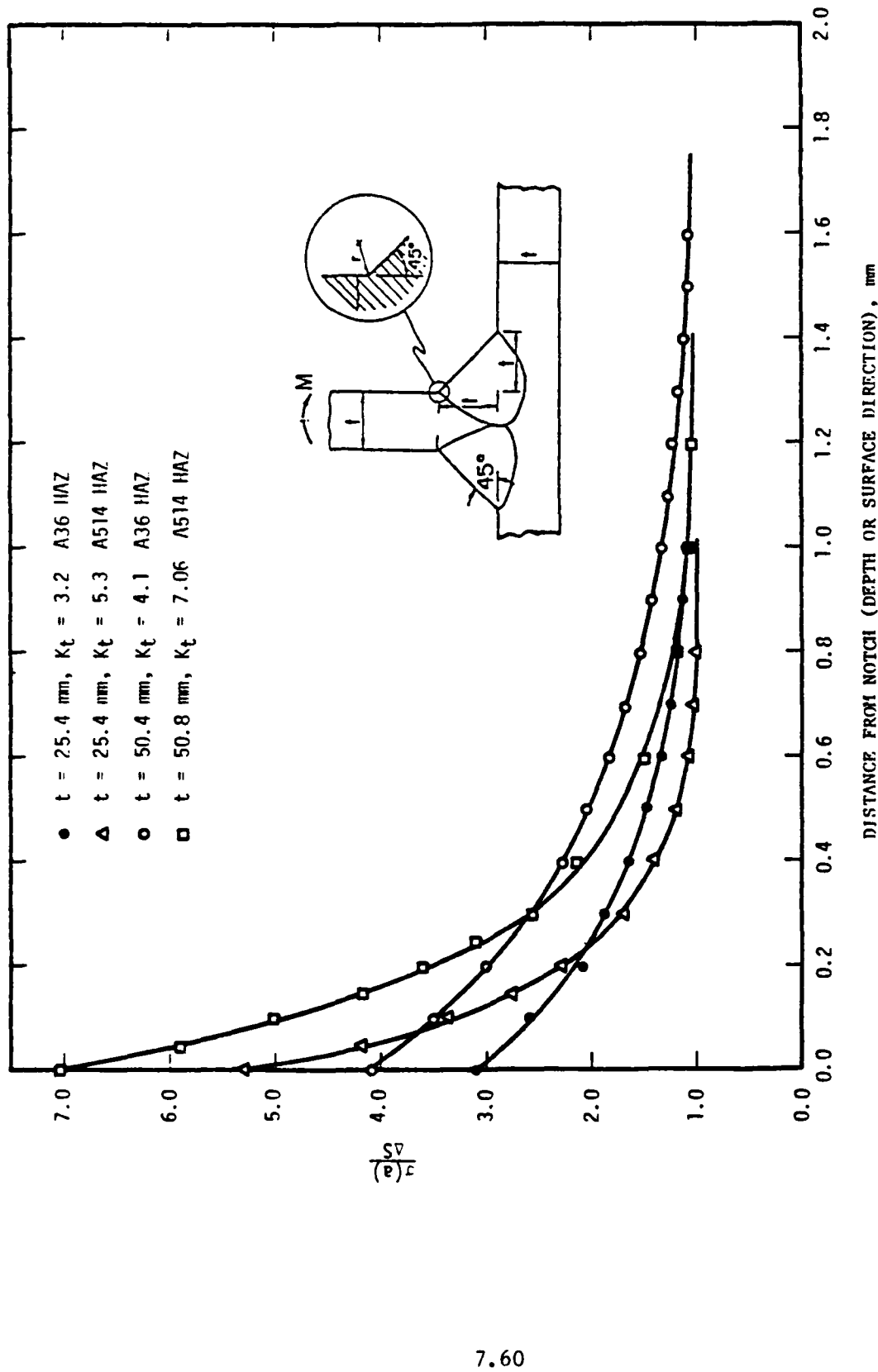


FIGURE 7.29. STRESS GRADIENT AT WELD TOE (UNCRACKED STATE) PLANAR T-JOINT

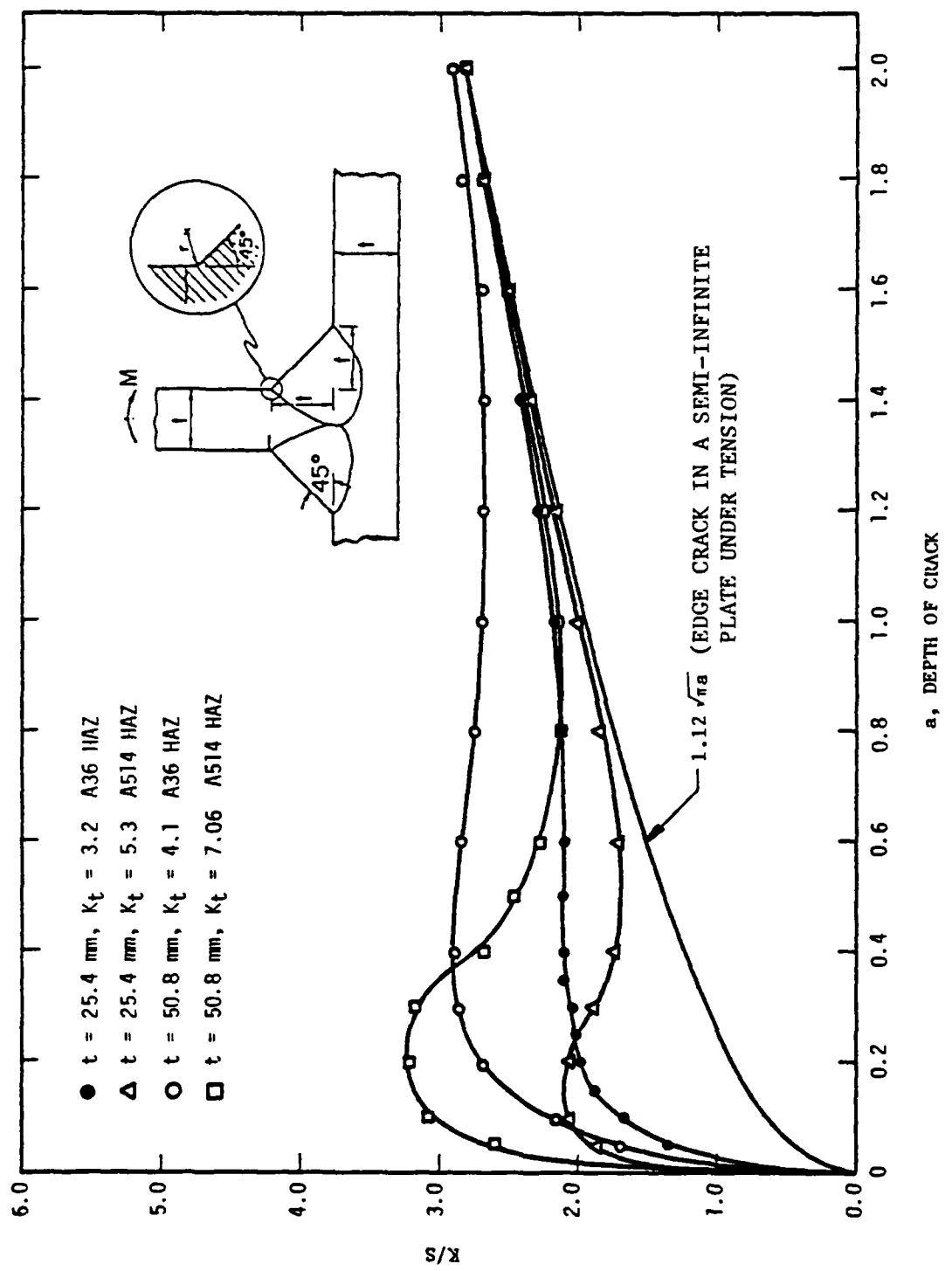


FIGURE 7.30. $\Delta K_I / \Delta S$ VERSUS DEPTH OF CRACK AT WELD TOE FOR A PLANAR T-JOINT

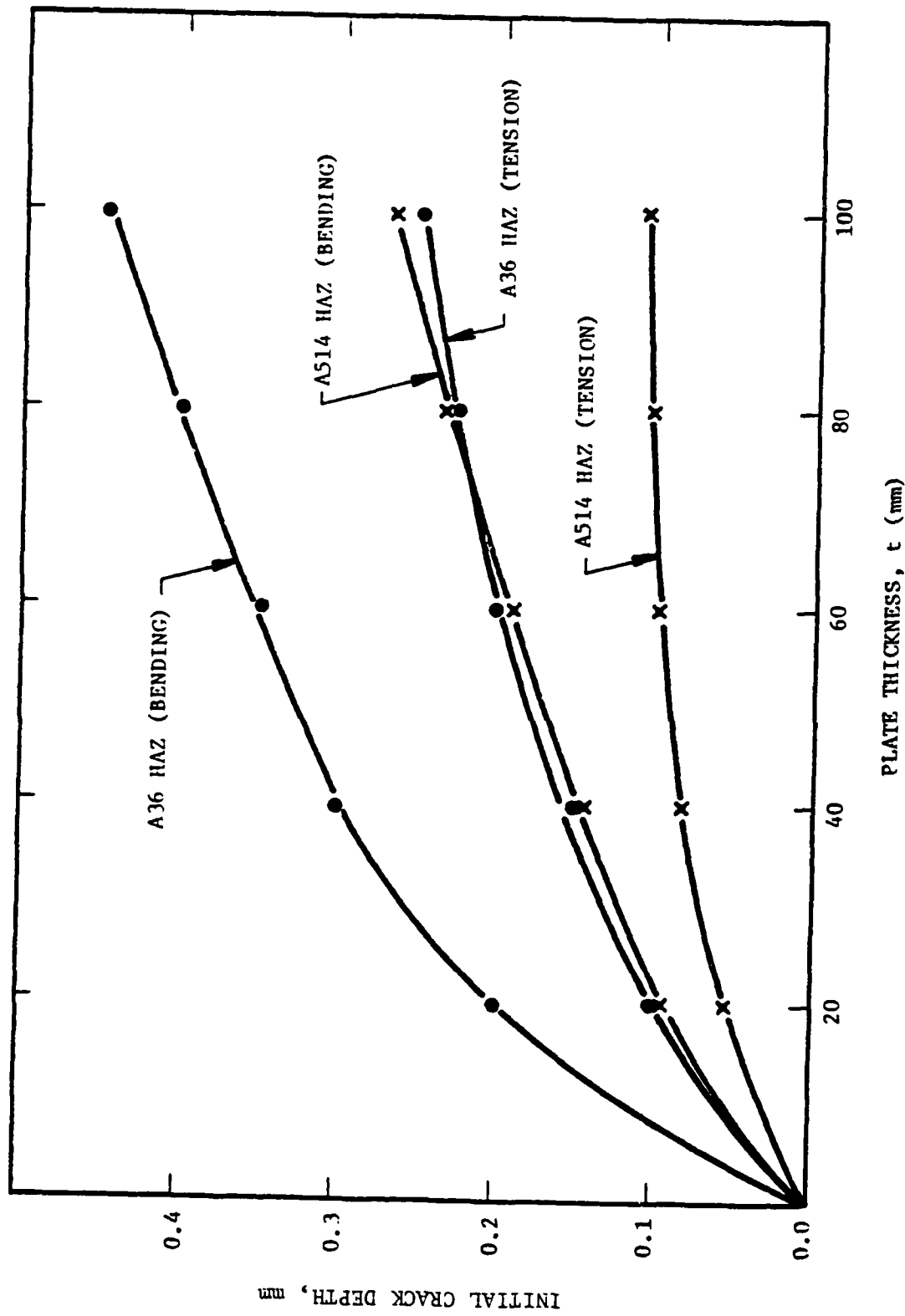


FIGURE 7.31. INITIAL CRACK DEPTH ASSUMPTION FOR CRACK GROWTH ANALYSIS

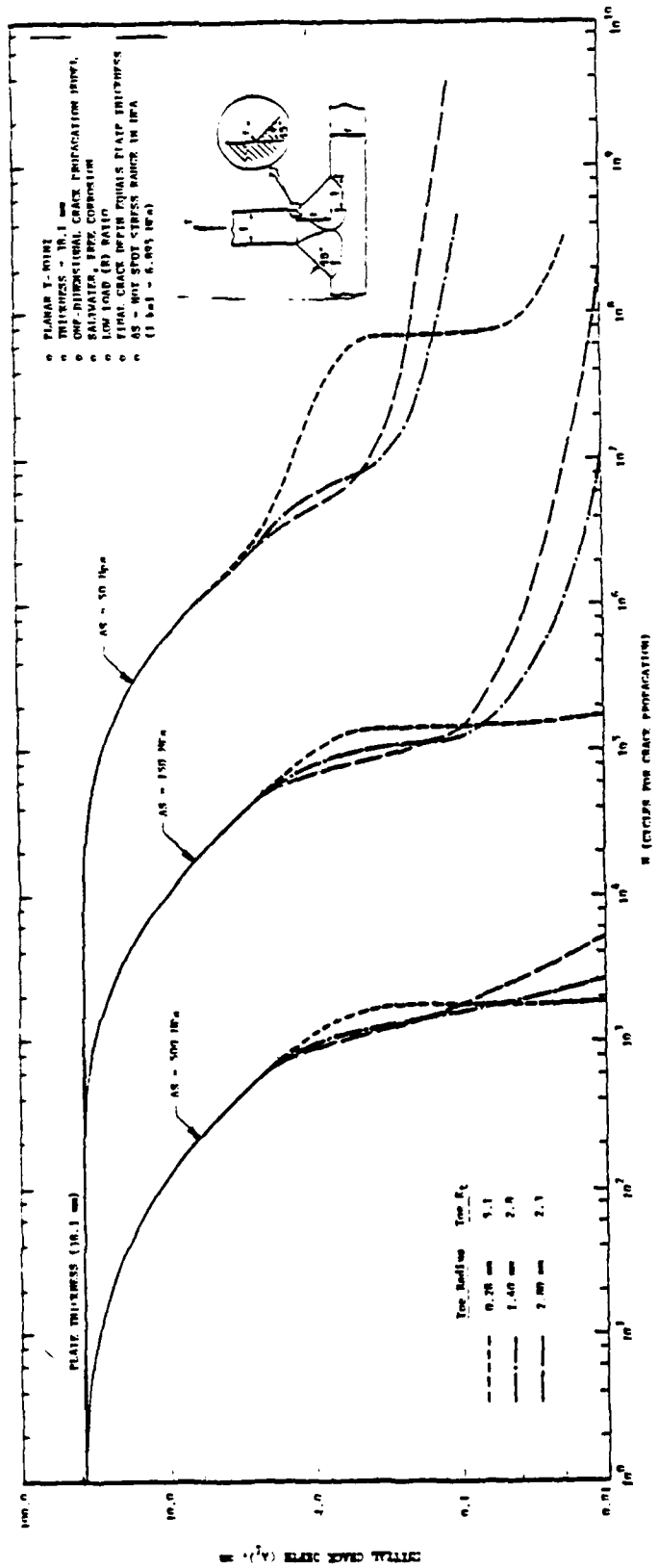


FIGURE 7.32. SENSITIVITY OF CRACK PROPAGATION LIFE TO WELD TOE RADIUS AND INITIAL CRACK DEPTH, LOW R-RATIO

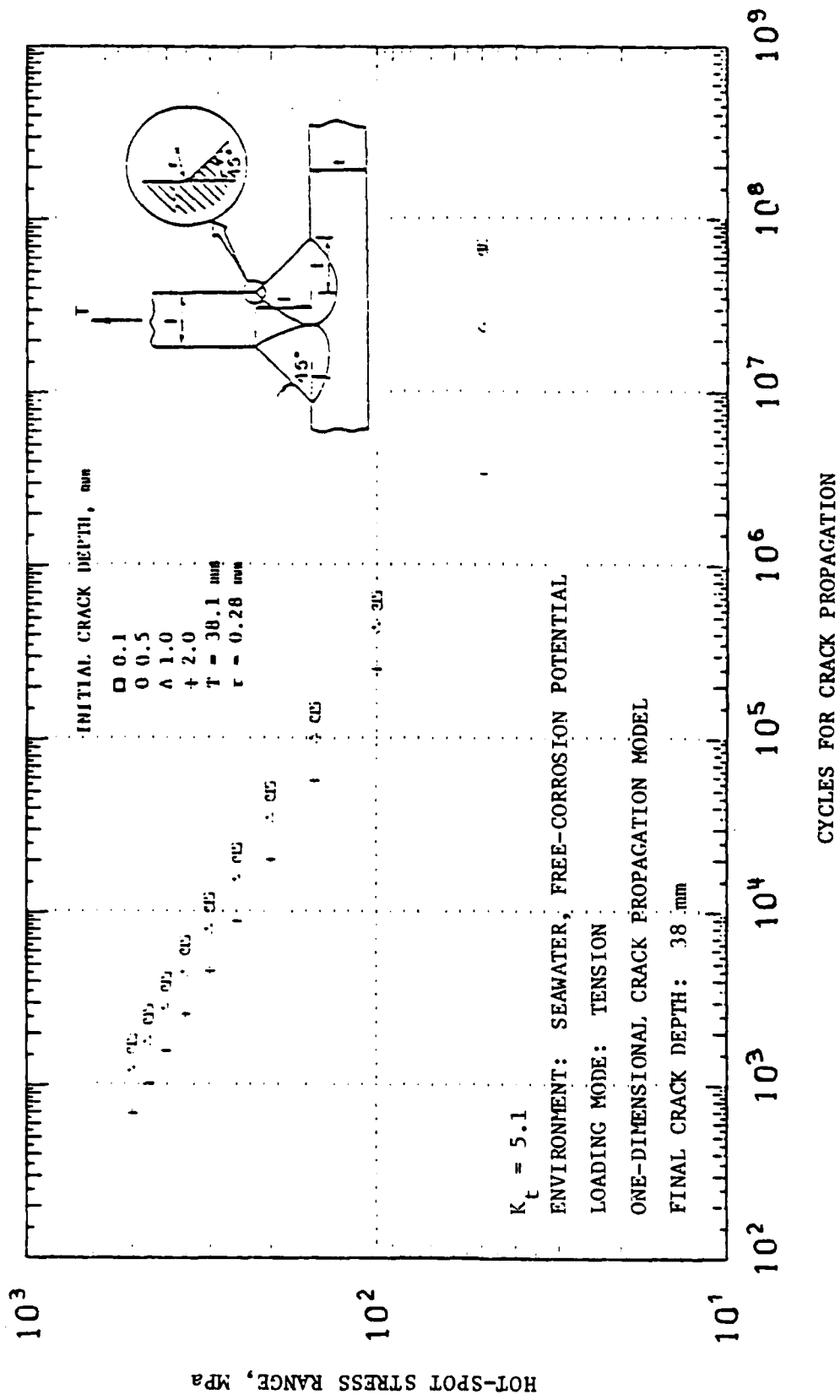


FIGURE 7.33. SENSITIVITY OF CYCLES FOR CRACK PROPAGATION TO INITIAL CRACK DEPTH (LOW LOAD (R) RATIO)

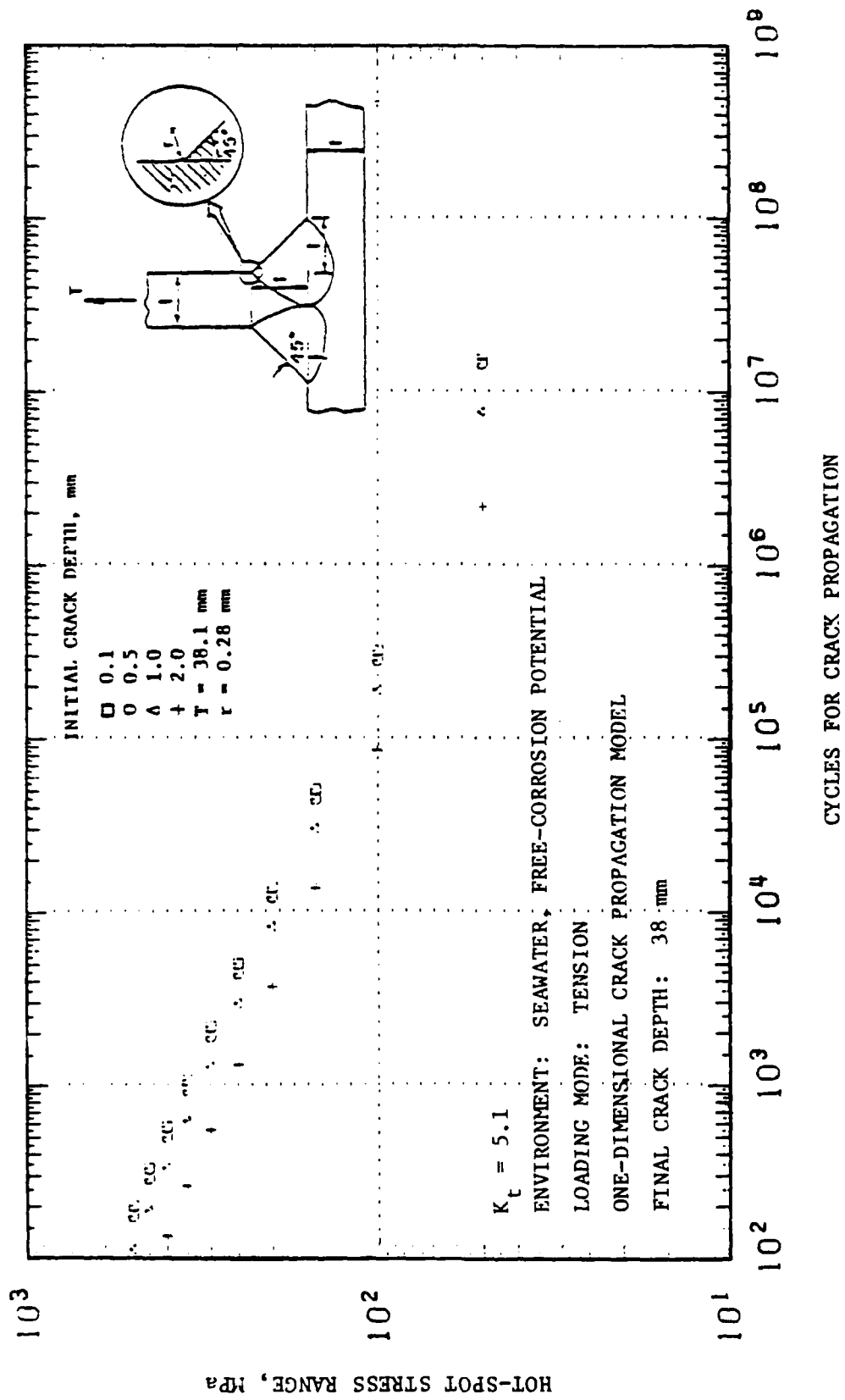


FIGURE 7.34. SENSITIVITY OF CYCLES FOR CRACK PROPAGATION TO INITIAL CRACK DEPTH
(HIGH LOAD (R) RATIO)

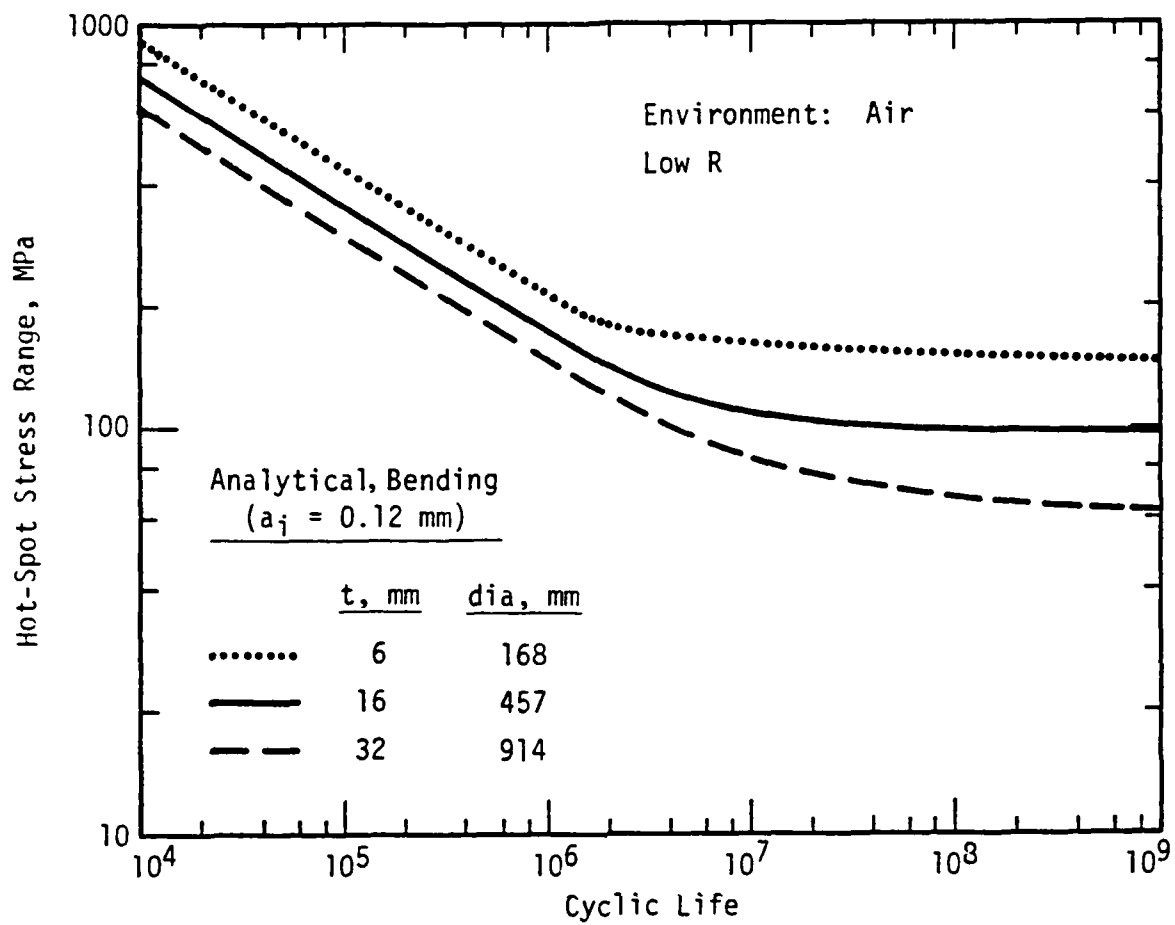


FIGURE 7.35. INFLUENCE OF CHORD SIZE ON FATIGUE LIFE
ASSUMING A CONSTANT INITIAL FLAW SIZE
OF $0.12 \text{ mm} \times 0.24 \text{ mm}$

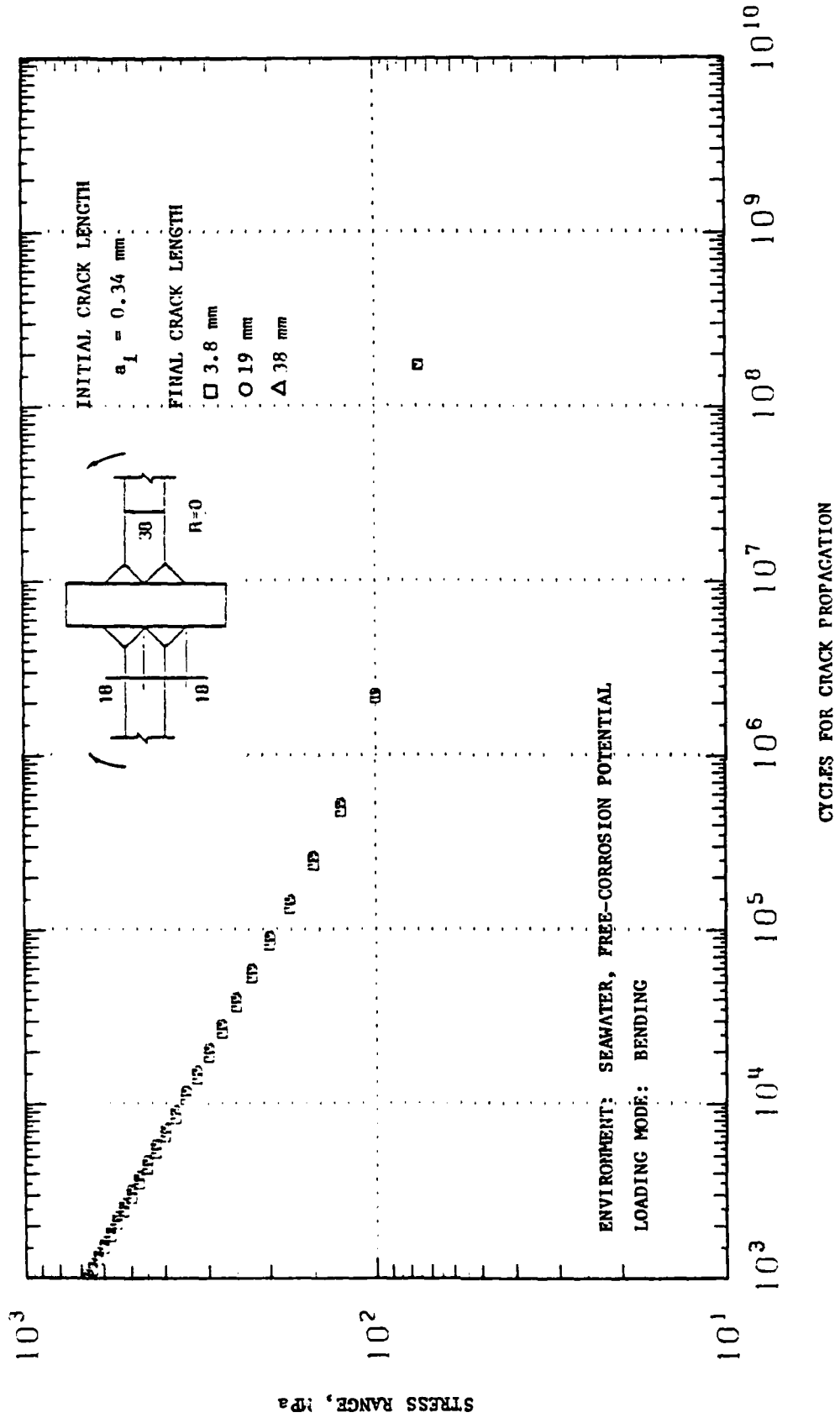
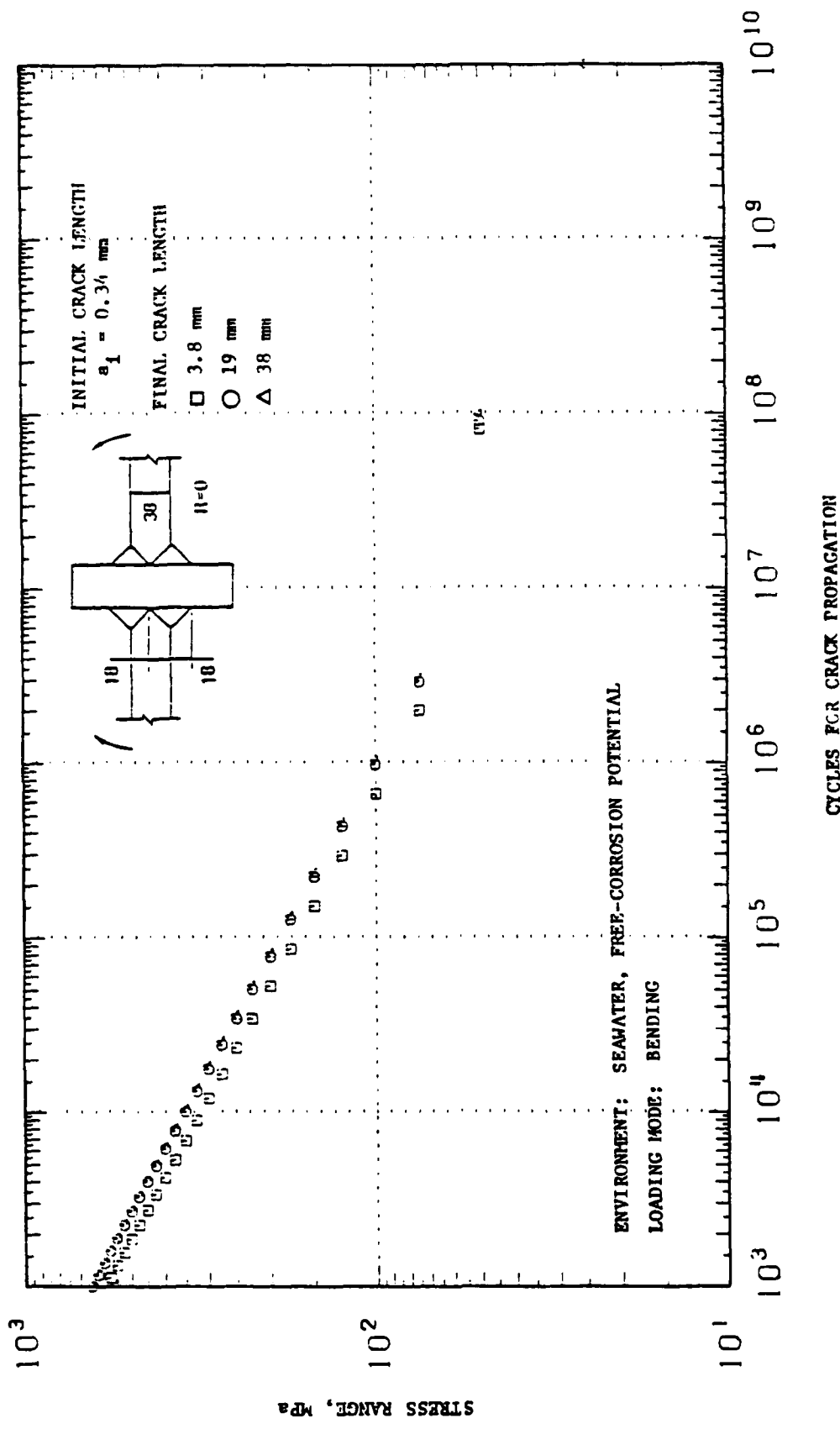


FIGURE 7.36. SENSITIVITY OF ONE-DIMENSIONAL CRACK PROPAGATION MODEL TO FINAL CRACK LENGTH



7.68

FIGURE 7.37. SENSITIVITY OF TWO-DIMENSIONAL CRACK PROPAGATION MODEL TO FINAL CRACK LENGTH

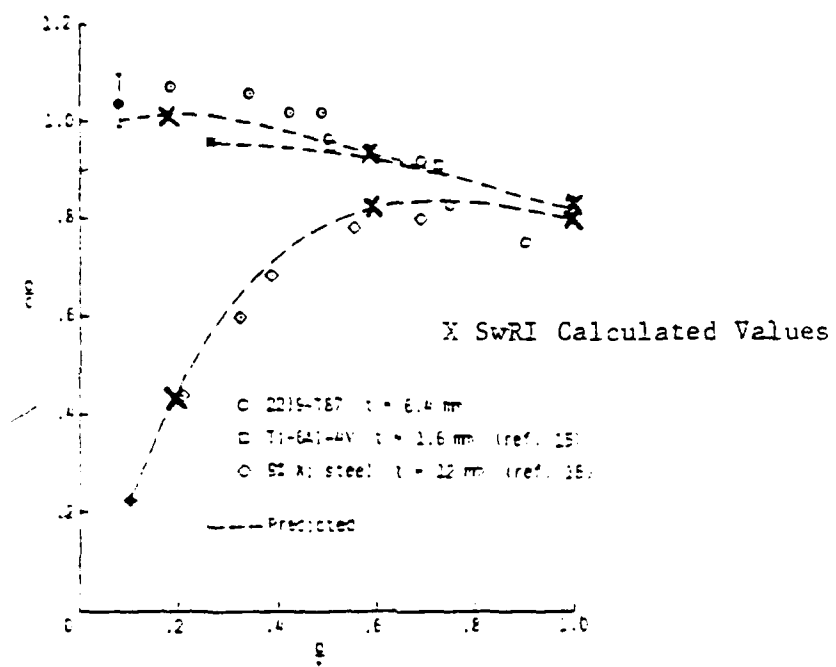


FIGURE 7.38. EXPERIMENTAL AND PREDICTED FATIGUE-CRACK GROWTH PATTERNS FOR A SURFACE CRACK IN A PLATE UNDER TENSION, FROM [6.34]. (SOLID SYMBOLS DENOTE INITIAL CONDITIONS.)

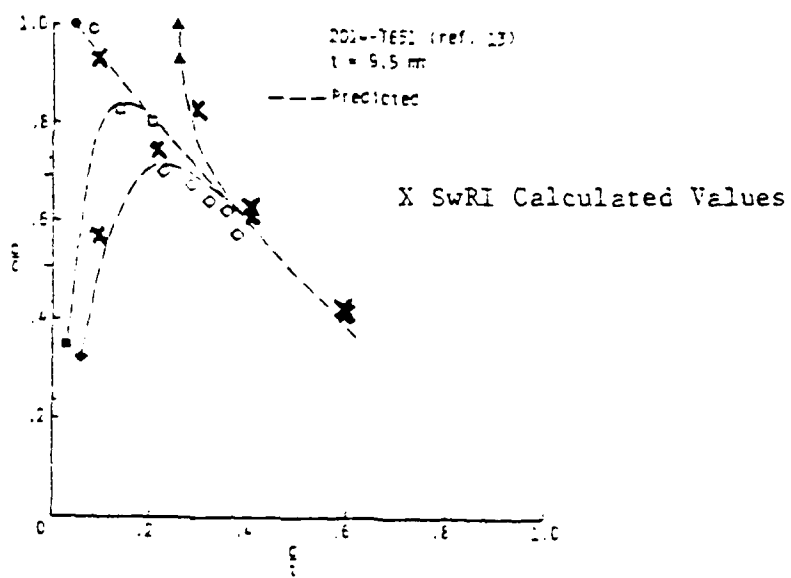


FIGURE 7.39. EXPERIMENTAL AND PREDICTED FATIGUE-CRACK GROWTH PATTERNS FOR A SURFACE CRACK IN AN ALUMINUM ALLOY CANTILEVER PLATE UNDER BENDING, FROM [6.34]. (SOLID SYMBOLS DENOTE INITIAL CONDITIONS.)

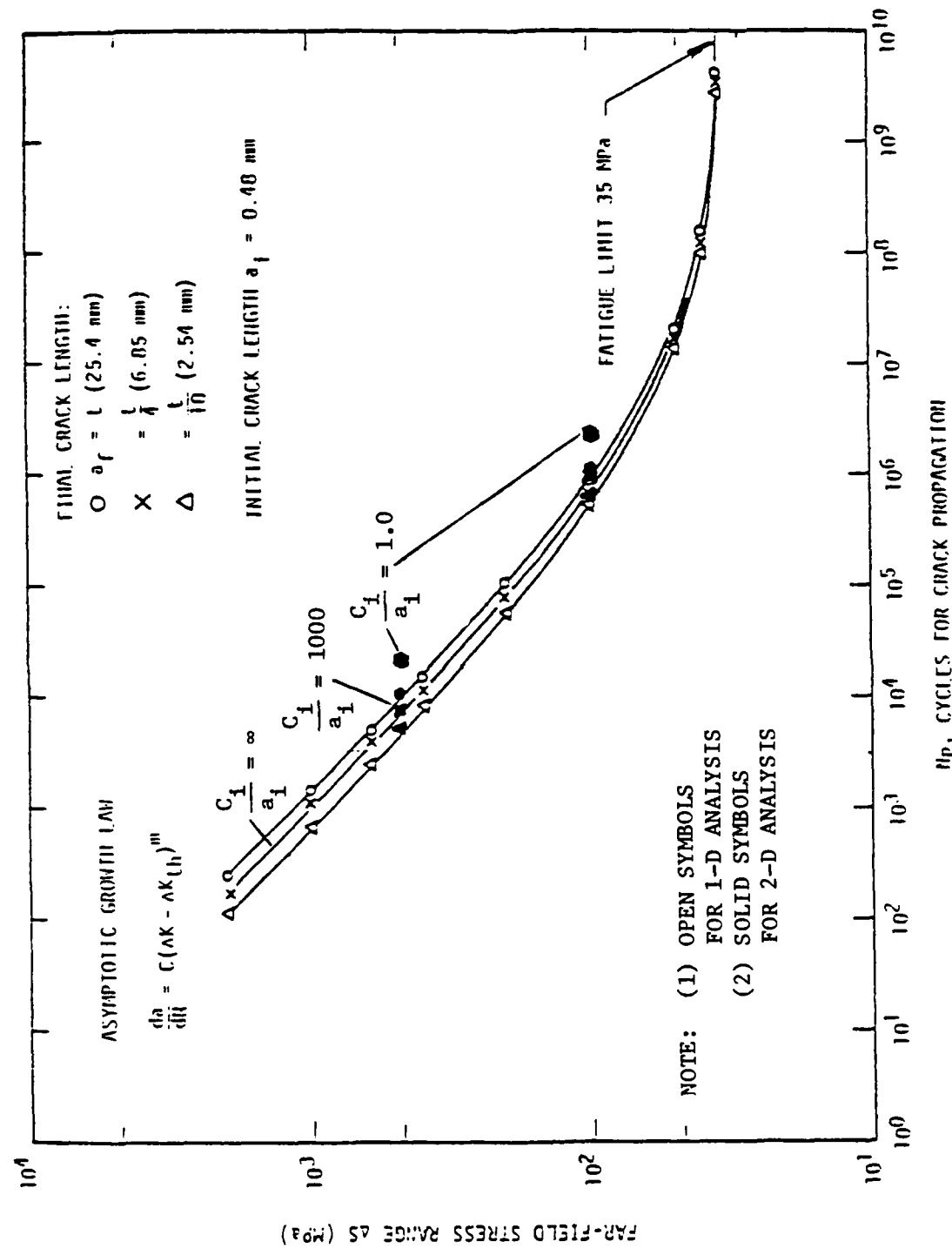


FIGURE 7.40. FATIGUE CRACK PROPAGATION CURVE FOR T-JOINT, A36 HAZ MATERIAL, ASYMPTOTIC GROWTH LAW, COMPARISON OF ONE-DIMENSIONAL AND TWO-DIMENSIONAL ANALYSES

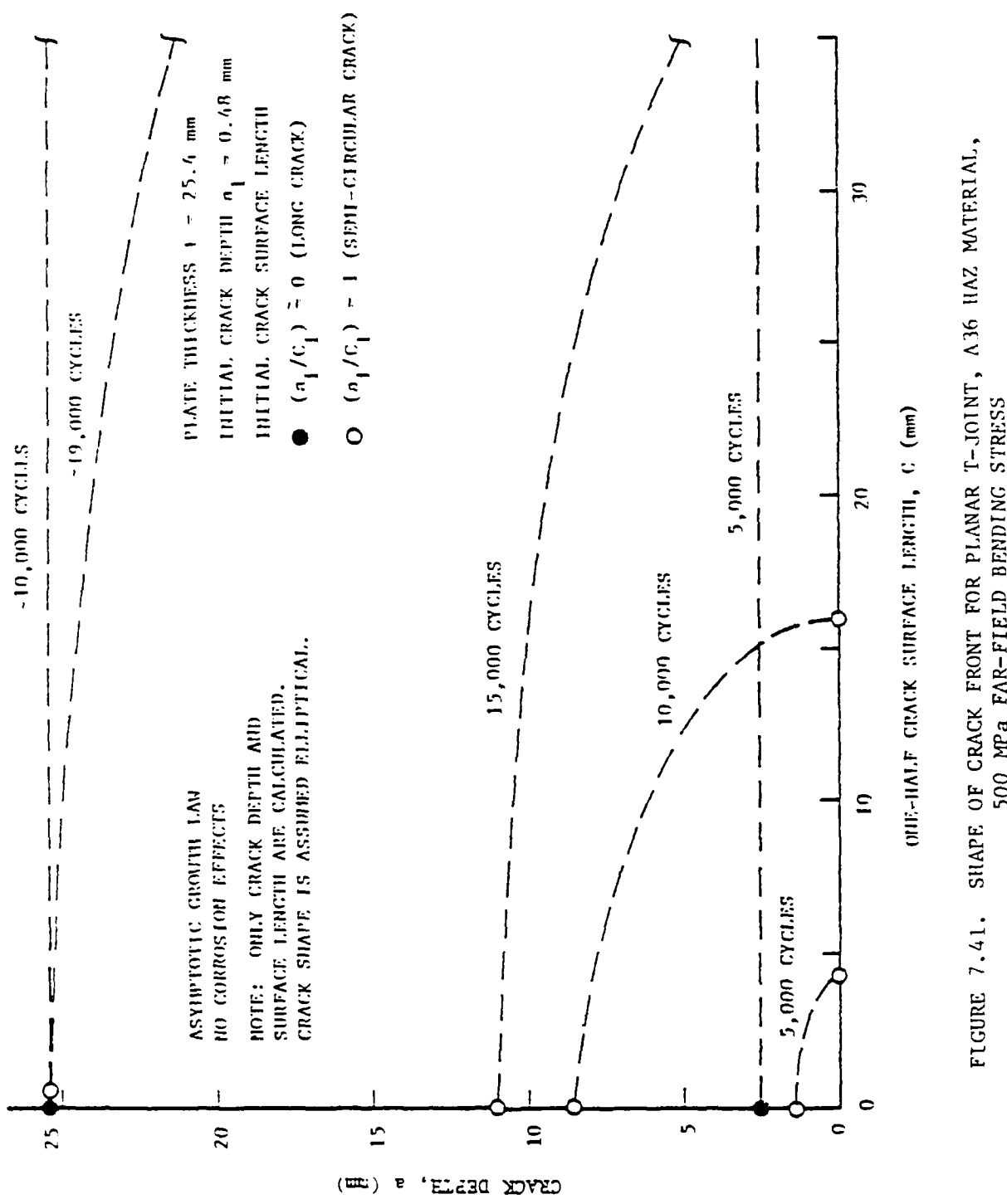


FIGURE 7.41. SHAPE OF CRACK FRONT FOR PLANAR T-JOINT, A36 HAZ MATERIAL,
500 MPa FAR-FIELD BENDING STRESS

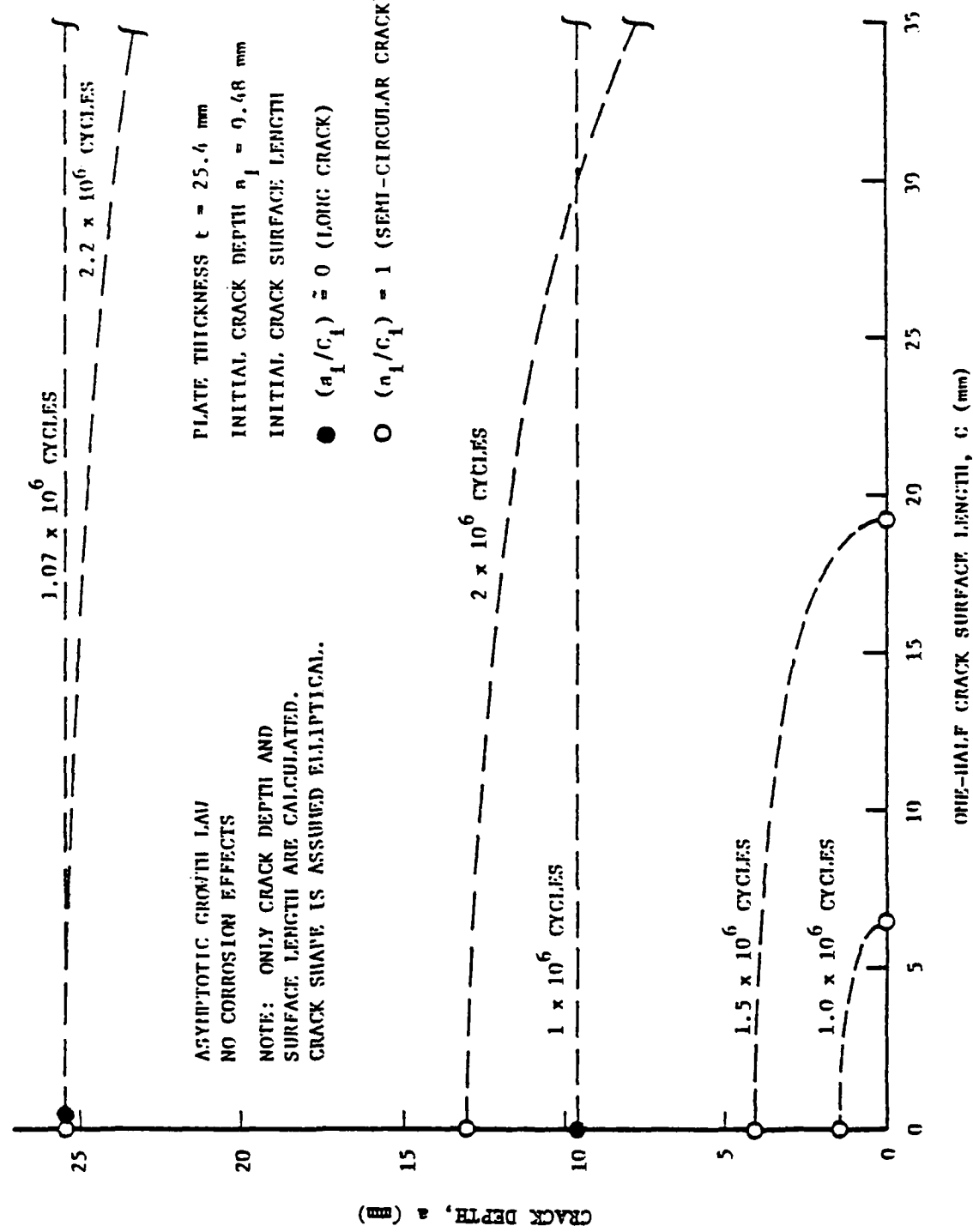


FIGURE 7.42. SHAPE OF CRACK FRONT FOR PLANAR T-JOINT, A36 HAZ MATERIAL,
100 MPa FAR-FIELD BENDING STRESS

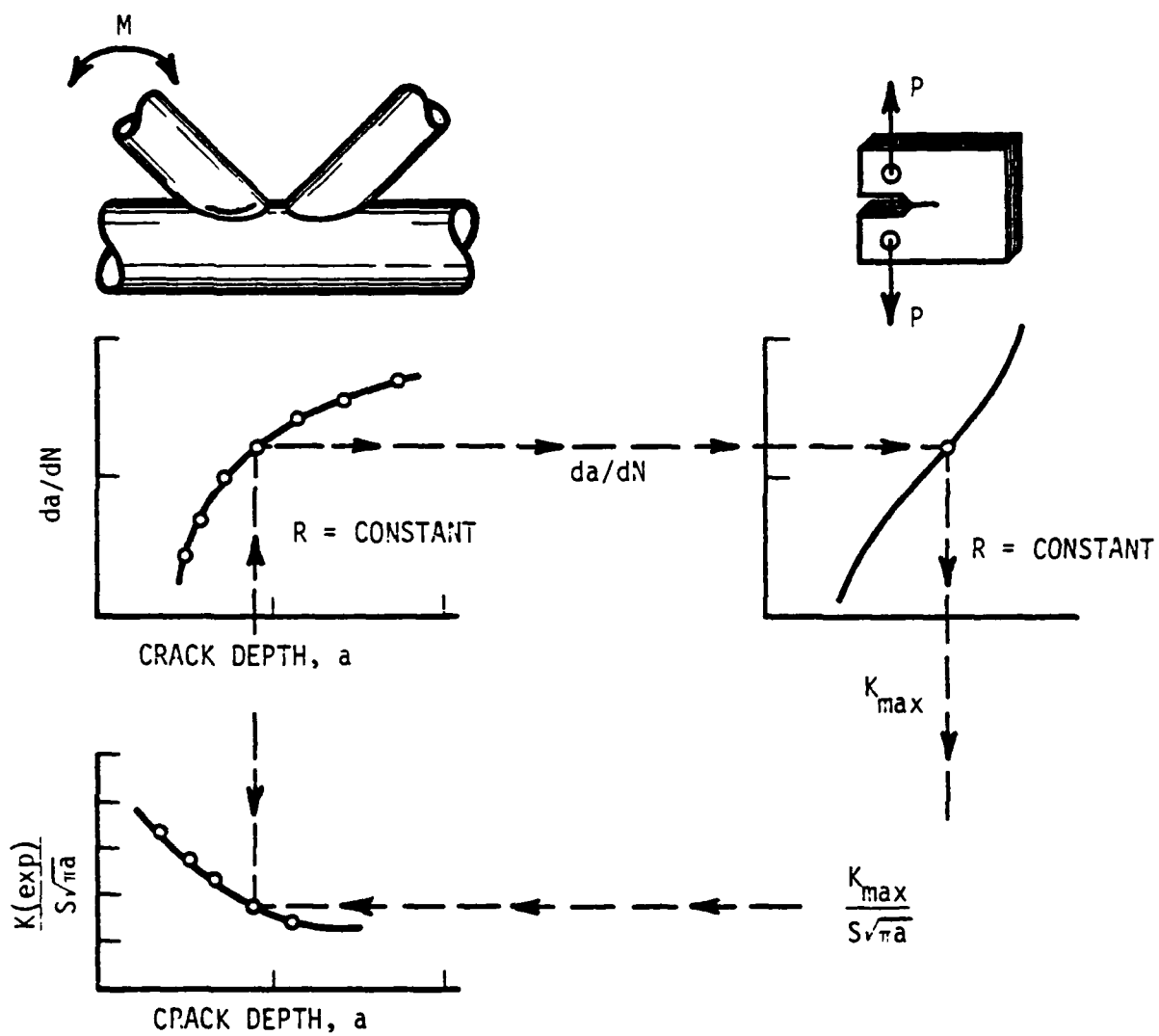


FIGURE 7.43. SCHEME FOR DETERMINATION OF EXPERIMENTAL STRESS INTENSITY FACTOR FROM CRACK GROWTH RATE INFORMATION

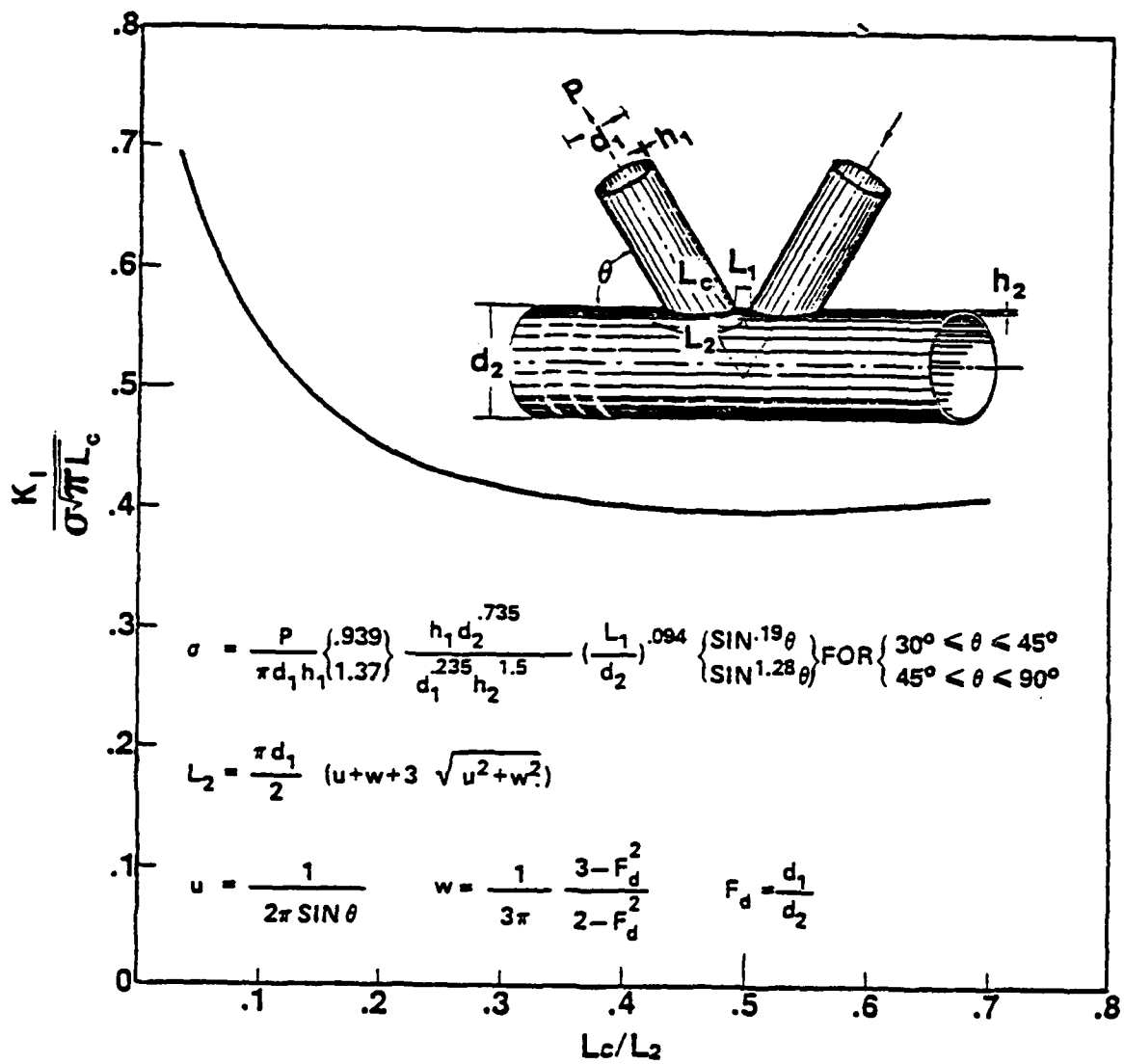


FIGURE 7.44. VARIATION OF EXPERIMENTALLY DETERMINED STRESS INTENSITY FACTOR WITH RELATIVE SURFACE CRACK LENGTH FOR TENSION CYCLING, FROM [7.14]

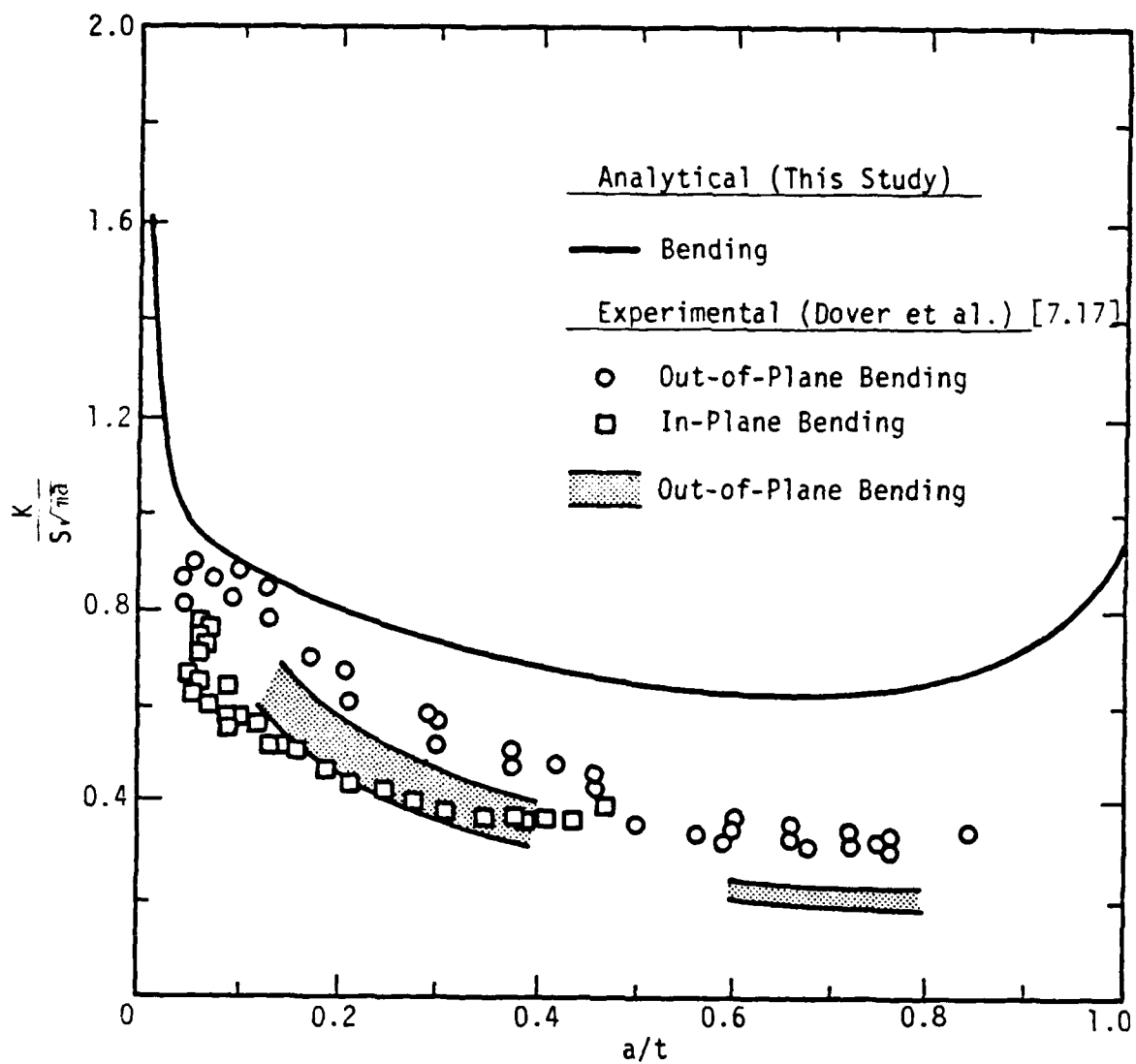


FIGURE 7.45. COMPARISON OF ANALYTICAL AND EXPERIMENTAL STRESS INTENSITY FACTORS FOR A T-JOINT

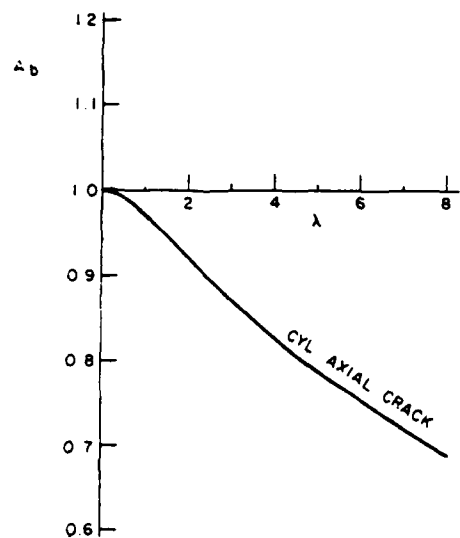


FIGURE 7.46. BENDING COMPONENT OF THE STRESS INTENSITY RATIO IN SYMMETRICALLY LOADED SHELLS, FROM [7.18]

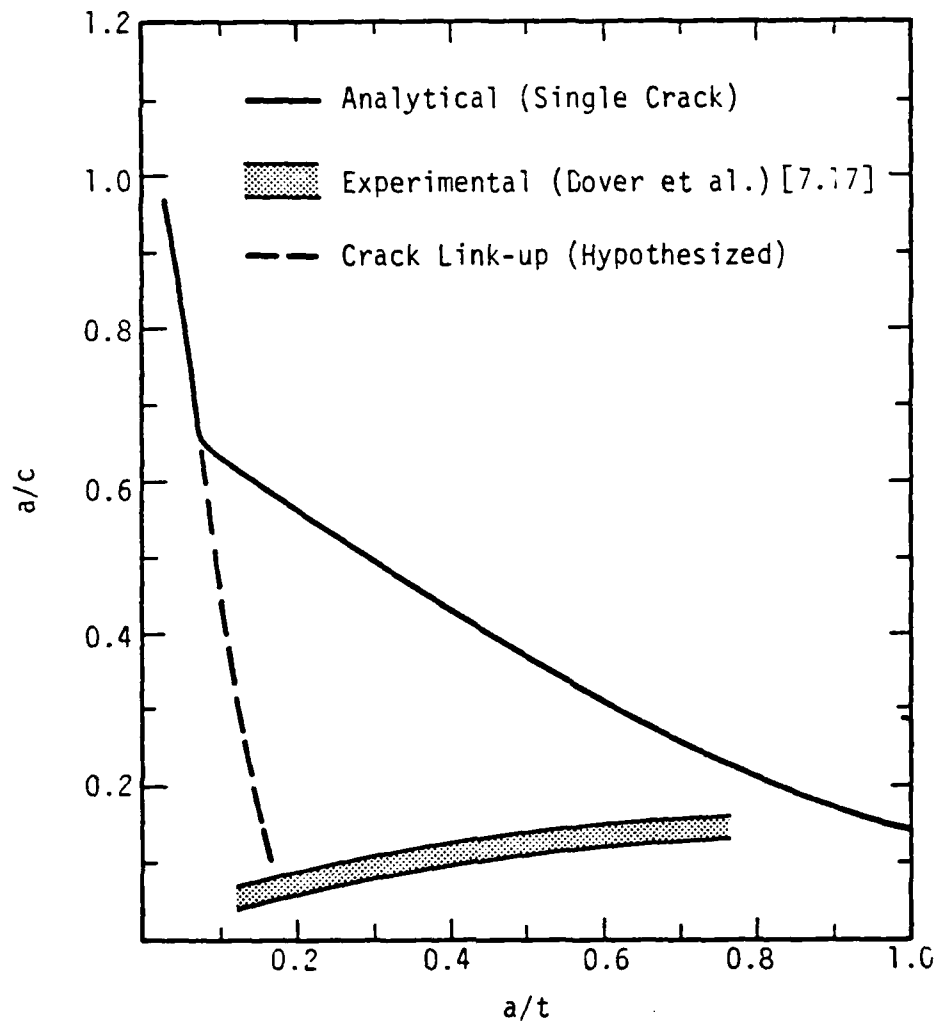


FIGURE 7.47. CHANGES IN CRACK SHAPE DURING
FATIGUE CRACK GROWTH IN A T-JOINT

8.0 PROBABILISTIC METHODOLOGY APPLIED TO THE CORROSION FATIGUE PROBLEM

8.1 Introduction

A probabilistic approach was implemented to investigate the following: (1) the sensitivity of the predicted fatigue life crack propagation analysis to the individual inputs, and (2) the effect on uncertainty in the predicted propagation model from the combined uncertainty of the several inputs. Whereas ordinarily a probabilistic S-N curve is derived directly from experimental fatigue data, the fatigue curve in this study is derived from the deterministic fracture mechanics model and experimental da/dN crack growth data addressed in previous chapters of this report. This approach analyzes the sources of uncertainty in the S-N curve in terms of the elements of the fracture mechanics analysis. Accomplishing this task required specifying the uncertainty, expressed as a mean and variance, and postulating the associated probability distributions, of the input parameters.

In lieu of a Monte Carlo simulation, a simplified, more approximate log-normal format was used with the corresponding linear (in logarithms) S-N, or $da/dN-\Delta K$, model. Subsequently, the logarithmic transformation approach was retained and applied to the more sophisticated three-component crack growth model. To accomplish this, an approximate analytical integration of the three-component model was developed, and construction of the corresponding probabilistic S-N curve was demonstrated. The lognormal format utilizes the assumption of a multiplicative function so that the model is linear in the logarithms. In studies of this type it is conventional practice to treat parameters as random variables if they are multiplicative and otherwise to treat them as constants. For example, the problem may be modeled so that the exponents of the multiplicative parameters are all constants [8.1].

In the lognormal format, the variables are also specified to be log-normally distributed. This restriction can be eliminated using either a Monte Carlo approach or the Rackwitz-Fiessler method [8.2]. The Rackwitz approach involves finding an optimum point in the space of the input variables. Published analyses, for example Reference [8.3], have demonstrated feasibility and superiority over Monte Carlo for relatively simple functional relations. Computer programs implementing the procedure often utilize numerical approximations of the partial derivatives in the optimization search. The present

study has developed analytical expressions for the partial derivatives of the functional relations derived from fracture mechanics. These are presented in the following material for subsequent incorporation into Rackwitz computer algorithms. Furthermore, these analytical tools enable use of first-order second-moment probabilistic analyses based on Taylor series expansions where linearization assumptions comparable to those of the lognormal format are specified. The results of these analyses presented in the following material accomplish the objectives of sensitivity analysis and probabilistic analysis of the present corrosion fatigue study. The details of the input distribution selection, the linear model analysis and results, and the three-component model development, analysis, and results are presented in the following sections. A discussion and conclusions section is also included on application of the several alternative probabilistic approaches to the problem.

8.2 Distribution of the Input Variables

The probability distributions of the input parameters are characterized by a central value, mean or median, and variance. Instead of variance, the ratio of standard deviation to the mean, the coefficient of variation, COV, may be specified. Where additional information is available or a particular distributional form enhances analytical tractability for sensitivity analysis, uncertainty studies, probabilistic life predictions, or reliability figure of merit calculations, such parametric distributional forms are identified. The variables whose distributions are needed are identified in the life prediction models to be considered. Furthermore, which variables are included would depend on the type of information to be developed. For example, where an S-N curve is being presented in probabilistic format, one set of parameters would be included as random variables conditional on assumed known (fixed) values of stress level. For a detailed reliability evaluation for service life mission, an additional set of parameters including random magnitude, order, damage accumulation effects, and cycles of stress during service life would be considered.

The life prediction models discussed in more detail in subsequent sections include the linear model and the three-component model. The linear model is so named because the log S-log N graph is a straight line. This corresponds to a straight line $\log da/dN - \log \Delta K$ graph under the assumption of

invariable proportionality of K to $Sa^{1/2}$. The linear model derived in Section 8.3 below is given by

$$\ln(N/N_T) = B - \ln C - (\frac{m}{2} - 1) \ln a_0 - m \ln Y - m \ln S_0 - \frac{m}{\xi} \ln(\ln N_T) - \ln N_T \quad (8.1)$$

where

N = cycles for crack propagation,
 B = constant, value depending on m , ξ , and rainflow correction if considered,
 $C = C' \pi^{m/2}$ where $da/dN = C'(\Delta K)^m$,
 a_0 = initial flaw size,
 m = power of ΔK in the crack growth rule,
 S_0 = once-in-a-lifetime stress range level,
 N_T = number of load cycles in service life,
and ξ = shape parameter of Weibull stress range distribution.

In this formulation the parameters C , a_0 , S_0 , and N_T are to be considered as random variables. The assumed constants, m and B , are considered to be precisely known from crack growth model or from S-N experimental data. Scatter in such data will be reflected in the parameter C . The three-component model is the solution of the differential equation,

$$dN/da = A_1/(\Delta K)^{n_1} + A_2/(\Delta K)^{n_2} - A_2/[(1-R)K_c]^{n_2} \quad (8.2)$$

where

n_1, n_2 = crack growth constants (corresponding to m in the previous model),
 A_1, A_2 = crack growth parameters (corresponding to C'^{-1} in the linear model),
 R = load ratio,
 K_c = fracture toughness (constant).

Approximate analytical solutions for this equation were developed in the low-, intermediate-, and high-cycle regions involving the same parameters combined

in different ways. For the high-cycle region, the three-component model derived in Section 8.4 below is given for a planar T-joint by

$$\begin{aligned}
 N = & \frac{A_1}{(1.12S \cdot \frac{\pi}{n_1})} \left\{ \frac{e^{n_1 H_0}}{-(n_1 H_1 + 1)} [a_0^{n_1 H_1 + 1} - a_1^{n_1 H_1 + 1}] \right. \\
 & \left. + \frac{1}{\frac{n_1}{(\frac{n_1}{2} - 1)}} [a_1^{-\frac{n_1}{2} - 1} - t^{-\frac{n_1}{2} - 1}] \right\} \\
 & + \frac{A_2}{(1.12S \cdot \frac{\pi}{n_2})} \left\{ \frac{e^{n_2 H_0}}{-(n_2 H_1 + 1)} [a_0^{n_2 H_1 + 1} - a_1^{n_2 H_1 + 1}] \right. \\
 & \left. + \frac{1}{\frac{n_2}{(\frac{n_2}{2} - 1)}} [a_1^{-\frac{n_2}{2} - 1} - t^{-\frac{n_2}{2} - 1}] \right\} \\
 & - \frac{A_2 (t - a_0)}{[(1-R)K_c]^{n_2}}
 \end{aligned} \tag{8.3}$$

where

$$a_1 = \frac{t}{35(K_t - 1)} \ln \frac{e^{\Delta} - 1}{K_t - 1},$$

$$H_1 = \ln (h_1/h_d)/\ln (a_1/a_d),$$

$$a_d = \frac{t}{35(K_t - 1)} \exp [((K_t - 1)/14.7)^{1/1.77}],$$

$$H_0 = \ln h_1 - H_1 \ln a_1.$$

$$h_i = [1 + (K_t - 1) \exp (-\frac{35(K_t - 1)a_i}{t})]^{-1} a_i^{-1/2}, \quad i = 1, d,$$

t = plate thickness,
 K_t = elastic stress concentration factor,
 S = stress range as before,
 Δ = approximation error constant.

The other parameters are as defined before. The parameters considered as random variables in the above model include a_0 , a_1 , H_0 , H_1 , A_1 , and A_2 . It is noted that a_1 , H_0 , and H_1 are associated random variables by their functional dependency on K_t , which depends on the weld toe radius, r , through another functional relation. In effect, then, the random variables for the three-component model are a_0 , A_1 , A_2 , and r . The random variability of S and N_T could be incorporated with the three-component model. The analytical approximation presented in Section 8.4 below for the three-component model suggests that a logarithmic transformation is tractable, and the linear model presented previously is in a logarithmic format. The summary of random variables is presented in Table 8.1.

8.2.1 Distribution of the Initial Flaw Size

In this study the initial flaw size distribution was obtained considering the $K_{f\max}$ approach and previously published results. From equation (7.5), the expression for initiated flaw size is given by

$$a_0 = 0.0198 (a_m t)^{1/2} / \alpha \quad (8.4)$$

where for a 25.4-mm-thick A36 HAZ T-Joint,

$$\begin{aligned} \alpha &= 0.19 \\ a_m &= 0.19 \text{ mm} \\ t &= 25.4 \text{ mm} \end{aligned} \quad (8.5)$$

For this case $a_0 = 0.23$ mm. This value is taken as the median value, and using the coefficient of variation for the flaw size distribution assumed in Reference [8.4], equation (13), the mean and variance of the logarithm of a_0 are given by

$$\mu_{\ln a_0} = \ln(0.000229) = -8.3818 \quad (8.6)$$

$$\sigma^2_{\ln a_0} = \ln\left(1 + \left(\frac{0.046 \text{ mm}}{0.125 \text{ mm}}\right)^2\right) = 0.127 \quad (8.7)$$

where the initial flaw size is in units of meters, m, and the 0.125 mm value is the observed mean initial flaw size from the Norwegian study.

8.2.2 Distribution of Weld Toe Radius and Parameters Y and K_t

The results of a study of the distribution of the weld toe radius, r, are reported in Reference [8.4] (Equation (2), and Table 2). A mean value of 2.7 mm and standard deviation of 2.2 mm were cited, and a best-fit Weibull distribution with shape parameter 1.11 and scale parameter 2.78 was reported. The median of this distribution is 2.00 mm, and its mean and standard deviations were estimated to be about 2.64 and 2.48 mm, respectively. Changing to the lognormal format, from the mean and standard deviation,

$$\mu_{\ln r} = \ln 0.0027 - \frac{1}{2} \ln \left(1 + \left(\frac{2.2}{2.7}\right)^2\right) = -6.169 \quad (8.8)$$

$$\sigma^2_{\ln r} = \ln \left(1 + \left(\frac{2.2}{2.7}\right)^2\right) = 0.509, \quad (8.9)$$

and from the best fit distribution,

$$\mu_{\ln r} = \ln 0.002 = -6.215 \quad (8.10)$$

$$\sigma^2_{\ln r} = \ln \left(1 + \left(\frac{2.48}{2.64}\right)^2\right) = 0.632 \quad (8.11)$$

where r is expressed in meters. The latter case has a smaller mean r and a larger variance; thus, it is the more conservative case.

The parameter Y is the stress intensity range proportionality factor in the relation

$$\Delta K = Y(a) S(\pi a)^{1/2}. \quad (8.12)$$

In this program, the parameter Y(a) model has been selected as

$$Y(a) = 1.12 [1 + (K_t - 1)e^{-35(K_t - 1)a/t}] , \quad (8.13)$$

where

$$K_t - 1 = a \left(\frac{t}{r} \right)^{1/2} . \quad (8.14)$$

These relations were developed in Sections 6.6.2 and 6.6.4. The initial value of Y(a) for crack growth is given by $Y(a_0)$. Thus, Y is a function of two random variables, a_0 and r. Using the first order second moment mean value (of logarithms) method for the 25.4-mm plate, and a equals 0.19 from Table 6.4, the mean and variance

$$\mu_{\ln Y(a_0)} = 0.55, Y_{.50} = 1.73 \quad (8.15)$$

$$\begin{aligned} \sigma_{\ln Y(a_0)}^2 &= (0.0756)^2 \sigma_{\ln a_0}^2 + (0.139)^2 \sigma_{\ln r}^2 \\ &= 0.000726 + 0.01221 \\ &= 0.013 \end{aligned} \quad (8.16)$$

were obtained. The development is shown in Appendix C. This first-order, second-moment method works well when the low-order Taylor series function approximation is good over the range of the random variable governed by its variance. The example development of Appendix C demonstrates this is true for the case presented. It is seen that the uncertainty in r dominates, contributing most to the variance of Y. For the linear model, a constant value Y is required. In this analysis, the initial value, $Y(a_0)$, will be used and considered a constant with respect to integration of dN/da , and considered a random variable with the distribution defined by the mean and variance in the logarithmic format. In conjunction with the three-component crack growth model, where the linear S-N curve restriction will be removed, the functional form of Y(a) expressed in equation (8.13) above will be retained in the integration of dN/da , and again considered a random variable because of its functional dependence on r.

The distribution of K_t , an intermediate relation in development for Y above, will also be required for analysis with the three-component model. Using the expression for $K_t - 1$ given above, the previously given conservative distribution values for r, and the logarithmic format, References [8.2] and [8.5], the distribution for K_t is then given by

$$\mu_{\ln(K_t - 1)} = -0.390 \quad (8.17)$$

$$\sigma_{\ln(K_t - 1)}^2 = (1/2)^2 \sigma_{\ln r}^2 = 0.158 \quad (8.18)$$

This information for K_t will be later used in the three-component model analysis.

8.2.3 Distribution of Crack Growth Parameters C, A₁, and A₂

The distribution for the crack growth parameter, C, for the linear model follows from the relation

$$C = C' \pi^{m/2} \quad (8.19)$$

where

$$\frac{da}{dN} = C' (\Delta K)^m$$

In Reference [8.4], the parameter m was considered a random variable with C' related to m by the expression,

$$\ln C' = -6.177 - 1.603 m, \quad (8.20)$$

equation (16) of Reference [8.4]. Reference [8.4] cited a mean value for m as 3.70 and standard deviation 0.11. From the relations above,

$$\sigma_{\ln C}^2 = \sigma_{\ln C'}^2 = (1.603)^2 (0.11)^2 = 0.031 \quad (8.21)$$

The value of the mean of $\ln C$ could be developed from the above; however, another approach will be used in the linear model analysis. In that approach only the variance of $\ln(N/N_T)$ will be considered and the central value related to the mean of $\ln C$ and m will be determined from the three-component model.

The distribution of A_1 and A_2 for the three-component model can be developed by considering the values given in Chapter 3.0 as the medians. The resulting da/dN models with these median values would then be evaluated and the residual differences between these evaluations and experimental data points determined. Then a statistical analysis of these residuals would be used to determine the distributions of the A's. Since the A's are related to the inverse of C, the variance of $\ln A_1$ and $\ln A_2$ corresponds to the variance of $\ln C$. As further information, Vosikovsky, Reference [8.6], reports da/dN data for an HSLA X-65 steel contained within a $\pm 50\%$ scatter band. This statement corresponds to $\sigma_{\ln A}^2 = 0.031$ if "all" the data are assumed to lie within $\pm 3.12 \sigma$. That is,

$$\ln 1.5 - \ln 0.5 = 2 (3.12 \sigma_{\ln A}) \Rightarrow \sigma_{\ln A}^2 = 0.031 \quad (8.22)$$

Analogous results can be obtained by consideration of the data shown in Chapter 3.0 of this report. From these considerations, we assume the values given in Table 8.2.

The variables for which probability distribution characteristics have been specified in Sections 8.2.1 through 8.2.3 above are the ones needed to derive the probabilistic S-N curves from the fracture mechanics approach and therein analyze the sources of uncertainty in the S-N curve. If reliability or life predictions of structures are to be made, then further consideration of random variability of the number of load cycles in the service life and uncertainty in the local stress range must also be considered. These are briefly addressed in Sections 8.2.4 and 8.2.5 below.

8.2.4 Distribution of Number of Load Cycles in Service Life

The number of load cycles, N_T , imposed on the structure during a specified service life, T_s , is given by

$$N_T = T_s/T_D \quad (8.23)$$

where T_D is the dominant cyclic stress period. Wirsching, in Reference [8.5], Section 4.5, indicates the coefficient of variation of T_D is 10 to 20 percent. From this information,

$$\begin{aligned}\mu_{\ln N_T} &= \ln T_s - \mu_{\ln T_D} \\ \sigma_{\ln N_T}^2 &= \ln (1 + C_{T_D}^2) = \{ \end{aligned}$$

0.01, $C_{T_D} = 0.10$
 $0.04, C_{T_D} = 0.20$

(8.24)

Although this parameter is needed for reliability assessment, it is not necessary to construction of the probabilistic S-N curve.

8.2.5 Distribution of Stress Range and Once-in-Lifetime Stress

As in the case of load cycles, stress range level for a structure need not be known to construct the S-N curve where a range level is assumed given. For reliability assessment, this information is needed. Utilizing a given distribution of stress range, the linear damage rule, and the linear model S-N formulation, the cycles to failure can be expressed in terms of the expected value of the m -th power of the stress range, $E\{S^m\}$. An analogous, but more complex, expression of cycles to failure could be obtained with the three-component model. If the stress range distribution is assumed to be Weibull, then

$$E\{S^m\} = S_o^m (\ln N_T)^{-m/\xi} \Gamma\left(\frac{m}{\xi} + 1\right) \quad (8.25)$$

indicating that the Weibull range parameter can be eliminated if the once-in-a-lifetime stress, S_o , is introduced. In the above expression, $\Gamma(\cdot)$ represents the gamma function, and the other parameters are as defined before. In general, the once-in-a-lifetime stress, S_o , could be used as a parameter for an arbitrarily specified stress range distribution.

Therefore, the once-in-a-lifetime stress range level can be used as a significant variable with general applicability. The once-in-a-lifetime value, S_o , is associated with the service cycles, N_T , since the greater the number of service cycles the greater the opportunity to experience a larger value of S_o . A relation expressing this association was incorporated in the expression for $E\{S^m\}$ given above and need not be considered further since the distribution for N_T has already been presented. The distribution of S_o itself depends on the distribution of seastate loading on a given marine structure,

and on the effect of the loading on the stress range at the location of interest in the structure. Wirsching, in Chapter 4 of Reference [8.5], has summarized ranges of estimates of bias and coefficient of variation of the stress range uncertainty factor, B, due to a variety of effects. These effects are tabulated in Table 8.3. If the uncertainty factor logarithm variances in Table 8.3 are applied to S_o , we obtain

$$\sigma_{\ln S_o}^2 = 0.21 \text{ to } 0.64, \quad (8.26)$$

The effects listed in Table 8.3 include uncertainty in manufacturing and fabrication, seastate, wave force, and member loads. To some extent these effects have already been incorporated in the random variables r , weld toe radius, and N_T , applied load cycles. Wirsching has indicated [8.7] a coefficient of variation of 0.50 for the factor B in general analysis of fixed offshore platforms, and a value of 0.25 as very representative of what is being considered in other applications. In the present study those values correspond to variances for the logarithm of S_o of 0.22 and 0.06, respectively. The uncertainty factors discussed above are considered applicable to determination of stress range in general, as well as to the once-in-a-lifetime stress range, S_o .

8.3 Linear S-N Model, Sensitivity, and Probabilistic Analysis

The underlying mathematical relations, the resulting sensitivity of cycles-to-failure to input variation, and the cycles-to-failure probabilistic analysis are presented in this section for the log-log linear S-N model. The use of this linear model is a simplification of the complex shape of crack growth curves over the range of ΔK considered in Chapter 3.0. In the $da/dN-\Delta K$ space the crack propagation rule is

$$\frac{da}{dN} = C' (\Delta K)^m, \quad (8.27)$$

corresponding to a straight line model in the $\ln (da/dN)$ versus $\ln (\Delta K)$ space. Using the expression

$$\Delta K = Y(a) S (\pi_a)^{1/2} \quad (8.28)$$

where

N = cycles-to-failure,
 a = crack size,
 C' = a constant,
 m = a constant,
 $Y(a)$ = proportionality factor,
and S = local stress range.

The function $Y(a)$ form will be retained in the three-component model analysis. However, for the present linear S-N model, $Y(a)$ will be assumed a constant, Y . Then the cycles-to-failure, N , can be obtained directly by integration.

The result is

$$S^m N(S) = [Y^m C a_0^{\frac{m}{2}} - \frac{(\frac{m}{2} - 1)}{2}]^{-1} = A(Y, C, a_0) \quad (8.29)$$

where it has been assumed that the terminal failure flaw size, a_f , is much greater than the initial size, a_0 , and the constant C is related to the original one by

$$C = C' (\pi)^{m/2} \quad (8.30)$$

The resulting expression,

$$N = A(Y, C, a_0)/S^m, \text{ or} \quad (8.31)$$

$$\ln N = -m \ln Y - \ln C - \frac{(\frac{m}{2} - 1)}{2} \ln a_0 - \ln \frac{(\frac{m}{2} - 1)}{2} - m \ln S,$$

is the basis for the probabilistic S-N curve where the cycles to failure, $N(S)$, at a given stress-range level, S , is a random variable because it is a function of the three random variables, Y , C , and a_0 .

Applying Miner's rule, with N representing the total number of cycles-to-failure, and with $N(S)$ given by the expression above, the fraction of service-to-failure-cycles consumed at stress range level S in the interval from S to $S + dS$ is given by $N_f(s)(S)dS/N(S)$, where $f_s(S)$ represents the probability density function of the local stress range. Assuming that the accumulated

fraction equal to 1.0 corresponds to failure, then integration of the fraction over the range of S values produces the probabilistic life prediction model.

$$E(S^m)N = A(Y, C, a_0) \quad (8.32)$$

where $E(S^m)$ is the expected value of the m -th power of S , a characteristic of the distribution of the stress range S . If the characteristic is expressed using the once-in-a-lifetime stress concept of Section 2.5 in Reference [8.5], and assuming $f_s(S)$ is Weibull, then

$$E(S^m) = S_0^m (\ln N_T)^{-m/\xi} \Gamma\left(\frac{m}{\xi} + 1\right) \quad (8.33)$$

where ξ denotes the shape parameter of the Weibull stress-range distribution. Using the above expressions to formulate the ratio N/N_T and taking the logarithm of the expression results in the final form

$$\ln(N/N_T) = B - \ln C - \left(\frac{m}{2} - 1\right) \ln a_0 - m \ln Y - m \ln S_0 - \frac{m}{\xi} \ln(\ln N_T) - \ln N_T$$

for the linear model where

$$B = -\ln\left(\frac{m}{2} - 1\right) - \ln \Gamma\left(\frac{m}{\xi} + 1\right). \quad (8.34)$$

The above linear model, so named because of the straight line form in the log-log space of S-N and $da/dN-\Delta K$, is also linear in terms of the logarithms of the random variables, C , a_0 , Y , S_0 , and N_T , except for a minor complication with N_T . The above equation forms the basis for probabilistic evaluations to express the structural reliability for a given service life. The Y , C , and a_0 terms are the basis for the probabilistic S-N curve, previously mentioned.

8.3.1 Sensitivity with Linear Model

Since the model is linear in the logarithms of the random variables (except N_T), no interaction of the effects of two or more variables exists. Thus, Table 8.4 expresses the sensitivity of the logarithm of N or of N/N_T to the logarithm of the respective variables. By the nature of the

logarithmic transformation, the sensitivities in this table can also be interpreted as the percentage change in N or in N/N_T to a 1 percent increase in the value of the corresponding variable. For example, if the initial flaw size were increased by 1 percent, for the case $m = 3.0$, $\xi = 1.0$, the cycles-to-failure would be decreased by 0.5 percent. Only considering the sensitivities, Table 8.4 indicates that cycles-to-failure, or ratio of failure-cycles-to-service-cycles, is most sensitive to variation in Y_0 and S , followed by N_T , C , and a_0 , in that order. This indication does not consider the degree of variability of each of the random variables. That will be considered below.

8.3.2 Probabilistic Analysis with the Linear Model

A probabilistic characteristic S-N curve and the variance of $\ln(N/N_T)$ are presented in this section for the linear model. The S-N curve derived from the linear fracture mechanics model is governed by the equation

$$\ln N = -\ln\left(\frac{m}{2} - 1\right) - \ln C - \left(\frac{m}{2} - 1\right) \ln a_0 - m \ln Y - m \ln S. \quad (8.35)$$

For the probabilistic S-N curve, the variance of $\ln N$ is given by

$$\sigma_{\ln N}^2 = \sigma_{\ln C}^2 + \left(\frac{m}{2} - 1\right)^2 \sigma_{\ln a_0}^2 + m^2 \sigma_{\ln Y}^2. \quad (8.36)$$

Using the high-cycle results from the three-component law, adjusting the results from $a_0 = 0.48$ mm to the median, 0.23 mm, and evaluating the variance from the above expression, a probabilistic S-N curve can be constructed. For a typical high-cycle case with corrosion effects, values of $m = 10.79$ and median $C = 2.394 \times 10^{-13}$ were obtained. The variance for this case is given by

$$\begin{aligned} \sigma_{\ln N}^2 &= \sigma_{\ln C}^2 + (4.395)^2 \sigma_{\ln a_0}^2 + (10.79)^2 \sigma_{\ln Y}^2 \\ &= 0.031 + (4.395)^2 (0.127) + (10.79)^2 (0.013) \\ &\quad (0.8\% + 61.3\% + 37.9\% = 100\%) \\ &= 4.0, \quad \text{COV}(N) = 7.3 \end{aligned} \quad (8.37)$$

Corresponding probability density functions are sketched in Figure 8.1 at 10^8 and 10^{10} cycles. The straight line through the medians of the two illustrated distributions is parallel to the high-cycle portion of the "with corrosion effects" three-component results and displaced by the effect of changing a_0 from 0.48 mm to the median 0.23 mm. The distributions are relatively broad and flat, with the $\pm 1.645 \sigma$ points marked in the figure.

For the high-cycle case without corrosion effects, values of $m = 6.309$ and median $C = 1.5087 \times 10^{-13}$ were specified. The variance for this case is given by

$$\begin{aligned}\sigma_{\ln N}^2 &= \sigma_{\ln C}^2 + (2.1545)^2 \sigma_{\ln a_0}^2 + (6.309)^2 \sigma_{\ln Y}^2 \\ &= 0.031 + (2.1545)^2 (0.127) + (6.309)^2 (0.013) \quad (8.38) \\ &\quad (2.7\% + 51.8\% + 45.5\% = 100\%) \\ &= 1.1, \text{ COV}(N) = 1.4\end{aligned}$$

The corresponding probability density functions are sketched in Figure 8.2 at 10^8 and 10^{10} cycles. Again, the line through the medians is parallel to, but displaced from, the "without corrosion effects" high cycle results corresponding to the values chosen for m and the median c . The distributions are relatively more peaked and narrower than in the case with corrosion effects, as a result of the smaller variance in this case. Since the inverse slope of the high-cycle S-N line enters directly into the variance determination, the variance is larger for the corrosion case where the high-cycle slope is smaller as expressed in Figures 8.1 and 8.2. The corresponding coefficients of variation of N are consistent with the observation that fatigue test data have considerable variability in some cases with coefficients of variation in excess of 1.0 [8.5]. For example, the high-cycle, without corrosion case, $m = 6.3$, presented above has $\text{COV}(N)$ equal to 1.4. This corresponds to a coefficient of variation in stress, $\text{COV}(S)$, equal to $1.4/6.3$, or 0.22. In an intermediate cycle regime the same $\text{COV}(S)$ would correspond to 1.0 $\text{COV}(N)$ for an intermediate-cycle m value of 4.5.

Furthermore, as a result of assumptions needed to produce the linear S-N form, the linear model results in more conservative (larger) variance and coefficient of variation than the more precise three-component

model. As will be shown in Section 8.4.2, the variance computed for the linear model is roughly twice as large as that of the three-component model. The corresponding coefficient of variation is therefore substantially larger for the linear model.

Based on the sensitivity, as well as on the random variability of the input variables for the probabilistic linear S-N curve, the most important variables are a_0 and Y, each contributing about 50 percent to the variance of $\ln N$. The variance of C contributes on the order of 1 and 3 percent.

For reliability evaluations, the variance of $\ln(N/N_T)$ is needed. The expression follows from the expression for $\ln(N/N_T)$,

$$\begin{aligned}\ln(N/N_T) &= B - \ln C - \left(\frac{m}{2} - 1\right) \ln a_0 - m \ln Y - m \ln S_0 \\ &\quad - \left(\frac{\mu}{\xi \mu \ln N_T} + 1\right) (\ln N_T - \mu \ln N_T)\end{aligned}\tag{8.39}$$

where the last term is a linear approximation to the nonlinear expression of N_T in the original equation. From this, one obtains

$$\sigma_{\ln(N/N_T)}^2 = \sigma_{\ln N}^2 + m^2 \sigma_{\ln S_0}^2 + \left(\frac{\mu}{\xi \mu \ln N_T} + 1\right)^2 \sigma_{\ln N_T}^2.\tag{8.40}$$

For a typical case with corrosion effects,

$$\begin{aligned}\sigma_{\ln(N/N_T)}^2 &= 2.0 + (10.79)^2 (0.21) + \left(\frac{10.79}{1.0 \ln 10^8} + 1\right)^2 (0.025) \\ &= 2.0 + 24.4 + 0.06 \\ &(7.6\% + 92.2\% + 0.2\% = 100\%) \\ &= 26.5\end{aligned}\tag{8.41}$$

For a typical case without corrosion effects,

$$\begin{aligned}\sigma_{\ln(N/N_T)}^2 &= 0.6 + (6.309)^2 (0.21) + \left(\frac{6.309}{1.0 \ln 10^8} + 1 \right)^2 (0.025) \\ &= 0.6 + 8.4 + 0.045 \quad (8.42) \\ (6.6\% + 92.9\% + 0.5\%) &= 100\% \\ &= 9.0\end{aligned}$$

These very large variances are the direct result of the uncertainty in the B factor, local stress range, as the calculations shown in equations (8.41) and (8.42) indicate. The values used for $\sigma_{\ln N}^2$ correspond to the three-component model results. These results indicate that uncertainty in determining local stress range is the predominant uncertainty source for reliability evaluations in the high-cycle regime.

8.4 Three-Component Model Approximate Analytical Expression

The three-component crack growth rule used in this study is

$$\frac{dN}{da} = \frac{A_1}{(\Delta K)^{n_1}} + \frac{A_2}{(\Delta K)^{n_2}} - \frac{A_2}{[(1-R)K_c]^{n_2}} \quad (8.43)$$

where

N = cycles-to-failure,

a = crack size,

R = a constant,

K_c = a constant,

A_1, A_2, n_1, n_2 = crack growth parameters,

and ΔK is given by

$$\Delta K = Y(a) S (\pi a)^{1/2}$$

$$Y(a) = 1.12 \left[1 + (K_t - 1) e^{-\frac{35(K_t - 1)a}{t}} \right], \quad (8.44)$$

for a plate T-joint.

In the above formulation, the parameters A_1 , A_2 , and K_t^{-1} are to be considered as constant with respect to integration, but as random variables with respect to uncertainty analysis. Upon manipulation of the above expressions, the cycles to failure N can be expressed as follows,

$$N = \frac{A_1}{(1.12S\sqrt{\pi})^{n_1}} \int_{a_0}^{a_f} (h(a))^{n_1} da + \frac{A_2}{(1.12S\sqrt{\pi})^{n_2}} \int_{a_0}^{a_f} (h(a))^{n_2} da - \frac{A_2 (a_f - a_0)}{[(1-R) K_c]^{n_2}} \quad (8.45)$$

where

$$h(a) = \left[1 + (K_t - 1) e^{-\frac{35(K_t - 1)a}{t}} \right]^{-1} a^{-1/2}. \quad (8.44)$$

The indicated integrations are not readily accomplished analytically; however, any straight-line segment approximation to $h(a)$ in the log-log $h(a)$ - a space is analytically integrable. Figure 8.3(a) illustrates the function $h(a)$ for the 1-in.-thickness case, $K_t = 3.2$. In the figure the crack size, a_1 , where $\ln h(a)$ differs from $-0.5 \ln a$ by 0.01 (an arbitrary departure criterion), is identified. A similar value, a_d , where $h(a)$ changes from concave upward to concave downward, is also shown. A straight line was drawn through the point

$(\ln a_d, \ln h(a_d))$ to the point $(\ln a_1, -0.5 \ln a_1)$. This straight-line approximation is applied in place of $h(a)$ for values of a below a_1 , and $-0.5 \ln a$ is applied in place of $h(a)$ for values of a above a_1 . In Figure 8.3, $h(a)$ is indistinguishable from $-0.5 \ln a$ above a_1 . For smaller values of K_t , the more probable values defined by the distribution of K_t as shown in Figure 8.3(b), the straight line approximation is more accurate than for the case illustrated in Figure 8.3(a). The terminal flaw size, a_f , is defined as the smaller of two values: (1) the thickness, t , of the plate in the T-joint, or (2) the value a_c for which the integrand dN/da becomes zero, corresponding to $da/dN = +\infty$. Thus, three cases must be considered:

- (1) $a_f = t$
- (2) $a_1 < a_f < t$
- (3) $a_0 < a_f < a_1$.

Considering the general form of a straight-line in the $\ln h - \ln a$ space,

$$\ln h(a) = H_0 + H_1 \ln a, \quad (8.46)$$

and recognizing that the first term of the integrand is negligible at the point where the integrand becomes zero, then an approximate expression for a_c is obtained

$$a_c = \left[\frac{1.12 S \sqrt{\pi}}{(1-R) K_c} \right] \frac{1}{H_1} e^{-\frac{H_0}{H_1}}. \quad (8.47)$$

Using $h(a) = 1/\sqrt{a}$, one obtains $H_0 = 0$ and $H_1 = -0.5$. Then the expression above can be used to define the three cases as follows

$$t < \left[\frac{1.12 S \sqrt{\pi}}{(1-R) K_c} \right]^{-2} \Rightarrow a_f = t, \text{ (High Cycle)} \quad (8.48)$$

$$a_1 < \left[\frac{1.12 S \sqrt{\pi}}{(1-R) K_c} \right]^{-2} < t \Rightarrow a_1 < a_f < t, \text{ (Intermediate Cycle)} \quad (8.49)$$

$$a_0 < \left[\frac{1.12 S \sqrt{\pi}}{(1-R) K_c} \right]^{-2} < a_1 \Rightarrow a_0 < a_f < a_1, \text{ (Low Cycle)} \quad (8.50)$$

The corresponding three values for a_f are given by

t , High Cycle

$$a_f = \left\{ \frac{1.12 S \cdot \pi}{(1-R) K_c} \right\}^{-2}, \text{ Intermediate Cycle} \quad (8.51)$$

$$\left[\frac{1.12 S \cdot \pi}{(1-R) K_c} \right] \frac{1}{H_1} e^{-\frac{H_0}{H_1}}, \text{ Low Cycle}$$

where

$$H_0 = \ln h(a_1) - H_1 \ln a_1$$

$$H_1 = \ln [h(a_1)/h(a_d)]/\ln (a_1/a_d)$$

$$a_d = \frac{t}{35(K_t - 1)} e^{\frac{(K_t - 1)}{14.7} t^{1/1.77}}$$

$$a_1 = \frac{t}{35(K_t - 1)} \ln \left(\frac{t}{e^\Delta - 1} \right).$$

In the above, Δ is the arbitrary error criterion previously used at $\Delta = 0.01$, and the expression for a_d is an approximate analytical solution to the transcendental equation,

$$K_t - 1 = \left(\frac{35(K_t - 1)a_d}{t} - 1 \right) e^{-\frac{35(K_t - 1)a_d}{t}}, \quad (8.52)$$

the defining expression for a_d .

Upon integration of dN/da for the three cases defined above, one obtains for the high-cycle regime,

$$\begin{aligned}
 N = & \frac{A_1}{(1.12, \frac{n_1}{\pi})} \left\{ \frac{e^{n_1 H_0}}{-(n_1 H_1 + 1)} [a_0^{n_1 H_1 + 1} - a_1^{n_1 H_1 + 1}] \right. \\
 & \left. + \frac{1}{\frac{n_1}{(\frac{n_1}{2} - 1)}} [a_1^{-\frac{n_1}{2} - 1} - t^{-\frac{n_1}{2} - 1}] \right\} \frac{1}{s} \\
 & + \frac{A_2}{(1.12, \frac{n_2}{\pi})} \left\{ \frac{e^{n_2 H_0}}{-(n_2 H_1 + 1)} [a_0^{n_2 H_1 + 1} - a_1^{n_2 H_1 + 1}] \right. \\
 & \left. + \frac{1}{\frac{n_2}{(\frac{n_2}{2} - 1)}} [a_1^{-\frac{n_2}{2} - 1} - t^{-\frac{n_2}{2} - 1}] \right\} \frac{1}{s} \\
 & - \frac{A_2 (t - a_0)}{[(1-R)K_c]^{\frac{n_2}{2}}} .
 \end{aligned} \tag{8.53}$$

For the intermediate-cycle regime,

$$\begin{aligned}
 N = & \frac{A_1}{(1.12, \frac{n_1}{\pi})} \left\{ \frac{e^{n_1 H_0}}{-(n_1 H_1 + 1)} [a_0^{n_1 H_1 + 1} - a_1^{n_1 H_1 + 1}] + \frac{1}{\frac{n_1}{(\frac{n_1}{2} - 1)}} a_1^{-\frac{n_1}{2} - 1} \right\} \frac{1}{s^{\frac{n_1}{2}}} \\
 & + \frac{A_2}{(1.12, \frac{n_2}{\pi})} \left\{ \frac{e^{n_2 H_0}}{-(n_2 H_1 + 1)} [a_0^{n_2 H_1 + 1} - a_1^{n_2 H_1 + 1}] + \frac{1}{\frac{n_2}{(\frac{n_2}{2} - 1)}} a_1^{-\frac{n_2}{2} - 1} \right\} \frac{1}{s^{\frac{n_2}{2}}} \\
 & - \frac{1}{(1.12, \frac{n_1}{\pi})^2} \left\{ \frac{A_1}{(\frac{n_1}{2} - 1) [(1-R)K_c]^{\frac{n_1}{2}-2}} + \frac{n_2 A_2}{(n_2-2) [(1-R)K_c]^{\frac{n_2}{2}-2}} \right\} \frac{1}{s^2} \\
 & + \frac{A_2 a_0}{[(1-R)K_c]^{\frac{n_2}{2}}} .
 \end{aligned} \tag{8.54}$$

For the low-cycle regime,

$$\begin{aligned}
 N = & \left\{ \frac{-A_1 e^{\frac{n_1 H_0}{a_0}} s^{\frac{n_1 H_1 + 1}{n_1}}}{(n_1 H_1 + 1)(1.12 \sqrt{\pi})^{\frac{n_1}{n_1}}} \right\} \frac{1}{s^{\frac{n_1}{n_1}}} + \left\{ \frac{-A_2 e^{\frac{n_2 H_0}{a_0}} s^{\frac{n_2 H_1 + 1}{n_2}}}{(n_2 H_1 + 1)(1.12 \sqrt{\pi})^{\frac{n_2}{n_2}}} \right\} \frac{1}{s^{\frac{n_2}{n_2}}} \\
 & + \frac{A_2 a_0}{[(1-R)K_c]^{\frac{n_2}{n_2}}} \\
 & + \left\{ \frac{A_1 e^{-H_0/H_1}}{(n_1 H_1 + 1)[(1-R)K_c]^{\frac{n_1 + 1/H_1}{n_1}} (1.12 \sqrt{\pi})^{-1/H_1}} \right. \\
 & \left. - \frac{A_2 e^{-H_0/H_1} n_2 H_1}{(n_2 H_1 + 1)[(1-R)K_c]^{\frac{n_2 + 1/H_1}{n_2}} (1.12 \sqrt{\pi})^{-1/H_1}} \right\} \frac{1}{s^{-1/H_1}}. \tag{8.55}
 \end{aligned}$$

From the definitions of the three cases, the switch point between the high-cycle and the intermediate-cycle model is given by

$$\left[\frac{1.12 S \sqrt{\pi}}{(1-R) K_c} \right]^{-2} = t. \tag{8.56}$$

No random variable is involved. For example values of $R = 0.8$, and $K_c = 160$ MPa, $\sqrt{\pi}$, the high/intermediate switching boundary is given by $S = 101$ MPa for $t = 25.4$ m. The switch point between the intermediate- and low-cycle models is given by

$$\left[\frac{1.12 S \sqrt{\pi}}{(1-R) K_c} \right]^{-2} = \frac{t}{35(K_t - 1)} \ln \left(\frac{K_t - 1}{e^{\Delta} - 1} \right). \tag{8.57}$$

One random variable, $K_t - 1$ is involved. For $K_t = 3.2$ and other parameters, as before, this switch point is $S = 382$ MPa. For K_t defined by the distribution of $\ln(K_t - 1)$ and using a first-order, second-moment method, this switch point is a random variable with $S_{0.05} = 187$ MPa, $S_{0.50} = 240$ MPa, and $S_{0.95} = 308$ MPa.

To compare the analytical approximation with the precise numerical integration results, Figure 8.4 was prepared. Figure 8.4 shows the case without corrosion effects with $K_t = 3.2$. The approximate analytical solution is very close to the precise numerical results in the high and intermediate regimes and errs conservatively in the low-cycle regime.

For marine structures, the high-cycle regime is of greatest interest. In this regime, as well as the others, the random variables to be considered for sensitivity and uncertainty analysis are A_1 , A_2 , $K_t - 1$, and a_0 .

8.4.1 Three-Component Model Sensitivity Analysis

Unlike the earlier linear model, the three-component model relates N , or the logarithm of N , to the random variables nonlinearly and with interaction among the effects of the variables. The analytical expressions for N from the three-component model, given previously, can be used to give accurate assessments of the changes in N , or $\ln N$, resulting from a change in one-variable-at-a-time, or from simultaneous changes in two or more of the parameters. The one-at-a-time change sensitivities can be obtained from Table 8.5 for the without corrosion case in the high-cycle regime.

As in the case for the linear model, the sensitivities presented in Table 8.5 can also be interpreted as the percentage change in N to a 1 percent increase in the value of the corresponding variable. The tabulated results indicate that a 1 percent increase in the initial flaw size, a_0 , the stress concentration addition, $K_t - 1$, and the crack-growth parameter, A , respectively, result in a 1.5 percent reduction, a 1.0 percent reduction, and a 1.0 percent increase in the characteristic cycles to failure. The expressions for the partial derivatives that can be evaluated to provide the sensitivities for other cases are presented in Appendix D.

8.4.2 Three-Component Model Probabilistic Analysis

A probabilistic S-N model was constructed for the three-component model as it was for the linear model presented previously. Numerical results were developed for the high-cycle regime without corrosion effects as an example. A first-order, second-moment method was chosen from among the alternative methods.

The alternative methods of probabilistic analysis for the three-component model included the lognormal format, Monte Carlo, response surface methodology, higher order higher moment methods, and the Rackwitz approach. Although a logarithmic format was retained as a useful transformation, the resulting expressions for cycles-to-failure, N , or $\ln N$, are not linear in the logarithms of the variables. Therefore, the lognormal format, Reference [8.2], cannot be used. The Monte Carlo approach could have been used with the three-component model realized either by the original numerical integration method, or by the newly developed approximate analytical solution. Response surface methodology is generation of data of the response, e.g., N , for selected combinations of values of the input variables, and subsequent low order multinomial regression modeling to obtain a simplified model for Monte Carlo or other method of probabilistic analysis. This approach was not used because a sufficiently simple approximate analytical model was obtained. Higher order, higher moment methods involve Taylor series expansions of the function N , or $\ln N$, in terms of the input variables and retaining terms in the expansion beyond the first order. The first order terms would be needed in such an approach.

The Rackwitz-Fiessler algorithm (Hasofer and Lind), Reference [8.2] involves finding an optimum point in the space of the input variables. Considering the nonlinear and transcendental nature of the expressions for N , or $\ln N$, this approach may be as costly as the direct Monte Carlo approach. For example, in Reference [8.3] two nonlinear functions of intermediate complexity were analyzed by the Rackwitz method and compared to the direct Monte Carlo approach. The first involved the square root of the sum of squares of two random variables. The Rackwitz method was 72 times faster than the Monte Carlo simulation employed. It is assumed that 10,000 simulations were used. In the second, a more complex nonlinear function involved sums, quotients, products, and fractional powers of six random variables. The Rackwitz approach was 28 times faster than the employed Monte Carlo case. The Monte Carlo simulation produces an estimate of the entire probability distribution of the function while the Rackwitz produces an estimate of the probability distribution at only one point in the range of the function. Therefore, an equivalent effort expended with the Rackwitz approach would produce 72 and 28 points, respectively, for the two cases in Reference [8.3], while the

Monte Carlo approach produced a much larger number of points on the probability distribution curve for the function. The methods to solve the necessary optimization/search problem usually involve partial derivatives evaluated either from analytical formulas or numerically by a method similar to the initial steps of the response surface methodology.

Since the first-order partial derivatives used in the simple first order, second moment method are therefore also useful to subsequent developments with other approaches, (for example, higher-order higher moment, or advanced first-order second-moment methods such as Rackwitz-Feissler), the first-order, second-moment approach in the logarithms of the variables was developed. Furthermore, this approach with the transformed input variables normally distributed is mathematically equivalent to the multiplicative log-normal format with the input variables lognormally distributed up to the point where other than additive (transformed) and multiplicative (untransformed) functions are considered as in the present study. Here the lognormal format cannot be used, but the transformed problem can be solved, approximately, by the first-order, second moment method.

When the coefficient of variation, COV, of the input variables is large, say over 10 percent, or the functional form is suspected to be highly nonlinear, then use of the first-order, second-moment method requires some type of validity check. An expedient checking method demonstrated in Appendix C was employed in this study.

The results of this probabilistic approach are presented in Table 8.6, and the corresponding probabilistic S-N curve is shown in Figure 8.5. The standard deviation of $\ln N$ at a given stress range level in the high-cycle regime (without corrosion effects) is on the order of 0.6 or 0.7. This three-component model result compares to the linear model result of $\sigma_{\ln N} = \sqrt{1.1} = 1.05$. These results indicate that the three-component results are more precise, with the variance about half the value obtained for the corresponding case with the linear model in Section 8.3.2. The distributions sketched in Figure 8.5 are correspondingly narrower than the linear model distributions sketched in Figure 8.2. For the linear model, $\ln a_0$ contributed about 52 percent and $\ln Y [\ln(K_t - 1)]$ about 46 percent to the variance of $\ln N$. For the three-component model, the respective values are about 61 percent and 36 percent.

8.5 Summary and Conclusions

Probabilistic S-N curves were constructed by synthesis from fracture mechanics models. These models are illustrated in Figures 8.1, 8.2, and 8.5. The associated variances in the logarithm of N , cycles-to-failure, in the high cycle regime, are 4.0 (standard deviation = 2.0) with corrosion effects from the linear model, 1.1 (standard deviation = 1.05) without corrosion effects from the linear model, and 0.5 (standard deviation about 0.7) without corrosion effects from the three-component model. The three-component model appears to be about twice as precise as the linear model in terms of the variance of the logarithm of cycles for crack propagation. Greater precision is manifest also in the flexibility of the three-component model in fitting crack growth data in high, intermediate, and low cycle regimes that must be modeled piece-wise with the linear model. The three-component and linear models both admit improved models of stress intensity as a function of flaw size as demonstrated with $h(a)$ in Section 8.4. The sensitivity of $\ln N$ to the logarithms of the several variables was also determined. The resulting percentage change in N , cycles-to-failure, due to a 1 percent increase in the values of the individual variables, is about -1 percent for the crack growth constant C , or $1/A_1$, on the order of -2 percent for the initial crack size, a_0 , without corrosion effects, and -1 or -2 percent for the elastic stress concentration effect, K_t^{-1} , without corrosion effects.

The probabilistic S-N models represent probabilistic life predictions and are a basis for structural reliability prediction. As a basis for structural reliability assessment, the S-N models would be combined with the uncertainty effects of stress quantification and load service life cycles presented in the foregoing text. For structural life or reliability prediction, the apparent uncertainty in the local stress range is the most significant.

CHAPTER 8.0 REFERENCES

- 8.1 Wirsching, P. H., "Probability-Based Fatigue Design Criteria for Offshore Structures," API-PRAC Project No. 81-15, Final Project Report, January 1983.
- 8.2 Wirsching, P. H., and Light, M. C., "Probability-Based Fatigue Design Criteria for Offshore Structures," API-PRAC Project No. 15, Final Report, First-Year Effort, November 1979.
- 8.3 McLain, S. D., Kelly, C. F., and Wirsching, P. H., "On the Performance of a New Algorithm for Computing Structural Reliability," for NASA-Lewis Research Center, Project No. NAG 3-41, June 1982.
- 8.4 Engesvik, K. M., and Moan, T., "Probabilistic Analysis of the Uncertainty in the Fatigue Capacity of Welded Joints," Unpublished Report, Division of Marine Structures, The Norwegian Institute of Technology, Trondheim.
- 8.5 Wirsching, P. H., "Probability-Based Fatigue Design Criteria for Offshore Structures," API-PRAC Project 80-15, Final Report, Second-Year Effort, February 1981.
- 8.6 Vosikovsky, O., "Fatigue-Crack Growth Rate in an X65 Line-Pipe Steel at Low Cyclic Frequencies in Aqueous Environments," Journal of Engineering Materials and Technology, Transactions of the ASME, Vol. 97, No. 4, October 1975, pp 298-304.
- 8.7 Wirsching, P. H., Private Communication, in review of progress report, February 28, 1983.
- 8.8 ASCE Committee on Fatigue and Fracture Reliability, "Fatigue Reliability," (A Four-Part State-Of-The-Art Summary on Fatigue Reliability), ASCE Proceedings, Journal of the Structural Division, Vol. 108ST, January-June 1982.

TABLE 8.1. RANDOM VARIABLE SUMMARY

Description	Application	Linear Model	Three-Component Model
Initial Flaw Size, a_0 (m)	S-N, Reliability	$\ln a_0$	$\ln a_0$
Weld Toe Radius, r (m)	S-N, Reliability	$\ln Y$	$\ln (K_t - 1)$
Crack Growth Parameter	S-N, Reliability	$\ln C$	$\ln A_1, \ln A_2$
Stress Range (MPa)	Reliability	$\ln S_0$	$\ln S_0$
Load Cycles in Service Life	Reliability	$\ln N_T$	$\ln N_T$

TABLE 8.2. A_1 AND A_2 DISTRIBUTIONS

	<u>Without Corrosion Fatigue Effects</u>	<u>With Corrosion Fatigue Effects</u>
$\mu_{\ln A_1}$	$\ln (8.35 \times 10^{13})$	$\ln (2.57 \times 10^{14})$
$\sigma^2_{\ln A_1}$	0.031	0.031
$\mu_{\ln A_2}$	$\ln (1.42 \times 10^{11})$	$\ln (2.35 \times 10^{15})$
$\sigma^2_{\ln A_2}$	0.031	0.031

TABLE 8.3. STRESS RANGE UNCERTAINTY FACTORS

	B_B	C_B	$\sigma_{\ln B}^2$
Manufacturing and Fabrication, B_M	0.90 to 1.30	0.10 to 0.30	0.01 to 0.09
Seastate, B_S	0.63 to 1.20	0.40 to 0.60	0.15 to 0.31
Wave Force, B_F	0.60 to 1.10	0.10 to 0.30	0.01 to 0.09
Member Loads, B_N	0.80 to 1.10	0.20 to 0.40	<u>0.04 to 0.15</u> 0.21 0.64

TABLE 8.4. LINEAR MODEL SENSITIVITIES

Case	$\frac{\delta \ln (N/N_T)}{\delta \ln C}$ (-1)	$\frac{\delta \ln (N/N_T)}{\delta \ln a_o}$ $\left(-\left(\frac{m}{2} - 1 \right) \right)$	$\frac{\delta \ln (N/N_T)}{\delta \ln Y}$ (-m)	$\frac{\delta \ln (N/N_T)}{\delta \ln S_o}$ (-m)	$\frac{\delta \ln (N/N_T)}{\delta \ln N_T}$ $\left(-\left(\frac{m}{\xi \ln N_T} + 1 \right) \right)$
$m = 2.67$ $\xi = 1.4$	-1	-0.335	-2.67	-2.67	$-1.138 @ 10^6$ cycles $-1.104 @ 10^8$ " $-1.083 @ 10^{10}$ "
$m = 3.0$ $\xi = 1.0$	-1	-0.5	-3.0	-3.0	$-1.217 @ 10^6$ cycles $-1.163 @ 10^8$ " $-1.130 @ 10^{10}$ "
$m = 3.5$ $\xi = 0.5$	-1	-0.75	-3.5	-3.5	$-1.507 @ 10^6$ cycles $-1.380 @ 10^8$ " $-1.304 @ 10^{10}$ "

TABLE 8.5. THREE-COMPONENT MODEL ONE-AT-A-TIME SENSITIVITIES
(WITHOUT CORROSION EFFECTS, HIGH-CYCLE MODEL)

S (MPa)	$N_{0.50}$ (Cycles)	$\frac{\delta \ln N}{\delta \ln A_1}$	$\frac{\delta \ln N}{\delta \ln A_2}$	$\frac{\delta \ln N}{\delta \ln (K_t^{-1})}$	$\frac{\delta \ln N}{\delta \ln a_o}$
101	1.0×10^6	0.22	0.78	-0.63	-0.57
50	3.9×10^7	0.80	0.20	-0.92	-1.26
30	1.2×10^9	0.97	0.03	-1.01	-1.46
20	2.1×10^{10}	0.99	0.01	-1.03	-1.49
10	2.8×10^{12}	1.00	0.00	-1.03	-1.50

TABLE 8.6. THREE-COMPONENT MODEL VARIANCE
OF LOGARITHM OF N

Source	S (MPa)				
	101	50	30	20	10
$\ln A_1$	0.0007 (0.6%)	0.0097 (2.8%)	0.0141 (3.1%)	0.0148 (3.2%)	0.0150 (3.2%)
$\ln A_2$	0.0092 (8.1%)	0.0006 (0.2%)	0.0000 (0.0%)	0.0000 (0.0%)	0.0000 (0.0%)
$\ln a_o$	0.0419 (36.7%)	0.2925 (58.4%)	0.2709 (60.6%)	0.2822 (60.9%)	0.2850 (61.0%)
$\ln (K_t^{-1})$	0.0623 (54.6%)	0.1342 (38.7%)	0.1618 (36.2%)	0.1663 (35.9%)	0.1674 (35.8%)
$\sigma_{\ln N}^2$	0.1141 (100%)	0.3470 (100%)	0.4468 (100%)	0.4633 (100%)	0.4674 (100%)

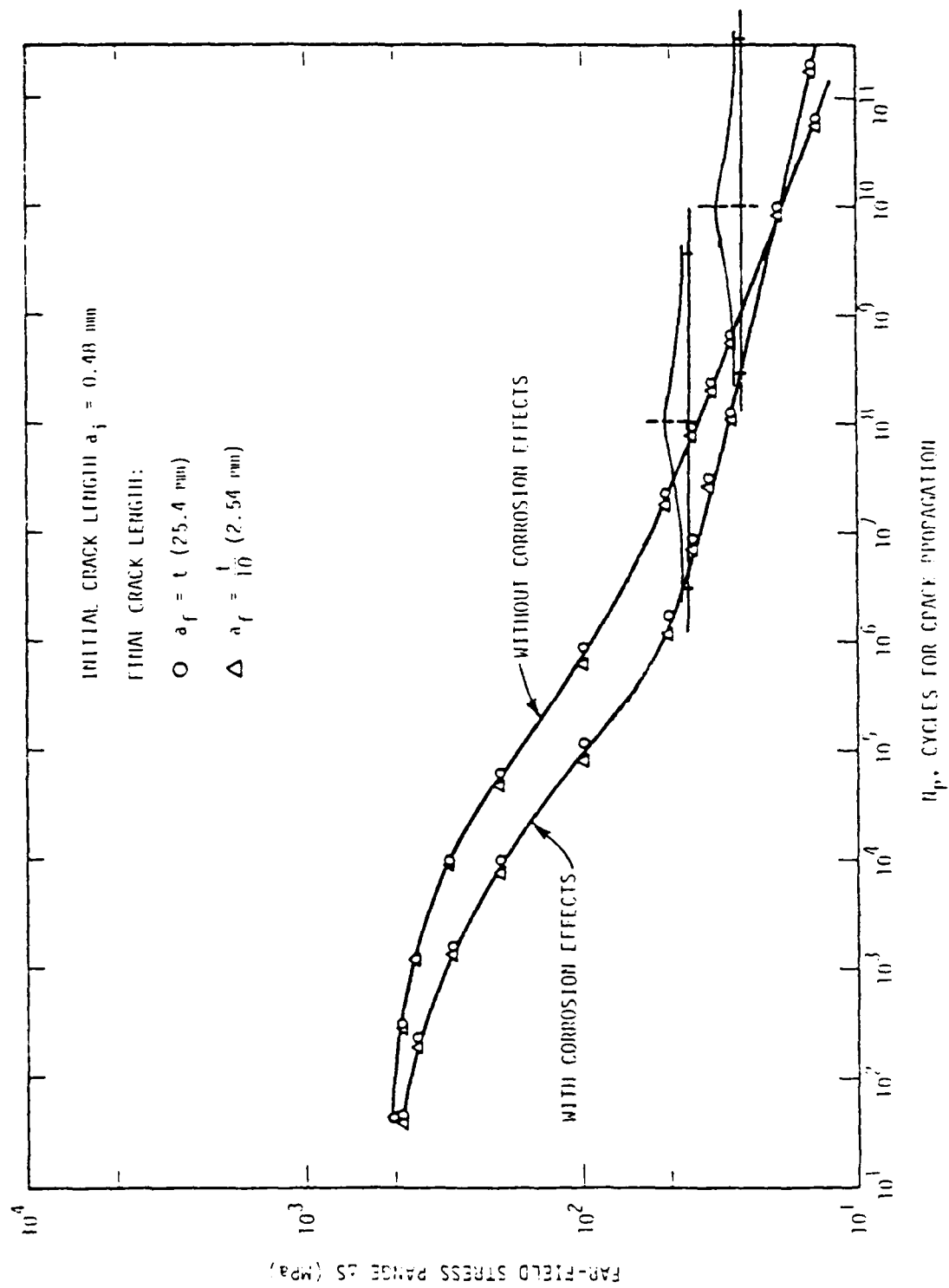


FIGURE 8.1. PROBABILISTIC S-N MODEL, LINEAR MODEL, WITH CORROSION EFFECTS

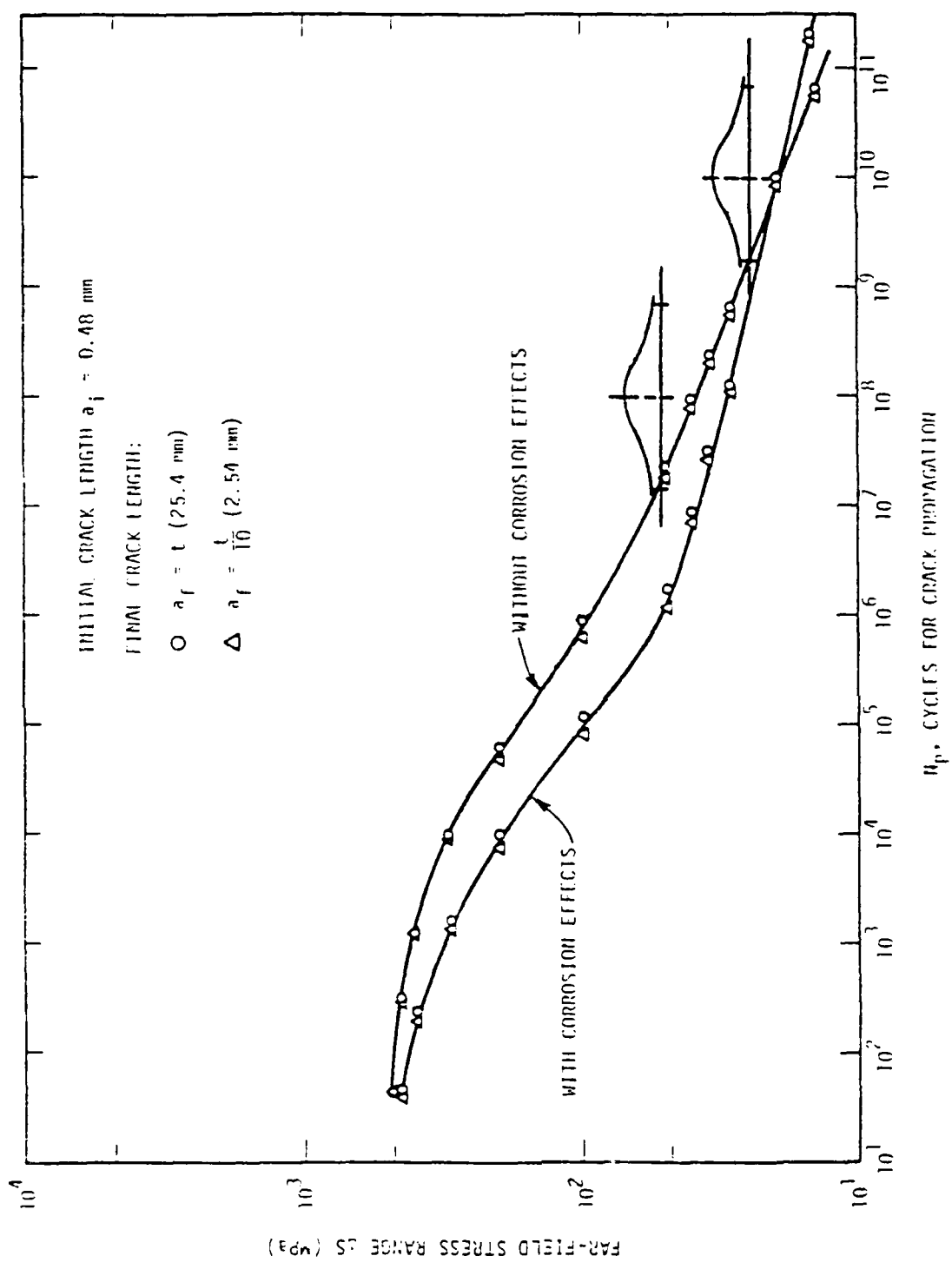
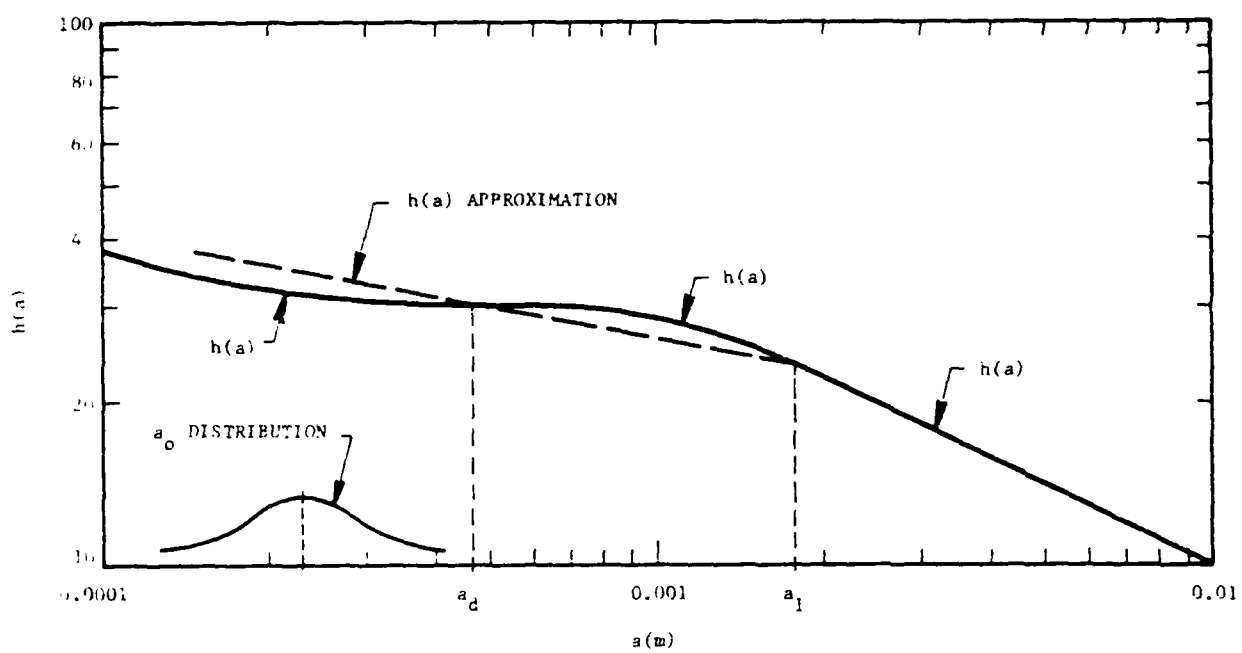
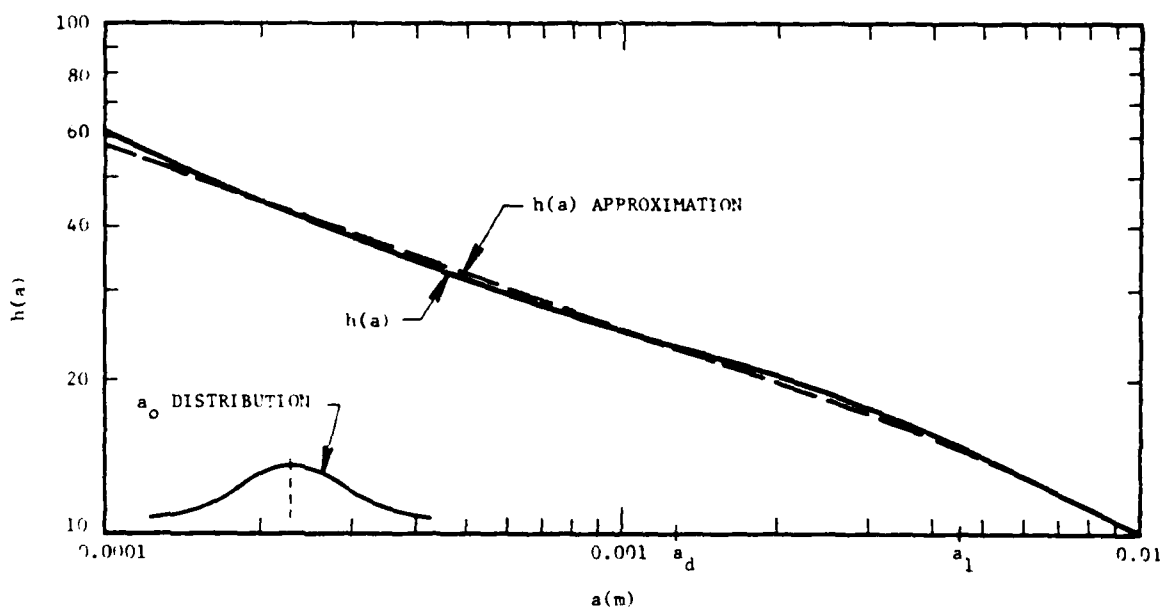


FIGURE 8.2. PROBABILISTIC S-N MODEL, LINEAR MODEL, WITHOUT CORROSION EFFECTS



(a) $K_t = 3.2$



(b) $K_t = 1.7$

FIGURE 8.3. APPROXIMATION OF $h(a)$

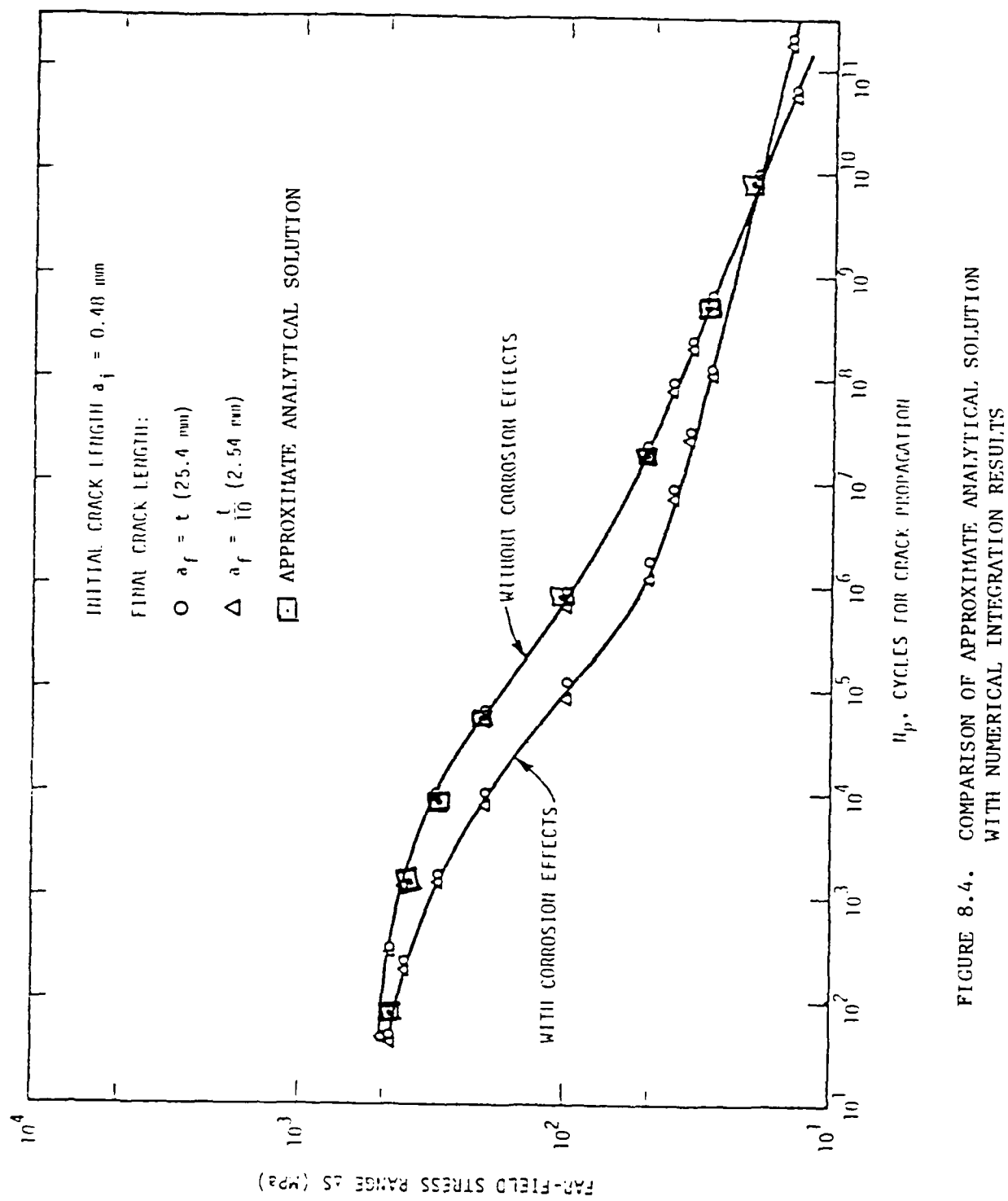


FIGURE 8.4. COMPARISON OF APPROXIMATE ANALYTICAL SOLUTION WITH NUMERICAL INTEGRATION RESULTS

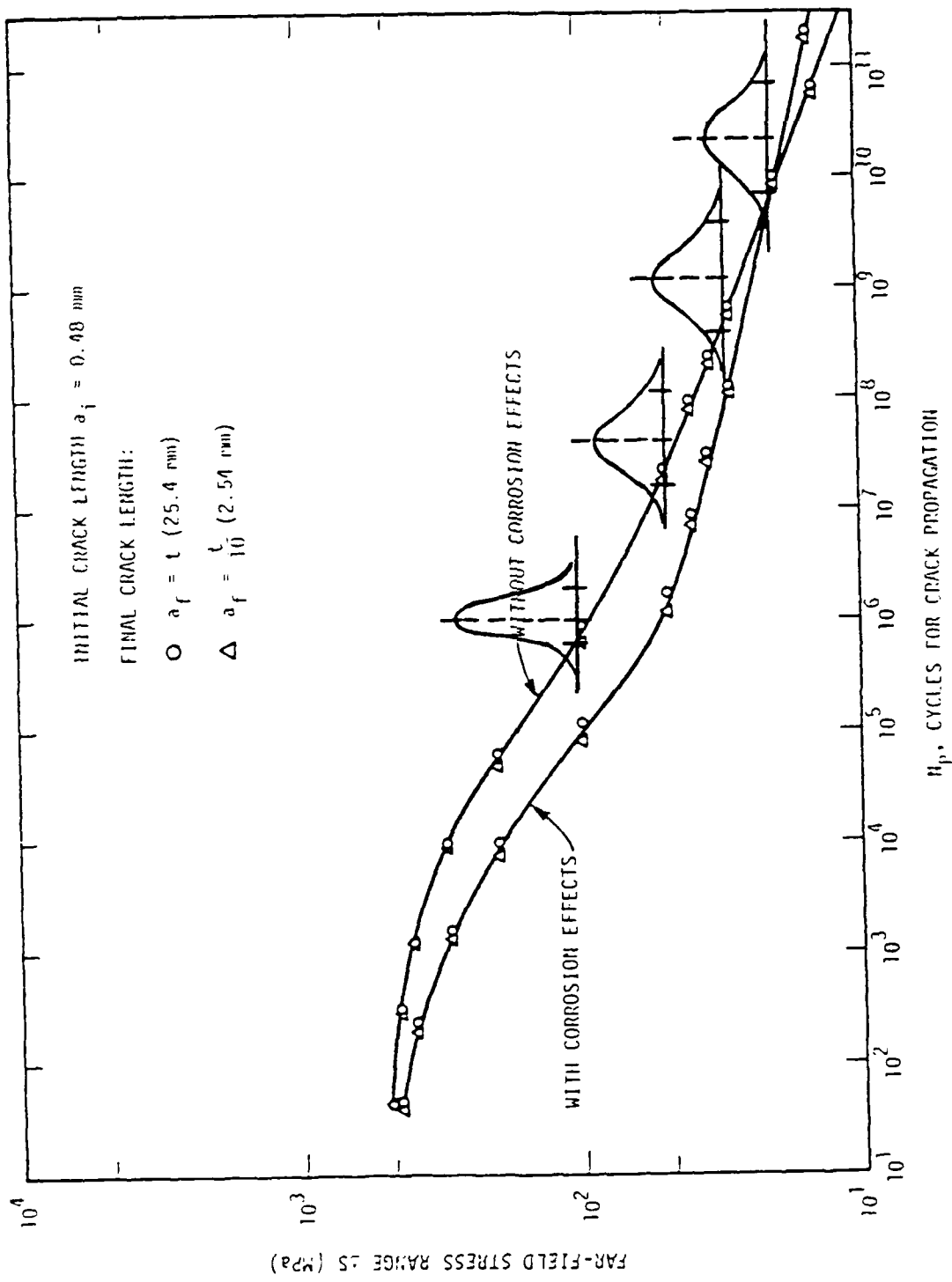


FIGURE 8.5. PROBABILISTIC S-N MODEL, THREE-COMPONENT MODEL,
WITHOUT CORROSION EFFECTS

9.0 SUMMARY, CONCLUSIONS, AND RECOMMENDATIONS

9.1 Summary

This report has presented the results of a comprehensive investigation into the phenomenon of corrosion fatigue in welded marine steels. Chapters 1.0-5.0 reviewed the effects of loading, environmental, materials, and fabrication variables on the corrosion fatigue resistance of welded joints. Chapter 6.0 discussed various methodologies for the deterministic evaluation of fatigue crack initiation and propagation life using local strain and fracture mechanics approaches, respectively. Analytical procedures, which considered weld toe geometry, joint geometry, plate thickness, and mode of loading were developed for both approaches.

In Chapter 7.0 analytical predictions on fatigue crack initiation were compared with experimental results. The lack of correlation with total life laboratory tests demonstrated that crack initiation constitutes only a small portion of the total fatigue life of the welded joint. A comparison of crack propagation predictions using air crack-growth data at low R shows excellent agreement with planar joint fatigue tests conducted in air. Agreement was not as good for predictions made at high-R or with effects of the corrosive seawater environment included. This may indicate a lack of reliable crack-growth data for these conditions.

The fracture mechanics model was extended to crack propagation in tubular joints. In this two-dimensional crack model, curvature effects of the chord and brace were found to be insignificant. The analytical predictions at low-R generally formed a lower bound on the experimental data conducted in air. Only a handful of tests have been conducted in seawater environment at a realistic wave frequency; for these cases, crack growth predictions and tests give reasonable correlation.

Chapter 8.0 utilized the deterministic crack growth model developed in Chapter 6.0 as the basis for a probabilistic model; this model was used to evaluate the sensitivities of fatigue life to various input variables including initial flaw size, weld toe radius, crack growth parameters, and stress range. The probabilistic analysis indicated that the most important factor contributing to uncertainty in fatigue life is the stress range. The importance of stress range is a manifestation of the strong dependence of crack growth rate on ΔK in the Region I low-growth rate regime.

9.2 Conclusions

This research program has attempted not only to critically review the state-of-the-art in corrosion fatigue of welded marine steels, but also to advance the science of fatigue life predictions. In the course of the review and in the formulation and validation of materials data and analytical methodologies, the program investigators were able to draw certain conclusions about the state of current technology. This section discusses 16 conclusions which the investigators feel reflect this study's findings. Imbedded in these discussions are recommendations for future areas of research which will lead to improved predictions of long-term corrosion fatigue in welded structures.*

1. Comparisons of experimental results on welded planar and tubular joints with crack initiation and crack growth predictions show that the fatigue lives of these components are controlled by crack growth, even in the high-cycle fatigue regime. In the low and intermediate fatigue life regime, crack initiation typically accounts for less than 10 percent of the fatigue life; in the high-cycle fatigue regime, crack initiation predictions, based on smooth specimen data, generally overpredict the life of welded components. The nonconservatism of the initiation analysis is due to the role of weld defects in non-post weld treated joints in virtually eliminating the need for the initiation processes which occur in smooth, unwelded specimens. In the statistical sense, this conclusion is even more applicable to offshore structures than to welded laboratory specimens because of the large size and large number of weldments contained in these structures. Based on the fracture mechanics analysis and SwRI's experience in failure analysis, fabrication defects in the range of 0.05 to 0.5 mm can be expected to be present in offshore structures; these will go undetected by nondestructive testing techniques (Sections 7.2 and 7.3).
2. Fracture mechanics crack growth predictions are in good agreement with fatigue lives measured on planar welded joints, provided low-R crack growth rate data are used. Although high-R life predictions might be expected to be more applicable to weldments due to welding residual stresses, these predictions are overly conservative. This

*These conclusions and recommendations are keyed to appropriate sections in this report.

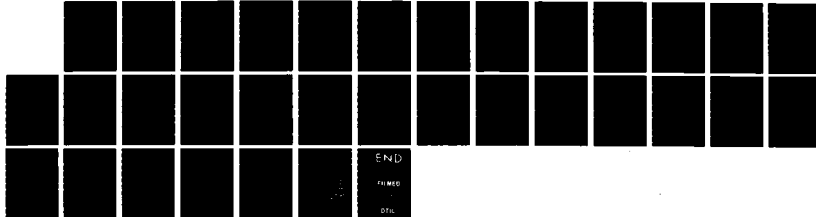
AD-A162 484 LONG-TERM CORROSION FATIGUE OF WELDED MARINE STEELS(U) 5/5
SOUTHWEST RESEARCH INST SAN ANTONIO TX
O H BURNSIDE ET AL. 1984 SR-1276 SSC-326

UNCLASSIFIED

DTCG23-80-C-20028

F/G 11/6

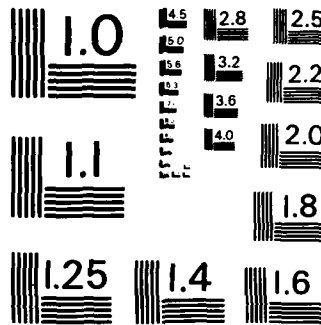
NL



END

THREE

DTI



MICROCOPY RESOLUTION TEST CHART
NATIONAL BUREAU OF STANDARDS - 1963 - A

conservatism may be due to an overly conservative selection of the high-R growth rate curve in Region I (Section 3.8). In tubular joints, fracture mechanics predictions in an air environment correlate well with measured lives provided low-R data and the bending mode of loading are used. Using the tension mode of loading gives a lower bound to the measured fatigue lives. These trends are consistent with the observation that local shell bending dominates the stress field in the vicinity of the weld (Sections 7.2 and 7.3).

3. The fracture mechanics crack growth analysis is in agreement with the size effects observed in measured fatigue lives on planar and tubular joints— specifically shorter lives occur for thicker welded joints (Sections 7.2 and 7.3). This effect is related to the growth of small cracks near the weld toe and is accounted for by including the influence of local weld toe geometry in the analysis. The invariant hot-spot stress—as usually defined—cannot account for this size effect because it does not incorporate the influence of local weld toe geometry (Section 7.7).
4. Although the explicit treatment of crack growth has been shown to be the physically correct approach to predicting fatigue lives in welded offshore structures (Sections 7.2 and 7.3), and fracture mechanics predictions have demonstrated a certain degree of success, various aspects of this approach need to be improved as cited below.
5. Existing crack growth rate data, $da/dN(\Delta K)$, in the low growth rate, high-cycle fatigue regime (Region I) are inadequate (also see Conclusions 6 and 7 below); this is particularly true for seawater data under both freely corroding and cathodic polarization conditions. This information needs to be generated as a function of cyclic frequency and load ratio. Innovative test techniques will be necessary to obtain the low frequency, low-growth rate data. Test systems with improved reliability over extended test durations are required as well as novel specimen geometries and test techniques which minimize required test times (Section 3.8).
6. The primary environmental variables affecting fatigue crack growth in seawater are temperature, oxygen content, and electrode potential. Most of these have been characterized for Region II growth rates;

- however, little information is available on the influence of these variables on crack-growth rates in Region I (Chapter 4.0).
7. The primary loading variables (apart from ΔK) affecting fatigue crack growth in seawater are load ratio, and cyclic frequency; however, just as in the case of environmental variables, little information is available on the influence of these variables on fatigue crack growth rates in Region I (Sections 3.2-3.4).
 8. The significance of load interaction effects during variable amplitude loading of offshore structures is an unresolved issue. Therefore, the applicability of linear damage accumulation methods such as the cycle-by-cycle analysis used herein or weighted-average approaches is uncertain. However, since retardation in growth rates following overloads is the predominant interaction, linear damage accumulation will provide conservative results. Although a variety of empirical and analytical models for crack growth retardation have been developed and are in use within the aircraft industry, the applicability of these models to offshore structures is unknown, primarily due to unknown interactions with environmental effects (Section 7.7).
 9. Stress intensity factor solutions for surface flawed plates appear to be applicable to tubular sections provided notch effects are included. Because of the magnitude of the shell parameter for typical tubular sections used in offshore structures, a correction factor for the curvature of the tube does not appear necessary when using plate solutions. However, this conclusion needs to be confirmed by more extensive analyses of tubular joints where typical joint configurations, modes of loading, and weld profile are considered (Section 7.6).
 10. The influence function approach for computing stress intensity factors appears to be accurate within 20 percent for notches typical of weld toe geometries. Using these values of ΔK may be sufficiently accurate in the Region II growth rate regime, but may produce considerable error for the low-growth rates in Region I (Section 6.6.2).
 11. Most previous fracture mechanics analyses of welded joints have utilized a simple power law relationship for $da/dN(\Delta K)$. Although, this relationship is only applicable for a limited range of growth

rates, it has been adequate for predicting the lives of welded coupon tests which have been conducted in the low-to-intermediate life regime. For tests which extend to long lives, as well as for actual structures, relations which represent the near-threshold growth rates (Region I) are necessary. In selecting such relations, those having an asymptotic behavior in Region I should be avoided since they can lead to extremely nonconservative life growth rate predictions (Section 3.7).

12. A number of crack-growth phenomena related to the presence of the seawater environment remain perplexing, including the influence of cathodic polarization, transient crack-growth responses, and crack size effects. Basic studies which focus on the issues of transport between the bulk and crack-tip environment and on the role of corrosion product/calcareous product wedging in corrosion fatigue are needed to understand these phenomena and assess their impact on the long-term corrosion fatigue behavior of offshore structures (Sections 3.5, 3.6 and 4.3).
13. Over the near term, design of offshore structures will continue to rely primarily on the classical approach to fatigue which involves S-N testing of welded specimens combined with operating experience. However, fracture mechanics will become an increasingly important tool for assessing the structural reliability of offshore structures--particularly in assessing the significance of defects discovered in service, extending the performance of structures beyond their originally intended life, and examining fracture critical locations in new generations of structures. The latter area will provide the impetus for introducing fracture mechanics into original design concepts since the use of novel designs with new modes of loading and new materials requirements (for example, tension-leg platforms) will limit the usefulness of existing S-N data and field experiences.
14. The information developed in the probabilistic analysis suggests areas for further research. For example, for the present model and the uncertainty of the data available in the literature, it is suggested that a more accurate determination of both the hot-spot and weld toe stress is needed to accomplish more accurate structural life predictions. The contribution of this uncertainty in stress is a

manifestation of the strong dependence of the growth rates, and therefore fatigue lives, on stress through the stress intensity factor.

15. A limitation to the extension of deterministic fracture mechanics models into the probabilistic realm is the relatively limited amount of information on the distribution functions of the primary input variables. Current probabilistic fracture mechanics models can be utilized to provide information on the relative sensitivity of the input variables, but cannot be utilized to give absolute quantitative measures of reliability. The distributions of the input variables may never be known exactly since data will probably never be available to fully develop the tails of the distributions. It is noted that the present probabilistic tools used in structural reliability and life prediction are based on the assumption of known input distributions. A confidence interval approach should be developed and implemented in probabilistic analysis. Such methods should provide further information on the effect of the limited amount of data on which the input distributions are based.
16. In view of the significance of stress amplitude and other loading variables on corrosion fatigue life predictions, advanced methods of forecasting stress histories need to be implemented in the design process. Specifically, these methods should interface with other emerging analytical methods relevant to fatigue life prediction, e.g., structural mechanics, probabilistic treatment of fatigue, and crack propagation modeling for variable amplitude loading. The spectral method of forecasting short-term stress histories facilitates the probabilistic interpretation of structural dynamic analysis. When simulations and rainflow cycle counting are used with this method, it offers a rational approach to estimating quantities which are required for implementation of advanced crack propagation modeling techniques for wide band loading, specifically the magnitude, mean, period and sequence of individual stress ranges.

9.3 Recommendations for Research Plans

Over the near term, design of offshore structures will continue to rely primarily on the classical approach to fatigue which involves S-N testing of welded specimens combined with operating experience. However, fracture mechanics will become an increasingly important tool for assessing the structural reliability of offshore structures--particularly in assessing the significance of defects discovered in service, extending the performance of structures beyond their originally intended life, and examining fracture critical locations in new generations of structures. The latter area will provide the impetus for introducing fracture mechanics into original design concepts since the use of novel designs with new modes of loading and new materials requirements (for example, tension-leg platforms) will limit the usefulness of existing S-N data and field experiences.

The current study has identified three broad areas where future research is needed. Such work would provide more reliable design and residual life assessments of offshore structures.

Materials

Fracture mechanics assessments for long-term corrosion fatigue require crack growth data, $da/dN(\Delta K)$, in the low-growth rate, high-cycle regime (Region I). Existing data are inadequate for materials currently being used in offshore structures, as well as for the higher-strength low-alloy steels suggested for future designs.

The primary loading, environmental, and materials variables affecting corrosion fatigue crack growth in offshore structures are summarized in Table 9.1. Also given are the possible ranges of these variables which can occur in offshore structures, along with comments addressing the interaction of variables, ranges judged to be most critical, and, where appropriate, recommended values for testing. Because of the large number of variables involved, as well as the wide range which certain variables can assume, it is not economically feasible to acquire data for all combinations of variables. Thus, judgements on which combination of variables are most critical need to be made. In certain instances these judgements depend on the specific structure, including its intended location. Thus the judicious selection of which data are most critical becomes an integral part of the design process. For example, selection of appropriate test variables (e.g., R-value, environmental

conditions and material) would differ for conventional designs in shallow water versus newer deep-water designs. Table 9.1 provides guidelines for such a selection process.

Overall, the most critical need for data exists at low crack growth rates and low cyclic frequencies--a combination which makes testing both difficult and costly. Thus, it is not surprising that little information is currently available on the influence of loading, environmental, and material variables within this regime.

In order to satisfy this need, an industry-wide commitment to long-range testing is required. For maximum effectiveness, such a program will require the development of test systems with improved reliability over extended test durations, combined with novel specimen designs and test techniques which minimize the required test times while precluding transient crack growth responses. However, any new test technique should be carefully qualified before being used as the basis for an extended program.

It is also important to recognize that a number of corrosion fatigue crack growth phenomena (discussed primarily in Chapter 3) remain unresolved and thereby confound the interpretation and application of data to design and reliability assessments. These phenomena--including the influence of cathodic polarization, transient crack growth responses, and crack size effects--need to be addressed, both in the test method verification and data generation phases of these programs. Since these phenomena appear to be controlled by underlying processes such as transport between the bulk and crack-tip environment and corrosion product wedging, parallel fundamental studies of these processes are needed to understand the above phenomena. Without such understanding, it may not be possible to properly interpret the test data and apply them to the prediction of corrosion fatigue in offshore structures. For example, basic, but nevertheless pragmatic, questions which need to be answered are as follows:

- o Can long crack data from conventional fracture mechanics test be utilized to predict the crack growth behavior of relatively small surface flaws?
- o Is cathodic polarization beneficial or detrimental to corrosion fatigue crack growth--particularly in high-strength, low-alloy steels selected for newer designs? If beneficial, what range is optimum?

- o Under what conditions do corrosion product wedging occur and is this phenomenon equally beneficial in laboratory tests and under actual service conditions?

In view of the significance of loading variables, including the potential for load-interaction effects, on corrosion fatigue performance, additional work utilizing variable amplitude loading is also needed. Critical questions which need to be addressed in this work are as follows. Is linear damage accumulation (that is, the use of Miner's rule and the implicit assumption that load-interaction effects are insignificant) unduly conservative for offshore structures? This question needs to be clearly resolved by conducting variable amplitude tests using load histories which properly simulate the wide-band loading which is experienced by offshore structures. If the answer to the above question is affirmative, the utility of available models for load-interaction effects needs to be evaluated for the material, environment, and loading conditions relevant to offshore structures. Such an evaluation is needed because available models are semi-empirical and therefore not universal; furthermore, these have evolved within the aircraft industry and thus their direct application to corrosion fatigue in general, and offshore structures in particular, is questionable. A related issue under corrosion fatigue conditions is whether or not the use of steady-state, constant amplitude crack growth rate properties in predictive models introduces additional conservatism when applied to offshore structures where cycle-by-cycle changes in mean stress and cyclic frequency are likely to produce transient crack growth responses.

Structural Analysis

The fracture mechanics approach for residual life predictions requires knowledge of the stress intensity factor range (ΔK). ΔK is a function of the structural geometry and the location, size, and shape of the crack. Analytical ΔK values for numerous structural configurations are available in the literature. Such solutions do not include welded joints, and stress intensity factors for such joints are generally based upon simpler known analytical solutions. Finite element calculations can be made for ΔK , but the process is computationally expensive, and the results difficult to express in a generalized form.

This study employed a surface crack in a flat plate solution combined with the stress field in a weld to compute stress intensity factors at the weld toe for both one- and two-dimensional cracks. Such a formulation is able to incorporate such factors as toe radius, plate thicknesses, and mode of loading. The technique used herein for computing stress intensity factors appears to be accurate within 20 percent for notches typical of weld geometries. Using these values of ΔK may be sufficiently accurate for residual life predictions in the Region II growth rate regime, but may produce considerable error for the low-growth rates in Region I. Therefore, to improve accuracy of crack growth calculations in this high-cycle regime, a research program is recommended to extend the influence function or a similar generalized approach for calculating ΔK to a variety of geometrical configurations and modes of loading typically found in offshore structures. An example would be the weld details with convex, flat, and concave profiles as described in the AWS Structural Welding Code, AWS D.1.1, Section 10.13 [5.32]. Effects of residual stresses due to welding should be included in the analytical formulation and correlated with crack growth data generated in the Materials recommendation. The results should be expressed in handbook form, which could be used by structural engineers in assessing fatigue life.

Probabilistic Analysis

The information developed in the probabilistic analysis of this report suggests several areas for future research. For example, for the fracture mechanics model used in this study and the uncertainty of the data available in the literature, it is suggested that a better understanding of the hot-spot stress range is needed to accomplish more precise structural life predictions. The contribution of this uncertainty in stress is a manifestation of the strong dependence of the growth rates, and therefore fatigue lives, on stress through the stress intensity factor (see Structural Analysis recommendation).

A limitation to the extension of deterministic fracture mechanics models into the probabilistic realm is the relative unavailability of information on the distribution functions of the primary input variables. Primarily because of this limitation, current probabilistic fracture mechanics models can be utilized to provide information on the relative sensitivity of the input variables, but cannot be utilized to give absolute quantitative measures of reliability.

Therefore, a program is recommended to further gather and statistically quantify data on the primary variables associated with fracture mechanics fatigue predictions. This includes:

- a) Crack growth parameter in Regions I and II including effects of environment and loading (frequency and R)
- b) Initial crack size and shape
- c) Weld toe geometry and weld shape
- d) Loading and hot spot stress concentration factors

Present probabilistic tools used in structural reliability and life prediction are based on the assumption of known input distributions. It is recognized that data to fully develop the tails of the distributions will never be available. Furthermore, modeling errors, and other errors, contribute to uncertainty of reliability and life predictions. A confidence interval approach could be developed and implemented that would augment the probabilistic methodologies, e.g., log-normal, first-order-second-moment, Monte Carlo, Rackwitz-Fiessler, to quantify uncertainty contributions of limited data and subjective estimates of other modeling errors. Such an approach would also be helpful in quantifying the benefits of research which seeks to improve reliability by adding to the data base.

TABLE 9.1 PRIMARY LOADING, ENVIRONMENTAL AND MATERIALS VARIABLES AFFECTING CORROSION FATIGUE CRACK GROWTH RESISTANCE IN OFFSHORE STRUCTURES

<u>Variable</u>	<u>Applicable Range</u>	<u>Comment</u>
<u>Loading Variables:</u>		
Stress Intensity Factor Range, ΔK	ΔK_{th} 2 MPa m to $\Delta K_c / (1-R)$ 200 MPa m	Practical values of corresponding da/dN vary from 10^{-11} to 10^{-3} m/cycle. However, for typical values of flaw size and design stress, $da/dN < 10^{-7}$ m/cycle will usually control the fatigue life.
Load Ratio, R	-1 to 0.9	High, positive R-values are most important; these occur at welds, provided residual stresses are not relaxed by plastic deformation, and in legs of tension leg platforms.
Cyclic Frequency, f	0.01 to 1 Hz	Generally, low frequencies ($f = 0.01$ to 0.2 Hz) are associated with high ΔK values, while high frequencies ($f = 0.1$ to 1.0) are associated with low ΔK values. Typically frequencies of 0.1 to 0.3 Hz are used in laboratory tests.
Cyclic Waveform	Trochoidal/Sinusoidal	Actual waveform is a trochoidal-sinusoidal hybrid; nevertheless, sinusoidal waveform is adequate for laboratory testing.
<u>Environmental Variables:</u>		
Temperature, T	0°C to 30°C	These variables are interrelated and also vary with geographic location, seawater depth, and time of year.
pH	6.5 to 8.5	Test temperature should be controlled to simulate water depth and geographic location. The relative merits of ASTM synthetic seawater versus natural seawater remain controversial.
Seawater Chemistry Variable		
Oxygen Content, [O]	0 to 8 ppm	Also interrelated to above variables. Low or near zero values of [O] are most representative of deep water or occluded regions, e.g., tight and/or deep cracks, crevices, or threaded connections. [O] content should be controlled during tests to simulate water depth and occluded nature of joints or connections.

TABLE 9.1 PRIMARY LOADING, ENVIRONMENTAL, AND MATERIALS VARIABLES AFFECTING CORROSION FATIGUE CRACK GROWTH RESISTANCE IN OFFSHORE STRUCTURES
 (continued)

<u>Variable</u>	<u>Applicable Range</u>	<u>Comment</u>
Electrode Potential, E	-0.6 to -1.2 V (vs Ag/AgCl)	Low negative values ($E = -0.6$ to -0.7) represent freely corroding conditions, while higher negative values represent cathodically "protected" or "overprotected" values which occur in service. Test plan should establish worst case potential depending on specific material-environment conditions.
Material Variables:		
Composition: Base metal Weld/HAZ	C-Mn/low alloy steel	Generally structural grades of C-Mn steels for existing structures; low alloy (higher strength) steels for new designs, e.g., tension-leg-platforms.
Strength Level	Yield Strength: 200-700 MPa	Typically C-Mn steels exhibit yield strengths of 200-400 MPa, while newer low alloy steels exhibit values of 550-700 MPa

APPENDIX A

GLOSSARY OF TERMS IN THE FIELDS OF CORROSION, FATIGUE, AND WELDING

Corrosion

active - the negative direction of electrode potential. (Also used to describe corrosion and its associated potential range when an electrode potential is more negative than an adjacent depressed corrosion rate [passive] range.)

anode - the electrode of an electrolytic cell at which oxidation is the principal reaction. (Electrons flow away from the anode in the external circuit. It is usually the electrode where corrosion occurs and metal ions enter solution.)

anodic polarization - the change of the electrode potential in the noble (positive) direction due to current flow. (See polarization.)

cathode - the electrode of an electrolytic cell at which reduction is the principal reaction. (Electrons flow toward the cathode in the external circuit.)

cathodic polarization - the change of the electrode potential in the active (negative) direction due to current flow. (See polarization.)

cathodic protection - a technique to reduce the corrosion rate of a metal surface by making it the cathode of an electrochemical cell.

concentration cell - an electrolytic cell, the emf of which is caused by a difference in concentration of some component in the electrolyte. (This difference leads to the formation of discrete cathode and anode regions.)

corrosion - the chemical or electrochemical reaction between a material, usually a metal, and its environment that produces a deterioration of the material and its properties.

corrosion fatigue - the process in which a metal fractures prematurely under conditions of simultaneous corrosion and repeated cyclic loading at lower stress levels or fewer cycles than would be required in the absence of the corrosive environment.

corrosion potential - the potential of a corroding surface in an electrolyte relative to a reference electrode measured under open-circuit conditions.

current density - the current flowing to or from a unit area of an electrode surface.

differential aeration cell (oxygen concentration cell) - a concentration cell caused by differences in oxygen concentration along the surface of a metal in an electrolyte. (See concentration cell.)

electrochemical cell - an electrochemical system consisting of an anode and a cathode in metallic contact and immersed in an electrolyte. (The anode and cathode may be different metals or dissimilar areas on the same metal surface.)

electrode potential - the potential of an electrode in an electrolyte as measured against a reference electrode. (The electrode potential does not include any resistance losses in potential in either the solution or external circuit. It represents the reversible work to move a unit charge from the electrode surface through the solution to the reference electrode.)

electromotive force series (EMF Series) - a list of elements arranged according to their standard electrode potentials, with "noble" metals such as gold being positive and "active" metals such as zinc being negative.

embrittlement - the severe loss of ductility or toughness or both, of a material, usually a metal or alloy.

erosion - the progressive loss of material from a solid surface due to mechanical interaction between that surface and a fluid, a multi-component fluid, or solid particles carried with the fluid.

erosion-corrosion - a conjoint action involving corrosion and erosion in the presence of a moving corrosive fluid, leading to the accelerated loss of material.

fretting corrosion - the deterioration at the interface between contacting surfaces as the result of corrosion and slight oscillatory slip between the two surfaces.

galvanic corrosion - accelerated corrosion of a metal because of an electrical contact with a more noble metal or nonmetallic conductor in a corrosive electrolyte.

galvanic couple - a pair of dissimilar conductors, commonly metals, in electrical contact. (See galvanic corrosion.)

hydrogen embrittlement - hydrogen-induced cracking or severe loss of ductility caused by the presence of hydrogen in the metal.

inhibitor - a chemical substance or combination of substances that, when present in the proper concentration and forms in the environment, prevents or reduces corrosion.

noble - the positive (increasingly oxidizing) direction of electrode potential.

open-circuit potential - the potential of an electrode measured with respect to a reference electrode or another electrode when no current flows to or from it.

oxidation - loss of electrons by a constituent of a chemical reaction. (Also refers to the corrosion of a metal that is exposed to an oxidizing gas at elevated temperatures.)

passivator - a type of inhibitor which appreciably changes the potential of a metal to a more noble (positive) value.

passive - the state of the metal surface characterized by low corrosion rates in a potential region that is strongly oxidizing for the metal.

pitting - corrosion of a metal surface, confined to a point or small area, that takes the form of cavities.

polarization - the change from the open-circuit electrode potential as the result of the passage of current.

potentiostat - an instrument for automatically maintaining an electrode in an electrolyte at a constant potential or controlled potentials with respect to a suitable reference electrode.

potentiostatic - the technique for maintaining a constant electrode potential.

reduction - the gain of electrons by a constituent of a chemical reaction.

rust - a corrosion product consisting primarily of hydrated iron oxide. (A term properly applied only to ferrous alloys.)

stress-corrosion cracking - a cracking process that requires the simultaneous action of a corrodent and sustained tensile stress. (This excludes corrosion-reduced sections which fail by fast fracture. It also excludes intercrystalline or transcrystalline corrosion which can disintegrate an alloy without either applied or residual stress.)

Fatigue

fatigue - the process of progressive localized permanent structural change occurring in a material subject to conditions which produce fluctuating stresses and strains at some point or points and which may culminate in cracks or complete fracture after a sufficient number of fluctuations.

fatigue life, N - the number of cycles of stress or strain of a specified character that a given specimen sustains before failure of a specified nature occurs.

stress cycle - the smallest segment of the stress-time function which is repeated periodically.

maximum stress, S_{max} - the stress having the highest algebraic value in the stress cycle, tensile stress being considered positive and compressive stress negative.

minimum stress, S_{min} - the stress having the lowest algebraic value in the cycle, tensile stress being considered positive and compressive stress negative.

mean stress (or steady component of stress), S_m - the algebraic average of the maximum and minimum stresses in one cycle, that is

$$S_m = (S_{max} + S_{min})/2$$

range of stress, S_r - the algebraic difference between the maximum and minimum stresses in one cycle, that is

$$S_r = S_{max} - S_{min}$$

stress amplitude (or variable component of stress), S_a - one half the range of stress, that is

$$S_a = S_r/2 = (S_{max} - S_{min})/2$$

stress ratio, R - The ratio of the minimum stress to the maximum stress, that is,

$$R = S_{min}/S_{max}$$

S-N diagram - a plot of stress against the number of cycles to failure.

fatigue strength at N cycles, S_N - a hypothetical value of stress for failure at exactly N cycles as determined from an S-N diagram. The value of S_N thus determined is subject to the same conditions as those which apply to the S-N diagram.

fatigue limit, S_l - the limiting value of the median fatigue strength as N becomes very large.

cycle ratio, C - the ratio of the number of stress cycles, n , of a specified character to the hypothetical fatigue life, N , obtained from the S-N diagram, for stress cycles of the same character, that is, $C = n/N$.

theoretical stress concentration factor (or stress concentration factor) K_t - the ratio of the greatest stress in the region of a notch or other stress concentrator as determined by the theory of elasticity (or by experimental procedures that give equivalent values) to the corresponding nominal stress.

fatigue notch factor, K_f - the ratio of the fatigue strength of a specimen with no stress concentration to the fatigue strength at the same number of cycles with stress concentration for the same conditions.

fatigue notch sensitivity, q - a measure of the degree of agreement between K_f and K_t . The definition of fatigue notch sensitivity is $q = (K_f - 1)/(K_t - 1)$.

Welding

as-welded - the condition of weld metal, welded joints, and weldments after welding prior to any subsequent thermal, mechanical, or chemical treatments.

backing - material (metal, weld metal, carbon, or granular) placed at the root of a weld joint for the purpose of supporting molten weld metal.

base metal - the metal to be welded, soldered, or cut.

brace intersection angle, (tubular structures) - the acute angle formed between brace center lines.

butt joint - a joint between two members aligned approximately in the same plane.

butt weld - a weld in a butt joint.

complete fusion - fusion which has occurred over the entire base metal surfaces exposed for welding and between all layers and passes.

complete joint penetration - joint penetration in which the weld metal completely fills the groove and is fused to the base metal throughout its total thickness.

complete joint penetration groove weld (tubular structures) - a groove weld having complete penetration and fusion of weld and base metal throughout the depth of the joint.

crater - in arc welding, a depression at the termination of a weld bead or in the molten weld pool.

defect - a discontinuity or discontinuities which by nature or accumulated effect render a part or product unable to meet minimum applicable acceptance standards or specifications.

discontinuity - an interruption of the typical structure of a weldment such as a lack of homogeneity in the mechanical or metallurgical or physical characteristics of the material or weldment. A discontinuity is not necessarily a defect.

edge angle, w (tubular structures) - the acute angle between a bevel edge made in preparation for welding and a tangent to the member surface, measured locally in a plane perpendicular to the intersection line. All bevels open to outside of brace.

filler metal - the metal to be added in making a welded, brazed, or soldered joint.

flash - the material which is expelled or squeezed out of a weld joint and which forms around the weld.

flux cored arc welding (FCAW) - an arc welding process which produces coalescence of metals by heating them with an arc between a continuous filler metal (consumable) electrode and the work. Shielding is provided by a flux contained within the electrode. Additional shielding may or may not be obtained from an externally supplied gas or gas mixture.

fusion - the melting together of filler metal and base metal, or the melting of base metal only, which results in coalescence.

fusion-type discontinuity - signifies slag inclusion, incomplete fusion, incomplete joint penetration, and similar discontinuities associated with fusion.

fusion zone - the area of base metal melted as determined on the cross-section of a weld.

gas metal arc welding (GMAW) - an arc welding process which produces coalescence of metals by heating them with an arc between a continuous filler metal (consumable) electrode and the work. Shielding is obtained entirely from an externally supplied gas or gas mixture. Some methods of this process are called MIG or CO₂ welding.

gas pocket - a cavity caused by entrapped gas.

groove angle, (tubular structures) - the angle between opposing faces of the groove to be filled with weld metal, determined after the joint is fitted up.

heat-affected zone - that portion of the base metal which has not been melted, but whose mechanical properties or microstructure have been altered by the heat of welding, brazing, soldering, or cutting.

hot-spot strain (tubular structures) - the cyclic total range of strain which would be measured at the point of highest stress concentration in a welded connection. When measuring hot-spot strain, the strain gage should be sufficiently small to avoid averaging high and low strains in the regions of steep gradients.

interpass temperature - in a multiple-pass weld, the temperature (minimum or maximum as specified) of the deposited weld before the next pass is started.

joint - the location of members or the edges of members which are to be joined or have been joined.

joint penetration - the minimum depth a groove or flange weld extends from its face into a joint, exclusive of reinforcement.

lap joint - a joint between two overlapping members.

leg of a fillet weld - the distance from the root of the joint to the toe of the fillet weld.

local dihedral angle, ψ (tubular structures) - the angle, measured in a plane perpendicular to the line of the weld, between tangents to the outside surfaces of the tubes being joined at the weld. The exterior dihedral angle, where one looks at a localized section of the connection, such that the intersecting surfaces may be treated as planes.

manual welding - a welding operation performed and controlled completely by hand.

partial joint penetration - joint penetration which is less than complete.

pass - a single longitudinal progression of a welding operation along a joint or weld deposit. The result of a pass is a weld bead or layer.

peening - the mechanical working of metals using impact blows.

piping porosity (general) - elongated porosity whose major dimension lies in a direction approximately normal to the weld surface. Frequently referred to as "pin holes" when the porosity extends to the weld surface.

porosity - cavity-type discontinuities formed by gas entrapment during solidification.

postweld heat treatment - any heat treatment subsequent to welding.

preheating - the application of heat to the base metal immediately before welding, brazing, soldering, or cutting.

preheat temperature - a specified temperature that the base metal must attain in the welding, brazing, soldering, or cutting area immediately before these operations are performed.

root face - that portion of the groove face adjacent to the root of the joint.

root of joint - that portion of a joint to be welded where the members approach closest to each other. In cross section, the root of the joint may be either a point, a line, or an area.

root of weld - the points, as shown in cross-section, at which the back of the weld intersects the base metal surfaces.

root opening - the separation, at the root of the joint, between the members to be joined.

shielded metal arc welding (SMAW) - an arc welding process which produces coalescence of metals by heating with an arc between a covered metal electrode and the work. Shielding is obtained from decomposition of the electrode covering. Pressure is not used and filler metal is obtained from the electrode.

submerged arc welding (SAW) - an arc welding process which produces coalescence of metals by heating with an arc or arcs between a bare metal electrode or electrodes and the work. The arc is shielded by a blanket of granular, fusible material on the work. Pressure is not used, and filler metal is obtained from the electrode and sometimes from a supplementary welding rod.

single electrode - one electrode connected exclusively to one power source which may consist of one or more power units.

parallel electrode - two electrodes connected electrically in parallel and exclusively to the same power source. Both electrodes are usually fed by means of a single electrode feeder. Welding current, when specified, is the total for the two electrodes.

tack weld - a weld made to hold parts of a weldment in proper alignment until the final welds are made.

throat of a fillet weld -

theoretical throat - the distance from the beginning of the root of the joint perpendicular to the hypotenuse of the largest right triangle that can be inscribed within the fillet weld cross section.

actual throat - the shortest distance from the root of a fillet weld to its face.

T-joint - a joint between two members located approximately at right angles to each other in the form of a T.

toe of weld - the junction between the face of a weld and the base metal.

tubular connection - a connection in the portion of a tubular structure which contains two or more intersecting tubular members.

tubular joint - a joint in the interface created by one tubular member intersecting another.

undercut - a groove melted into the base metal adjacent to the toe or root of a weld and left unfilled by weld metal.

weld - a localized coalescence of metals produced either by heating to suitable temperatures, with or without the application of pressure or by the application of pressure alone, and with or without the use of filler metal.

weldability - the capacity of a metal to be welded under the fabrication conditions imposed into a specific, suitably designed structure and to perform satisfactorily in the intended service.

weld bead - a weld deposit resulting from a pass.

welding - a metal joining process used in making welds.

welding sequence - the order of making the welds in a weldment.

weldment - an assembly whose component parts are joined by welding.

APPENDIX B

ECSC OFFSHORE TUBULAR JOINT TEST
DATA SHEET

OFFSHORE TUBULAR JOINT TEST DATA SHEET

ECSC Pg. F7

Type	
Loading	
Laboratory	
Specimen nr.	

GEOMETRY actual values in mm	outside diameter	wall thickness	Post weld stress relief H.T. Yes No
	D	T	
	d ₁	t ₁	
	d ₂	t ₂	

ACTUAL PROPERTIES OF CRACKED MEMBER

BASE METAL	Grade :						STD :					
	C %	Si %	Mn %	S %	P %	Al %						

WELD BEAD GEOMETRY AT THE HOT SPOT applied STD : AWS - API - ...	WELDING PROCEDURE																							
	Position																							
	Nr of runs																							
	Energy (kj/m)																							
	preheat. temp. (° C)																							
	postheat. temp. (° C)																							
POST WELDING TREATMENT																								
Heat treatment - tig or plasma dressing																								
Shoot peening - grinding																								

WELD METAL DEPOSIT	C %	Si %	Mn %	S %	P %	Ni %						

TENSILE PROPERTIES	Base metal	weld metal
Yield strength σ_y (N/mm ²)		
Tensile strength σ_u (N/mm ²)		

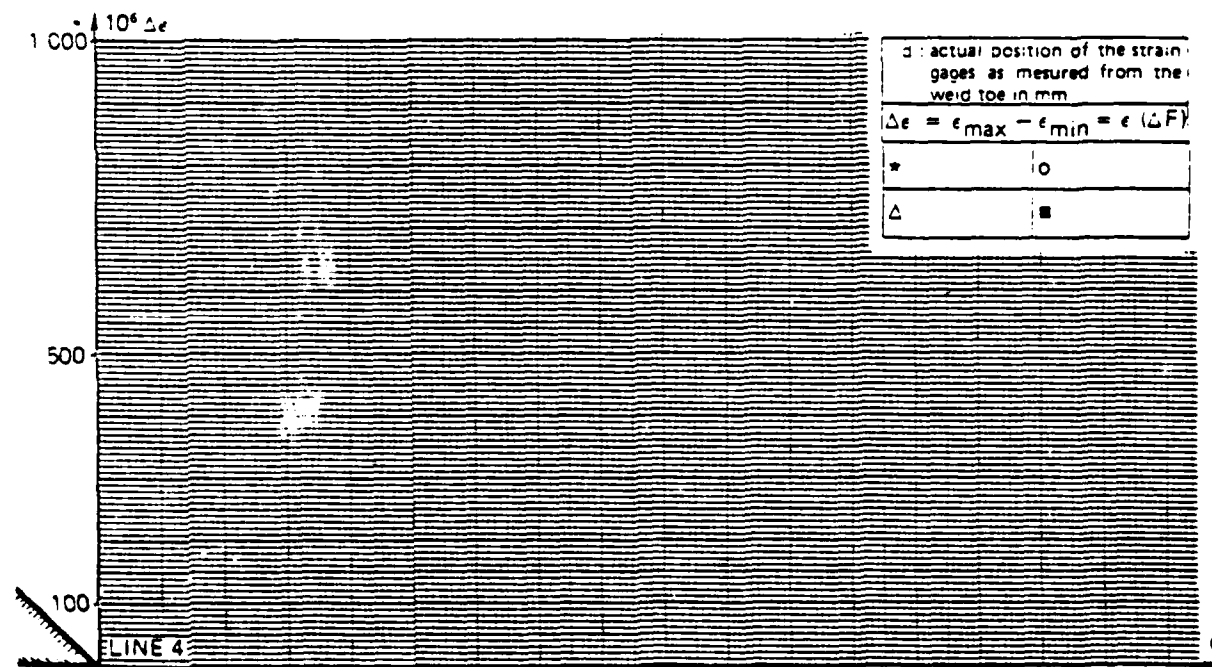
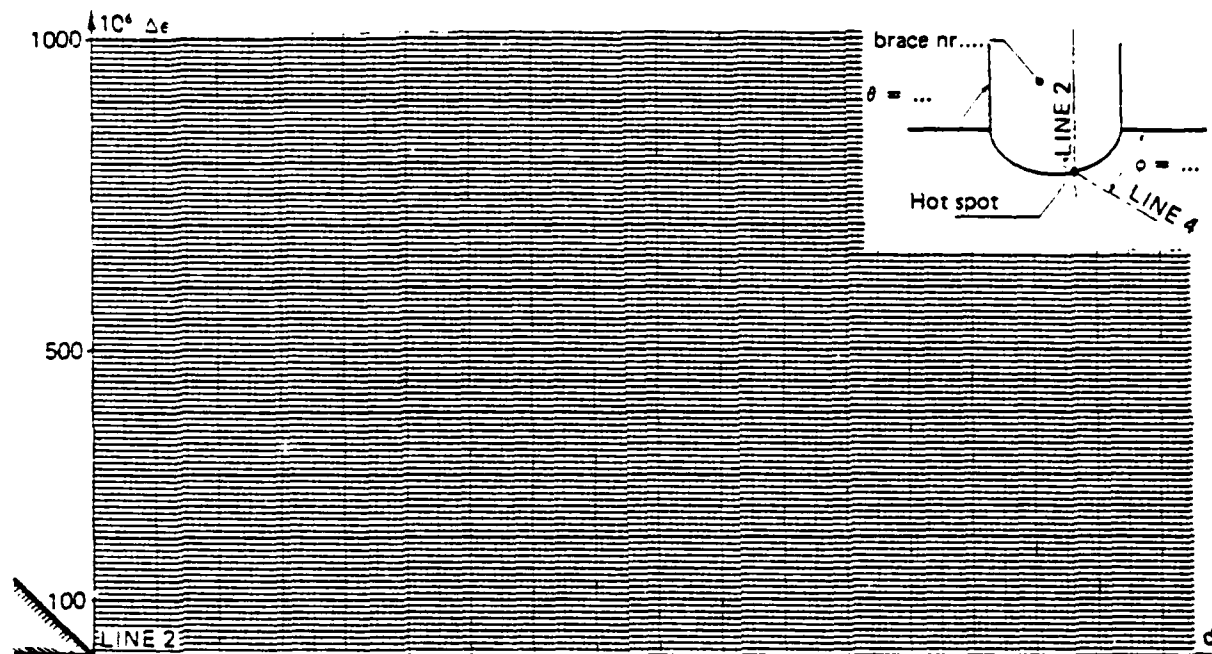
Other properties
see page 4

MEASUREMENTS BEFORE FATIGUE TESTING

Number of cycles before measurements : ...

cycles

F_{\min} (kN)	F_{\max} (kN)	R_S	T (°C)	Frequencies (Hz)	Actuator displacement for ΔF (mm)

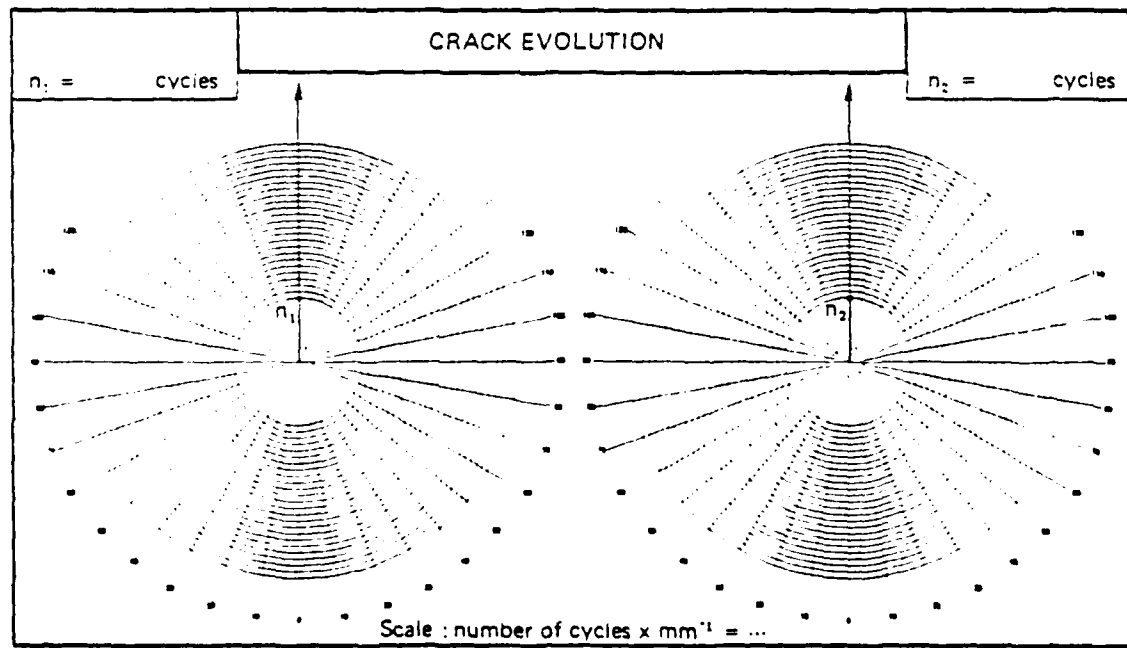
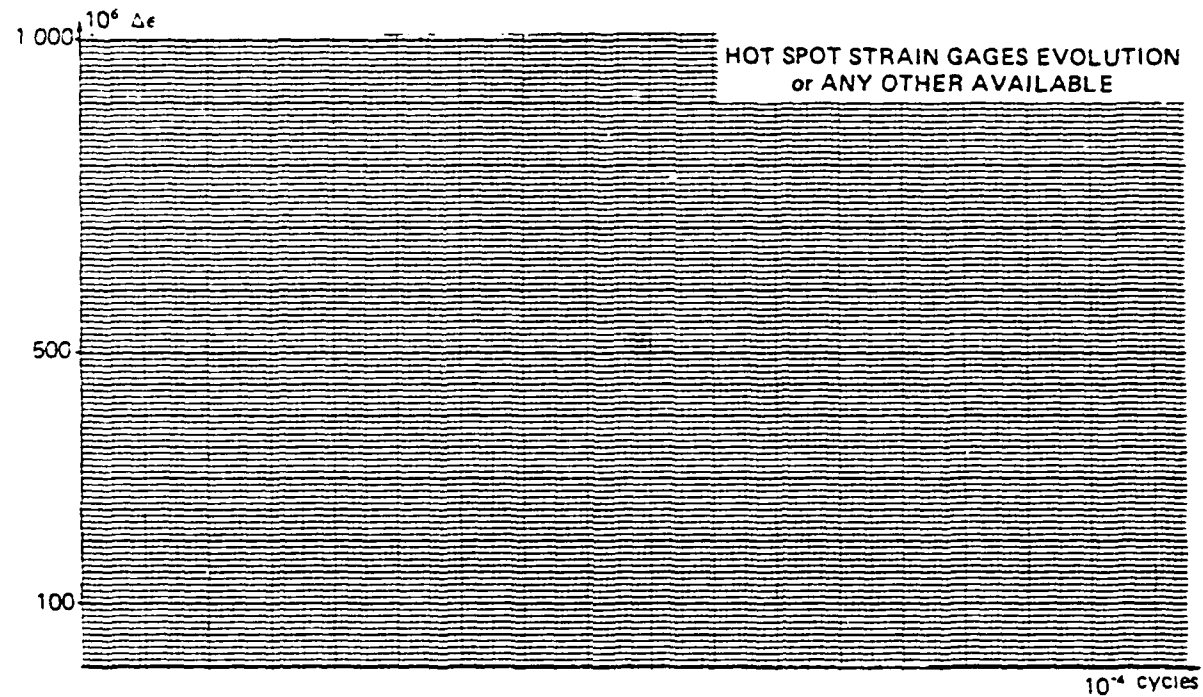


MEASUREMENTS DURING FATIGUE TESTING

FATIGUE TESTING CONDITIONS : in air/in sea water – with/without protection.

FAILURE CRITERION	$\Delta\epsilon = 15\%$	Visual crack ~ 30 mm	Through crack	End of the test (1)	Static residual strength (kN)
Number of cycles					

A : complete failure
 B : actuator displacement = ... mm
 C : secondary cracking total length = ... mm
 D : other reason : ...



OTHER RELEVANT INFORMATIONS

CFS Part 2 80-K78

APPENDIX C

FIRST-ORDER, SECOND-MOMENT EXAMPLE CALCULATION

The first-order second-moment method is developed in this appendix for the function

$$Y(a_0, r) = 1.12 [1 + Z_2], \quad (C-1)$$

$$\text{where } Z_2 = a\sqrt{t} e^{Z_1 - X_2/2}, \quad (C-2)$$

$$Z_1 = -35 a\sqrt{t}/t e^{X_1 - X_2/2} \quad (C-3)$$

$$X_1 = \ln a_0 \quad (C-4)$$

$$X_2 = \ln r \quad (C-5)$$

Equations (C-1) through (C-5) correspond to equations (8.13) and (8.14) in the text. It is given that

$$\mu_{X_1} = -8.3818 \quad (C-6)$$

$$\sigma_{X_1}^2 = 0.127 \quad (C-7)$$

$$\mu_{X_2} = -6.215 \quad (C-8)$$

$$\sigma_{X_2}^2 = 0.632 \quad (C-9)$$

Define

$$y = \ln Y. \quad (C-10)$$

Then (C-1) becomes

$$y(X_1, X_2) = \ln 1.12 + \ln (1 + Z_2) \quad (C-11)$$

with Z_2 defined by (C-2) through (C-5). The objective is to obtain μ_y and σ_y^2 by the first-order second moment method and show that the first order Taylor series employed in this approach is accurate.

The Taylor series approximation of y is given by

$$y(X_1, X_2) \approx y(\mu_{X_1}, \mu_{X_2}) + \frac{\partial y}{\partial X_1} \Big|_{\mu_{X_1}, \mu_{X_2}} (X_1 - \mu_{X_1}) + \frac{\partial y}{\partial X_2} \Big|_{\mu_{X_1}, \mu_{X_2}} (X_2 - \mu_{X_2}) \quad (C-12)$$

When equation (C-11) is evaluated with $t = 0.0254$ m and $a = 0.19$ with $X_1 = -8.3818$ and $X_2 = -6.215$ from equations (C-6) and (C-8), respectively, then

$$y(\mu_{X_1}, \mu_{X_2}) = 0.5496 \quad (C-13)$$

is obtained. The partial derivative of y with respect to X_1 follows from equations (C-2), (C-3), and (C-11). The expression is

$$\frac{\partial y}{\partial X_1} = Z_1 Z_2 / (1 + Z_2) \quad (C-14)$$

and evaluated at the means given by (C-6) and (C-8) results in

$$\left. \frac{\partial y}{\partial X_1} \right|_{\mu_{X_1}, \mu_{X_2}} = -0.07556 \quad (C-15)$$

The derivative of y with respect to X_2 also follows from (C-2), (C-3), and (C-11). The expression is

$$\frac{\partial y}{\partial X_2} = -0.5 (1 + Z_1) Z_2 / (1 + Z_2), \quad (C-16)$$

and evaluated at the means results in

$$\left. \frac{\partial y}{\partial X_2} \right|_{\mu_{X_1}, \mu_{X_2}} = -0.1390 \quad (C-17)$$

Upon substituting (C-17), (C-15), and (C-13) in (C-12) the approximate expression for y is obtained,

$$y(X_1, X_2) = 0.5496 - 0.07556 (X_1 + 8.3818) - 0.1390 (X_2 + 6.215) \quad (C-18)$$

The approximate expression for y , $\ln Y$, from equation (C-18) is compared in Figure C.1 with the exact expression for y , $\ln Y$, from equation (C-11) at the mean value of X_1 , as an example. The figure shows that the approximation is adequate over the range of X_2 specified by a distribution of X_2 with mean and variance given by (C-8) and (C-9).

The expression for the variance of y follows from equation (C-18). It is

$$\sigma_y^2 = (0.7556)^2 \sigma_{X_1}^2 + (.1390)^2 \sigma_{X_2}^2 \quad (C-19)$$

and when evaluated with (C-7) and (C-9) is

$$\sigma_{\ln Y}^2 = 0.013 \quad (C-20)$$

The expression for the mean of y follows from (C-18) also. It is

$$\mu_{\ln Y} = 0.5496 \quad (C-21)$$

completing the objective of this appendix.

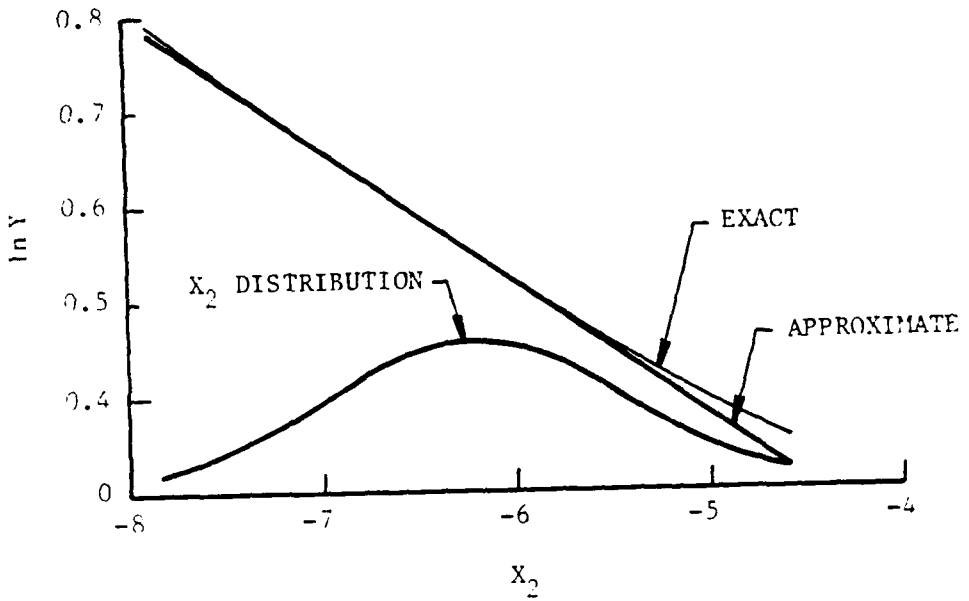


FIGURE C.1. APPROXIMATE AND EXACT EXPRESSIONS
FOR $y(u_{X_1}, X_2)$

APPENDIX D

THREE-COMPONENT HIGH-CYCLE MODEL PARTIAL DERIVATIVES

In this appendix the partial derivatives are presented for the logarithmically transformed cycles for crack propagation. The notation corresponds precisely to that used in Section 8.4 of the text.

$$N = \frac{A_1}{(1.12S\sqrt{\pi})^{n_1}} Q_1 + \frac{A_2}{(1.12S\sqrt{\pi})^{n_2}} Q_2 - \frac{A_2(t - a_o)}{[(1-R)K_c]^{n_2}} \quad (D-1)$$

$$Q_1 = e^{n_1 H_0} [n_1 H_1 + 1]^{-1} [a_1^{n_1 H_1 + 1} - a_o^{n_1 H_1 + 1}] \\ + [\frac{n_1}{2} - 1]^{-1} [a_1^{-(\frac{n_1}{2} - 1)} - t^{-(\frac{n_1}{2} - 1)}] \quad (D-2)$$

$$Q_2 = e^{n_2 H_0} [n_2 H_1 + 1]^{-1} [a_1^{n_2 H_1 + 1} - a_o^{n_2 H_1 + 1}] \\ + [\frac{n_2}{2} - 1]^{-1} [a_1^{-(\frac{n_2}{2} - 1)} - t^{-(\frac{n_2}{2} - 1)}] \quad (D-3)$$

$$\frac{\partial \ln N}{\partial \ln X_i} = \frac{1}{N} \frac{\partial N}{\partial \ln X_i}, \quad X_i = A_1, A_2, a_o, K_t^{-1}. \quad (D-4)$$

$$\frac{\partial N}{\partial \ln A_1} = \frac{A_1}{(1.12S\sqrt{\pi})^{n_1}} Q_1, \quad (D-5)$$

$$\frac{\partial N}{\partial \ln A_2} = \frac{A_2}{(1.12S\sqrt{\pi})^{n_2}} Q_2 - \frac{A_2(t - a_o)}{[(1-R)K_c]^{n_2}}, \quad (D-6)$$

$$\frac{\partial N}{\partial \ln a_0} = \frac{-A_1}{(1.12S\sqrt{\pi})^{n_1}} e^{n_1 H_0} a_0^{n_1 H_1 + 1} + \frac{-A_2}{(1.12S\sqrt{\pi})^{n_2}} e^{n_2 H_0} a_0^{n_2 H_1 + 1} \\ (D-7)$$

$$+ \frac{A_2 a_0}{[(1-R)K_c]^{n_2}},$$

$$\frac{\partial N}{\partial \ln(K_t^{-1})} = \frac{A_1}{(1.12S\sqrt{\pi})^{n_1}} \frac{\partial Q_1}{\partial \ln(K_t^{-1})} + \frac{A_2}{(1.12S\sqrt{\pi})^{n_2}} \frac{\partial Q_2}{\partial \ln(K_t^{-1})}. \quad (D-8)$$

$$\text{Define } x = \ln(K_t^{-1}). \quad (D-9)$$

$$\frac{\partial Q_1}{\partial x} = \frac{n_1}{n_1 H_1 + 1} e^{n_1 H_0} [a_1^{n_1 H_1 + 1} - a_0^{n_1 H_1 + 1}] [\frac{\partial H_0}{\partial x} - \frac{1}{n_1 H_1 + 1} \frac{\partial H_1}{\partial \ln x}] \\ (D-10)$$

$$+ \frac{e^{n_1 H_0}}{n_1 H_1 + 1} [(n_1 H_1 + 1) a_1^{n_1 H_1} \frac{\partial a_1}{\partial x} + (\ln a_1) a_1^{n_1 H_1 + 1} n_1 \frac{\partial H_1}{\partial x} \\ - a_0^{n_1 H_1 + 1} (\ln a_0) n_1 \frac{\partial H_1}{\partial x}] - a_1^{-\frac{n_1}{2}} \frac{\partial a_1}{\partial x},$$

$$\frac{\partial Q_2}{\partial x} = \frac{n_2}{n_2 H_1 + 1} e^{n_2 H_0} [a_1^{n_2 H_1 + 1} - a_0^{n_2 H_1 + 1}] [\frac{\partial H_0}{\partial x} - \frac{1}{n_2 H_1 + 1} \frac{\partial H_1}{\partial x}] \\ (D-11)$$

$$+ \frac{e^{n_2 H_0}}{n_2 H_1 + 1} [(n_2 H_1 + 1) a_1^{n_2 H_1} \frac{\partial a_1}{\partial x} + (\ln a_1) a_1^{n_2 H_1 + 1} n_2 \frac{\partial H_1}{\partial x} \\ - a_0^{n_2 H_1 + 1} (\ln a_0) n_2 \frac{\partial H_1}{\partial x}] - a_1^{-\frac{n_2}{2}} \frac{\partial a_1}{\partial x},$$

$$\frac{\partial H_0}{\partial x} = \frac{1}{h_1} \frac{\partial h_1}{\partial x} - \frac{H_1}{a_1} \frac{\partial a_1}{\partial x} - (\ln a_1) \frac{\partial H_1}{\partial x}, \quad (D-12)$$

$$\frac{\partial H_1}{\partial x} = \frac{1}{\ln(a_1/a_d)} [\frac{1}{h_1} \frac{\partial h_1}{\partial x} - \frac{1}{h_d} \frac{\partial h_d}{\partial x} - \frac{H_1}{a_1} \frac{\partial a_1}{\partial x} + \frac{H_1}{a_d} \frac{\partial a_d}{\partial x}], \quad (D-13)$$

$$\frac{\partial h_1}{\partial x} = - \frac{1}{2} a_1^{-1.5} \frac{\partial a_1}{\partial x}, \quad (D-14)$$

$$\frac{\partial h_d}{\partial x} = \frac{-h_d(K_t-1)a_d}{\frac{-35(K_t-1)a_d}{[1 + (K_t-1)e^{-t}]}} [1 - \frac{35(K_t-1)}{t} (a_d + \frac{\partial a_d}{\partial x})] - \frac{h_d}{2a_d} \frac{\partial a_d}{\partial x}, \quad (D-15)$$

$$\frac{\partial a_1}{\partial x} = \frac{t}{35(K_t-1)} [1 - \ln(\frac{e^{\Delta}-1}{e^{\Delta}-1})], \quad (D-16)$$

$$\frac{\partial a_d}{\partial x} = a_d [(\frac{1}{1.77} - 1) (\frac{K_t-1}{14.7})^{\frac{1}{1.77}} - 1]. \quad (D-17)$$

Committee on Marine Structures
Marine Board
National Academy of Sciences - National Research Council

The Committee on Marine Structures provides technical advice to the Interagency Ship Structure Committee's research program.

Mr. A.D. Haff, Chairman, Annapolis, MD
Prof. A.H.-S. Ang, University of Illinois, Champaign, IL
Mr. G.C. Lee, Griff C. Lee, Inc., New Orleans, LA
Mrs. M. Ochi, Gainesville, FL
Prof. D.L. Olson, Colorado School of Mines, Golden, CO
Mr. P.W. Marshall, Shell Oil Company, Houston, TX

MATERIALS ADVISORY GROUP

Prof. D.L. Olson, Colorado School of Mines, Golden, CO
Mrs. N.C. Cole, Combustion Engineering, Inc., Chattanooga, TN
Prof. G.T. Bahn, Vanderbilt University, Nashville, TN
Prof. W.H. Hart, Florida Atlantic University, Boca Raton, FL
Dr. S. Ibarra, Gulf Science & Technology Co., Pittsburgh, PA
Mr. J.J. Schmidt, Lukens, Inc., Coatesville, PA
Mr. R.E. Somers, Welding Consultant, Bellfonte, PA
Dr. N. Zettlemoyer, Exxon Production Research Co., Houston, TX

PROJECT ADVISORS

Mr. P.W. Marshall, Shell Oil Company, Houston, TX
Prof. P. Wirsching, University of Arizona, Tucson, AZ
Dr. R.D. Glasfeld, General Dynamics Quincy Shipbuilding, Quincy, MA

SHIP STRUCTURE COMMITTEE PUBLICATIONS

- SSC-316 Ship Structure Committee Long-Range Research Plan: Guidelines for Program Development by E.M. MacCutcheon, O.H. Oakley and R.D. Stout, 1983, AD-A140275
- SSC-317 Determinations of Strain Rates in Ship Hull Structures: A Feasibility Study by J. G. Giannotti and K. A. Stambaugh, 1984
- SSC-318 Fatigue Characterization of Fabricated Ship Details for Design by W. H. Munse, T. W. Wilbur, M. L. Tellalian, K. Nicoll and K. Wilson, 1983, AD-A140338
- SSC-319 Development of A Plan to Obtain In-Service Still-Water Bending Moment Information for Statistical Characterization by J. W. Boylston and K. A. Stambaugh, 1984
- SSC-320 A Study of Extreme Waves and Their Effects on Ship Structures by W. H. Buckley, 1983, AD-A140317
- SSC-321 Survey of Experience Using Reinforced Concrete in Floating Marine Structures by O.H. Burnside and D.J. Pomeroy, 1984
- SSC-322 Analysis and Assessment of Major Uncertainties Associated With Ship Hull Ultimate Failure by F. Kaplan, M. Seneta, J. Bentson and T.A. Achteridis, 1984
- SSC-323 Updating of Fillet Weld Strength Parameters for Commercial Shipbuilding by R.P. Krumpen, Jr., and C.G. McRae, 1984
- SSC-324 Analytical Techniques for Predicting Corrosion Fatigue Life by J.D. Porricelli and J.N. Boyd, 1984
- SSC-325 Correlation of Theoretical and Measured Mechanical Properties for the S4-7 Grade Ship and the S4-14 Grade Hull Casting by S. J. Omtz by E.H. Chen, Y.S. Chin & J.B. Aulick, 1984
- SSC-326 Long-Term Corrosion Behavior of Welded Marine Steels by O.H. Burnside, S.J. Omtz, E. Oelkers, E. Chen, and R.J. Mackie, 1984
- None Ship Structure Committee Publications - A Special Bibliography AD-A140339

END

FILMED

1-86

DTIC